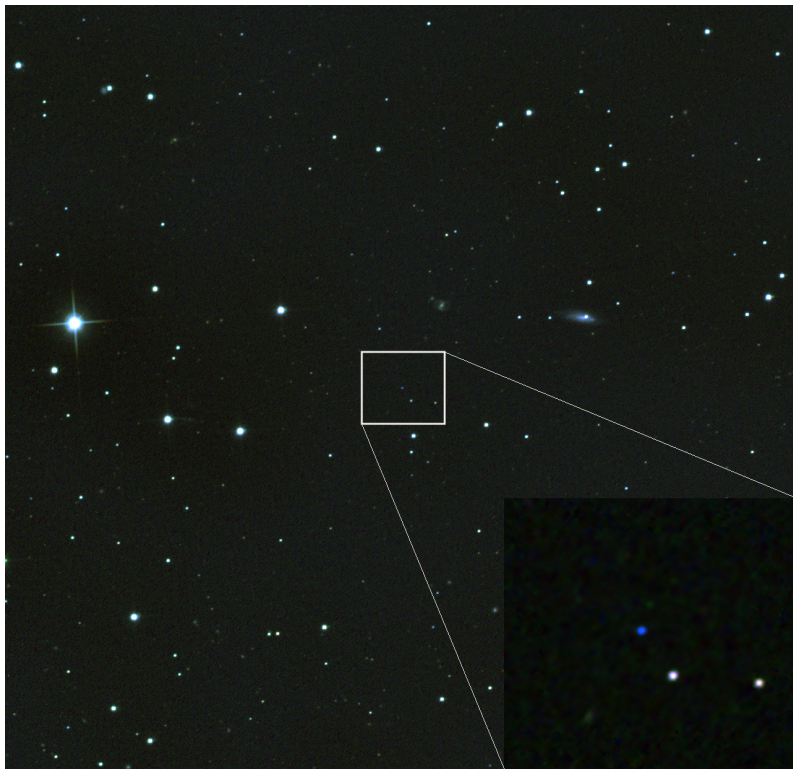

Evolutionary fingerprints on the chemical composition of He-sdO stars

Quantitative optical and UV NLTE spectral
analysis of twelve He-sdO stars

- first revised version -



Der Naturwissenschaftlichen Fakultät
der Friedrich-Alexander-Universität
Erlangen-Nürnberg

zur

Erlangung des Doktorgrades Dr. rer. nat

vorgelegt von

Markus Schindewolf
aus Bamberg

Als Dissertation genehmigt
von der Naturwissenschaftlichen Fakultät
der Friedrich-Alexander-Universität Erlangen-Nürnberg.

Tag der mündlichen Prüfung: 27.06.2018

Vorsitzende/r des Promotionsorgans: Prof. Dr. Georg Kreimer
Gutachter: Prof. Dr. Ulrich Heber
Prof. Dr. Stefan Dreizler

überarbeitete Fassung vom 16.07.2018

The image on the titelpage shows the Hypervelocity He-sdO US708. The image was taken at the Dr. Karl Remeis Observatory Bamberg with the Ernst-Hartwig-Telescope (EHT) by the author using a L-RGB filterset.

Das Bild auf der Titelseite zeigt den Hypervelocity He-sdO US708. Es wurde vom Autor an der Dr. Karl Remeis Sternwarte Bamberg mit dem Ernst Hartwig Teleskop und einem L-RGB Filtersatz aufgenommen.

Abstract

Helium rich hot subdwarf O stars (He-sdO stars) are known to exist in three flavors, depending on the enrichment of carbon and/or nitrogen in their atmospheres. It is believed that the chemical composition can be seen as a direct link to their evolutionary history. To examine on this link, a sample of twelve He-sdO stars was analyzed. To model the stellar atmosphere as accurately as possible, all available elements were included in NLTE conditions. Despite hydrogen and helium, the atmospheres contained carbon, nitrogen, oxygen, neon, magnesium, aluminum, silicon, phosphorus, sulfur, iron and nickel.

In a first step, the atmospheric parameters of each star were measured. To do so, different grids of model atmospheres with a different metal content were calculated and extensively tested and compared to previous analyses. It turned out that a pure hydrogen/helium grid is not a good choice for atmospheric examinations of He-sdO stars as the changes in temperature stratification are tremendous when compared to a fully blanketed model. However, these differences could not be reproduced to the same extend when fitting line profiles. In this work, a HHeCNO grid was mainly used. This grid offers the best compromise between computational effort and accuracy of stratification reproduction and only shows minor temperature differences compared to a fully blanketed model.

To determine the abundances of all elements included in the atmosphere, archival optical and UV spectra were used and a global fit of individual lines was applied to one element after the other iteratively. To get a first idea of the abundances, models without iron and nickel were computed using opacity distribution functions and applying them to optical data. After including iron and nickel in the opacity sampling mode, all elements were re-fitted using optical and UV data. Afterwards, photometric measurements were compared with the spectral energy distribution resulting from the calculated atmosphere to check for discrepancies and get an idea of the distance and the reddening assuming the canonical mass for He-sdOs of $0.47 M_{\odot}$. It turned out that there are basically two groups of He-sdO stars in the sample, those enriched in nitrogen and those enriched in carbon and nitrogen. The carbon-rich stars were found to belong to the same class as the carbon/nitrogen rich ones, at least for the stars in this sample. For the nitrogen-rich subsample, the slow merger of two He-core White Dwarfs seems the most plausible scenario as it reproduces the observed abundance pattern best. A cutback is that none of the N-rich stars shows any significant rotation as it would be expected from a merger scenario. The deep-mixing hot flasher scenario succeeds in explaining the CN-rich stars of the sample. Small deviations between model and measurements for certain elements can be explained by deficiencies in the modeling process of the stellar evolution. As some of the CN-rich stars show significant rotation it was tested if they can be explained by the composite merger scenario, but no matches were found.

A cooperation with ASTROSERVER.ORG was initialized to analyze the fasted star known so far, the He-sdO US708. This was necessary as the available UV COS spectra were of too poor quality to apply the usual fitting method to the data. In the Astroserver approach all available spectra are fitted together and all included elements are varied at the same time in each iteration step. Of special interest were the iron and nickel contents of the stellar atmosphere as they allow to draw

direct conclusion on how US708 was accelerated to such a high speed. The common theory claims the ejection by a double detonation of a C/O White Dwarf in a supernova Type Ia. The supernova ejecta would hit US708 and could be seen in its atmosphere. Indeed, a significant enrichment of iron and nickel, trace elements for a SN Ia, was found compared to a He-sdO from the same N-rich class and with similar atmospheric parameters. This would be in principle a direct evidence for the supernova ejection theory, as well as the high rotational velocity. But as an ejection from the Galactic disk would require too extreme masses, not in accordance with evolutionary tracks for this type of star, an alternative scenario in which US708 is in fact a pre-He WD ejected from a very close binary system in the Galactic Halo by a supernova Ia, is proposed.

Zusammenfassung

Es wird angenommen, dass sich Helium reiche heiße Unterzwerge des Spektraltypes O (He-sdOs) in drei Klassen einteilen lassen, je nachdem wie viel Kohlenstoff und oder/Stickstoff sich in ihren Atmosphären findet. Wahrscheinlich lässt sich die chemische Zusammensetzung direkt mit ihrer Entstehungsgeschichte verknüpfen. Um diese Verbindung zu untersuchen wurden zwölf He-sdOs analysiert. Um ihre Atmosphären so gut wie möglich zu modellieren wurde alle Elemente (H, He, C, N, O, Ne, Mg, Al, Si, P, S, Fe, Ni) unter NLTE Bedingungen eingebaut.

Als erstes wurden die atmosphärischen Parameter der Sterne bestimmt. Hierzu wurden Modellgitter von Atmosphären mit einer unterschiedlichen Metallhäufigkeit erstellt und ausgiebig getestet indem ihre Resultate mit früheren Analysen der selben Sterne verglichen wurde. Es zeigte sich dass ein reines H/He Gitter unzureichend ist da die Temperaturschichtung der Sternatmosphäre, im Vergleich zu einer solchen mit allen oben genannten Elementen, nicht exakt genug reproduziert werden kann. Beim Fitten einzelner Linien zeigte sich dass die Unterschiede bezüglich der effektiven Temperatur kleiner sind als es die Temperaturschichtung vermuten lässt. In dieser Arbeit wurde Großteils ein HHeCNO Gitter verwendet, welches einen guten Kompromiss zwischen Genauigkeit und Rechenaufwand bietet und nur geringe Abweichungen der effektiven Temperatur im Vergleich zu einem Modell mit allen verfügbaren Elementen aufweist.

Um die Metallhäufigkeiten zu bestimmen wurden optische und UV Spektren aus verschiedenen Archiven benutzt und mit einem globalen Fit individueller Linien für jedes einzelne Element untersucht. In einem ersten Schritt wurden Modelle ohne Eisen und Nickel auf optische Daten angewendet um einen ersten Eindruck der Häufigkeiten zu bekommen. Nach dem Hinzufügen von Eisen und Nickel wurden alle Elementhäufigkeiten erneut gefittet, dieses Mal unter Berücksichtigung optischer sowie UV Daten. Danach wurden photometrische Messungen mit einer aus den Berechnungen resultierenden spektralen Energieverteilung verglichen um etwaige Diskrepanzen zu entdecken und um einen Eindruck für die vorhandene Rötung und die Entfernung zu bekommen.

Entgegen der Annahme wurden in der untersuchten Probe nur Stickstoff- und Kohlenstoff/Stickstoffreiche Sterne gefunden, keine mit alleiniger Kohlenstoffanreicherung. Für die stickstoffreichen Sterne erscheint die langsame Verschmelzung zwei weißer Zwerge mit Heliumkern das wahrscheinlichste Entstehungsszenario zu sein, da es die gemessenen Häufigkeiten richtig vorhersagt. Allerdings zeigt keiner dieser Sterne eine signifikante Rotation wie man sie nach der Verschmelzung zweier Sterne erwarten würde. Für die CN-reichen Sterne scheint das „deep-mixing hot flasher“ Szenario die beste Lösung zu sein. Kleinere Abweichungen zwischen Modell und Beobachtung lassen sich durch Unzulänglichkeiten der Modellierung erklären. Da einige der Sterne rotieren wurde getestet ob eine Kombination aus langsamer und schneller Verschmelzung zweier He-WDs eine passende Erklärung liegen könnte, was aber nicht der Fall war.

Um den schnellsten bisher bekannten He-sdO, US708, zu analysieren wurde eine Kooperation mit ASTROSERVER.ORG gestartet, da die vorhandenen COS UV Spektren von zu schlechter Qualität waren um sie mit der sonst angewandten Methode zu analysieren. Das Astroserver Programm kann alle verfügbaren Elemente gleichzeitig

unter Berücksichtigung aller Spektren, sowohl optischer als auch UV Natur, fitten. Von besonderem Interesse waren die Häufigkeiten von Eisen und Nickel da sich mit ihrer Hilfe direkt Rückschlüsse auf den Beschleunigungsmechanismus von US708 ziehen lassen. Die gängige Theorie beschreibt die Beschleunigung als das Ergebnis einer „double detonation“ Supernova Ia, deren Ausstoß US708 trifft und in dessen Atmosphäre nachzuweisen wären. In der Tat wurde eine signifikante Anreicherung von Eisen und Nickel im Vergleich zu einem anderen stickstoffreichen He-sdO mit ähnlichen atmosphärischen Parametern gefunden. Dies bedeutet, in Kombination mit der hohen Rotationsgeschwindigkeit von US708 das die Möglichkeit der Beschleunigung durch eine Supernova Explosion sehr wahrscheinlich ist. Aber da eine Beschleunigung aus der Galaktischen Scheibe zu extreme Massen benötigen würde, welche nicht im Einklang mit den gängigen Entwicklungspfaden für solche Sterne sind, wurde eine alternative Theorie aufgestellt. Diese besagt dass US708 ein pre-He Weißer Zwerg ist der durch eine Supernova Ia Explosion aus einem sehr engen Doppelsternsystem im Galaktischen Halo geschossen wurde.

Contents

1	Introduction	1
2	Astrophysical background	3
2.1	Stellar parameters	3
2.1.1	Fluxdensity, luminosity & effective temperature	3
2.1.2	Stellar classification	4
2.1.2.1	The Harvard Classification	4
2.1.2.2	Morgan-Keenan Classification	5
2.1.2.3	Hertzsprung-Russell Diagram	6
2.1.3	Focusing on sdO stars	7
2.1.3.1	General information	7
2.1.3.2	Possible formation mechanisms	8
2.2	Structure of stars	13
2.3	Nuclear fusion & the origin of elements	14
2.3.1	Burning processes	14
2.3.1.1	pp-chain	15
2.3.1.2	CNO-bi-cycle	17
2.3.1.3	Subsequent reactions	17
2.3.2	Supernovae	19
2.3.2.1	Core collapse Supernovae	20
2.3.2.2	Type Ia	21
2.3.3	Neutron captures	22
2.4	Runaway stars	22
2.4.1	Supernova ejection scenario	23
2.4.2	Hills mechanism	24
2.4.3	Disruption of satellite galaxies	24
2.4.4	Dynamical Acceleration	26
3	Model atmospheres and synthetic spectra	28
3.1	Radiative transfer	28
3.2	Simplifications for model atmospheres	31
3.3	Level population (LTE vs. NLTE)	34
3.4	Line formation & -broadening	36
3.5	Rotation and Macroturbulence	38
4	Numerical methods	40
4.1	Complete Linearization	40
4.2	Accelerated Lambda Iteration	41
4.3	Acceleration of convergence	44
4.4	OS vs ODF	45
4.5	Influence of Fe/Ni elements	46

4.6	TLUSTY	47
4.6.1	CL/ALI-method	48
4.6.2	Tricks and hints	49
4.6.3	TLUSTY vs TMAP	51
4.7	Synspec	52
4.8	SPAS	53
4.9	General procedure for abundance determination	54
4.10	Comparison of modelgrids	60
4.11	XTGRID	64
4.12	Photometry and color indices	65
5	Spectrographs	67
5.1	Types of Spectrographs	67
5.2	Scientific Instruments	69
5.2.1	UVES	69
5.2.2	XSHOOTER	69
5.2.3	FEROS	71
5.2.4	The High Resolution Echelle Spectrometer (HIRES)	72
5.2.5	The Echellette Spectrograph and Imager (ESI)	73
5.2.6	Hubble Space Telescope instrumentations	74
5.2.6.1	The Space Telescope Imaging Spectrograph (STIS)	75
5.2.6.2	The Cosmic Origin Spectrograph(COS)	76
5.2.7	The International Ultraviolet Explorer (IUE)	78
5.2.8	The Far UV Spectroscopic Explorer (FUSE)	78
5.3	Data reduction	80
6	Analysis of He-sdO stars	83
6.1	Nitrogen rich He-sdO stars	83
6.1.1	CD-31° 4800	83
6.1.1.1	General information	83
6.1.1.2	Spectral analysis	84
6.1.1.3	Spectral energy distribution	96
6.1.2	HE 1511-1103	98
6.1.2.1	General information	98
6.1.2.2	Spectral analysis	99
6.1.2.3	Spectral energy distribution	104
6.1.3	HZ1	105
6.1.3.1	General information	105
6.1.3.2	Spectral analysis - XSHOOTER & SPY/UVES	106
6.1.3.3	Spectral energy distribution	114
6.1.4	HZ44	117
6.1.4.1	General Information	117
6.1.4.2	Spectral analysis	117
6.1.4.3	Spectral energy distribution	124
6.2	Carbon rich He-sdO stars	126
6.2.1	[CW83] 0904-02	126
6.2.1.1	General information	126
6.2.1.2	Spectral analysis	126
6.2.1.3	Spectral energy distribution	133

6.2.2	HE 0958-1151	134
6.2.2.1	General information	134
6.2.2.2	Spectral analysis	134
6.2.2.3	Spectral energy distribution	140
6.3	Carbon and Nitrogen rich He-sdO stars	141
6.3.1	LSS 1274	141
6.3.1.1	General information	141
6.3.1.2	Spectral Analysis	141
6.3.1.3	Spectral energy distribution	149
6.3.2	LSIV +109	151
6.3.2.1	General information	151
6.3.2.2	Spectral Analysis	151
6.3.2.3	Spectral energy distribution	158
6.3.3	[CW83] 0832-01	160
6.3.3.1	General information	160
6.3.3.2	Spectral analysis	160
6.3.3.3	Spectral energy distribution	166
6.3.4	GALEX J095256.6-371940	167
6.3.4.1	General information	167
6.3.4.2	Spectral Analysis	168
6.3.4.3	Spectral energy distribution	174
6.4	The Halo He-sdO star BD+39° 3226	175
6.4.1	General information	175
6.4.2	Spectral analysis	175
6.4.3	Spectral energy distribution	183
6.5	Discussion on errors	184
6.5.1	Statistical and systematic errors	184
6.5.2	Optical vs UV data	185
6.5.3	Wrong broadening data	186
6.5.4	Undetermined abundances of iron and nickel	187
6.5.5	Errors of solar abundances	189
6.6	An eye on radial velocities	191
6.7	The Pickering Problem	193
7	Evolutionary scenarios	197
7.1	Formation history of N-enriched He-sdOs	197
7.2	Formation history of C-enriched He-sdOs	200
7.3	Formation history of CN-enriched He-sdOs	204
7.4	Remarks on the formation history of BD+39° 3226	213
8	Analysis of US708	214
8.1	General procedure	215
8.2	Revisiting CD -31° 4800	215
8.3	Spectral analysis of US708	225
8.3.1	Atmospheric parameters	225
8.3.2	Abundances of US708	226
8.3.3	Atmospheric parameters - revisited	232
8.4	Acceleration mechanism	234
8.4.1	Abundances of iron & nickel	234

8.4.2	Kinematic properties	240
8.4.3	Evolutionary and ejective scenarios	244
8.4.3.1	Ejection by triple disruption in the Galactic centre .	244
8.4.3.2	Ejection by an asymmetric core-collapse supernova .	244
8.4.3.3	Ejection from the disk by a thermonuclear supernova	246
8.4.3.4	Ejection from the halo by a thermonuclear supernova	247
9	Summary & Conclusion	250
	Bibliography	255
	List of Figures	265
	List of Tables	271
	Appendix	276
.1	Data of analyzed spectra	277
.1.1	CD -31° 4800	277
.1.2	[CW83] 0904-02	278
.1.3	LSS 1274	279
.1.4	LSIV +10 9	280
.1.5	[CW83] 0832-01	280
.1.6	HE 1511-1103	281
.1.7	HE 0958-1151	281
.1.8	HZ1	281
.1.9	HZ44	283
.1.10	GALEX J095256.6-371940	283
.1.11	BD+39° 3226	285
.1.12	US 708	286
.2	Additional spectral fits for HZ1	287
.2.1	XSHOOTER	287
.2.2	SPY/UVES	289
.3	Abundance plots for CD -31° 4800 and US708	292
.3.1	CD -31° 4800	292
.3.2	US708	292
.3.3	Comparison of CD -31° 4800 and US708	293
.4	Linelist	295
.4.1	Optical Helium lines	295
.4.2	Optical metal lines	295
.4.3	UV lines	299

1 Introduction

“- Hey, Timon, ever wonder what those sparkly dots are up there?”

- Pumba, I don't wonder; I know.

- Oh. What are they?

- They're fireflies. Fireflies that, uh... got stuck up on that big bluish-black thing.

- Oh, gee. I always thought they were balls of gas burning billions of miles away.

- Pumba, with you, everything's gas.“

Timon&Pumba, Disney's The Lion King, 1997

When was the last time you have looked into the night sky and were amazed by the sheer amount of stars you can see up there?

With no artificial light around, up to 3000 stars can be observed with the naked eye. The closer to light-polluted areas we come, the fewer stars can be seen. If we want to try to describe the shining gas balls we see in the sky, different properties can be used. Especially their position on the firmament and their relative position to each other is usually known since thousands of years. Other characteristics like their brightness or their color complete the image we get and allow us to draw direct conclusions on the physical properties of the respective star. Speaking of the stellar color, most of the stars we can see in the night sky appear to be white or reddish. There are hardly any stars with a bluish appearance. Only telescopes and other scientific instruments reveal where most of them hide in the darkness of the sky.

Amongst the blue stars, a small quantity is represented by hot subluminescent stars of spectral type O or B, the sdO and sdB stars. These core helium burning stars only feature very thin hydrogen envelopes. They are usually associated with a rather interesting and probably violent past, as only some extreme events can cause a star to lose almost all of its hydrogen envelope.

A special subgroup among the hot subluminescent stars are the He-sdO stars. Those stars are characterized by the large amount of helium in their atmospheres and their helium line dominated spectra without virtually any hydrogen lines. Their formation history is thought to be different compared to normal sdO stars. Several theories have been made up to explain their origin, some of them involving binary interaction, others focusing on rather complicated thermonuclear processes in single stars. Up to now, the He-sdO stars are grouped into three subgroups, depending on their chemical composition and the most abundant metal: The carbon-, nitrogen- and carbon&nitrogen rich ones. Other, heavier elements have also been found in this type of stars, amongst them i.e. neon, silicon, sulfur up to iron and nickel. Recent studies also give evidence for the presence of elements heavier than iron, like germanium, strontium or lead. Some of the He-sdO stars do not match the standard scheme with dominating helium lines and poor hydrogen. In their spectra helium and hydrogen lines co-exist at a comparable strength. While not being a classical, pure He-sdO, these stars may be classified as intermediate He-sdOs .

But the question remains if the chemical composition of a He-sdO star gives a direct

link to the formation history. Or in other words: Do the members of the single subgroups form a homogeneous sample if more elements than carbon, nitrogen and oxygen are taken into consideration. And what about the intermediate He-sdOs? Are they also belonging to one of the subgroups or is their evolutionary history completely different? To make profound statements it is not enough to look at optical data as some of the interesting elements are only present in the UV wavelength range or dominate in the optical UV.

subgroups, an evolutionary scenario will be presented and discussed. One of the most extreme and interesting He-sdO stars is US708. This rather dim helium star is the fastest known star to mankind at the time of writing this thesis. Currently it is located in the halo and heading towards the outer parts of our Galaxy with a restframe velocity larger than 1200 kms/s. Of course, such a high speed needs an extreme event of acceleration. Again, different theories have been discussed. The acceleration by the black hole in the centre of the Milky Way was ruled out recently, as well as the acceleration in dense stellar cluster. Up to now, the acceleration as the result of a thermonuclear supernova is favored, however without proof. To do so, some direct evidence for a Typ Ia supernova would have to be found on US708. The best candidate is a clear enrichment in iron and nickel as both elements get produced in this type of stellar explosion. As already mentioned UV data are necessary for this kind of measurements. If such an enrichment can be confirmed, US708 could serve as a milestone for several parts of astronomy. It would not only help to test current mass models of the Milky Way, enhance our understanding of binary interactions and binary evolution but also offer the possibility apply crosschecks on the modeling of supernovae Ia.

This thesis has the aim to deal with the two main problems described here. By analyzing a large sample of He-sdO stars to determine their atmospheric parameters and chemical abundances, it will be tried to search for common, or uncommon, chemical patterns or striking abundances of single elements. As understanding and determining atmospheric parameters is not as easy as it may sound, extensive research on different approaches and models of this topic was conducted. Grouping the analyzed stars will not only be tried based on their chemistry but also their atmospheric parameters. For each of the chemical subgroups an evolutionary scenario will be presented and discussed.

These questions will also be asked on US708 to get hints on its past and maybe future development. Not only the evolution and nature of the star itself will be examined but also the events that lead to its acceleration. As the data available for US708 are not of best quality, a cooperation with ASTROSERVER.ORG [Németh, 2017] was established to get as much information from the different spectra as possible.

To give a help in understanding the different scenarios, models and procedures used and described in this work, a short introduction on the most important topics from the astrophysical background and the theory of modeling stars in a computer will be presented hereafter, followed by an overview on the instruments used for gathering spectral data. Chapters on the analysis of the sample stars and their evolutionary history are followed by a single chapter on US708 as this star differs from the rest of the sample by means of analysis and parameters. In the end a summary and conclusion is presented.

2 Astrophysical background

This chapter is intended to give an overview about certain stellar parameters that are indispensable to understand the scientific analysis and results explained later on. Afterwards, information on the structure and life of stars will be presented, followed by a short overview on the nuclear processes that let the stars shine and produce their energy.

2.1 Stellar parameters

All the information we get from stars comes from the analysis of their emitted light, whether as spectra, lightcurves or position measurements. Depending on how we measure that light, certain parameters can be defined to describe the nature of the star and to make it comparable to others.

2.1.1 Fluxdensity, luminosity & effective temperature

Each star emits energy in form of electromagnetic radiation. The specific intensity I_ν is the radiated energy ΔE per frequency interval $\Delta\nu$, per time Δt , passing through a projected surface element ΔA in direction of the solid angle $\Delta\omega$; Or written as a formula

$$I_\nu = \frac{\Delta E}{\Delta\nu\Delta t\Delta\omega\Delta A \cos(\theta)} \quad (2.1)$$

The total intensity can be derived by integrating over all frequencies.

$$I = \int_0^\infty I_\nu d\nu \quad (2.2)$$

As all stars (except for the sun, of course) are too far away to resolve the stellar disk (at least in the optical wavelengths), we have to integrate the observed light over the stellar disk which leads to a quantity called flux density F_ν , or simply F if integrated over all frequencies.

$$F = \int_{4\pi} I \cos(\theta) d\omega = \int_0^\infty F_\nu d\nu \quad (2.3)$$

The luminosity L of a star is defined as

$$L = \int_S F_S dA \quad (2.4)$$

This is the total energy coming from a surface S . By making the plausible assumption of a spherical star with radius R , the luminosity modifies to

$$L = 4\pi R^2 F_S \quad (2.5)$$

Another important parameter to characterize a star is its temperature. But this is not as trivial as it may seem. The atmosphere of a star has a more or less complicated temperature stratification and the stellar surface is not as sharply defined as one may assume. In addition the definition of a temperature only applies to objects in complete thermodynamical statistical equilibrium. This is not the case in most of the stellar atmospheres. Therefore it is necessary to introduce a characteristic value, called the effective temperature T_{eff} . This is done by comparing the flux of the star to a black body radiator. According to the Stefan-Boltzmann law the “black body flux“ is defined as

$$F_B = \sigma T^4 \quad (2.6)$$

with the Stefan-Boltzmann constant σ . The effective temperature is therefore linked to the Flux of a star F_S via

$$F_S = \sigma T_{\text{eff}}^4 \quad (2.7)$$

and

$$L = 4\pi R^2 \sigma T_{\text{eff}}^4 \quad (2.8)$$

The effective temperature for stars spans from a few thousand Kelvin for the cool late-type stars and up to over 100000 K for the hottest early-type stars.

This large temperature range implies that is appropriate to use other parameters than this of classify stellar objects.

2.1.2 Stellar classification

2.1.2.1 The Harvard Classification

Stellar spectroscopy began in the late 19th century and led to the so called “Harvard Classification“ that was established in the early 20th century. It uses absorption lines to determine between different types of stars and is therefore only linked indirectly to the temperature. Stars are assigned a capital letter O, B, A, F, G, K or M ¹ according to the features they show in their spectra. Rayne [1925] concluded that the spectral sequence is a sequence of decreasing temperature. The early-type stars (O, B, A) are hot objects with temperatures between ~ 10000 K (A-stars) and over ~ 30000 K)O-stars. In contrast, the late-type stars (K, M) are comparatively cool with temperatures between 2500 K and 5000 K

As the ionization state of elements increases with temperature, hotter stars usually show strong absorption lines of hydrogen and helium as well as metal lines in high ionization levels. It shall be mentioned that the term “metals “ refers to all elements except hydrogen and helium. Cooler stars can be characterized by the occurrence of molecule bands and lines of neutral elements.

Up to now, several additional classes have been introduced, covering rather extreme objects like Wolf-Rayet stars (class WR). Fig. 2.2 gives an overview on the lines and ionization stages visible at certain temperatures in the stellar spectrum.

¹Oh Be A Fine Girl Kiss Me

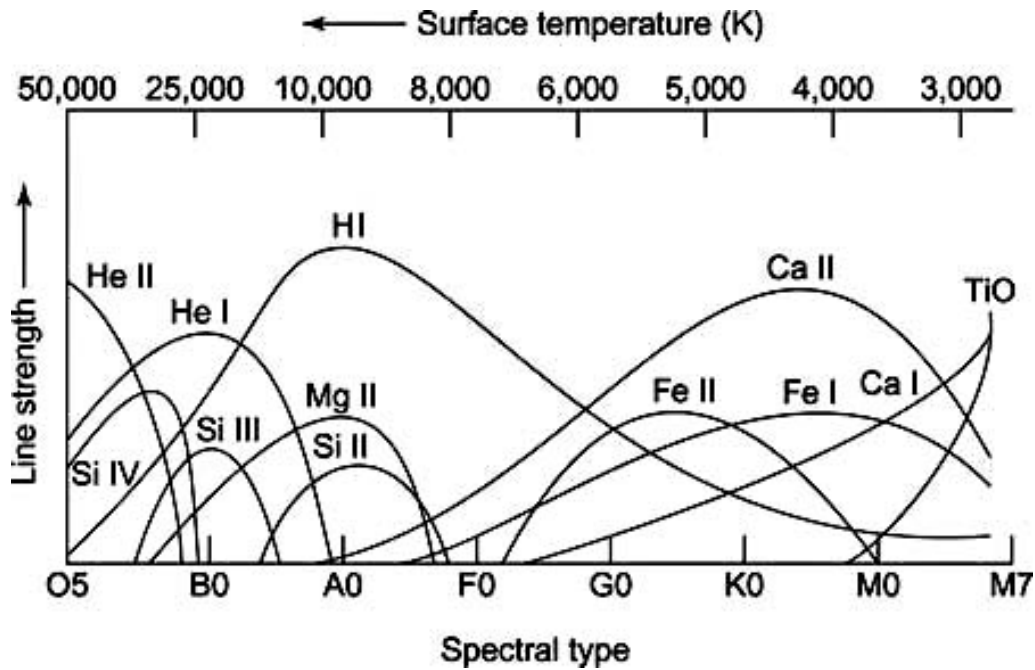


Figure 2.1: The equivalent width of several elements and ionization stages plotted versus temperature and spectral class. Taken from: ¹

2.1.2.2 Morgan-Keenan Classification

The Harvard classification was extended to account for differences in luminosity (Yerkes classification). This two-dimensional scheme was finally worked out by Morgan and Keenan in the 1950s. An indirect connection to the surface gravity of a star is given as a lower gravity results in a less pronounced pressure broadening effect. In detail the width of hydrogen lines and the line strength of ionized elements is used.

The MK Classification utilizes roman numbers from 0 to VII to describe the luminosity of a star. Class 0 is assigned to the largest hypergiant stars, V are the main sequence dwarf stars and finally white dwarfs have a luminosity class of VII. Table 2.1 gives an overview on the different classes.

0	Hypergiants
I	Supergiants
II	luminous giants
III	normal giants
IV	Subgiants
V	dwarfs (main sequence stars)
VI	Subdwarfs
VII	White dwarfs

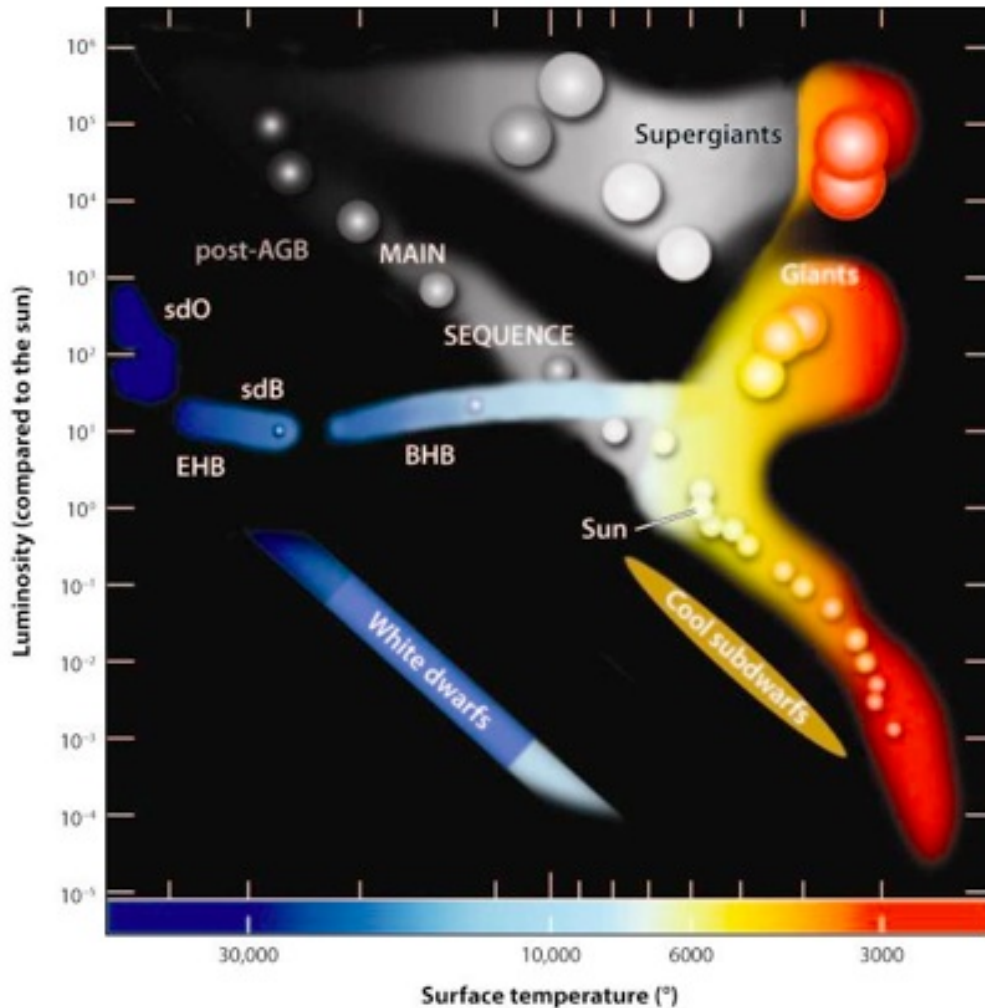
Table 2.1: Luminosity classes of different types of stars

¹http://ccphysics.us/henriques/a1051/spectral_types.jpg

2.1.2.3 Hertzsprung-Russell Diagram

To get an overview of possible classes of stellar populations or to search for correlations between different parameters, a graphical visualization is helpful.

The most common one in astronomy is the so called “Hertzsprung-Russell Diagram“ (named after E. Hertzsprung and H. Russel). In this kind of graphic, the Luminosity is plotted versus the spectral class or the effective temperature of a star. Fig. 2.2 shows a typical H-R-Diagram. Some regions contain much more stars than oth-




 Heber U. 2009.
Annu. Rev. Astron. Astrophys. 47:211–51

Figure 2.2: A Hertzsprung-Russell diagram. The luminosity is plotted versus the effective temperature.

ers and form clear patterns. The most obvious and densely populated is the main sequence (MS). During its lifetime, a star “moves“ through the HRD and crosses several areas as its inner parameters like temperature and luminosity slowly change. Each star starts its life on the Zero Age Main Sequence (ZAMS) when it begins to burn hydrogen in the core. The main sequence is the area where a star spends most of its lifetime. When the hydrogen supply is depleted, the star is at the TAMS, the

Terminal Age Main Sequence.

The next step in the stellar evolution is the red giant branch, which is characterized by hydrogen shell burning. If a star is massive enough, and therefore can develop temperatures high enough, it is able to start helium burning in the core. The less massive ones will start to cool down and evolve to He-core white dwarfs. This final stage of stellar evolution has a low luminosity and is placed far below the main sequence in the HRD. It basically consists of the remaining core of a red giant after the ejection of the outer layers and mainly consists of the products of the helium fusion, carbon, nitrogen and oxygen. If the white dwarf is or becomes too massive it will end its life in a thermonuclear explosion (see Sect. 2.3.2 for details). If not, it will simply cool down and become less and less luminous. As long as a red giant burns helium in the core and hydrogen in the shell it can be found on the horizontal branch (HB), which follows the red giant stage. A special part of the horizontal branch is the extreme horizontal branch EHB. Its stars show a much higher temperature than their cooler comrades, possibly due to a higher helium abundance [Lee et al., 2005]. Their thin hydrogen envelope doesn't allow for H-shell burning. Massive stars that can burn helium in a shell around their inert carbon/oxygen core and sustain hydrogen shell burning at the same time can be found on the asymptotic giant branch (AGB) and are therefore called AGB-stars.

A quite small but rather interesting area can be found beyond the EHB. The sdB and sdO stars there are very hot (and therefore blue) and show a similar luminosity compared to the larger main sequence stars. The following section will deal with these special type in particular.

2.1.3 Focusing on sdO stars

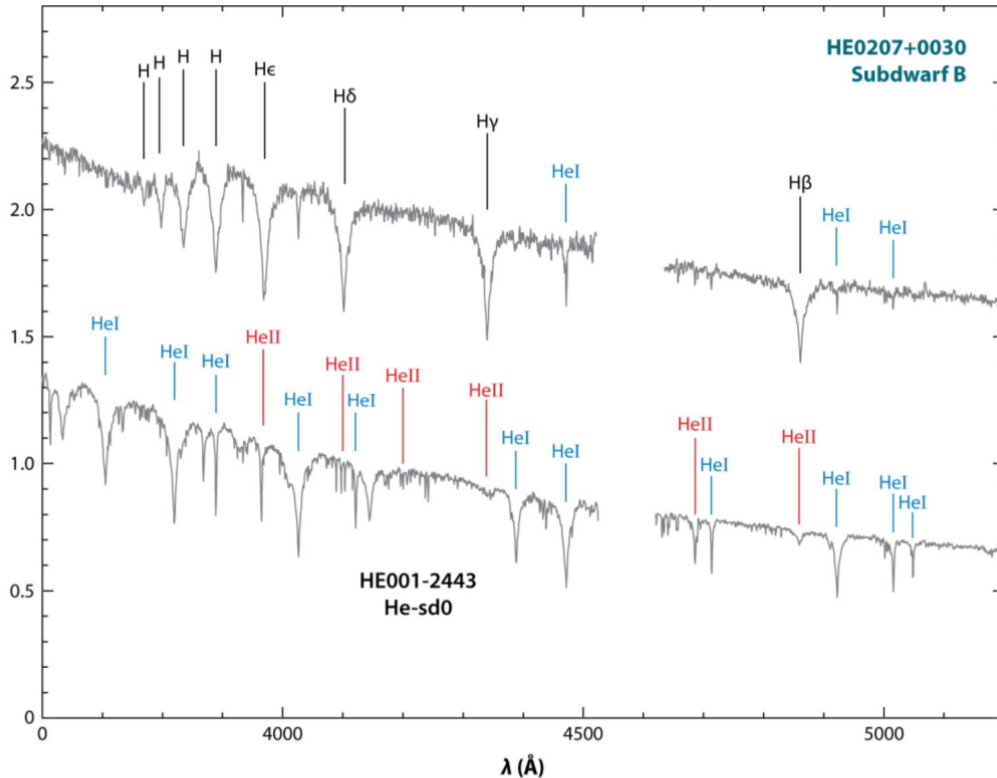
Subdwarf stars are low mass stars in a late evolutionary state. They can be divided into B- and O-type stars and are therefore called sdB or sdO stars. These stars dominate the population of faint, blue stars at high galactic latitudes and can be found in the old disk and the halo [Ferraro et al., 1997].

2.1.3.1 General information

To distinguish between sdB and sdO stars, which have a different evolutionary history, a quick look at their spectra is all that is needed. The spectra of sdBs are dominated by the hydrogen lines of the Balmer series and virtually no HeII lines. On the other side sdO stars are usually hydrogen poor and show much stronger helium lines, especially the HeII line at 4686Å. A special subtype, the He-sdO is characterized by the absence of hydrogen Balmer lines. In general, one can say that most evolved low mass stars with clearly visible HeII lines are sdO stars, with the exception of i.e. DO white dwarfs or the PG1159 stars. In Fig. 2.3 typical spectra of sdB and sdO stars can be found, including with markers of the most important lines.

SdB stars are assigned to models for Extreme Horizontal Branch stars. They show core-helium burning and are unable to sustain hydrogen burning. Progenitors of sdBs have to lose almost their complete hydrogen envelope. The remaining hydrogen envelope is inert and not able to sustain any nuclear burning. The mass loss is believed to be caused by binary interactions through Roche lobe overflow or the formation and ejection of a common envelope, depending on the speed of the

mass transfer. This theory is supported by the spectra of sdB stars, among which a significant part was found to be composite spectra [Ferguson et al., 1984]. The companions were, in most cases F, G or K-type stars [Stark and Wade, 2003]. As




 Heber U. 2009.
Annu. Rev. Astron. Astrophys. 47:211–51

Figure 2.3: Typical spectra of sdB and sdO stars with indication of important hydrogen and helium lines. Taken from Heber [2009].

this work deals with He-sdO stars, the following lines will describe them in detail. The typical temperature range of He-sdOs varies from around 40000 K to about 46000 K, while the $\log(g)$ spans from ~ 5.5 to ~ 5.9 [Heber, 2008].

He-sdOs can be divided in different abundance classes, depending if the spectra show strong Carbon and/or Nitrogen lines. These subtypes depend on the formation mechanism which will be dealt with in the following section.

In contrast to sdB stars, the fraction of close binaries among sdO stars is rather small with approximately only 4%.

2.1.3.2 Possible formation mechanisms

There are several possibilities how sdO, and especially He-sdO stars can be formed. The two main scenarios are the hot flasher and the merger scenario which will be described hereafter.

Hot flasher

A core helium flash is a thermonuclear runaway reaction that produces carbon from

helium through the triple alpha process.



If the core of a star with a mass below $2.2 M_\odot$ runs out of hydrogen for the pp reaction, the core starts to contract, the central temperature increases and the electron gas becomes degenerate. The pressure of the degenerated electrons gas stabilizes the core. Once a temperature of around 100 Mil. K is reached, the helium fusion kicks in and enhances the temperature even more. As the equation of state is independent of the temperature, the newly started helium fusion does not lead to any expansion. All the released energy is absorbed in the shells of the star. Once the temperature is high enough to lift the degeneracy, the core expands and settles to a quasi-static state after a few million years, burning helium in the core.

Not all red giant stars show a helium flash. Some of them, the so called flash-manqué stars, evolve towards high temperatures before helium core burning stars, instead they evolve towards the White Dwarf cooling track where they might still ignite helium and become a late hot flasher.

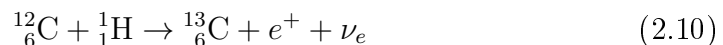
There are three subtypes of the hot flashing scenario, depending at which time of the evolution the flash occurs [Heber, 2016]. In the **Early hot flasher scenario** the helium core flash happens after the departure from the Red Giant Branch, before the star enters the WD cooling track, leading to subdwarf stars with standard H/He envelopes.

If the star is already on the white dwarf cooling track, the **late hot flasher** scenario becomes important. It has to be distinguished between three different possibilities [Lanz et al., 2004].

- **Deep mixing**

In this case, the energy produced by the hydrogen shell burning can be neglected and the inner convective zone reaches up to the outer, hydrogen rich layers. This leads to the mixing of hydrogen into deeper layers, close to the core where it can be burnt and increase the energy output. This is the start of a runaway process, because it creates an entropy barrier at the layer where the hydrogen burning occurs, splitting the convective zone into two subzones. It grows into upper layers and more protons are pushed downwards which then increase again the energy output that drives the convection zone further out. This scenario is called a H-flash and it consumes almost all of the formerly present hydrogen, leading to very hydrogen deficient stars. Fig. 2.4 shows a schematic Kippenhahn diagram of such a deep mixing process. It can be seen that hydrogen rich envelope declines more and more as the convective zones start to merge.

The surface of such a star would show a large enrichment in helium and carbon. Nitrogen enrichment is possible if the $^{12}_6\text{C}$ was burnt to $^{14}_7\text{N}$ by hydrogen ignition.



- **Shallow mixing**

In this scenario the inner convection zone reaches the hydrogen rich outer

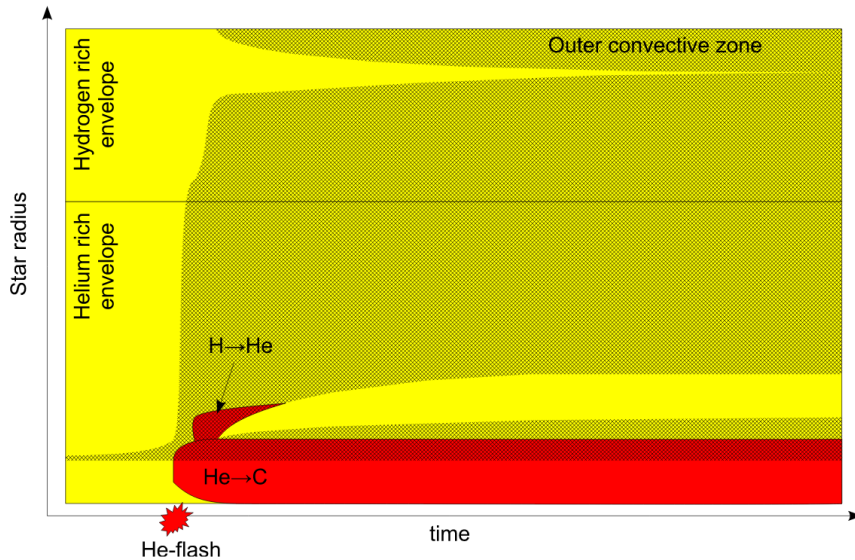


Figure 2.4: Kippenhahn diagram for the deep mixing scenario, Adopted from: Hirsch [2009].

layers, but cannot push enough protons to the deeper layers to ignite the runaway H-flash. Only little hydrogen is burnt before the two convective zones merge. If helium is ignited while the hydrogen shell burning still produces significant amounts of energy, the CNO burning sets up an entropy barrier. This prevents the inner convection zone from reaching too far upwards. In Fig. 2.5 this barrier is clearly visible in the upper panel, separating the two convective zones. Carbon enriched material is mixed in the inner envelope by the interior convection zone. The zone will slowly shrink and start to move outwards. As the star evolves, another, outer convection zone establishes and starts to move inwards. Once the two zones merge, the products of the CNO burning and of the helium flash are mixed into the outer hydrogen envelope.

- **composite mixing**

Of course, not all late hot flasher can be strictly divided in one of the two cases. For those with weak, but not negligible hydrogen shell burning, a composite scenario can be set up as seen in Fig. 2.6. In this cases, the inner convective zone reaches the hydrogen rich layers, but the runaway process is not initiated as the amount of protons mixed to the center of the star is too low. After ~ 6000 years, the convective zones start merging. The surface composition of the resulting sdO would still be depleted in hydrogen, but not as much as in the other scenarios.

The problem with these scenarios becomes apparent in the $T_{\text{eff}}/\log(g)$ diagram, as the observed distribution of stars does not match the predictions from theoretical models. As the evolutionary timescales are much shorter than the helium burning phase of a sdO, it would be expected that these stars accumulate on or near the helium main sequence. However, this is not observed for all sdO stars, many of which appear to have too low gravities.

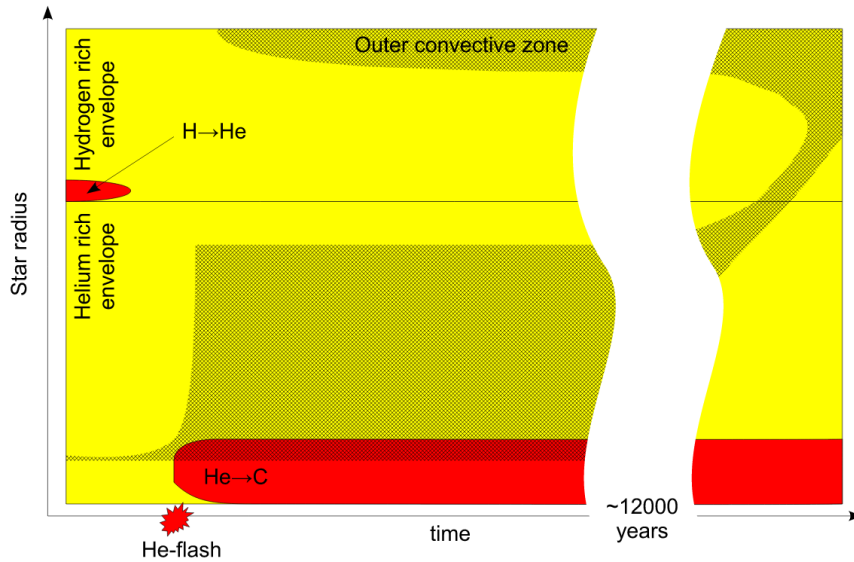


Figure 2.5: Kippenhahn diagram for the shallow mixing scenario. Adopted from Hirsch [2009].

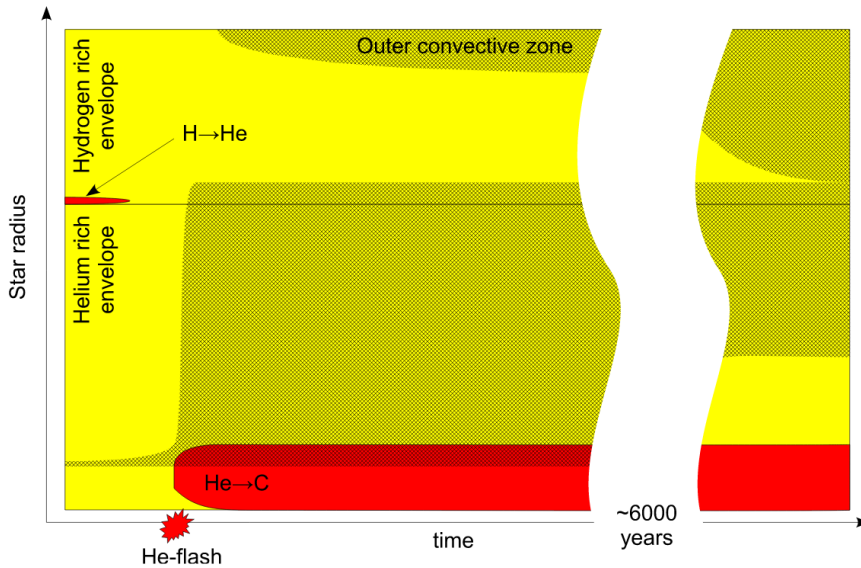


Figure 2.6: Kippenhahn diagram for the composite mixing scenario. Adopted from Hirsch [2009].

The second proposed scenario is the merging of two He core White Dwarfs.

Merging of two He core WDs

The merger scenario was proposed by Webbink [1984] and is directly linked to close binary evolution. To form a sdO star, a short period binary system consisting of two white dwarfs with He cores is needed. This system has to lose orbital energy, i.e. by emitting gravitational waves. Zhang and Jeffery [2012] computed models for merging helium white dwarfs and differentiated between three different modes, the fast-, the slow-mergers and a combination of both. A schematic overview on the three models can be found in Fig. 2.7. If the two bodies get close enough to-

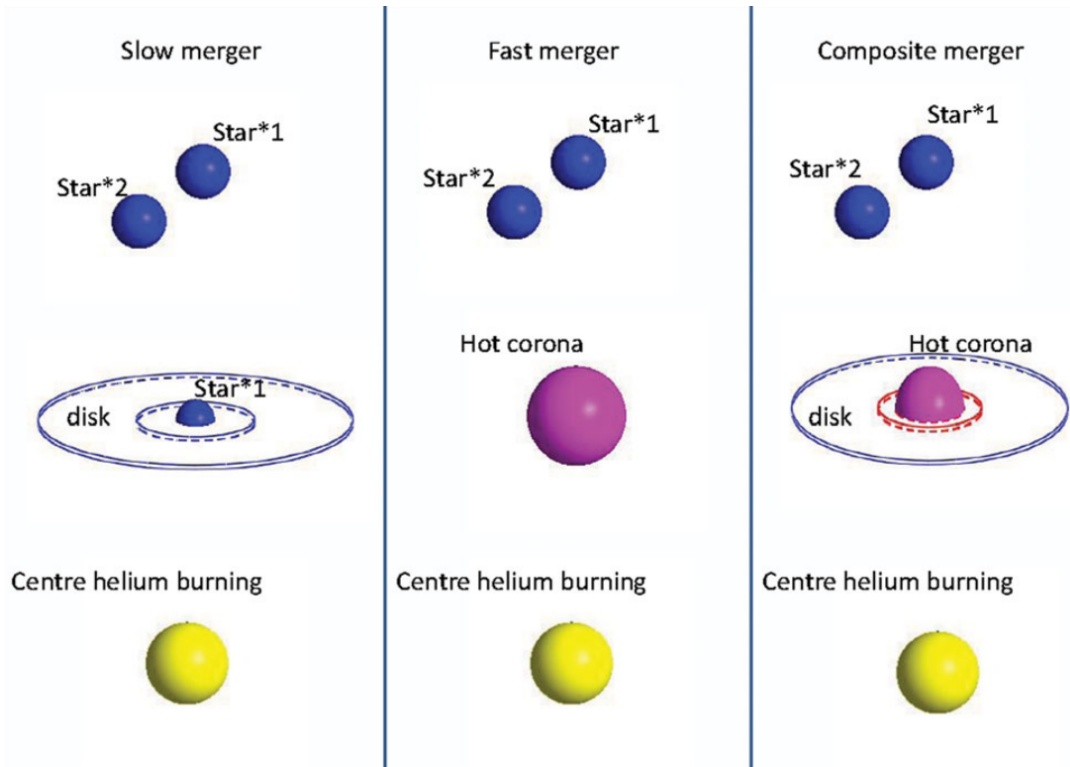


Figure 2.7: Schematic overview on the three different merging models for helium white dwarfs. Taken from Zhang and Jeffery [2012].

gether, the less massive one fills its Roche lobe and run-away mass transfer starts towards the other white dwarf. Due to the mass/radius relation for White Dwarfs, an increase in mass leads to a shrinking of the star, meaning a smaller radius. In the slow model, the larger of the two stars fills its Roche lobe and the transferred mass forms a disk around the companion. The accretion on the surface happens slowly and temperatures remain low. During the fast merging model in contrast, the accreted matter falls directly onto the companion’s surface without establishing a circumstellar disk first. This process leads to very high temperatures around 10^8 K and the heated material expands and forms a corona around the star [Heber, 2016]. In the third model, a part of the matter forms a disk while the rest is directly accreted and transferred to the corona mentioned beforehand.

The chemical composition of the remaining star depends on the favored model. The slow merger model does not reach high temperatures which would be sufficient for nuclear burning to occur and therefore no change in the chemical structure is expected. It matches the chemical pattern of the disrupted star which is thought to be nitrogen rich due to the CNO bi-cycle.

In the fast case, the temperature is high enough for nuclear reactions and carbon can be produced via the triple- α process. The formation of convective zones could bring up material from deeper layers to the surface resulting in an enrichment of carbon.

For the third scenario, the chemical structure depends on the mass of the merger. In high mass mergers ($M > 0.65 M_{\odot}$, [Zhang and Jeffery, 2012]) the strong convection zones mix nitrogen- and carbon-rich material and traces of both can be found in the spectra. For lower masses, the surfaces remains nitrogen-rich as no convection

mixes carbon from deeper layers into the accreted material.

This implies that the chemical composition gives a remark on the stellar mass, as carbon-rich stars should be heavier than nitrogen rich ones [Hirsch, 2009].

The conversion of angular momentum leads to a high rotational velocity of the resulting star. However, Gourgouliatos and Jeffery [2006] showed that the rotational velocity of a merger outcome can easily exceed its breakup velocity. This leads to the question which processes may reduce the angular momentum to keep the star bound. One theory involves high magnetic fields that breaks down the rotation of the star by the dynamo effect. The necessarily strong magnetic fields have been found in some sdB and sdO systems [Valyavin et al., 2006], however, recent measurements are only showing upper limits for the magnetic field strength. Despite this, a high mass loss rate could be responsible as it transfers angular momentum outwards, away from the stellar surface.

2.2 Structure of stars

Describing the inner structure of stars is a difficult task. Several assumptions are made to simplify the necessary calculations. In many cases, stars can be regarded as spherically symmetric and in hydrostatic equilibrium, neglecting mass loss, magnetic fields, rotation and so on.

The structure can be described by four differential equations, linking the radial distribution of several parameters with each other. For more detailed information, see e.g. “*An Introduction to Modern Astrophysics*“ by Carroll&Ostlie [2006].

The first equations demands a hydrostatic equilibrium, meaning that the outward pressure gradient produced in the interiors of the star (by the electrons and ionized atoms) is compensated by the gravitational force pulling inwards.

$$\frac{dP(r)}{dr} = -\frac{GM(r)\rho(r)}{r^2} \quad (2.12)$$

$P(r)$ is the pressure at a certain radius r from the centre of the star, G is the gravitational constant, ρ is the density and $M(r)$ describes the mass enclosed within a radius r .

The following equation describes the distribution of mass in a star, based on mass conservation. Again, $M(r)$ is the mass within a radius r .

$$\frac{dM(r)}{dr} = 4\pi r^2 \rho(r) \quad (2.13)$$

Each star produces energy by nuclear fusion in its inner parts (see Sect. 2.3 for more details). As the fundamental physical principles hold everywhere in the universe, energy conservation applies to stars, too. This is described by:

$$\frac{dL(r)}{dr} = 4\pi r^2 \rho(r) \left(\epsilon - T \frac{dS}{dT} \right) \quad (2.14)$$

where the star produces an amount of energy ϵ , passing through a surface with radius r and resulting in a luminosity L at this surface point. The parameter S describes the entropy of the matter that builds the star. The entropy can be linked to the

heat Q via the temperature by $dQ = TdS$, implying that energy can be transported in form of heat.

This energy can be transported in three ways: Conduction, convection and radiation. In general, the temperature gradient $\frac{dT}{dr}$ plays an important role when it comes to the transportation of energy in stars. The normal star is not dense enough for conduction to be efficient, therefore it will not be described here any further. The remaining two cases have to be dealt with separately.

For convective layers, as they occur in the envelope of cool stars, the temperature gradient dT/dr can be described via

$$\frac{dT(r)}{dr} = \left(1 - \frac{1}{\gamma}\right) \frac{T(r)}{P(r)} \frac{dP(r)}{dr} \quad (2.15)$$

with the adiabatic exponent γ . For radiative layers, the following equation is appropriate.

$$\frac{dT(r)}{dr} = -\frac{3}{4ac} \frac{\rho\kappa}{T^3} \frac{L(r)}{4\pi r^2} \quad (2.16)$$

The factor a is the radiation constant and κ is a coefficient describing absorption, c is the speed of light.

To decide if radiative energy transfer occurs or if convection is more likely, the temperature gradients for both cases have to be compared to the adiabatic temperature gradient. If the radiative temperature gradient is smaller than the adiabatic one, radiation is the principle of choice, otherwise convection takes place (Schwarzschild criterion).

In theory the emission of neutrinos is a fourth source of cooling for a stellar object, which is relevant in very hot and dense matter, such as the early stages of white dwarf evolution, during which neutrinos can be emitted through non-nuclear production.

2.3 Nuclear fusion & the origin of elements

This section focuses on the details of the nuclear fusion processes that are taking place in all kinds of stars and that are necessary to form the elements heavier than hydrogen and helium. The last part deals with supernovae and the formation of elements heavier than iron.

2.3.1 Burning processes

Today it is assumed that all stars start their life after a gas cloud collapsed due to gravitational instabilities. During the collapse the central region of the gas cloud starts to heat up until, eventually, it becomes hot enough for fusion processes to kick in at a sufficient rate to form a stable, self-sustaining thermonuclear fusion reaction. As mentioned in a previous section, such a newborn star is settled on the main sequence where it burns hydrogen to helium and spends most of its lifetime. Nuclear fusion is among the most efficient, energy-producing processes in the Universe. To understand why energy is released during the fusion of, i.e. hydrogen atoms, it is helpful to take a look at the binding energy per nucleon for different atoms (Fig. 2.8).

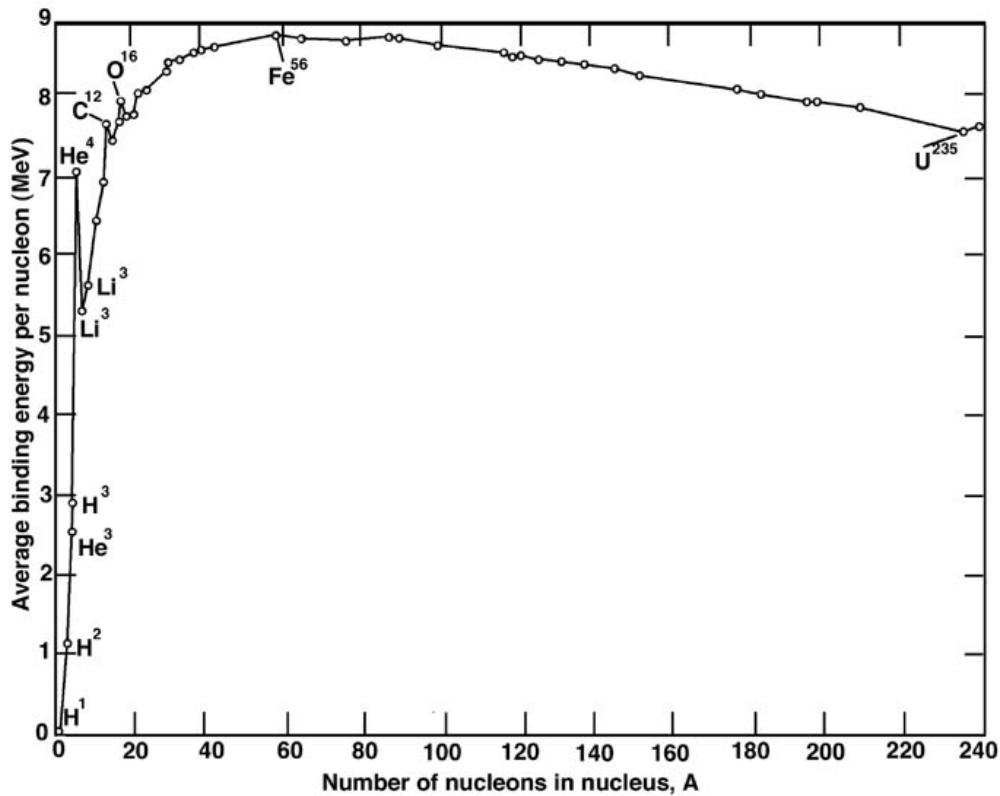


Figure 2.8: Binding energy per nucleon plotted versus number of nucleons.
Taken from: ¹

For the light elements like hydrogen, helium, lithium etc. the binding energy per nucleon is comparatively small. The more nucleons an element hosts, the stronger is the binding between them. This value peaks at ${}^{56}_{26}\text{Fe}$ and drops slowly for even heavier elements.

This means, that by combining lightweight elements to heavier ones, the resulting cores have an excess of binding energy, which is released. The largest “energy gap“ between two elements can be found for hydrogen (${}^1_1\text{H}$) and helium (${}^4_2\text{He}$), meaning that this fusion reaction releases the largest amount of energy.

There are in principal two main possibilities to get from hydrogen to helium. The proton-proton-chain (pp) and the CNO-bi-cycle. Both will be dealt with in the following subsections.

2.3.1.1 pp-chain

The main reaction of the pp-chain is



The mass of the resulting He atom is about 0.7% smaller than the mass of the educts. This mass defect is released as energy ΔE according to Einstein’s formula $E=mc^2$.

¹http://imagine.gsfc.nasa.gov/Images/educators/posters/elements/booklet/energy_big.jpg

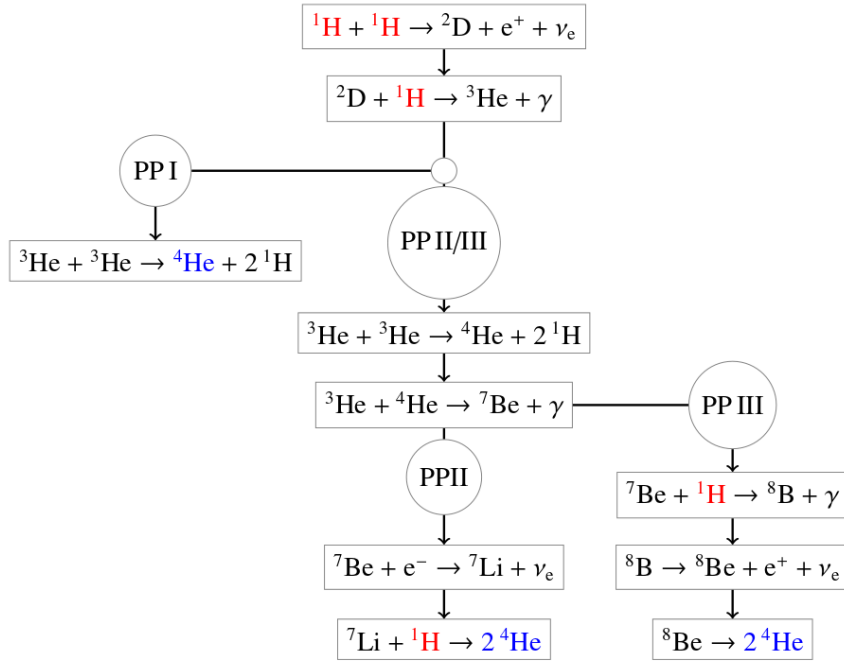


Figure 2.9: Schematic overview on the pp-chain mechanism. The resulting helium is colored blue, while the burnt hydrogen is red. Taken from Irrgang [2014].

However this picture is strongly simplified, and the ongoing reactions are much more complicated. A detailed overview is presented in Fig. 2.9.

The first steps are the fusion of two protons to a deuteron under emission of a positron and an electron neutrino (β^+ decay). This first step also has the smallest crosssection and therefore takes most of the time to happen. This bottleneck explains why a star can spend such a long part of its lifetime burning hydrogen. Afterwards the resulting deuteron captures another proton and forms a ^3He nucleus. The following reactions depend on the temperature in the star and occur at different probabilities.

- For solar temperatures the first sub-chain PPI has the highest probability. It simply fusions two of the ^3He nuclei to a “normal“ ^4He nucleus and emits two protons.
- With a probability of $\sim 9\%$ the second sub-chain PPII forms ^7_4Be that decays into ^7_3Li . The lithium absorbs a free proton and decays into two ^4_2He nuclei.
- The last reaction ist the most unlikely one. Here the produced ^7_4Be becomes ^8_5B by absorbing a proton. Afterwards ^8_4Be is produces in an inverse β -decay. The ^8_4Be than decays into two helium4-cores.

The speed at which the pp-chain takes place is dependent on the temperature of a star. The hotter the star is, the higher the kinetic energy of the particles. A high kinetic energy increases the probability of a particle to tunnel through the Coulomb barrier of another equally charged nucleus and allow the strong force to become

dominant over the electrostatic repulsion. Of course, also the local density ρ plays a certain role. To sum up, the probability of the pp chain can be described via

$$q_{pp} \propto \rho T^4 \quad (2.18)$$

2.3.1.2 CNO-bi-cycle

The second possibility to produce helium is the CNO (bi-)cycle. In these reactions, carbon, nitrogen and oxygen (CNO) act as catalysts to produce helium and are produced and destroyed continuously. However, the sum of C,N and O nuclei stays constant.

Fig. 2.10 illustrates all the ongoing reactions and produced particles like photons, positrons and neutrinos. The reactions in the CNO network are extremely sensitive to temperature:

$$q_{\text{CNO}} \propto \rho T^{16} \quad (2.19)$$

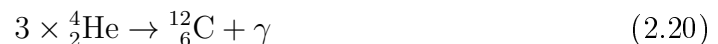
This leads to a peak of the energy production in the very center of the star and a steep gradient pointing outwards. In contrast to the pp-chain, the CNO (bi-)cycle is also dependent on the amount of catalyst atoms that can be found in the fusion region.

The different sub-reactions in the CNO cycle happen on different timescales. A bottle neck is the reaction ${}^{14}_7\text{N} + {}^1_1\text{H} \rightarrow {}^{15}_8\text{O} + \gamma$. This leads to a higher nitrogen abundance and a depletion of carbon in stars where the CNO cycle takes place in equilibrium. If a star produces its energy by the pp-chain or via the CNO-network is dependent on its temperature and therefore mass. At around $1.5 M_{\odot}$ the contribution of pp and CNO are comparable. At higher temperatures/higher masses, the CNO cycle is the dominant energy source.

2.3.1.3 Subsequent reactions

After a star has produced helium, the question arises how heavier elements are produced.

The most common way is the capturing of helium nuclei, also called α -capture. A special form is the so called triple alpha process.



Here, three ${}^4_2\text{He}$ nuclei merge together to form a carbon nucleus. In detail, two α -particles collide and build an intermediate ${}^8\text{Be}$ nucleus which captures another α -particle and turns into carbon. The collisions have to occur on a very short timescale ($\sim 10^{-16}\text{s}$), otherwise the intermediate ${}^8\text{Be}$ nucleus might break up again.

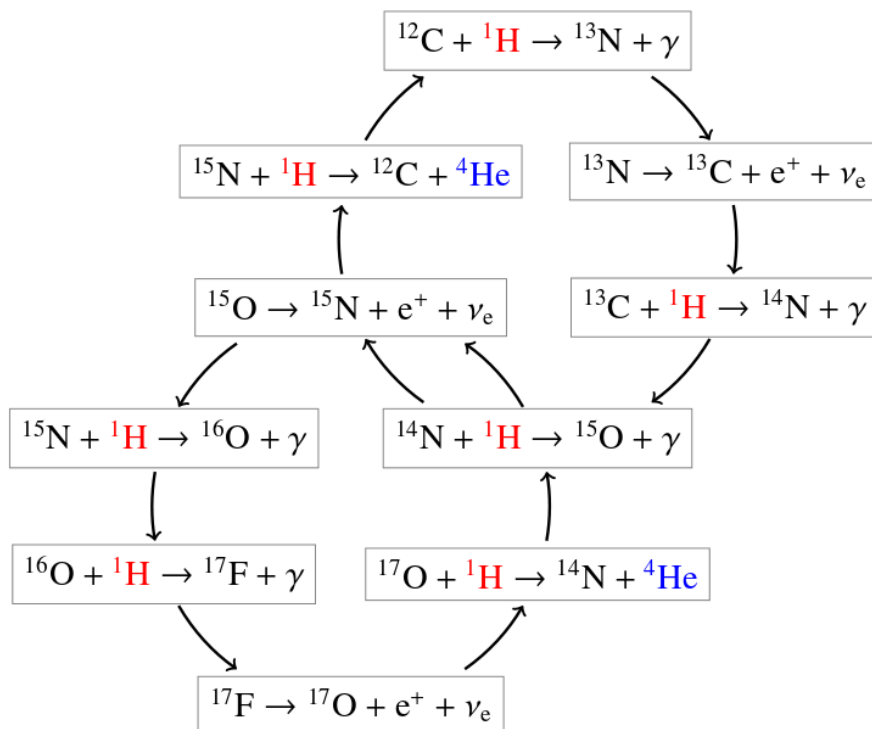
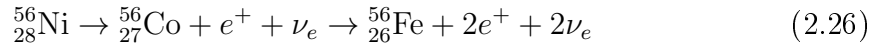
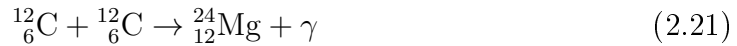


Figure 2.10: Schematic overview on the CNO bi-cycle. The resulting helium is colored blue, while the burnt hydrogen is red. Taken from Irrgang [2014].

Even heavier elements can be built up by capturing more alphas. But there is another, more direct way, which is explained in the following equations.



Of course, these reactions cannot occur in all stars. The heavier the produced element, the more restrict are the necessary conditions on the inner parameters, like temperature and pressure, of the star. Only the heavy stars above $\sim 8 M_\odot$ can i.e. ignite the carbon fusion and a even higher mass is required to burn elements up to nickel or iron.

Creating many elements with different masses changes the inner structure of the star. At the beginning each element is burnt in the stellar core. As the fuel there is exhausted, the fusion zone moves outwards and shell burning is initiated. The ashes of each step begin to sink to the center of the star where they accumulate and can be burnt further if the temperatures allow for this reaction. The ashes are stabilized by the pressure of the degenerate electron gas. The structure resembles an onion with shells of different elements as it can be seen in Fig. 2.11. The different fusion stages take different times. While a star can spend millions of years burning hydrogen to helium, the fusion of silicon to nickel is a matter of a few hours up to days.

This onion-like structure with an iron core, where fusion is not possible anymore, is the starting point of a core collapse supernova explosion which will be described in detail in the following section.

2.3.2 Supernovae

Supernovae are among the most energetic events known to mankind and mark the final end of a star's life. Today some of them can be used as standard candles to measure cosmic distances or to understand the cosmic circle of matter and the origin of the chemical elements. Supernovae are mostly caused by the collapse of a stellar iron core, however a special type (Type Ia) only occurs in binary systems containing white dwarfs. Observationally, they can be classified by their spectra and the presence of hydrogen absorption lines. Supernovae of Type I contain no hydrogen lines in their spectra, while Type II supernovae show spectral traces of hydrogen. For each type, there are several subtypes which are listed in the following overview.

- **SN Ia**
no H lines and Si lines
- **SN Ib**
no H lines, weak Si lines, large amount of He

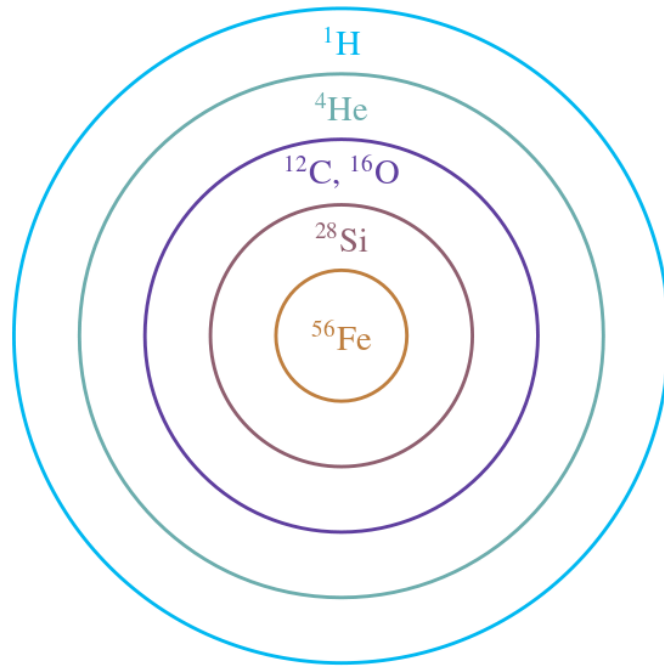


Figure 2.11: Onion-like structure of an evolved, massive star, not to scale. Taken from Irrgang [2014].

- **SN Ic**
no H lines, no Si lines, small amount of He
- **SN II-L**
H Lines, linear decrease of brightness after maximum
- **SN II-P**
H lines, brightness remains at plateau after maximum for some time

2.3.2.1 Core collapse Supernovae

As mentioned beforehand, core collapse supernovae can only take place in stars that have built up an iron core by fusing lighter elements. This means that the stellar mass has to exceed $\sim 8M_{\odot}$. Lighter stars do not match the criteria to burn carbon. As soon as the central fuel is depleted and the nuclear reactions stop, the iron core starts to contract. In addition photodesintegration starts to play a more and more important role. This process describes the break up of nuclei by the absorption of hard gamma radiation. The iron atoms are split up into neutrons and alpha particles, which then can be split into protons and neutrons. As the photons get absorbed during this process, it acts as a cooling mechanism for the inner part of the star. But not only does it decrease the temperature, also the radiative pressure is lowered even more as the photons get absorbed. These effects initiate the contraction and results in an increase of the density.

The core is enriched with neutrons, a state that is supported by $\beta+$ decays, that turn protons and electrons into neutrons and neutrinos. The stabilizing pressure of the degenerate electron gas is lowered as more and more electrons react. The neutrinos

can escape the high density regions and take energy with them which accelerates the cooling and contraction even more - a runaway process has started.

At some point the neutron gas cannot be compressed anymore because the neutrons are in a degenerate state and the resulting pressure is counteracting the collapse. This only works if the mass of the neutron star is below the Oppenheimer-Volkoff-Limit ($\sim 3 M_{\odot}$). Otherwise the core would continue to collapse and form a black hole.

Assuming a stable neutron core, the infall of the outer shells is suddenly stopped when the material hits the core, as it cannot be compressed any further because of the degeneracy. The momentum impacted on the neutron star leads to vibrations which drive the shockfront outwards. As they reach the remaining outer shells, they heat up their environment and start enhancing or igniting further fusion reactions with a large amount of neutrinos via pair production. The density may become so high, that even the weakly interacting neutrinos can be absorbed and contribute to the heating. As the shockwaves gain more and more energy, the result is gigantic explosion that tears the remaining star completely apart. Only the neutron star remains. The processed materials (mainly helium and α -elements) are ejected.

2.3.2.2 Type Ia

Supernovae Ia are among the most important standard candles and can be used to measure the expansion of the universe.

This type of supernovae can be distinguished from other type I supernovae by the presence of silicon absorption lines in the spectra.

They occur in close binary systems that contain a CO white dwarf. The progenitor stars are not massive enough to sustain carbon or oxygen burning and therefore mainly consist of these elements (see Sect. 2.3). The electron gas in the core is degenerated and therefore the temperature cannot get high enough for nuclear fusions, even if the core would compress even more. If the companion in a close binary system exceeds its Roche lobe, matter can be transferred on the white dwarf. The matter is accreted there and the mass and temperature starts to increase, while the radius of the White Dwarf decreases (Mass/Radius relation for white dwarfs). At a certain point of roughly $1.4 M_{\odot}$ (Chandrasekhar limit, depending on actual chemical composition) the temperature is high enough for carbon burning to start, but as the electron gas is degenerate, the increasing temperature does not result in an increasing pressure nor in an expansion. This leads to even more fusion reactions, carbon is burnt to mostly iron, incomplete burning results in silicon. At some point, the carbon fusion reactions that started in small parts of the star flash over the whole sphere and are usually strong enough to disrupt the star completely, as the binding energy of the White Dwarf is exceeded. In the occurring reactions, Supernovae Type Ia produce most of the iron in the Universe.

Several models for SN Ia have been developed. Recently the double detonation models have been suggested. This event requires a WD, accreting helium from a companion. The donor star could be a sdB or sdO star, which have ample helium in the envelope to transfer to the WD. At some point, helium rich material can be transferred onto the WD, i.e. by Roche lobe overflow. If about $0.1 M_{\odot}$ has been transferred, the helium ignites and the resulting shockwave triggers the ignition of carbon in the core, leading to the supernova. This process does not require the WD to be pushed over the Chandrasekhar mass. The critical mass is lower than the the

Chandrasekhar mass, possibly as low as $0.9M_{\odot}$. Double detonation supernovae are also referred to as underluminous supernovae as their brightness is usually below the one of normal SN Ia.

2.3.3 Neutron captures

However, even with the tremendous energy release during a supernova, the processes described so far would not be able to explain the existence of elements heavier than iron.

The origin of these elements lies in the slow and rapid neutron capturing reactions. The slow one takes place at comparatively low neutron fluxes as they can be found in stellar interiors during certain fusion reactions, while the rapid capturing requires extreme neutron fluxes as they can occur just before and during a supernova, when the neutronisation and photodisintegration of the atoms has already started. Another recently discussed possibility for the r-process is the merger of two neutron stars (Kilonovae). Because the neutrons are uncharged, the normal coulomb repulsion has no effect on the particles and they can get absorbed by the nuclei without problems.

- **slow process (s)**

In the s process the time between two capturings of a neutron is so long that the corresponding β -decay can happen and decrease the number of neutrons in the nucleus. As there are different cross sections for the capturing of neutrons, some elements are more stable than other and can be enriched. These are mainly isotopes which nuclear shells have been filled completely with neutrons, respectively with neutron numbers $n = 50, 82$ and 126 .

- **rapid process (r)**

If the r process takes place, the neutron flux and the neutron absorption rate are so high, that the time between two absorptions is not long enough for a β -decay. This leads to extremely neutron rich nuclei in which the outer neutrons experience only a small binding energy. As the neutron flux decreases, the decay rate takes over and the neutron enrichment is reduced until long-lived or stable isotopes have been formed. The r process can also stop if instable isotopes are reached that suffer from spontaneous fission, like Curium or Rutherfordium.

Only the r process can explain the very heavy and neutron rich elements which can be found towards the end of the periodic table.

2.4 Runaway stars

After having focused on the stellar evolution and burning processes, a special class of stars needs to be discussed in more detail: The runaway- or hypervelocity stars.

As indicated by their name, hypervelocity stars (HVS hereafter) show a much

higher velocity than average stars, even exceeding the Galactic escape velocity. This type of stars was first mentioned by Brown [2015] and their origin is associated with the tidal interaction between the supermassive black hole in our Galactic center and the disruption of a binary system, leading to the acceleration of one component.

Some of these stars can reach speeds larger than the galactic escape velocity, which means that they are unbound to our galaxy. One example of such an unbound HVS is US708, the second discovered HVS [Hirsch et al., 2005], belonging to the class of He-sdO stars. It was measured to have a Galactic rest frame velocity of 708 ± 15 km/s, resulting in this name. A recent analysis by Geier et al. [2015a] included the transversal space velocity, which revealed the full space velocity of around 1200 km/s at a distance of about 19 kpc and a fast rotation of 115 km/s. This could be a hint for acceleration by a thermonuclear supernova in a former close binary system (see Sect.2.4.1). A reconstruction of the stellar trajectory excluded the Galactic center as a possible region for the origin of US708. Despite these facts, there is still no final proof that this star was really ejected by a supernova, as there is still no direct proof for a nearby supernova explosion in US708's atmosphere.

With the discovery of HE 0437-5439, a main sequence star with a radial velocity of 723 ± 3 km/s [Edelmann et al., 2005], the first HVS most likely originating from the Large Magellanic Cloud was discovered [Gualandris and Portegies Zwart, 2007]. While not being able to reach its current position from the Galactic center within its lifetime, a dynamical ejection from a dense stellar cluster within the LMC is imaginable.

It is not only about discovering new record-breaking stellar velocities, HVS can also be used to determine several properties of our Galaxy. If they originate from the Galactic center, their physical properties, chemical composition and trajectories can be utilized to draw conclusions about the innermost regions that are hardly observable because of the dense dust clouds around it. Not only the mass in the Galactic center, also the mass distribution in the Milkyway halo, so to speak the gravitational potential can be examined as it influences the path of the ejected star. There are different mass models that can be tested when being confronted with HVS tracks [Irrgang, 2014]. Even assumptions on the distribution of the mysterious dark matter halo and its shape can be drawn from the stellar tracks.

But to fully understand the nature of HV-stars, it is essential to know about their origin and the different possible acceleration scenarios.

2.4.1 Supernova ejection scenario

One possible explanation for HVS is them originating from a former binary system in which one of the components underwent a supernovae explosion. Depending on the type and mass of the stars in the system, there are two different scenarios. If the companion is a massive star near the end of his lifetime, a core-collapse supernova is likely to occur. The star needs a mass above $8 M_{\odot}$ for this ending. An example for a HVS which is believed to originate from this scenario is HD271791 [Schaffenroth et al., 2015]. In the other scenario, the companion is a white dwarf. These types of stars are much

to lightweight for a core collapse supernova, but in close binary systems with a helium rich companion, where mass (helium) transfer from one star to the other is possible by i.e stable Roche lobe overflow, the white dwarf can gain enough matter to undergo a double detonation event.

In both scenarios the remaining star is set free (as long as it survived the explosion) and moves at its former orbital velocity. In close binary systems, this orbital velocity can be high enough for the ejected star to be classified as a HVS.

Combined with a fast rotation, the chemical structure of the atmosphere can serve as a clear indicator whether a supernova was involved or not. During the explosion the α -elements generated in the star are ejected and should be found both in the surrounding interstellar medium as well as in the HVS. HIP 60350 can be used as an example. Irrgang et al. [2010] conducted an analysis and showed that the required α -overabundance is consistent with the data.

For stars set free during a SN Ia, Pan et al. [2012] calculated several scenarios to probe the distribution of gas and other matter after the explosion. From their work, they were able to calculate the ratio of nickel to hydrogen on the remnant. It ranges from 10^{-6} for a red giant companion to 10^{-3} for a helium star companion. This is in agreement with results from Liu et al. [2013b] who find an enrichment of iron and nickel of the same magnitude.

2.4.2 Hills mechanism

The Hills mechanism was first described by Hills [1988] to provide evidence for a supermassive black hole (SMBH) in the center of our Galaxy by observing fast, single stars.

In this approach a close binary systems approaches the Galactic black hole and gets disrupted by the strong tidal forces. In this three-body interactions, one of the components stays bound in the gravitational potential of the SMBH while the other one is ejected at a speed up to 4000 km/s. A possible confirmation for this theory was given by Genzel et al. [2010] who observed a cluster of young, B-type stars in the innermost part (0.04 pc) of the Galactic center. This so called S-star cluster (see Fig. 2.12) has a somewhat puzzling nature, as it assumed that stars of all ages should be found in this region. A possible explanation could be the Hills mechanism and therefore the S-cluster consists of the remains of former close binary systems from which one part got ejected. In addition, the elliptical orbits predicted by the Hills mechanism have been observed for the S-stars, as shown in Fig. 2.13.

2.4.3 Disruption of satellite galaxies

Another scenario was proposed by Abadi et al. [2009]. It was discovered that a large fraction of the examined HVS sample seem to cluster in the constellation of Leo and that these stars share a velocity below the average. Some of the trajectories could not be traced back to the galactic center. An explanation might be the disruption of a satellite dwarf galaxy in this region. The common

¹<http://www.astronomynotes.com/ismnotes/s9.htm>

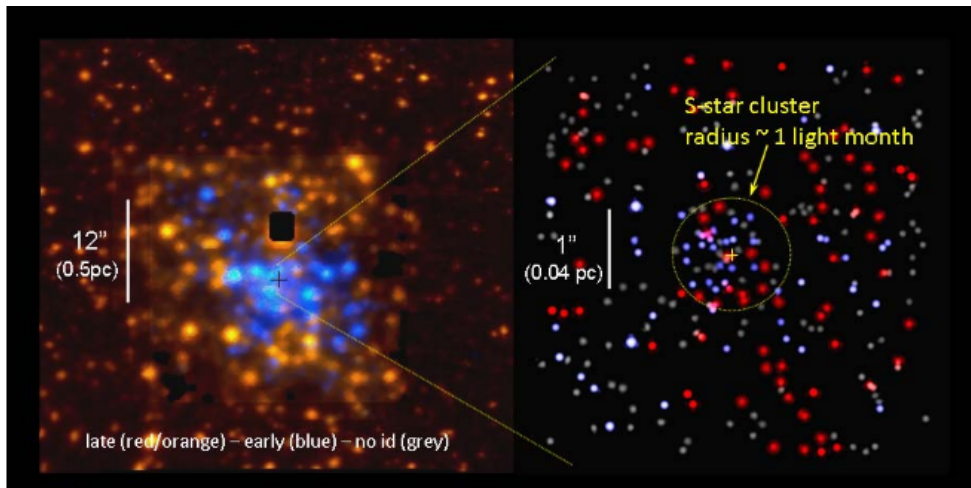


Figure 2.12: Distribution of late-type stars (red) and early-type stars (blue) within one parsec around the central galactic region. The panel on the left shows the S-cluster. Taken from Genzel et al. [2010].

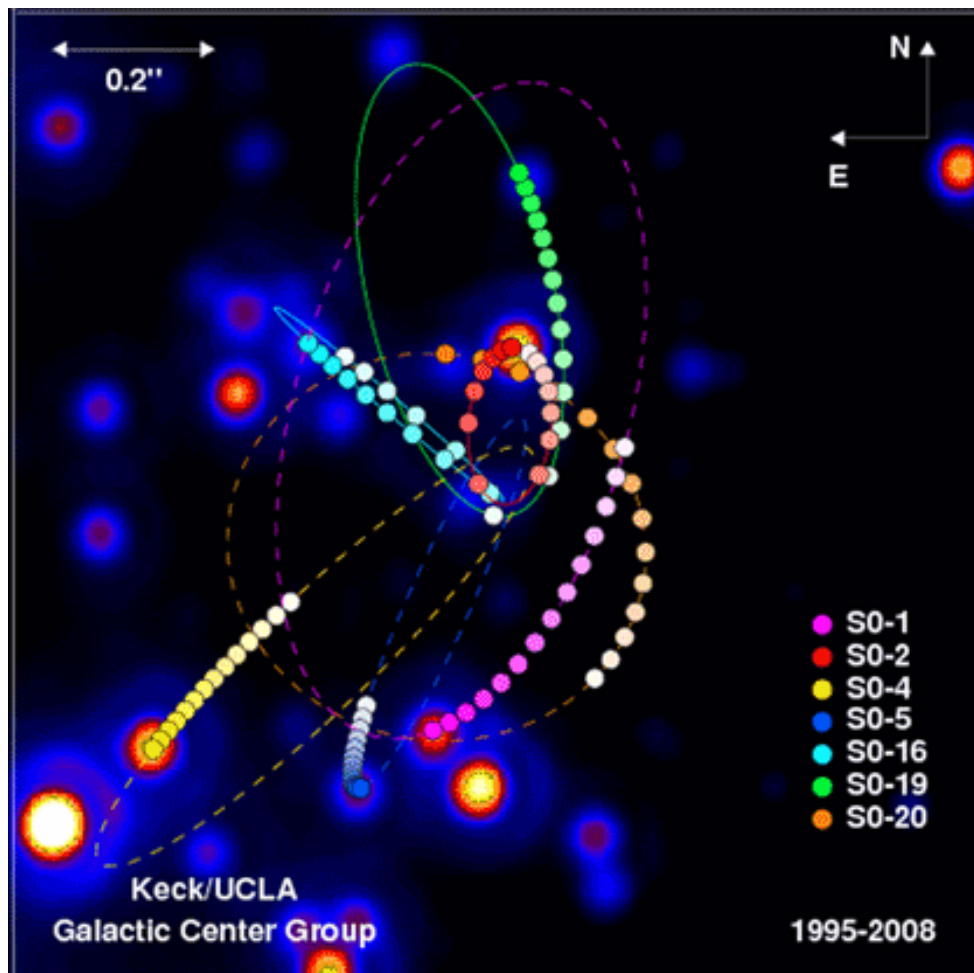


Figure 2.13: Orbits of several S-stars. Taken from ¹

travel time of the stars of about 200 Myrs can be explained with this approach

as well as the angular clustering, being caused by projection effects as the “former galaxy“ was seen edge on. The Hills mechanism would not be able to explain this clustering, as it predicts an isotropic distribution over the sky. In Fig. 2.14 the angular distribution of the observed HVSs across the sky can be seen.

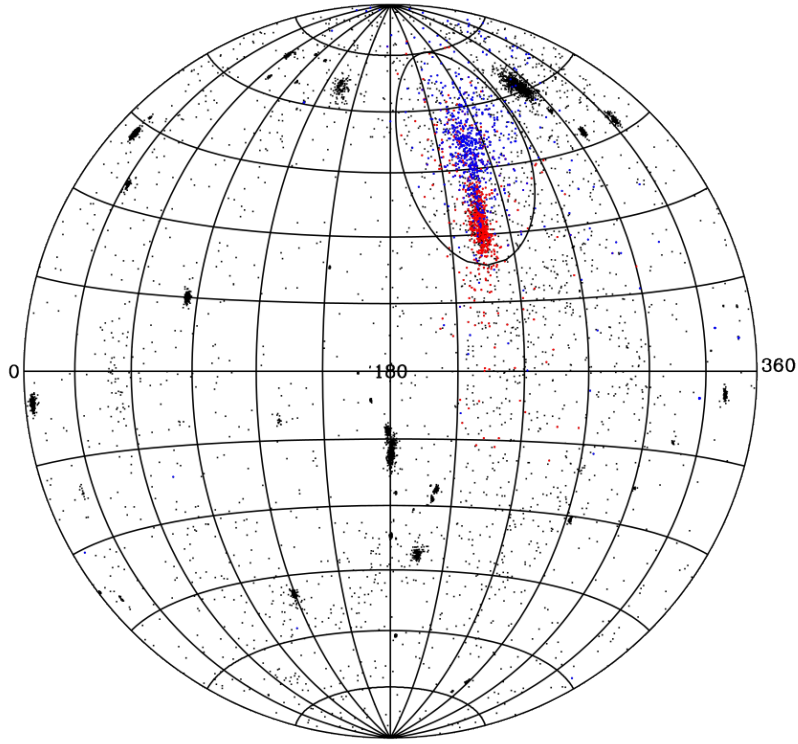


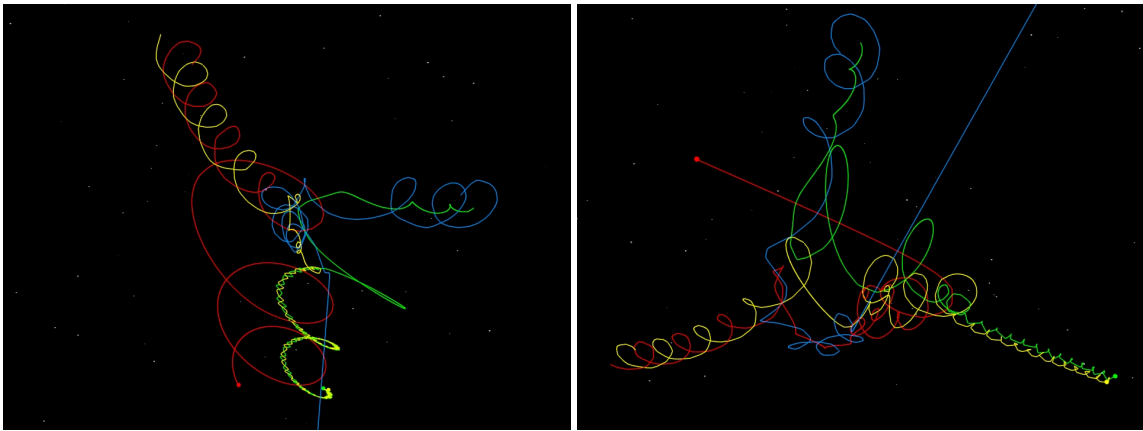
Figure 2.14: Aitoff projection showing stars from a disrupted satellite galaxy (red) and HV stars with velocities $> 400\text{km/s}$ in the tidal stream (blue). The drawn circle has a radius of 26° and almost fully contains the stream. Taken from Abadi et al. [2009]

2.4.4 Dynamical Acceleration

In this scenario HV stars are generated by the gravitational interaction between many stars or binary systems as they happen to occur i.e. in dense stellar clusters. Especially the interactions between two binary systems can accelerate one star from such systems to very high velocities close to 1000 km/s [Leonard, 1991]; The remaining stars form a triplet system.

In another case the two interacting binary systems can form a new double star systems while one star from each former group is accelerated and ejected.

Figure 2.15 illustrates these two scenarios. As interactions in clusters are much more likely because of the higher density of possible interacting partners, the amount of cluster run-aways stars generated this way should be higher than for any other scenario. However, the maximal velocity for such stars remains quite low compared to the other scenarios as shown by simulations [Poveda et al., 1967].



(a) Ejection of a single star

(b) Ejection of two runaway stars

Figure 2.15: Visualization of dynamical interaction between binary systems. Figures kindly provided by Dr. Andreas Irrgang (priv. com.). The two binaries (red&yellow and blue&green) are incoming from the right. (a) formation of a triplet system and ejection of the blue star. (b) formation of a new binary and the ejection of two stars.

3 Model atmospheres and synthetic spectra

This chapter is mainly based on the series of seminar talks on stellar atmospheres given by Prof. Ulrich Heber at the Remeis Observatory Bamberg in April 2016 and the textbook of Carroll & Ostlie from 2006. If any information from other sources are used, they are cited in the usual way.

A short introduction on the stellar interiors had already been given in the previous chapter. This part deals with the stellar atmosphere in particular. By definition, the stellar atmosphere is the interface between the interior parts of a star and outer space and also the part of the star from where the line spectrum emerges and which produces most of the stars radiated energy. The following sections are to explain the ongoing processes in more detail, starting with the basic properties of radiative transfer, followed by necessary simplifications for setting up model atmospheres and the differences between the LTE and the NLTE approach. After discussing line formation and line broadening, the focus will be laid on macroscopic influences like rotation and macroturbulence. Finally a short introduction on photometry and the spectral energy distribution is given.

3.1 Radiative transfer

Spectral lines usually are the most unique feature of a spectrum and differ from star to star. Together with the continuum they originate from absorption and emission processes of radiation in the stellar atmosphere.

Emissions can be treated and described via the emission coefficient η_ν . This equals the number of possible emitters ($\#$) times the frequency-dependent transition probability $\sigma_{\text{transition}}$, summed up over all possible transitions n .

$$\eta_\nu = \#_{\text{emitters}} \times \sum_n \sigma_{\text{transition}}(\nu) \quad (3.1)$$

The absorption can be described in a similar way with the absorption coefficient κ_ν . It consist of the number ob absorbers ($\#$) times the frequency dependent atomic cross section σ_{abs} .

$$\kappa_\nu = \#_{\text{absorbers}} \times \sigma_{\text{abs}}(\nu) \quad (3.2)$$

Another name for κ_ν is opacity.

There are mainly four different processes that make up stellar absorption processes:

- **bound-bound absorption (bb)**

Bound-bound transitions occur within an atom when an electron absorbs a photon of a certain energy and is excited to a higher energy level. Only

photons with an energy exactly matching the band gap between two levels can be absorbed. This process leads to the formation of absorption lines as it is unique for each element and transition.

The atomic probability W_{nm} for a transitions between two levels m and n are linked to the Einstein coefficients. Emission of a photon and therefore the transition from a higher level can be described via

$$W_{nm} = B_{nm} \cdot w_\nu(\nu) \quad (3.3)$$

where $w_\nu(\nu)$ is the spectral energy density and B_{nm} is the Einstein coefficient for this kind of transition. The Einstein coefficient itself derives from the quantum-mechanical transition probability [Demtröder, 2010].

$$B_{nm} = \frac{2}{3} \frac{\pi^2 e^2}{\epsilon_0 h^2} \left| \int \psi_n^* r \psi_m d\tau \right|^2 \quad (3.4)$$

where $e \int \psi_n^* r \psi_m d\tau$ is the transition dipole moment p_{nm} , ψ_m and ψ_n are the wave functions describing the two energy states.. Equation 3.4 can therefore be rewritten as

$$B_{nm} = \frac{2}{3} \frac{\pi^2}{\epsilon_0 h^2} |p_{nm}|^2 \quad (3.5)$$

- **bound-free absorption (bf)**

The bound-free absorptions resemble the (outer) photo effect. Electrons bound to the nucleus can absorb an incoming photon which raises their energy. If the resulting energy is larger than the binding energy for that particular electron, it can leave the atomic union with a kinetic energy E_{kin} and become unbound.

$$E_{kin} = h\nu - (E_{ion} - E_n) \quad (3.6)$$

The kinetic energy can cover various values and therefore the bound-free absorptions contribute to a continuous opacity.

- **free-free transition (ff)**

The free-free transitions describe the changes in energy of a free electron that passes close to an ionized atom. The negatively charged electron is attracted by the positive ion and therefore accelerated. This acceleration of a charge results in the emission of a photon, better known as Bremsstrahlung. In special cases an electron can gain energy while passing an ion by absorbing a photon emitted by the ion.

As these two possibilities neither produce nor require certain energy states, free-free transitions contribute to the continuum of stellar spectra.

- **scattering (s)**

The scattering of photons with unbound electrons is called Thomson scattering. The scattering does not change the number of photons but alters their energy distribution and deflects them from their original path. It can be thought as the absorption of an initial and the emission of final photon with different energies. The changes in energy distribution have an effect on the global opacity of the plasma as well.

As all these processes contribute to the opacity, κ can be rewritten as

$$\kappa = \kappa_{bb} + \kappa_{bf} + \kappa_{ff} + \kappa_s \quad (3.7)$$

In some cases it is preferable to use an averaged opacity. If so, the different wavelength-dependent opacities have to be weighted somehow to take care of their distribution to the overall absorption. This can be done in two ways:

- Weighting with the Planck black body radiation energy density distribution $B_\nu(T)$:

$$\kappa_{\text{Planck}} = \left(\frac{\pi}{\sigma T^4} \right) \int_0^\infty \kappa_\nu B_\nu(T) d\nu \quad (3.8)$$

- Weighting with the temperature derivative of the Planck distribution
This so called Rosseland opacity takes the temperature derivative $u(\nu, T)$ of the Planck distribution to calculate the inverse of the opacity ¹.

$$u(\nu, T) = \frac{\partial B_\nu(T)}{\partial T} \quad (3.9)$$

and

$$\kappa_{\text{Rosseland}} = \frac{\int_0^\infty u(\nu, T) d\nu}{\int_0^\infty \kappa_\nu^{-1} u(\nu, T) d\nu} \quad (3.10)$$

In modern computer programs, the optical depth discretization is based on the Rosseland opacity.

Except for scattering, all the described reactions change the number of photons in an atmosphere and therefore the radiation field, while scattering only alters the direction of radiation. These changes can be described via the radiative transfer equation.

$$dI_\nu = \eta_\nu ds - \kappa_\nu I_\nu ds \quad (3.11)$$

I_ν is the specific intensity as described in equation 2.1 and ds is an infinitesimal small distance element.

The ratio of emission- to absorption coefficient is called source function S_ν .

$$S_\nu = \frac{\eta_\nu}{\kappa_\nu} \quad (3.12)$$

This allows to rewrite the radiative transfer equation.

$$\frac{dI_\nu}{ds} = \kappa_\nu (S_\nu - I_\nu) \quad (3.13)$$

At this step it is helpful to introduce the optical depth τ , for details see Sect. 3.2.

$$d\tau = \kappa dt \quad (3.14)$$

and

$$\tau(\nu, t) = \int_{t=0}^t \kappa_\nu(t') dt' \quad (3.15)$$

¹<http://www-star.st-and.ac.uk/~kw25/teaching/stars/STRUC7.pdf>

The parameter t is measuring the depth in the atmosphere, starting on the outside. The optical depth is an indicator how strongly radiation is damped. It is characteristic for each individual star and is an indicator on how the number of photons is changed by absorption and (re-)emission processes.

A formal solution to the radiative transfer equation can be written as

$$I_\nu(\tau_1, \mu) = I_\nu(\tau_2, \mu) \exp\left(-\frac{\tau_2 - \tau_1}{\mu}\right) + \int_{\tau_1}^{\tau_2} S_\nu \exp\left(-\frac{t_\nu - \tau_1}{\mu}\right) \frac{dt_\nu}{\mu} \quad (3.16)$$

with $\mu = \cos \Theta$ and Θ being the angle to the normal of the plane (see Fig. 3.1).

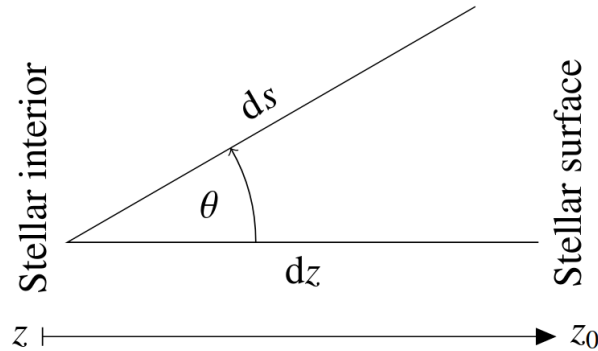


Figure 3.1: Measuring of angle Θ . Adopted from Irrgang et al. [2013].

The specific intensity emitted at a depth τ_2 is exponentially absorbed on its way to depth τ_1 , as described by the first term. In the second term of the equation, the gain in intensity by reemission at t_ν is described. On its way to τ_1 this additional radiation is again partly absorbed. t_ν is just an integration variable ranging from τ_2 to τ_1 .

However Eq. 3.16 is just a formal solution to the radiative transfer equation as the radiation field interacts with the matter and changes its properties which determine the source function by the absorption and emission coefficients. The source function is therefore a function of the specific intensity.

3.2 Simplifications for model atmospheres

It should have become clear by now that the description of stellar atmospheres is nothing close to trivial. Life gets even harder if one wants to model the mentioned processes with a computer in order to get synthetic spectra. Because of this, some assumptions are made on the atmospheres to simplify both description and modeling.

a) **stationarity**

All time-dependent effects and processes are not taken into account. These could be i.e. pulsations or temporary cooler spots on the surface of the star.

b) **no magnetism**

The stars are assumed to show no magnetic fields which could lead to Ze-

mansplitting of lines and therefore would change the form and shape of the calculated synthetic spectra.

c) **homogeneity**

For calculation purposes the stellar atmosphere is usually divided into several layers. The more layers, the more accurate the result. Typically around 70 different ones are used. It is assumed that each of these layers is homogeneous within itself. Possible variations concerning temperature, chemical abundance etc can only be found between different layers.

There are two standard coordinate systems that can be used to describe which thickness (or layer) of the atmosphere is dealt with at the moment. The first one utilizes a parameter z (geometrical depth) that increases outwards and therefore is zero at the center of the star. The second one is a bit more sophisticated. It is expressed by the optical depth τ_ν which is zero at the stellar surface. It is defined by using the frequency dependent absorption coefficient:

$$\tau_\nu = - \int_{z_0}^z \kappa_\nu dz \quad (3.17)$$

where z refers to the other coordinate system introduced beforehand. For a definition of τ in the other coordinate system, see Eq. 3.15. In Fig. 3.2 an overview on the two different systems is given. Measuring the position in the

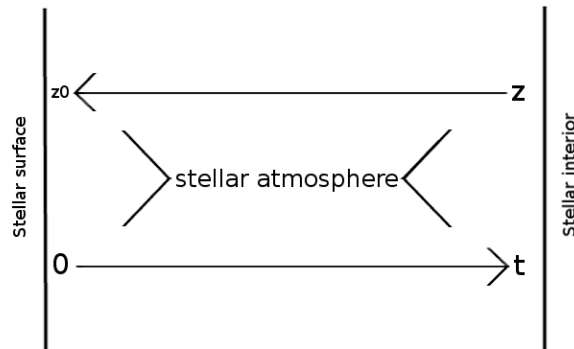


Figure 3.2: Overview on the different stellar coordinate systems and their starting & end values.

atmosphere by the optical depth has the wavelength/frequency dependence as a big disadvantage. It can be solved by switching to the the Rosseland-opacity (see Eq. 3.10).

$$\tau_\nu = - \int_{z_0}^z \kappa_{Rosseland} dz \quad (3.18)$$

This can serve as a frequency-independent indicator for extinction in the stellar atmosphere.

d) **plan-parallel geometry**

The thickness of a stellar atmosphere is usually very small compared to the radius of the star.

$$\frac{\Delta R_{atmo}}{R_*} \ll 1 \quad (3.19)$$

This is why effects occurring from spherical geometry can be neglected. The curvature of the star is not taken into account when calculating model atmospheres as the important processes happen on such small distances (i.e. the mean free path of a photon or an electron) that the neglect of curvature does not induce any negative effect.

e) **radiative equilibrium**

The temperature of a star has a main influence on how energy is transported in the atmosphere. In hot stars, energy transport by radiation is the main process, while convection becomes less important with higher temperatures. The impact of convection on the energy transport is neglectable for the type of stars discussed in this work.

If an atmosphere is in radiative equilibrium, the energy lost per unit volume due to emission has to be compensated by the absorbed energy and vice versa.

$$\int_0^\infty \int_{4\pi} \kappa_\nu I_\nu d\Omega d\nu \equiv \int_0^\infty \int_{4\pi} \eta_\nu d\Omega d\nu \quad (3.20)$$

The energy conservation is directly linked to flux conservation. However, the flux can be linked to the effective temperature by the Stefan-Boltzmann law.

$$T_{\text{eff}} = \sqrt[4]{\frac{F}{\sigma}} \quad (3.21)$$

f) **hydrostatic equilibrium**

The atmosphere is assumed to be in hydrostatic equilibrium. Equation 2.12 has to be modified to adopt the effects of radiative acceleration g_{rad} .

$$g_{\text{rad}} = \frac{1}{\rho(z)c} \int_0^\infty \kappa_\nu F_\nu d\nu \quad (3.22)$$

The modified equation of hydrostatic equilibrium is given by

$$\frac{dP}{dz} = -\rho(z)(g - g_{\text{rad}}) \quad (3.23)$$

with g , the constant surface gravity.

$$g = \frac{GM}{R_*^2} \quad (3.24)$$

g) **static atmosphere**

Some stars feature a strong stellar wind which usually goes hand in hand with a large mass loss over time. This stellar wind could easily affect the cores of weak lines and the effects grows the further out in the atmosphere the lines are produced. Lines formed in deeper layers of the atmosphere are usually not affected.

As Kudritzki [1992] showed for main sequence O-stars, even small mass loss rates can affect the line cores. However, as sdO stars show a much higher surface gravity than main sequence O-stars and are not known for having strong winds, the mass loss is usually negligible. A counterexample would be

LSE 153, a post-AGB star which is more luminous than a normal He-sdO and shows an asymmetry in a N V resonance doublet, pointing towards a significant mass loss rate [Haas, 1997]

All the assumptions (and simplifications) mentioned here lead to a set of differential equations that refer to the temperature and the surface gravity. In combination with other equations (e.g. charge conservation) they have to be solved simultaneously to calculate an representative atmosphere. The details and methods of calculations will be explained in Sect.4

3.3 Level population (LTE vs. NLTE)

To understand the basic physics in stellar atmospheres and get insight on statistical plasma properties, two main approaches can be used. The LTE and the NLTE approach.

LTE stands for Local Thermodynamical Equilibrium, with an emphasis on local. This implies that the temperature is the same for certain, non-infinitesimal, plane-parallel layers. In this description, interactions with electrons dominate any radiative processes. The occupation numbers for the energy levels can be determined from the Saha and Boltzmann equation (Eq. 3.27) in combination with the assumed Maxwell energy distribution

$$p(\nu)d\nu = \left(\frac{m}{2\pi kT}\right)^{3/2} \exp\left(-\frac{m\nu^2}{2kT}\right) 4\pi\nu^2 d\nu \quad (3.25)$$

and the demanded conservation of charge.

$$\sum_I N_I Z_I - n_e = 0 \quad (3.26)$$

Z_I is the charge associated with level I . The Saha ionization equation for two neighboring ionization states N_{up} and N_{low} reads

$$(N_{\text{up}}/N_{\text{low}}) = \frac{A(kT)^{3/2}}{N_e} \exp -\chi_0/kT \quad (3.27)$$

χ_0 is the ionization energy, N_e is the number density of free electrons and A is a constant factor. The Boltzmann excitation formula can be written as

$$\frac{n_i}{n_j} = \frac{g_j}{g_i} \exp\left(-\frac{E_j - E_i}{kt}\right) \quad (3.28)$$

with the statistical weights g_i, g_j , the energy of the i th excited state E_i and the corresponding occupation number density.

All these equations make the calculation of the local source function possible. However, there are certain cases where the LTE approach is not accurate enough anymore.

Especially in hot stars and giants with a low particle density, deviations start to occur. In the first case, the high temperature comes hand in hand with an intense radiation field ($\propto T^4$) where the mean free path for photons is larger than for an

electron. In the second case, low densities result in a larger mean free path for photons, making it easier to link two zones with different temperatures, resulting in interactions.

Both problems can be dealt with by using the Non-LTE approach (NLTE). Here the occupations numbers have to be determined simultaneously with the radiation field, which itself is dependent from the temperature in all layers and the local occupation numbers there. This drastically increases the complexity of the problem and therefore the numerical efforts that have to be conducted to solve the occurring problems.

While the Maxwell distribution is still valid, the Saha-Boltzmann equations has to be replaced by demanding statistical equilibrium, where the occupation number of a certain level, n_i are no longer determined by the local temperature, but shall be invariant over time.

$$\frac{dn_i}{dt} = 0 \quad (3.29)$$

This means that populating and depopulating processes between two levels i and j have to be balanced. This can be expressed in the rate equation, where rate coefficients for radiative transitions (R) and collisionally transitions (C) are used and have to be balanced.

$$n_i \sum_{j \neq i} (R_{ij} + C_{ij}) = \sum_{j \neq i} n_j (R_{ji} + C_{ji}) \quad (3.30)$$

The left hand side of the the equation are the processes depopulating level i , the right hand side shows the processes populating level i . Contributions to R_{ij} come from radiative transitions like line absorption and -emission as well as from photoionization and recombination while C_{ij} is based on inelastic collisions like line excitation and de-excitation or collisional excitations/recombinations.

For radiative bound-free transitions R_{ij} can be written as

$$R_{ij} = 4\pi \int_{\nu_0}^{\infty} \alpha_{ij}(\nu) \frac{J_\nu}{h\nu} d\nu \quad (3.31)$$

with the atomic cross-section α_{ij} , the specific intensity J_ν integrated over all angles and the threshold frequency ν_0 which defines the energy needed for the transition to a free state. The downward process is given by R_{ji} .

$$R_{ji} = \frac{n_i^*}{n_j^*} \cdot 4\pi \int_{\nu_0}^{\infty} \alpha_{ij}(\nu) \left[\frac{2h\nu^3}{c^2} + J_\nu \right] \exp\left(-\frac{h\nu}{kT}\right) d\nu \quad (3.32)$$

with n_i^*/n_j^* being the ratio of LTE occupation numbers according to the Saha equation.

Collisional excitations can be described as

$$C_{ij} = n_e \int_{\nu_0}^{\infty} \sigma_{ij} f(\nu) \nu d\nu \quad (3.33)$$

with the collisional cross-section σ_{ij} , the electron density n_e and the velocity distribution $f(\nu)$. Again ν_0 is is the minimum energy necessary for the transition to

occur. From the balance equation, C_{ji} is defined as

$$C_{ji} = \frac{n_i^*}{n_j^*} C_{ij} \quad (3.34)$$

with the ratio of LTE population numbers $\frac{n_i^*}{n_j^*}$.

3.4 Line formation & -broadening

Absorption lines are the key feature of stellar spectra. They originate from discrete transitions between different atomic states. The wavelength dependent absorption coefficient κ_ν at the line wavelength is higher than the continuum opacity as additional bound-bound transitions can occur at certain energies. Photons from spectral lines originate from outer parts of the atmosphere, compared to continuum photons. This implies that the spectral lines come from cooler parts of the atmosphere.

The width of spectral lines can give valuable information about stellar properties, i.e. the surface gravity. Unfortunately there are several processes involved in broadening the lines, making it more difficult to measure these properties. The most common effects are discussed hereafter.

- **Natural damping**

Even under optimal conditions absorption lines cannot be infinitesimally sharp. By having in mind that every excited state in an atom or ion has a finite lifetime $\Delta\tau$ and applying Heisenbergs uncertainty principle

$$\Delta E \times \Delta\tau \geq \frac{\hbar}{2} \quad (3.35)$$

it can be seen that the finite lifetime results in an uncertainty of the energy level ΔE . The lifetime of a level is directly linked to the Einstein coefficient for spontaneous emission A_{jk} between level j and k.

$$\Delta\tau = \frac{1}{\sum_{j \leq k} A_{jk}} \quad (3.36)$$

The natural line width can be described via a Lorentz profile:

$$I(\omega) = I_0 \frac{\gamma/2\pi}{(\omega - \omega_0)^2 + (\gamma/2)^2} \quad (3.37)$$

with ω_0 , the central frequency [Demtröder, 2010].

- **Pressure broadening**

Pressure broadening occurs when the radiating atom collides with other particles, i.e electrons or ions. During these collisions the phase of the originally emitted radiation gets disturbed. The profile function for the pressure broadening is a Lorentz profile with the damping constant $\gamma = 2/\tau$, whereas τ is indirectly proportional to the density of collision partners. τ is also the mean time between two collisions.

- **Stark effect**

The Stark effect is closely related to the pressure broadening and describes the splitting and/or shifting of energy levels (and therefore spectral lines) in static electric fields. The stronger the electric field, the stronger the splitting gets. As a high pressure leads to a closer distance between two atoms, the Coulomb forces will get stronger in this case, leading to an enhanced electric field.

The Stark effect can be divided in the linear - and the quadratic Stark effect. The first one depends linear on the electric field and affects atoms with an intrinsic dipole moment, such as HeII, while the second one shows a quadratic dependence on the electric fields and shifts the levels of the other atoms.

- **Thermal Doppler broadening**

As all particles in the stellar atmosphere are in constant motion, the Doppler effect plays an important role, at least if absorbing atoms are considered to be moving within the line of sight of absorbed radiation. This expands the range of absorbable frequencies to doppler-shifted ones. The particle velocities along the line of side follow a Maxwell distribution

$$\omega_x(v_x) = \frac{1}{\sqrt{\pi}v_{\text{thermal}}} \cdot \exp\left(-\frac{v_x^2}{v_{\text{thermal}}^2}\right) \quad (3.38)$$

The resulting absorption profile represents a Gaussian profile, centered at the restframe velocity v_0 . By introducing Δv as $v - v_0$ it is described via

$$\varphi_v = \frac{1}{\sqrt{\pi}\Delta v_{\text{thermal}}} \cdot \exp\left(-\frac{\Delta v^2}{v_{\text{thermal}}^2}\right) \quad (3.39)$$

- **Microturbulence**

Microturbulence is a free parameter that is often necessary to bring together model spectra and data. It describes chaotic, non-thermal turbulences on scales much smaller than optical wavelength and is modeled similar to the thermal movement, the only difference is the usage of the micro velocity v_{micro} instead of the thermal velocity.

$$\omega_x(v_x) = \frac{1}{\sqrt{\pi}v_{\text{micro}}} \cdot \exp\left(-\frac{v_x^2}{v_{\text{micro}}^2}\right) \quad (3.40)$$

Again, the calculated profile is a Gaussian one.

All the effects described beforehand occur in a star at the same time. Therefore, the profiles of the different effects overlap, which has to be taken into account. Mathematically, the overlap of the different profiles is treated with a convolution. The Gaussians of microturbulence and thermal broadening are convolved and form another Gaussian, while the two Lorentzians profiles of natural damping and pressure broadening form another Lorentzian. In the end, the convolution of a Gaussian and a Lorentzian results in a Voigt function. This type of function cannot be expressed analytically and has to be approximated numerically.

However, it can be written as

$$V = \frac{1}{\sqrt{\pi}\Delta\nu_D} \times H(a, v) \quad (3.41)$$

with

$$H(a, v) = \frac{a}{\pi} \int_{-\infty}^{+\infty} \frac{\exp(-y^2)}{(v-y)^2 + a^2} dy \quad (3.42)$$

3.5 Rotation and Macroturbulence

All the effects discussed in the previous section occur on a microscopic scale and are based more or less on the interactions of atoms, ions and electrons. There are other processes that take place on a more macroscopic scale.

The most prominent effect is the rotational broadening. A certain number of stars is known to have rotational velocities well above 10 km/s. Especially the supernova-ejection-remnant candidates among the hypervelocity stars rotate very fast due to the conservation of angular momentum. The rotational velocity of a star around its pole cannot be directly measured. The only approach is to measure the velocity projected on the line of sight to that star. Seeing the star under an inclination i , the measurable velocity $v_{rot,m}$ is defined as

$$v_{rot,m} = v_{rot} \sin(i) \quad (3.43)$$

As it is not possible to resolve the surface of a star today (but possibly in the future, see e.g. Dravins et al. [2010]) the flux measured with a detector is always the integrated flux over the whole stellar disk. But as the star rotates, and one part of the atmosphere moves towards us and induces a Doppler shift towards the blue, the other side is moving away from us, resulting in a Doppler shift towards the red. These different shifts lead to a broadening of lines. Technically it is treated by convolving the measured flux with a rotational profile which is implemented in the analysis program SPAS (see Sect. 4.8). The following image (Fig. 3.3) illustrates the influence of rotational velocities on stellar profiles.

Another property of several stars is macroturbulence. This large scale turbulent motion in „cells“ is very similar to microturbulence. According to Aerts et al. [2009] it is directly linked to pulsational effects. Each of the cells causing macroturbulent effects moves at a certain velocity within the stellar interior and the atmosphere and therefore emits a specific Doppler shifted spectrum. The size of these cells is large enough for photons not to interact with other areas. As already explained beforehand it is not possible to resolve a stellar surface and therefore the detected flux is integrated over all Doppler shifted cells, leading to a broadening of spectral lines.

¹<http://www.astro.uu.se/~ulrike/Spectroscopy/PS/Rotationsprofil.jpg>

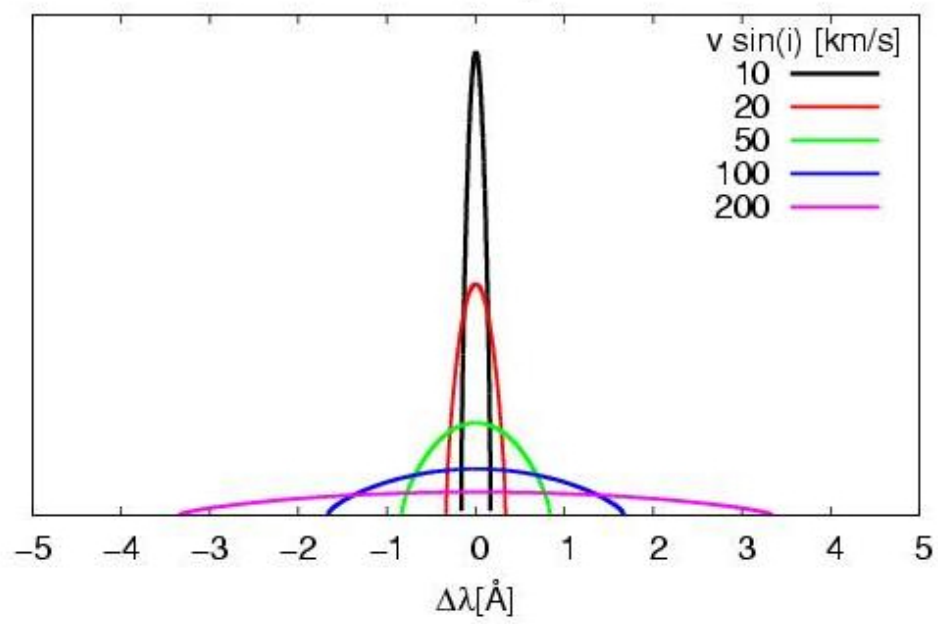


Figure 3.3: Influence of the rotational velocity on a line profile at different velocities. Adopted from: ¹

4 Numerical methods

To calculate model atmospheres of stellar objects it is necessary to keep all of the properties and physical processes in mind and implement them into a program. Especially NLTE model atmospheres are a much harder task than pure LTE atmospheres as the total line opacity can be determined locally. But even LTE conditions are difficult enough, as the sheer number of lines requires some statistical method to be dealt with in a reasonable time (see Sect. 4.1).

Usually being developed years and even decades ago, the codes to model stellar atmospheres suffered from the lack of computing power in those days and therefore were only able to bare a low number of lines and transitions. As the power of CPUs has risen, so did the abilities of the programs. Today, the calculation of millions of lines under full NLTE conditions is possible. However, without certain assumptions and simplifications, even today's computer could hardly handle the sheer amount of necessary calculations. In addition there are several (mathematical and numerical) tricks and techniques that help to reduce the calculation time to a minimum.

In a first step, several of these techniques will be explained, followed by a detailed insight of the programs used in this thesis.

4.1 Complete Linearization

The problem in computing model atmospheres is solving a highly coupled set of non-linear equations. These equations are the radiative transfer equation, the equation of hydrostatic equilibrium, the equations for conservation of charge and particle number, the radiative equilibrium equation and equations defining the opacities. A first steps towards solving this mathematical mess were made by Auer and Mihalas [1969] by introducing the method of complete linearization which is described hereafter. For a brief summary, see also Hubeny and Lanz [2003].

The idea is to describe a stellar atmosphere by a set of vectors ψ_d for all different depth-points. The depth-points range from 1 to ND, the number of depth-points. Each vector ψ_d can be written as

$$\psi_d = (J_1, \dots, J_{NF}, N, T, n_e, n_1, \dots, n_{NL}) \quad (4.1)$$

The meaning of the different symbols is:

- J_i is the mean intensity of radiation at the i th frequency point
- N : total particle number density
- T : temperature
- n_e : electron density
- n_j : number density population of level j

- NF: number of frequencies
- NL: number of energy levels

According to Hubeny and Lanz [1995] the set of equations can be rewritten as

$$P(x) = 0 \quad (4.2)$$

with x being a new vector formed from the previous vectors ψ_d .

$$x = (\psi_1, \dots, \psi_{ND}) \quad (4.3)$$

Equation 4.2 can be solved with the Newton-Raphson method:

$$x^{n+1} = x^n - J[x^n]^{-1}P[x^n] \quad (4.4)$$

with the Jacobi matrix J , being defined as

$$J_f(a) = \frac{\partial f}{\partial x}(a) = \frac{\partial(f_1, \dots, f_m)}{\partial(x_1, \dots, x_n)}(a) \quad (4.5)$$

In this special case (finite difference solutions, maximum of second order equations), J has a block-triagonal form. This implies that equations 4.2 can be rewritten as [Mihalas, 1978]:

$$-P_d[x^n] = A_d^n \delta \psi_{d-1}^n + B_d^n \delta \psi_d^n - C_d^n \delta \psi_{d+1}^n = L_d^n \quad (4.6)$$

Resulting from the Newton-Raphson method, the number of iterations is represented by n , while A, B and C are matrices of the dimension $NN \times NN$ with $NN = NF + NL + 3$. L_d^n is the residuum vector at the depth-point d , NF is the number of frequencies, NL is the number of levels.

Instead of explicitly inverting the Jacobian, equation 4.4 can be solved by applying a block-Gaussian elimination procedure [Hubeny and Lanz, 1995]. This means that for each depth point, only one $NN \times NN$ matrix has to be inverted.

The total computation time scales as

$$NN^3 \times ND \times N_{iter}$$

4.2 Accelerated Lambda Iteration

The second, big approach to solve the problems coming hand in hand with atmospheric calculations is the Lambda iteration. In principle it evaluates the source function from the equation of statistical equilibrium

$$S = (1 - \epsilon)J + B\epsilon \quad (4.7)$$

Here, B is the Planck function, J is the mean intensity averaged over all frequencies and ϵ is the collisional destruction probability for an excited level. Afterwards, the radiative transfer equation (Eq. 3.11) can be solved with the new source function.

A formal solution to equation 3.11 is

$$I_{\mu\nu} = \Lambda_{\mu\nu}[S_\nu] \quad (4.8)$$

with the Lambda Operator Λ operating on S_ν . As Hubeny and Lanz [2003] showed, the source function can be rewritten as

$$S = (1 - \epsilon)\Lambda[S] + \epsilon B \quad (4.9)$$

As the method is called Lambda iteration, this step is conducted multiple times and therefore

$$S^{n+1} = (1 - \epsilon)\Lambda[S^n] + \epsilon B \quad (4.10)$$

The main advantage is that, in contrast to the complete linearization, the time consuming matrix inversion can be skipped completely because all coupling is treated iteratively. But it turned out that the solutions of this method tend to stabilize at a certain point before reaching real convergence, therefore the global minimum of the best solution is hardly reached.

To improve the method, a technique called operator splitting can be introduced [Cannon, 1973]. As a result, the Lambda operator can be written as

$$\Lambda = \Lambda^* + (\Lambda - \Lambda^*) \quad (4.11)$$

where Λ^* is called approximate Lambda operator. Applying this to Eq. 4.9 provides

$$S^{n+1} = (1 - \epsilon)\Lambda^*[S^{n+1}] + (1 - \epsilon)(\Lambda - \Lambda^*)[S^n] + \epsilon B \quad (4.12)$$

It can be seen that the former Lambda operator now consists of two parts, whereas the approximate Lambda operator (Λ^*) acts on the latest step of the iterated source function and the difference between the exact operator and the approximate one acts on the known “old” source function [Hubeny and Lanz, 2003].

According to Hubeny and Lanz [2003] Equation 4.12 can be rewritten as

$$\delta S^n \equiv S^{n+1} - S^n = [1 - (1 - \epsilon)\Lambda^*]^{-1}[S^{FS} - s^n] \quad (4.13)$$

Here S^{FS} stands for the formal solution of the source function. The term $[1 - (1 - \epsilon)\Lambda^*]^{-1}$ is called the “acceleration operator”.

According to Hubeny and Lanz [1995] the ALI method can also be described with regard to the mean intensity:

$$J_\nu^n = \Lambda_\nu^* S_\nu^n + (\Lambda_\nu - \Lambda_\nu^*) S_\nu^{n-1} \quad (4.14)$$

The mean intensity is described via two terms, a correction term, known from the previous iteration and the first one, describing the influence of a simplified lambda operator on the source function. The radiative transfer equations are eliminated from the coupled systems [Hubeny and Lanz, 1995].

The main advantages of the ALI method all come back to the approximated lambda operator. This operator has to be easy and cheap to invert and must still describe the underlying physics well enough. The three main forms of the approximated lambda operator are the diagonal form, the tridiagonal or multi-band form and the

Gauss-Seidel approximate operator. Mainly the diagonal form

$$\Lambda^* = \Lambda^*(\tau)\mathbf{1} \quad (4.15)$$

(with the unit diagonal matrix $\mathbf{1}$) is used in today's applications and referred to as Jacobi method. Its construction will be explained in more detail hereafter. The usage of a diagonal operator is comparatively simple as its inversion is just a scalar division. There are several methods to get to a diagonal form of the exact lambda operator.

- **General approach**

The diagonal element of the Λ matrix at a certain depth point d equals the mean intensity for a source function which is zero everywhere but at the selected depthpoint d ($S_d = 1$ and $S_i = 0, (i \neq d)$) [Hubeny and Lanz, 2003].

$$\Lambda_{dd} = \Lambda[\delta(\tau_d - \tau)] \quad (4.16)$$

If the lambda operator is frequency and angle-dependent, the specific intensity instead of the mean intensity has to be used. Unfortunately the convergence speed decreases with spatial resolution.

- **Short characteristics**

Olson and Kunasz [1987] suggested applying the method of short characteristics to evaluate the approximate lambda operator and to get an explicit expression for Λ^*

$$\Lambda_\nu^* = 1 - \frac{1}{2} \int_0^1 \left(\frac{1 - e^{-\Delta\tau_{d-1/2}}}{\Delta\tau_{d-1/2}} + \frac{1 - e^{-\Delta\tau_{d+1/2}}}{\Delta\tau_{d+1/2}} \right) d\mu \quad (4.17)$$

where

$$\Delta\tau_{d-1/2} = \tau_d - \tau_{d-1} \quad (4.18)$$

The idea of short characteristics is to divide the medium into different cells and approximate the source function by a linear or quadratic polynomial in each of these cells. The formal solution for the specific intensity within one cell would be given by

$$I(\tau_d) = I(\tau_{d+1})e^{-\Delta\tau_{d+1/2}} + \int_{\tau_d}^{\tau_{d+1}} S(t)e^{-(t-\tau_d)} dt \quad (4.19)$$

The integral can be evaluated analytically and the boundary values of the specific intensity are constrained by boundary conditions or the emerging intensity from neighboring cells [Hubeny and Lanz, 2003].

- **Feautrier scheme**

Rybicki and Hummer [1991] applied an approach based on the Feautrier method, where symmetric and antisymmetric parts of the specific intensity are used .

$$j_{\mu\nu} = [I(+\mu, \nu) + I(-\mu, \nu)]/2 \text{ and } h_{\mu\nu} = [I(+\mu, \nu) - I(-\mu, \nu)]/2 \quad (4.20)$$

Hubeny and Lanz [2003] showed that

$$\mu(dh_{\mu\nu}/d\tau_\nu) = j_{\mu\nu} - S_\nu \quad (4.21)$$

$$\mu(dj_{\mu\nu}/d\tau_\nu) = h_{\mu\nu} \quad (4.22)$$

If $h_{\mu\nu}$ is eliminated, the following form can be applied

$$\mu^2(d^2J_{\mu\nu}/d\tau_\nu^2) = j_{\mu\nu} - S_\nu \quad (4.23)$$

Now, S_ν is assumed to be fully specified and equation 4.23 can be solved for one ν -point at a time. After tedious algebra and properly set boundary conditions, a tridiagonal system is found.

$$-A_d j_{d-1} + B_d j_d - C_d j_{d+1} = \bar{S}_d \quad (4.24)$$

d is again the depth point and \bar{S}_d equals the source function everywhere but at the boundaries at $d=1$ and $d=ND$, with ND =number of depth points. Equation 4.24 can be solved by a standard Gaussian elimination method [Hubeny and Lanz, 2003].

However, despite all the useful simplifications that the ALI method offers, a non-linear system of equations arises if Eq. 4.14 is used within the equations for the statistical, hydrostatic and radiative equilibrium.

While the ALI method can be dealt with comparatively fast by computers, it still tends to converge slower than the method of complete linearization.

4.3 Acceleration of convergence

There are several approaches to speed up the calculations. Most of them aim at reducing the sizes of the matrices to be inverted, reducing the number of levels or the necessary iterations to reach convergence. The two most common ones are briefly described in this short section. For a more complete overview, also on other possible methods, see i.e Hubeny and Lanz [2003]

- **Ng-acceleration**

The Ng-accelerations in of the the mathematical acceleration of convergence procedures [Auer, 1987]. The basic idea is to re-use solutions from previous iterations in combination with the last one to construct the state vector describing the desired parameters. Usually, a linear combinations of the previous iterates is used. The Ng accelerations is usually not used for every iteration. The typical usage is to start it at or around the 7th iteration and repeat it every 4 iterations [Hubeny and Lanz, 2003].

- **Kantarovich acceleration**

In the Kantarovich accelerations, the inverse of the Jacobian is kept fix after a certain number of iterations so that all following steps use the same matrix. This shortcuts the time consuming matrix inversions. Hubeny and Lanz [2003] claim that this method is very robust and only two to four iterations at the beginning are needed to set up a “good enough“ Jacobian. After several

iterations, the matrix should be refreshed by recalculating it using the current solution. A detailed description and analysis of the Kantarovich acceleration method and its application to complete linearization is provided by Hubeny and Lanz [1992].

Additional concepts like opacity sampling, superlines, superlevels or the hybrid CL/ALI approach are helping in speeding up the calculations. The following sections give an overview on these topics.

4.4 OS vs ODF

No matter which method is chosen to compute the stellar atmosphere, a reduction of the number of frequency points (easily several millions; one million lines, five or more frequency points per line) is always helpful to reduce the necessary computation time. To get a sufficiently correct model, each absorption line of every present element would have to be included. However, this is not practical at all in real life. On the one hand, not all the absorption lines are known, on the other hand, the number of required frequency points would easily get out of hand. To compensate for this problem, two approaches are common today and will be presented hereafter. The **Opacity sampling (OS)** is a statistical approach to estimate the total opacity. Described i.e. by Carbon [1984] the OS method consists of choosing a grid of frequency points covering the interesting part of a spectrum and evaluating the necessary equations only at these points. This means that for each tic, the total opacity of that point is added up, no matter from which line and transition it originates. The density of grid points is adjusted to the desired wavelength range and density of lines. The more frequency points are used, the better the results, partly because the line cores, that originate from the largest opacities, are usually quite narrow. However, according to Hubeny and Lanz [1995] not more than 1000 points are required to match a model to observational data without significant deviations. If too few points are used, the danger of missing the core of some important lines increases.

With the **Opacity distribution function (ODF)** the actual cross sections are represented by a smooth varying function. Therefore the spectra is divided into equal parts. In each of these sections, the absorption probabilities are rearranged so that they can be represented by a function, the opacity distribution function. This can be represented by a much smaller amount of points than the actual, detailed opacities. It's peak is placed at the mean frequency of the selected frequency range, weighted by the cross sections. Usually a monotonically decreasing function towards the strongest individual line is chosen. For a detailed description, see i.e. Hubeny and Lanz [1995]. As with the OS method, narrowing the frequency intervals enhances the accuracy, while introducing cutbacks on the computation time. While being completely insensitive to missing opacities and a significantly reduced computation time, the ODF method has large disadvantages when it comes to overlapping transitions this would lead to discontinuity at the edges of the representational functions. In addition the chemical composition of the atmosphere has to be fixed beforehand.

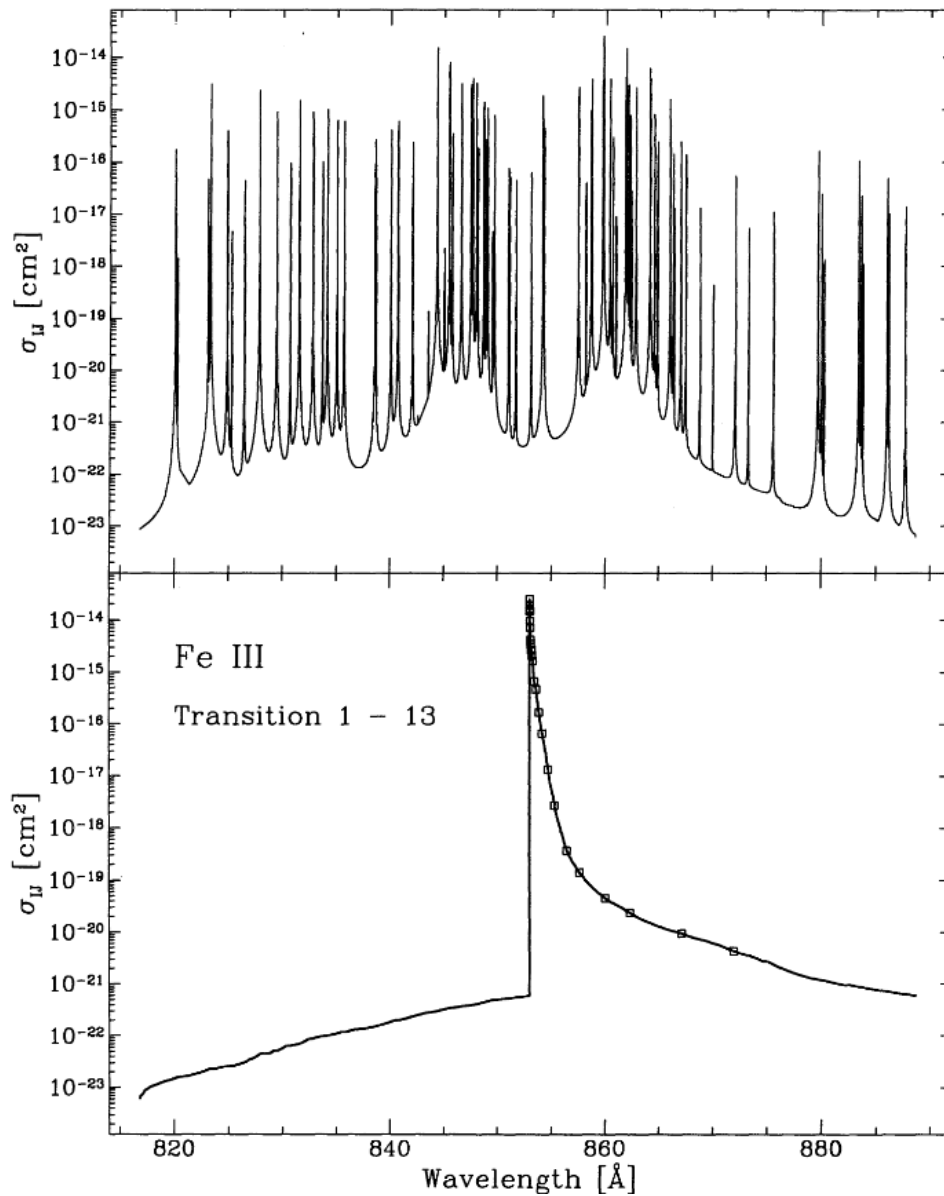


Figure 4.1: .

Comparison between actual cross sections (upper panel) and the ODF constructed from it (lower panel). The small square indicate the frequency points for representing the function. Adopted from Hubeny and Lanz [1995].

4.5 Influence of Fe/Ni elements

Among all the elements that can be included in a calculated atmosphere, the so called Iron group elements play a special role.

Iron is the most stable element, as it has the highest binding energy per nucleon in the core. It has numerous valence electrons and together with a not completely filled 3D shell, a variety of excited energy states is possible. These different states result in an enormous amount of absorption lines. However, most of them cannot be seen in optical spectra. In the UV, or even worse, in the extreme UV, there's a real wealth of iron lines, so that basically each visible line of another element is blended with iron. For low resolution spectra this might lead to a new "quasi" continuum

level, which is lower than the normal continuum and therefore might lead to lower abundances and incorrect values for atmospheric parameters. In such cases, it is always helpful to have optical spectra to crosscheck the data.

But the numerous lines of iron group elements do not only affect the (E)UV spectra where those lines are visible, but also the line profiles in the optical by effects of line blanketing. This describes the influence of absorption and emission to the temperature stratification and enhances the red to IR part of the spectra on the cost of the UV and blue one. It can be divided in three different processes, blocking, surface cooling and backwarming. Blocking is the absorption of radiated energy by one of the numerous metal absorption lines. But as the total flux has to be conserved, more flux has to come from the continuum. This can be reached by a steeper temperature gradient that increases the temperature in the parts of the atmosphere where the continuum is “produced“ (backwarming).

Surface cooling describes the effect of a temperature reduction in the outer parts of the stellar atmosphere by collisionally excitation, followed by radiative de-excitation. The radiated photons are likely to leave the (thin) atmosphere without any following interactions. Their energy is transported away, lowering the surface temperature [Haas, 1997],

All the discussed effects remain valid for nickel, which has even more lines than iron and shows much stronger effects on the properties of the atmosphere and the spectra. Some stars show a very high nickel abundance, well above one. This can be caused by the radiative pressure which drives nickel to upper parts of the atmosphere, where it can be detected more easily. This counteraction against gravitational sedimentation becomes more easy when the element has a high radiative crosssection, meaning it can absorb photons of different energies well. Nickel with its large amount of lines fulfills this criterion excellently [Chayer et al., 1994].

Unfortunately, it is very time consuming to include iron and nickel in stellar atmospheres, as all the lines consume a huge amount of CPU time. Therefore, these elements are usually included in a later stage of the analysis, when abundances for lighter elements have already been (roughly) calculated and can be used as starting values for the atmospheres with iron and nickel.

But it is usually worth the effort, because especially the iron abundance can tell a lot about the life and the history of a star. It can be used to determine the affiliation to stellar populations and give a very rough estimate on the stellar age. As in the case of US708 it can be used to proof or refute the supernova scenario as origin of the high velocity.

4.6 TLUSTY

There are several programs to compute model stellar atmospheres which include one or more of the approaches explained above. One of them is the Fortran77 based TLUSTY ¹, which features a unique combination of methods. The idea is to combine the advantages of the complete linearization and the accelerated lambda iteration without suffering from their specific disadvantages.

¹<http://nova.astro.umd.edu/>

4.6.1 CL/ALI-method

In the so called CL/ALI approach, the frequency points are divided into two different groups. The first group is treated with complete linearization and contains the frequencies at the strongest opacities, i.e. the line cores, and some points near important continuum edges. The rest of the frequencies is treated within the ALI formalism.

This technique allows any transition to be represented by frequency points from both groups, CL and ALI. Depending on how many frequencies are assigned to which group, the program can operate in full CL or full ALI mode, while within general use, it will always use a combination of both. Hubeny and Lanz [1995] claim that by assigning at least some explicit frequencies (to the CL mode) the time per iteration increases whereas the total number of iterations drops.

Another improvements over previous codes is the inclusion of superlevels and superlines. Especially for atoms with a very complex level structure, like iron or nickel with their 10^6 to 10^7 transitions, the code would no longer operate in useful timescales. Therefore TLUSTY uses superlevels to reduce the necessary computation time. Superlevels are groupings of levels with similar properties. In details, they have the same NLTE departure coefficients and all the single levels are in a Boltzmann equilibrium with each other. To constrain the choice of levels forming a superlevel, several requirements have to be met.

- All levels in a superlevel share the same parity
- The energy differences between the single levels must be small
- Not too many superlevels, as this would counteract with the idea of saving computation time
- Only levels with measured energies (no predicted ones) can be part of a superlevel

Usually each ion has about 20 to 30 superlevel in the most sophisticated model atom file. Transitions between different superlevels are referred to as superlines. The following graphic, Fig. 4.2, shows a visualization of the superline/-level concept in a Grotrian diagram. Another specialty of TLUSTY is the way the ODF is calculated. As the ODF depends on the depth in the atmosphere, the most accurate treatment would be to calculate it at each depth point. However, this is not only time consuming, but also not necessary. TLUSTY computes three ODFs at three different depth indices. One at the surface of the atmosphere, one at the characteristic depth, where the lines (super)lines are supposed to form and one at the last depth point. In between the three functions, a logarithmic interpolation in depth indices is used. Fig. 4.3 shows these three functions computed for several transitions in FeIII. It can be seen that the differences between the surface function and the one at the characteristic depth are negligible. The ODF from the deepest point in the atmosphere varies significantly, however this not a real problem, as the formation of lines happens in much higher parts of the atmosphere and due to the logarithmic interpolation, the deep ODF contributes only very little.

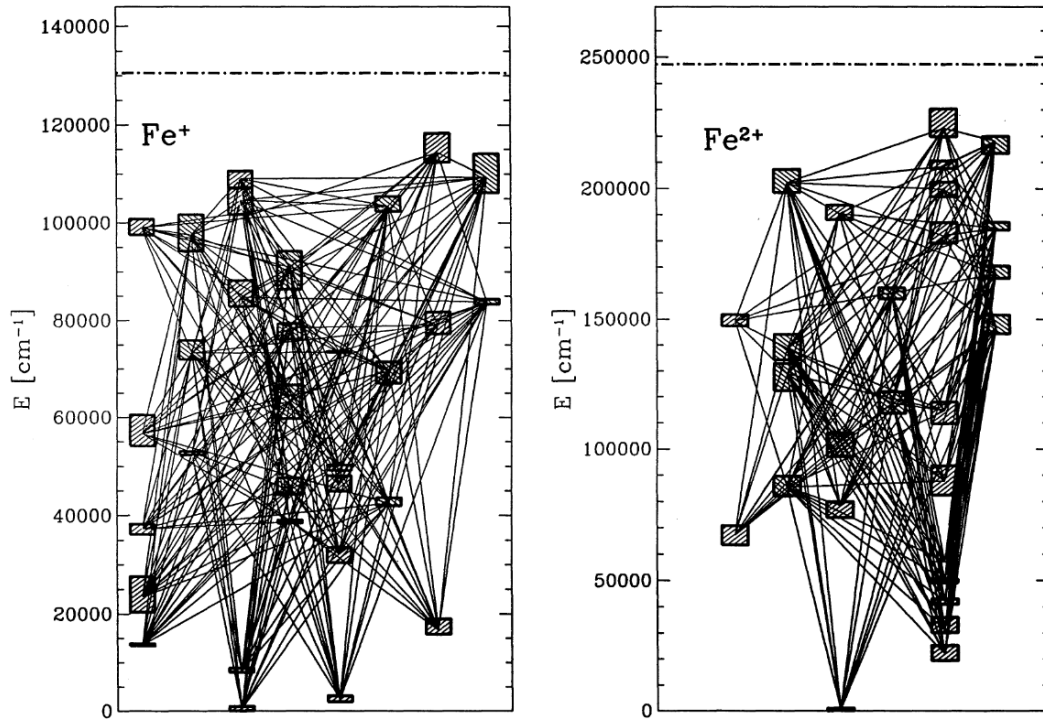


Figure 4.2: Superlevels and -lines for FeII and FeIII in a Grotrian diagram. Superlevels are marked as boxes, corresponding superlines are connecting lines. The dot-dashed line at the top marks the ionization level and the y-axis shows the energy. The superlevels are arranged into columns with alternating parity. Adopted from Hubeny and Lanz [1995].

4.6.2 Tricks and hints

During the work with TLUSTY and after the calculation of numerous atmospheres, some tricks have turned out to be quite useful and time saving. To preserve them for other people working with TLUSTY, a short summary is given hereafter.

- **General layout for NLTE atmospheres**

If one wants to calculate a NLTE atmosphere from scratch, the starting point has to be a gray atmosphere with the correct temperature and gravity, while the helium abundance should be kept low. Values of about $0.01 \times H$ have proven to work fine. In a gray atmosphere, it is assumed that the absorption coefficient is constant for all frequencies. Usually only one iterations is enough to get a model “good enough“ to continue with. The next step is to switch on the LTE mode in the fort.5 file and recalculate the model with the desired maximal number of iterations. If this was successful, the code switch for NLTE treatment can be activated. Only after the model converged in complete NLTE, the abundance for helium shall be increased to the desired value. Afterwards, other metals can be included one after the other, starting at low abundances (around 10^{-10} for CNO). It is important to add elements in order of increasing proton number.

- **Negative numbers in output file**

Sometimes the fort.7 output file contains negative numbers. TLUSTY does

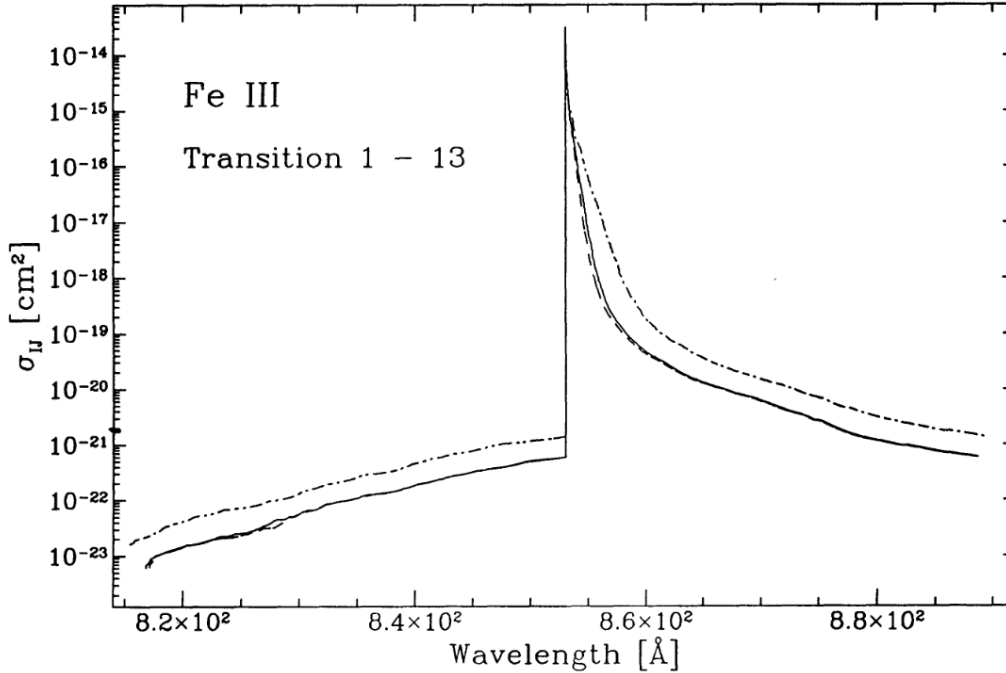


Figure 4.3: ODFs computed for three different depth points. Surface: dashed lines, characteristic depth: full line, last depth point: dash-dotted line. Adopted from Hubeny and Lanz [1995].

not display an error when reading in these files, but the program will crash with a “slow convergence in ELCOR“ error. The negative numbers are usually associated with a bad convergence as documented in the fort.13 file.

- **Including iron and nickel**

The inclusion of iron and nickel is basically the same as for other metals. It should start at low abundances (around 10^{-6}) and then be increased. But for iron and nickel, there are four different input files for each ionization stage, available from the TLUSTY homepage. In addition the flags2 file has to be modified. The ISPDF switch has to be set to unity. This implies switching from ODF to OS mode. This is recommended for fully blanketed models. Furthermore the value for DDNU has to be set up. It defines the stepsize for the opacity sampling expressed in fiducial Dopplerwidths of iron. At last, CNU1, the switch for the highest frequency at which lines are taken into account should be activated. This maximum frequency is defined as

$$\nu_{\max} = \text{CNU1} \times T_{\text{eff}} \times 10^{11} \quad (4.25)$$

- **Ignoring certain levels**

For some model atoms it turned out that the inclusion of all levels results in the feared slow convergence error. In such cases commenting out several of the last levels in the file is helpful. Then the atmosphere is computed again and hopefully converges. Afterwards some levels can be added and after several iterations all levels can be included. However for the NIII model atom that

was mainly used in this work, it was not possible to include the very last level, so it had to be left out.

- **Number of iterations**

The maximum number of iterations can be set in the flags2 file. If a converging atmosphere with several metals is already available, the number of iterations normally does not exceed ~ 40 . However, for some areas in the parameter range the iterations can go up to over 100. Numbers larger than 120 have not been observed during this thesis. However, atmospheres with such a high number of iterations usually show a worse convergence than others. For some cases TLUSTY tends to oscillate around the best solution and converges only very slowly. If this happens it is recommended to re-calculate the atmosphere by using the one with the large number of iterations as an input and not changing anything in the fort.5 file.

- **Convergence in grids**

If larger grids are calculated it is natural that some of the atmospheres are not converging. One possibility would be to increase the abundance from the previous atmosphere manually with a smaller stepsize. As this is quite time consuming, a more elegant approach is to go to the model with the same abundance but a higher $\log(g)$ and decrease the gravity. In the regime of He-sdO stars, changes by 0.1 dex are usually no problem.

4.6.3 TLUSTY vs TMAP

Some of the stars from this thesis have already been analyzed in terms of atmospheric parameters and basic abundances. As most of the previous work didn't make use of TLUSTY but of TMAP this offers a good possibility to compare the two codes.

TMAP stands für Tübingen Model Atmosphere Package [Werner and Dreizler, 1999]. It is based on the ALI method and accounts for metal line blanketing. It shares the same assumptions with TLUSTY so that the generated synthetic spectra should match at most parts. However, differences in the used model atoms or the broadening tables lead to differences in the line shape.

The idea to compare the output of the two codes arose from the $\log(g)$ problem in CD -31° 4800, where a large difference in surface gravity was observed depending on which models were used (see also Sect. 6.1.1)

To achieve the highest possible comparability, pure H/He models were compared by simply overplotting the synthetic spectra at a certain point from the used grid. The Tlusty grid contained additional carbon, nitrogen and oxygen in LTE at a number abundance of $1 \cdot 10^{-10}$. This was necessary to ensure that the output spectrum was calculated in the desired wavelength range by Synspec. Being typical for the He-sdO stars, the temperature was selected to be 45000 K, the surface gravity 5.6 and the helium to hydrogen ratio was 100 by numbers. Fig. 4.4 shows a small selection of helium lines. Only lines with clearly visible differences and without a shift introduced by different line lists were used. It can be seen that some of the linecores of the TLUSTY spectra are more shallow than with TMAP and show slight emission features. The hydrogen component in the HeII 4859 line is much more clearly visible in the TLUSTY line. Also slight differences in the wings of the

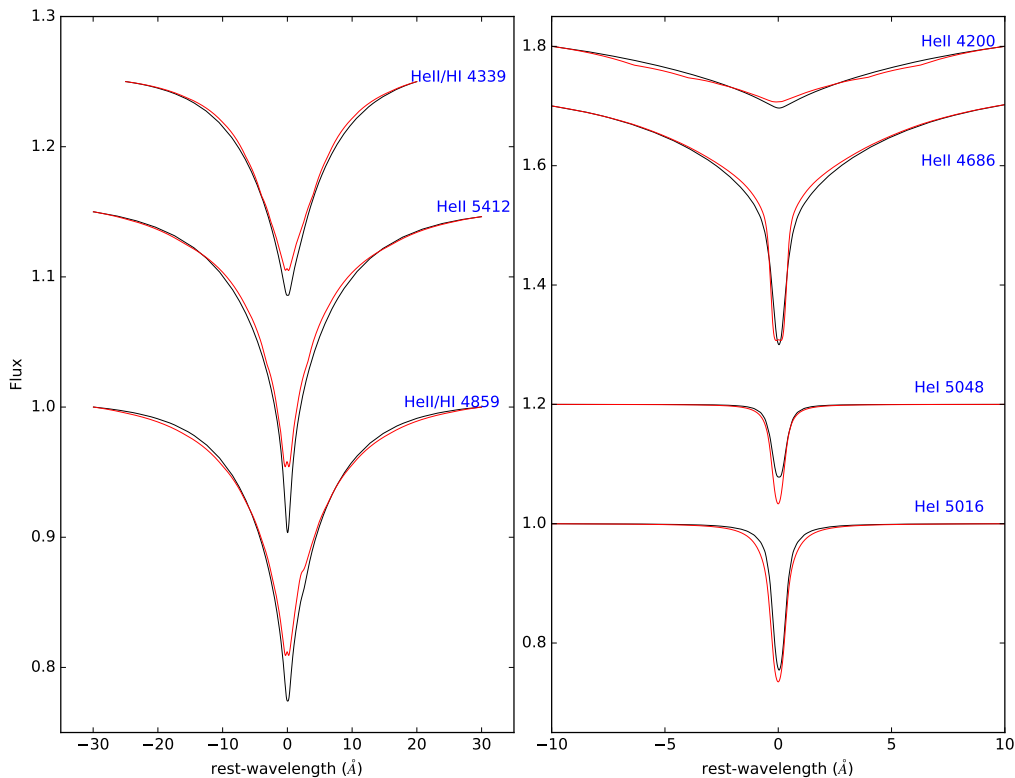


Figure 4.4: Comparison of selected helium lines of a TLUSTY model spectrum (red) and a TMAP model spectrum (black).

lines can be observed. As temperature and surface gravity are quite insensitive in that parameter range, such large differences in the line cores can result in significantly different values for the atmospheric parameters.

For another comparison of TMAP and TLUSTY at much higher temperatures (~ 700000 K) and higher surface gravities (~ 9.0) see Nemeth [2010].

4.7 Synspec

To calculate the synthetic spectra from the TLUSTY output atmospheres, the general spectrum synthesis code SYNSPEC(48)¹ was used. A more detailed description on this program can be found in Hubeny et al. [1985].

SYNSPEC uses the same control file as TLUSTY and expects a model atmosphere as input. A general line list is provided via another input file. The program selects lines that might contribute to the total opacity by selecting a characteristic depth in the atmosphere. This depth can be specified by the user and should resemble the depth at which the continuum optical depth is of the order of unity. The normal depth index used in this work was 40. After reading in all the lines, the line center opacity is calculated for each line. If the line opacity is smaller than a predefined fraction of the continuum opacity, the line is rejected and not used in further calculations. To enhance the accuracy of the models, the corresponding RELOP parameters was set to 10^{-5} .

¹<http://nova.astro.umd.edu/Synspec49/synspec.html>

As the desired spectral range is set in the SYNSPEC control file (fort.55), the code divides the spectrum in many small subranges which are calculated independently. Each frame consists of about 120 wavelength points. To derive the pure continuum opacity, the program uses the endpoints of each frame and linearly interpolates in between them. The first two points of each set are used for the determination of the continuum radiation field, while the rest describes the spectrum with all its features. The wavelength points are not set equally (except the program is forced so by the user) but distributed depending on the number of lines in a subframe of the spectrum. At each line center one wavelength point is set up, as well as equidistantly between two neighboring lines. The non-covered space in between is filled up with additional points to cover the line wings and the continuum.

In addition to this standard mode, several other options are available, i.e. the continuum mode in which the line opacity is set to zero or the molecular mode for cooler stars which allows the usage of molecular lines.

SYNSPEC can deal with both LTE and NLTE, or even a combination of both. If TLUSTY atmospheres are used, the treatment of lines depends on the implementation in the model atmosphere. transitions between levels of elements that were included in complete NLTE are also treated that way in SYNSPEC, while the rest is treated as LTE transitions.

The intrinsic line profiles are classical Voigt functions. The broadening effects of natural, Stark, thermal and Van-der-Waals interactions are taken into account.

4.8 SPAS

The analysis of spectra was done by using the program SPAS, the *Spectra Plotting and analysis suite* by Heiko Hirsch [Hirsch, 2009]. It is a reimplementation of Ralf Napiwotzki's *FITSB2* [Napiwotzki et al., 2004], upgraded with a graphical user interface and some other features. The program fits synthetic spectra to the observed data by making use of χ^2 -minimization via a simplex algorithm. The user can select spectral lines and change the wavelength window to be used for the fit. If more than one line is selected, a choice between global line fitting and individual line fitting can be made. In the first case, the program will try to fit all the line at the same time and return the parameter set that results from the lowest χ^2 of all lines together. If the lines are fitted individually, the parameter set is calculated for each single line and the mean value from all parameter sets as well as the standard deviation is returned.

For a good fitting result it is not only necessary to fit the core and the wings of the line well, a good reproduction of the continuum is also inevitable. If a fit misses the continuum, SPAS offers the opportunity to force the fit to match the end points of the continuum in the local fit window. This usually results in a worse fit for the line core and the wings. The synthetic spectra are usually interpolated from grids of NLTE model atmospheres including metal line blanketing (see Sect. 3 and following), the errors are calculated with the Bootstrapping algorithm. The synthetic spectra are convolved to match the resolution of the data, which can be given for each line individually, Therefore it is possible to fit data from different instruments simultaneously. It does not matter if the data are normalized or not as the program (re-) normalizes the spectra for each fitting window.

At first, no model atmospheres are used. In this step only the shift between the

observed position of the line and the expected position is calculated by fitting a combination of Gaussians and Lorentzians to the line profiles. The user can select appropriate lines (best S/N ratio, no blends etc.). Afterwards the model atmospheres are taken into account to calculate the atmospheric parameters, like effective temperature, surface gravity and helium abundance, or to calculate metal abundances with given atmospheric parameters. This can be done for each spectrum separately or after coadding them to improve the S/N ratio and therefore the visibility of the lines.

SPAS offers the possibility to fit the rotational velocity of a star that causes line broadening. The rotational broadening of the lines is not needed to be implemented in the models as the program uses a standard rotational profile that can be applied to every line.

In Fig. 4.5, a screenshot of *SPAS* output showing fits to several Balmer lines of a sdB star is displayed.

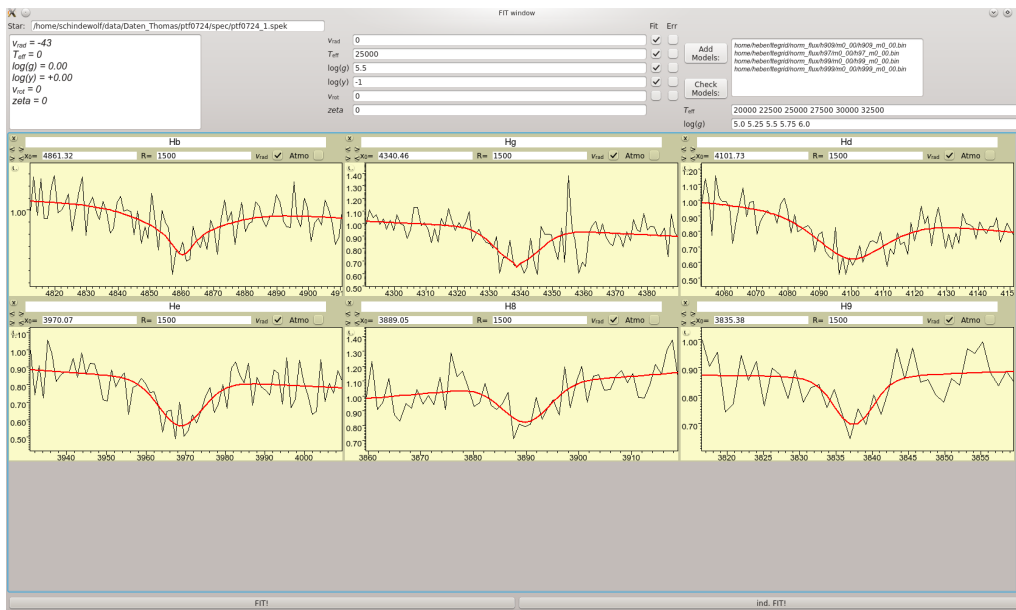


Figure 4.5: Screenshot of SPAS output, showing fits to several Balmer lines of a faint sdB star.

4.9 General procedure for abundance determination

As the aim of this thesis is to study the properties of He-sdB stars, it is necessary to determine the atmospheric parameters (effective temperature, surface gravity, ratio of helium to hydrogen) as well as the abundances for as many other elements as possible. To do so, model atmospheres and -spectra were calculated with the programs and techniques described above. The outcome was fitted to observational data using SPAS. This section outlines the established fitting procedure.

In the beginning all available data for a certain star was collected from online archives. If there were more than one spectrum in a wavelength range, they were

coadded to enhance the signal to noise ratio. The radial velocity shift of the spectra was measured with SPAS and corrected in all following steps by shifting the model spectra in the fitting program.

To get a first idea of the atmospheric parameters, a H/He grid was used to fit them. The grid covered a temperature range from 30000 K to 56000 K, the $\log(g)$ spans from 5.0 to 6.2 and the ratio of (He/H) was selected from (1, 10, 100, 300, 500, 700, 900, 1100, 1300, 1500, 2000) by number abundances. The large coverage of the parameter space was necessary to cover as many possible subtypes of stars as possible and to allow the individual line fits to deviate from the globally fitted solution as much as possible if necessary. Despite hydrogen and helium, carbon, nitrogen and oxygen were included as LTE components at an abundance of $(H/X)=(1/1^{-10})$. This proved necessary to get synthetic spectra over the whole desired range as SYN-SPEC automatically cuts the edges of spectra if no lines are present there. At this abundance the elements have no noticeable influence on the atmospheric structure of the star.

All possible lines were fitted, however the region around $H\alpha$ sometimes had to be left out as it caused SPAS to crash with a segmentation fault error more than once, most likely because the maximum number of datapoints was exceeded in high resolution spectra. At this point of the fitting procedure, only the global fit was used, as the individual one would lead to an undetermined value for the hydrogen/helium ratio for almost all helium lines as they contain no trace of hydrogen in their profile. Exceptions are the regions around $H\alpha$, $H\beta$, $H\gamma$, $H\delta$ and so on.

After this step, it was decided by manual inspection of the spectra if the star was more enriched in carbon or nitrogen. A first model atmosphere with the previously determined parameters was set up in which the other metals (C,N,O,Ne, Mg, Al, Si, P, S) were set to the solar number abundance as a starting point. Afterwards the carbon or nitrogen abundance (depending on the type of the star) was increased from its current value to about a ratio to hydrogen of one. For each step, a synthetic spectrum was calculated and used to determine the abundance of that element. In the next step, the H/He grid was upgraded by including carbon or nitrogen only, at the correct abundance in full NLTE conditions. To save computation time, the parameter range was shrunk down to a reasonable range around the known atmospheric parameters. By including another element, more explicitly: more opacity, the temperature structure of the atmosphere is changed and the computed results should lie closer to the true values. After refitting the atmospheric parameters, a new atmosphere with these ones was set up and again, all other metals were set to the solar abundance.

After having analyzed four He-sdO stars by June 2016, this procedure changed a bit. The H/He grid got replaced by a H/He/C/N/O grid that contained C,N and O at full NLTE conditions with an abundance of 10 times solar for carbon and nitrogen and the solar abundance for oxygen. The helium abundance varied from 0.1 to 10000. For each helium abundance, the C,N,O values were set differently to keep the ration between the elements at solar/10x solar. The value of (H+He) was scaled to unity so that the conversion factors for C, N and O are:

- $C_{10xsol} = 1/2.479 \cdot 10^{-3}$
- $N_{10xsol} = 1/6229 \cdot 10^{-4}$

- $C_{sol} = 1/4.513 \cdot 10^{-4}$

Table 4.1 gives an overview on the different subgrids and the actually used number abundances. For the atmospheric structure it does not matter that much if the el-

He/H	H+He	C/H (10x)	N/H (10x)	O/H
0,1	1.1	$2.727 \cdot 10^{-3}$	$6.852 \cdot 10^{-4}$	$4.964 \cdot 10^{-4}$
1	2	$4.958 \cdot 10^{-3}$	$1.249 \cdot 10^{-3}$	$8.903 \cdot 10^{-4}$
10	11	$2.727 \cdot 10^{-2}$	$6.852 \cdot 10^{-3}$	$4.964 \cdot 10^{-3}$
100	101	$2.504 \cdot 10^{-1}$	$6.291 \cdot 10^{-2}$	$4.558 \cdot 10^{-2}$
1000	1001	2.482	$6.235 \cdot 10^{-1}$	$4.518 \cdot 10^{-1}$
10000	10001	24.79	6.23	4.51

Table 4.1: Summary of the different number abundances of helium, carbon, nitrogen and oxygen in the calculated HECNO grid

ements are actually at their correct abundances; What is important is that there is enough opacity introduced to push the atmosphere closer to its true state in terms of temperature stratification. Models with a too shallow or too steep stratification would result in a wrong temperature.

To validate and justify the usage of such a HHeCNO grid, an examination on the temperature stratification of the atmosphere of CD-31° 4800 was performed with models containing different amounts of metals. The testbed was CD-31° 4800, a star analyzed later in this work (see Sect. 6.1.1). A pure NLTE atmosphere with only hydrogen and helium was constructed at the corresponding atmospheric parameters of CD-31° 4800 ($T_{\text{eff}}=42230$ K, $\log(g)=5.6$, $n(\text{He})/n(\text{H})=407$) and the temperature stratification over $\tau_{\text{rosseland}}$ was determined. Afterwards different metals were included at the correct abundance for CD-31° 4800 and the stratification was re-evaluated. Fig. 4.6 shows the results for the H/He atmosphere. In addition, the results for one atmosphere containing additional nitrogen, one with the carbon, nitrogen and oxygen, one with all the available intermediate mass elements plus aluminum and a last one with additional iron and nickel. The model with iron and nickel is the results from the abundance determination for CD-31° 4800 (see Sect. 6.1.1) and was used as a reference, meaning Fig. 4.6 shows the temperature offset of the different atmospheres to the one containing iron and nickel. It can be clearly seen that the pure H/He and H/He/N models show large deviations from the Fe/Ni model. In the parts of the stellar atmosphere where most of the lines are produced (column depth 0.01 to 1), the maximum difference is almost 4000 K. This is in good agreement with the results found by Bauer and Husfeld [1995]. Considering the normal temperature of an He-sdO, this is about 10%. The difference between the CNO and the full model is much less pronounced and only becomes important in the outer parts of the atmosphere where some strong resonance lines are formed. In addition the offset to the Fe/Ni model in the important region is only 500 K to 1000 K, or up to 2.5%. The more metals are in the atmosphere, the more pronounced the effects of line blanketing are. The induced opacity (especially of iron and nickel with its millions of transitions) results in surface cooling and backwarming and therefore in a steeper stratification. Photons produced in the inner part of the star are more likely to be absorbed closer to their origin. The pronounced difference between the

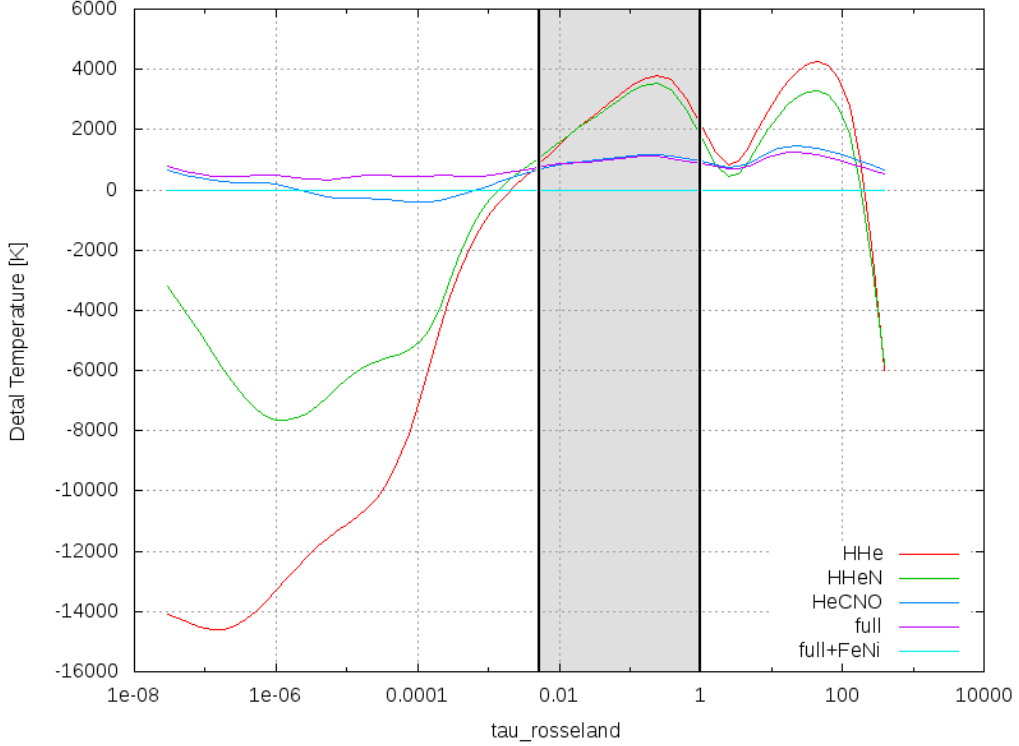


Figure 4.6: Relative temperature stratification of the atmosphere of CD-31° 4800 for models with different metal contents. The x axis gives the logarithm of $\tau_{\text{Rosseland}}$ while the y-axis represents the temperature. The reference ($\Delta T=0$) is given by the complete model atmosphere containing iron and nickel. The line forming region is indicated by the gray area between the two black bars.

models for HHeN and HHeCNO (with respect to the low abundance of carbon and oxygen) can be explained by the formation of strong resonance lines in the outer parts of the atmosphere.

To validate these results, the procedure was repeated for [CW83] 0904-02, another star analyzed later on in this work. [CW83] 0904-02 is a carbon rich He-sdO with slightly other atmospheric parameters. It has an effective temperature of $T_{\text{eff}}=47000$ K, $\log(g)=5.7$ and helium is $100 \times$ more abundant than hydrogen. Instead of using a HHeN atmosphere, a HHeC atmosphere was used, containing the exact amount of carbon as derived from the analysis of [CW83] 0904-02. Fig. 4.7 shows the temperature stratification of [CW83] 0904-02 for models with a different amount of metals with respect to the complete model atmosphere containing iron and nickel as a reference. It can be clearly seen that the differences between the single models are far less pronounced than in the case of CD-31° 4800. While the pure HHe model clearly sticks out and reveals temperature differences of up to 2500 K in the line forming regions, there is hardly any difference between the rest of the models. Temperatures are different by below 1000 K. Only in the outer regimes, differences become more pronounced again. This means that even the HHeC models should deliver trustworthy results in this case. It is unlikely that all the differences result only from the different abundances, but from the different effective temperature and surface gravity of the star. Considering the necessary computing time for a complete model

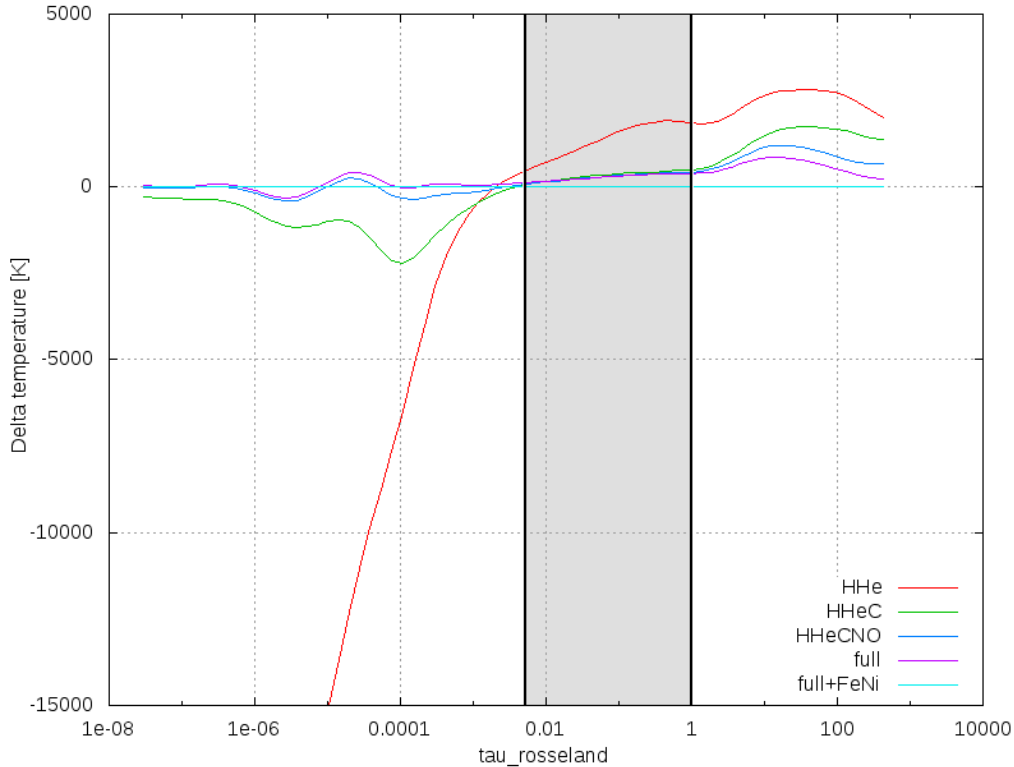


Figure 4.7: Relative temperature stratification of the atmosphere of [CW83] 0904-02 for models with different metal contents. The x axis gives the logarithm of $\tau_{\text{rosseland}}$ while the y-axis represents the temperature. The reference ($\Delta T=0$) is given by the complete model atmosphere containing iron and nickel. The line forming region is indicated by the gray area between the two black bars.

with iron and nickel and the differences in stratification and line shape presented here, the HHeCNO grid seems to be the best trade off between accuracy and time spent. It was therefore used for most of the analyzes in this work. Exceptions are indicated in the corresponding sections.

One final test was to cross-check if the differences in temperature stratification really plays such a big role concerning the determination of the atmospheric parameters. To do so, the final synthetic spectrum of CD-31° 4800 was used as the deviations between the temperature structures were most pronounced for this star. As described in Sect. 6.1.1 the atmospheric parameters were determined using a HHeN grid, while the final result contained all the NLTE intermediate elements as well as iron and nickel. The HeI and HeII lines of the synthetic spectrum were fitted using the HHeCNO grid and the atmospheric parameters were determined. Fig. 4.8 shows the fits to the selected lines. No artificial noise was added to the lines from the synthetic spectrum to avoid encountering errors from the fit caused by the noise and to make deviations more easy to spot. Despite some lines missing in the HHeCNO grid or being too pronounced there, no big difference is perceptible.

The atmospheric parameters with which the reference model was calculated are an effective temperature of 42230 K, a surface gravity of $\log(g)=5.6$ and a helium abundance of $\log(y)=2.60$.

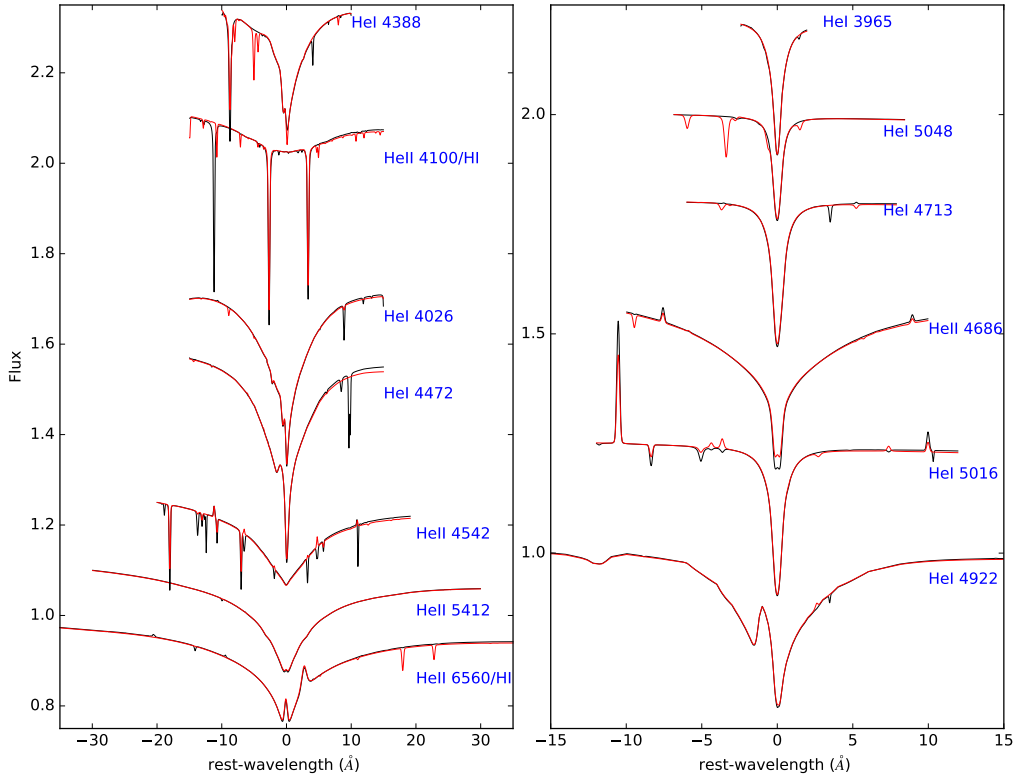


Figure 4.8: Fits to several He I and HeII lines derived from a synthetic spectrum of CD-31° 4800 using the HHeCNO grid.

The fit with the HHeCNO grid resulted in the following parameters:

- $T_{\text{eff}} = 42190 \pm 500 \text{ K}$
- $\log(g) = 5.57 \pm 0.15$
- $\log(n(\text{He})/n(\text{H})) = 2.51 \pm 0.30$

It can therefore be concluded that the shifts in temperature predicted from the stratification do not play such an important role in the determination of atmospheric parameters. The wings of the helium lines form in regions where the spacing between the different stratifications is comparatively small. The line core however should be much more affected. Looking at Fig. 4.8 proofs that wrong with only slight errors in a few lines like HeII 4686, HeI 4388, or HeI 4922.

A detailed comparison of the modelgrids used in this work and their resulting different atmospheric parameters is shown in the following section. In addition, a comparison to previous analyses is shown.

After having provided the atmospheric parameters in one or the other way, the following step was the determination of the abundances for all the metals included in the model so far. For this purpose, one element after the other was enhanced in its abundance iteratively, while all steps were saved and transformed to synthetic spectra. From these subgrids the abundances were fitted. The resulting final atmosphere already matched the observed spectra quite well in most cases. For fitting, usually both a global fit to all lines and an individual fit were performed. As the resulting abundances should be the same (in a perfect world), the individual abundances for

each line were closely looked at to check for any outliers. Those lines were removed from the fit. Usually it was only necessary to delete one or two lines per element. The next step was the analysis of the UV data. This consequently demanded the inclusion of iron and nickel in the models (see also Sect. 4.5). At first, only iron was included and a small subgrid was set up to determine the corresponding abundance from UV spectra. Afterwards the same step was repeated for nickel. Of course the iron-group elements with their millions of lines have a huge influence on every atmosphere, especially in the UV and the continuum part. Therefore it is necessary to re-measure all abundances from new subgrids that contain iron and nickel. As the computation time increased dramatically for these steps, the subgrids were centered around the known values and in addition the range was cut down to save time. If abundances from optical and UV data were available, the “final“ abundance was the error weighted average of the result of both spectral range and the average error was used.

The following table 4.2 shows which ionization stages were commonly used for which element in the standard model atmospheres and how many levels and superlevels were used. If no traces of an element could be found by visual inspection of the regions where the most prominent lines were suspected, the corresponding elements were of course not included.

For NIII, the original data file contained 40 levels. However the last of them always produced slow convergence errors when included. It was therefore left out. For some elements, like magnesium or aluminum, higher ionization stages than included are expected at the typical temperatures of He-sdOs. Unfortunately therefore no data files are available for TLUSTY. The data file for NiIII was not usable either as its including resulted in an invalid memory reference. Including any CII data files resulted in an error with the maximum of transitions that could be stored in the PRFLIN vector when operating in OS mode. This could not be solved by increasing the DDNU value, which represents the step size for the opacity sampling. A recompilation of TLUSTY solved this problem, but caused a segmentation fault for the iron group elements. Therefore the C II stage was not used in the final models containing iron and nickel, but only in the modelgrids that were used for the determination of the atmospheric parameters. As the He-sdO stars analyzed in this work usually show no CII lines, this is nothing to worry about. A small test fit with a HHeCNO subgrid, once with and once without CII, to selected carbon lines of [CW83] 0904-02 showed difference in the resulting carbon abundance of 0.02 dex, which is far below the errors for the fit.

4.10 Comparison of modelgrids

Although the HHeCNO grid has proven to be most suitable when it comes to reproducing the temperature stratification of a stellar atmosphere, a comparison of the resulting atmospheric parameters when using different grids is still missing. Therefore, it was decided to compare the results of different versions of the grid (different metals included) with previous results. CD -31° 4800, LSIV +10 9, [CW83] 0832-01, [CW83] 0904-02 and LSS 1274 were chosen as the old CASPEC spectra used in the analysis by Bauer and Husfeld [1995] and Dreizler [1993] were still available. For each star, the starting point was a pure H/He grid. The lines and their fitting windows used in this step were not altered afterwards to ensure comparability. The

Element	Ionization stage	# L	#SL
H	0	16	1
HeI	0	24	0
HeII	1	20	0
CIII	2	34	12
CIV	3	35	2
NII	1	32	10
NIII	2	39*	9
NIV	3	34	14
NV	4	21	4
OII	1	36	12
OIII	2	28	13
OIV	3	31	8
NeII	1	23	9
NeIII	2	12	2
MgII	1	21	4
AlIII	2	19	4
SiIII	2	31	15
SiIV	3	19	4
PIV	3	14	0
PV	4	12	4
SIII	2	29	12
SIV	3	33	5
FeIII	2	0	50
FeIV	3	0	43
FeV	4	0	42
NiIV	3	0	38
NiV	4	0	48

Table 4.2: The different ionization stages and number of levels (L)+superlevels (SL) used in the standard model atmosphere. For *, see the following text

nex step was using a grid containing additional carbon or nitrogen, depending on the most enriched element in the star. In the end, the lines were fitted with the HHeCNO grid. Table 4.3 shows the different atmospheric parameters originating from the different fits. The last column shows the results from fitting high resolution spectra from FEROS or UVES. For details, see the corresponding sections of the single stars. As Dreizler [1993] used a fixed helium to hydrogen ration of 100 for determining the atmospheric parameters, the same value was fixed in this analysis. The parameters of CD -31° 4800 given by Bauer and Husfeld [1995] are falling out of the series, as they were not determined using helium but silicon lines of different ionization stages. This seemed necessary because of the Pickering Problem (for details, see i.e. Sect. 6.1.1). This analysis used the helium lines and excluded the problematic pickering lines if necessary. For [CW83]0904-02, a rotational velocity of 35 km/s was used.

For all stars, the results from Bauer and Husfeld [1995] or Dreizler [1993] are in

good agreement with the results of this work displayed in the last column. Details are given in the corresponding sections of the stars.

The results from all different grids are in agreement with the results from previous work. This is a very good sign, that the general method of fitting applied in this work is trustworthy and the calculated models give similar results.

For CD -31° 4800, only the H/He grid gives a too low surface gravity when compared to the results from the high resolution spectra.

For LSIV +10 9, all grids give a too high temperature compared to the parameters from the UVES spectra. However, the difference is only about 500 K and therefore negligible.

For [CW83] 0832-01, only the H/He grid gives a too low surface gravity.

The same holds for [CW83] 0904-02 and LSS 1274, in which both the H/He and the H/He+C grid fail to match the $\log(g)$ of the high resolution data.

As a general scheme, it can be observed that the models with a higher content of metals deliver a higher surface gravity and a maybe slightly lower temperature (which is not significant!). This can be explained by the backwarming effect of the additional metals which increase the opacity and therefore contribute to a hotter photosphere. The temperature needed to maintain the ionization equilibrium is therefore lowered, but to keep the line profiles the same, a higher $\log(g)$ is required. As the temperature shows a T^4 dependence in the flux relation, its changes are very small. This can be confirmed when comparing the different grids among each other.

Star	previous results	H/He-grid	H/He+X grid	HHe+CNO grid	results (this work)
CD -31° 4800	44000 ± 2000	42790 ± 700	42570 ± 500	42790 ± 700	42230 ± 300
	5.4 ± 0.3 [Bauer and Husfeld, 1995]	5.41 ± 0.08 2.5 (fixed)	5.5 ± 0.07 2.5 (fixed)	5.63 ± 0.09 2.5 (fixed)	5.6 ± 0.06 2.61 ± 0.06
LSIV +109	44500 ± 1000	45880 ± 500	45420 ± 750	45490 ± 500	43850 ± 600
	5.55 ± 0.15 [Dreizler, 1993]	5.48 ± 0.05 2.0 (fixed)	5.58 ± 0.08 2.0 (fixed)	5.70 ± 0.10 2.0 (fixed)	5.43 ± 0.20 2.73 ± 0.19
[CW83]0832-01	44500 ± 1000	45460 ± 850	45870 ± 660	45480 ± 560	45700 ± 800
	5.55 ± 0.15 [Dreizler, 1993]	5.54 ± 0.05 2.0 (fixed)	5.66 ± 0.05 2.0 (fixed)	5.75 ± 0.07 2.0 (fixed)	5.70 ± 0.09 3.0 (fixed)
[CW83]0904-02	46500 ± 1000	48093 ± 800	48098 ± 750	47750 ± 500	47000 ± 700
	5.55 ± 0.15 [Dreizler, 1993]	5.40 ± 0.07 2.0 (fixed)	5.49 ± 0.07 2.0 (fixed)	5.62 ± 0.05 2.0 (fixed)	5.70 ± 0.10 2.0 ± 0.10
LSS 1274	44500 ± 1000	43320 ± 590	43700 ± 500	44400 ± 500	44270 ± 400
	5.55 ± 0.15 [Dreizler, 1993]	5.22 ± 0.05 2.0 (fixed)	5.25 ± 0.07 2.0 (fixed)	5.47 ± 0.06 2.0 (fixed)	5.48 ± 0.07 2.17 ± 0.25

Table 4.3: Comparison of the results of fitting atmospheric parameters with grids containing different amounts of metals. The spectral data were taken with CASPEC at an resolution of R=18000. For each star, the size and position of the fitting windows was kept constant. X stands for either carbon or nitrogen, depending on which element is more abundant in the star.

4.11 XTGRID

As an alternative to the standard fitting procedure, spectral fitting was performed by the χ^2 minimization program XTGRID for some stars (mainly CD -31° 4800 and US708). This python-based program, developed by Dr. Peter Németh combines the simplex- and steepest-descent algorithm in an iterative way to fit multi-wavelength data of hot stars. It can fit the atmospheric parameters, metal abundances, radial velocity and rotational velocity.

(For a detailed description of XTGRID, see i.e. Németh et al. [2012].)

The program uses TLUSTY to calculate small grids of model atmospheres and fits them to the observational data. At first the general direction follows the gradient of the steepest descent with a step size that is as large as accepted by TLUSTY without being in danger of convergence errors. For each parameter the new step directions and -sizes can be calculated by a simplex approach. If temperature or gravity change, a new model atmosphere is calculated, while changes in the abundances of the included elements are dealt with by new synthetic spectra. The directions are calculated from the new fits and the starting model gets replaced by a new one. These steps are repeated until the relative changes for all free parameters are below 0.5 % in three consecutive iterations. In addition, the maximum allowed step size must at least get halved.

XTGRID also features a special approach to compare the models to the data, especially the continuum. The spectrum is sampled in small sections to account for problems occurring because of strong line broadening, blanketing effects or poor spectral resolution. In each segment, the synthetic spectrum is normalized to the data by finding the ratio of their median fluxes. Adapting the resolution of the observed spectra, the synthetic ones are convolved with a Gaussian profile of appropriate width.

To estimate the quality of the fits, the parameter errors are calculated for 60, 90 and 99 % confidence levels. Therefore the $\Delta\chi^2$ is mapped with respect to the final parameter. The ranges are

- $-0.99 < (\Delta X/X) < 100$
- $-0.26 < (\Delta T/T) < 0.26$
- $-0.195 < (\Delta \log(g)/\log(g)) < 0.195$

with the final abundance for a specific element X . Parameters are changed until the limit for 60 % confidence level is reached at a given number of free parameters.

XTGRID uses a certain technique to enhance the computation speed. It makes use of the faster convergence rate of temperature and gravity compared to the abundances and includes parameter relaxation. Temperature and gravity can be kept fixed for five iterations if their relative changes become smaller than 0.5 %. This allows for faster convergence of the other parameters. This also saves a lot of time as only SYNSPEC is used to treat the changes in abundance. After a total number of 14 iterations, all models are recalculated with TLUSTY for three iterations. If the models do not converge at this point, the loop is repeated for another 14 iterations until the convergence limit is reached.

4.12 Photometry and color indices

Up to now, only the stellar spectra and their calculations played an important role in this work. But also photometry can be used to derive certain atmospheric parameters or to provide a cross-check for the stellar values derived from a spectroscopic analysis. The idea of using standardized interference filters for spectral classifications dates back to the 1960s.

One of the most important systems is the Stroemgren filter set [Strömngren, 1956]. It consists of six filter which properties can be found in the following table.

Filter	$\lambda_0/\text{\AA}$	FWHM/ \AA
u	3500	380
v	4100	200
b	4700	100
y	5500	200
β_s	4864	30
β_w	4864	150

Table 4.4: Overview on the different Stroemgren filters with their center wavelength and FWHM

In addition, there are the so called Stroemgren indices, which are basically the difference between two ore more filters.

- (b-y)
- (u-b)
- $c1=(u-v)-(v-b)$
- $m1=(v-b)-(b-y)$
- $\beta = \beta_s - \beta_w$

The difference between the narrow-/smallband and the wideband filter is used to account for the continuum around the $H\beta$ line

The (b-y) index measures the slope of a spectrum between the two center wavelength of the filter (4700 \AA and 5500 \AA) and can be used as a temperature indicator for cool stars. (u-b) and c1 are more or less centered around the Balmer jump and provide information on the effective temperature in hot stars. Finally, the β filter difference is utilized to measure the equivalent width of the $H\beta$ absorption line. This width serves a an indicator for the surface gravity.

Fig.4.9 gives a graphical overview on the different filters and their passbands as well as center wavelength.

Of course, there are also other filters and filter sets that can be used, like the Johnson filters, WISE- or 2Mass filters. In general, the photometric datasets are inhomogeneous, both with respect to bandwidth as well as to accuracy.

In this thesis, the photometry was used to crosscheck if the calculated spectra and

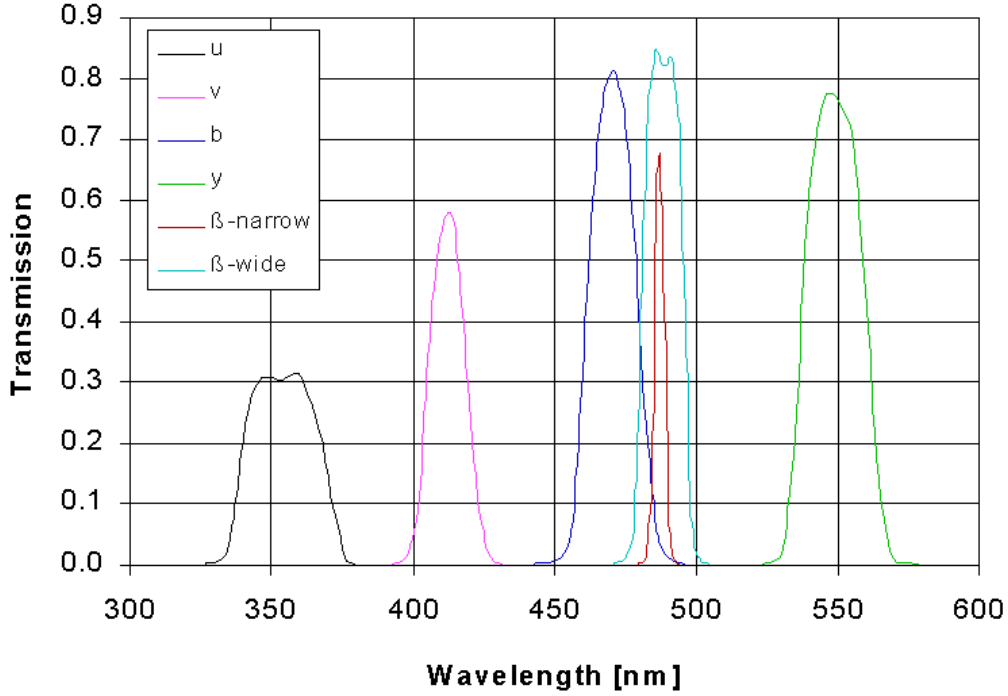


Figure 4.9: The different stroemgren filter passbands. Adopted from: ¹

derived atmospheric parameters were correct. To do so, a spectral energy distribution (SED) of the star was calculated and all available filter magnitudes and colors were collected. In addition, three boxes were set up between 1300 Å & 1800 Å, 2000 Å & 2500 Å and 2500 Å & 3000 Å. The magnitudes for these filters were calculated from low resolution IUE spectra, that were not used for the analysis of the stars themselves. This was necessary, because there are hardly any measurements available (with calibrated filters) that cover the UV regime.

Afterwards, the magnitudes from all available filters were overplotted over the SED to check for any discrepancies. To obtain the distance (resulting from the angular diameter θ) to the star and the reddening, the SED was shifted and stretched automatically until the the SED matched the observations best. Interstellar extinction is accounted for by multiplying the synthetic flux with a reddening factor $10^{-0.4A(\lambda)}$ using the extinction curve of Fitzpatrick [1999]. The extinction parameter was set to $R_V = A(V)/E(B - V) = 3.15$. The SED is usually shown as as flux density times the wavelength to the power of three ($F_\lambda \lambda^3$) as a function of wavelength to reduce the steep slope of the SED on such a broad wavelength range. To fasten up this process, an ISIS script was written that needs the filter names, -magnitudes, magnitude uncertainties and type of filter and produces a printable output. If not indicated otherwise, a canonical mass of $0.47 M_\odot$ was used for all stars. If no errors for magnitude or color measurements were found, a standard error of 0.025 mag for magnitudes and 0.01 for colors was applied. For details on the procedure see e.g. Heber et al. [2017].

¹<http://www.konkoly.hu/staff/racz/stromgren-s.gif>

5 Spectrographs

After having calculated model atmospheres, they have to be compared to the data and tested. But to get data in the first place is inevitable to understand how they are measured, so to speak how the starlight is collected and transformed in a spectra using a spectrograph.

In this chapter the different spectrographs which's data were used in this thesis are described and the general mode of operations is explained. Towards the end, a short summary on the data reduction process is given.

5.1 Types of Spectrographs

There are different types of spectrographs. The most prominent and widely used ones are the longslit spectrograph and the echelle one. In summary it can be said that the first one is more sensitive on the cost of spectral resolving power, while the other one can deliver better resolved spectra but on the cost of sensitivity for dim targets. As both feature a similar inner structure (except one element) their properties will be described together hereafter.

All common spectrographs share several parts:

- **Slit**
The slit operates as an elongated, very narrow aperture and prevents straylight from entering the instrument. Its width has an influence on the quality of the spectra.
- **Collimator**
The collimating system provides a beam of parallel light for the dispersion element following afterwards.
- **Dispersion element**
This element separates the incoming light into the different wavelength and actually creates the spectra. It can be a prism or a (in most cases reflecting) grating.
- **Focusing system**
Several lenses and optical components image the obtained spectrum onto the detector.
- **Detector**
The detector creates a digital image of the spectrum. Most common are CCDs, but especially in the UV-spectrographs other detector, e.g. multi-channel plates, can be used.

In modern spectrographs, a blaze-grating is used as dispersion element. It consists of a series of grooves, tilted by the blaze angle (θ) (measured to the surface normal) and coated with a reflective surface. The grating equation reads

$$d(\sin \alpha + \sin \beta) = \Delta s = n\lambda \quad (5.1)$$

with the path difference Δs and the wavelength λ . α is the entrance angle, β is the reflected angle (where $\alpha + \beta = 2\Theta$) and d is the grating constant, giving the distance between two grooves. The integer number n is called diffraction order.

To describe a spectrograph, the resolving power R is commonly used. It is defined as

$$R = \frac{\lambda}{\Delta\lambda} \quad (5.2)$$

and describes the ability of resolving a wavelength difference of $\Delta\lambda$ at a certain wavelength λ . There are mainly two effects limiting the resolving power of a spectrograph. Diffraction by a grating always comes hand in hand with an inherent smearing of lines. Thus the resolving power of the grating is defined as

$$R_{\text{grating}} = \left(\frac{\lambda}{\Delta\lambda} \right)_{\text{grating}} = nN \quad (5.3)$$

with the number of grooves that are actually illuminated N . The other limiting effect is the finite slit size. As it cannot be infinitesimally small, the light beam behind the slit will never be completely parallel, but always a little bit inclined. This leads to an uncertainty of the incident angle and results in a finite resolving power R_{slit} [pra, 2015]

$$R_{\text{slit}} = \frac{n \cdot f_{\text{coll}}}{d \cdot b \cos \alpha} \lambda \quad (5.4)$$

The resolving power of the slit is usually significantly smaller than the one of the grating.

Getting high resolution spectra is desirable because they might reveal details and small line features that are not visible in lower resolution spectra. To increase resolution it is helpful to decrease the slitwidth or to observe in higher diffraction orders. However, both approaches have their disadvantages.

Due to distortions in the atmosphere, the image of a star is not point like anymore (as it would be without atmosphere) but shows a finite angular size. This increases the diameter of the projection of the star in the focal plane of the telescope. If the slitwidth is smaller than that size, light is lost and the exposure time would have to be extended to compensate for. In case of fiber coupled spectrographs, the diameter of the fiber defines the size of the star's image.

The decision to observe in higher orders is made difficult by the overlapping of orders. To nevertheless make use of them nevertheless, these orders have to be separated. This can be achieved by placing a second dispersion element in the spectrograph which is placed between the blaze-grating and the objective, resulting in an Echelle-spectrograph. The direction of dispersion of this so called cross disperser is perpendicular to that of the blazed grating. This doesn't only make use of the complete CCD chip but also enhances the resolving power drastically. The drawback is a lower sensitivity as all the available light of the star entering the spectrograph is spread over entire chip instead of only some lines of it.

5.2 Scientific Instruments

In this part the focus is laid on the different spectrographs, their technical details and (dis-)advantages. It will start with the optical spectrographs, while the UV ones follow in the end.

5.2.1 UVES¹

UVES is an optical echelle spectrograph of ESO. It is mounted at the Nasmyth B focus of the second Unit Telescope of VLT (“Kueyen“). It features two arms, one for the red and one for the blue. The first one can reach a resolving power up to $R=110000$, the blue one up to $R=80000$. Both arms can be used separately or at the same time when using a beam splitter. The wavelength ranges are 3000 \AA to 5000 \AA and 4200 \AA to 11000 \AA respectively. In addition to the light coming from the telescope, a fiber port is available for the red arm.

The instrument itself consists of two parts. The first part, attached to the telescope rotator, holds the calibration lamps, a iodine cell for RV calibration, different image slicers and a derotator that is connected to the second part of the instrument, the actual spectrograph.

Before being directed to one of the two arms, the light passes through the preslit area which holds additional optical components, i.e. a depolarizer. Depending on which arm is used, the light either directly passed through the slit for the red arm or is directed to the blue slit with a flat mirror.

Within the spectrograph the light beams are collimated and sent to the echelle grating and then resent to the main collimators. However, a small fraction of the light ($\sim 1\%$) is fed to the exposure meters, that measure the amount of light from both sky and object within the system. The lion’s share hits the cross-disperser units via mirrors and transfer collimators and enters the CCD where it is recorded. The cameras are connected to a liquid nitrogen cryostat in order to reduce the noise of the chips. The CCD in the red arm is a bit different from the blue one as it consists of two single chips with a small gap in between them. This leads to the loss of one echelle order around the selected central wavelength. Fig. 5.1 an overview on the layout of the UVES spectrograph and its different subparts.

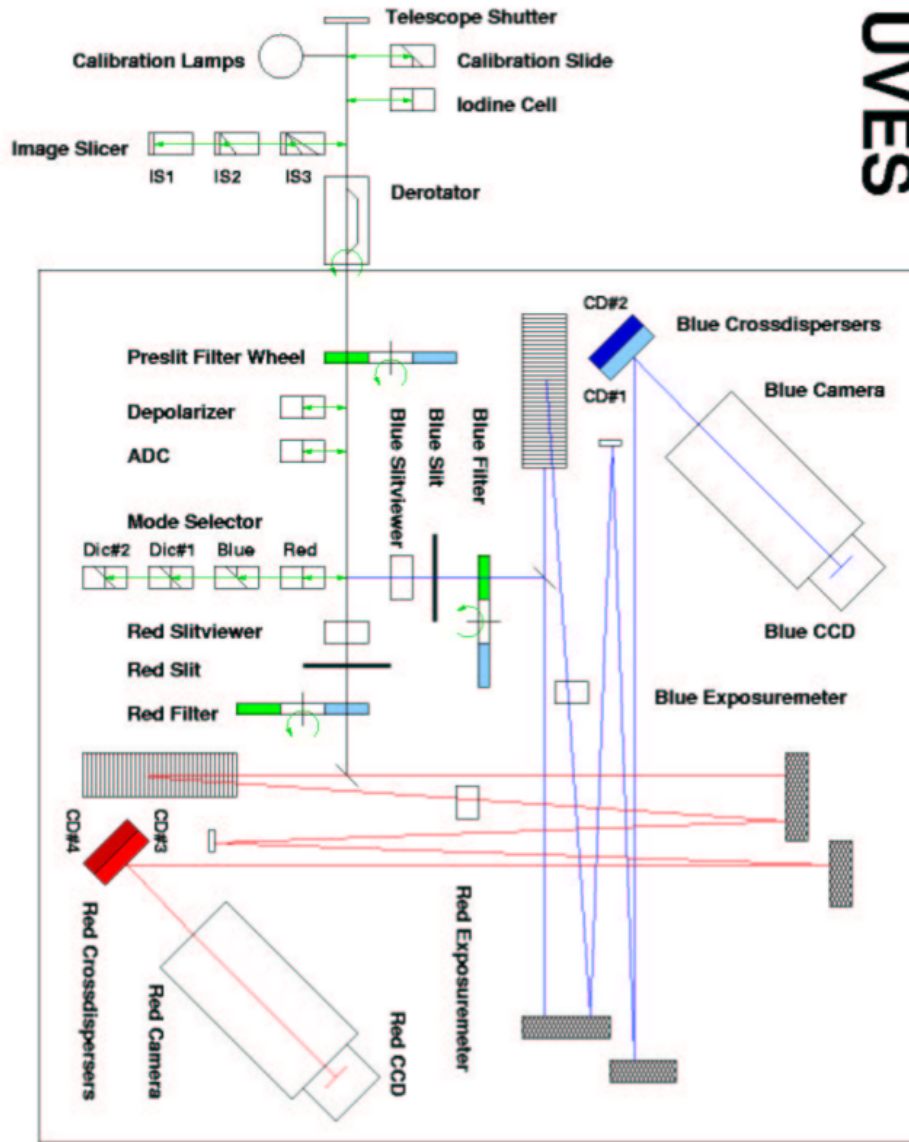
5.2.2 XSHOOTER²

The XSHOOTER spectrograph was installed at the ESO VLT on Cerro Paranal in 2009. It is a multi-wavelength spectrograph, consisting of three independent subunits to maximize the sensitivity. It can cover a vast spectral range from the visible UV to the near infrared. The three single echelle spectrographs and their wavelength range are

- UVB: 3000 \AA to 5595 \AA
- VIS: 5595 \AA to 10240 \AA
- NIR: 10240 \AA to 24800 \AA

¹Based on information given in the ESO UVES manual. http://www.eso.org/sci/facilities/paranal/instruments/uves/doc/VLT-MAN-ESO-13200-1825_v99.pdf

²Based on the information given in Vernet et al. [2011]



UVES

Figure 5.1: Schematic overview on the UVES optical layout. Adopted from: http://www.eso.org/sci/facilities/paranal/instruments/uves/doc/VLT-MAN-ES0-13200-1825_v93.pdf

A schematic overview on the optical design is given in Fig. 5.2. The backbone of XSHOOTER (not visible in Fig. 5.2) can be directly mounted to the derotator of the Cassegrain focus of one of the VLTs. It is a supporting structure containing, among others, the instrument shutter, lamps for flatfields and wavelength calibration, a guiding camera and an Integrated Field Unit (IFU). This redirects the incoming light in order to easily pass it to the three spectrographs. Two dichroics are used to split the beam. The first one sends light to the UV spectrographs, while the second one splits the beam for the VIS and NIR one. Following each dichroic is a small piezo-mounted mirror that can compensate for flexures of the telescope or the supporting structure. For the UV and VIS channel, an Atmospheric Dispersion

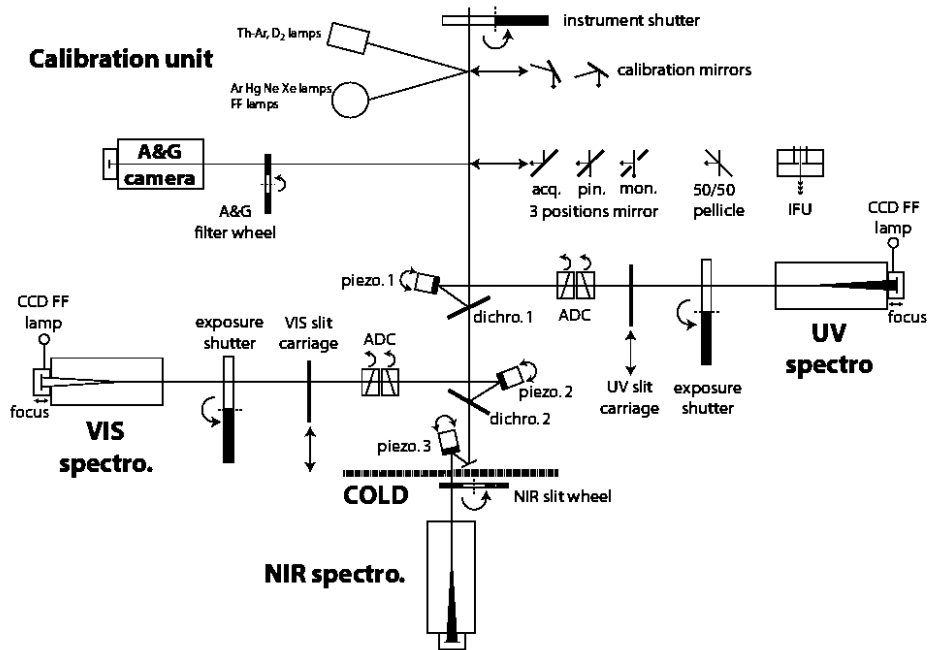


Figure 5.2: Schematic overview on the XSHOOTER optical layout. Taken from: Vernet et al. [2011]

Corrector (ADC) is placed in the beam, compensating for atmospheric dispersion to enhance the amount of light reaching the spectrograph.

The NIR spectrograph, in contrast to the two other ones, is placed in a cryostat with liquid nitrogen to reduce the emission of infrared light due to thermal emission. Light can enter the cryostat through a sealed window. For each channel, different slits are available, positioned on a wheel for easy changing. A field lens is placed in front of every slit to (re-)focus the incoming light on the grating and, again, enhance the sensitivity.

5.2.3 FEROS¹

The Fiber-fed Extended Range Optical Spectrograph (FEROS) is basically a classical echelle spectrograph that has some unique equipment features. It is mounted at the 2.2m MPG/ESO telescope at La Silla. The spectrograph basically consists of three main parts: The spectrograph itself, a calibration unit and an adapter that allows to instantly change between taking spectra and imaging with the Wide Field Imager (WFI). As this adapter is mounted directly at the Cassegrain focus, the light coming from the telescope has to be directed to the spectrograph standing in a separate room with an optical fiber. FEROS has two fibers to obtain spectra from the desired object and the sky simultaneously. Both fibers are separated by about 2.9 arcminutes on the sky. To minimize the loss of light, microlenses are positioned in front of the fibers. The complete adapter can be slightly rotated to avoid stars lying on the sky fiber. The fibers from the calibration unit (with flat field and wavelength calibration lamps) are also mounted to the adapter and their light can be guided

¹Based on the official FEROS User's manual. <https://www.eso.org/sci/facilities/lasilla/instruments/feros/doc/manual>

to the science fibers via the Sliding Calibration Sector Mirros (SCSM). Fig. 5.3

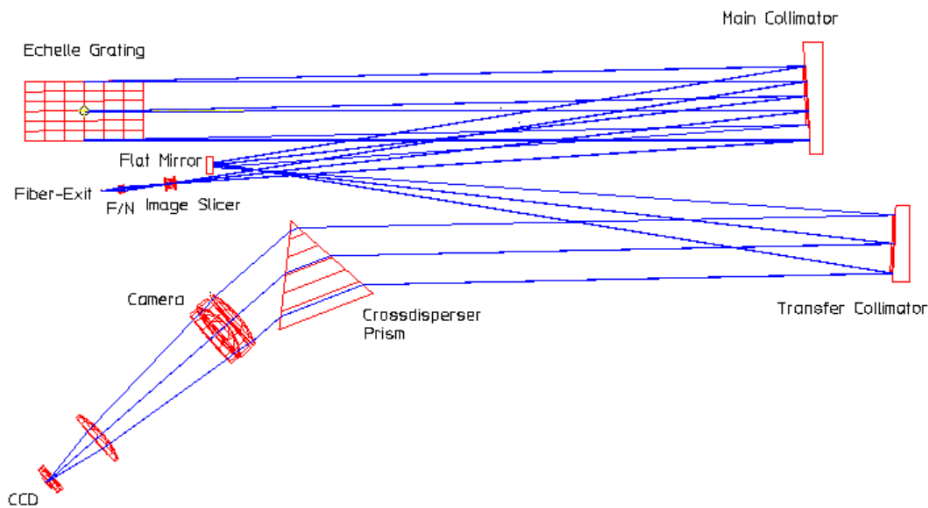


Figure 5.3: Schematic overview on the FEROS optical layout. Adopted from: <https://www.lsw.uni-heidelberg.de/projects/instrumentation/Feros/Description.html>

gives an overview on the optical layout of the FEROS spectrograph. After passing the optical fibres the light passes an image slicer and is collimated. The light is then directed to the echelle grating. This grating features 79 lines/mm, resulting in a resolving power of the spectrograph of ~ 48000 . After the grating the light is sent back to the main collimator and via a flat mirror to a second collimator. Then it hits the crossdisperser element, a prism. Finally it is focused on a CCD chip by various lenses.

FEROS covers a very wide wavelength range from 3560 \AA to 9200 \AA in a fixed setup. The data reduction is straight forwards, because only a single operation mode is available.

5.2.4 The High Resolution Echelle Spectrometer (HIRES) ¹

HIRES, the High Resolution Echelle Spectrometer, is a standard type echelle spectrograph mounted on the right Nasmyth focus of the KECK I telescope on Mauna Kea, Hawai. Its layout was designed to meet the specifications, limits and environment conditions of its workplace on the summit. It covers the optical wavelength and depending on the used slit and the different gratings, the spectral resolving power varies between 24000 and 85000. A schematic overview on the path of light inside the spectrograph is presented in Fig. 5.4. After entering the slit, the light passes a wheel, where several filters are mounted in order to modulate the incoming light. In front of the slit, several calibration lamps and a iodine cell are placed. Behind the filter wheel and a shutter, the light hits one of two tilted spherical mirrors. They collimate the light and redirect it towards the echelle grating. Two different mirrors are available, each with a special coating optimized either for the blue or the red

¹Based on the information given in Vogt et al. [1994]

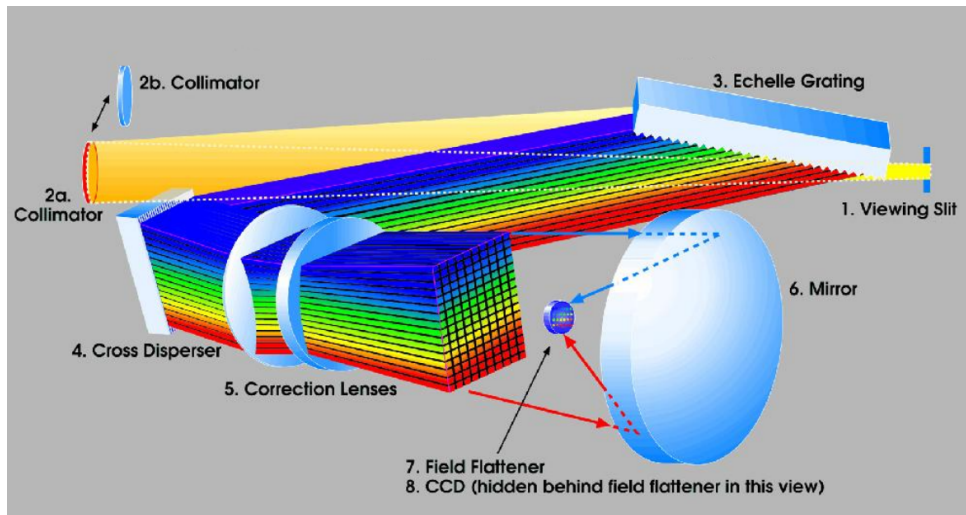


Figure 5.4: Schematic path of light in the HIRES spectrograph. Adopted from <https://www2.keck.hawaii.edu/inst/hires/>

part of the wavelength range. The echelle grating consists of three single gratings that were mosaicked together and features a rather steep blaze angle of over 70° . The large size of the grating is necessary to optimize the throughput of the system and to minimize the loss of light. A cross disperser splits the beam coming from the echelle grating again. Via several correction optics, it is sent to the detector which is placed behind a field flattener. The detector itself is a standard CCD detector with a tailored setup of lenses in front of it, again, to maximize the efficiency.

5.2.5 The Echellette Spectrograph and Imager (ESI)¹

The Echellette Spectrograph and Imager (ESI) is a multipurpose instrument currently mounted at the Cassegrain focus of the KECK II telescope on Mauna Kea, Hawaii. It features three different observing modes: A standard Echellette mode, a high efficiency low dispersion mode and the direct-imaging configuration. In Fig. 5.5 the optical layout of the ESI spectrograph operating in echellette mode is pictured. Coming from the telescope, the light passes a slit and filter wheel before reaching a collimator which can be actively moved in three dimensions. This item provides flexure and focus control for the spectrograph. In Echellette mode, the light is then forwarded to a double-pass prism, pre-crossdispersing the light before it hits the grating. After the grating the beam of light passed through the first prism again and is cross-dispersed a second time. After being directed through a second prism, the light is forwarded to the camera. This mode provides a resolving power of up to $R=13000$. In the high-efficiency mode, a plane silvered mirror is placed in front of the grating so that the light is only dispersed by the two prisms. To accommodate for the new dispersion direction, the slit can be rotated by 90° . In this configuration, the resolving power varies between $R=1000$ and $R=6000$. In the direct imaging mode, a mirror is placed in the path of light, sending the light directly to the camera, bypassing all dispersing elements.

¹Based on information given in Sheinis et al. [2002].

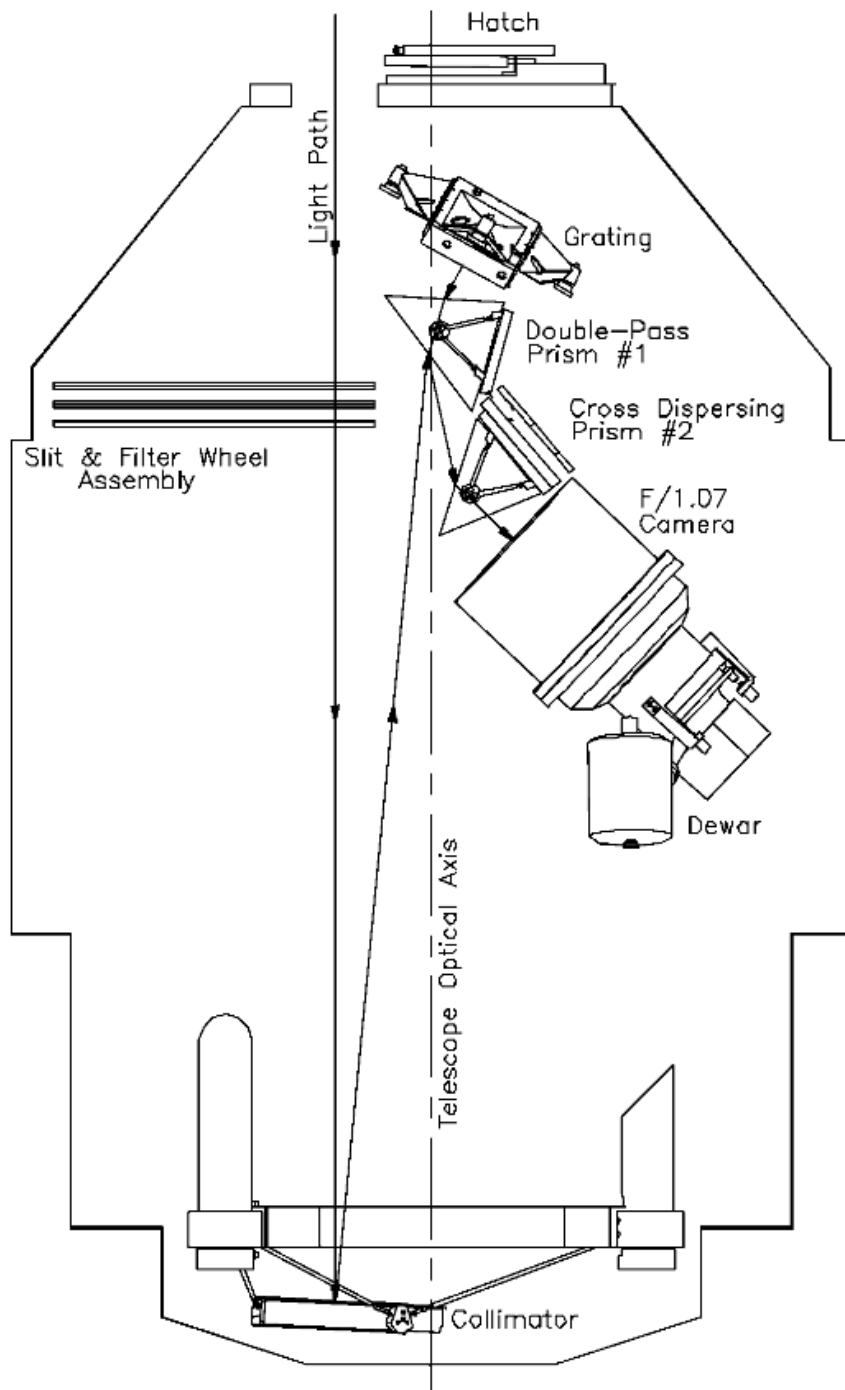


Figure 5.5: Schematic path of light in the ESI spectrograph operating in echellette mode. Taken from Sheinis et al. [2002].

5.2.6 Hubble Space Telescope instrumentations

The Hubble Space Telescope (HST) features several scientific instruments, among them the two spectrographs described below.

The first idea for a space observatory was formulated by Lyman Spitzer in 1946¹.

¹<https://www.spacetelescope.org/about/history/timeline/>

But it took almost 45 years until the first space telescope, the Hubble Space Telescope, was finally launched. Planning focused on launching it four years earlier, but the Challenger space shuttle disaster and the following compulsive break for all Shuttle flights also stalled this intend. When the telescope was finally in an orbit around Earth, it was discovered that the shape of the main mirror and therefore the optical quality suffered from a manufacturing error, resulting in strong spherical aberrations. During the first service mission in 1993, the COSTAR (Corrective Optics Space Telescope Axial Replacement) optics was installed. This device features different mirrors for each of the scientific instruments that counteract the aberrations from the main mirror and established a parallel wavefront again. As all future instruments had already built-in corrective optics, COSTAR was decommissioned in 2009 and replaced by COS, the Cosmic Origin Spectrograph (see Sect. 5.2.6.2) during the last service mission. As Shuttle flights are no longer possible to maintain the telescope future failures can no longer be repaired.

If there are no instrument failures, the satellite should be functional until around the year 2024 when the orbit will have declined to such an extend that the telescope will re-enter the atmosphere and burn up¹. It is planned that the HST will be succeeded by the James Webb Space telescope (JWST, launched probably in 2018), an infrared telescope. While the HST was able to gather data from the far UV to the infrared, this is a major step-back for many fields of astronomy.

5.2.6.1 Space Telescope Imaging Spectrograph (STIS)²

The Space Telescope Imaging Spectrograph (STIS) was installed in 1997 and is a multi purpose instrument capable of doing both, spectroscopy and imaging. By using different kinds of detectors, it is sensitive from the UV to the near infrared for longslit spectroscopy and on the UV (1150 Å to 3100 Å) for echelle spectroscopy.

Fig. 5.6 gives an overview on the different components of STIS. After being directed to the entrance of the spectrograph by the telescope mirrors, the light passes through the first and the second correction mirror that compensate for the spherical aberrations. Depending if calibrations frames are taken or not, a small mirror can be inserted in the path of light that blocks all light coming from the telescope and reflects the lines from the calibration lamps to the detector. The calibration system actually consists of two subsystems, one for providing the flat fields and one for the wavelength calibration and slit illumination. No matter where the light is coming from, the next optical element is a collimation mirror, followed by the slit wheel. This device contains the slits for spectroscopy and the different apertures and filters for the imaging mode. To select between the different modes, the nutating Grating Wheel is used. It stores the first-order grating for longslit spectroscopy, the cross-disperser grating for the echelle mode and a selection of prisms and mirrors, necessary for imaging. With the echelle grating a resolution between $R \sim 30000$ and $R \sim 114000$ can be achieved, while the resolving power for the longslit mode is lower, between 500 and 17000. However the big advantage of STIS with its long slits is that it can gather multiple spectra of extended objects at the same time. Of course,

¹<http://www.deeпаstronomy.com/how-the-hubble-space-telescope-will-die-video.html>

²Based on the STIS instrument handbook for cycle 24 [Biretta, 2016].

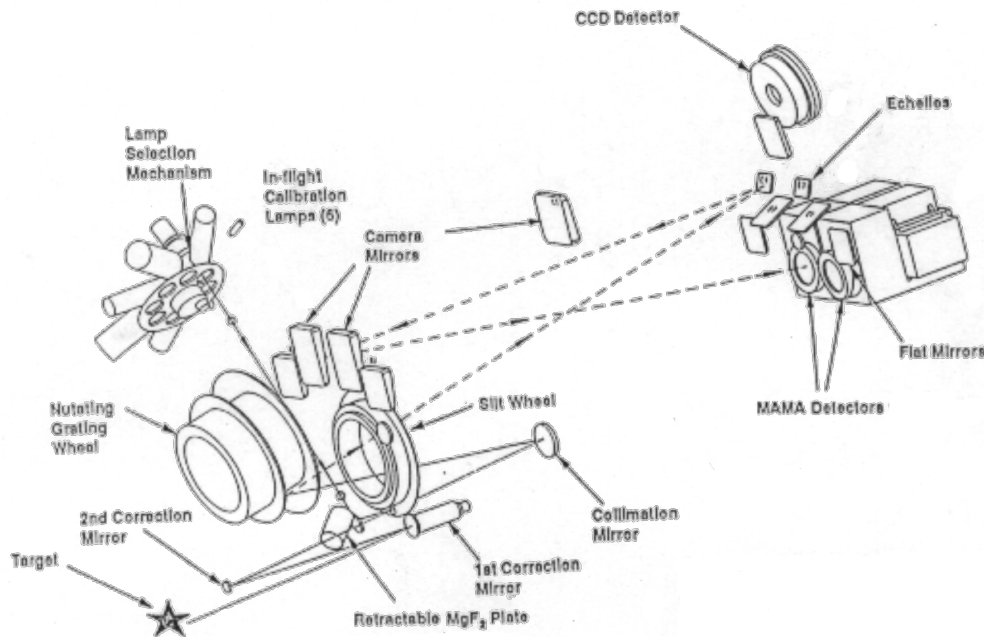


Figure 5.6: Layout of the STIS spectrograph with its most important components; Adopted from Biretta [2016].

this is not possible in echelle mode, where the spectra is spread over the surface of the chip. Only the “traditional“ longslit mode where the spectra only occupy several pixel rows on the chip is suitable for this kind of observation.

STIS makes use of three different detectors: A CCD operating from 1640 Å to 10300 Å and two Multi-Anode Microchannel Array (MAMA, similar to the ones used in COS) detectors, one for the far UV (1150 Å to 1700 Å) and one for the near UV from 1600 Å to 3100 Å. Different mirrors are used to guide the light to one of the detectors.

5.2.6.2 The Cosmic Origin Spectrograph(COS) ¹

The Cosmic Origin Spectrograph (COS) was installed on HST in May 2009 and replaced the COSTAR optics. It is a slitless UV spectrograph and consists of two separate channel, one for the far UV (FUV), ranging from 900 Å to 2150 Å and one for the near UV (NUV) from 1650 Å to 3200 Å. The two channels are independent from each other and cannot be used simultaneously. In Fig. 5.7 the layout of the optical system is shown to scale, including the different possible paths of light. After being reflected by the mirrors of the Hubble telescope, the light passes through an external shutter and encounters one of the four apertures, turnably mounted on the Aperture Mechanism. The most important apertures are the Primary Science Aperture (PSA) and the Bright Object Aperture (BOA). The remaining two ones are for wavelength calibration and flat fielding. The PSA is basically a circular field stop with a diameter of 0.7 mm which corresponds to 2.5 arcseconds. The BOA has the same geometrical properties, but holds a neutral density filter ND2 with a

¹Based on the official COS Handbook, Cycle 24 [Debes, 2016]

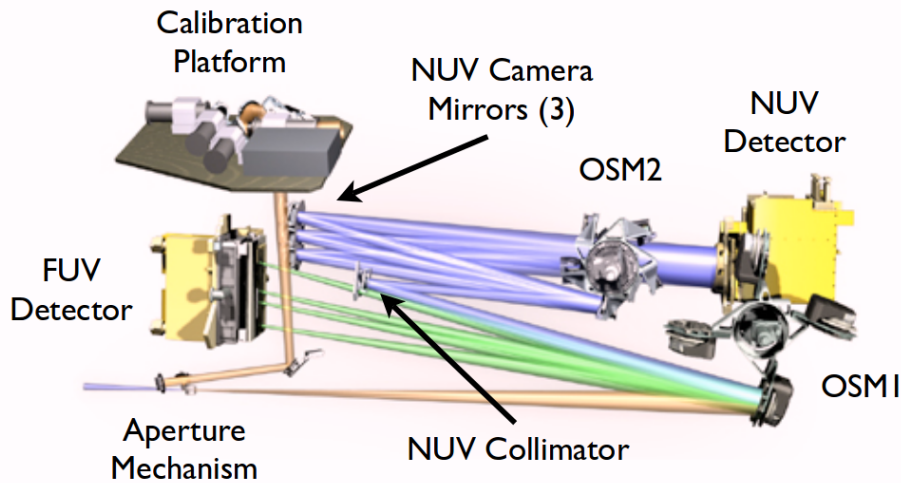


Figure 5.7: Schematic layout of the COS optical layout, including FUV and NUV channel. Taken from Debes [2016].

transmission of about 0.6%. It is used for observing bright stars as the detectors would otherwise exceed their maximum brightness limit. The light then reaches the Optics Select Mechanism 1 (OSM1). This device can either insert a flat mirror to direct the light to the NUV channel, or locate one of three gratings for the FUV channel. As this thesis only used data from the FUV, a description of the NUV channel will be omitted. Fig. 5.8 gives an overview on the optical path for the FUV channel. The gratings are not only used to disperse the light and focus it, but also

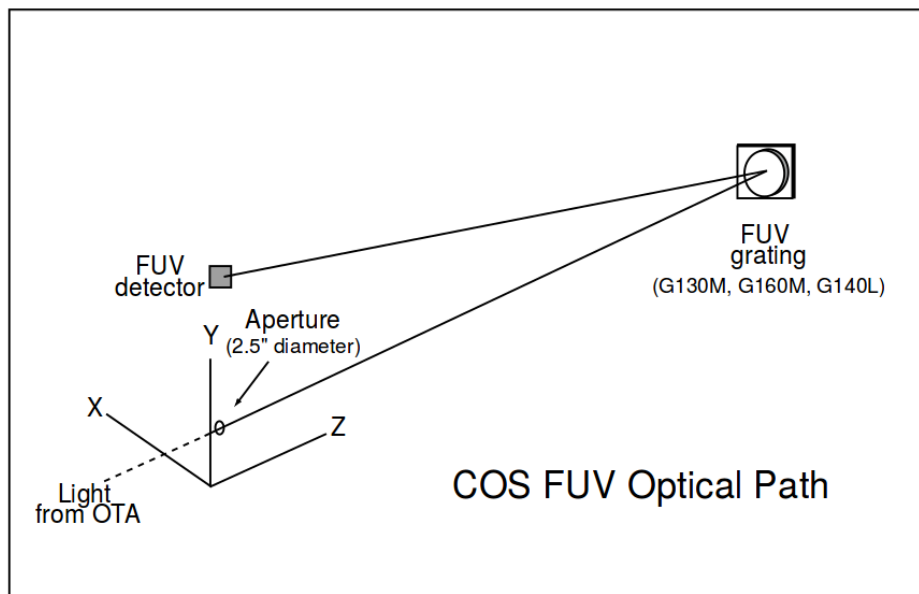


Figure 5.8: Schematic layout of the COS FUV channel. Taken from ?

to correct for the aberrations caused by the HST primary mirror. The usage of only one optical surface for these purposes enhances the sensitivity of the spectrograph

in the UV, as each reflection etc. causes the loss of a certain percentage of light. The detector used in COS is a windowless cross delay line, similar to that one used on the FUSE satellite (see Sect. 5.2.8). The detector consists of two photon-counting micro channel plates (MCPs), similar to a photomultiplier, separated from each other by a ~ 9 mm gap. The detector's surfaces is curved to match the non-flat focal plane. The charge cloud produced by an incoming photon and the micro-channel plates is hitting a delay-line anode (two for each detector, x- and y -direction). To determine the location of that event, the arrival times for such a charged pulse are calculated and digitized. To reduce the background rate, an ion-repeller grid is placed in front of the detector, preventing thermal ions to be detected.

5.2.7 The International Ultraviolet Explorer (IUE)¹

The International Ultraviolet Explorer (IUE) was a UV sensitive space based spectrograph. It was launched in 1978 as a cooperation project between American and European scientists and gathered data until 1996.

The satellite basically consisted of a 45 cm Ritchey Chrétien telescope and two attached spectrographs (see also Fig. 5.9), one for the near UV and one for the far UV.

After passing through the hole in the primary mirror, the light passed the aperture select mechanism. There were two apertures for each of the spectrographs; The small aperture had a circular diameter of 3 arcseconds, while the large aperture had a rectangular shape of about 10×20 arcseconds. For spectro-photometric measurements, the larger aperture is recommended as the small one could suffer from light loss.

Two independent guiding sensors ("Fine error sensor") were placed near the aperture wheel and fed with light by some semi reflective mirrors.

The beam of light hits one of the two collimator mirrors, depending on the wavelength band being observed. The NUV band covered 1850 \AA to 3300 \AA , the FUV one 1150 \AA to 2000 \AA . After being collimated, the next optical element was the Dispersion select mechanism that placed either an echelle grating and a cross disperser or the disperser alone in the lightpath. In the first case, a resolution of $\sim 0.2 \text{ \AA}$ was achievable, the second configuration yielded about 6 \AA . The light was then detected by one of two redundant cameras for each arm with an attached UV converter to enhance the sensitivity of the system.

5.2.8 The Far UV Spectroscopic Explorer (FUSE)²

As IUE, the Far UV Spectroscopic Explorer (FUSE) is a spacecraft carrying an (F)UV sensitive spectrograph. Launched in 1999 it was operational until a defect in a rotation wheel stopped its mission in 2007.

FUSE operated in the UV waveband from about 900 \AA to 1190 \AA which is technologically very difficult to handle. In this comparatively small window, the optical

¹Based on information provided by the Space Telescope Science Institute; <https://archive.stsci.edu/iue/instrument.html>

²Based on the official FUSE instrument handbook <https://archive.stsci.edu/fuse/instrumenthandbook/index.html>

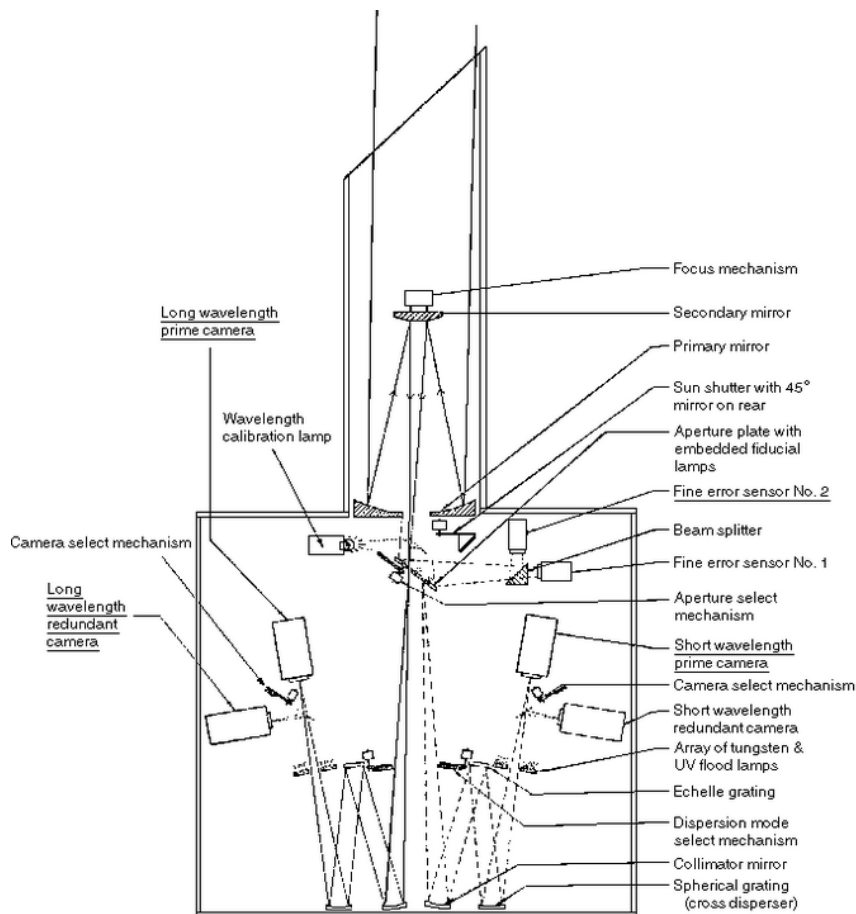


Figure 5.9: Layout of the IUE satellite with its most important components; Adopted from: https://archive.stsci.edu/iue/instrument/obs_guide/fig2.1.gif.

systems was designed to reach a maximum throughput. To do so, the system consists of four individual optical paths. Each path holds an off-axis parabolic mirror that collects the star light and a Focal Plane Assembly Unit at the mirror's focal plane that basically serves as an entrance aperture. It holds a flat mirror with holes cut out of it. The size of the four different holes determines the spectral resolving power of the system. There was one aperture for high-, medium-, and low-resolution, as well as a pinhole that was never used for any observation. The portion of light that hit the flat mirror and didn't fall through one of the apertures was reflected back to one of the FES, the Fine Error Sensor, sitting in the "LiF"-channel (see below), serving as a guiding camera and surveying the pointing accuracy.

The four channels are not identical. To optimize the performance, two of them are tailored to high reflectivity from 905 to 1100 Å by using a silicon carbide (SiC) coating on top of an aluminum layer. The latter one guaranteed a higher thermal stability. The remaining two mirrors and gratings used lithium fluoride (LiF) on top of aluminum. The optimized passband of this channel is 1025-1187 Å. According to their coating, the optical paths are referred to as "LiF" and "SiC" channels. Fig. 5.10 shows an schematic overview on the FUSE layout. After passing the coated gratings, the light enters the detectors. As there are only two detectors, each of

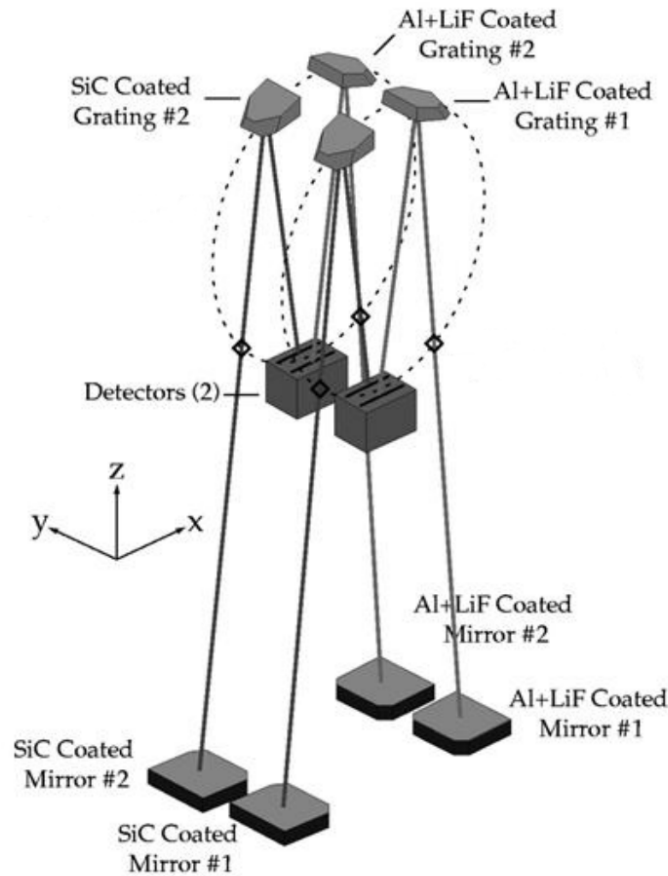


Figure 5.10: Optical layout of the FUSE spacecraft; Adopted from: https://archive.stsci.edu/fuse/instrumenthandbook/chapter2.html_Toc102014442.

them captures a LiF and a SiC spectrum. To prevent overlapping, the spectra were offset perpendicular to the direction of dispersion. Furthermore, each detector was divided into two segments, separated by a small gap. Each segment covers almost the entire wavelength range, important key regions are in the overlapping area on both parts.

The detectors themselves are Double Delay Line detectors with microchannel plates and an ion-repeller grid placed in front of them.

5.3 Data reduction

As all spectrographs use camera-like structure to obtain the spectra, the resulting data can be found as an image showing the light distribution on the CCD chip in most cases. To transfer this image to a machine-readable (ascii) file, several actions and transformations have to be taken. These will be described hereafter. Depending on the type of spectrographs, the steps may vary a bit, but nevertheless, the general concept remains the same.

- **Removal of cosmics**

Cosmics are unwanted, bright pixels, or pixel structures on the CCD image that are caused by incoming, highly energetic charged particles from cosmic rays. Depending on the angle of impact, they can be found somewhere between single illuminated pixels and elongated (mostly linear) bright traces. The longer the exposure time, the larger the number of cosmics. Their signal strength is usually much larger than the signal caused by the “normal” photons. This makes it easier to eliminate the cosmics by applying numerical filters, tailored to detect the typical signature of cosmic particles on CCD chips.

- **Subtraction of Bias Frames**

In a CCD chip, a constant offset is added to all the pixel values to avoid negative signals during the readout process. As this affects the values of all other signals, too, the offset is subtracted by using a bias frame. These frames are taken with a closed shutter and the minimal exposure time. In an ideal world the signal would only consist of the readout noise and pixel offset. But as there are natural fluctuations, several bias frames are taken and averaged afterwards. The averaged bias can then be subtracted from all other images.

- **Subtraction of Dark Frames**

As the CCD chip has a finite temperature and uses non-zero exposure times, all images will be affected by dark-current. This results from thermal excitations within the semiconductor material of the chip and increases the value of several pixels (some more than others). To subtract the dark current, an exposure with the same CCD temperature and the same exposure time as the science frame is taken but with the shutter closed and then subtracted from the corresponding light exposure. This kind of correction frame also eliminates stray light that might occur within the spectrograph as well as hot pixels, i.e. malfunctioning pixels, that show a signal no matter if light was present or not. If dark frames are used, it is not necessary to obtain bias frames as each dark also contains the readout noise and offset. With professional spectrographs, it is common to take only bias frames and no darks as the chips are cooled to such low temperatures that there is virtually no dark current anymore.

- **Subtraction of the sky background**

Some spectrographs (e.g. FEROS) offer the possibility to obtain two spectra, one of the target and one of the surrounding sky. The second spectrum can be used to estimate the background signal overlaid to the target spectrum. This makes it easier to subtract the obstructive sky background. This way the influence of sky illumination by the moon or artificial light sources i.e. street lamps can be reduced to a large extent.

- **Flat field correction**

Flat fielding is important to get rid of artificial trends in the spectrum. The intensity profile of a spectrograph is dominated by the blaze function (see Sect. 5.1). In addition damaged pixels in the CCD can have a lower sensitivity than the rest of them which would result in a lower flux at the corresponding wavelength. To get rid of both effects, several flat field frames must be taken. They are obtained with a light source that emits pure white light (which is of

course not 100% possible in the real world) and an open shutter. The science frames are divided by the flat field to remove the trend resulting from the blaze function or the non-linear pixel responses.

- **Wavelength calibration**

As the data still has intensity per pixel values, it is necessary to convert the pixel- into a wavelength scale, that is to determine the dispersion relation. This is done by making use of calibration lamps. Most common are Thorium Argon (ThAr) lamps, which provide thousands of sharp lines which's center wavelength are known very accurately from laboratory measurements.

- **Rebinning**

In this step, the individual spectral orders are extracted from the two-dimensional image and are converted to a one-dimensional spectrum

- **Merging of orders**

If an echelle spectrograph was used, it is necessary to merge the individual orders to a single one, covering the complete accessible wavelength range. If spectral orders overlap, the data in those regions are averaged.

- **Normalization**

It is common to use normalized spectra, at least for quantitative spectral analysis. In these cases, the continuum value is set to unity (=1). However it is difficult to normalize spectra as a function has to be fitted to the data that represents the general slope of the continuum without being influenced by the spectral absorption lines. If fitting this function was successful, the data can be divided by it to reach a normalized continuum.

6 Analysis of He-sdO stars

This chapter hosts the results of the analysis of the different He-sdO stars, dealt with during this thesis. For a better overview, they have been divided into three classes, depending on the enrichment of carbon and/or nitrogen in their atmospheres. An exception is US708 which is described in chapter 8 due to the non-standard method of analysis used on this star.

For every star, an overview on its known parameters and the results of previous analysis is presented, followed by a brief description of the data used in this work. If possible, a comparison between the resulting spectroscopic data (SED) and all available photometric indices is made to test and crosscheck the results as well as to obtain a distance and reddening parameters.

6.1 Nitrogen rich He-sdO stars

As CD -31° 4800 was the first He-sdO analyzed during this work, the description of the modeling process and the used programs will be more detailed than for the rest of the sample.

6.1.1 CD -31° 4800

6.1.1.1 General information

CD-31° 4800 is a bright ($m_v = 10.6$) He-sdO star located at $\alpha = 07^{\text{h}} 36^{\text{m}} 30.2^{\text{s}}$ and $\delta = -32^{\circ} 12' 43.7''$. A parallax of $\pi = 7.62 \pm 1.51$ was measured by the Hipparcos satellite. This translates to a distance of 131_{-22}^{+32} pc [Hirsch, 2009].

It was discovered as CPD -31 1701 by Garrison and Hiltner [1973] during a survey of southern OB stars. They described it as a bright object located in the plane of the Milky Way. Its spectrum is dominated by stark broadened HeI and HeII lines. An analysis of the atmospheric parameters and metal abundances was conducted by Bauer and Husfeld [1995]. They found a temperature of 44000 ± 2000 K and a surface gravity of $\log(g) = 5.4 \pm 0.3$. In addition they noticed the strong helium enrichment as well as an overabundance of nitrogen compared to carbon and oxygen. Despite that, they encountered a problem with fitting the line cores of HeII lines belonging to the Pickering series. The model was always deeper than the actual line, while fitting the other lines perfectly. This problem is addressed in Sect. 6.7.

The latest analysis of this interesting object was done by Hirsch [2009]. He used pure H/He grids as well as ones with additional carbon or nitrogen to determine the atmospheric parameters. His results depend on the used grid. For H/He only, a temperature of 43000 K, a surface gravity of 5.84 and a helium abundance of 2.75 was found. The values changed with a H/HE/N grid and were determined to $T_{\text{eff}} = 44100$ K, $\log(g) = 6.06$ and $\log(y) = 1.84$. For all models the rotational velocity was below 10 km/s.

By comparing the results from the different analysis it is striking that the surface gravity spans a comparatively large range of over 0.6 dex. As already mentioned beforehand, the helium lines in this regime are quite insensitive to gravitational broadening so that the quality of the analyzed data has to be well above average to get trustworthy results. This aspect, as well as others, will be revisited in the following section.

6.1.1.2 Spectral analysis

For the spectral analysis, the quality of the data is essential. Spectra covering an extended wavelength range allow to use multiple helium and hydrogen lines for the determination of the atmospheric parameters, while a high S/N ration in combination with a good spectral resolution show line features that might have remained hidden in worse data.

For CD-31° 4800 spectra from UVES, FEROS, FUSE, IUE and the COS spectrograph from the Hubble Space Telescope were used. Information about each dataset can be found in the tables in Sect. .1 in the appendix. If more than one spectrum was available, they were coadded to enhance the signal to noise ratio.

As CD-31° 4800 was the first He-sdO analyzed during this thesis, the workflow is a bit different compared to the rest of the sample. The first step was the determination of the atmospheric parameters from the UVES spectra.

This was done by using an adopted pure NLTE H/He grid provided by Dr. Peter Németh. This grid included CNO at a very low abundance (10^{-10} by numbers) in LTE to ensure the synthetic spectra would be calculated in the complete desired wavelength range. A global fit of the atmospheric parameters resulted in an effective temperature of $T_{\text{eff}} = 41400 \pm 300$ K, a surface gravity of 5.47 ± 0.1 and a helium abundance of $\log(n(\text{He})/n(\text{H})) = 2.77 \pm 0.1$.

As CD-31° 4800 is known to be nitrogen rich, a pure H/He grid is not the best approach to model the stellar atmosphere as the nitrogen has an influence on the structure of the atmosphere, the stratification and the depths of line formation. Therefore the nitrogen abundance was determined from a subgrid, set up around the temperature, gravity and helium abundance determined beforehand. Nitrogen was then included in the H/He grid at a value of $\log(n(\text{N})/n(\text{H})) = -0.19$, being equivalent to $n(\text{N}) = 0.65 \cdot n(\text{H})$. Fitting this grid to the UVES spectrum resulted in

- $T_{\text{eff}} = 42230 \pm 300$ K
- $\log(g) = 5.60 \pm 0.03$
- $\log(n(\text{He})/n(\text{H})) = 2.61 \pm 0.06$
- $v_{\text{rot}} < 5$ km/s
- “Model 1“

This model is referred to as “ Model 1“. The fits to selected HeI and HeII lines are shown in Fig. 6.1

Despite these parameters are typically normal for a He-sdO star, they show a large difference from the values determined in the latest analysis of this system by Hirsch [2009]. Especially the surface gravity is about 0.24 dex to 0.46 dex to low, depending

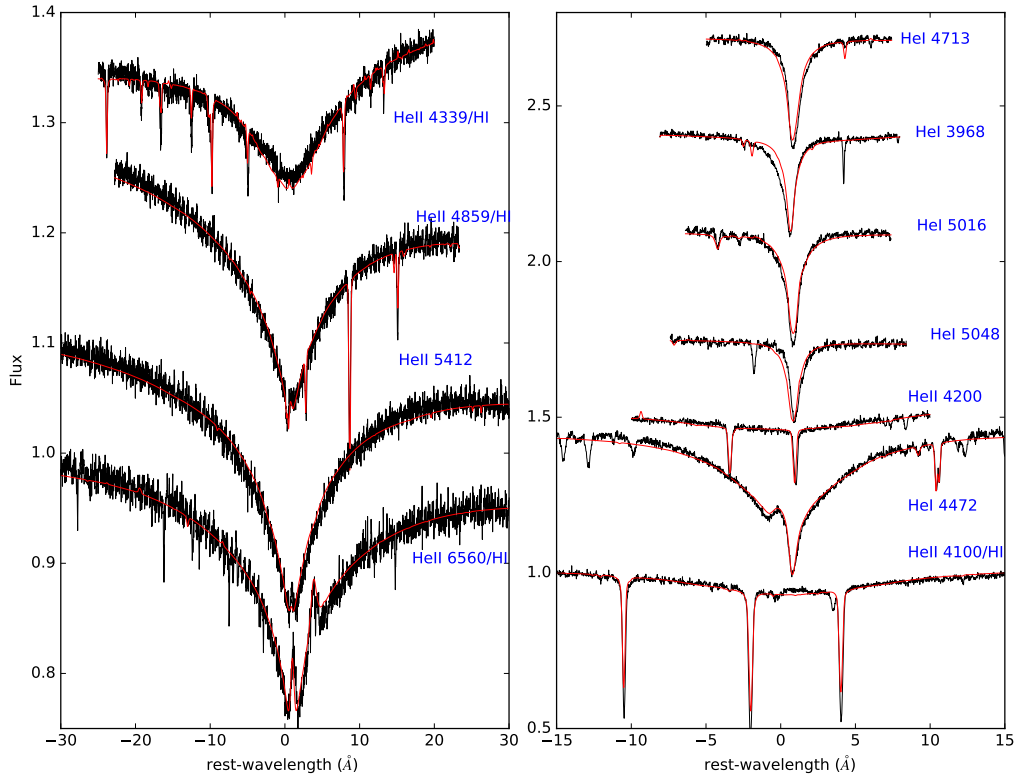


Figure 6.1: Visualization of several HeI and HeII lines of CD-31° 4800, some with a hydrogen component. The black lines show parts of the UVES spectrum, the best-fitting model is represented by the red lines. The flux levels had been adjusted for better representation.

on the model used by Hirsch [2009]. As it was not possible to find any reason for the discrepancy, it was decided to go back to the older FEROS spectrum and analyze it with the same HHeN grid.

Resulting from the fits shown in Fig. 6.2, the derived atmospheric parameters change and are now much closer to the values from Hirsch [2009].

- $T_{\text{eff}} = 43170 \pm 350 \text{ K}$
- $\log(g) = 5.90 \pm 0.05$
- $\log(n(\text{He})/n(\text{H})) = 2.70 \pm 0.08$
- $v_{\text{rot}} < 5 \text{ km/s}$
- “Model 2”

To decide between the two possible set of parameters, a subgrid with varying nitrogen abundance was calculated for each possibility to test the ionization equilibrium. Although NII, NIII and NIV lines are visible in the both datasets, NII was dismissed from the test, as fits of this ionization stage generally looked worse than for the other two ions and often resulted in emission lines where the spectra showed a clear absorption profile. If the temperature of the star is correct, each ionization stage should give the same nitrogen abundance if fitted solely. A too low or too

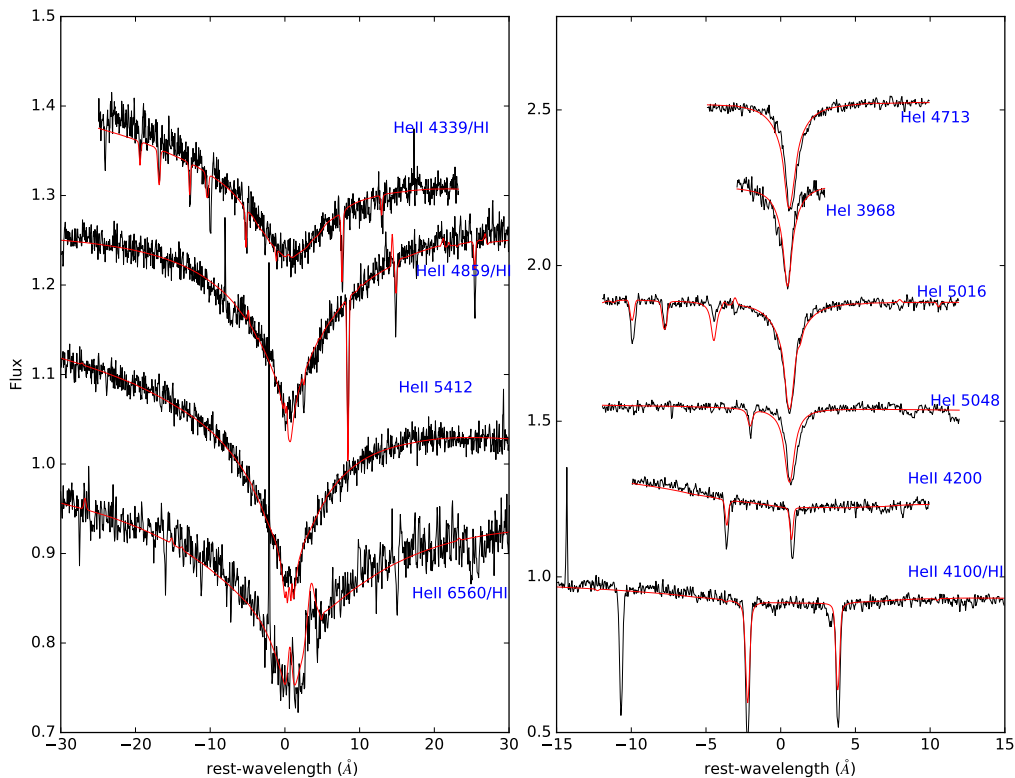


Figure 6.2: Visualization of several HeI and HeII lines of CD-31° 4800. The black lines show parts of the FEROS spectrum, the best-fitting model is represented by the red lines. The flux levels had been adjusted for better representation.

	44230 K/5.60/2.61	43170 K/5.9/2.7
NIII	-0.24 ± 0.012	0.01 ± 0.02
NIV	-0.27 ± 0.03	-0.05 ± 0.04

Table 6.1: Comparison of ionization equilibriums for CD-31° 4800

high temperature would lead to a shift towards opposite directions of abundances for each ion. As it can be seen in table 6.1, the abundances derived from NIII and NIV are equal within the error ranges. As it cannot be decided which model is correct (or closer to reality), the following analysis was done simultaneously for both sets of parameters. For a trustworthy claim on the correct surface gravity, the parallaxes and distances from GAIA would be very helpful. Unfortunately, the data on CD-31° 4800 will not be published before April 2018 in DR2, as it was excluded in DR1 because of its very blue color. See also chapter 9 for a discussion of the $\log(g)$ problem.

It is worthwhile to mention that the same problem with fitting the line cores of the HeII Pickering series was encountered as described by Bauer and Husfeld [1995]. The 4399 HeII line and the 4200 HeII line were not fitable together with the rest of the lines and therefore excluded from the determination of the atmospheric parameters. In Fig. 6.1 the miss-fitted 4339 line can be seen. The same problem appeared with the FEROS spectrum (see Fig. 6.2) but to a smaller extent. But as

CD-31° 4800 is not the only sample star to show this problem, it will be discussed in more detail in Sect. 6.7. After the work on this star was finished, an old FORS spectrum was provided. Despite having only a resolution of $R=1900$, it features an excellent signal to noise ratio. To test the atmospheric models, it was divided into six subparts and fitted with a H/He modelgrid (see Fig. 6.3). As the nitrogen features in this spectrum are all blended with other elements, the omission of nitrogen in the grid results in better fits. As the low resolution covers all hydrogen features

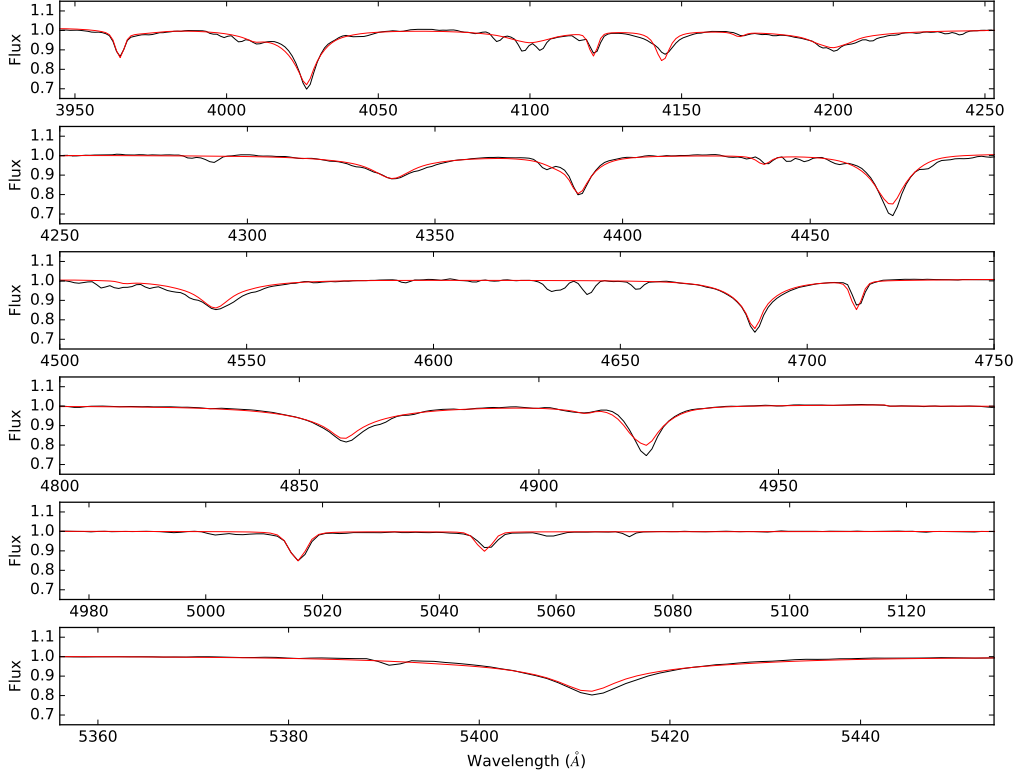


Figure 6.3: Fit to several parts of the FORS spectrum of CD-31° 4800, containing various HeI and HeII lines.

in the He lines and therefore makes it impossible to calculate the H/He ratio, the $\log(y)$ was set to 2.61 in accordance with the values from UVES. A change to a value of $\log(y)=2.7$ (result from FEROS) resulted in no significant change of the atmospheric parameters. The resulting effective temperature is $T_{\text{eff}} = 42730 \pm 600$ K and $\log(g) = 5.74 \pm 0.15$. This is compatible with both results from either UVES or FEROS. The FORS spectrum is especially helpful because it was not taken with an echelle spectrograph but with a longslit one. This eliminates all problems that might occur from artifacts of normalization, merging of the single echelle orders or de-blaizing and is therefore particularly trustworthy.

As CD-31° 4800 was the only star in the sample for which a NUV-IUE spectrum with a reasonable S/N ratio was available, the atmospheric parameters could be tested using the HeII Foulmer lines. They originate from electrons descending to level $n=3$ in the $2x$ ionized helium atom. Fig. 6.4 shows an overplot of model to these lines. Fitting the lines was not possible as the temperature showed a scatter around 3000 K and the surface gravity varied between 5.3 and 5.9, depending on the selected fitting window. This can be explained by the low sensitivity of the HeII lines

(especially in this wavelength region) to changes of the atmospheric parameters in combination with the bad S/N ratio of the data. By the naked eye, no differences were visible between both models, therefore, only model 1 is shown here and it matches the observation quite well.

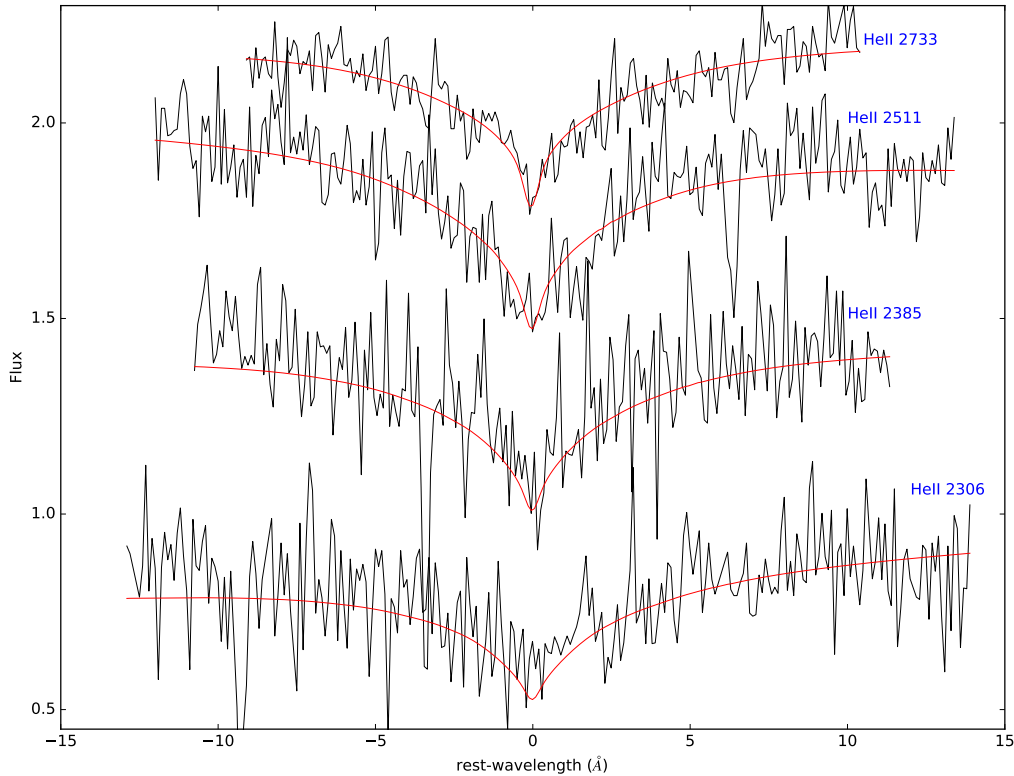


Figure 6.4: The Fowler lines from the IUE spectrum of CD-31° 4800 overplotted with model 1.

The determination of the different elements' abundances was done as described in Sect. 4.9. In a first step only the optical UVES data was used. For each element, both a global fit of all usable lines as well as an individual fit of each line was done. In theory, both methods should lead to the same results. In practice it turned out that the width of the window around each fitted line (aka the number of data-points in the selected spectral range) has an influence on how each line is weighted in the global fit. Therefore, the results derived from the global and individual fit may vary. To account for that, an error-weighted average of both abundances was calculated and used for further calculations.

Table 6.2 shows the first results of the UVES fit. The given numbers are the $\log(n(X)/n(H))$ ratio in number abundances. In general, the values of model 2 are a bit larger, due to the higher helium abundance. The given errors are the errors of the global fit. For sulfur, no satisfying fit was possible, as the line profiles were not matchable with the data. It was therefore fitted by eye. As this problem was found with other He-sdO models, it might indicate a problem with the sulfur model atoms.

After this first fit, the models were upgraded by including iron and nickel at solar abundance and the spectra were refitted. This time, the IUE spectra were included, but fitted separately. Again, the same routine concerning the combination of global

Element	# lines	Model 1	Model2
C	7	-2.48 ± 0.02	-2.24 ± 0.01
N	35	-0.35 ± 0.02	-0.18 ± 0.02
O	8	-2.21 ± 0.06	-2.06 ± 0.05
Ne	13	-1.16 ± 0.03	-0.96 ± 0.03
Mg	1	-1.58 ± 0.02	-1.37 ± 0.03
Al	5	-2.63 ± 0.02	-2.48 ± 0.02
Si	7	-1.57 ± 0.03	-1.43 ± 0.02
S	5	set to -4	set to -3.8

Table 6.2: Metal abundances derived from the optical UVES spectra of CD-31° 4800. Given is the $\log(n(X)/n(H))$ in number abundances. (Models without Fe/Ni). The second column gives the number of lines used for fitting a specific element.

and individual fit was applied. Because of the lower resolution, the worse S/N ratio and the crowding of lines, the errors on the UV fits are generally larger than for the optical fits. This means that the final abundances are dominated by the optical data.

Element	lin. Opt./UV	#1 Optical	#1 UV	#2 Optical	#2 UV
C	7/4	-2.28 ± 0.02	-2.47 ± 0.37	-2.09 ± 0.02	-2.3 ± 0.37
N	39/18	-0.30 ± 0.01	-0.32 ± 0.12	-0.13 ± 0.02	-0.29 ± 0.13
O	8/10	-2.25 ± 0.02	-1.67 ± 0.17	-2.01 ± 0.02	-1.18 ± 0.4
Ne	13/10	-0.98 ± 0.02	-1.20 ± 0.3	-0.82 ± 0.01	-0.74 ± 0.29
Mg	1/6	-1.56 ± 0.03	-1.70 ± 0.34	-1.34 ± 0.02	-1.48 ± 0.33
Al	5/4	-2.61 ± 0.02	-3.20 ± 0.18	-2.44 ± 0.02	-3.03 ± 0.17
Si	8/11	-1.45 ± 0.02	-1.41 ± 0.14	-1.41 ± 0.02	-1.30 ± 0.17
S	6/2	-2.73 ± 0.12	(-3.01 ± 1.14)	-2.40 ± 0.25	(-2.89 ± 2.0)
Fe	0/32	—	-1.85 ± 0.09	—	-1.64 ± 0.1
Ni	0/22	—	-3.02 ± 0.2	—	-2.59 ± 0.14

Table 6.3: Metal abundances derived from the optical UVES and ultra-violet IUE spectra of CD-31° 4800. Given is the $\log(n(X)/n(H))$ in number abundances. (Models with Fe/Ni). The second column gives the number of lines used for the fit of a specific element. Values in brackets show extremely large errors and have to be dealt with care.

The inclusion of iron and nickel has improved the quality of fit for the sulfur lines. Despite still being far off optimal, the results looked much better than with the models lacking both iron group elements. However, fits to sulfur lines in the UV show extremely large errors and have to be dealt with care. As the final abundances are the error weighted average of optical and UV abundances, the abundances from optical data are dominating. The following figures show parts of the UVES and IUE spectrum. Overplotted is the model with the final parameters. For reasons of clarity only fits of model 1 are shown. However, the general quality of fit is very similar between the two models.

Element	FUSE Mod.1	FUSE Mod.2
C	$-1.91 \pm 0.15(6)$	$-2.17 \pm 0.16(6)$
N	$-0.39 \pm 0.06(15)$	$-0.31 \pm 0.06(14)$
O	$-1.92 \pm 0.10(4)$	$-1.99 \pm 0.11(4)$
Ne	$-1.20 \pm 0.25(3)$	$-0.60 \pm 0.21(3)$
Mg	—	—
Al	$-2.93 \pm 0.30(2)$	$-2.22 \pm 0.20(1)$
Si	$-1.45 \pm 0.09(6)$	$-1.58 \pm 0.10(5)$
S	$-2.09 \pm 0.25(2)$	$-2.02 \pm 0.20(3)$
Fe	$-2.01 \pm 0.25(9)$	$-1.98 \pm 0.17(10)$
Ni	$-2.83 \pm 0.17(6)$	$-2.29 \pm 0.20(6)$

Table 6.4: Metal abundances derived from a Far-UV FUSE spectrum of CD-31° 4800. Given in brackets is the number of lines used for each element and model.

After the work on CD-31° 4800 was finished, a FUSE spectrum was discovered and it was decided to use the existing models to fit the additional UV data. Table 6.4 shows the results. In general the FUSE results show a good consistency with the older abundances. Interestingly, the FUSE abundances do not appear to be generally higher than those determined from IUE as it would be expected based on the better resolution and therefore the weaker pseudocontinuum. In addition the sulfur lines match much better, resulting in smaller errors.

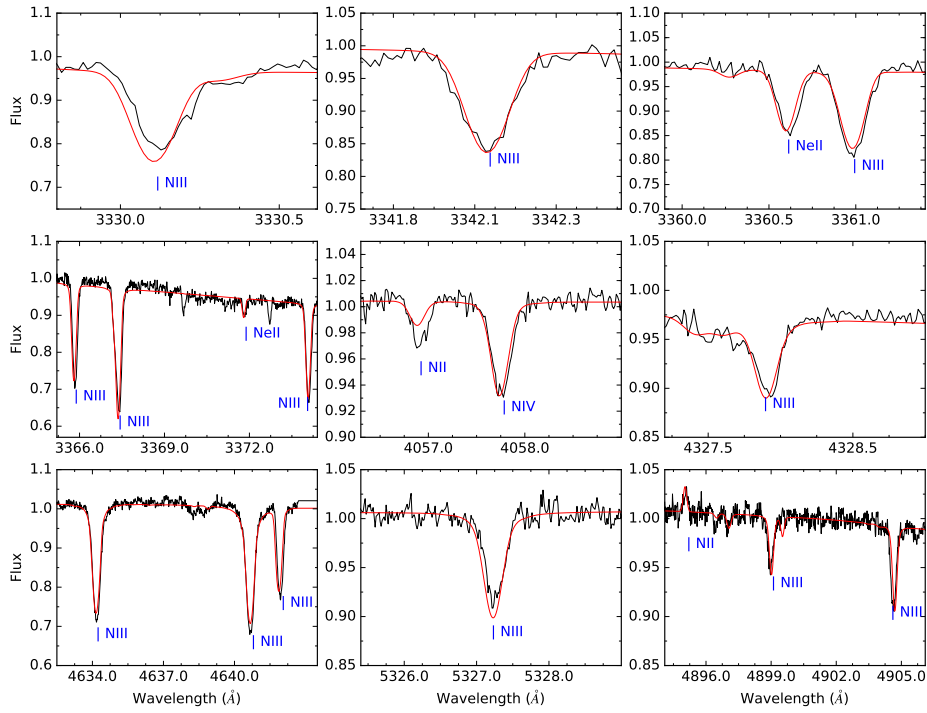


Figure 6.5: Visualization of several nitrogen lines with different ionization stages of CD-31° 4800 (UVES spectrum) in comparison with the final synthetic spectrum. The x-axis of each subplot shows the wavelength, the y-axis the flux.

The main advantage of UV data is the possibility to crosscheck the results from the optical. In the case of CD-31° 4800 where only one IUE spectrum was available, it was difficult to find strong single lines which are not blended with other metals. Especially concerning iron and nickel this was not possible. Some elements showed hardly any strong lines in the UV. For those the resulting abundances show large errors and should be interpreted as upper limits.

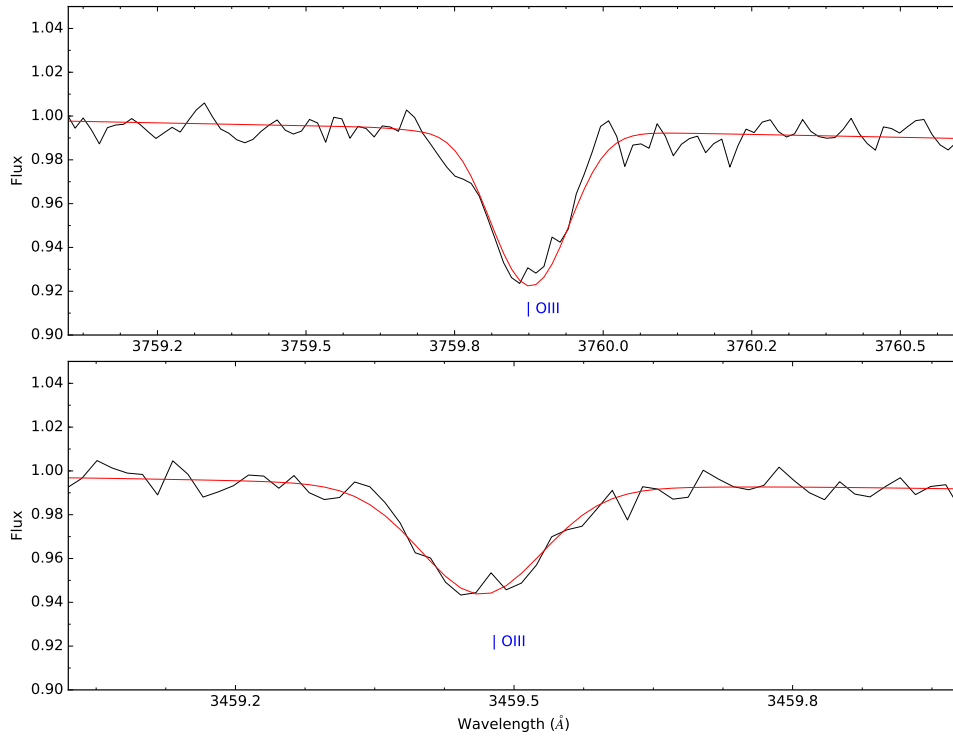


Figure 6.6: Visualization of several OIII lines of CD-31° 4800 (UVES spectrum) in comparison with the final synthetic spectrum.

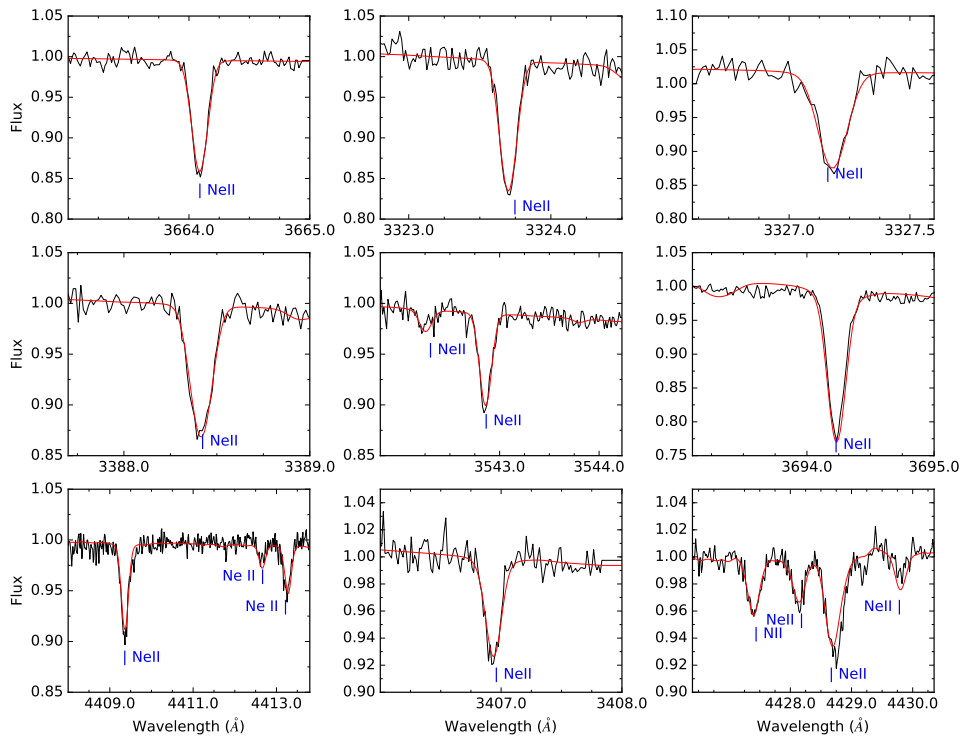


Figure 6.7: Visualization of several NeII lines of CD-31° 4800 (UVES spectrum) in comparison with the final synthetic spectrum.

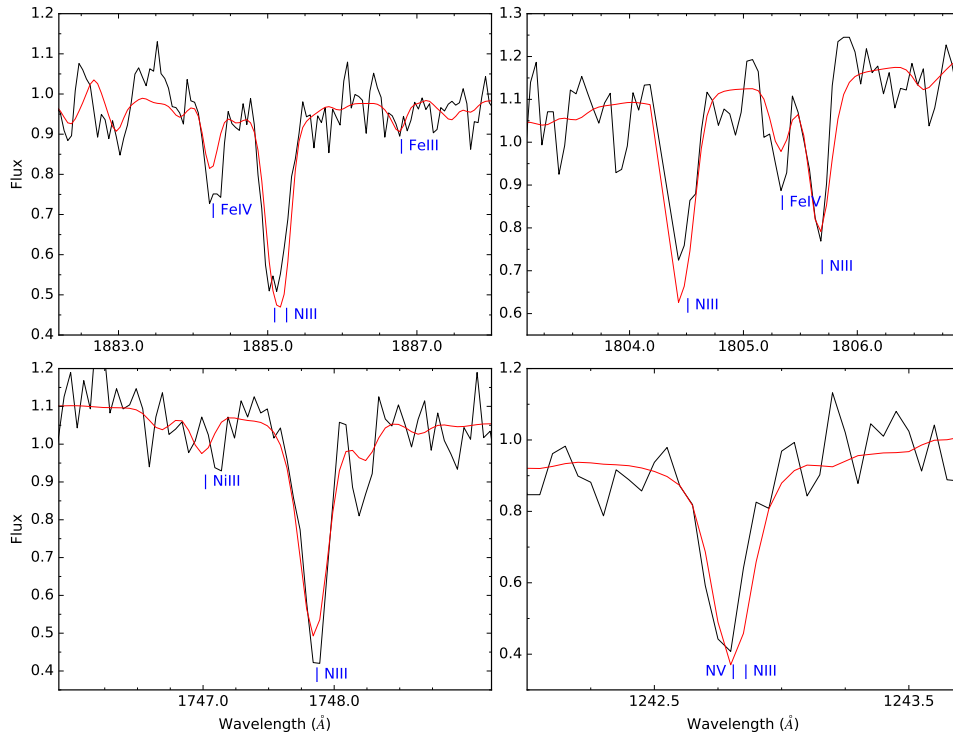


Figure 6.8: Visualization of several nitrogen lines with different ionization stages of CD-31° 4800 (IUE spectrum) in comparison with the final synthetic spectrum.

If the metal abundances derived from the optical and the UV data are compared, it can be noticed that the values are usually smaller in the UV. This is caused by the strong pseudocontinuum, a common event in low resolution UV spectra. If the resolving power of the spectrograph is not strong enough to separate the individual lines, no continuum is visible. What appears to be the continuum in the data is not the real level, but somewhat deeper, depending on the crowding and the resolution of the data. Fitting lines in such a case is difficult as the programs tend to treat the pseudocontinuum like the real one and therefore propose lines that are more shallow than they really are. This is no big deal as long there is resolved optical data for comparison. The difficulty arises with iron and nickel which have no clear lines in the optical and therefore can only be analyzed from the UV.

Fig. 6.10 shows the abundances derived from the optical and from the UV for model 1.

The median difference between the abundances is 0.2 dex. This shift can be applied to the abundances of iron and nickel to shift them towards more reasonable values.

To better compare the derived results, table 6.5 gives the mass abundance for each element compared to the solar mass abundance. Fig. 6.11 shows a visual representation of table 6.5. The abundances of CD-31° 4800 show a classical CNO pattern; Nitrogen is enriched while carbon and oxygen are depleted. The rest of the intermediate mass elements is about solar in both models. Iron is slightly depleted, while the value for nickel depends on the model. Model 1 shows a slight underabundance compared to the solar value, while it is slightly overabundant in model 2. This can

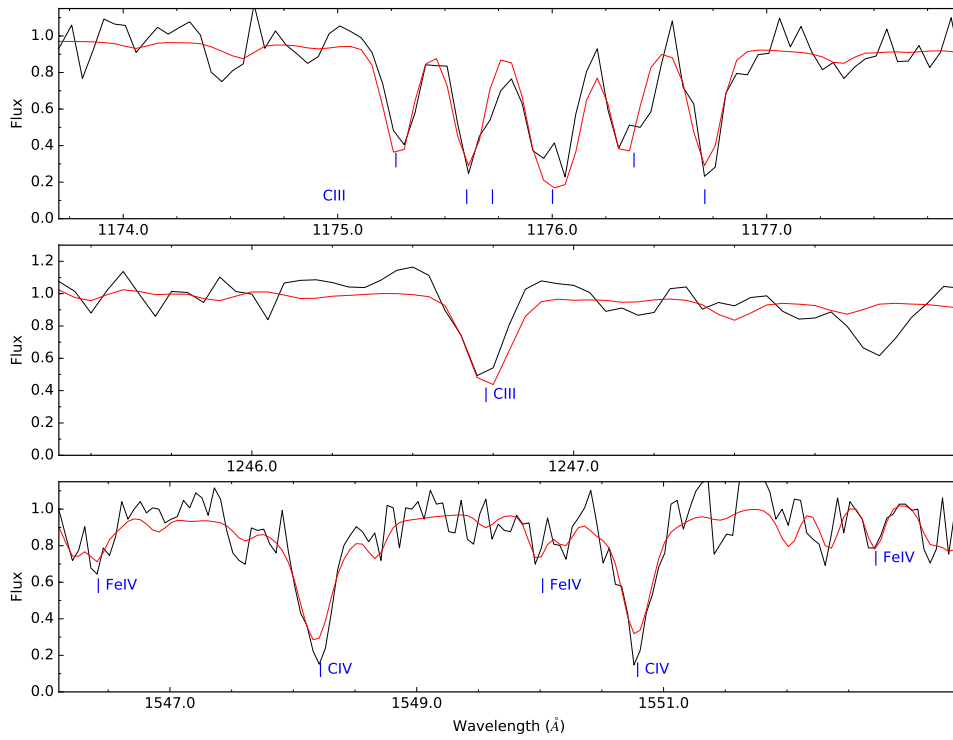


Figure 6.9: Visualization of several carbon lines with different ionization stages of CD-31° 4800 (IUE spectrum) in comparison with the final synthetic spectrum.

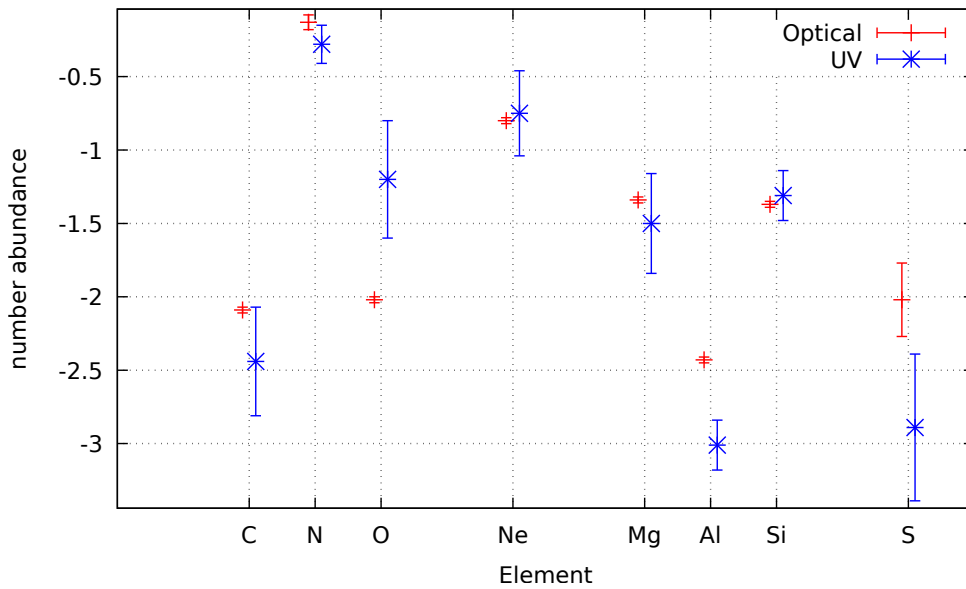


Figure 6.10: Comparison between the metal abundances derived from fits to the UVES and the IUE spectrum. Shown is the number abundance versus the corresponding chemical element.

be caused by a different selection of lines for the two fits as not all spectral lines matched equally well in both models. A detailed discussion of the abundances and

Element	β/β_{\odot} Model 1	β/β_{\odot} Model2
H	$8.26 \cdot 10^{-4}$	$6.77 \cdot 10^{-4}$
He	$3.98^{+1.12}_{-0.95}$	$3.97^{+1.15}_{-1.08}$
C	$(1.84^{+0.54}_{-0.88}) \cdot 10^{-2}$	$(2.03^{+0.20}_{-0.98}) \cdot 10^{-2}$
N	$5.98^{+1.87}_{-1.43}$	$7.13^{+2.48}_{-1.84}$
O	$(1.07^{+0.86}_{-0.53}) \cdot 10^{-2}$	$(1.85^{+2.05}_{-0.78}) \cdot 10^{-2}$
Ne	$1.01^{+1.01}_{-0.50}$	$1.24^{+1.07}_{-0.62}$
Mg	$0.552^{+0.565}_{-0.274}$	$0.759^{+0.751}_{-0.386}$
Al	$0.571^{+0.33}_{-0.191}$	$0.772^{+0.444}_{-0.249}$
Si	$0.927^{+0.402}_{-0.265}$	$0.881^{+0.443}_{-0.277}$
S	$0.104^{+0.450}_{-0.083}$	$0.201^{+0.599}_{-0.104}$
Fe	$0.363^{+0.091}_{-0.048}$	$0.444^{+0.111}_{-0.070}$
Ni	$0.473^{+0.202}_{-0.150}$	$1.04^{+0.420}_{-0.291}$

Table 6.5: Mass abundances for the different elements in CD-31° 4800 compared to the solar mass abundance.

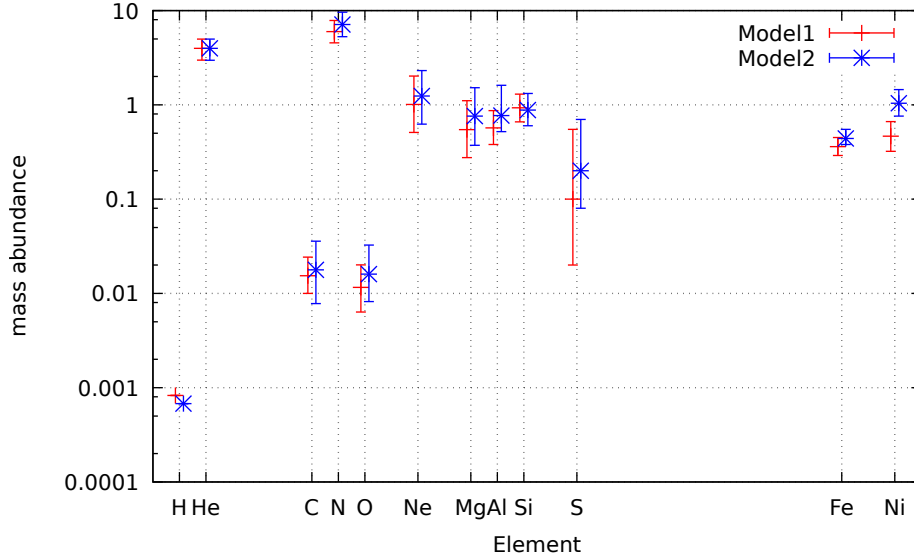


Figure 6.11: Relative mass abundances for CD-31° 4800 compared to their solar value.

their implication for the formation history will be given in Sect. 7.1.

As both models show reasonable abundances, it is still not clear which of the parameter sets fits better to the star. Another approach to solve this dilemma is presented in the following section.

6.1.1.3 Spectral energy distribution

By comparing the Spectral Energy Distribution (SED) of a star to measured fluxes (magnitudes) in different filters and to different colors it is possible to judge if the basic parameters of the system are reasonable. Despite that, the distance and the reddening can be calculated.

In the case of CD-31° 4800, a vast set of different measurements was available and allowed for a detailed analysis of the SED. To determine the reddening and the distance, the SED was shifted and stretched until it matched the observations best (see sect. 4.12 for a more detailed description). The photometric measurements can be found in table 6.6.

Fig. 6.12 and Fig. 6.13 show the fit of the SED from both model to the available observations. As it can be seen, there is hardly any difference between both of the models. Especially the $H\beta$ line, which is an indicator for the accuracy of the surface gravity is perfectly reproduced by each of the models. Unfortunately this means that no better constraint on one or the other $\log(g)$ is possible so far.

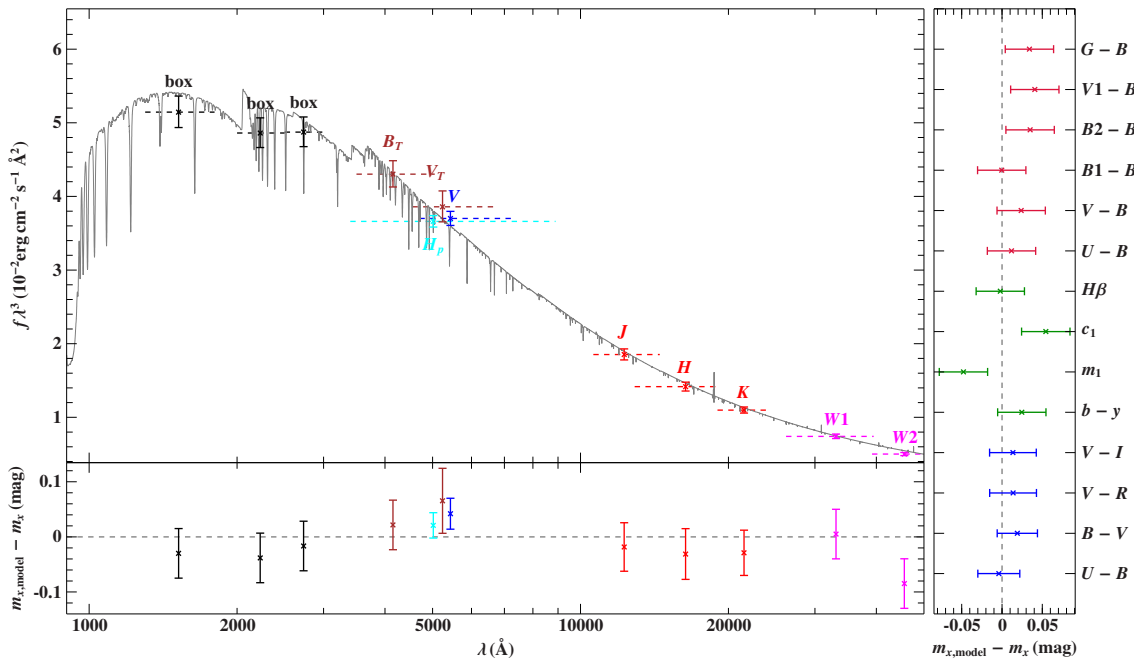


Figure 6.12: SED for model 1 of CD-31° 4800 compared with photometric measurements (magnitudes and colors). The bottom and right panels show the residuals for the magnitude and color measurements.

For model 1 a reddening of 0.0262 and a θ -value of $3.515 \cdot 10^{-11}$ was determined. This translated to a spectroscopic distance of 227_{-35}^{+43} pc for the canonical mass of $0.47M_{\odot}$. For model 2 the distance was 163_{-32}^{+39} pc, determined from $\theta = 3.563 \cdot 10^{-11}$ with a reddening of 0.0234. As θ is virtually the same for both models, the distance is mainly influenced by the different surface gravities.

There is a Hipparcos measurement for CD-31° 4800 which translates to a distance of 131_{-22}^{+32} pc. This would strongly point to Model 2 with the higher surface gravity. Changing the mass of the star until the emerging distance from Model 1 complies with the Hipparcos measurement would lead to unphysically low masses. However, in the past, there were some cases in which the Hipparcos measurement was sig-

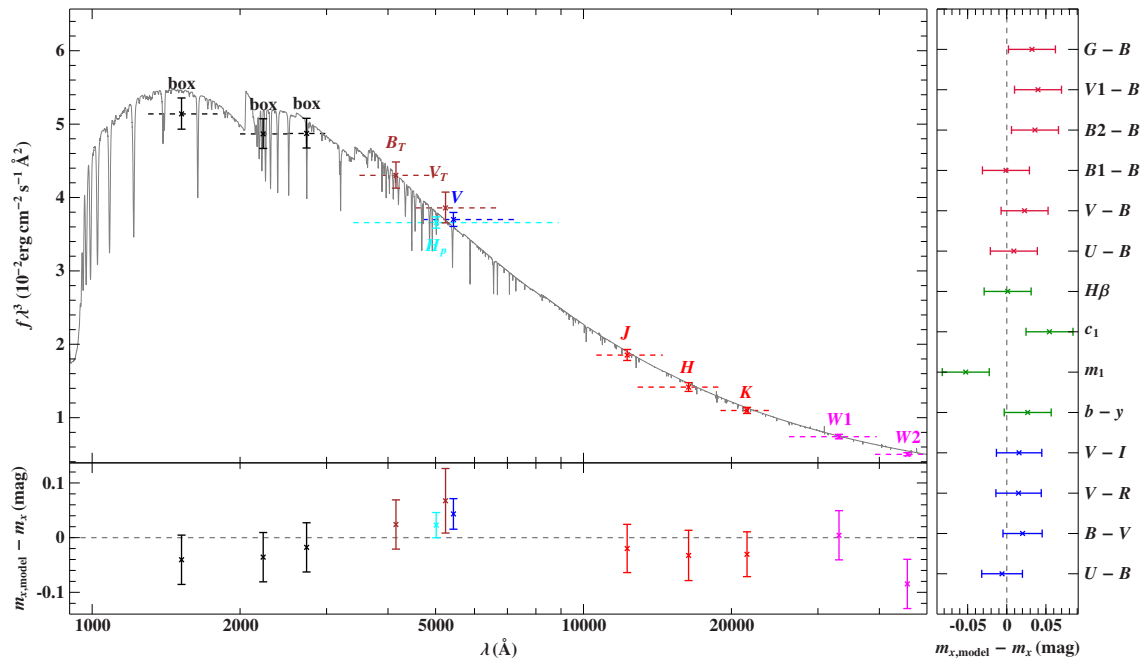


Figure 6.13: SED for model 2 of CD -31° 4800 compared with photometric measurements (magnitudes and colors). The bottom and right panels show the residuals for the magnitude and color measurements.

nificantly off, especially for blue subdwarf stars [Heber, priv. com]. Therefore it is necessary to wait for GAIA to get trustworthy parallax measurements.

Filter	value	error	type	reference
J	11.246	0.024	magnitude	Cutri et al. [2003]
H	11.376	0.026	magnitude	Cutri et al. [2003]
K	11.48	0.021	magnitude	Cutri et al. [2003]
UmB	-1.20	0.006	color	Mermilliod [1997]
BmV	-0.309	0.005	color	Mermilliod [1997]
V	10.5	0.008	magnitude	Renson and Manfroid [2009]
VmR	-0.131	0.009	color	van Leeuwen [2007]
VmI	-0.293	0.009	color	van Leeuwen [2007]
bmy	-0.138	–	color	Paunzen [2015]
m1	0.072	–	color	Paunzen [2015]
c1	-0.243	–	color	Paunzen [2015]
H β	2.54	–	color	Renson and Manfroid [2009]
VmB	1.316	–	color	Rufener [1988]
B1mB	0.738	–	color	Rufener [1988]
B2mB	1.661	–	color	Rufener [1988]
GmB	2.561	–	color	Rufener [1988]
Hp	10.4301	0.003	magnitude	van Leeuwen [2007]
Bt	10.148	0.025	magnitude	Høg et al. [2000]
Vt	10.449	0.039	magnitude	Høg et al. [2000]
W1	11.538	0.025	magnitude	Cutri [2012]
W2	11.674	0.025	magnitude	Cutri [2012]
box1	6.6014	–	magnitude	-
box2	7.5702	–	magnitude	-
box3	7.9832	–	magnitude	-

Table 6.6: Photometric measurements for CD-31° 4800.

6.1.2 HE 1511-1103

6.1.2.1 General information

HE 1511-1103 is a comparatively dim ($m_v = 14.9$) He-sdO star located at $\alpha = 15^{\text{h}} 14^{\text{m}} 16.9$ and $\delta = -11^{\circ} 14' 12.5''$. It was first mentioned in the Palomar-Green catalog of UV-excess stellar objects [Green et al., 1986] and classified as a sdO star by Kilkenny et al. [1988]. The first sophisticated determination of the atmospheric parameters was provided by Stroeger et al. [2007] who used TMAP and H/He models. In addition to the classification as being enriched in carbon and nitrogen, they determined an effective temperature of 42298 K, a surface gravity of $\log(g)=5.68$ and a helium abundance of $\log(y)=1.1$. The results found by Hirsch [2009] (using TMAP and H/He/(C/N)) differ somewhat. He found an effective temperature of 41090 ± 86 K and a surface gravity of $\log(g)= 5.46 \pm 0.03$, while classifying the star as only nitrogen rich. He found the projected rotational velocity to be below 10 km/s.

6.1.2.2 Spectral analysis

The different available SPY/UVES spectra were folded to a common resolution of $R=25000$, as arising from the DIMM seeing monitor data. This value results from the worse seeing for an individual spectra. Note that this is still better than the resolving power of 18000 determined by the slit width of the SPY setup.

By visual inspection, strong hydrogen features become apparent in the spectrum, especially the $H\alpha$ emission feature superimposed on the HeII line at 6560 \AA . Other hydrogen features seem to be hidden in the noise level. Using the HHeCNO grid to fit the atmospheric parameters results in the following values.

- $T_{\text{eff}} = 42700 \pm 600 \text{ K}$
- $\log(g) = 5.63 \pm 0.07$
- $\log(n(\text{He})/n(\text{H})) = 0.87 \pm 0.05$
- $v_{\text{rot}} < 5 \text{ km/s}$

Fig. 6.14 shows a visual representation of selected HeI and HeII lines. These results

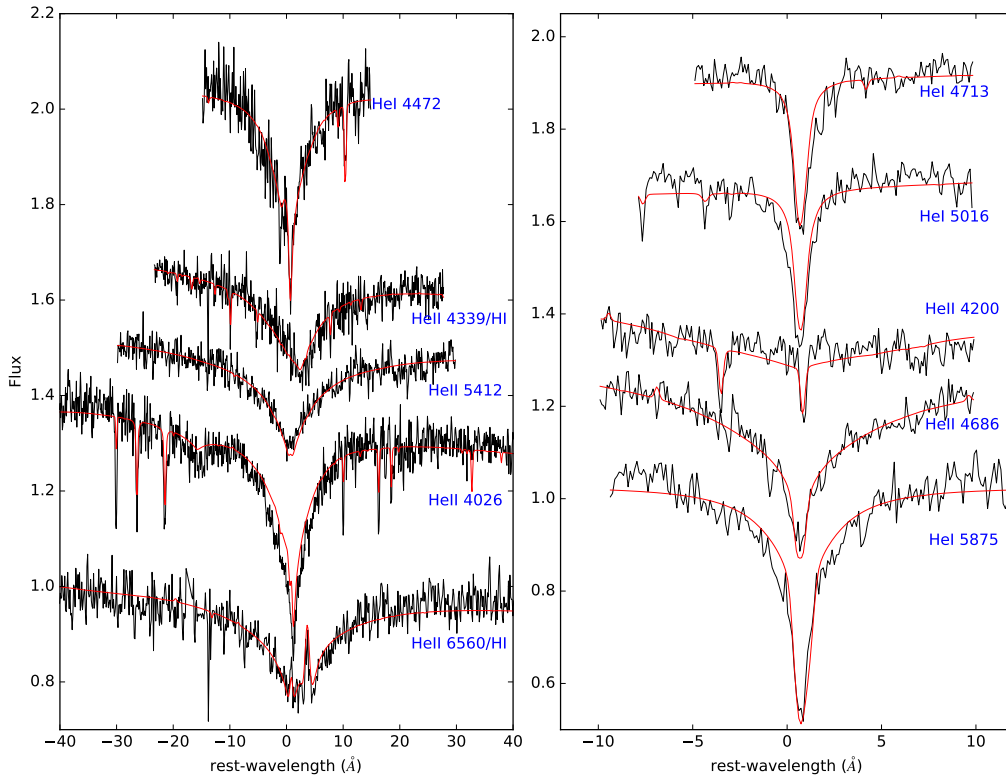


Figure 6.14: Visualization of several HeI and HeII lines of HE 1511-1103, some with a hydrogen component. The black lines show parts of the SPY/UVES spectrum, the best-fitting model is represented by the red lines. The flux levels had been adjusted for better representation.

are closer to those found by Stroerer et al. [2007], although the helium abundance is significantly different. But as especially the HeII line at 6560 \AA with the $H\alpha$ feature is modeled very well, the helium abundance of $\log(n(\text{He})/n(\text{H})) = 0.87 \pm 0.05$

is regarded as trustworthy. No signs of rotations were found, neither by broadened helium nor metal lines. The helium content of $7.4\times$ hydrogen is remarkably low for a He-sdO star. However, as all the other criteria of a He-sdO star are matched, the classification is valid.

The determination of the metal lines followed the standard scheme (see Sect. 4.9). The results of the first run on metal abundances can be found in Table 6.7. Phosphorus was fitted by eye, as the resulting line profiles from SPAS diverged to much from the data.

Element	# lines	abundance
C	5	-3.35 ± 0.15
N	15	-1.80 ± 0.04
O	4	-3.45 ± 0.18
Ne	5	-2.35 ± 0.11
Mg	1	-3.00 ± 0.10
Al	2	-4.00 ± 0.3
Si	4	-3.10 ± 0.25
P	1	-4.60 (fit by eye)
S	4	(-3.80 ± 0.5)

Table 6.7: Metal abundances derived from the optical SPY/UVES spectra of HE 1511-1103. Given is the $\log(n(X)/n(H))$ in number abundances. (Models without Fe/Ni). The second column gives the number of lines used for fitting a specific element. Values in brackets show extremely large errors and have to be dealt with care.

As no suitable UV spectra are available, it is not possible to determine abundances for iron and nickel. But as these elements have an influence on the profiles of all other lines and the temperature stratification, it was decided to include them in full NLTE conditions. They were both set to solar (mass) abundance with respect to the current state of the stellar atmosphere.

The results from the second round of abundance determinations is shown in Table 6.8. Again, phosphorus was fitted by eye. As in the case of CD-31° 4800, the inclusion of iron and nickel increased the quality of the fits to sulfur lines slightly. Figs. 6.15 to 6.17 show metal line profile fits for nitrogen, neon and magnesium for illustration.

Fig. 6.18 shows a visual representation of table 6.9. HE 1511-1103 is enriched in nitrogen, and depleted in carbon and oxygen. This contradicts the classification of Stroeer et al. [2007] who classified the star as strong lined concerning carbon and nitrogen. Neon shows a small enrichment of around twice the solar mass abundance, while the rest of the intermediate elements is consistent with the solar level. Only sulfur is below that level, but as the error bars for sulfur (and phosphorus) are quite large (resulting from weak lines and a high noise level), the results for these two elements should be taken with a grain of salt.

Element	# lines	abundance
C	5	-3.50 ± 0.16
N	13	-1.93 ± 0.04
O	3	-3.25 ± 0.24
Ne	6	-2.25 ± 0.11
Mg	1	-2.93 ± 0.14
Al	2	-4.10 ± 0.16
Si	5	-2.93 ± 0.10
P	2	-5.2 (fit by eye)
S	4	-3.90 ± 0.34

Table 6.8: Metal abundances derived from the optical SPY/UVES spectra of HE 1511-1103. Given is the $\log(n(X)/n(H))$ in number abundances. (Models with Fe/Ni). The second column gives the number of lines used for fitting a specific element.

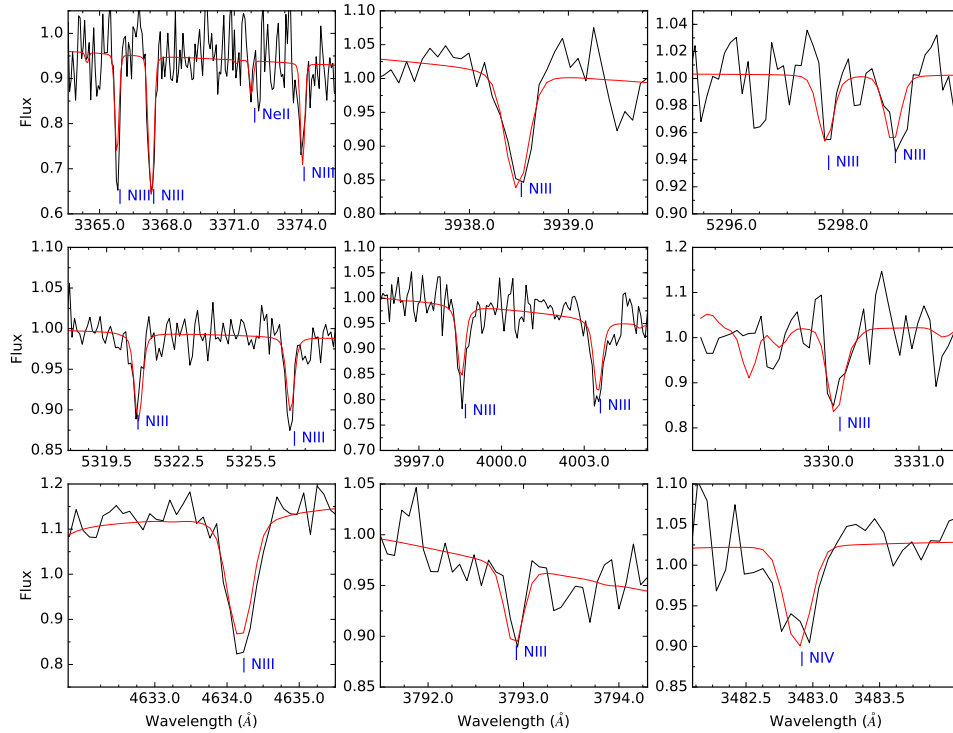


Figure 6.15: Visualization of several nitrogen lines with different ionization stages of HE 1511-1103 (SPY/UVES spectrum) in comparison with the final synthetic spectrum.

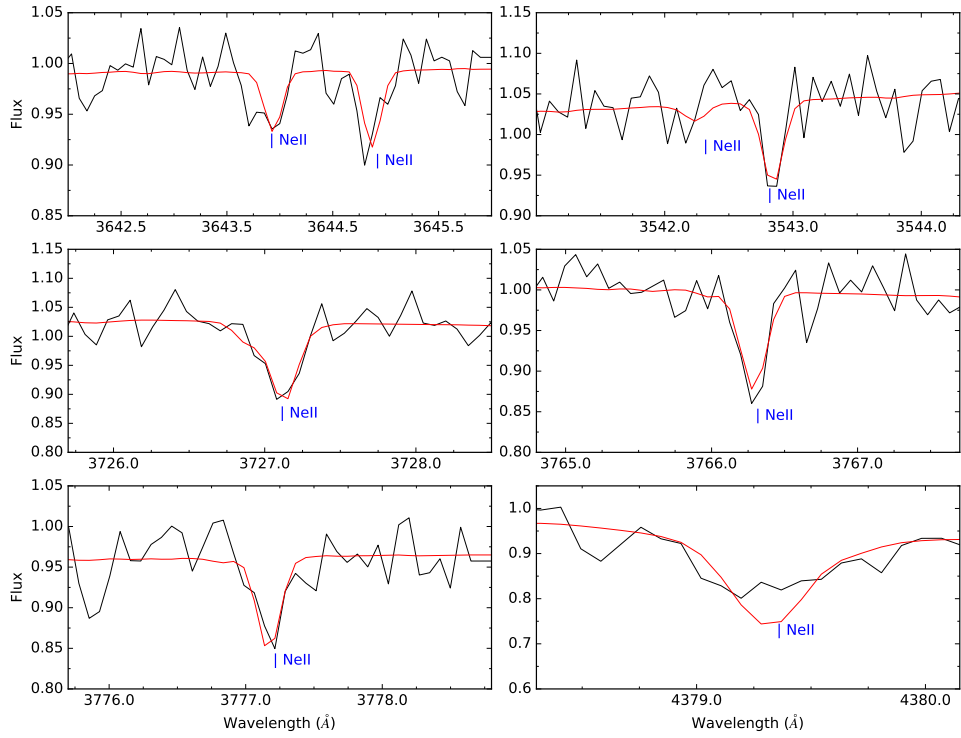


Figure 6.16: Visualization of several NeII lines of HE 1511-1103 (SPY/UVES spectrum) in comparison with the final synthetic spectrum.

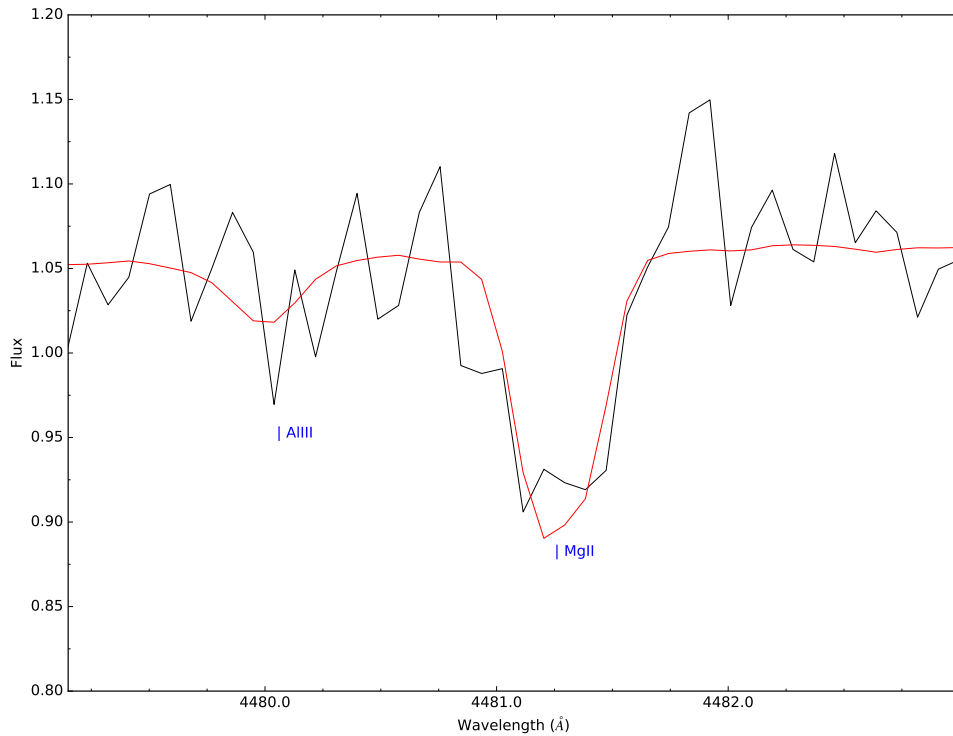


Figure 6.17: Visualization of the unresolved MgII duplet at 4481.5 Å of HE 1511-1103 (SPY/UVES spectrum) in comparison with the final synthetic spectrum.

Element	mass abundance ratio β/β_{\odot}
H	$3.41 \cdot 10^{-2}$
He	$2.97^{+1.70}_{-1.05}$
C	$(4.01^{+1.14}_{-0.91}) \cdot 10^{-2}$
N	$5.93^{+0.88}_{-0.77}$
O	$(3.92^{+2.89}_{-2.25}) \cdot 10^{-2}$
Ne	$2.26^{+0.58}_{-0.47}$
Mg	$1.00^{+0.38}_{-0.28}$
Al	$0.963^{+0.437}_{-0.303}$
Si	$1.24^{+0.32}_{-0.26}$
P	$0.851^{+0.846}_{-0.420}$
S	$0.332^{+0.393}_{-0.181}$
Fe	1
Ni	1

Table 6.9: Abundances by mass for the different elements in HE 1511-1103 compared to the solar mass abundances.

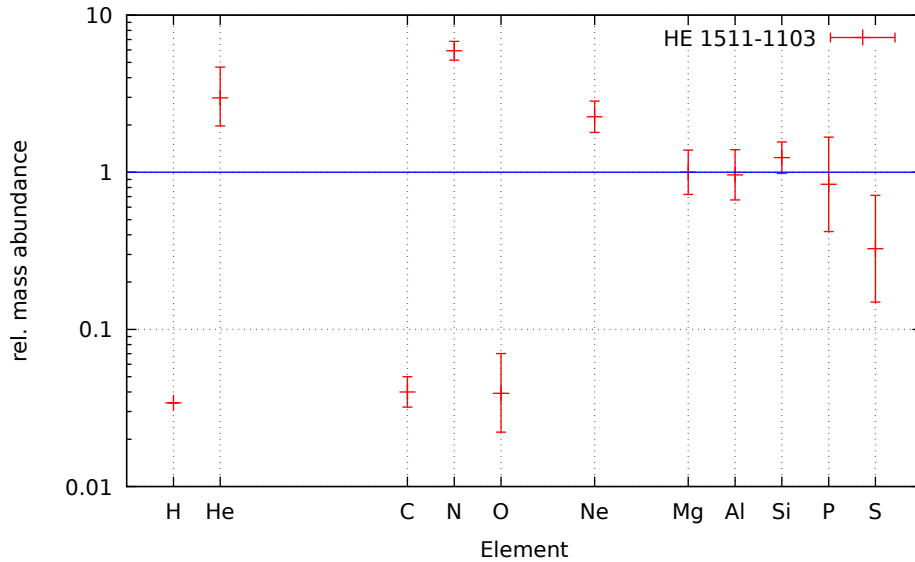


Figure 6.18: Relative mass abundances for HE 1511-1103 compared to their solar value.

6.1.2.3 Spectral energy distribution

For HE 1511-1103, there are not very many photometric measurements. Table 6.10 shows the ones available online. In Fig. 6.19, the computed spectral energy distribution of HE 1511-1103 is shown, together with the available measurements. Although some measurements are off (i.e. R) the general slope of the SED is confirmed by the measured magnitudes. As neither UV data nor filters below the Balmer jump are available, no constraints on the UV part of the SED are available. An angular diameter of $\theta = 4.6032 \cdot 10^{-12}$ and a reddening of $E(B-V)=0.0501$, a distance of $1.70_{-1.32}^{+1.43}$ kpc was derived, adopting a mass of $0.47M_{\odot}$ for the star.

Filter	value	error	type	reference
J	15.60	0.024	magnitude	Cutri et al. [2003]
H	15.65	0.026	magnitude	Cutri et al. [2003]
K	11.31	0.021	magnitude	Cutri et al. [2003]
R	15.09	–	magnitude	Zacharias et al. [2004]
BmV	-0.167	0.009	color	Henden et al. [2016]
V	14.97	0.05	magnitude	Henden et al. [2016]
b1	14.85		magnitude	Roeser et al. [2010]
W1	15.99	0.066	magnitude	Cutri [2012]
W2	16.14	0.2425	magnitude	Cutri [2012]

Table 6.10: Photometric measurements for HE 1511-1103.

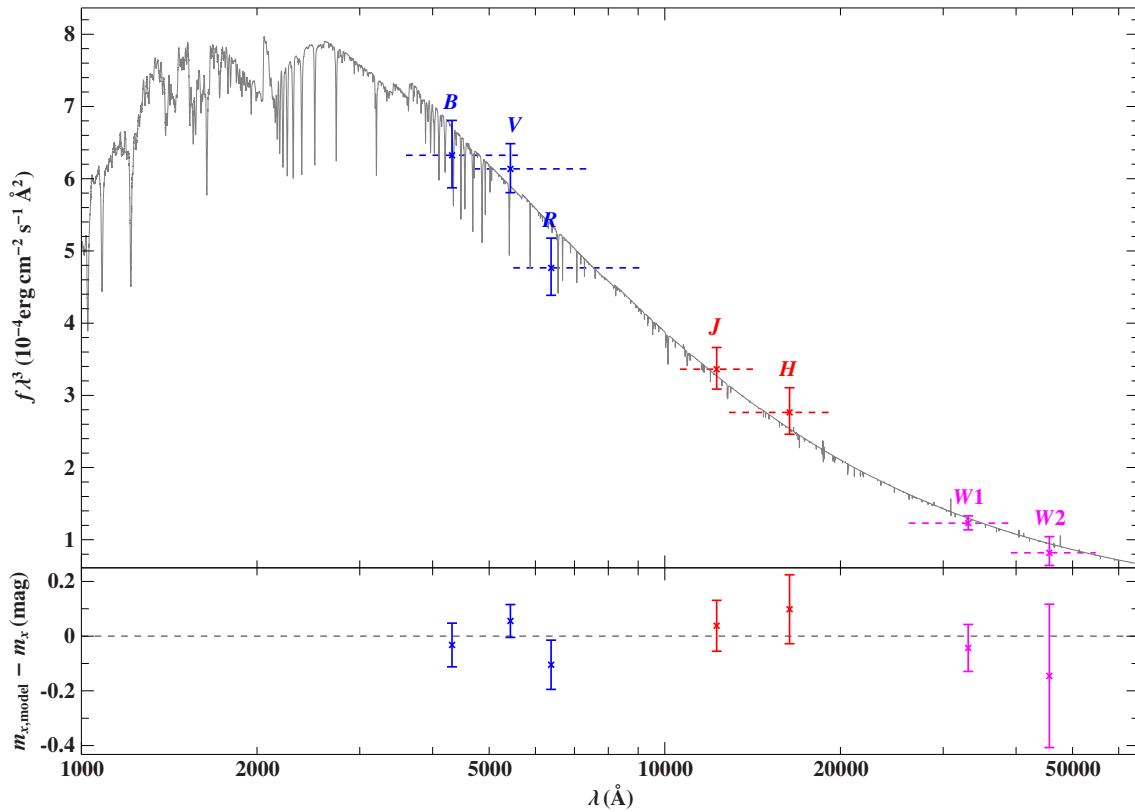


Figure 6.19: SED of HE 1511-1103 in comparison with photometric magnitudes. The bottom panel shows the residuals for the magnitude measurements.

6.1.3 HZ1

6.1.3.1 General information

HZ1 is a 12.66 mag He-sdO located at $\alpha = 04^{\text{h}} 50^{\text{m}} 13.5^{\text{s}}$ and $\delta = 17^{\circ} 42' 06.2''$. It was the first star in the Humanson-Zwicky (HZ) search for faint blue stars in 1947, the first survey for such objects ever. Greenstein [1966] examined the nature of faint blue stars and mentioned a strong reddening for HZ1 (see Sect. 6.1.3.3). HZ1 was listed by Kilkenny et al. [1988] in the catalog of spectroscopically identified hot subdwarfs, however without atmospheric parameters. These were firmly determined by Stroerer et al. [2007] using TMAP and H/He models. They found HZ1 to be a nitrogen rich He-sdO with an effective temperature of 41344 K, a surface gravity of 5.68 and a helium to hydrogen ratio of 1000. In the same year, Rodríguez-López et al. [2007] confirmed that HZ1 showed no significant pulsations during an extended search campaign for sdO pulsators. Hirsch [2009] delivered an update of the atmospheric parameters, using again TMAP but more sophisticated modelgrids than Stroerer et al. [2007]. He derived a new effective temperature of 40545 ± 250 K, $\log(g) = 5.54 \pm 0.05$ and a projected rotational velocity below 10 km/s. The classification as nitrogen rich remained valid and carbon as well as a nitrogen abundance was determined.

For HZ1 high quality spectra are available from XSHOOTER and SPY/UVES.

This offers the possibility to perform the analysis separately on both spectra and compare the results.

6.1.3.2 Spectral analysis - XSHOOTER & SPY/UVES

The available XSHOOTER spectra were collected and coadded to enhance the S/N ratio. By visual inspection of the spectral position of hydrogen features in the helium lines, a somewhat mixed impression arises. While the H α emission is clearly visible, the fit fails to reproduce the core of the HeII line at 6560 Å. The very high S/N ratio made fitting with the HHeCNO grid quite struggling as even small line features became apparent, which were usually hidden in noise. The fit resulted in the following parameters. The rotational velocity was determined using selected, sharp nitrogen lines.

- $T_{\text{eff}} = 40660 \pm 600 \text{ K}$
- $\log(g) = 5.60 \pm 0.10$
- $\log(n(\text{He})/n(\text{H})) = 2.90 \pm 0.30$
- $v_{\text{rot}} = 5 \pm 3 \text{ km/s}$

The fits to the helium lines is seen in Fig. 6.20. Because of the high S/N ratio, deviations can be seen at the position of some carbon lines, where the HHeCNO grid uses a wrong carbon abundance for a nitrogen rich He-sdO. As explained beforehand, this is nothing to worry about as it is the sharp carbon lines do not affect the fit. The high helium abundance of about 800 times hydrogen is in accordance with the missing hydrogen features in H β , however, the emission peak in the HeII 6560 Å line would be expected to be less pronounced at this abundance. In general, it can be said that the fits are far from being perfect. Several line cores do not have the correct depth. independent from the ionization stage. Also the line wings were very hard to reproduce. As already mentioned, this is due to the “missing“ noise that would usually cover these imperfections which are represented by the comparatively large errors.

However, the results are in perfect agreement with the parameters provided by Hirsch [2009] and Stroeer et al. [2007].

The available SPY/UVES spectra were coadded as well to enhance the S/N ratio. The SPY setup utilized a 2" slit which would result in a resolving power of about R=19000. Caused by the good seeing at Paranal observatory, the stellar image is often significantly smaller than the slit, resulting in a higher resolving power. To use the correct resolution for the optimize_wavegrid function (used for avoiding over- or undersampled data) the average seeing of the observing nights were taken from the ESO archive (DIMM seeing monitor) and the resolving power was recalculated. Values varied between 1.5" (R~27000) and 0.89" (R~48000). To accommodate for both extreme cases and everything in between, all data were folded to R=30000.

The fit of the atmospheric parameters was done using the standard HHeCNO grid and resulted in the following parameters. The rotational velocity was determined from nitrogen lines as well.

- $T_{\text{eff}} = 40700 \pm 1200 \text{ K}$

- $\log(g)=5.78 \pm 0.25$
- $\log(n(\text{He})/n(\text{H}))= 2.50 \pm 0.37$
- $v_{\text{rot}} = 6 \pm 4 \text{ km/s}$

The emission feature of $\text{H}\alpha$ is apparent and this time, the core of the HeII line at 6560 \AA could be reproduced as well. The results are in good agreement with the ones by Hirsch [2009] and Stroeer et al. [2007], however, the errors are quite large making this statement somewhat squishy.

In general, it can be said that the fits of helium lines for both spectra show a very high level of agreement. Clearly visible are too strong carbon lines in the model, especially around the HeII line at 6560 \AA , resulting in a wrong carbon abundance in the HHeCNO model for such a nitrogen rich He-sdO. The wrong abundance of carbon is unlikely to distract the fit and should have no result on the final parameters.

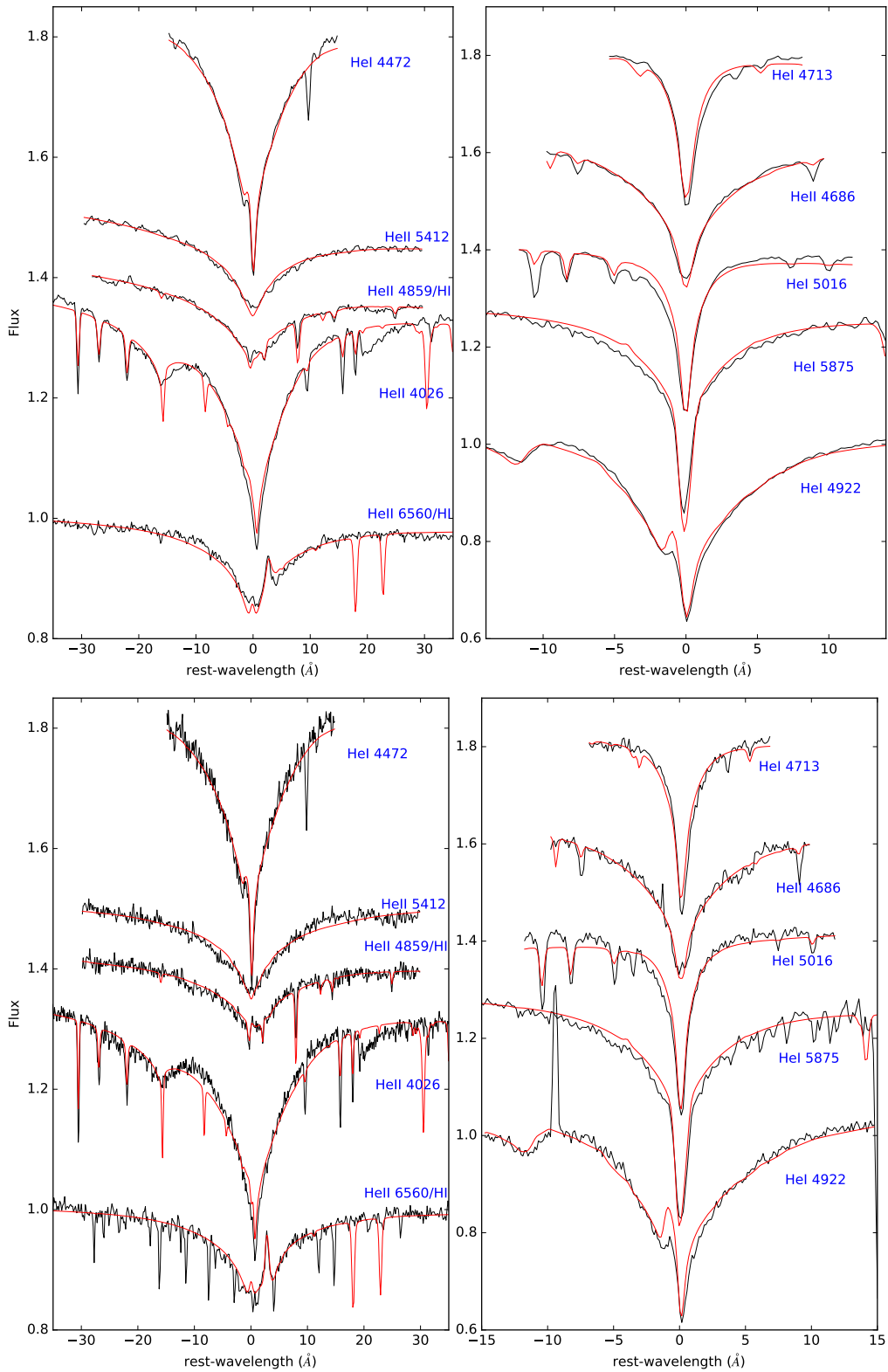


Figure 6.20: Visualization of several HeI and HeII lines of HZ1, some with a hydrogen component. The black lines show parts of the spectrum, the best-fitting model is represented by the red lines. The flux levels had been adjusted for better representation. The upper panels shows the XHSOOTER data, the bottom panel represents the SPY/UVES data.

Determining the metal abundances followed the standard scheme for both stars. Due to the high S/N ratio, and therefore well visible weak features, a high number of lines could be used, especially in the XSHOOTER data. Table 6.11 shows the results of the first iteration for both spectra.

Element	# lines(X)	abundance(X)	# lines (U)	abundance(U)
C	19	-2.47 ± 0.11	19	-2.27 ± 0.07
N	56	-0.19 ± 0.09	58	-0.48 ± 0.04
O	11	-2.40 ± 0.37	10	-2.40 ± 0.30
Ne	19	-0.90 ± 0.09	20	-1.35 ± 0.07
Mg	1	-0.96 ± 0.15	1	-1.47 ± 0.23
Al	5	-2.67 ± 0.20	6	-3.03 ± 0.13
Si	11	-1.47 ± 0.09	13	-2.01 ± 0.06
P	2	(-3.34 ± 0.57)	3	(-4.05 ± 0.64)
S	6	-2.05 ± 0.26	5	-1.95 ± 0.14

Table 6.11: Metal abundances derived from the optical XSHOOTER and SPY(UVES spectra of HZ1. Given is the $\log(n(X)/n(H))$ in number abundances. (Models without Fe/Ni). The second and forth column gives the number of lines used for fitting a specific element. (X) indicates the XSHOOTER data, (U) the SPY/UVES data. Values in brackets show extremely large errors and have to be dealt with care.

Unfortunately, there is only one high-res IUE spectrum for HZ1, which turned out to be not suitable for fitting as is looked like pure noise. Therefore, the abundances of iron and nickel were set to the solar mass abundance, with reference to the composition of the model atmosphere at the time of the fixture.

Table 6.12 shows the results for the abundance analysis after the second iteration, when the models contained iron and nickel. Fits to selected nitrogen and neon lines from both spectra are shown in Fig. 6.21 and Fig. 6.22. Fits to other metal lines can be found in the Appendix .2. The phosphorus lines in the spectra of HZ1 are very tiny and hard to distinguish from noise, which explains the larger errors for this element.

Element	# lines(X)	abundance(X)	# lines(U)	abundance(U)
C	19	-2.11 ± 0.10	18	-2.46 ± 0.07
N	60	-0.14 ± 0.06	60	-0.55 ± 0.05
O	12	-2.30 ± 0.31	10	-2.61 ± 0.31
Ne	18	-0.79 ± 0.09	21	-1.26 ± 0.06
Mg	1	-1.27 ± 0.34	1	-1.75 ± 0.19
Al	6	-2.45 ± 0.14	6	-2.95 ± 0.10
Si	15	-1.28 ± 0.08	15	-1.94 ± 0.07
P	4	-3.40 ± 0.45	4	(-4.28 ± 0.51)
S	6	-2.40 ± 0.30	9	-2.20 ± 0.17

Table 6.12: Metal abundances derived from the optical XSHOOTER and SPY/UVES spectra of HZ1. Given is the $\log(n(X)/n(H))$ in number abundances. (Models with Fe/Ni). The second and forth column gives the number of lines used for fitting a specific element. (X) indicates the XSHOOTER data, (U) the SPY/UVES data. Values in brackets show extremely large errors and have to be dealt with care.

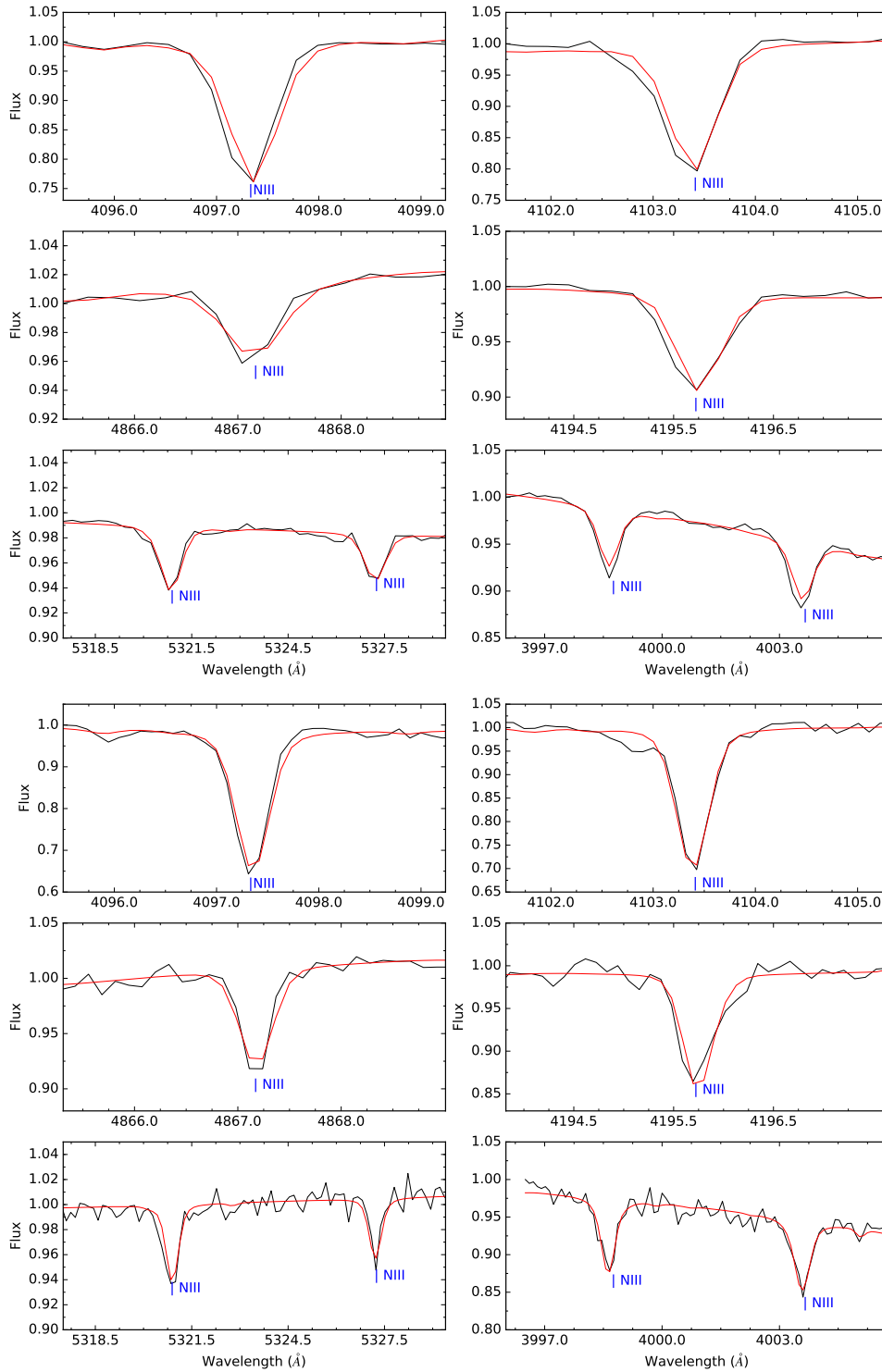


Figure 6.21: Visualization of several NIII lines of HZ1 in comparison with the final synthetic spectrum. The upper panel shows the fits to the XSHOOTER spectrum, the bottom panel the fits to the UVES/SPY data.

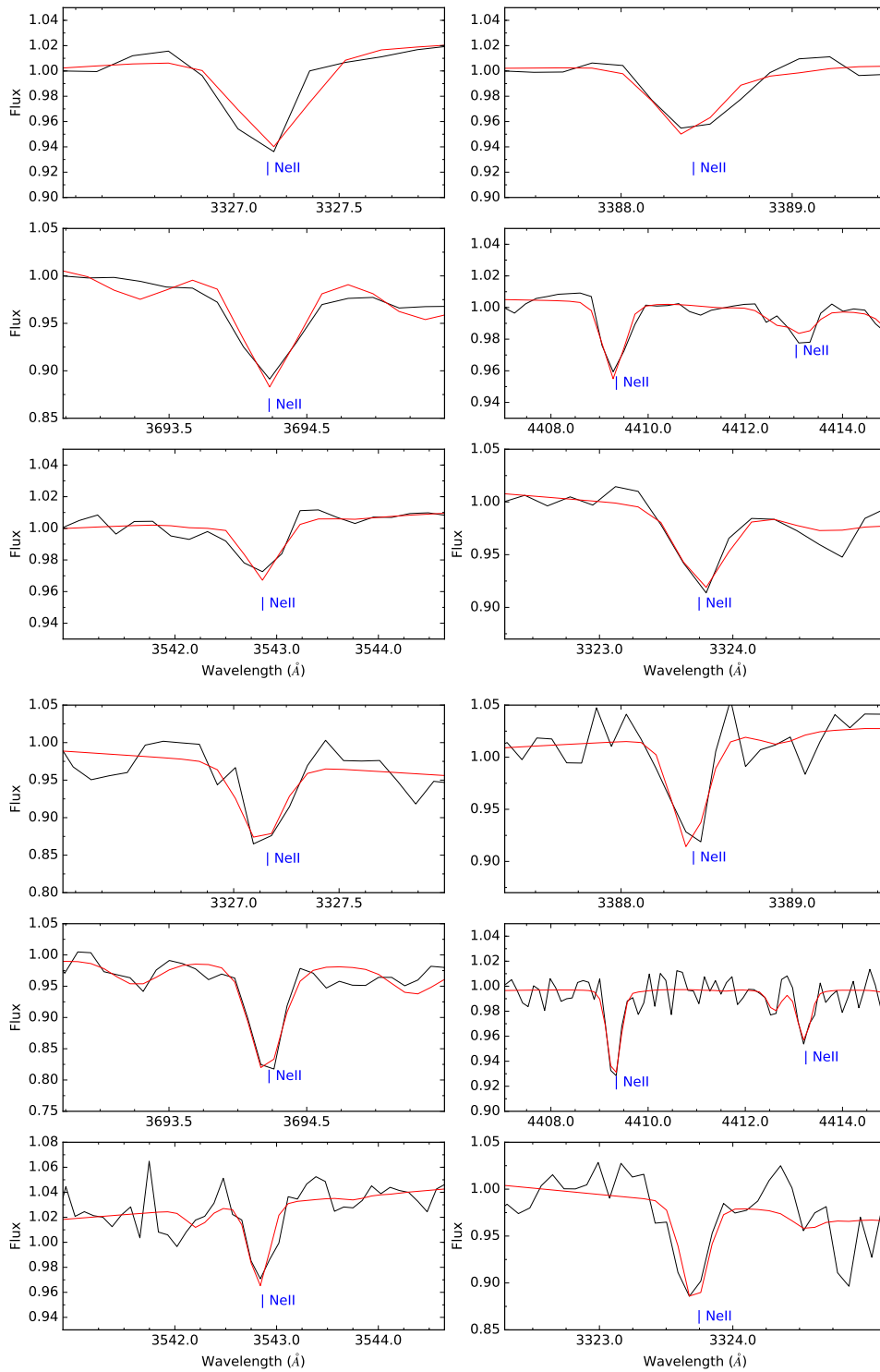


Figure 6.22: Visualization of several NeII lines of HZ1 in comparison with the final synthetic spectrum. The upper panel shows the fits to the XSHOOTER spectrum, the bottom panel the fits to the UVES/SPY data.

In Table 6.13 the abundances have been compared to mass abundances with respect to the solar value, Fig. 6.23 shows a visual representation of these values. HZ1 shows the classical pattern of the CNO burning bi-cycle. Nitrogen is enriched, while carbon and oxygen are depleted. The intermediate elements are all solar or slightly sub-solar.

Both the XSHOOTER and SPY/UVES analysis shows a remarkably well agreement. The helium abundance is virtually identical, the CNO pattern shows up in both datasets with hardly any difference in the values. Concerning the intermediate mass elements, neon, magnesium and silicon are matching very well. For aluminum, the errorbars are not overlapping, but the errors given by SPAS are very small considering the quality of the fit. The abundances for phosphorus differ significantly, however this is compensated by the large errors for the fit. The same nearly holds for sulfur, which abundances also differ but here the errors are overlapping very slightly. This most likely has the same cause as the other problems with sulfur fits encountered in this work. As it was very hard to get good line fits for sulfur, even slight differences in the lines or e.g. the noise level can lead to significantly different abundances.

The fact that elements with clearly visible lines from both datasets result in the same mass abundance ratios and even similar errorbars is a very good sign and proves the reproducibility of the analysis method. For the rest of the elements, the lines were only weakly visible so that even slight deviations in the spectra can have a huge influence on the determined enrichments and errors.

Element	β/β_{\odot} (XSHOOTER)	β/β_{\odot} (SPY/UVES)
H	$4.03 \cdot 10^{-4}$	$1.10 \cdot 10^{-3}$
He	$3.98^{+3.96}_{-1.99}$	$3.96^{+5.33}_{-2.27}$
C	$(1.23^{+0.49}_{-0.44}) \cdot 10^{-2}$	$(1.37^{+0.36}_{-0.31}) \cdot 10^{-2}$
N	$4.57^{+0.68}_{-0.59}$	$4.45^{+0.54}_{-0.44}$
O	$(4.46^{+3.55}_{-2.45}) \cdot 10^{-3}$	$(5.30^{+2.21}_{-1.98}) \cdot 10^{-3}$
Ne	$0.811^{+0.212}_{-0.173}$	$0.691^{+0.108}_{-0.085}$
Mg	$0.587^{+0.684}_{-0.314}$	$0.480^{+0.261}_{-0.171}$
Al	$0.545^{+0.211}_{-0.152}$	$0.430^{+0.108}_{-0.088}$
Si	$0.693^{+0.137}_{-0.125}$	$0.384^{+0.051}_{-0.037}$
P	$0.659^{+1.434}_{-0.450}$	$0.218^{+0.466}_{-0.147}$
S	$0.134^{+0.200}_{-0.076}$	$0.511^{+0.303}_{-0.192}$
Fe	1	1
Ni	1	1

Table 6.13: Mass abundances for the different elements in HZ1 compared to the solar mass abundance.

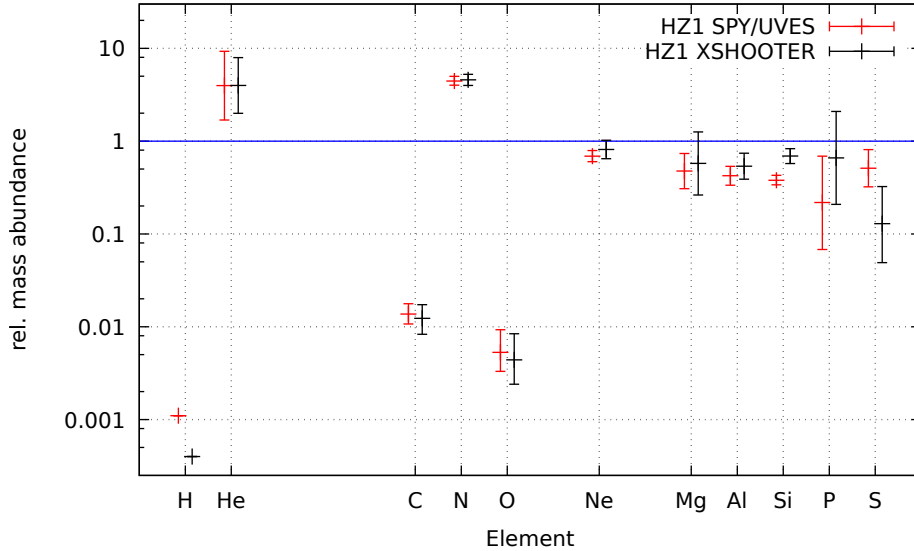


Figure 6.23: Relative mass abundances for HZ1 derived from SPY and XSHOOTER data, compared to their solar value. The solar abundances of iron and nickel are not shown.

6.1.3.3 Spectral energy distribution

In table 6.14 the available measured magnitudes and computed colors for HZ1 are shown. The following figures show the calculated SED for HZ1 from both XSHOOTER and SPY/UVES data in comparison with the data from table 6.14. It is apparent, that there is virtually no difference visible with the naked eye, as expected by the comparable abundances and atmospheric parameters.

What strikes the eye is the shape of the SED. Compared to the energy distribution of other He-sdOs in this thesis, the maximum of the emitted flux is shifted towards the red and lies at around 5000 \AA . This is caused by the large reddening of HZ1, as already mentioned by Greenstein [1966]. The $E(B-V)$ value for HZ1 is 0.2602 (XSHOOTER) and 0.2593 (SPY/UVES) respectively. This indicates the strong interstellar reddening as these values are about 0.2 dex larger than for the other sample stars. With $\theta_{\text{SPY}} = 1.9650 \cdot 10^{-11}$ and $\theta_{\text{XSHOOTER}} = 1.9489 \cdot 10^{-11}$ a distance of 335_{-85}^{+113} pc and 416_{-45}^{+51} pc respectively is obtained. As for CD-31° 4800, the difference in distance is caused by the different surface gravities to most extend. The magnitudes and color indices fit the SED very well without any obvious deviations. Only the U-B value is a bit off, which is nothing to worry about at this level.

Filter	value	error	type	reference
J	12.746	0.021	magnitude	Cutri et al. [2003]
H	12.8486	0.024	magnitude	Cutri et al. [2003]
K	12.865	0.029	magnitude	Cutri et al. [2003]
UmB	-0.06	–	color	Penston [1973]
BmV	-1.01	–	color	Penston [1973]
r	12.751	–	magnitude	Zacharias et al. [2012]
i	12.978	–	magnitude	Zacharias et al. [2012]
V	12.645	–	magnitude	Kharchenko [2001]
B	12.59	–	magnitude	Kharchenko [2001]
Vt	12.648	–	magnitude	Høg et al. [2000]
W1	12.973	0.025	magnitude	Cutri [2012]
W2	13.005	0.003	magnitude	Cutri [2012]
box1	9.882	–	magnitude	-

Table 6.14: Photometric measurements for HZ1.

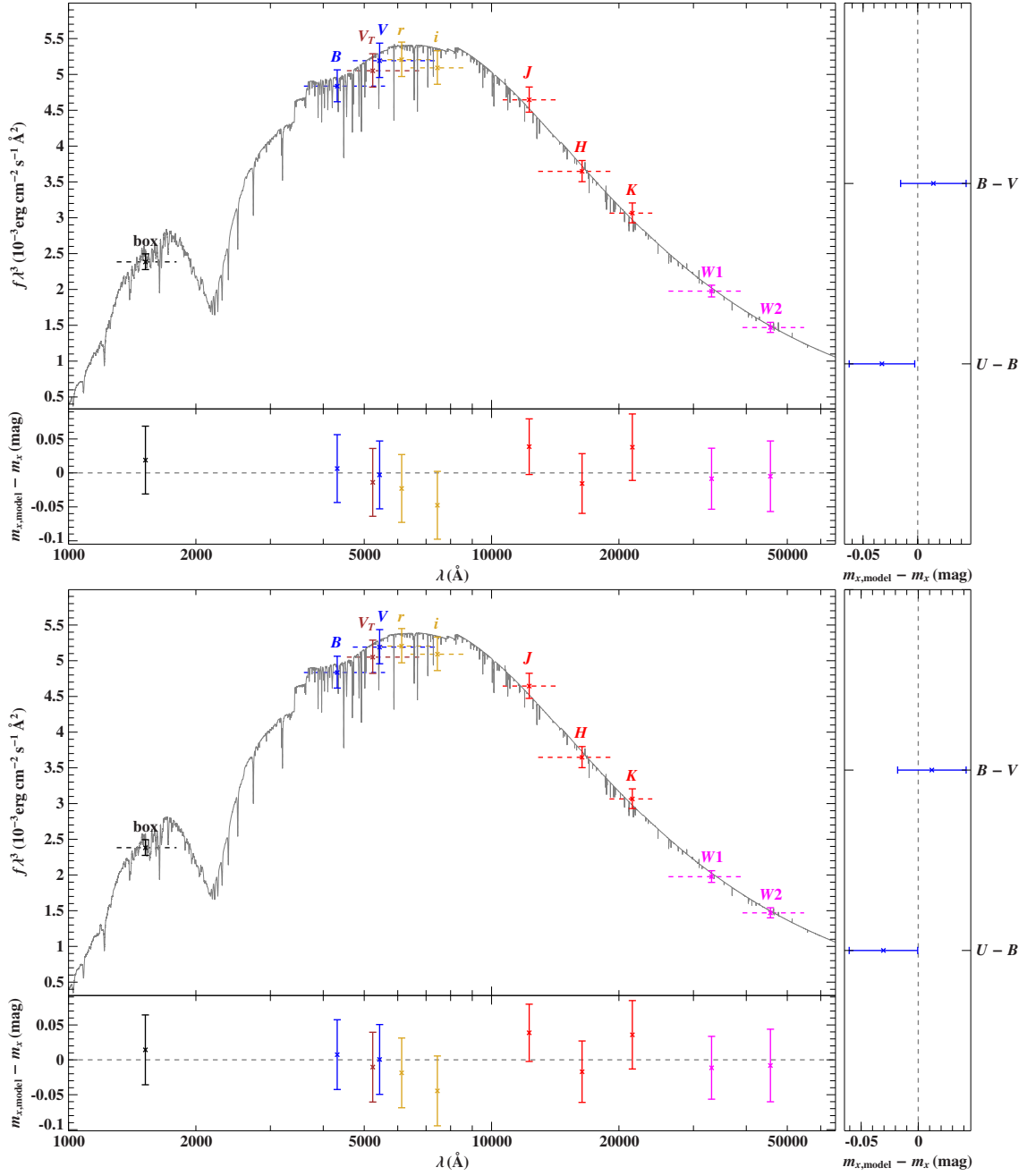


Figure 6.24: SED of HZ1(XSHOOTER) in comparison with photometric measurements (magnitudes and colors). The bottom and right panels show the residuals for the magnitude and color measurements. The large upper panels gives the XSHOOTER SED, the lower large panel the SED resulting from SPY/UVES data.

6.1.4 HZ44

6.1.4.1 General Information

HZ44 is a He-sdO star located at $\alpha = 13^{\text{h}}23^{\text{m}}35.7$ and $\delta = +36^{\circ}07'59.6''$ with a visual magnitude of $V=11.65$. Despite being a spectroscopic standard star for i.e. HST, its nature and parameters have hardly been analyzed. It was first listed by Humason and Zwicky [1947] in their search for faint blue stars. Greenstein [1966] classified it as a helium rich sdO star with an additional enrichment of nitrogen. The first atmospheric parameters were given by Kilkenny et al. [1988] who stated an effective temperature of 39800 K and a $\log(g)$ between 5.3 and 5.7. HZ44 was examined by O'Toole [2004] and several elements beyond the iron group were found, e.g. silicon, germanium, tin and lead. A search for a companion on a long period orbit conducted by Schork [2017] did not find any companion. A companion on a short period orbit could not be excluded but was considered highly unlikely.

6.1.4.2 Spectral analysis

For HZ44, several optical spectra are available. The first intention to use a high resolution, good S/N HIRES spectra to determine the atmospheric parameters had to be put down as the spectrum suffered from jumps and discontinuities resulting from incorrect order merging. Most of the HeI and HeII lines covered more than one order and were useless for fitting. Fortunately, several low resolution spectra from TWIN, ISIS and CAFOS were available. During the fitting process, it turned out that HZ44 features a very low helium abundance, at least for a He-sdO star. The hydrogen Balmer lines are clearly visible in the spectra, a confusion with the corresponding HeII lines can be excluded as the radial velocities of the lines confirm their hydrogen nature. For the fitting a HHe grid had to be used as the standard HHeCNO or HHeN grids featured too strong lines that were not visible in the low resolution spectra and therefore failed to deliver reasonable fits. From the fit of the coadded spectra of the single instruments, three sets of atmospheric parameters were determined.

TWIN

- $R \sim 2000$
- $T_{\text{eff}} = 40500 \pm 600 \text{ K}$
- $\log(g) = 5.70 \pm 0.10$
- $\log(n(\text{He})/n(\text{H})) = 0.20 \pm 0.07$

ISIS

- $R \sim 3000$
- $T_{\text{eff}} = 38200 \pm 600 \text{ K}$
- $\log(g) = 5.60 \pm 0.18$
- $\log(n(\text{He})/n(\text{H})) = 0.00 \pm 0.10$

CAFOS

- $R \sim 1100$
- $T_{\text{eff}} = 38900 \pm 900 \text{ K}$
- $\log(g) = 5.60 \pm 0.11$
- $\log(n(\text{He})/n(\text{H})) = 0.00 \pm 0.12$

From these three sets of parameters, an average was formed and used throughout the rest of the analysis. The overall agreement between the three different parameter sets is very good.

averaged atmospheric parameters

- $T_{\text{eff}} = 39200 \pm 600 \text{ K}$
- $\log(g) = 5.65 \pm 0.10$
- $\log(n(\text{He})/n(\text{H})) = 0.10 \pm 0.20$

Fig. 6.25 shows the fit of the TWIN spectrum.

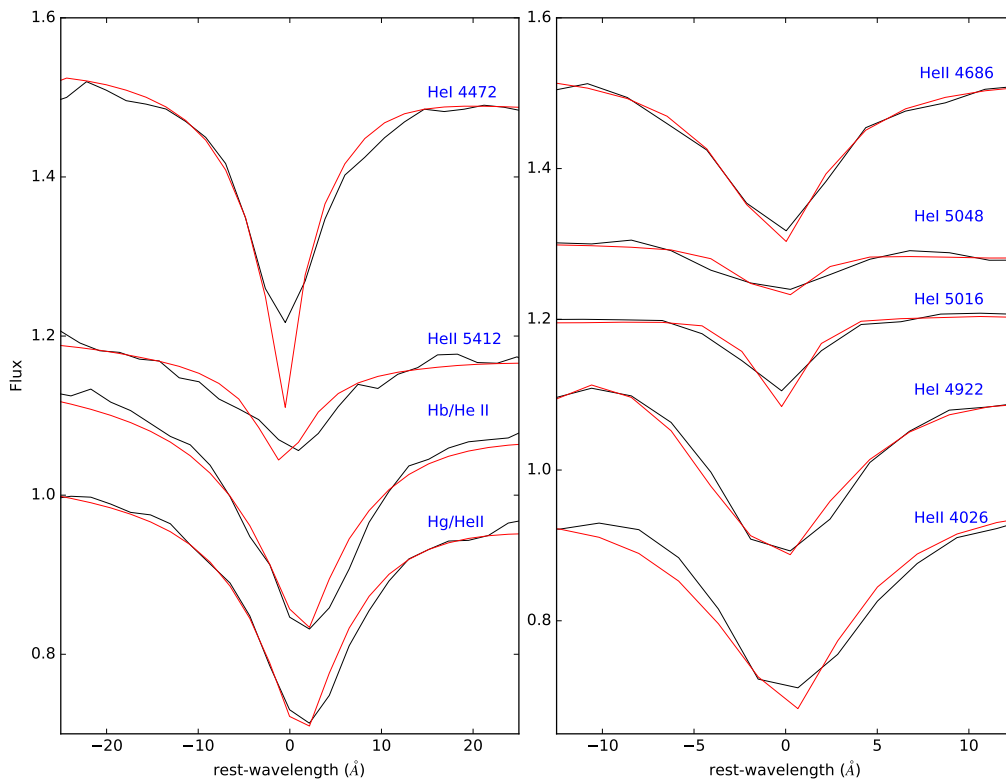


Figure 6.25: Visualization of several Hydrogen, HeI and HeII lines of HZ44. The black lines show parts of the TWIN spectrum, the best-fitting model is represented by the red lines. The flux levels had been adjusted for better representation.

The value on the helium abundance error was selected higher than usual to account for the low resolution of the optical spectra which makes it more difficult to

resolve and fit the helium and/or hydrogen features in certain lines. The HeI line at 4472 Å is clearly off. However, it was not possible to improve the quality of fit for this particular line. As the other HeI lines are fitted well, this has no influence on the reliability of the ionization equilibrium. The hydrogen lines H β and H γ are indeed hydrogen lines and not the corresponding helium ones as the hydrogen lines show the same radial velocity as the rest of the lines visible in the spectra. The helium lines would show a shift of over 100 km/s compared to the other lines.

To determine the metal abundances, the HIRES spectra could be used as the metal lines are sharp and narrow enough to be well covered within one order. Table 6.15 shows the results of the first iteration with models containing no iron and nickel. After finishing the work on the optical spectrum, iron and nickel were included and fitted from the available FUSE spectrum. The IUE spectrum suffered from a too poor S/N ratio to allow for any fits. In Table 6.16 the results from the second iteration including iron and nickel at the solar level in the models are shown. Unfortunately it turned out that the HIRES spectrum could not be used for abundance determination and therefore the results from the HIRES have to be dropped. Only the UV data were used hereafter.

Element	# lines	abundance
C	16	-4.61 ± 0.03
N	47	-3.22 ± 0.04
O	9	-4.55 ± 0.03
Ne	16	-4.10 ± 0.02
Mg	2	-4.45 ± 0.10
Al	6	-5.57 ± 0.03
Si	12	-4.36 ± 0.06
P	3	-6.70 ± 0.17
S	8	-4.27 ± 0.05

Table 6.15: Metal abundances derived from the optical HIRES spectra of HZ44. Given is the $\log(n(X)/n(H))$ in number abundances. (models without Fe/Ni). The second column gives the number of lines used for fitting a specific element.

It is worthwhile to mention that in HZ44 the N II lines fitted much better than in any other He-sdO from the sample. For stars with higher temperatures, the fit often resulted in unwanted emission in the model, while the line shape clearly demands absorption. This behavior is far less pronounced in HZ44. The lower temperature of this star shifts the ionization equilibrium from NIII towards NII. Although this should have no general affect how the lines are fitted, it improved the usability of NII lines.

Table 6.17 shows the metal abundances of HZ44 in comparison with their solar values. The same is represented by Fig. 6.31.

Element	# lines (opt.)	abundance (opt.)	# lines (UV)	abundance (UV)
C	0	--	6	-4.45 ± 0.12
N	0	--	16	-3.07 ± 0.07
O	0	--	6	-4.06 ± 0.12
Ne	0	--	2	-4.11 ± 0.37
Mg	0	--	0	--
Al	0	--	1	-3.55 ± 0.10
Si	0	--	4	-3.93 ± 0.12
P	0	--	4	-6.50 ± 0.20
S	0	--	1	(-4.53 ± 1.17)
Fe	0	--	12	-4.66 ± 0.25
Ni	0	--	7	-3.85 ± 0.21

Table 6.16: Metal abundances derived from optical and UV spectra of HZ44. Given is the $\log(n(X)/n(H))$ in number abundances. (Models with Fe/Ni). The second column gives the number of lines used for fitting a specific element. Values in brackets show extremely large errors and have to be dealt with care.

The FUSE fit of sulfur could only use one line and therefore suffers from a large error.

Element	β/β_{\odot}
H	$9.06 \cdot 10^{-2}$
He	$1.34^{+0.69}_{-0.46}$
C	$(1.19^{+0.36}_{-0.33}) \cdot 10^{-2}$
N	$1.14^{+0.20}_{-0.17}$
O	$(1.61^{+0.48}_{-0.44}) \cdot 10^{-2}$
Ne	$(8.25^{+11}_{-4.70}) \cdot 10^{-2}$
Mg	--
Al	$9.05^{+2.34}_{-1.87}$
Si	$0.331^{+0.110}_{-0.084}$
P	$0.124^{+0.071}_{-0.038}$
S	$0.198^{+2.796}_{-0.195}$
Fe	$(6.27^{+5.38}_{-3.01}) \cdot 10^{-2}$
Ni	$6.30^{+4.62}_{-2.73}$

Table 6.17: Mass abundances for the different elements in HZ44 compared to the solar mass abundance.

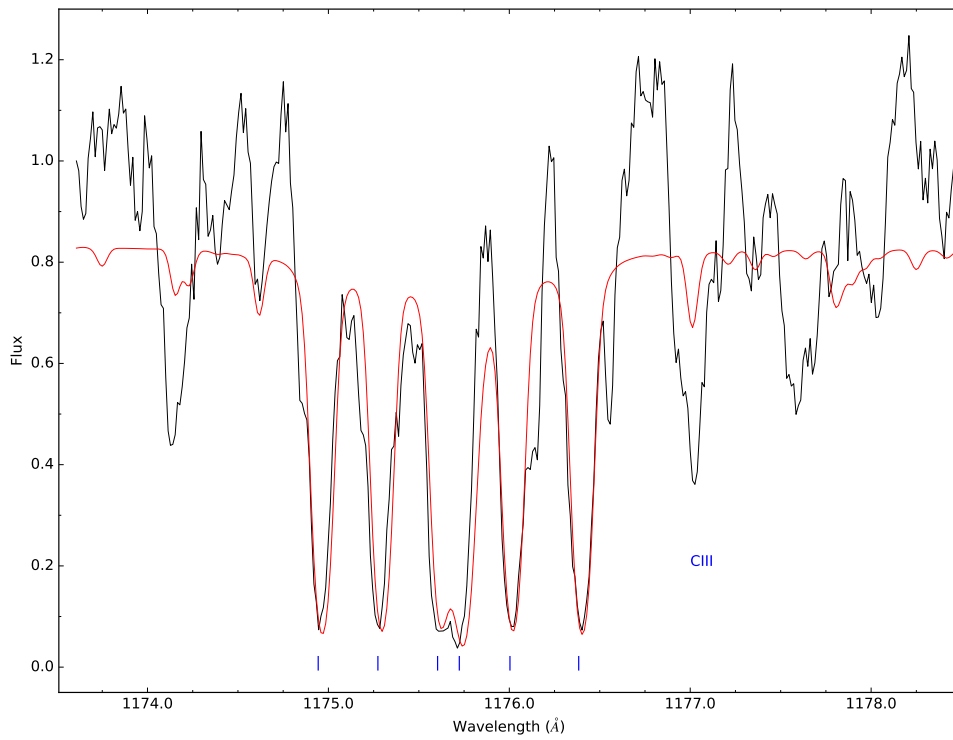


Figure 6.26: Visualization of the C III septuplet of HZ44 (FUSE spectrum) in comparison with the final synthetic spectrum. The continuum placement is the best trade-off as a higher continuum resulted in wrong lines cores and worse (i.e. too broad) wings.

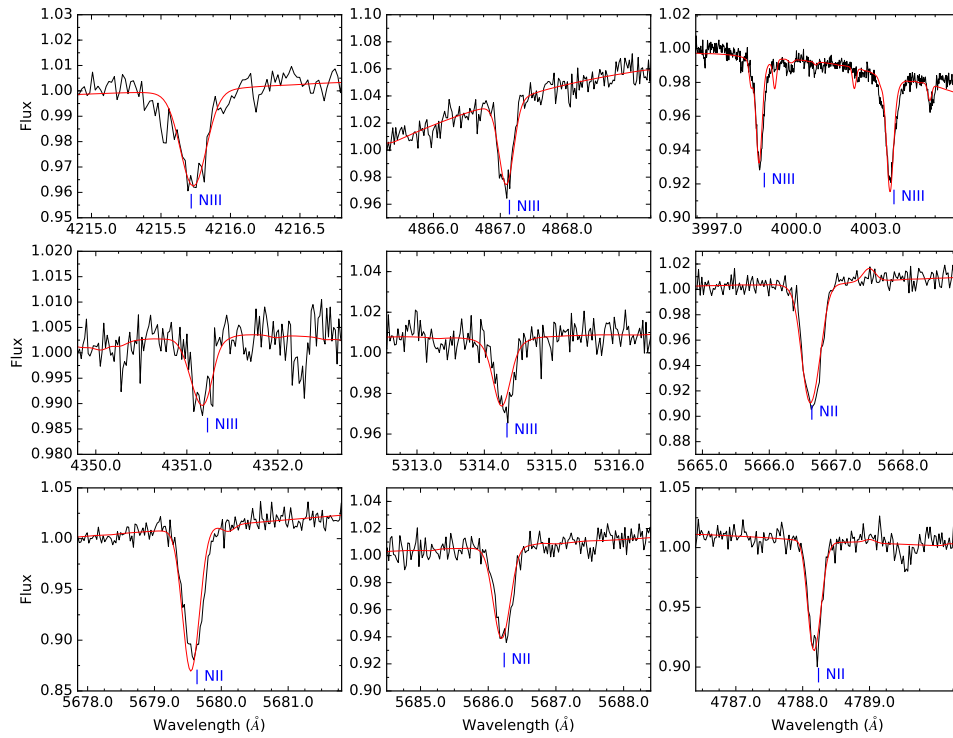


Figure 6.27: Visualization of several nitrogen lines with different ionization stages of HZ44 (HRES spectrum) in comparison with the final synthetic spectrum.

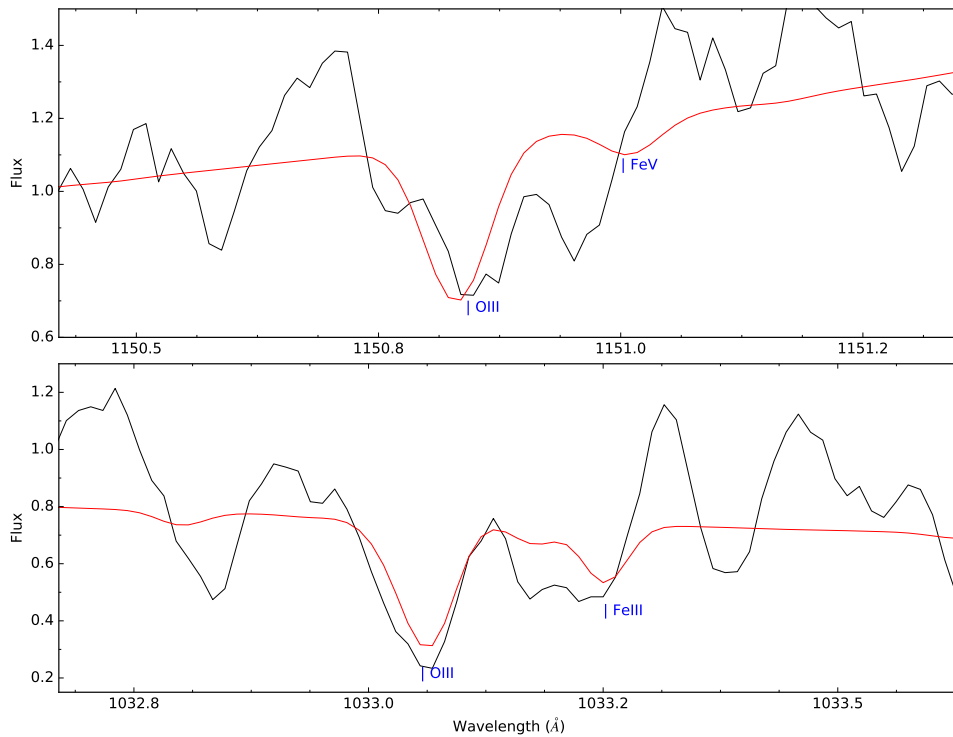


Figure 6.28: Visualization of several OIII lines of HZ44 (FUSE spectrum) in comparison with the final synthetic spectrum.

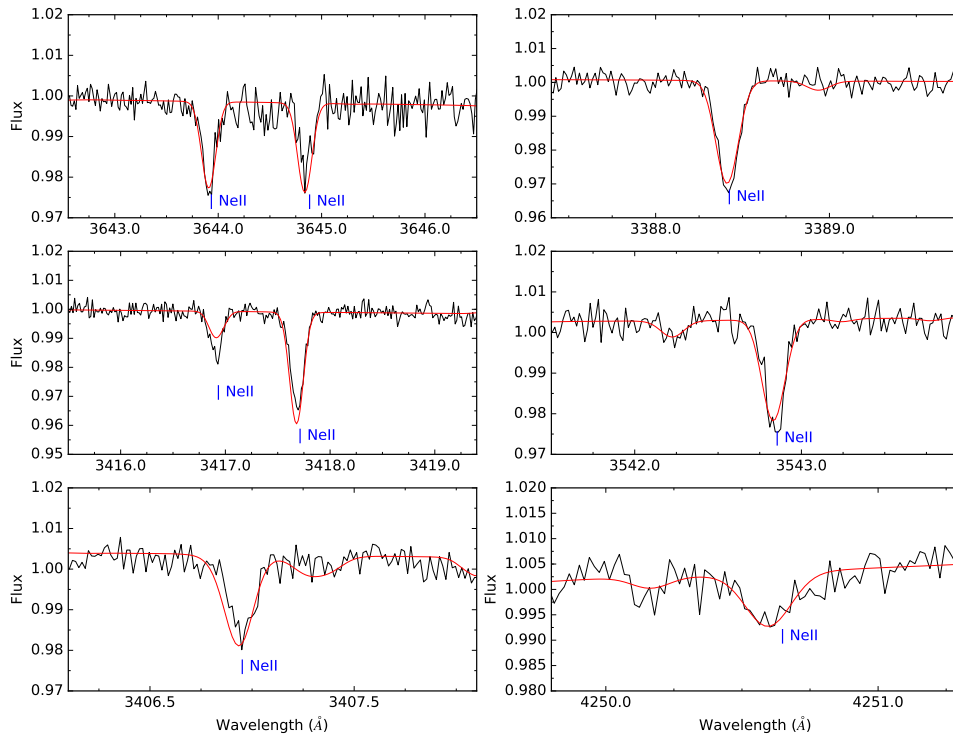


Figure 6.29: Visualization of several NeII lines of HZ44 (HRES spectrum) in comparison with the final synthetic spectrum.

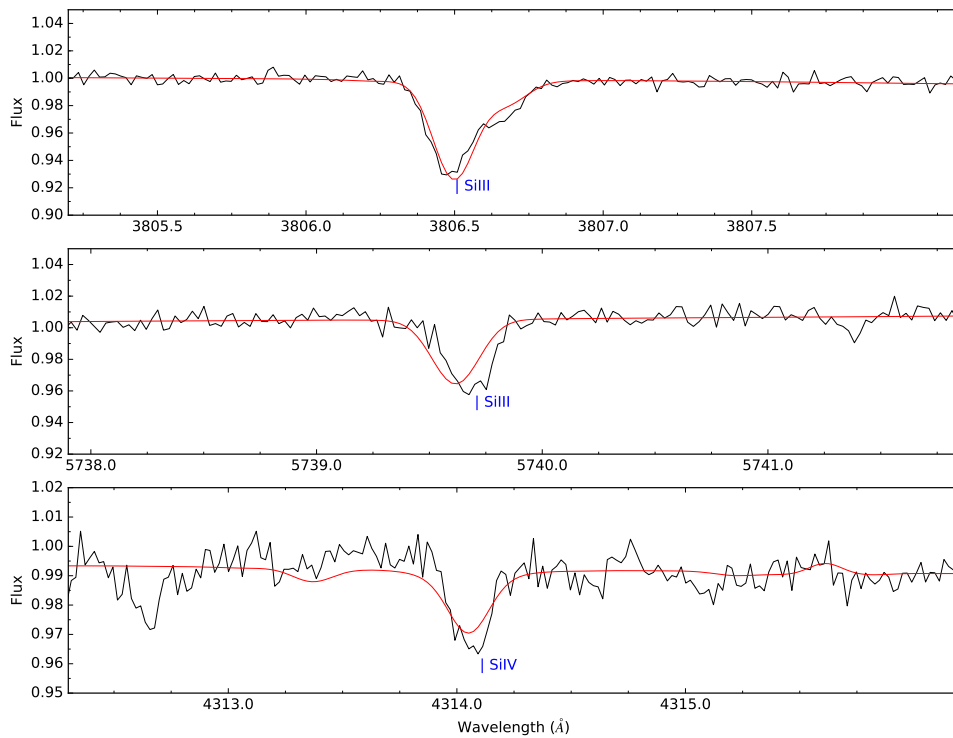


Figure 6.30: Visualization of several silicon lines with different ionization stages of HZ44 (HRES spectrum) in comparison with the final synthetic spectrum.

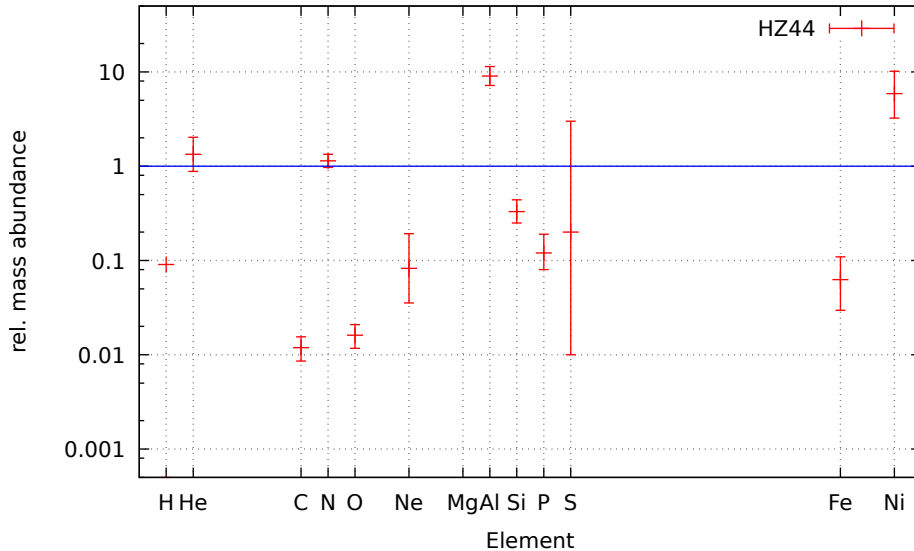


Figure 6.31: Relative mass abundances for HZ44 compared to their solar value.

It is apparent that HZ44 is not a typical He-sdO star. Helium and hydrogen are present at approximately the same abundance by number. While helium has an about solar mass abundance, hydrogen is only depleted to one tenth by mass. As a result hydrogen Balmer lines are clearly visible in the spectrum. This basically disqualifies HZ44 as a pure He-sdO star. It should be rather classified as an intermediate He-sdO.

The classical CNO bi-cycle abundance pattern is well visible. Nitrogen reaches the solar level, while carbon and oxygen are at one hundredth of the solar level. All the intermediate mass elements are depleted without any specifically recognizable pattern. Aluminum is significantly enriched, but as this was not seen in any other star in this work, a fitting error is likely. Iron is subsolar while nickel is clearly above the solar level.

6.1.4.3 Spectral energy distribution

In Fig. 6.32, the computed spectral energy distribution of HZ44 is shown, together with the available measurements. The measured magnitudes show a good, but not overwhelming, agreement between measurements and SED. Especially the first box filter between 1300 Å and 1800 Å is significantly off. As the measurements confirm the general slope of the SED, an outlier is the most likely explanation for this offset. A distance of 356_{-39}^{+44} pc results from $\theta = 2.1500 \cdot 10^{-11}$ and the gravity by adopting a mass of $0.47 M_{\odot}$. The reddening is 0.02 mag.

Filter	value	error	type	reference
J	12.386	0.022	magnitude	Cutri et al. [2003]
H	12.569	0.023	magnitude	Cutri et al. [2003]
K	12.672	0.027	magnitude	Cutri et al. [2003]
U	10.186	–	magnitude	Landolt and Uomoto [2007]
I	11.995	–	magnitude	Landolt and Uomoto [2007]
UmB	-1.16	–	color	Mermilliod [1997]
BmV	-0.27	–	color	Mermilliod [1997]
bmy	-0.151	–	color	Hauck and Mermilliod [1997]
m1	0.104	–	color	Renson and Manfroid [2009]
c1	-0.233	–	color	Renson and Manfroid [2009]
g	11.45	0.02	magnitude	Zacharias et al. [2012]
r	11.89	0.04	magnitude	Zacharias et al. [2012]
V	12.65	0.05	magnitude	Zacharias et al. [2012]
B	11.42	0.04	magnitude	Zacharias et al. [2012]
R	12.00	0.08	magnitude	Zacharias et al. [2012]
Bt	11.156	–	magnitude	Høg et al. [2000]
Vt	11.254	–	magnitude	Høg et al. [2000]
W1	12.737	0.024	magnitude	Cutri [2012]
W2	12.822	0.020	magnitude	Cutri [2012]
box1	7.932	–	magnitude	-
box2	8.631	–	magnitude	-
box3	9.070	–	magnitude	-

Table 6.18: Photometric measurements for HZ44.

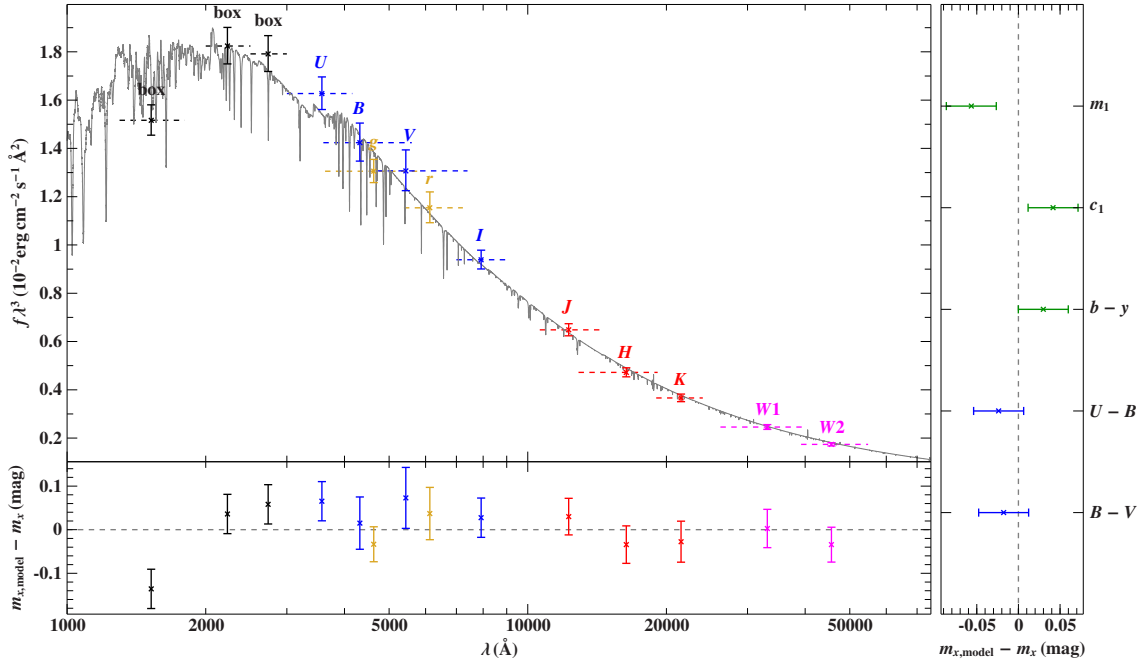


Figure 6.32: SED of HZ44 in comparison with photometric measurements (magnitudes and colors). The bottom and right panels show the residuals for the magnitude and color measurements.

6.2 Carbon rich He-sdO stars

6.2.1 [CW83] 0904-02

6.2.1.1 General information

[CW83] 0904-02 is a spectroscopically rarely analyzed He-sdO with a visual magnitude of 12.25 ± 0.27 [Høg et al., 2000]. It is located at $\alpha = 09^{\text{h}}07^{\text{m}}08.11^{\text{s}}$ and $\delta = -03^{\circ}06'13.97''$.

It was first mentioned by Berger and Fringant [1980] who describe the spectrum as dominated by HeI and HeII lines with an absence of hydrogen. Kilkenny et al. [1988] listed it in their catalog of spectroscopically identified hot subdwarf stars and classify it as a He-sdO.

Dreizler [1993] did the first analysis of this system, aiming at the atmospheric parameters and metal abundances. He found an effective temperature of $T = 46500 \pm 1000$ K and a surface gravity of $\log(g) = 5.55 \pm 0.15$. While the spectrum is dominated by helium lines, the HeI lines are weaker compared to the HeII lines, while for the rest of analyzed He-sdOs, both ionization stages had lines of comparable strength. An enrichment in carbon and a slighter enrichment in nitrogen was found, as well as a solar neon content and sub-solar magnesium and silicon abundances.

Up to now this system has mainly been used for analyzing the chemical composition of the interstellar medium.

6.2.1.2 Spectral analysis

For the spectral analysis of [CW83] 0904-02 data from many different instruments was available (FEROS, FUSE, IUE, STIS). An overview on the used data can be found in Sect. .1.

The FEROS spectra were used for determining the atmospheric parameters, which was aggravated by the bad S/N ratio of these spectra. In a first step, the pure H/He grid was used and resulted in an effective temperature of $T_{\text{eff}} = 49000 \pm 700$ K, $\log(g) = 5.70 \pm 0.1$ and a helium abundance of $\log(y) = 1.5 \pm 0.1$. These values are significantly different from those found by Dreizler [1993], especially the temperature is off by about 3000 K. As [CW83] 0904-02 shows strong carbon lines and only weak nitrogen lines in the optical spectra, it was decided to include carbon in the H/He grid to enhance the compliance with the observational data. The carbon abundance was found to be $0.148 \times n(\text{H})$ from CIII and CIV lines. In addition the carbon lines were found to be broadened by rotation and a projected rotational velocity of $v_{\text{rot}} = 33 \pm 2$ km/s was measured. However, as the new H/He/C grid results in almost the same values as the H/He grid, the visible CIII and CIV lines were used to check the ionization equilibrium as an indicator for the correct temperature. The carbon abundance only from CIII lines was $0.029 \times n(\text{H})$, while it grew to $1.080 \times n(\text{H})$ when using CIV lines. This result was confirmed by the analysis of the STIS data, which showed one clear CIII and CIV line. As both abundances should be about the same when the temperature is correct, the discrepancy indicates that the current model is too hot. As all tries to push the fitting results towards a lower effective temperature (different starting values, selection of lines etc.) failed, the only remaining option was to go back to “fitting by eye“. By careful adjustment and visual inspection of the the data and the overplotted models, the following combination of atmospheric

parameters was found (the errors are those from the fit with the H/He grid):

- $T_{\text{eff}} = 47000 \pm 700 \text{ K}$
- $\log(g) = 5.70 \pm 0.1$
- $\log(n(\text{He})/n(\text{H})) = 2.0 \pm 0.1$
- $v_{\text{rot}} = 35 \pm 2 \text{ km/s}$

The succeeding check of the ionization equilibrium confirmed that the temperature was now much closer to the real value, as the carbon abundance showed a difference of 0.25 dex from FEROS and 0.06 dex from STIS. How well the manually fitted parameters seem to match the ones of [CW83] 0904-02 can be seen in Fig. 6.33.

To crosscheck the rotation, the FUSE spectra were used. In Fig. 6.35 several carbon lines from the UV together with the fitted line profiles are shown. In addition, the theoretical line profiles of a non-rotating star are given in green. As the broadening and resulting smearing of the single lines is clearly observable, the rotational velocity can be seen as being confirmed by the FUSE spectra which gave a projected rotational velocity of $v_{\text{rot}} = 30 \pm 4 \text{ km/s}$. This is in good agreement with the value from the optical data. The determination of the metal abundances followed the

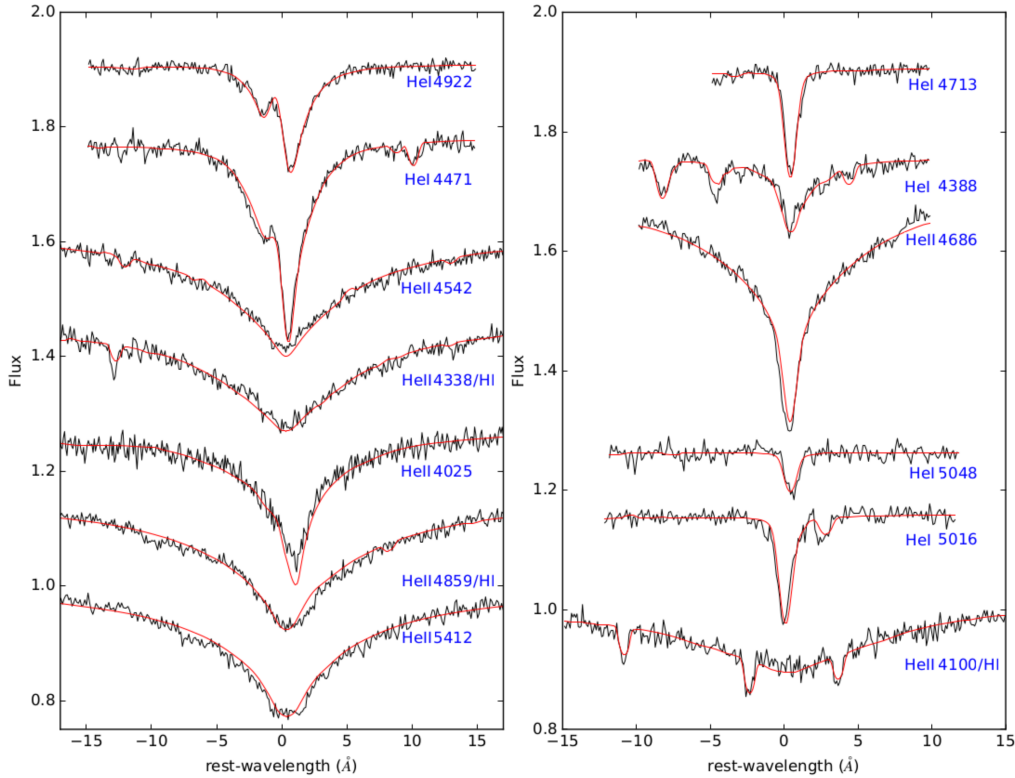


Figure 6.33: Visualization of several HeI and HeII lines of [CW83] 0904-02, some with a hydrogen component. The black lines show parts of the FEROS spectrum, the best-fitting model is represented by the red lines. The flux levels had been adjusted for better representation.

same scheme as for the other stars. On overview on the values is given in table 6.20

Element	# lines	FEROS
C	19	-0.14 ± 0.05
N	19	-1.75 ± 0.1
O	4	-2.44 ± 0.4
Ne	3	-1.21 ± 0.15
Mg	1	-2.47 ± 0.17
Al	(1	$-3.54 \pm 0.7)$
Si	4	-2.45 ± 0.15
P	1	—
S	(2	$-3.9 \pm 1)$

Table 6.19: Overview on the number abundances for [CW83] 0904-02 determined from the optical FEROS spectrum. Given is the $\log(n(X)/n(H))$ in number abundances. (Models without Fe/Ni). The second column gives the number of lines used for the fit of a specific element. Values in brackets show very large errors and have to be dealt with care.

Element	FEROS	FUSE	IUE	STIS
He	2.0 ± 0.1	—	—	—
C	$-0.22 \pm 0.07(20)$	$0.07 \pm 0.05(5)$	$0.05 \pm 0.15(4)$	$0.10 \pm 0.16(2)$
N	$-1.87 \pm 0.07(19)$	$-1.44 \pm 0.09(7)$	$-1.75 \pm 0.21(8)$	$-1.35 \pm 0.13(3)$
O	$(-2.28 \pm 0.60)(5)$	$-1.66 \pm 0.15(3)$	—	—
Ne	$-0.98 \pm 0.25(4)$	$(-0.90 \pm 0.50)(2)$	$(-0.96 \pm 0.70)(3)$	—
Mg	$-2.41 \pm 0.12(1)$	—	$(-1.75 \pm 0.90)(2)$	—
Al	$-3.10 \pm 0.47(2)$	$-2.69 \pm 0.22(2)$	$(-2.91 \pm 0.82)(2)$	—
Si	$-2.51 \pm 0.15(4)$	$-2.29 \pm 0.28(4)$	$(-2.35 \pm 0.7)(3)$	$(-2.76 \pm 0.70)(1)$
P	—	-4.16 ± 0.2	—	—
S	—	—	(-4.19 ± 1.00)	—
Fe	—	-2.68 ± 0.23	$-2.84 \pm 0.14(11)$	$-2.64 \pm 0.64(1)$
Ni	—	-3.11 ± 0.21	$-3.62 \pm 0.12(5)$	$-3.86 \pm 0.2(4)$

Table 6.20: Overview on the number abundances for [CW83] 0904-02 determined from different spectra. Given is the $\log(n(X)/n(H))$ in number abundances. (Models with Fe/Ni). The number of lines used for fitting each element is displayed in brackets following the abundances. Abundances in brackets show very large errors and have to be dealt with care.

Although the oxygen abundances from FEROS and FUSE differ by about 0.6 dex, the error ranges are still overlapping. Given the much smaller errors from FUSE, the final oxygen abundance is dominated by this value. For neon the global fit gave values differing by about 1 dex, while the values from the individual fit were consistent and only changing very little. Hence the abundance from the individual fit was used. Overplotting the corresponding model and the different spectra showed no significant deviations. As there is, unlike in CD-31° 4800, no significant trend that the abundances from the UV are smaller or larger than those from the optical, no de-trending for iron and nickel was necessary. This can be explained by the much better resolution of the FUSE and STIS data which allow for a much more

accurate determination of the real continuum level. Hence the problem with the pseudocontinuum is much less pronounced and only occurs in crowded areas of the spectra. The quality of the IUE data was comparatively bad and suffered from a poor S/N ratio, which explains the low number of lines and the large errors for certain elements.

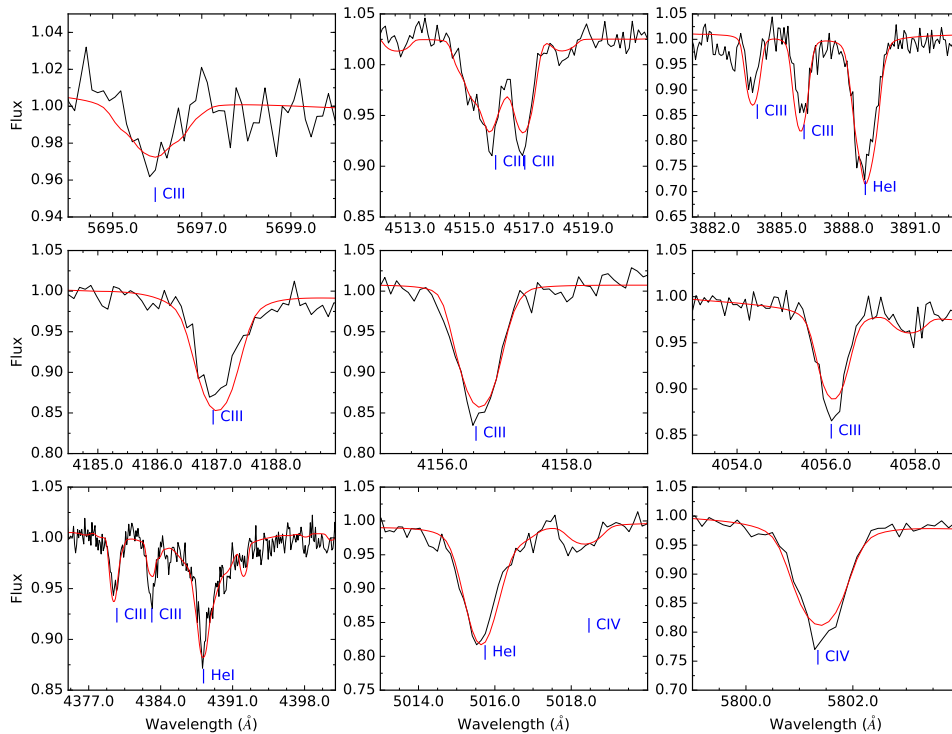


Figure 6.34: Visualization of several carbon lines with different ionization stages of [CW83] 0904-02 (FEROS spectrum) in comparison with the final synthetic spectrum.

For reasons of comparison the number abundances were converted to mass abundances and compared to the solar mass abundance (see table 6.21).

Fig. 6.38 shows a visualization of these values. It can be clearly seen that [CW83] 0904-02 lacks the classic CNO-pattern as seen with the nitrogen-enriched He-sdO stars. This points to a different formation history that will be discussed in Sect. 7.2. The results from Dreizler [1993] were confirmed. Not only the carbon enrichment was found, also the subsolar magnesium and silicon abundances were verified. Only the slight nitrogen enrichment could not be confirmed, as the results shown here would be compatible with a solar nitrogen content. As with most of the other stars, the determination of the sulfur content was very difficult because the line were strongly blended or extremely hard to fit.

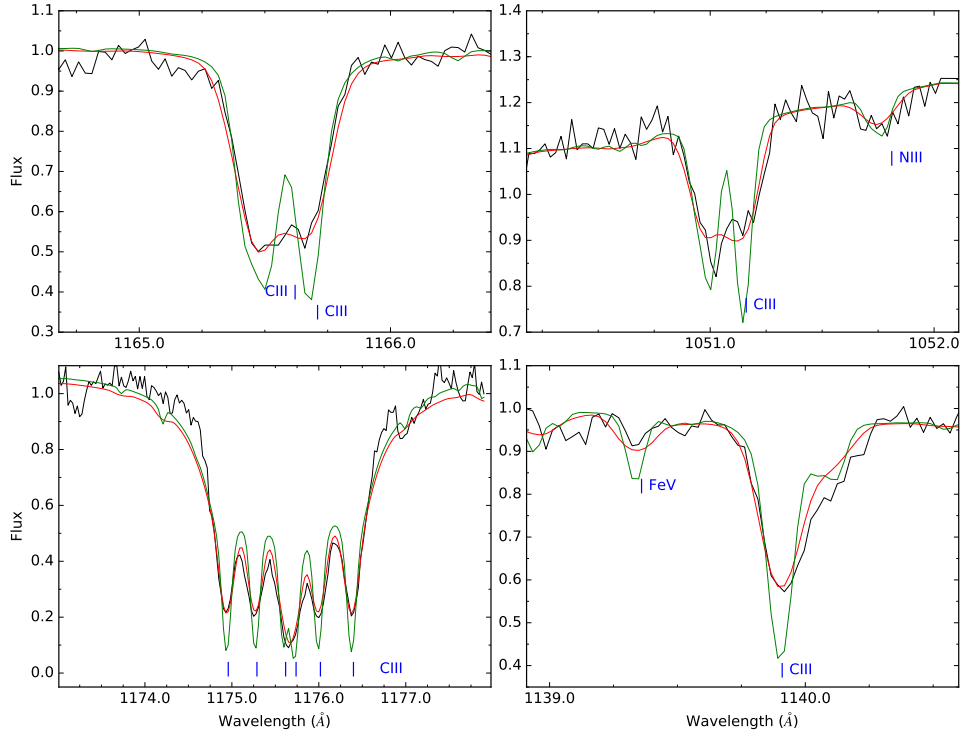


Figure 6.35: Visualization of several CIII lines of [CW83] 0904-02 (UV spectra) in comparison with the final synthetic spectrum. Given in green are the assumed line profiles for the same carbon abundance if the star would show no rotational broadening.

Element	mass abundance ratio
H	$3.24 \cdot 10^{-3}$
He	$3.85^{+3.83}_{-1.92}$
C	$9.68^{+2.51}_{-1.99}$
N	$1.22^{+0.32}_{-0.25}$
O	$0.129^{+0.133}_{-0.070}$
Ne	$4.64^{+3.61}_{-2.03}$
Mg	$0.524^{+0.34}_{-0.188}$
Al	$1.54^{+3.32}_{-1.05}$
Si	$0.323^{+0.194}_{-0.125}$
P	$0.877^{+0.518}_{-0.329}$
S	$(3.12^{+23.1}_{-2.50}) \cdot 10^{-2}$
Fe	$0.160^{+0.103}_{-0.063}$
Ni	$0.558^{+0.330}_{-0.212}$

Table 6.21: Mass abundances for the different elements in [CW83] 0904-02 compared to their solar value.

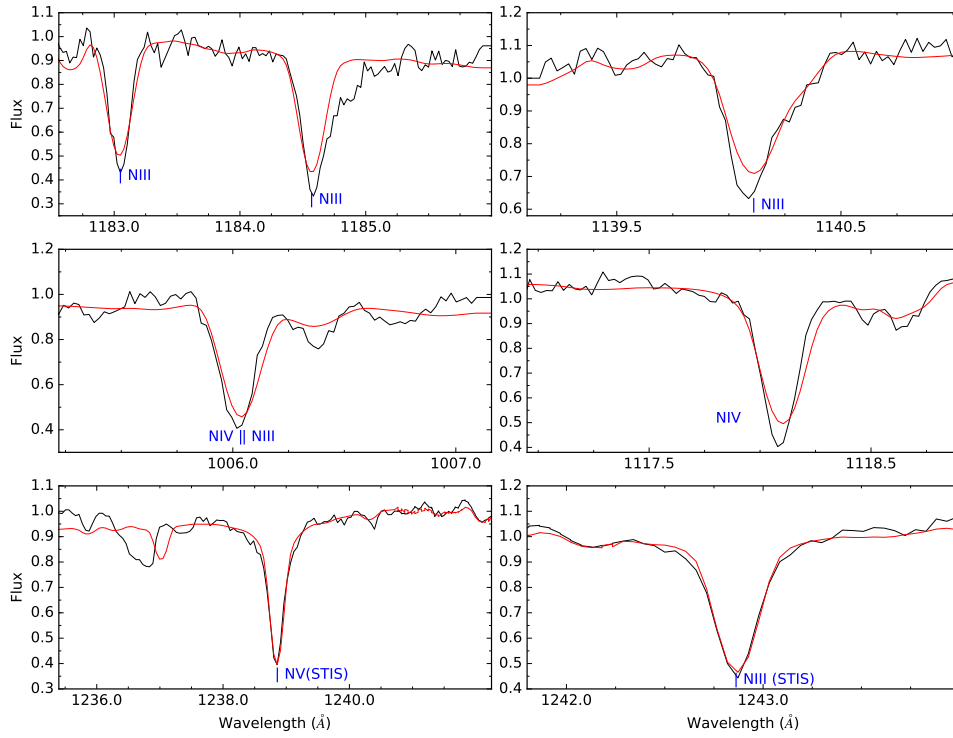


Figure 6.36: Visualization of several nitrogen lines with different ionization stages of [CW83]0904-02 (UV spectra) in comparison with the final synthetic spectrum.

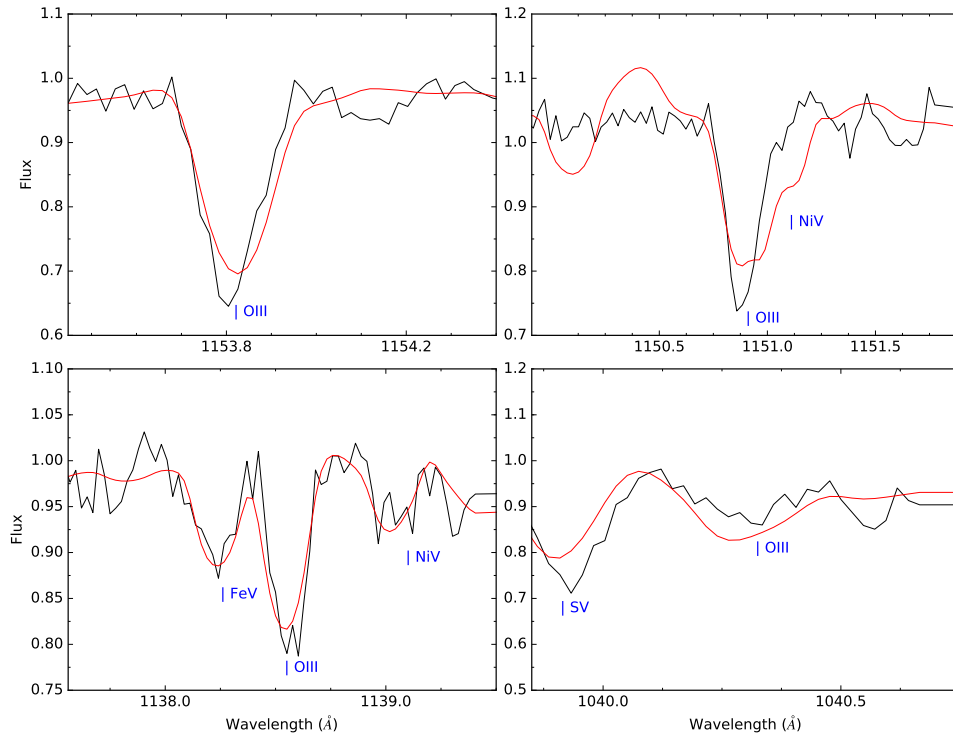


Figure 6.37: Visualization of several O III lines of [CW83]0904-02 (UV spectra) in comparison with the final synthetic spectrum.

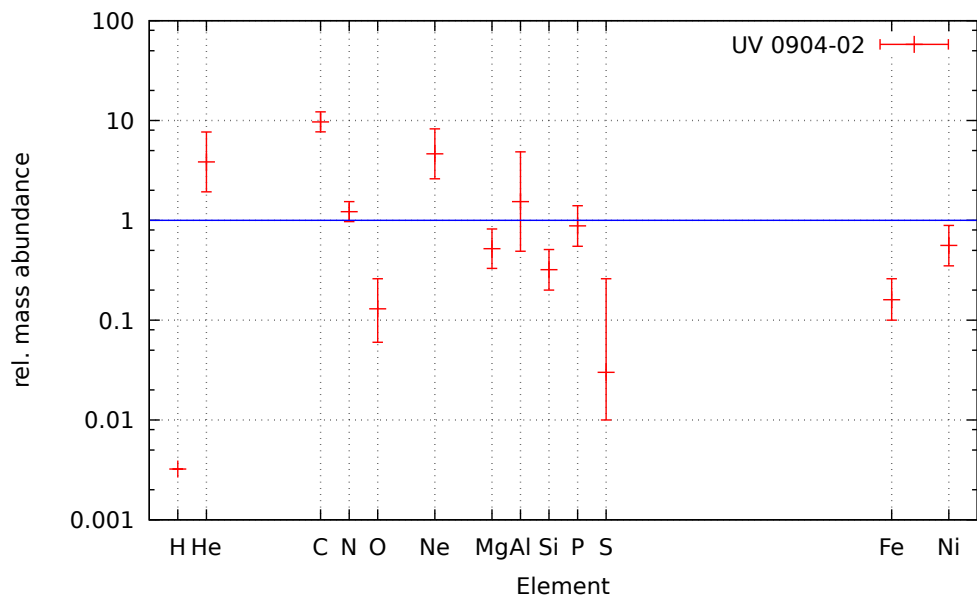


Figure 6.38: Visualization of the mass abundance ratio of [CW83] 0904-02. The solar level of the different elements is given by the blue line

6.2.1.3 Spectral energy distribution

As usual, the SED of a star with the calculated parameters was compared with photometric measurements to check for consistency. The following table (table 6.22) gives an overview on the used photometric measurements.

Filter	value	error	type	reference
J	12.639	0.028	magnitude	Kharchenko [2001]
H	12.799	0.030	magnitude	Kharchenko [2001]
K	12.884	0.037	magnitude	Kharchenko [2001]
B	11.72	0.11	magnitude	Egret et al. [1992]
V	12.25	0.27	magnitude	Zacharias et al. [2004]
bmy	-0.134	–	color	Paunzen [2015]
m1	0.040	–	color	Paunzen [2015]
c1	-0.237	–	color	Paunzen [2015]
u	12.009	–	magnitude	Hudelot et al. [2012]
g	15.528	–	magnitude	Hudelot et al. [2012]
r	15.147	–	magnitude	Hudelot et al. [2012]
i	15.045	–	magnitude	Hudelot et al. [2012]
z	14.338	–	magnitude	Hudelot et al. [2012]
Bt	11.545	0.108	magnitude	Høg et al. [2000]
Vt	12.169	0.271	magnitude	Høg et al. [2000]
W1	12.975	0.024	magnitude	Cutri [2012]
W2	13.059	0.029	magnitude	Cutri [2012]
box1	7.910	–	magnitude	-
box2	8.844	–	magnitude	-
box3	9.312	–	magnitude	-

Table 6.22: Photometric measurements for [CW83] 0904-02.

The comparison between the SED constructed from the model atmosphere and the measured photometric values revealed no significant deviations. Only the Johnson V and the Tycho V_t indices are almost out of the given errorrange. But as all the other values match way better and the errors are comparatively large anyway, it is more likely a problem with the measurement of V and V_t than a problem with the SED. It is interesting to notice that the measurements from Tycho and Johnson have an identical errorrange but their absolute value is slightly different. According to the SED fit, [CW83] 0904-02 is located at 419_{-86}^{+108} pc ($\theta = 1.728 \cdot 10^{-11}$ and $0.47 M_\odot$) and is affected by a reddening of 0.0201. This is in agreement with the distance given by Dreizler [1993] which is 520 ± 90 pc.

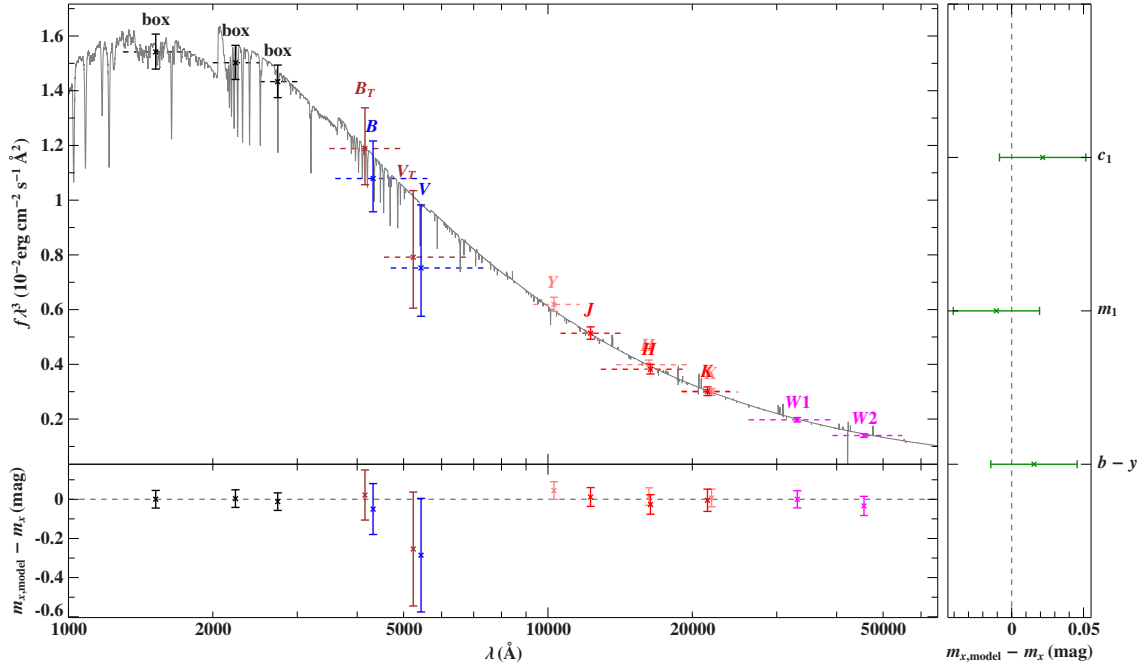


Figure 6.39: SED of [CW83] 0904-02 in comparison with photometric measurements (magnitudes and colors). The bottom and right panels show the residuals for the magnitude and color measurements.

6.2.2 HE 0958-1151

6.2.2.1 General information

HE 0958-1151 is a comparatively little analyzed He-sdO star ($m_V=14.05$) located at $\alpha = 10^{\text{h}}00^{\text{m}}42.6^{\text{s}}$ and $\delta = -12^{\circ}05'52.96''$. Despite being mentioned in several catalogs (i.e. Green et al. [1986] and Kilkenny et al. [1988]), the first detailed spectroscopic analysis was done by Stroeger et al. [2007] who classified the system as carbon rich with only a weak nitrogen component. The atmospheric parameters they found are $T_{\text{eff}}=44125$, $\log(g)=5.51$ and $\log(y)=1.85$. An analysis by Hirsch [2009] revealed a similar temperature of 44230 K, while the surface gravity was a bit lower with $\log(g)=5.39$. The classification as carbon rich was confirmed. Both analyses were based on TMAP.

6.2.2.2 Spectral analysis

The UVES spectra for HE 0958-1151 were taken from the ESO-phase3 archive, folded to a common resolution of $R=19000$ and coadded. Despite being classified as “science ready“, the spectra suffered from various cosmics which were not removed correctly during data processing. Therefore the most prominent ones and those contaminating other spectral lines were removed by hand. The flux values of the pixel containing the cosmic were replaced by the average of the neighboring pixel.

The fitting of the HeI and HeII with the HECNO grid revealed the following atmospheric parameters

- $T_{\text{eff}} = 45500 \pm 500$ K
- $\log(g)=5.36 \pm 0.10$

- $\log(n(\text{He})/n(\text{H})) = 3$ (fix)
- $v_{\text{rot}} = 20 \pm 2 \text{ km/s}$

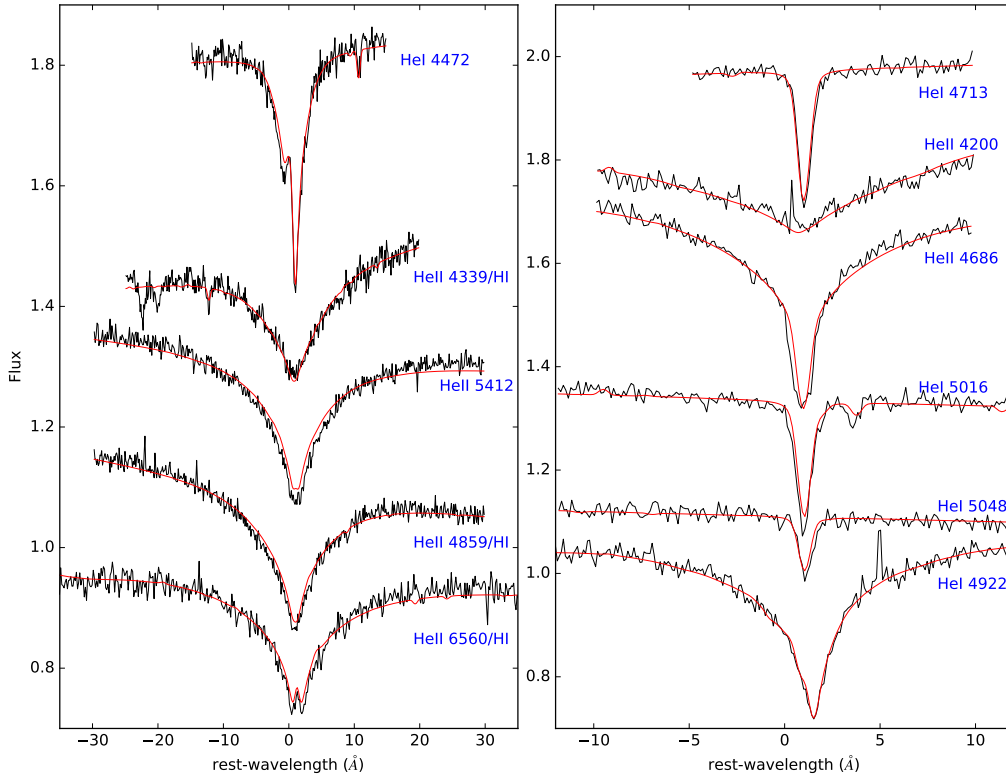


Figure 6.40: Visualization of several HeI and HeII lines of HE 0958-1151, some with a hydrogen component. The black lines show parts of the SPY/UVES spectrum, the best-fitting model is represented by the red lines. The flux levels had been adjusted for better representation.

The spectra showed almost no visible contribution from hydrogen. As the $\log(y)$ varied a lot during the fitting process, it was fixed at $1000\times$ hydrogen. The rotation was measured from the broadening of carbon lines.

The determination of the metal lines followed the standard scheme. The results of the first run on metal abundances can be found in table 6.23. Aluminum was fitted by eye, as the resulting line profiles from SPAS diverged to much from the data. As no lines were visible in the spectra, the value has to be interpreted as an upper limit.

As no suitable UV spectra are available, it is not possible to determine abundances for iron and nickel. But as these elements have an influence on the profiles of all other lines and the temperature stratification, it was decided to include them in full NLTE conditions. They were both set to solar (mass) abundance with respect to the current state of the stellar atmosphere.

The results from the second round of abundance determinations is shown in table 6.24. Again, aluminum was fitted by eye, an error of 0.3 dex was adopted but the value has to be interpreted as an upper limit.

The following figures show metal lines of different elements and, overimposed, the best-fitting model for the specific element.

Element	# lines	abundance
C	15	0.83 ± 0.10
N	14	-0.55 ± 0.07
O	5	-0.85 ± 0.20
Ne	6	-0.36 ± 0.08
Mg	1	-1.45 ± 0.15
Al	2	$-2(\text{fit by eye})$
Si	2	-1.55 ± 0.16
P	2	(-2.6 ± 0.6)
S	2	-2.30 ± 0.40

Table 6.23: Metal abundances derived from the optical SPY/UVES spectra of HE 0958-1151. Given is the $\log(n(X)/n(H))$ in number abundances. (Models without Fe/Ni). The second column gives the number of lines used for fitting a specific element. Abundances in brackets suffer from large uncertainties and have to be dealt with care.

Element	# lines	abundance
C	16	0.66 ± 0.07
N	13	-0.60 ± 0.15
O	5	-0.82 ± 0.20
Ne	7	-0.29 ± 0.07
Mg	1	-1.38 ± 0.19
Al	2	-2.4 ± 0.30
Si	2	-1.50 ± 0.16
P	2	-2.96 ± 0.35
S	3	(-2.14 ± 0.50)

Table 6.24: Metal abundances derived from the optical SPY/UVES spectra of HE 0958-1151. Given is the $\log(n(X)/n(H))$ in number abundances. (Models with Fe/Ni). The second column gives the number of lines used for fitting a specific element. Abundances in brackets suffer from large uncertainties and have to be dealt with care.

Fig. 6.44 shows a visual representation of table 6.25. HE 0958-1151 is enriched in carbon, while the nitrogen level is consistent with the solar level. Oxygen is depleted. This classifies HE 0958-1151 as carbon-rich. Neon is only slightly enriched to twice the solar abundance. All the other elements seem to be unaderabundant, except phosphorus, which would be consistent with the solar amount of this element.

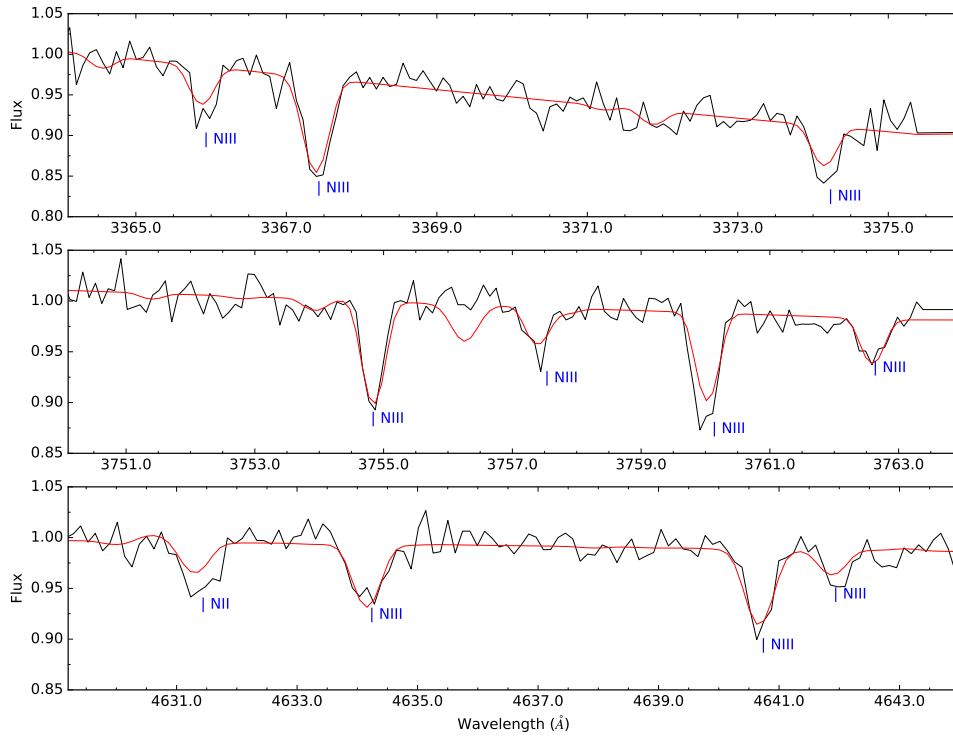


Figure 6.41: Visualization of several nitrogen lines with different ionization stages of HE 0958-1151 in comparison with the final synthetic spectrum.

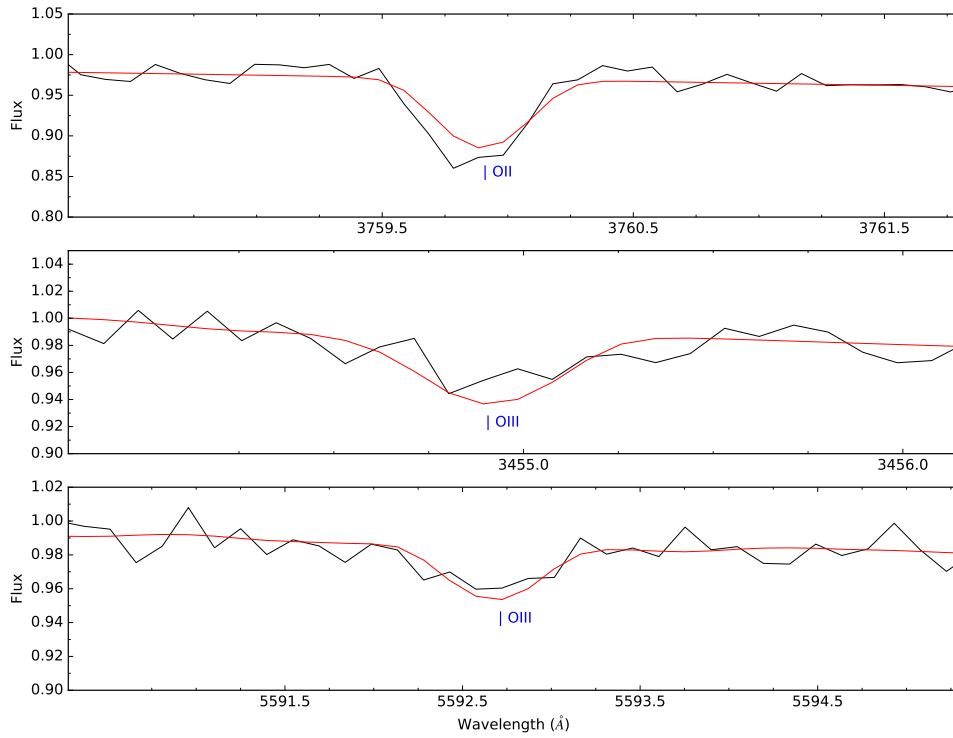


Figure 6.42: Visualization of several oxygen lines with different ionization stages of HE 0958-1151 in comparison with the final synthetic spectrum.

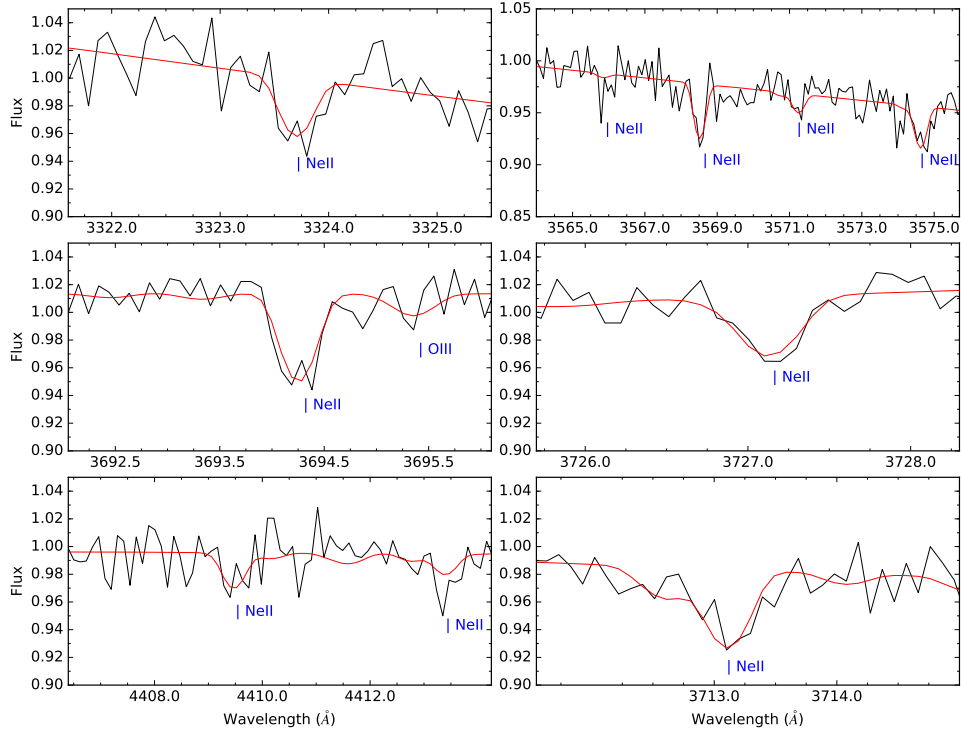


Figure 6.43: Visualization of several NeII lines of HE 0958-1151 in comparison with the final synthetic spectrum.

Element	mass abundance ratio β/β_{\odot}
H	$2.95 \cdot 10^{-4}$
He	$3.93^{+2.30}_{-1.45}$
C	$5.68^{+1.30}_{-1.06}$
N	$1.24^{+0.51}_{-0.36}$
O	$0.104^{+0.049}_{-0.041}$
Ne	$2.00^{+0.349}_{-0.304}$
Mg	$0.350^{+0.196}_{-0.118}$
Al	$0.473^{+0.482}_{-0.245}$
Si	$0.327^{+0.146}_{-0.107}$
P	$1.470^{+1.420}_{-0.711}$
S	$0.192^{+0.402}_{-0.128}$
Fe	1
Ni	1

Table 6.25: Mass abundances for the different elements in HE 0958-1151 compared to the solar mass abundance.

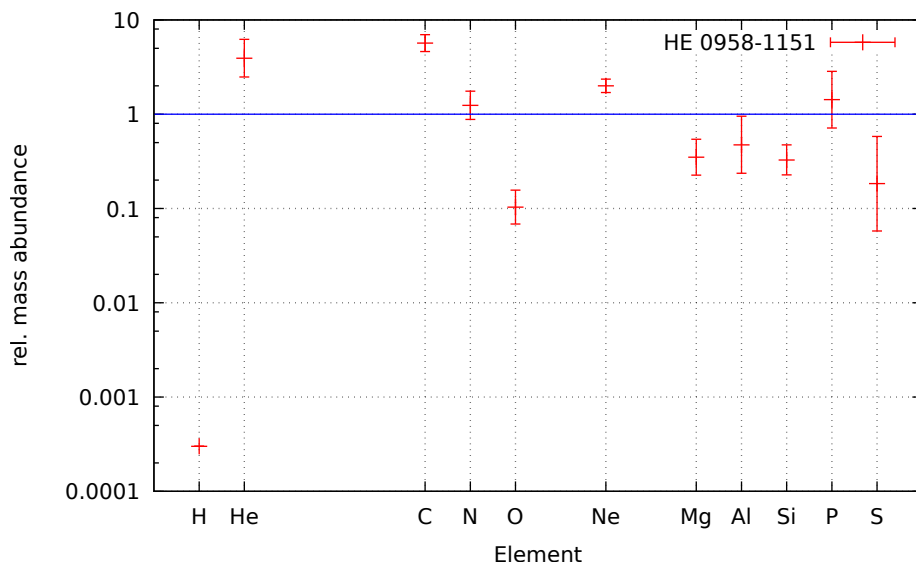


Figure 6.44: Relative mass abundances for HE 0958-1151 compared to their solar value. The adopted solar abundances of iron and nickel are not shown.

6.2.2.3 Spectral energy distribution

The SED of a star with the calculated parameters was compared with photometric measurements to check for consistency. Table 6.26 gives an overview on the photometry used.

Filter	value	error	type	reference
J	14.656	0.032	magnitude	Kharchenko [2001]
H	14.748	0.074	magnitude	Kharchenko [2001]
K	15.0824	0.177	magnitude	Kharchenko [2001]
R	14.30	0.11	magnitude	Fedorov et al. [2011]
B	13.84	0.03	magnitude	Egret et al. [1992]
V	14.05	0.02	magnitude	Zacharias et al. [2004]
B-V	-0.24	0.05	color	Kilkenny et al. [1997]
U-B	-1.17		color	Kilkenny et al. [1997]
B1	13.73		magnitude	Monet et al. [2003]
B2	14.07		magnitude	Monet et al. [2003]
g	13.85	0.04	magnitude	Hudelot et al. [2012]
r	14.29	0.03	magnitude	Hudelot et al. [2012]
i	14.63	0.06	magnitude	Hudelot et al. [2012]
W1	14.929	0.04	magnitude	Cutri [2012]
W2	15.123	0.132	magnitude	Cutri [2012]

Table 6.26: Photometric measurements for HE 0958-1151.

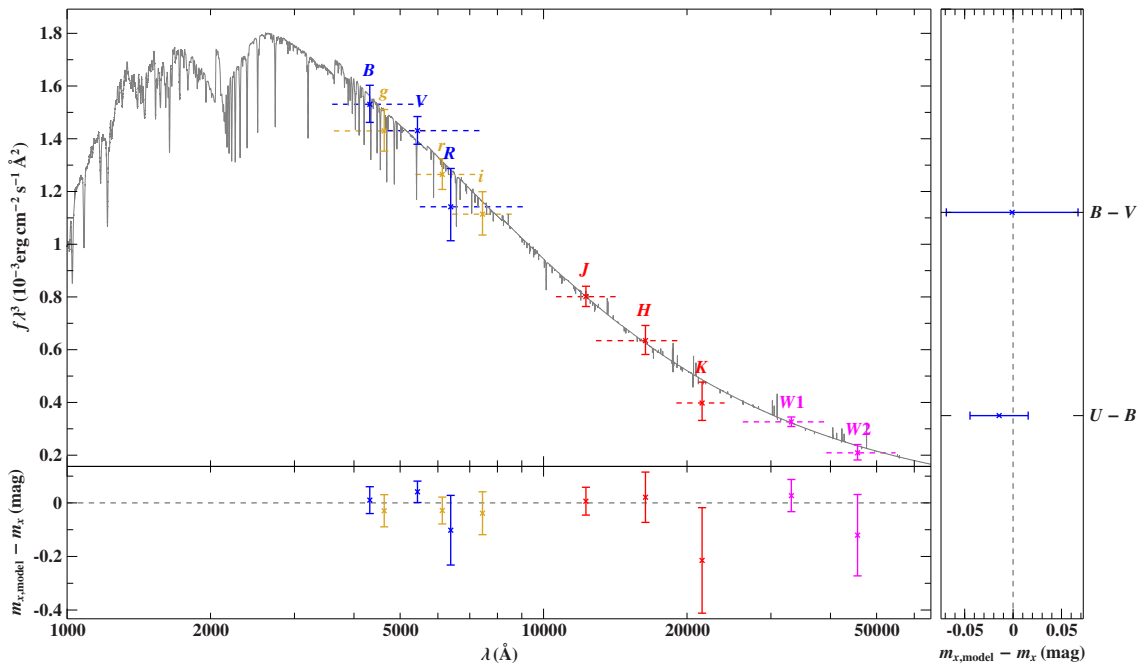


Figure 6.45: SED of HE 0958-1151 in comparison with photometric measurements (magnitudes and colors). The bottom and right panels show the residuals for the magnitude and color measurements.

The comparison between the SED constructed from the model atmosphere and the measured photometric values revealed no significant deviations. Only the K magnitude is slightly off, but regarding the large error, there is no need for concerns. With a reddening of 0.0695, a mass of $0.47 M_{\odot}$ and $\theta = 7.0717 \cdot 10^{-12}$, a distance of $1.512_{-1.64}^{+1.84}$ kpc results.

6.3 Carbon and Nitrogen rich He-sdO stars

6.3.1 LSS 1274

6.3.1.1 General information

LSS 1274 is a Helium sdO located at $\alpha = 09^{\text{h}}18^{\text{m}}56^{\text{s}}$ and $\delta = -57^{\circ}04'25.4$. It has a V-magnitude of 12.387 [Høg et al., 2000].

It was first mentioned by Kilkenny et al. [1988] in their catalog of spectroscopically identified hot subdwarf stars. A first detailed analysis of the atmospheric parameters was done by Dreizler [1993]. He used NLTE models for the spectroscopic analysis and determined a temperature of 44500 ± 1000 K, and a surface gravity of 5.55 ± 0.15 . The hydrogen abundance was lower than 0.1 by number and an enrichment in carbon, nitrogen and neon was detectable.

Recently it has been used to study the interstellar medium, especially the deuterium to hydrogen ratio.

6.3.1.2 Spectral Analysis

The UVES spectrum of LSS 1274 shows large gaps in wavelength-coverage. so that the number of available HeII lines is comparatively low. The exceptions are HeII 4026 HeII 4859, HeII 5412 and HeII 6560. But as the HeII 5412 line was problematic to fit and showed large deviations between model and data, it was not used for the determination of atmospheric parameters. Without several HeII lines it is difficult to determine the atmospheric parameters correctly. Therefore an old CASPEC spectrum was included in the fitting process. Despite the low resolution, it covered the essential HeII lines. Both spectra were fitted together, with the CASPEC data filling up the UVES gaps and adopting the proper resolution for each spectral range. The results of the fit can be seen in Fig. 6.46. The resulting parameters from a fit with a HHeC grid are

- $T_{\text{eff}} = 44270 \pm 400$ K
- $\log(g) = 5.48 \pm 0.20$
- $\log(n(\text{He})/n(\text{H})) = 2.17 \pm 0.25$
- $v_{\text{rot}} = 5 \pm 3$ km/s

These results are in perfect agreement with the values from Dreizler [1993].

The combined UVES+CASPEC spectrum was also used for the following determination of the metal abundances which followed the common scheme. But because of the low resolution of the CASPEC data, it was only suitable for elements with strong and clear lines, like carbon, nitrogen or neon.

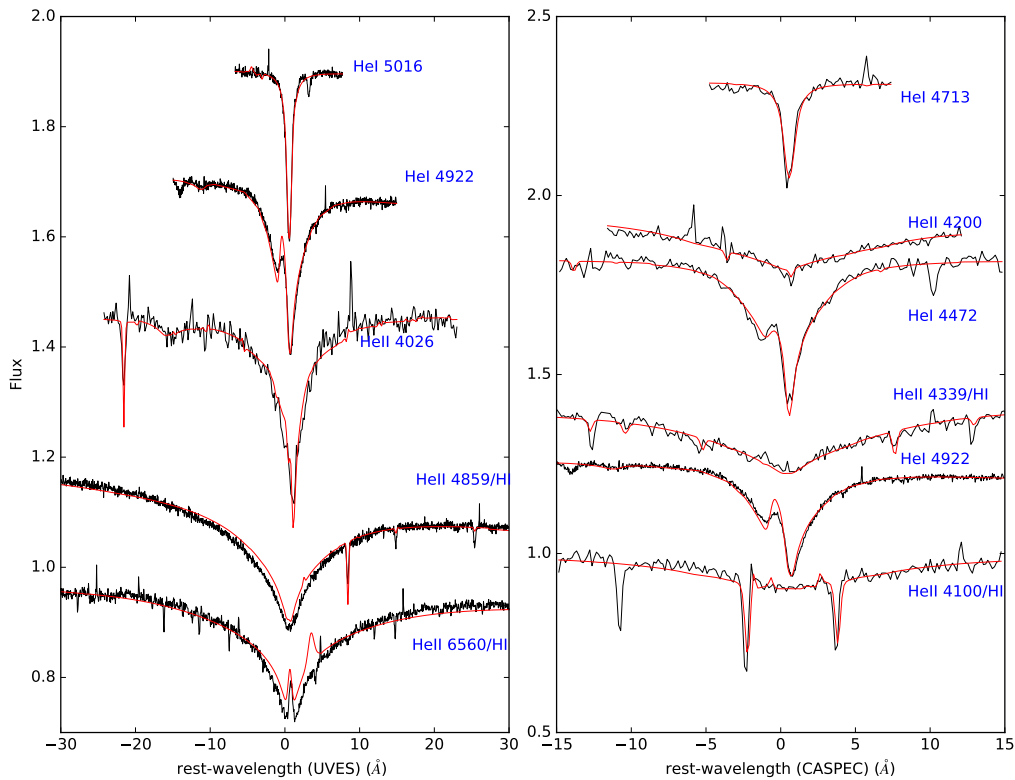


Figure 6.46: Visualization of several HeI and HeII lines of LSS 1274, some with a hydrogen component. The black lines show parts of the CASPEC and UVES spectrum, the best-fitting model is represented by the red lines. The flux levels had been adjusted for better representation.

Table 6.27 shows the results of the first analysis run on the optical data. The models contained no iron or nickel. No significant phosphorus lines were detectable.

Element	# lines	UVES+CASPEC
C	16	-0.40 ± 0.08
N	33	-1.14 ± 0.12
O	11	-1.76 ± 0.10
Ne	17	-0.72 ± 0.09
Mg	2	-2.15 ± 0.40
Al	3	-2.96 ± 0.12
Si	6	-2.00 ± 0.09
P	0	—
S	6	$-(3.05 \pm 0.50)$

Table 6.27: Overview on the number abundances for LSS 1274 determined from the optical UVES+CASPEC spectra. Given is the $\log(n(X)/n(H))$ in number abundances. (Models without Fe/Ni). The second column gives the number of lines used for the fit of a specific element. Abundances in brackets suffer from large uncertainties and have to be dealt with care.

A FUSE spectrum of good quality was available for LSS 1274. Because of the

Element	UVES+CASPEC	FUSE
He	2.17 ± 0.25	–
C	$-0.03 \pm 0.06(16)$	$0.08 \pm 0.11(5)$
N	$-1.11 \pm 0.05(35)$	$-1.05 \pm 0.07(10)$
O	$-1.81 \pm 0.15(11)$	$-1.74 \pm 0.25(7)$
Ne	$-0.71 \pm 0.04(16)$	$-0.79 \pm 0.50(3)$
Mg	$-1.96 \pm 0.27(1)$	–
Al	$-2.90 \pm 0.08(3)$	$-2.25 \pm 0.29(2)$
Si	$-2.01 \pm 0.05(5)$	$-2.20 \pm 0.12(4)$
P	–	$-3.92 \pm 0.14(4)$
S	$-2.69 \pm 0.15(6)$	$-2.81 \pm 0.10(4)$
Fe	–	$-2.42 \pm 0.15(11)$
Ni	–	$-2.62 \pm 0.25(8)$

Table 6.28: Overview on the number abundances for LSS 1274 determined from different spectra. Given is the $\log(n(X)/n(H))$ in number abundances. (Models with Fe/Ni). The number of lines used for fitting each element is displayed in brackets following the abundances.

high resolution of the FUSE data, no problems with the pseudocontinuum occurred. The abundances from the UV show no clear trend compared to the results from the optical (see Table 6.28). The following figures show selected lines for different elements and the final model overplotted to them.

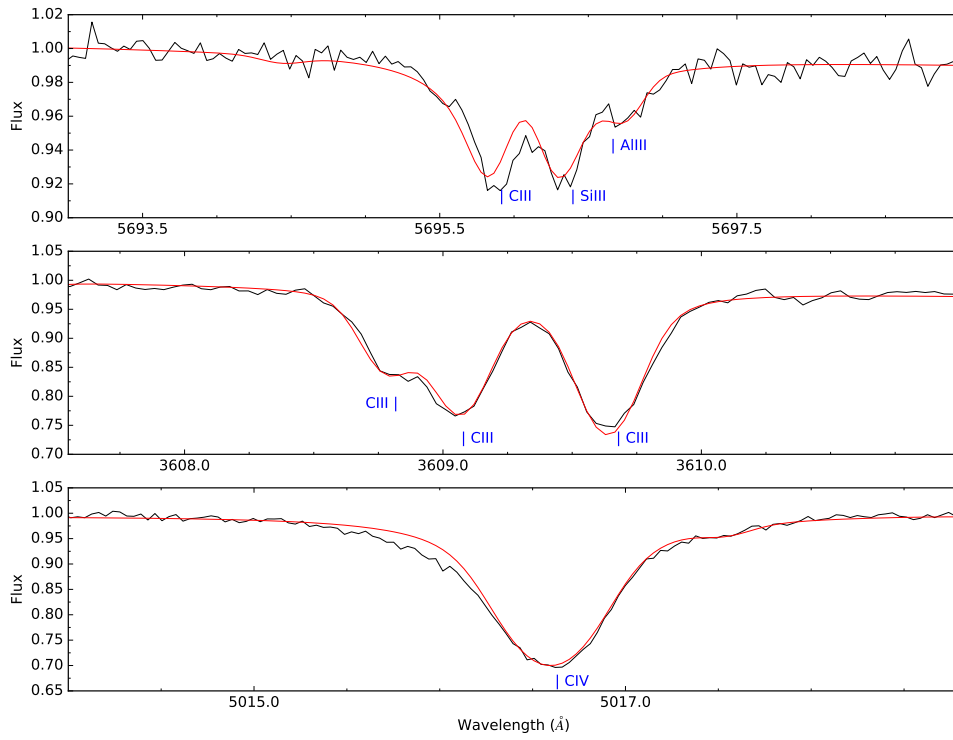


Figure 6.47: Visualization of several carbon lines with different ionization stages of LSS 1274 (optical spectra) in comparison with the final synthetic spectrum.

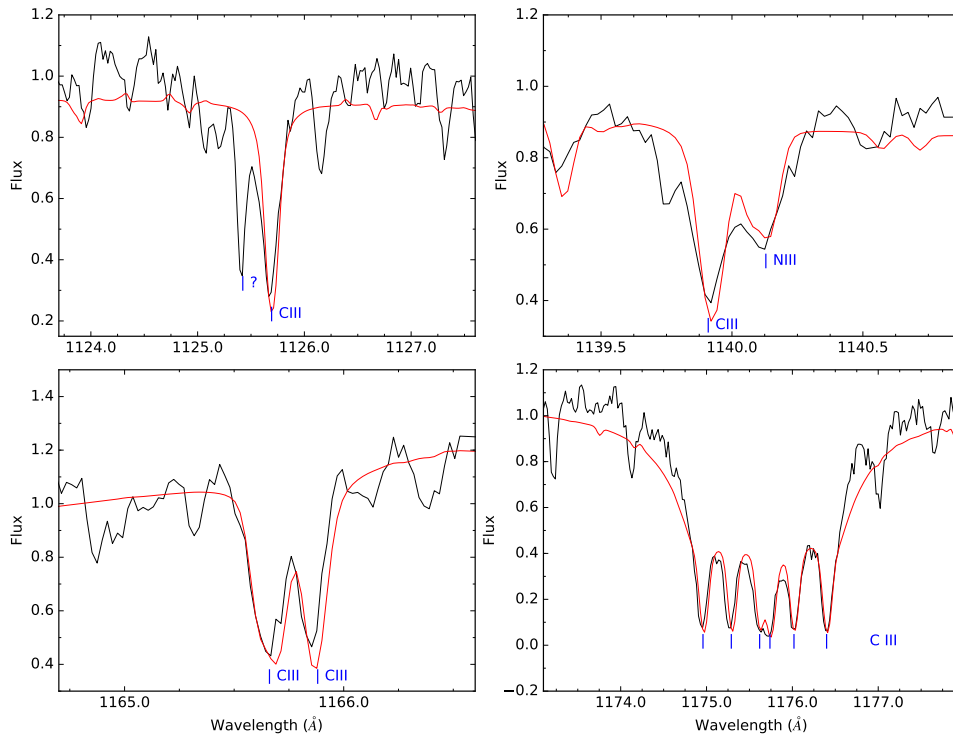


Figure 6.48: Visualization of several C III lines of LSS 1274 (UV spectra) in comparison with the final synthetic spectrum. The line marked with a ? in the first left panel could not be identified.

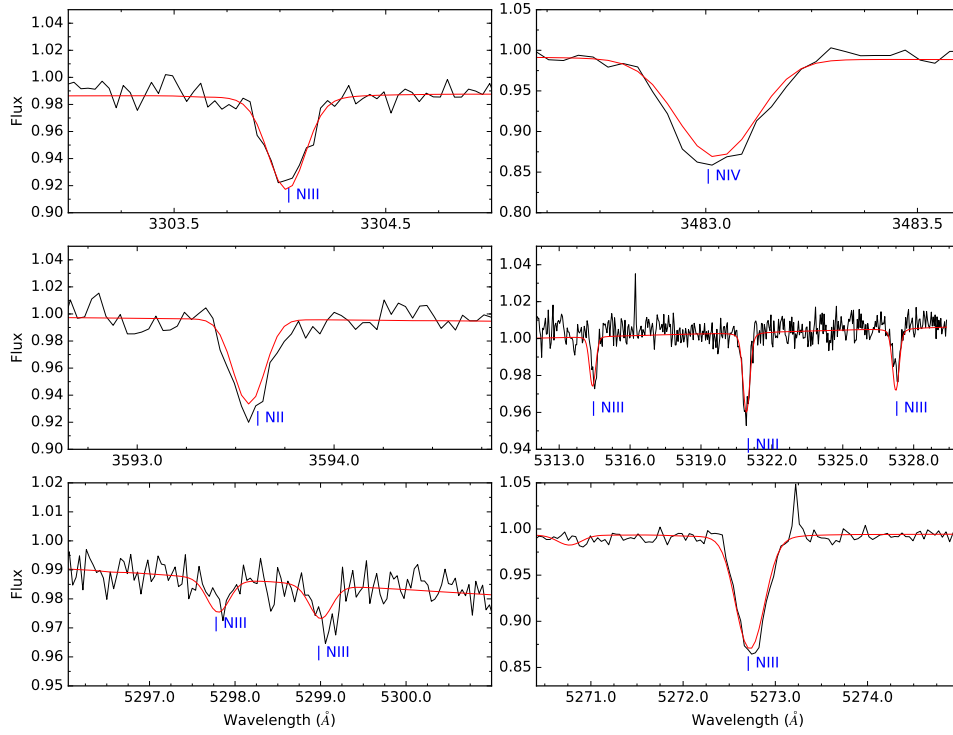


Figure 6.49: Visualization of several nitrogen lines with different ionization stages of LSS 1274 (optical spectra) in comparison with the final synthetic spectrum.

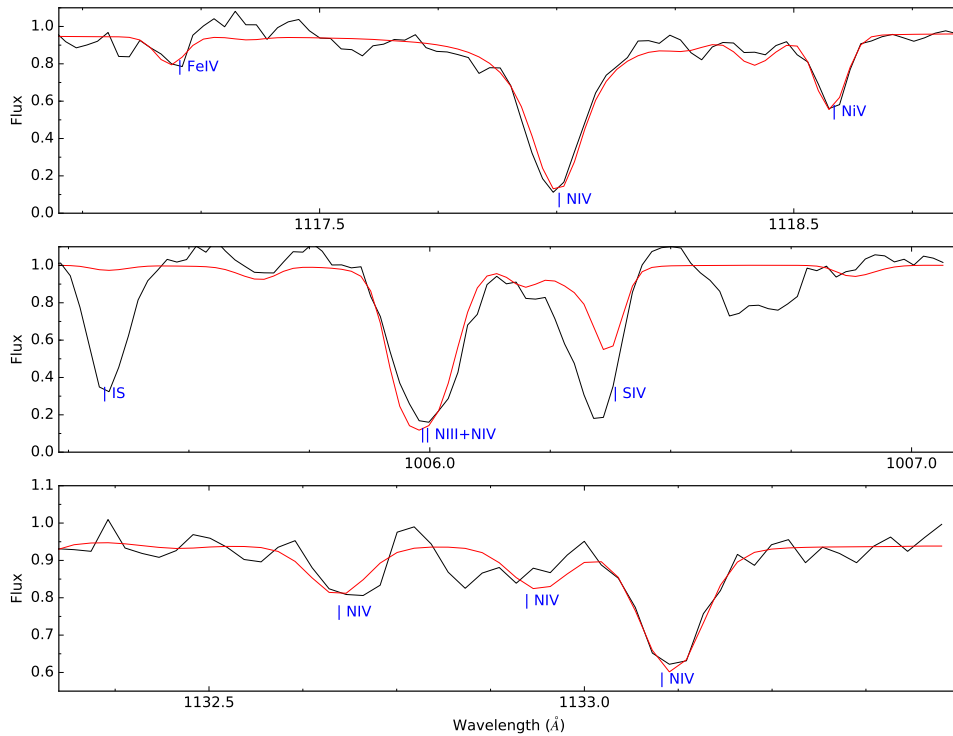


Figure 6.50: Visualization of several nitrogen lines with different ionization stages of LSS 1274 (UV spectra) in comparison with the final synthetic spectrum. An interstellar line is marked with IS.

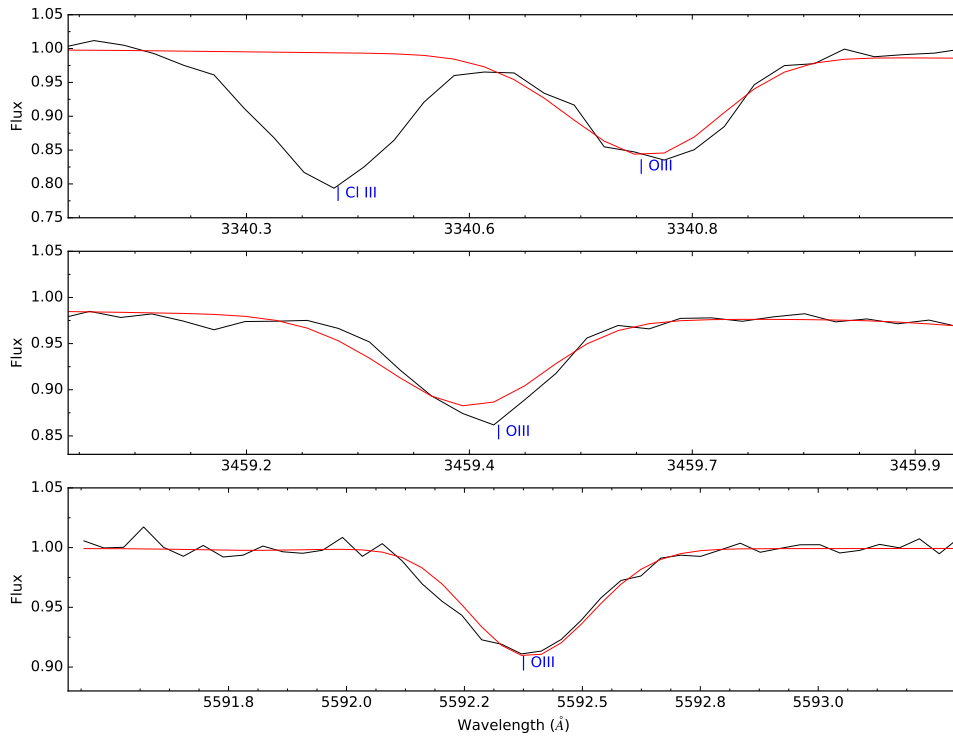


Figure 6.51: Visualization of several OIII lines of LSS 1274 (optical spectra) in comparison with the final synthetic spectrum.

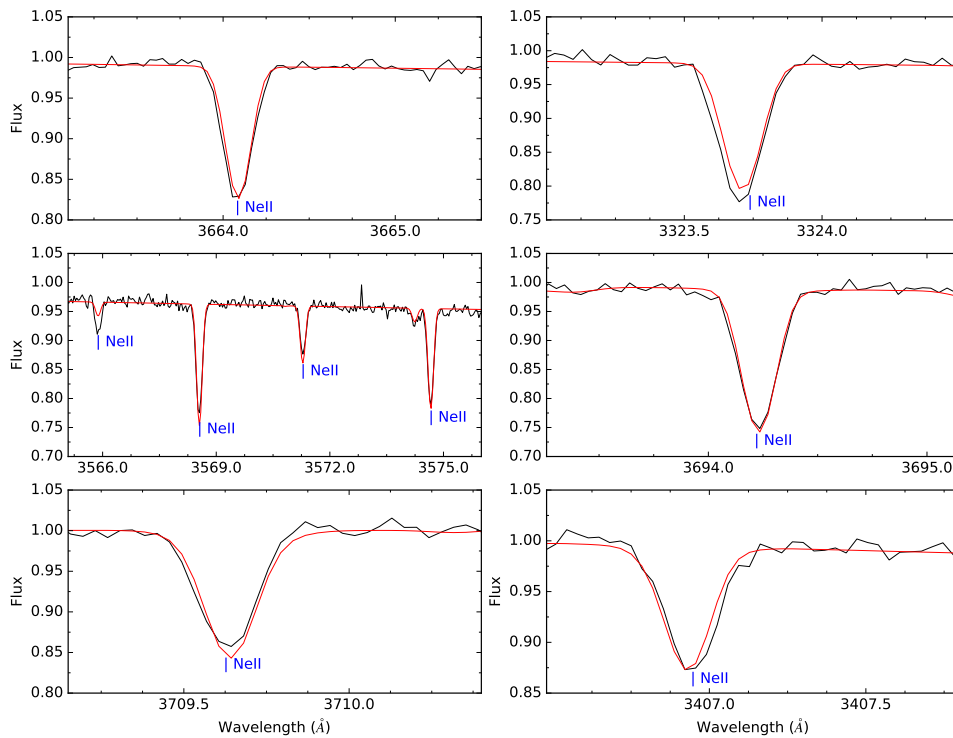


Figure 6.52: Visualization of several NeII lines with different ionization stages of LSS 1274 (optical spectra) in comparison with the final synthetic spectrum.

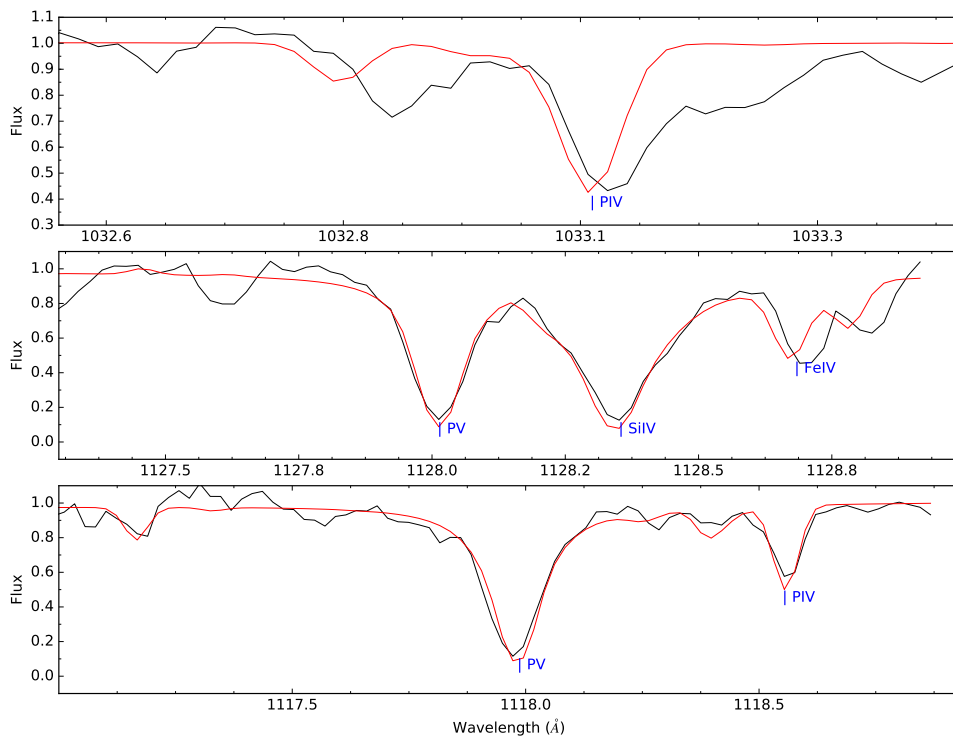


Figure 6.53: Visualization of several phosphorus lines with different ionization stages of LSS 1274 (UV spectra) in comparison with the final synthetic spectrum.

Table 6.29 lists the mass abundances of LSS 1274 with respect to their corresponding solar value and Fig. 6.54 shows a visual representation.

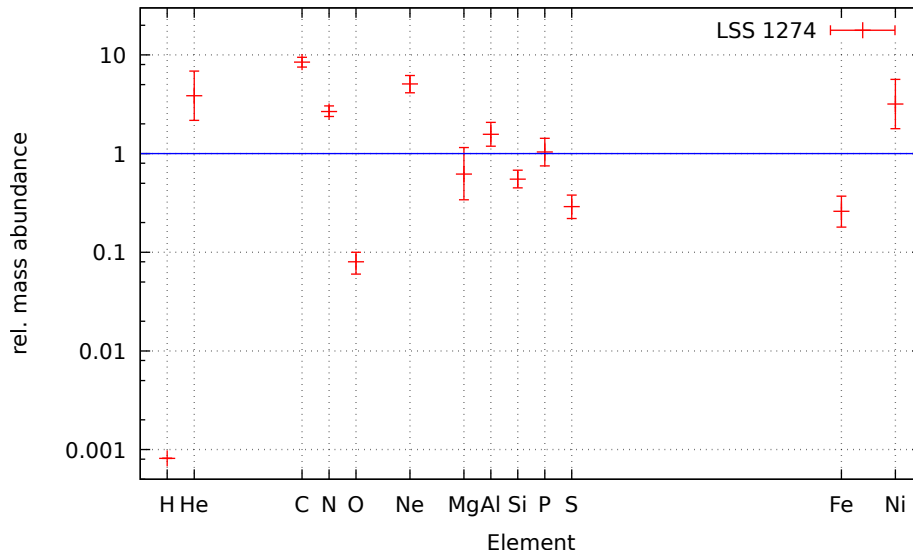


Figure 6.54: Mass abundances for the different elements in LSS 1274 compared to their solar value.

LSS 1274 shows a clear enrichment in helium and carbon. Nitrogen is also enriched, but only slightly but significantly over the solar level, while oxygen is depleted. The common CNO pattern is missing, giving hints to the formation history (see Sect. 7.3). Neon is well above solar, reaching almost the level of carbon, while the rest of the intermediate mass elements scatters around the solar level. Iron is depleted and nickel is clearly enriched, however, the errorbars on the Ni abundance are comparatively large.

Element	mass abundance ratio
H	$6.09 \cdot 10^{-4}$
He	$3.86^{+3.00}_{-1.69}$
C	$8.45^{+1.03}_{-0.92}$
N	$2.67^{+0.37}_{-0.29}$
O	$(8.03^{+2.49}_{-2.12}) \cdot 10^{-2}$
Ne	$5.09^{+1.10}_{-0.95}$
Mg	$0.621^{+0.533}_{-0.275}$
Al	$1.57^{+0.503}_{-0.382}$
Si	$0.555^{+0.133}_{-0.104}$
P	$1.04^{+0.39}_{-0.29}$
S	$0.293^{+0.099}_{-0.065}$
Fe	$0.256^{+0.112}_{-0.082}$
Ni	$3.21^{+0.93}_{-0.72}$

Table 6.29: Mass abundance ratio for LSS 1274.

6.3.1.3 Spectral energy distribution

As usual, the SED of a star with the calculated parameters was compared with photometric measurements to check for consistency. The following table (Table 6.30) gives an overview on the photometry used. If no error is given, the standard error for magnitudes and colors was used (see Sect. 4.12). Measurements in brackets were not used for the fit.

The comparison between the photometric values and the SED calculated from the model is good. Only the WISE2 index is slightly off. Compared to the other measurements, the error of the Johnson V filter is tremendous. However, as this occurred several time with V-band measurements for other stars, no reason to worry is given and the measurement was not used for the fit, only overplotted. Due to a lack of low resolution IUE spectra, only one box filter could be calculated. From the shift of the SED, a distance of 711^{+130}_{-105} pc, based on $\theta = 1.298 \cdot 10^{-11}$ was obtained. The reddening is 0.339. Dreizler [1993] suggests a distance of 580 ± 100 pc, which is overlapping within the errorbars with the result from this work.

Filter	value	error	type	reference
J	13.34	–	magnitude	Kharchenko [2001]
H	13.516	–	magnitude	Kharchenko [2001]
K	13.524	–	magnitude	Kharchenko [2001]
B	12.4	–	magnitude	Egret et al. [1992]
V	12.86	0.002	magnitude	Høg et al. [2000]
b-y	-0.047	–	color	Paunzen [2015]
m1	0.027	–	color	Paunzen [2015]
B-V	-0.212	–	color	Landolt and Uomoto [2007]
U-B	-1.187	–	color	Landolt and Uomoto [2007]
V-R	-0.07	–	color	Landolt and Uomoto [2007]
R-I	-0.092	–	color	Landolt and Uomoto [2007]
V-I	-0.166	–	color	Landolt and Uomoto [2007]
W1	13.656	0.05	magnitude	Cutri [2012]
W2	13.810	0.06	magnitude	Cutri [2012]
box1	9.389	–	magnitude	-
box2	10.385	–	magnitude	-
box3	10.596	–	magnitude	-

Table 6.30: Photometric measurements for LSS 1274.

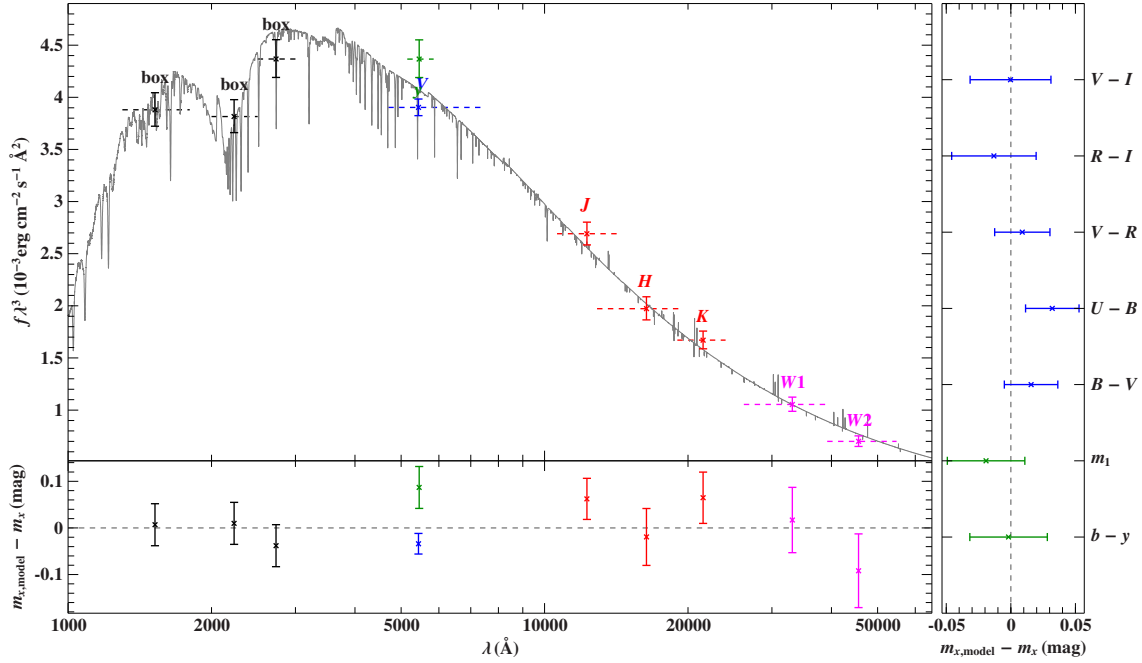


Figure 6.55: SED of LSS 1274 in comparison with photometric measurements (magnitudes and colors). The bottom and right panels show the residuals for the magnitude and color measurements.

6.3.2 LS IV +109

6.3.2.1 General information

LS IV +109 is a $11.99 m_V$ [Schonberner and Drilling, 1984] bright helium sdO located at $\alpha = 20^{\text{h}}43^{\text{m}}02.5^{\text{s}}$ and $\delta = 10^{\circ}34'21''$. It was first listed by Nassau and Stephenson [1963].

A first overview on the spectral features is given by Walker [1981]. They describe the spectrum as being dominated by HeI and HeII lines and almost no visible contribution from hydrogen in the blended H/He lines. They refer to the strong Stark broadening of lines and note the absence of the Pickering series of the HeII lines.

A more sophisticated analysis was presented by Schonberner and Drilling [1984]. They derived the temperature of the star from the slope of the continuum in UV spectra, taken with the IUE satellite and give a constraint on the distance from color magnitude information to $d = 230 \pm 100$ pc. The derived temperature is very high (65000 K) for a star of that spectral type. As in the optical range, the UV spectra show strong HeII lines and the $L\alpha$ absorption is comparatively small.

Dreizler [1993] used optical spectra to determine the atmospheric parameters and the abundances of several elements. His results for the effective temperature are in contrast to the value from the UV spectrum (44500 ± 1000 K) but seem to be more reasonable for a He-sdO star. The value for the surface gravity is 5.55 ± 0.15 . He found an enrichment in helium, carbon nitrogen and neon and a depletion of oxygen. Ulla and Thejll [1998] searched for IR excesses and claimed to have found one in LS IV +109 and classify it as a binary candidate (see Sect. 6.3.2.3 & 6.6 for more information).

6.3.2.2 Spectral Analysis

As LS IV +109 features the same wavelength gaps in the optical spectrum as LSS 1274, the amount of usable HeII lines was comparatively low. In addition the data from the red arm was missing, only raw-data was available. It was tried unsuccessfully to convert the raw data to a usable extracted spectrum. Unfortunately, no additional CASPEC spectrum was available at the time of analysis.

The fitting of the atmospheric parameters was done using the HHeCNO grid. In a first fit with a resulting surface gravity of $\log(g) = 5.53$, nearly all HeI lines were too shallow, while the HeII lines at 4100\AA and 4200\AA seemed fine. It was therefore decided to adjust the parameters by eye and compare the resulting models to the data by overplotting. Luckily, only the $\log(g)$ had to be lowered, while the other parameters from the fit remained constant. The lower $\log(g)$ had a positive effect on the fit of the HeI lines while hardly affecting the HeII lines. A visualization of the final model is presented in Fig. 6.56. The resulting parameters are

- $T_{\text{eff}} = 43850 \pm 600$ K
- $\log(g) = 5.43 \pm 0.20$
- $\log(n(\text{He})/n(\text{H})) = 2.73 \pm 0.19$
- $v_{\text{rot}} < 5$ km/s

Both temperature and surface gravity are well consistent with the values by Dreizler [1993]. The initial value for the surface gravity ($\log(g)=5.53$) is closer to Dreizler's results, but as the new one is also matching within the error range no further actions were taken on this topic. No significant rotation was measured. To get a first impression of the chemical composition, only the optical UVES spectrum was used. The models contained no iron or nickel to speed up the calculations. The summary of the results can be found in Table 6.31

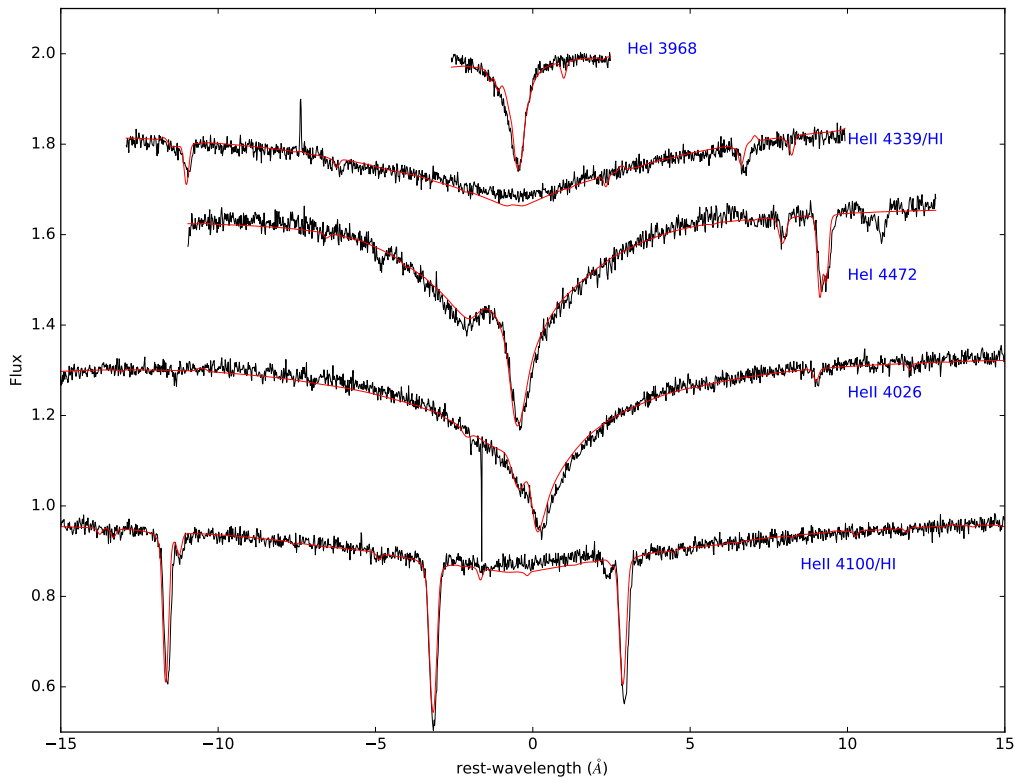


Figure 6.56: Visualization of several HeI and HeII lines of LSIV +109, some with a hydrogen component. The black lines show parts of the UVES spectrum, the best-fitting model is represented by the red lines. The flux levels had been adjusted for better representation.

Element	# lines	UVES
C	12	0.10 ± 0.20
N	30	-0.13 ± 0.02
O	7	-0.80 ± 0.07
Ne	14	0.05 ± 0.02
Mg	1	-1.29 ± 0.03
Al	2	-2.19 ± 0.04
Si	5	-1.05 ± 0.05
P	2	-2.87 ± 0.07
S	3	-3.60 ± 0.30

Table 6.31: Overview on the number abundances for LSIV +10 9 determined from the optical UVES spectra. Given is the $\log(n(X)/n(H))$ in number abundances. (Models without Fe/Ni). The second column gives the number of lines used for the fit of a specific element.

After iron and nickel were added, all available spectra were analyzed in parallel (Table 6.32). The following figures show the most important and/or significant lines from different spectra and the matching of the final model. Sulfur was excluded from the models and set to the solar value as, in this case, the inclusion of iron and nickel had no positive effect on the line fits. By comparing both UV-abundances to those from the optical data, the difference between FUSE and IUE becomes apparent. The errors on the IUE fits are much larger than on the FUSE ones. This can be explained by the lower resolution and the far worse S/N ratio which results in less fitted lines. Interestingly, the IUE results are not significantly lower than the FUSE or UVES ones, hence the pseudo continuum seem to be much less pronounced. As the resolution of IUE is constant for all used observations, this can only be explained by less line crowding for LSIV +10 9.

The abundances were transformed to the relative mass abundances (Table 6.33) and visualized in Fig. 6.63.

Element	UVES	FUSE	IUE
He	2.73 ± 0.25	—	—
C	$0.17 \pm 0.03(12)$	$0.10 \pm 0.02(4)$	$0.20 \pm 0.10(2)$
N	$-0.16 \pm 0.04(28)$	$-0.38 \pm 0.05(9)$	$-0.13 \pm 0.20(6)$
O	$-0.67 \pm 0.05(8)$	$-0.80 \pm 0.10(5)$	—
Ne	$0.07 \pm 0.02(14)$	$(0.25 \pm 0.60)(2)$	$0.25 \pm 0.40(4)$
Mg	$-1.21 \pm 0.04(1)$	—	$(-1.13 \pm 0.50)(1)$
Al	$-2.13 \pm 0.04(3)$	$(-2.21 \pm 0.60)(2)$	$-1.98 \pm 0.30(1)$
Si	$-1.04 \pm 0.04(5)$	$-1.07 \pm 0.14(2)$	$-1.10 \pm 0.40(3)$
P	$-2.87 \pm 0.10(2)$	$-3.50 \pm 0.10(5)$	$-3.2 \pm 0.40(2)$
S	—	—	—
Fe	—	$-1.89 \pm 0.12(10)$	$(-1.51 \pm 0.84)(9)$
Ni	—	$-2.20 \pm 0.29(7)$	$-2.67 \pm 0.15(7)$

Table 6.32: Overview on the number abundances for LSIV +10 9 determined from different spectra. Given is the $\log(n(X)/n(H))$ in number abundances. (Models with Fe/Ni). The number of lines used for fitting each element is displayed in brackets following the abundances. Abundances in brackets show large errors and have to be dealt with care.

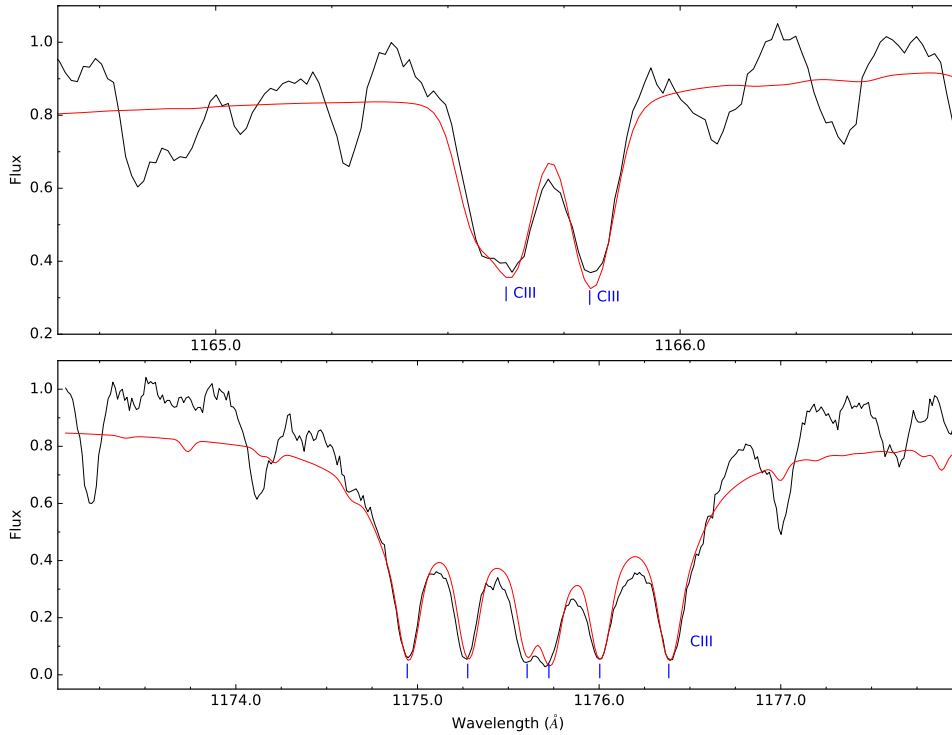


Figure 6.57: Visualization of several CIII lines of LSIV +10 9 (UV spectra) in comparison with the final synthetic spectrum.

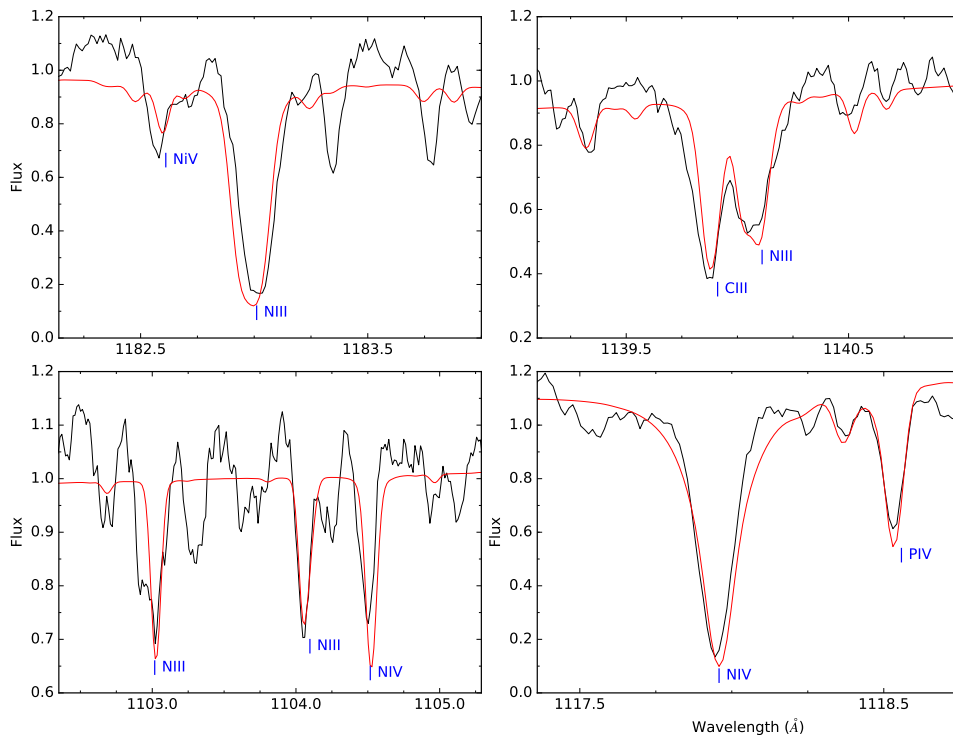


Figure 6.58: Visualization of several nitrogen lines with different ionization stages of LSIV +109 (UV spectra) in comparison with the final synthetic spectrum.

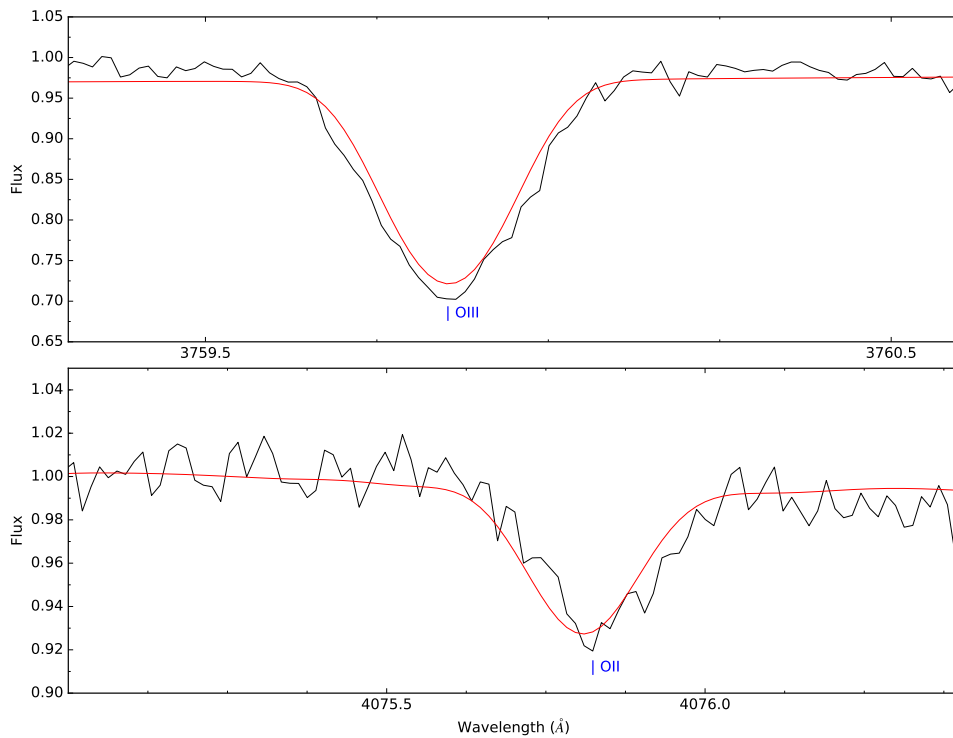


Figure 6.59: Visualization of two oxygen lines with different ionization stages of LSIV +109 (optical spectra) in comparison with the final synthetic spectrum.

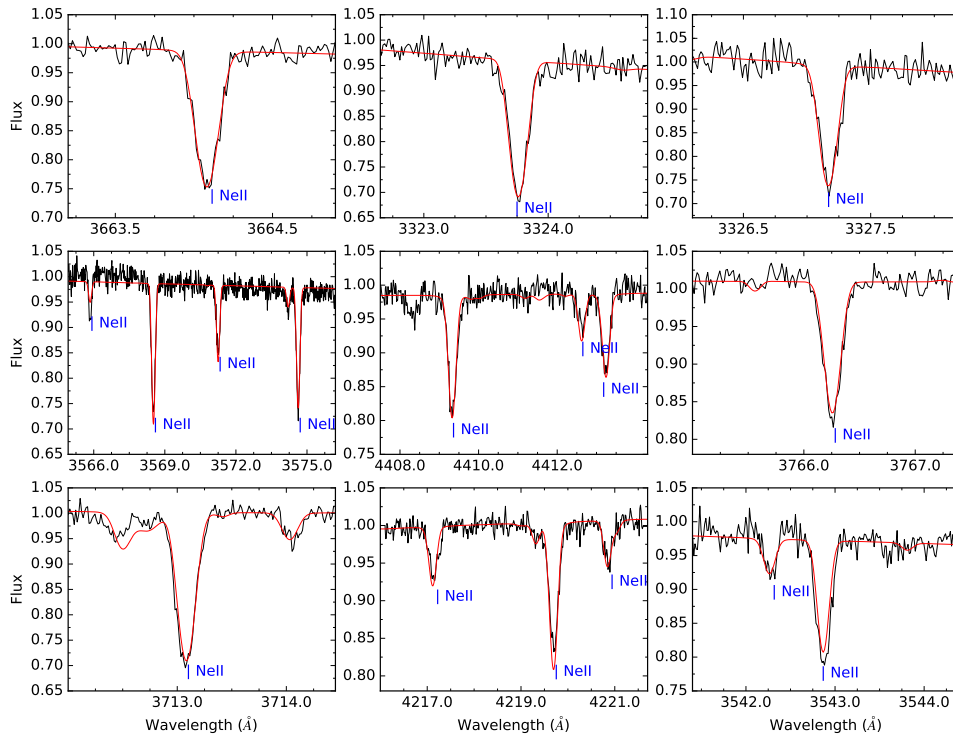


Figure 6.60: Visualization of several NeII lines of LSIV +109 (optical spectra) in comparison with the final synthetic spectrum.

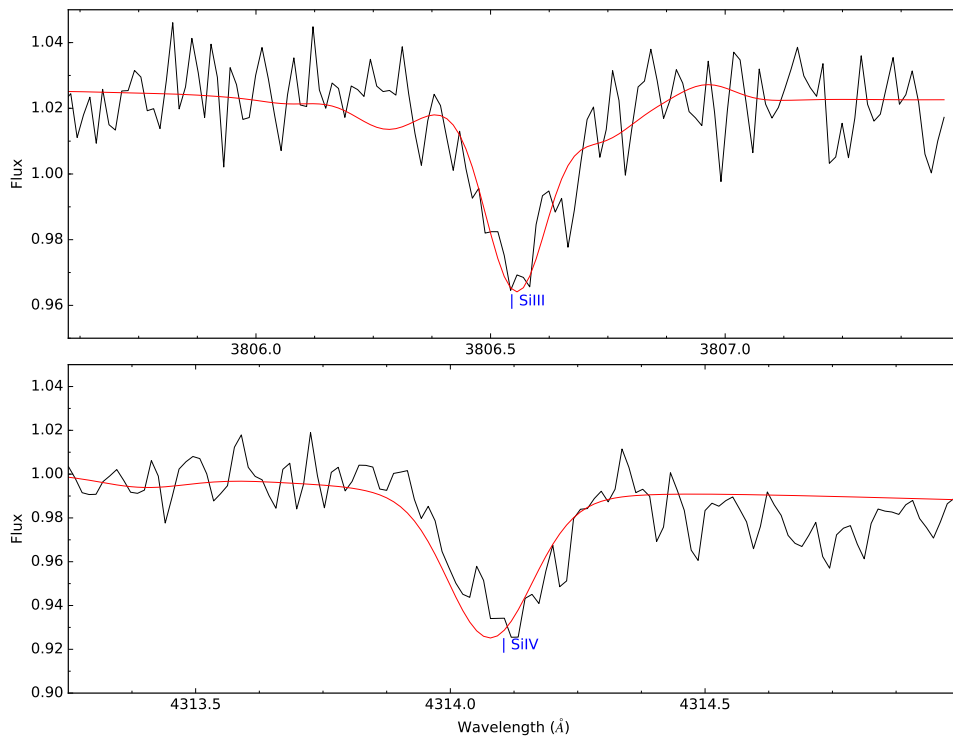


Figure 6.61: Visualization of several silicon lines with different ionization stages of LSIV +109 (optical spectra) in comparison with the final synthetic spectrum.

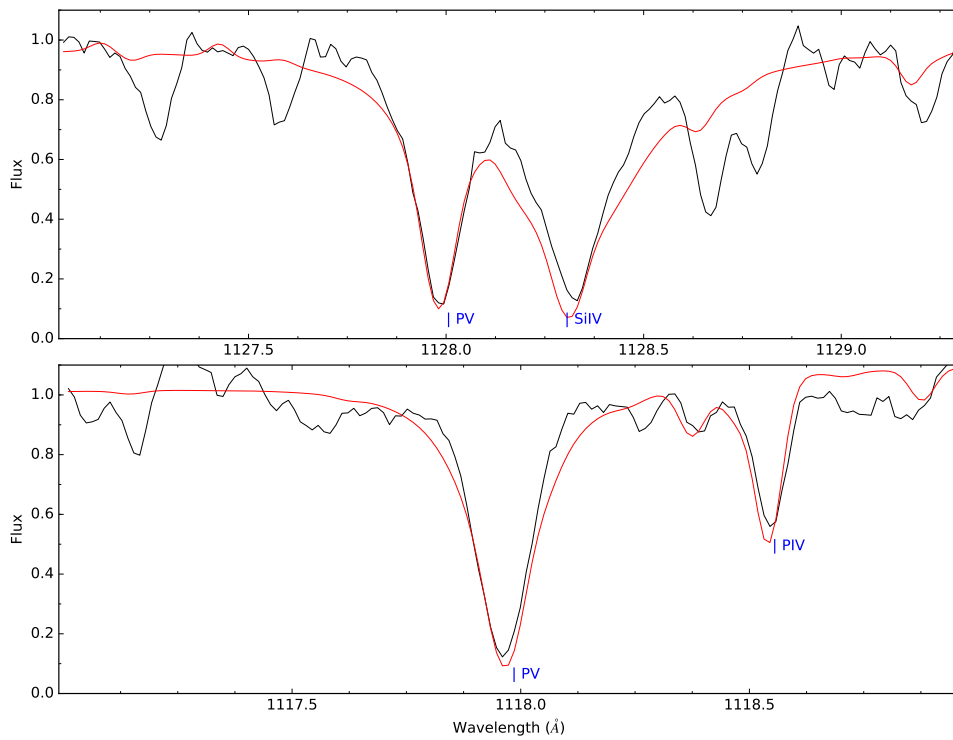


Figure 6.62: Visualization of two phosphorus lines with different ionization stages of LSIV +109 (UV spectra) in comparison with the final synthetic spectrum..

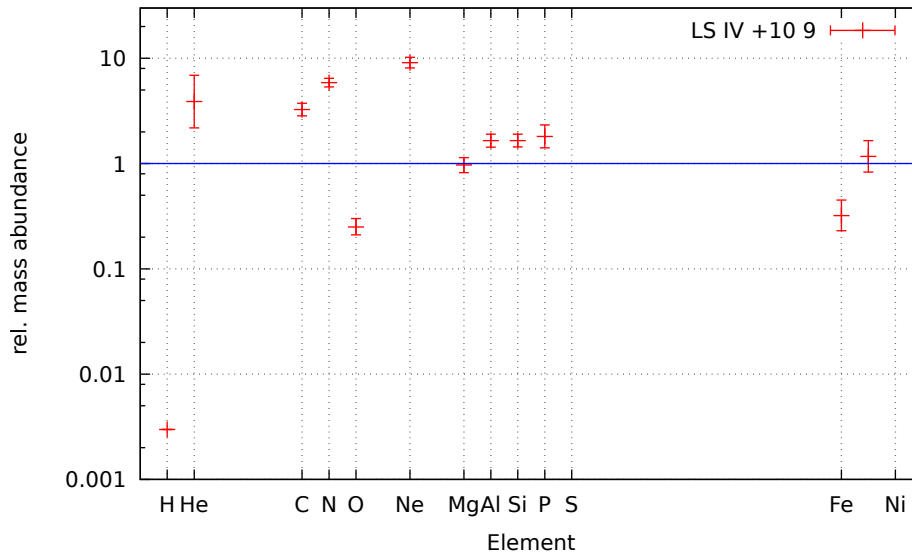


Figure 6.63: Mass abundances for the different elements in LSIV +10 9 compared to their solar value.

LSIV +10 9 shows the classical enrichment in helium, as well as an enrichment in carbon and nitrogen. In contrast to LSS 1274, nitrogen is more abundant than carbon. As usual, oxygen is depleted. Neon is enriched to almost 10x solar. Magnesium is at the solar level, but the rest of the intermediate mass elements is enriched significantly. As all the intermediate mass elements seem to be more present than usual, some sort of systematic error cannot be excluded. Iron is subsolar, while the level of nickel is in accordance with a solar content.

6.3.2.3 Spectral energy distribution

As usual, the SED of a star with the calculated parameters was compared with photometric measurements to check for consistency. The following table (table 6.34) gives an overview on the used photometric measurements.

The photometric measurements of LSIV +10 9 show larger deviations from the calculated SED than in other stars. While the color indices fit the desired mean value within the errorbars, some magnitudes are quite off. Especially Bt and V are well higher than the errors on the measurement would allow, while Vt is too low. The J, H and K magnitudes show a slight, but not significant trend. While J is on the upper limit of the range, H and K are at the lower one.

As the star is quite dim for the Tycho measurements, the standard error used for measurements without any given official error, is too small. The same applies for the Johnson V band as it is not clear how and with which instrument the data had been taken. The scatter of the other photometric magnitudes is much harder to explain. But as no clear trend from UV to infrared is present, the results are interpreted as trustworthy. The reddening is 0.0513 and $\theta = 1.7919 \cdot 10^{-11}$ which translates to a distance of 550_{-83}^{+98} pc. This is in very good agreement with the distance of 510 ± 90 pc as suggested by Dreizler [1993]. The distance given by Schonberner and Drilling [1984] of 230 ± 100 pc is not in agreement with neither the results of Dreizler [1993] nor with the distance given in this work. But as already the temperature given

Element	mass abundance ratio
H	$2.22 \cdot 10^{-3}$
He	$3.88_{-1.70}^{+3.02}$
C	$3.26_{-0.42}^{+0.48}$
N	$5.87_{-0.52}^{+0.57}$
O	$0.251_{-0.039}^{+0.047}$
Ne	$9.09_{-0.99}^{+1.11}$
Mg	$0.970_{-0.152}^{+0.169}$
Al	$1.65_{-0.22}^{+0.25}$
Si	$1.65_{-0.21}^{+0.25}$
P	$1.81_{-0.40}^{+0.52}$
S	--
Fe	$0.324_{-0.090}^{+0.125}$
Ni	$1.17_{-0.34}^{+0.48}$

Table 6.33: Mass abundance ratios for LSIV +109.

Filter	value	error	type	reference
J	12.632	0.03	magnitude	Kharchenko [2001]
H	12.813	0.02	magnitude	Kharchenko [2001]
K	12.916	0.04	magnitude	Kharchenko [2001]
V	11.98	–	magnitude	Egret et al. [1992]
Vt	12.064	–	magnitude	Høg et al. [2000]
Bt	11.606	–	magnitude	Høg et al. [2000]
bmy	-0.107	–	color	Paunzen [2015]
m1	0.034	–	color	Paunzen [2015]
c1	-0.213	–	color	Paunzen [2015]
B-V	-0.24	0.09	color	Henden et al. [2016]
W1	13.970	0.024	magnitude	Cutri [2012]
W2	13.050	0.033	magnitude	Cutri [2012]
box1	9.195	–	magnitude	-
box2	9.514	–	magnitude	-
box3	8.269	–	magnitude	-

Table 6.34: Photometric measurements for LSIV +109.

by Schonberner and Drilling [1984] was way off compared to other results, not too much interpretation should be put into this discrepancy.

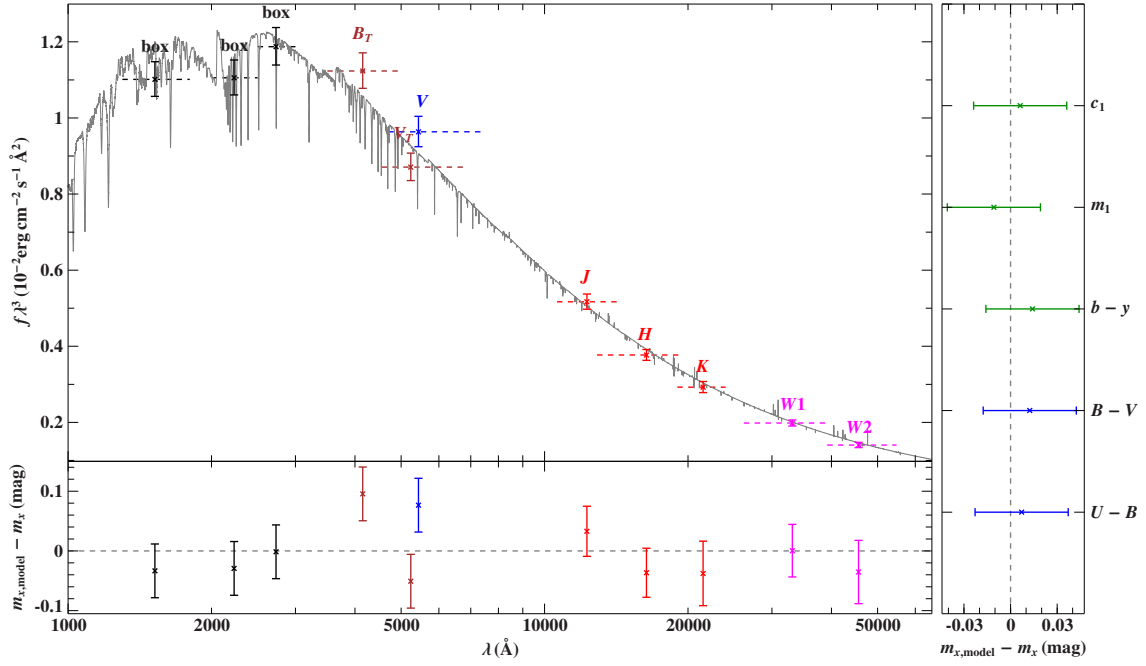


Figure 6.64: SED of LSIV +109 in comparison with photometric measurements (magnitudes and colors). The bottom and right panels show the residuals for the magnitude and color measurements.

6.3.3 [CW83] 0832-01

6.3.3.1 General information

[CW83] 0832-01 has a visual magnitude of $m_V = 11.51$. It is located at $\alpha = 08\text{h}35\text{m}23.9\text{s}$ and $\delta = -01^\circ55'52.7''$. Its first classification as sdO star was performed by Berger and Fringant [1980]. They mentioned the absence of hydrogen features in the helium lines and noted the presence of CIII-lines, hence the classification as a carbon rich He-sdO is obvious. Kilkenney et al. [1988] listed it in their catalog of spectroscopically identified hot subdwarf stars, without any further analysis. Five years later Dreizler [1993] conducted a first analysis of optical spectra, resulting in an effective temperature of 46500 K, a surface gravity of $\log(g)=5.55$ and a helium abundance of $\log(n/\text{He})/n(\text{H})$ above one. An enrichment in carbon, nitrogen and neon was found, together with solar magnesium and silicon content, as well as a depletion in oxygen. A subsequent analysis by Hirsch [2009] with a fixed helium abundance of $100\times$ hydrogen revealed an effective temperature of 44000 K and a slightly higher surface gravity of $\log(g)=5.64$.

6.3.3.2 Spectral analysis

For the analysis of [CW83] 0832-01 several FEROS spectra were coadded. By visual inspection, both carbon and nitrogen lines were observable in the spectra, while no traces of hydrogen were visible. The fit of the atmospheric parameters was done with the HHeCNO grid and resulted in the following parameters.

- $T_{\text{eff}} = 45700 \pm 800 \text{ K}$
- $\log(g)=5.70 \pm 0.09$

- $\log(n(\text{He})/n(\text{H}))= 3(\text{fix})$
- $v_{\text{rot}} = 17 \pm 3 \text{ km/s}$

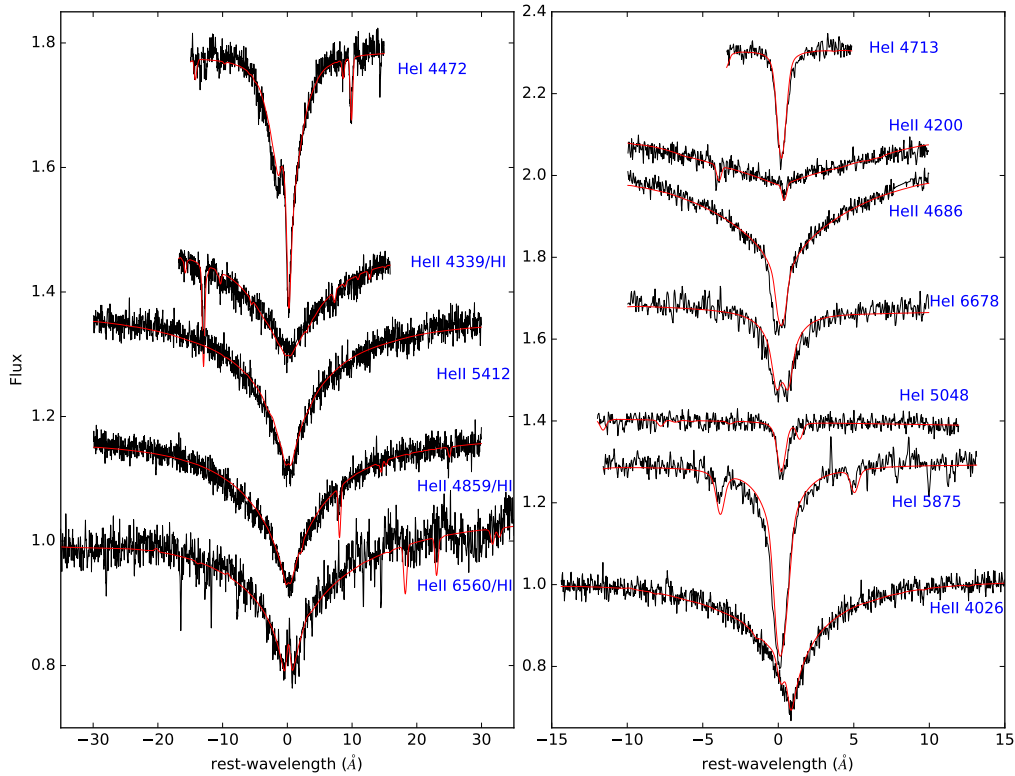


Figure 6.65: Visualization of several HeI and HeII lines of [CW83] 0832-01, some with a hydrogen component. The black lines show parts of the FEROS spectrum, the best-fitting model is represented by the red lines. The flux levels had been adjusted for better representation.

The helium abundance was fixed at $1000\times$ hydrogen as no hydrogen was visible and the abundance varied widely during the fitting process. From the helium lines, the rotational velocity was found to be 15kms/s , while the projected rotational velocity $v_{\text{rot}} = 17 \pm 3 \text{ km/s}$ originates from measuring the broadening of selected carbon lines.

The difference of the results to previous ones is quite significant. The helium abundance of $100\times$ hydrogen used by Hirsch [2009] seems too low, which might also explain the discrepancy concerning the effective temperature and surface gravity. As Dreizler [1993] gives no errors on his results it is hard to judge how large the potential overlap is, but the effective temperatures seem quite close together, while the surface gravity is off by 0.15 dex . The determination of the metal lines followed the standard scheme. The results of the first run on metal abundances can be found in Table 6.35. Phosphorus was fitted by eye, as the resulting line profiles from SPAS diverged to much from the data. The number of used neon lines is comparatively low as the spectra missed large parts of the blue end where neon lines tend to cumulate.

As no suitable UV spectra are available, it is not possible to determine abundances for iron and nickel. But as these elements have an influence on the profiles of

Element	# lines	abundance
C	10	0.60 ± 0.23
N	12	-0.30 ± 0.12
O	4	-1.00 ± 0.20
Ne	4	-0.11 ± 0.06
Mg	1	-1.11 ± 0.07
Al	1	-1.80 ± 0.22
Si	4	-1.05 ± 0.20
P	1	-2.8 (fit by eye)
S	2	-1.70 ± 0.25

Table 6.35: Metal abundances derived from the optical FEROS spectra of [CW83]0832-01. Given is the $\log(n(X)/n(H))$ in number abundances. (Models without Fe/Ni). The second column gives the number of lines used for fitting a specific element.

all other lines and the temperature stratification, it was decided to include them in full NLTE conditions. They were both set to solar (mass) abundance with respect to the current state of the stellar atmosphere.

The results from the second round of abundance determinations is shown in Table 6.36. Again, phosphorus was fitted by eye. By comparing the errors of both fitting runs, it becomes obvious that the inclusion of iron and nickel significantly reduced the errors for all the other elements.

The following figures show metal lines of different elements and, overimposed, the best-fitting model for the specific element.

Element	# lines	abundance
C	9	0.80 ± 0.07
N	12	-0.24 ± 0.05
O	5	-0.64 ± 0.30
Ne	5	0.31 ± 0.10
Mg	1	-0.99 ± 0.05
Al	2	-1.90 ± 0.09
Si	4	-1.18 ± 0.16
P	1	-2.8 (fit by eye)
S	2	-1.57 ± 0.20

Table 6.36: Metal abundances derived from the optical FEROS spectra of [CW83]0832-01. Given is the $\log(n(X)/n(H))$ in number abundances. (Models with Fe/Ni). The second column gives the number of lines used for fitting a specific element.

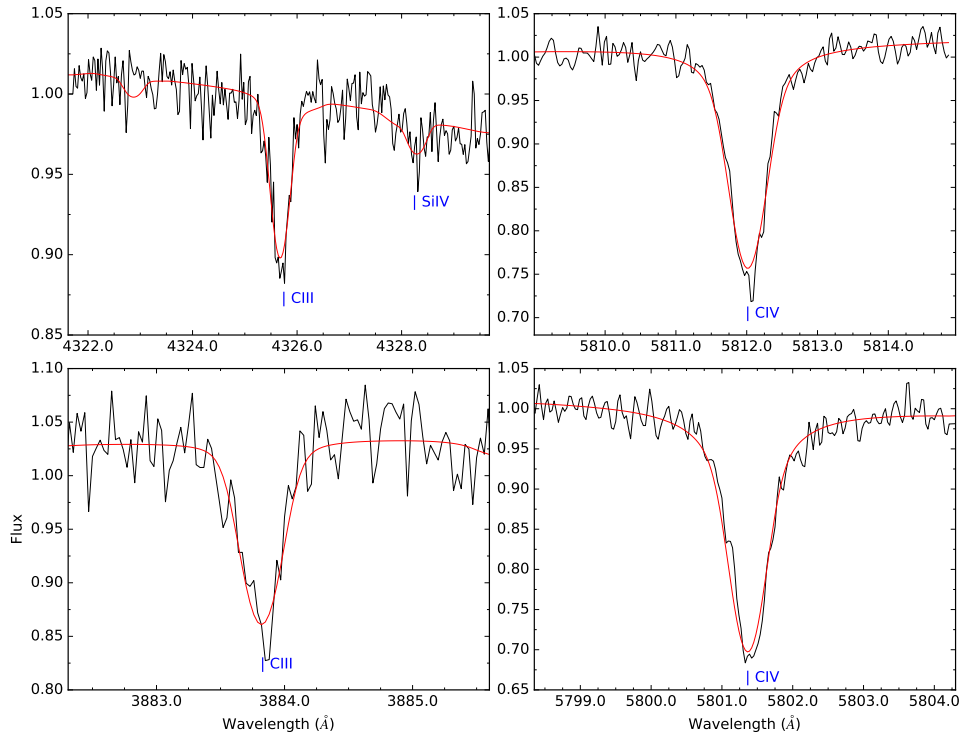


Figure 6.66: Visualization of several carbon lines with different ionization stages of [CW83] 0832-01 (UVES spectrum) in comparison with the final synthetic spectrum.

Element	mass abundance ratio β/β_{\odot}
H	$3.08 \cdot 10^{-4}$
He	$3.87^{+2.27}_{-1.43}$
C	$7.73^{+0.94}_{-0.84}$
N	$2.80^{+0.34}_{-0.31}$
O	$0.154^{+0.119}_{-0.072}$
Ne	$7.90^{+1.82}_{-1.48}$
Mg	$0.847^{+0.109}_{-0.090}$
Al	$1.47^{+0.38}_{-0.30}$
Si	$0.673^{+0.224}_{-0.163}$
P	$2.02^{+2.02}_{-1.02}$
S	$0.666^{+0.394}_{-0.251}$
Fe	1
Ni	1

Table 6.37: Mass abundances for the different elements in [CW83] 0832-01 compared to the solar mass abundance.

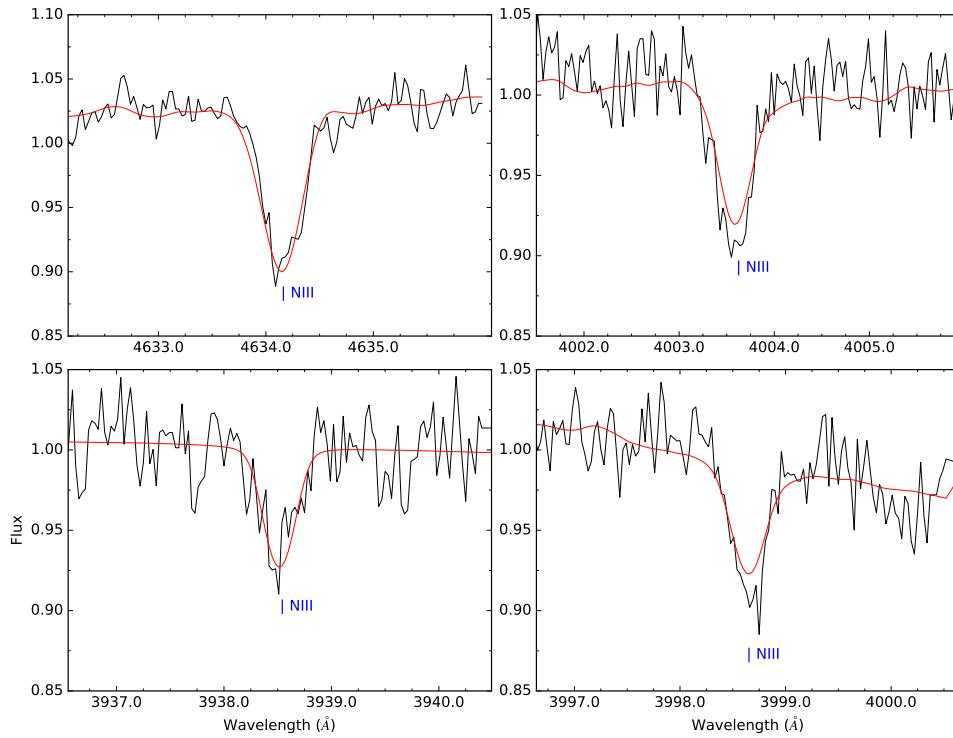


Figure 6.67: Visualization of several NIII lines of [CW83] 0832-01 (UVES spectrum) in comparison with the final synthetic spectrum.

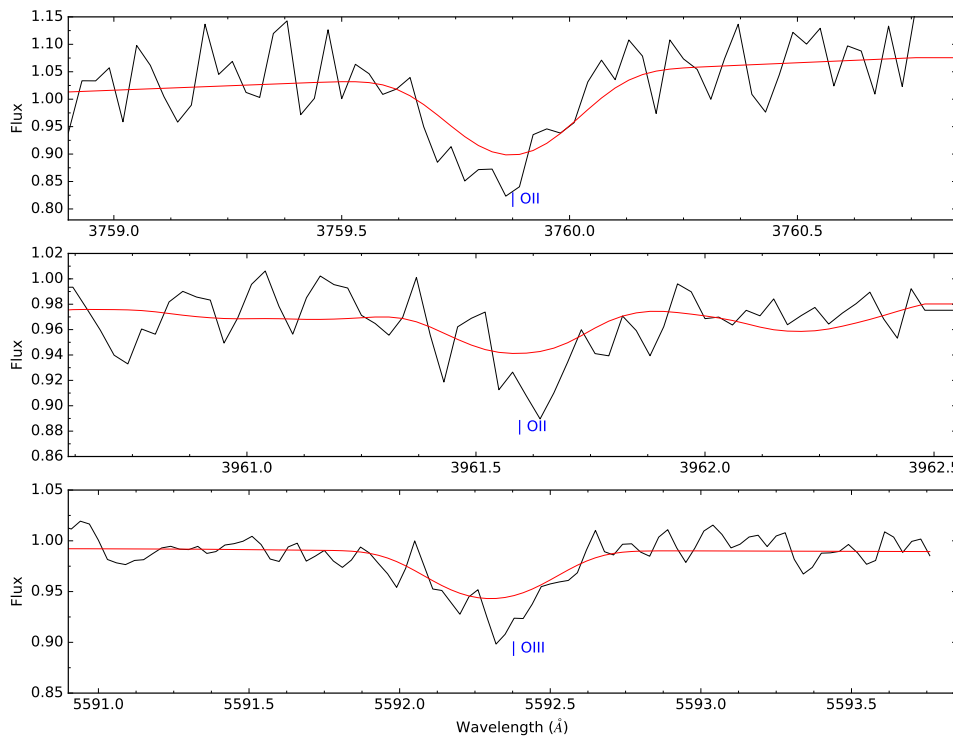


Figure 6.68: Visualization of several oxygen lines with different ionization stages lines of [CW83] 0832-01 (UVES spectrum) in comparison with the final synthetic spectrum.

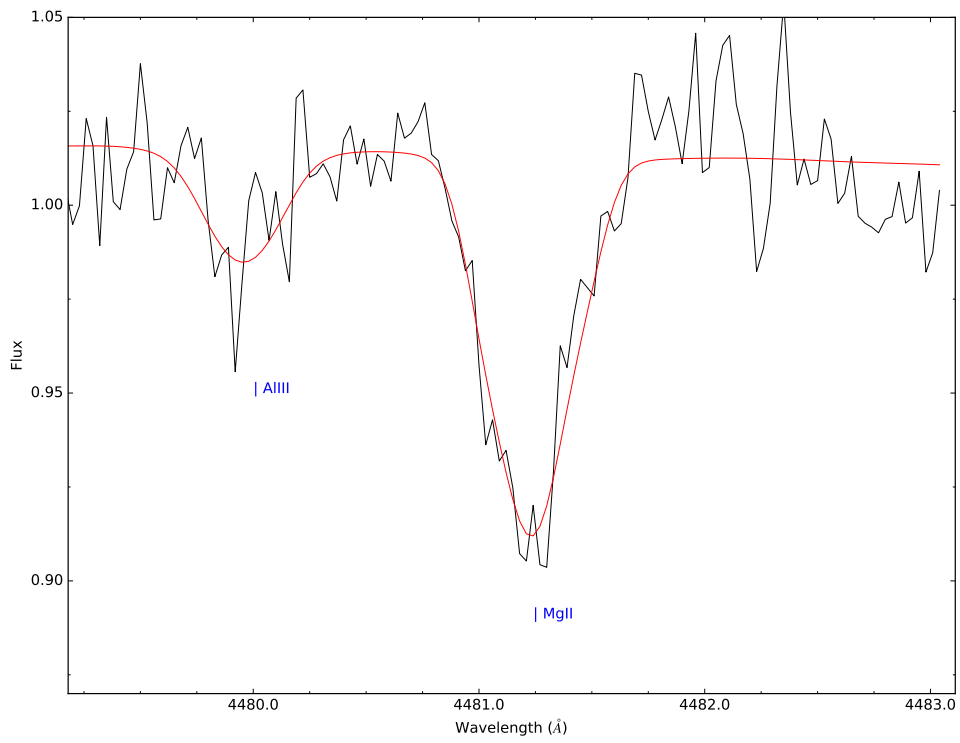


Figure 6.69: Visualization of one MgII line of [CW83] 0832-01 (UVES spectrum) in comparison with the final synthetic spectrum.

Fig. 6.70 shows a visual representation of table 6.37. [CW83]0832-01 is enriched in both carbon and nitrogen, while oxygen is depleted. The neon abundance is quite high and even exceeds carbon compared to the respective solar level. The intermediate elements all scatter around solar enrichment without any clear visible trend.

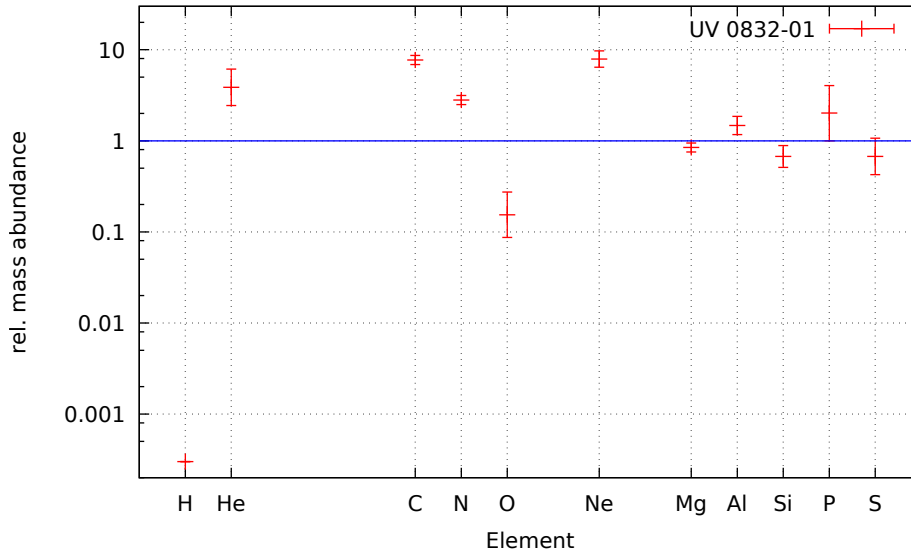


Figure 6.70: Relative mass abundances for [CW83]0832-01 compared to their solar value. The solar abundances of iron and nickel are not shown.

6.3.3.3 Spectral energy distribution

The SED of [CW83]0832-01 shows a very good agreement with photometric measurements. All residuals scatter around zero without any outliers. At a distance of 328_{-32}^{+36} pc ($\theta = 2.207 \cdot 10^{-11}$ and $M=0.47 M_{\odot}$) the reddening is 0.024 mag. This agrees with the value given by Dreizler [1993] (390 ± 70 pc). Again, the V-magnitude suffers from large errors.

Filter	value	error	type	reference
J	12.094	0.03	magnitude	Kharchenko [2001]
H	12.271	0.03	magnitude	Kharchenko [2001]
K	12.359	0.03	magnitude	Kharchenko [2001]
V	11.51	0.1	magnitude	Egret et al. [1992]
B	11.18	–	magnitude	Zacharias et al. [2004]
B1	10.87	–	magnitude	Monet et al. [2003]
R1	11.64	–	magnitude	Monet et al. [2003]
bmy	-0.118	–	color	Paunzen [2015]
m1	0.022	–	color	Paunzen [2015]
c1	-0.222	–	color	Paunzen [2015]
W1	12.462	0.024	magnitude	Cutri [2012]
W2	12.542	0.024	magnitude	Cutri [2012]
W3	12.347	0.498	magnitude	
box1	7.491	–	magnitude	-
box2	8.353	–	magnitude	-
box3	8.762	–	magnitude	-

Table 6.38: Photometric measurements for [CW83] 0832-01.

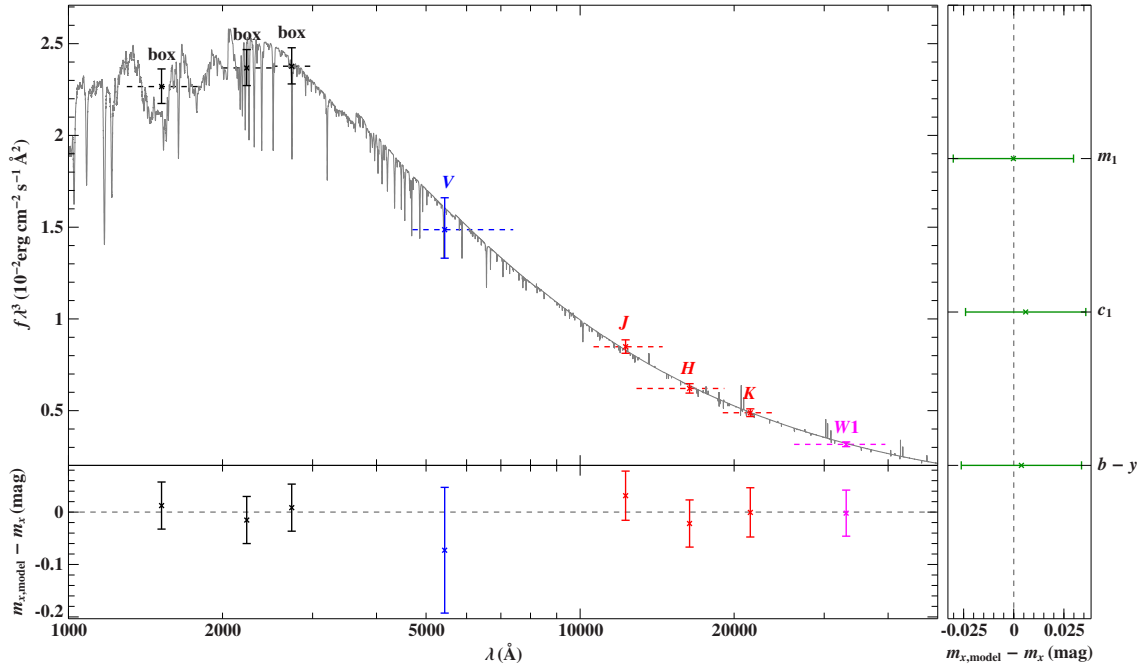


Figure 6.71: SED of [CW83] 0832-01 in comparison with photometric measurements (magnitudes and colors). The bottom and right panels show the residuals for the magnitude and color measurements.

6.3.4 GALEX J095256.6-371940

6.3.4.1 General information

GALEX J095256.6-371940 or TYC 7180-740-1 is a 12.67 mag He-sdO located at $\alpha = 09^{\text{h}}52^{\text{m}}56.8^{\text{s}}$ and $\delta = -37^{\circ}01'41''$. Up to now, it was hardly analyzed, with the

only appearance in Vennes et al. [2011]. In this work, rough atmospheric parameters were shown to be settled at an effective temperature of 43000 ± 4000 K, a surface gravity of 5.44 ± 0.3 and a $\log(y)$ of $1.2^{+0.5}_{-0.3}$.

6.3.4.2 Spectral Analysis

For GALEX J095256.6-371940, optical spectra from FEROS and XSHOOTER are available. Unfortunately, the FEROS data suffer from massive spikes in the data, probably due to an insufficient removal of cosmics. Therefore it was tried to re-reduce the raw data using the FEROS pipeline. The normal reduction resulted in the same, spike polluted spectra. One of the spikes was exactly at the position of the $H\alpha$ emission feature in the HeII 6560 line. Using the optimized extraction mode reduced the amplitude of the spikes but was not able to remove them completely. A little spike that could be interpreted as a hydrogen emission feature remained in the HeII 6560 line. It was therefore decided to dump the FEROS data and focus on the XSHOOTER data. From this sample several single spectra were available from each channel that were coadded to enhance the S/N ratio.

The analysis was done by using the HHeCNO grid. The following atmospheric parameters resulted. The rotational velocity was checked using isolated, sharp nitrogen lines.

- $T_{\text{eff}} = 44450 \pm 250$ K
- $\log(g) = 5.50 \pm 0.10$
- $\log(n(\text{He})/n(\text{H})) = 3$ (fix)
- $v_{\text{rot}} = 22 \pm 3$ km/s

By eye, hardly any hydrogen features can be seen at the $H\alpha$ and $H\beta$ position. As all the fits went to an extremely high helium to hydrogen ration of over 1000, the $\log(y)$ was fixed at 3.0. The fits at 3.0 were indistinguishable from those at higher helium abundances. Fig. 6.72 shows the result of the fit.

As already known, the HeII 4200 Å and HeII 4339 Å lines were not fittable together with the other ones and show (much) too deep line cores. In addition, the HeII 4542 Å line shows the same problem. All three were excluded from the fit and are shown as an overplot in Fig. 6.72.

By comparing these results to those described in Vennes et al. [2011], it can be seen that the surface gravity matches perfectly while the temperature is about 500 K too high. The helium abundance is at least 1.3 dex off. As almost no hydrogen feature is visible in the XSHOOTER data, the value from Vennes et al. [2011] seems too low.

The determination of the metal lines followed the standard scheme. The results of the first run on metal abundances can be found in table 6.39.

As no suitable UV data are available for GALEX J095256.6-371940, it was not possible to determine the correct abundances for iron and nickel. Therefore, both were set to their solar mass abundance and all the lines were refitted. The result can be found in table 6.40. Interestingly, the inclusion of iron and nickel helped in reducing the large error for the magnesium line but on the other hand increased the uncertainty of the phosphorus determination,

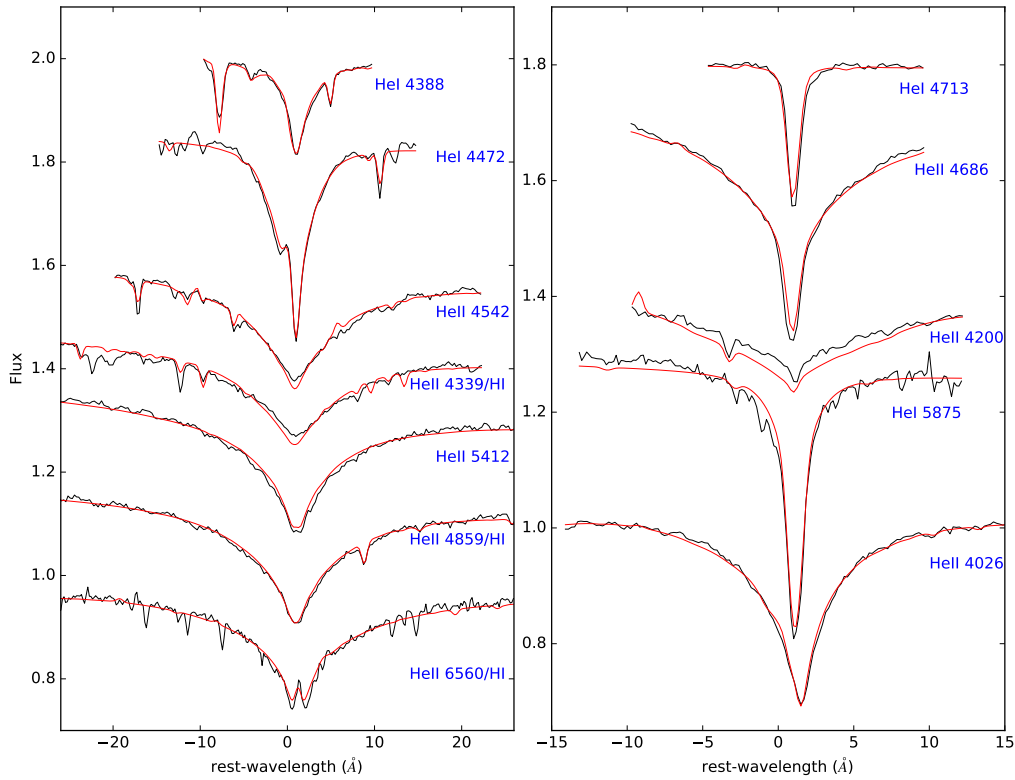


Figure 6.72: Visualization of several HeI and HeII lines of GALEX J095256.6-371940, some with a hydrogen component. The black lines show parts of the XSHOOTER spectrum, the best-fitting model is represented by the red lines. The flux levels had been adjusted for better representation.

Element	# lines	abundance
C	20	0.50 ± 0.12
N	60	-0.12 ± 0.09
O	11	-0.20 ± 0.35
Ne	19	0.15 ± 0.12
Mg	1	(-1.00 ± 1.00)
Al	5	-2.11 ± 0.15
Si	12	-0.80 ± 0.18
P	3	-2.6 ± 0.39
S	5	-1.70 ± 0.26

Table 6.39: Metal abundances derived from the optical XSHOOTER spectra of GALEX J095256.6-371940. Given is the $\log(n(X)/n(H))$ in number abundances. (Models without Fe/Ni). The second column gives the number of lines used for fitting a specific element. Abundances in brackets suffer from large uncertainties and have to be dealt with care.

The abundances derived from the fits were transferred to mass abundances and compared to the solar value of the corresponding element. The result is shown in table 6.41 and visualized in Fig. 6.77.

GALEX J095256.6-371940 shows an enrichment in both carbon and nitrogen

Element	# lines	abundance
C	22	0.50 ± 0.09
N	64	0.03 ± 0.08
O	11	-0.23 ± 0.16
Ne	21	0.21 ± 0.10
Mg	1	-0.97 ± 0.38
Al	5	-2.00 ± 0.17
Si	12	-0.72 ± 0.15
P	3	(-2.77 ± 0.53)
S	5	-1.53 ± 0.21

Table 6.40: Metal abundances derived from the optical XSHOOTER spectra of GALEX J095256.6-371940. Given is the $\log(n(X)/n(H))$ in number abundances. (Models with Fe/Ni). The second column gives the number of lines used for fitting a specific element. Abundances in brackets suffer from large uncertainties and have to be dealt with care.

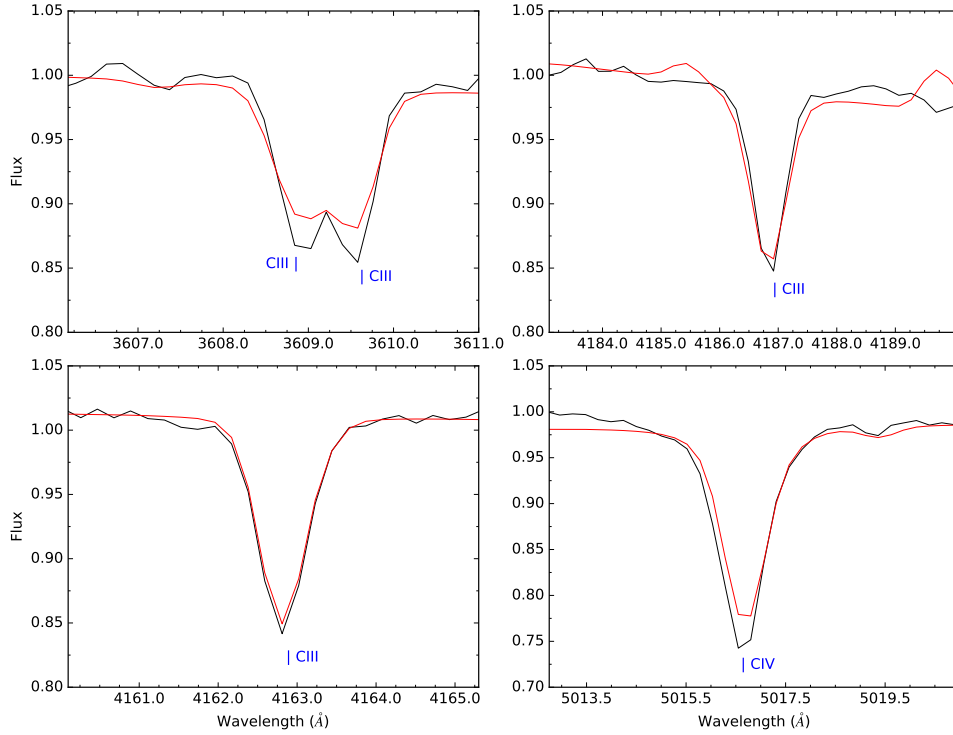


Figure 6.73: Visualization of several carbon lines with different ionization stages of GALEX J095256.6-371940 (XSHOOTER spectrum) in comparison with the final synthetic spectrum.

to roughly the same level while oxygen is depleted to a sub-solar value. Neon is clearly enriched to over six times the solar level. The rest of the intermediate mass elements is consistent with solar level enrichment, only silicon sticks out with a slightly enhanced amount of the element.

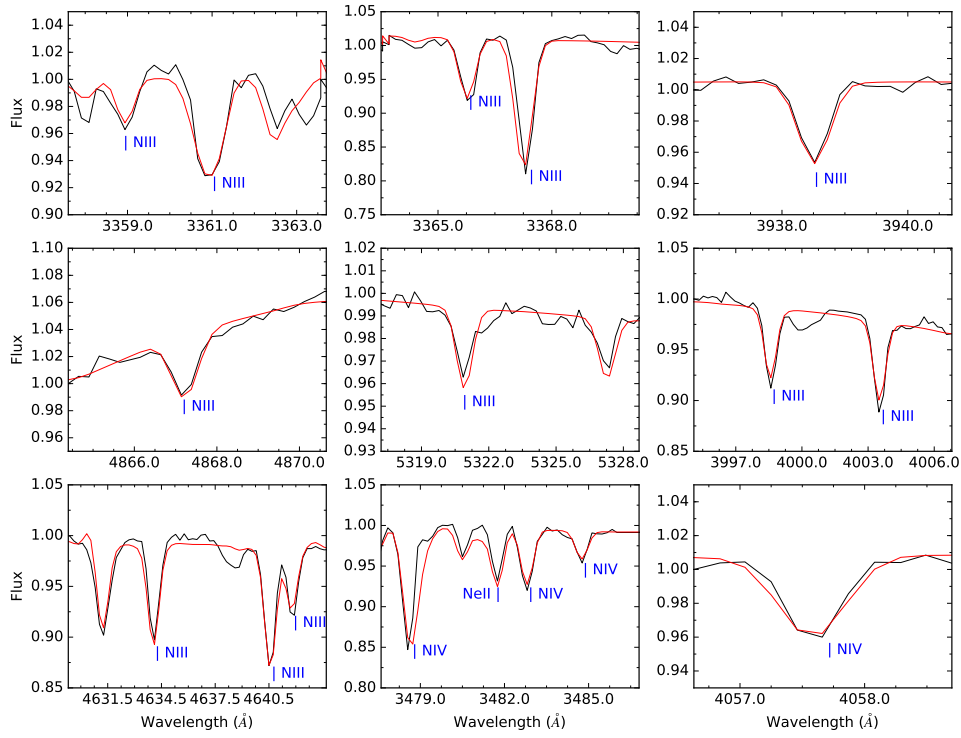


Figure 6.74: Visualization of several nitrogen lines with different ionization stages of GALEX J095256.6-371940 (XSHOOTER spectrum) in comparison with the final synthetic spectrum.

Element	mass abundance ratio β/β_{\odot}
H	$3.06 \cdot 10^{-4}$
He	$3.90^{+3.89}_{-1.95}$
C	$3.90^{+0.79}_{-0.66}$
N	$5.26^{+1.07}_{-0.89}$
O	$0.393^{+0.236}_{-0.150}$
Ne	$6.39^{+1.66}_{-1.30}$
Mg	$0.894^{+1.250}_{-0.524}$
Al	$1.18^{+0.69}_{-0.44}$
Si	$1.95^{+1.14}_{-0.72}$
P	$2.19^{+8.80}_{-1.80}$
S	$0.743^{+0.745}_{-0.372}$
Fe	1
Ni	1

Table 6.41: Mass abundances for the different elements in GALEX J095256.6-371940 compared to the solar mass abundance.

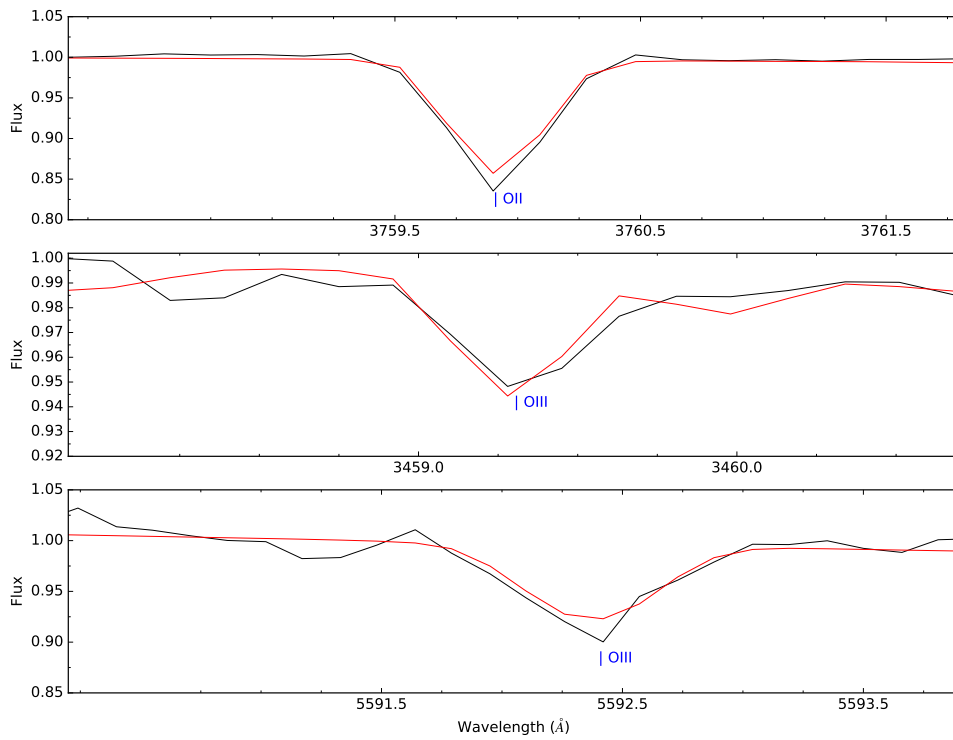


Figure 6.75: Visualization of several oxygen lines with different ionization stages of GALEX J095256.6-371940 (XSHOOTER spectrum) in comparison with the final synthetic spectrum.

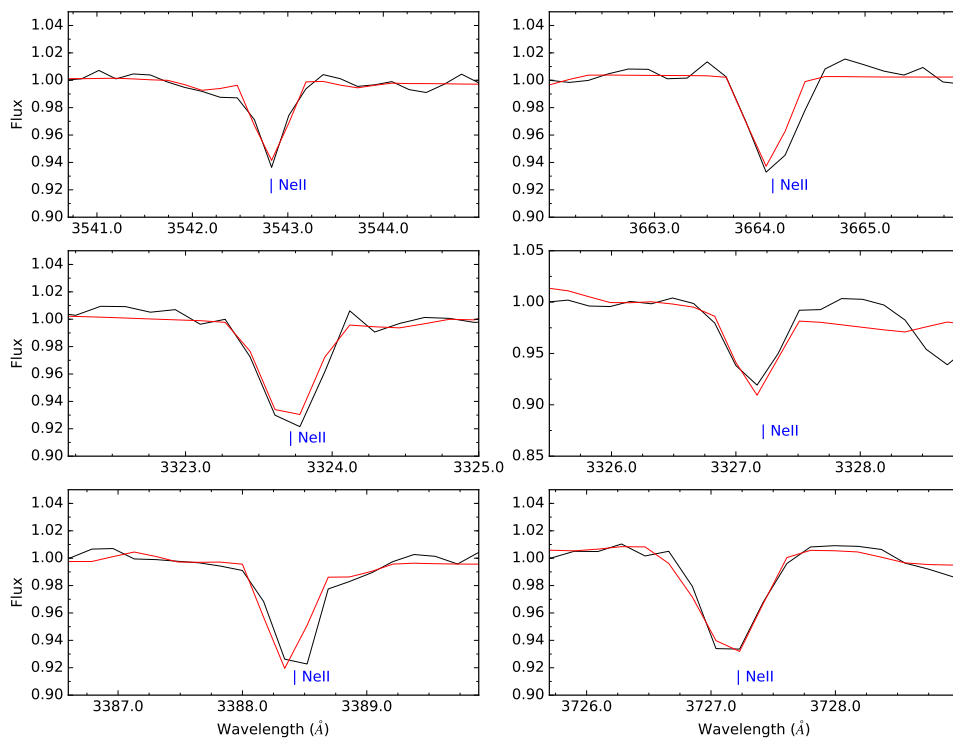


Figure 6.76: Visualization of several NeII lines of GALEX J095256.6-371940 (XSHOOTER spectrum) in comparison with the final synthetic spectrum.

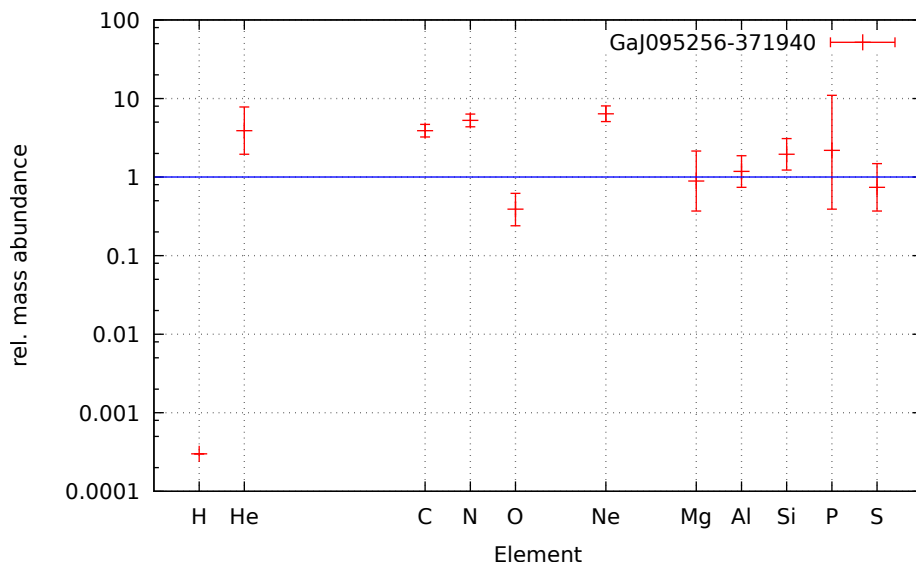


Figure 6.77: Relative mass abundances for GALEX J095256.6-371940 compared to their solar value. The solar abundances of iron and nickel are not shown

6.3.4.3 Spectral energy distribution

Working with the SED of GALEX J095256.6-371940 turned out to be a difficult task. Not only is there solely one measurement for a color index, the existing magnitudes, especially V/Vt and B/Bt show a large scatter and huge errorbars. Trying to use averaged values for V/Vt and B/Bt did not improve the situation. Therefore it was decided to drop the B and V measurements and rely on the APASS magnitudes g,r and i instead. From the fit, a distance of 852_{-94}^{+105} pc, a value of $\theta = 1.0673 \cdot 10^{-11}$ and a reddening of 0.0418 mag would emerge.

Filter	value	error	type	reference
J	13.858	0.032	magnitude	Cutri et al. [2003]
H	14.005	0.047	magnitude	Cutri et al. [2003]
K	14.031	0.067	magnitude	Cutri et al. [2003]
g	13.084	0.03	magnitude	Henden et al. [2016]
r	13.510	0.018	magnitude	Henden et al. [2016]
i	13.795	0.045	magnitude	Henden et al. [2016]
W1	14.0152	0.030	magnitude	Cutri [2012]
W2	14.090	0.047	magnitude	Cutri [2012]
B-V	-0.213	0.03	color	Henden et al. [2016]

Table 6.42: Photometric measurements for GALEX J095256.6-371940.

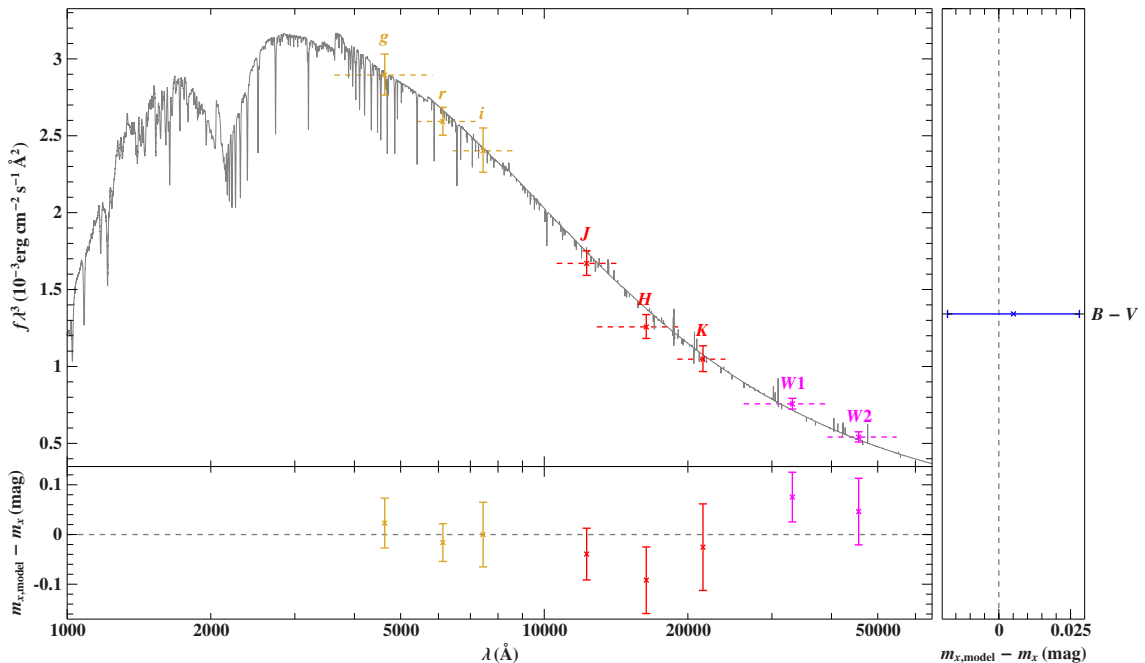


Figure 6.78: SED of GALEX J095256.6-371940 in comparison with photometric measurements (magnitudes and colors). The bottom and right panels show the residuals for the magnitude and color measurements.

6.4 The Halo He-sdO star BD+39° 3226

6.4.1 General information

BD+39° 3226 is He-sdO with a visual magnitude of $m_V=10.2$. It is located in the Halo of the Galaxy at $\alpha = 17^{\text{h}}46^{\text{m}}31.9^{\text{s}}$ and $\delta = +39^{\circ}19'09.1''$.

It was first mentioned by Barbier et al. [1978] as a helium rich UV object. In the same year, Berger and Fringant [1978] announced the discovery of three new hot subdwarfs, among them BD+39° 3226. They classified the spectrum as being dominated by HeI and HeII lines. No signs of hydrogen were found and a general lack of carbon and nitrogen lines was observed. Kilkenney et al. [1988] listed BD+39° 3226 in their catalog of spectroscopically identified hot subdwarf stars and gave an effective temperature of 44670 K and a surface gravity of 5.5. The classification as a helium rich hot subdwarf remained untouched. The star was checked for pulsations by Rodríguez-López et al. [2007] during their search for sdO pulsators but no indications for those were found. They give quite imprecise atmospheric parameters with an effective temperature of 44700 ± 5000 K and $\log(g) = 5.5 \pm 0.5$.

6.4.2 Spectral analysis

The available HIRES spectra were not suitable for determining the atmospheric parameters as they suffered from the same problems as mentioned for HZ44, poor order merging, jumps and steps in the continuum etc. Fortunately, it was possible to get hands on a KECK ESI spectrum, which also suffered from certain jumps over the spectral range but not as much as the HIRES one. Most of the HeI and HeII lines were not affected. The fit with the HHeCNO grid resulted in the following set of atmospheric parameters.

- $T_{\text{eff}} = 46200 \pm 500$ K
- $\log(g) = 5.90 \pm 0.15$
- $\log(n(\text{He})/n(\text{H})) = 1.30 \pm 0.12$

Namely, this is in good agreement with the parameters given by Rodríguez-López et al. [2007], but mainly because of their large errors on temperature and surface gravity and therefore no statement that should be taken too serious. In Fig. 6.79 the fit to several helium lines is shown. Well visible is the shift of the lines towards smaller wavelengths due to the large radial velocity of BD+39° 3226. The fit to the HeII line looks poor, especially the core is not deep enough and as a consequence the $H\alpha$ feature is too pronounced in the model. The $H\beta$ and $H\gamma$ features on the other HeII lines instead is well modeled. This indicated that the determined hydrogen to helium ratio cannot be as wrong as the fit to the HeII 6560 line might indicate.

By visual inspection it is apparent that the star is very metal poor as hardly no metal lines are visible to the naked eye.

To determine the metal abundances, the HIRES spectrum could be utilized as the steps were unlikely to affect one of the few lines. Table 6.43 shows the metal abundances from the HIRES spectrum. The values for iron and nickel in this first iteration were determined from the available, coadded IUE spectrum. It has to be mentioned that the overall fitting suffered from the poor data. While the visible lines were not

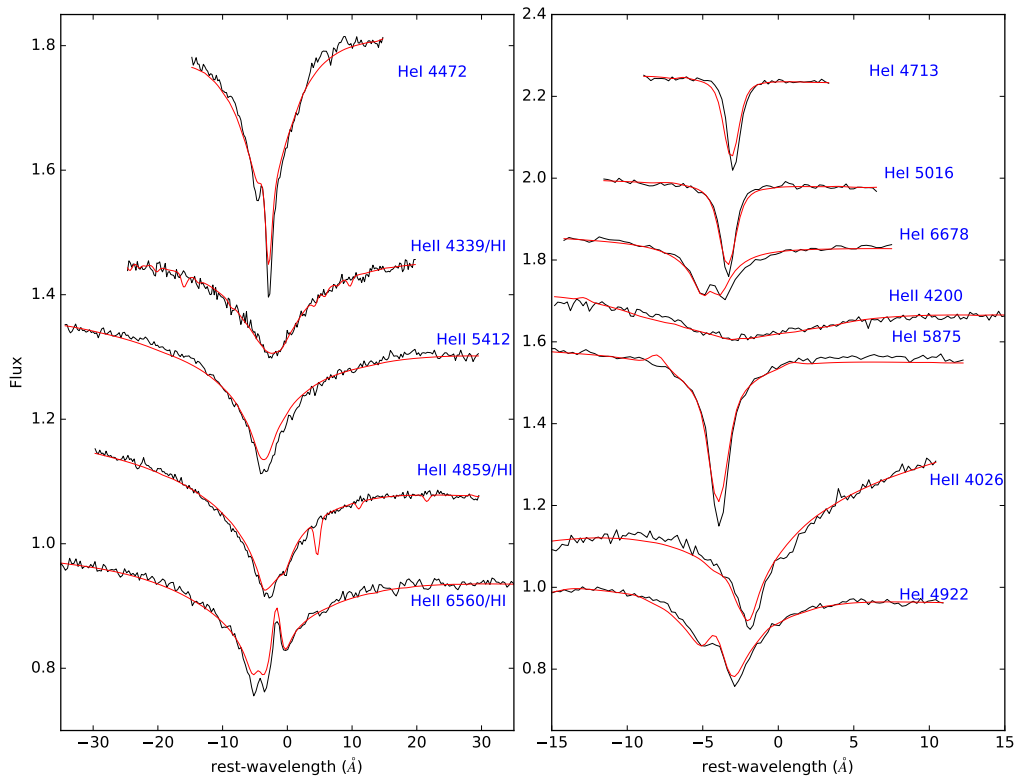


Figure 6.79: Visualization of several HeI and HeII lines of BD+39° 3226. The black lines show parts of the ESI spectrum, the best-fitting model is represented by the red lines. The flux levels had been adjusted for better representation.

Element	# lines	abundance
C	9	-4.27 ± 0.10
N	7	-3.60 ± 0.10
O	1	-4.68 ± 0.05
Ne	5	-4.41 ± 0.17
Mg	1	-3.03 ± 0.05
Al	2	-5.57 ± 0.35
Si	2	-4.26 ± 0.05
P	2	-5.94 ± 0.06
S	2	$-(6.36 \pm 0.50)$

Table 6.43: Overview on the number abundances for BD+39° 3226 determined from the optical HIRES spectrum. Given is the $\log(n(X)/n(H))$ in number abundances. (Models without Fe/Ni). The second column gives the number of lines used for the fit of a specific element. Abundances in brackets suffer from large uncertainties and have to be dealt with care.

or only hardly affected by the jumps in the data, these drawbacks affected the fits in which no line was visible in the data and which would result in an upper limit for the specific element. Adjusting the continuum level by eye slightly helped in reducing the problem.

Including iron and nickel did not help in improving the fits. Table 6.44 lists the abundances from the optical and UV spectra in the second iteration, after including iron and nickel. Especially silicon sticks out as the optical abundance is more than one dex off the one from the first iteration, while the UV values also agree with the higher abundance from the first iteration. It is therefore likely that this specific abundance might have been misfitted. Additionally, there is often a large spread between the three spectra concerning the resulting abundances. For aluminum, sulfur and iron, the IUE abundances are significantly lower than the FUSE ones, while STIS tends to give the highest abundances. This could, in principal, be explainable with the lower resolution of IUE and therefore a stronger pseudocontinuum compared to FUSE and STIS. But as some elements are not affected, like nitrogen, neon and silicon it is questionable if the wrong continuum level can be a valid answer. Of course line-crowding is more or less pronounced, depending on the region of wavelength that is used. In a metal poor star, like BD+39° 3226, in which only few lines were used for an element in the IUE data, selection effects play an important role, while they are likely to average out if more lines are used. In general, the low resolution of the IUE data makes it difficult to obtain trustworthy results at such a low metallicity as in BD+39° 3226, also explaining the large errors. As the final abundances were calculated as the error-weighted average, the IUE results tend to play only a small roll compared to the values from STIS and FUSE.

Especially in the HIRES data, it was difficult to find usable metal lines for fitting. Often, only one line was available, in other cases, visible lines were overimposed on broader helium lines, like in the case of many nitrogen lines. The same holds for the STIS data, which only covered a small wavelength range.

By comparing the abundances from the different spectra, it is apparent that the FUSE and STIS data give quite similar results, except for phosphorus which was only fitted by eye in the STIS range. The resolving power of both instruments is high enough to avoid the pseudocontinuum induced by line crowding, at least in such a metal-poor star. Table 6.45 shows the mass abundances of the certain elements as well their mass abundances compared to the solar level. Fig. 6.86 shows a visual representation of these values.

Figures 6.80 to Fig. 6.84 show several fits to selected lines from the optical and the UV spectra. Especially in Fig. 6.81 the bad wavelength calibration of the FUSE data can be seen. As this line was matching in other star's FUSE data, an error in the linelist is highly unlikely. Also Fig. 6.80 shows slight deviations concerning the wavelength.

In BD+39° 3226, the hydrogen to helium ratio lies in the typical regime for He-sdO stars. The CNO bi-cycle abundance pattern is well visible, although the overall abundances of all elements are much lower compared to the rest of the sample. The intermediate mass elements seem to cluster around 0.025 to 0.05 the solar value with magnesium sticking out. It is enriched to almost the solar level while phosphorus is depleted below one hundredth solar. As seen before, iron is less abundant than nickel and at the same level as the intermediate mass elements

For a more detailed discussion on the abundance pattern, see Sect. 7.4.

Element	HIRES	FUSE	IUE	STIS
He	–	–	–	–
C	$-4.48 \pm 0.40(4)$	$-4.45 \pm 0.08(4)$	$(-4.51 \pm 0.56)(2)$	$-4.33 \pm 0.04(2)$
N	$-3.51 \pm 0.07(7)$	$-2.76 \pm 0.13(12)$	–	$-2.51 \pm 0.05(4)$
O	$-4.67 \pm 0.04(1)$	$-4.04 \pm 0.15(6)$	–	$-4.35 \pm 0.08(2)$
Ne	$-4.8 \pm 0.40(5)$	$-3.58 \pm 0.50(4)$	$(-3.53 \pm 0.78)(5)$	–
Mg	$-3.02 \pm 0.05(1)$	–	$-2.95 \pm 0.25(4)$	–
Al	$(-5.7 \pm 1.8)(1)$	$-3.4 \pm 0.20(1)$	$-4.81 \pm 0.45(3)$	–5 (fity by eye)
Si	$-5.34 \pm 0.35(2)$	$-4.16 \pm 0.08(5)$	$(-4.19 \pm 1.5)(5)$	$-3.91 \pm 0.05(1)$
P	$-6.23 \pm 0.30(1)$	$-6.25 \pm 0.25(3)$	–	–
S	–	$-4.5 \pm 0.20(3)$	$(-5.5 \pm 1.10)(3)$	–
Fe	–	$-3.82 \pm 0.10(18)$	$-5.21 \pm 0.40(10)$	$-3.63 \pm 0.10(10)$
Ni	–	$-4.18 \pm 0.15(8)$	$-4.87 \pm 0.30(10)$	$-4.61 \pm 0.1(16)$

Table 6.44: Overview on the number abundances for BD+39° 3226 determined from different spectra. Given is the $\log(n(X)/n(H))$ in number abundances. (Models with Fe/Ni). The number of lines used for fitting each element is displayed in brackets following the abundances. Abundances in brackets suffer from large uncertainties and have to be dealt with care.

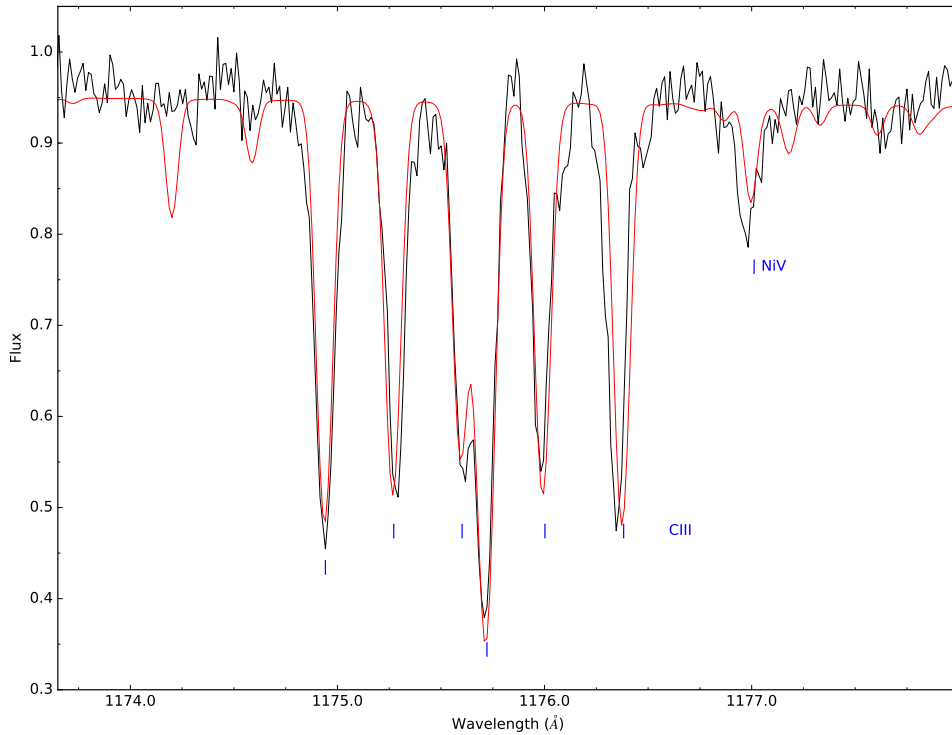


Figure 6.80: Visualization of the CIII septuplet of BD+39° 3226 (FUSE spectrum) in comparison with the final synthetic spectrum.

Element	logarithmic mass abundance	mass abundance ratio
H	-1.95	$1.52 \cdot 10^{-2}$
He	-0.05 ± 0.11	$3.56^{+1.47}_{-1.04}$
C	-5.37 ± 0.17	$0.002^{+0.001}_{-0.001}$
N	-3.96 ± 0.10	$0.160^{+0.056}_{-0.038}$
O	-5.25 ± 0.13	$0.001^{+0.001}_{-0.001}$
Ne	-4.59 ± 0.24	$0.022^{+0.025}_{-0.011}$
Mg	-3.53 ± 0.12	$0.417^{+0.169}_{-0.121}$
Al	-5.62 ± 0.21	$0.043^{+0.053}_{-0.024}$
Si	-5.20 ± 0.12	$0.001^{+0.003}_{-0.002}$
P	-6.70 ± 0.16	$0.035^{+0.020}_{-0.013}$
S	-5.05 ± 0.16	$0.029^{+0.017}_{-0.011}$
Fe	-4.31 ± 0.15	$0.038^{+0.022}_{-0.014}$
Ni	-4.52 ± 0.18	$0.423^{+0.326}_{-0.190}$

Table 6.45: Logarithmic mass abundances for the different elements in BD+39° 3226 compared to their solar value.

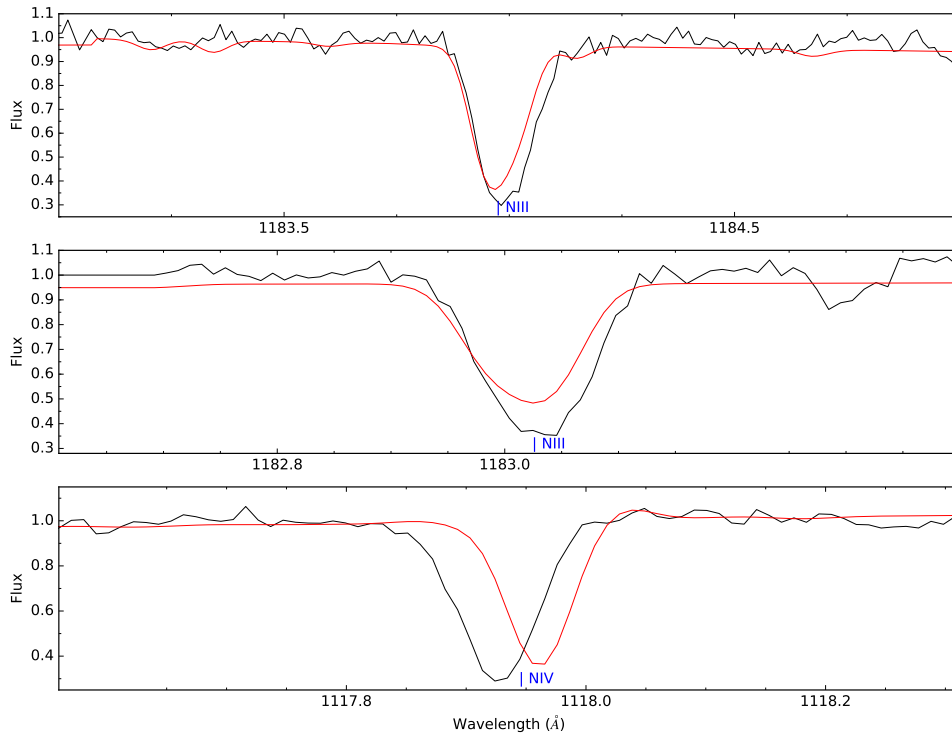


Figure 6.81: Visualization of several nitrogen lines with different ionization stage of BD+39° 3226 (FUSE spectrum) in comparison with the final synthetic spectrum. The bad wavelength calibration is clearly visible.

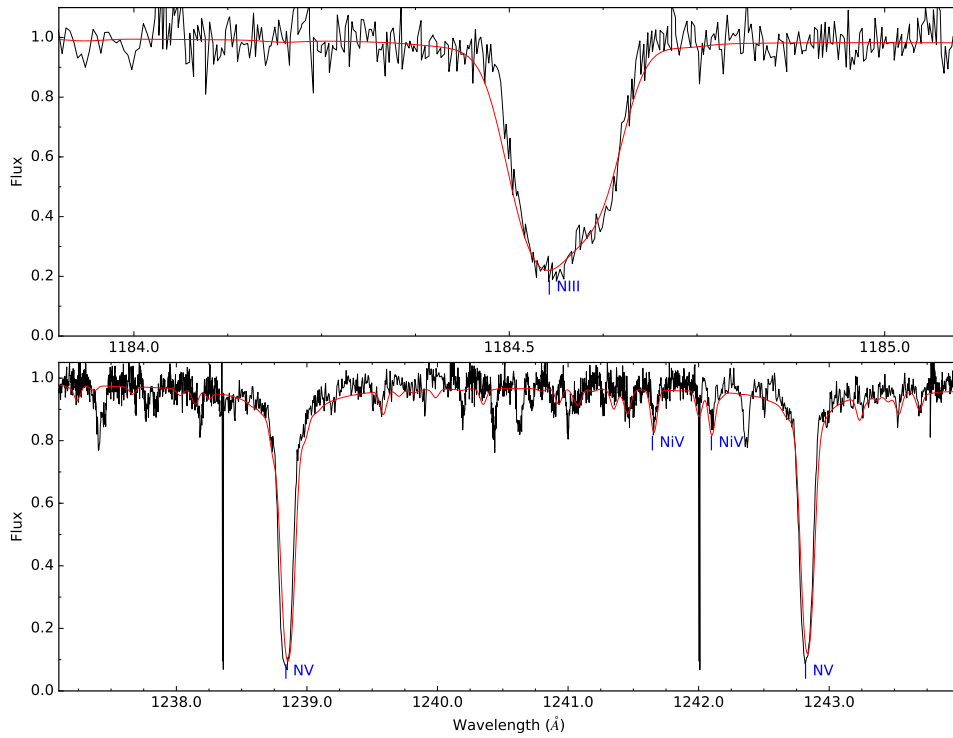


Figure 6.82: Visualization of several nitrogen lines with different ionization stage of BD+39° 3226 (STIS spectrum) in comparison with the final synthetic spectrum.

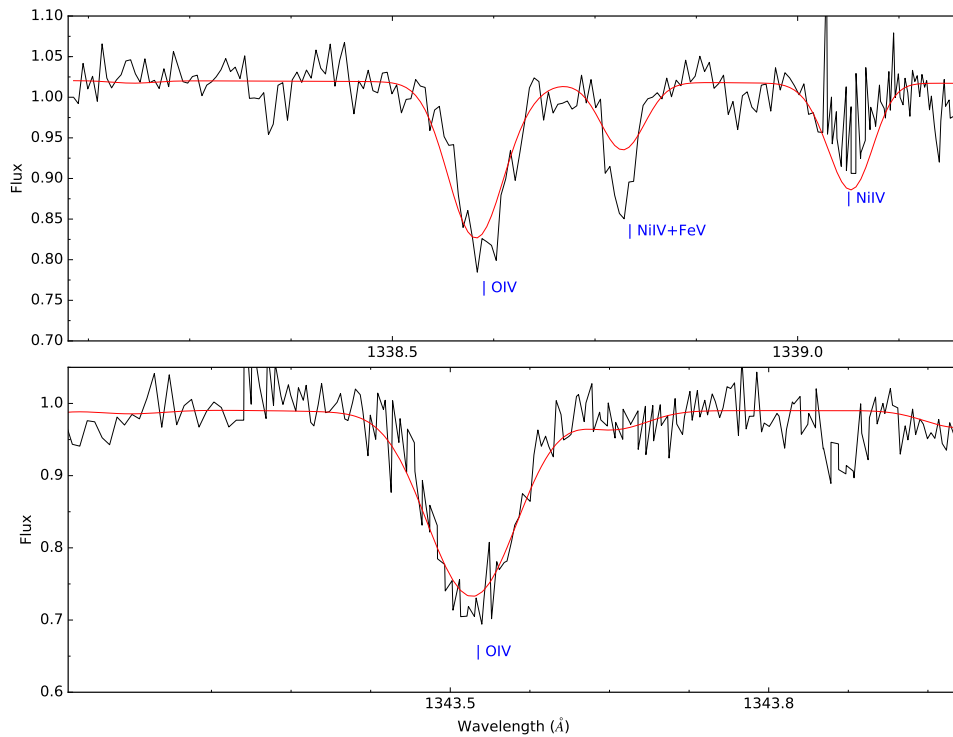


Figure 6.83: Visualization of several O IV lines of BD+39° 3226 (STIS spectrum) in comparison with the final synthetic spectrum.

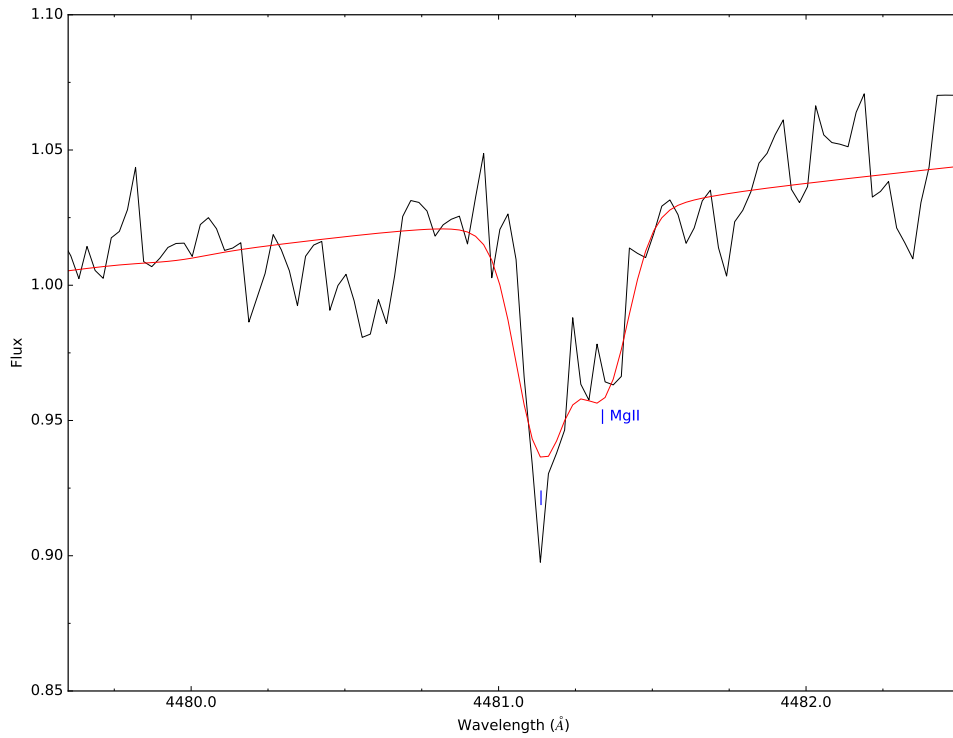


Figure 6.84: Visualization of several MgII lines of BD+39° 3226 (optical data) in comparison with the final synthetic spectrum.

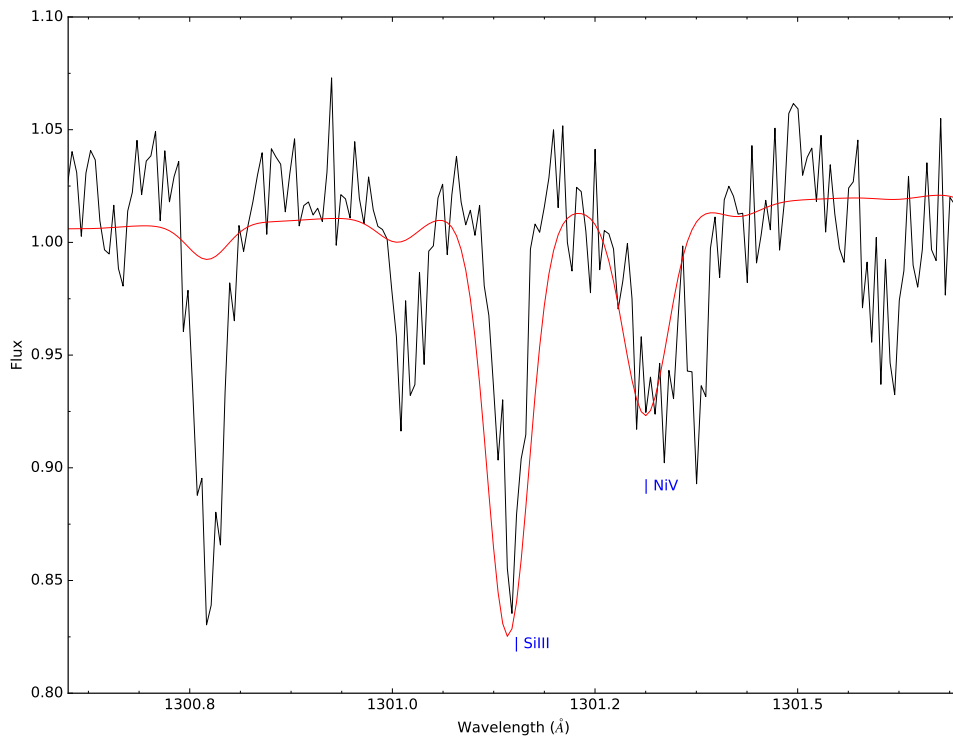


Figure 6.85: Visualization of one SiIII line of BD+39° 3226 (STIS spectrum) in comparison with the final synthetic spectrum.

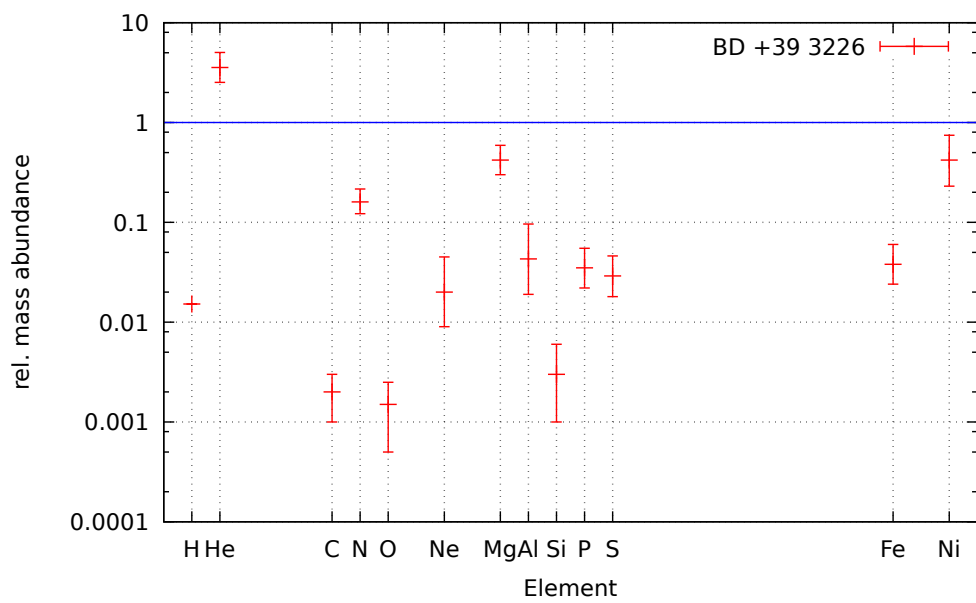


Figure 6.86: Visualization of the mass abundance ratio of BD+39^o 3226. The solar level of the different elements is given by the blue line.

6.4.3 Spectral energy distribution

In Fig. 6.87, the computed spectral energy distribution of BD+39° 3226 is shown, together with the available measurements. Except Johnson V and R all magnitudes match the SED within the errorrange very nicely. In addition, both color indices are matching very well.

There is a Hipparcos parallax of 4.27 ± 1.16 mas for this star [van Leeuwen, 2007]. This translates to a distance of 234_{-50}^{+87} pc. Assuming a mass of $0.47 M_{\odot}$ for BD+39° 3226, the photometric distance is 146_{-24}^{+27} pc. The errorranges for the two measurements are almost overlapping. Just slight deviations from the canonical mass of $0.47 M_{\odot}$ would lead to a better overlap between the Hipparcos measurements and the value arising from the SED fit.

Filter	value	error	type	reference
J	10.873	0.021	magnitude	Cutri et al. [2003]
H	11.023	0.022	magnitude	Cutri et al. [2003]
K	11.097	0.017	magnitude	Cutri et al. [2003]
UmB	-1.21	–	color	Dworetzky et al. [1982]
BmV	-0.29	–	color	Dworetzky et al. [1982]
R	10.39	–	magnitude	Zacharias et al. [2012]
V	10.2	–	magnitude	ESA [1997]
B	9.9	–	magnitude	ESA [1997]
Vt	10.149	–	magnitude	Høg et al. [2000]
Bt	9.813	–	magnitude	Høg et al. [2000]
W1	11.173	0.023	magnitude	Cutri [2012]
W2	11.262	0.021	magnitude	Cutri [2012]
box1	6.144	–	magnitude	-
box2	7.116	–	magnitude	-
box3	7.518	–	magnitude	-

Table 6.46: Photometric measurements for BD+39° 3226.

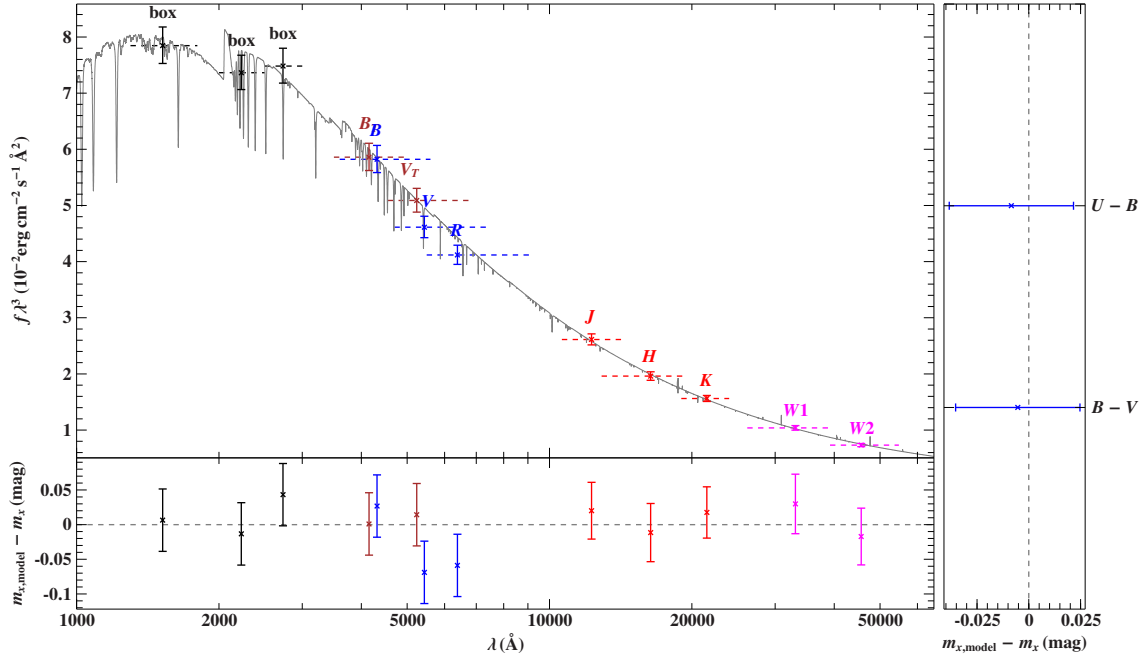


Figure 6.87: SED of BD+39° 3226 in comparison with photometric measurements (magnitudes and colors). The bottom and right panels show the residuals for the magnitude and color measurements.

6.5 Discussion on errors

6.5.1 Statistical and systematic errors

If not indicated otherwise, all the errors given for the stars presented in this thesis are the statistical fitting errors provided by SPAS.

Of course, possible sources for systematic errors also have to be kept in mind. These are i.e. errors in the model atoms or the broadening tables. Both would affect the shape and/or depths of lines and lead to wrong abundances. Another effect, mostly observed with NII lines, was lines going into emission where they should stay in absorption. Those lines were not used for fitting. Also lines with clear mismatches between data and model were rejected. To help identifying those mismatching lines, the results of a global fit in which all selected lines are fitted together and an individual fit in which each line is fitted solely and the result got averaged afterwards, was compared. Regarding the individual fit, all lines with abundances being off the median by 1 dex were rejected. At the same time the ionization equilibrium was checked for the available ionization stages. If abundances of one ionization stage are continuously higher or lower compared to other ionization stages of the same element, a wrong effective temperature in the models becomes likely.

Ideally the global and individual fit would deliver exactly the same abundances, in practice difference usually were between 0.1 and 0.2 dex. This is likely to be caused by the implementation of the error calculation in SPAS. The weight for a line in the global fit is based on the number of datapoints in that specific window. Broad lines like the helium ones or several single lines lying close together and fitted in one window tend to dominate the fit. This has to be kept in mind when adjusting fit windows or rejecting lines. Of course a certain, human selection bias can never be

ruled out.

Another point is the number of available lines for a specific element. Depending on the chemical composition of the He-sdO, nitrogen, carbon or neon usually had no lack of usable lines. Elements like aluminum, magnesium, phosphorus and sulfur tend to have only few feasible lines which are often hidden within the noise of the data. With few lines, outliers become more important and influence the fit stronger than with multiple lines. This is visible in the given error for the different element abundances which is usually larger for the intermediate mass elements. Iron and nickel play a special role in this game. Single iron or nickel lines are hard to find in the UV, especially in the low resolution COS and IUE spectra. The used fitting windows always contained more than just one iron or nickel line so that each line fit was an average on several lines itself. This brought the abundances originating from each fit window closer together and resulted in lower average errors than for the other elements.

6.5.2 Optical vs UV data

The analysis of UV spectra is not as straight forward as it is in the optical regime. As already mentioned in Sect. 6.1.1 the determined abundances from optical and UV spectra might vary significantly. The spectral lines of a star should lead to the same abundances, not matter at which wavelength the line is. The most important reason for different abundances in the UV is the linecrowding. The number of spectral lines usually starts to increase towards the blue. In the UV there can be so many lines that they start to blend into each other and become indistinguishable. If enough lines start to blend no single line are visible and the real continuum level starts to vanish. This is called a pseudocontinuum. Depending on the number and crowding of lines, the difference between the real, physical continuum and the pseudocontinuum might vary. Additionally iron and nickel contribute millions of small lines in the UV so that basically every line in the UV is blended with iron and/or nickel.

The fitting program used in this thesis cannot deal with a pseudocontinuum and treats it as a normal continuum, leading to lower abundances from the UV. Of course this is no sweeping statement. If the resolving power of an UV spectrograph is high enough, single lines can be resolved (although it is virtually impossible to resolve all the tiny iron and nickel lines). Additional facts like rotation (contributing to line blending/smearing) and low abundances of a star (reducing line crowding) also have to be taken into account.

To get an impression of the role of resolution concerning UV spectra, IUE and FUSE data were compared. The resolution of FUSE is about twice as high than the IUE one. Unfortunately they only feature a small overlap between the observed wavelength ranges. Fig. 6.88 shows two CIII multiplets of [CW83]0904-02 from FUSE and IUE data together with the best carbon fit. From FUSE a $\log(n(\text{C})/n(\text{H}))$ of -0.14 ± 0.09 for the 1165.65 Å lines and $+0.06 \pm 0.11$ for the 1175.5 Å lines was measured. In the IUE spectra, these values changed to -0.87 ± 0.30 and -0.73 ± 0.17 respectively. The scatter for a certain dataset is within the expected range. The measured difference between the abundances can be up to roughly 1 dex! Of course it has to be considered that these lines are at the far red end of FUSE and the far blue end of IUE, meaning that the S/N ratio is not the best, especially not for IUE. Fig. 6.89 shows how much the continuum level would have to be increased manually

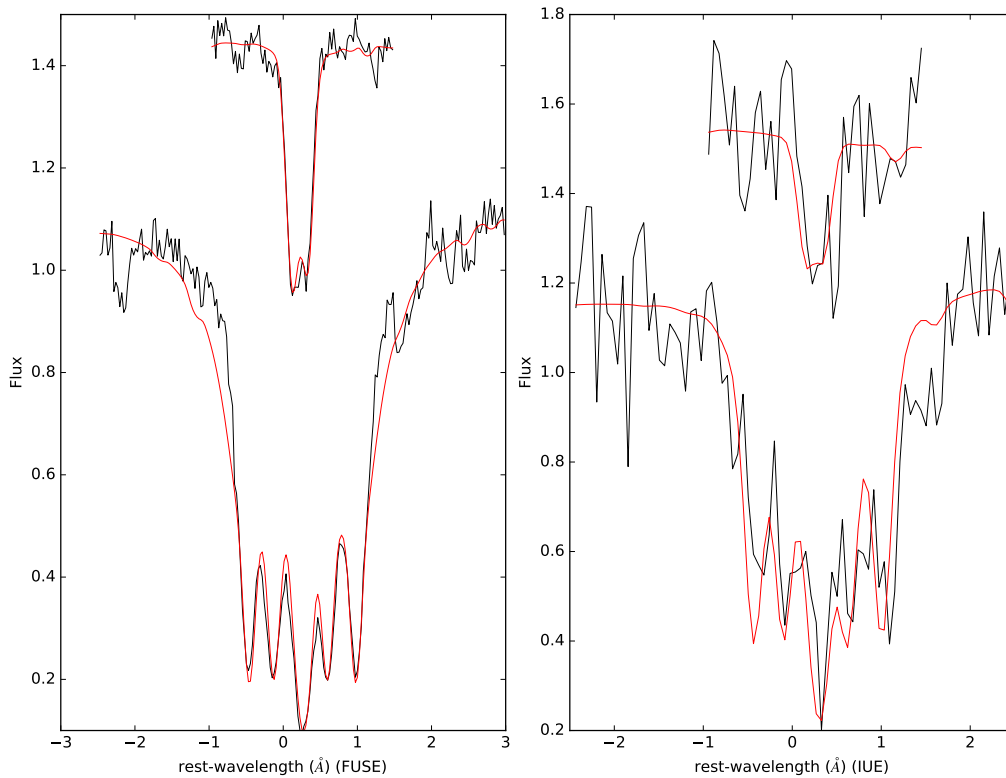


Figure 6.88: Comparison of a fit of the CIII triplet around 1165.65 Å and the CIII septuplet around 1175.5 Å for a FUSE and an IUE spectrum of [CW83] 0904-02.

until the measured abundances of the line in IUE matched with the one in FUSE. Of course this is not practical when determining the abundances as it introduces a significant error when placing the continuum level by eye for each line.

When comparing FUSE and IUE abundances for the stars which featured both spectra, the difference is less pronounced than one might expect from the figures above. The mean difference is 0.21 ± 0.04 dex. Of course the line crowding is not the same for all the spectral range. There are regions with fewer lines in which the difference between continuum and pseudocontinuum is less pronounced. When fitting multiple lines, the continuum level is averaged, resulting in smaller differences than in the “worst-case” scenario above.

6.5.3 Wrong broadening data

Especially when fitting the CIII septuplet around 1175.5 Å, it turned out very difficult to fit the line cores together with the wings and the continuum level. In most cases, the wings in the model were much broader than in the data. The problem was first encountered in [CW83] 0904-02 and extensively tested there. The first idea of a wrong carbon abundance and a too high projected rotational velocity could not be confirmed as even a fit of only this line with both parameters allowed to vary, no better results could be obtained. For some stars, as BD+39° 3226, the septuplet could be fitted extremely well, most likely because no broad wings are observable and the sharp carbon lines blend with the continuum level without any apparent

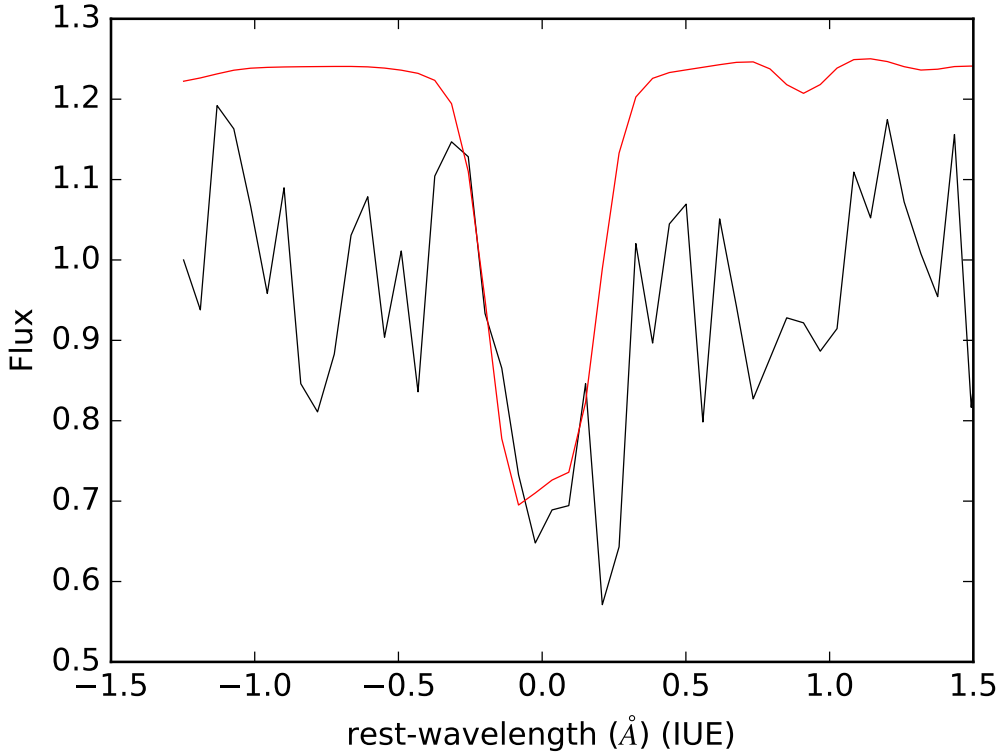


Figure 6.89: CIII triplet around 1165.65 Å in [CW83] 0904-02 with adopted continuum level.

broadening. This could indicate that the metallicity has something to do with the problem. An additional factor might be wrong broadening data. A wrong value for the damping constant or the Stark broadening parameters might explain the observed behavior.

6.5.4 Undetermined abundances of iron and nickel

For some of the stars presented in this thesis, there are either no UV spectra available or the available ones are of too poor quality to determine the abundances of iron and nickel. In these cases, both elements have been set to solar abundance, knowing that this value is unlikely to represent the true state.

Wrong abundances of one element have two effects. Firstly the total weighted particle number, necessary to convert number- to mass abundances is too low or too high.

$$\beta(X) = \frac{u_X}{\sum_{i=1}^{i=y} n_i u_i} n(X) \quad (6.1)$$

This has an effect on all other element abundances, but only on a very tiny scale. The total particle number is highly dominated by helium, carbon and nitrogen, at least in the He-sdO stars. Uncertainties induced this way are below 0.1% for all elements.

Secondly (and more importantly) iron and nickel have an influence on the stellar atmosphere and the temperature stratification as they add a certain amount of opacity by their millions of lines. This additional opacity can lead to a shift of the

continuum (with effects largest in the UV) and to a “deformation“ of all other line profiles.

To quantify how much a wrong iron (or nickel) abundance influences the fit of other elements, the nitrogen content of HE 1511-1103 was used as a testbed. The subgrid to determine the nitrogen abundance after the first iterations (so after having determined abundances for all elements and after including iron and nickel at solar abundance) was modified. The iron abundance was shifted from solar level to 0.1 solar level. To save calculation time only nitrogen abundances for 10^{-3} , 10^{-2} and 10^{-1} times hydrogen by number were calculated with the low iron level. Afterwards several strong nitrogen lines were fitted with both subgrid. In the subgrid with the solar iron content, only the files representing 10^{-3} , 10^{-2} and 10^{-1} times hydrogen by number were selected to avoid any bias. Fig. 6.90 shows the fits of selected nitrogen

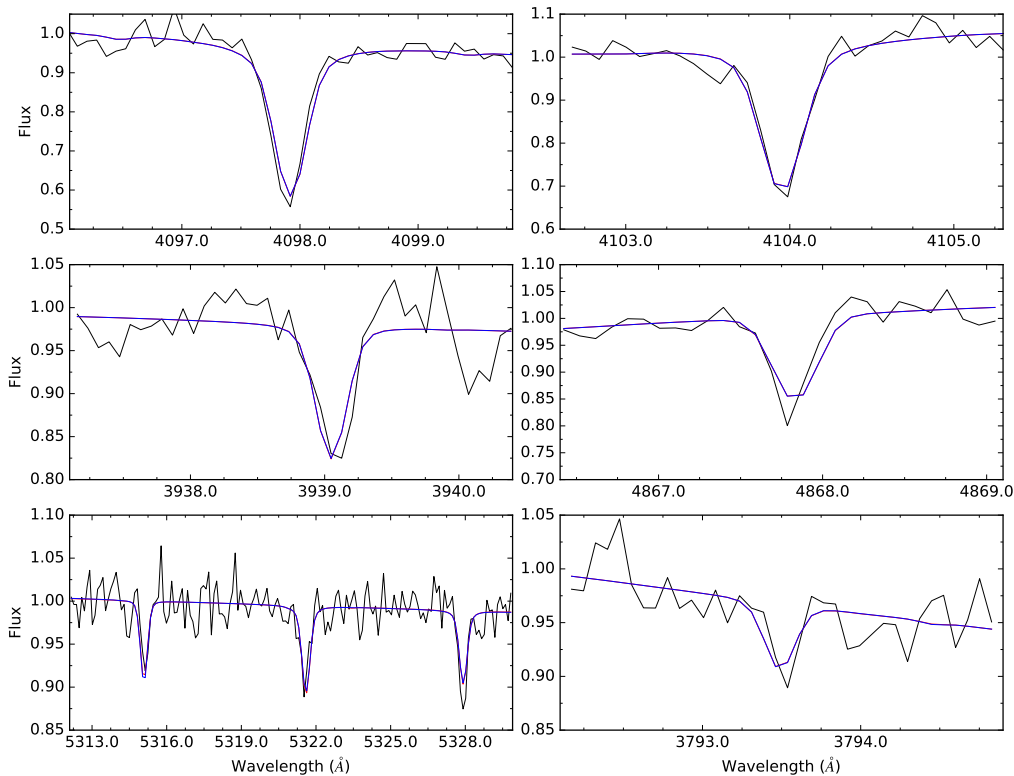


Figure 6.90: Comparison of models with different iron contents for NIII lines in HE 1511-1103. The (almost invisible) red line represents the model with a solar iron abundance.

III lines. The red curve represents the model with the solar iron abundance, while in the blue model, iron had been depleted. It can be clearly seen, that there is hardly any difference visible to the naked eye. The only slight differences in the line cores can be seen at 5315.2 \AA and 5321.56 \AA in the bottom left panel. The resulting abundances from a global fit are

- $\log(y)=1.96 \pm 0.05$ for the low iron abundance and
- $\log(y)=1.95 \pm 0.05$ for the higher iron abundance

The fitted wavelength ranges for each line as well as the continuum level was not changed. The bluest nitrogen line was around 3790 \AA , while the red end lies around

5320 Å. Both the most blue and the most red end of the spectrum was well covered. To sum it up, it seems that the correct level for the iron (and nickel) abundance only has a minor, neglectable effect, at least while fitting optical spectra of He-sdO stars.

6.5.5 Errors of solar abundances

To put the derived number- and mass abundances in reference with the solar values, the photospheric abundances given in Asplund et al. [2009] were used. They are listed in table 6.47. For the noble gases marked with * only atmospheric estimates were used. Especially neon and argon have particularly large errors. This results from the lack of lines for the noble gases in the photospheric spectrum of the sun. For their abundances, indirect methods relying on i.e. the corona had to be used. The last column gives the error for each element that was used in the python code for calculating the mass abundances and the solar references. The errors for each element were not used individually, but grouped according to the size of the error. The errors were rounded up to assure that the errors used in the code are in case of doubt larger than the actual errors and not underestimated. The NLTE-only elements which were used in all analysis (except US708) were marked with an upper case N. Except for neon, all the NLTE-only elements have errors not larger than 10%.

Element	photospheric abundance (log)	error
H	0	- N
He	-1.07 ± 0.01 *	2.5% N
Li	-10.95 ± 0.10	25%
Be	-10.62 ± 0.09	25%
B	-9.30 ± 0.20	50%
C	-3.57 ± 0.05	10% N
N	-4.17 ± 0.05	10% N
O	-3.31 ± 0.05	10% N
F	-7.44 ± 0.30	100%
Ne	-4.07 ± 0.10 *	20% N
Na	-5.76 ± 0.04	10%
Mg	-4.4 ± 0.04	10% N
Al	-5.55 ± 0.03	7% N
Si	-4.49 ± 0.03	7% N
P	-6.59 ± 0.03	7% N
S	-4.88 ± 0.03	7% N
Cl	-6.50 ± 0.30	100%
Ar	-5.6 ± 0.13 *	35%
K	-6.97 ± 0.09	25%
Ca	-5.66 ± 0.04	10%
Sc	-8.85 ± 0.04	10%
Ti	-7.05 ± 0.05	10%
V	-8.07 ± 0.08	20%
Cr	-6.36 ± 0.04	10%
Mn	-6.57 ± 0.04	10%
Fe	-4.50 ± 0.05	10% N
Co	-7.01 ± 0.07	20%
Ni	$-5,78 \pm 0.04$	10% N
Cu	-7.91 ± 0.05	10%
Zn	-7.44 ± 0.05	20%

Table 6.47: Solar photospheric abundances taken from Asplund et al. [2009]. NLTE elements are marked with an N, a * indicates that an indirect method was used to determine the abundance.

6.6 An eye on radial velocities

One of the key questions concerning stellar formation and evolutions is if the star is actually a binary system or not. There are several possibilities to answer this question for a certain system, i.e. photometric measurements and measurements of radial velocities. A “invisible“ companion would alter the radial velocity of the system periodically although being not directly visible in the spectrum. Other companions like cool main sequence stars could be spotted by an infrared excess.

For all stars analyzed in this work, Sect. .1 in the appendix displays the measured radial velocities for each available, single spectrum that was used in this analysis. The radial velocity was determined by using SPAS and fitting Voigt profiles to selected sharp metal lines, mostly nitrogen or neon. If this was not possible, mainly due to a lack of those lines (like in the case of BD+39° 3226) or because of a too low resolution (like with the COS spectra), broader helium lines were used.

If possible interstellar or telluric lines were used to crosscheck the RVs and correct them if necessary.

While comparing the SED of the analyzed stars with photometric measurements, no sign of an IR excess was seen for any of the sample stars, therefore a cool MS companion can be excluded for all of them.

For most of the measured stars, the radial velocities are consistent, meaning that the values overlap withing the errorranges. Or in other words, the radial velocity did not change in the observed period of time. However, for some stars, outliers were detected and will be discussed in more detail hereafter.

- **LSS 1274**

For LSS 1274, the available CASPEC spectrum sticks out with a RV of 40 ± 7 km/s compared to values centered around 15k km/s for the UVES and FUSE measurements. Unfortunately, no detailed information on when this spectrum was taken could be obtained, only the year of 1987 was available from the corresponding publication. As the UVES and FUSE are data consistent among each other, it is hard to tell where this offset originates from. Regarding the long time between the CASPEC data and the other observations, it is possible that the RV did indeed change and a hint for a long periodical companion is given. On the other hand, the available data are not well enough distributed over the years to draw any firm conclusions. Another RV data point was provided by Drilling and Heber [1987] who found a value of 24 ± 1 km/s. This lies between the CASPEC value and the rest and is dated to the 9th of April, 1985.

- **LSIV +10 9**

LSIV +10 9 shows significant deviations between almost all available used spectra. Interestingly, the UVES spectrum and two of the FUSE ones are matching, while The IUE and one FUSE spectrum are also matching but at about 30 km/s less. While the IUE spectrum is from the 1980s, the matching FUSE one is from 2004 and the other two spectra are two years older. If available, interstellar lines were crosschecked to validate the results. This shift points to an unseen companion to LSIV +10 9. Ulla and Thejll [1998] claimed to have found an IR excess and mentioned that LSIV +10 9 is a binary. By looking at the SED of this star, no IR excess or any other indication for bi-

	Ulla and Thejll [1998]	Cutri et al. [2003]
J	11.15 ± 0.03	12.632 ± 0.03
H	10.98 ± 0.05	12.813 ± 0.02
K	10.90 ± 0.05	12.916 ± 0.04

Table 6.48: Comparison of photometric magnitudes J, H and K from Ulla and Thejll [1998] and Cutri et al. [2003].

narity could be found. The measured distance of 550 pc and the reddening of 0.0513 also seem perfectly normal. To understand this discrepancy, the values for the J, H and K magnitudes measured by Ulla et al. were compared to those used for fitting the SED in this work, downloaded from the VIZIR online catalog. They are displayed in the table 6.48. The values from Cutri et al. [2003] are also given by other catalogs, so they can be regarded as trustworthy. Although the IR excess could not be confirmed by more recent measurements, the questions on the origin of the RV variations remains valid. Although not visible in the spectrum or the SED, LSIV +10 9 might have a companion and be therefore part of a binary system.

It has to be mentioned that irregular RV variations without any obvious explanation have already been observed during the MUCHFUSS project [Geier et al., 2015b].

- **BD+39° 3226**

In the case of BD+39° 3226 (see Sect. 6.4) the IUE spectrum shows a tremendous offset of around 280 km/s compared to the HIRES and FUSE data, which are consistent among each other. It is most likely that the IUE data was transferred to the restframe and is therefore useless for comparing radial velocities. Dworetzky et al. [1982] report the following four measurements of radial velocities:

- 23.07 1975: -258 ± 8 km/s
- 26.07 1975: -293 ± 15 km/s
- 24.08 1975: -261 ± 19 km/s
- 28.08 1975: -281 ± 11 km/s

While the measurement of -258 ± 8 km/s is not in agreement with neither the velocities derived from HIRES, FUSE and STIS data, nor with the other velocities proposed by Dworetzky et al. [1982], it can be regarded as an outlier. Bluhm et al. [1999] give a radial velocity of -289.1 ± 6.5 km/s, which is the same magnitude as the other measurements. Hence, we conclude that BD+39° 3226 is not RV variable.

- **CD-31° 4800**

For CD-31° 4800, several RV measurements are available from history:

- 36 ± 7 km/s from Giddings [1981]
- 37 ± 1 km/s from Drilling and Heber [1987]
- 18 ± 4 km/s from Kilkenny and Muller [1989]

While the value of Giddings [1981] are in agreement with the presented measurements, the results from Drilling and Heber [1987] and Kilkenny and Muller [1989] expand the RV range to both ends. No real trend is observable and CD-31° 4800 might be another candidate for the irregular RV variations presented by Geier et al. [2015b].

- **General XSHOOTER data**

By looking at the RVs determined from XSHOOTER data, it becomes apparent that the single channels show a systematic shift of a few km/s between each other. This is not much and usually covered by the error estimations, but should not remain unmentioned here.

In general, data from some instruments are more likely to show inconsistent RVs than others. Especially FUSE data often suffers from a more or less poor wavelength calibration as it can be seen in some of the stars presented in this work. Dixon et al. [2007] claim that the wavelength accuracy of FUSE depends, among other parameters, also on the angle under which light hits the optics and suggest a systematic error of up to 10 km/s resulting from this behaviour. Also the HIRES spectrograph not only suffers from an inefficient flat field correction, also the wavelength calibration seem to be problematic as shifts between certain lines of about 7 km/s have been observed in one spectrum.

6.7 The Pickering Problem

While fitting the atmospheric parameters of several He-sdO stars presented in this thesis, a problem was encountered with the He II Pickering lines. In some stars it was impossible to fit the He II 4200 Å and the He II 4339 Å line together with the other helium lines without significant deviations. Especially the line core could not be reproduced and were too deep in the models. The most affected stars are CD-31° 4800, LSIV +10 9 and GALEX J095256.6-371940. Fig. 6.91 and Fig. 6.92 show the He II 4200 Å and the He II 4339 Å line from different stars overplotted with the final model for the corresponding spectral range. Note that the radial velocity has not been corrected for in the plots.

It is obvious that the He II 4200 Å line barely matches in any star. The deviations between data and model is only small for [CW83] 0832-01, [CW83] 0904-02 and (visible as a slight continuum offset) for LSS 1274. In all other stars the line core in the model is too deep. For the He II 4339 Å line, the deviations are far less pronounced. Only in CD-31° 4800, LSIV +10 9 and GALEX J095256.6-371940 significant differences between model and data are visible. For the rest of the stars, the differences are explainable with noise. The three stars with strong discrepancies in the He II 4339 Å line are also those with the largest offset concerning the He II 4200 Å line. This problem was already discussed by Bauer and Husfeld [1995] who encountered it while fitting CASPEC spectra of CD-31° 4800. In their work, several possible sources of error were ruled out, like data reduction, stellar rotation, hydrogen contribution in the helium lines, level dissolution, inadequate model atoms, mass loss and binarity (see Bauer and Husfeld [1995], page 484f). These aspects shall be revisited here.

- **Data reduction**

As the Pickering Problem was encountered in different stars, with spectra

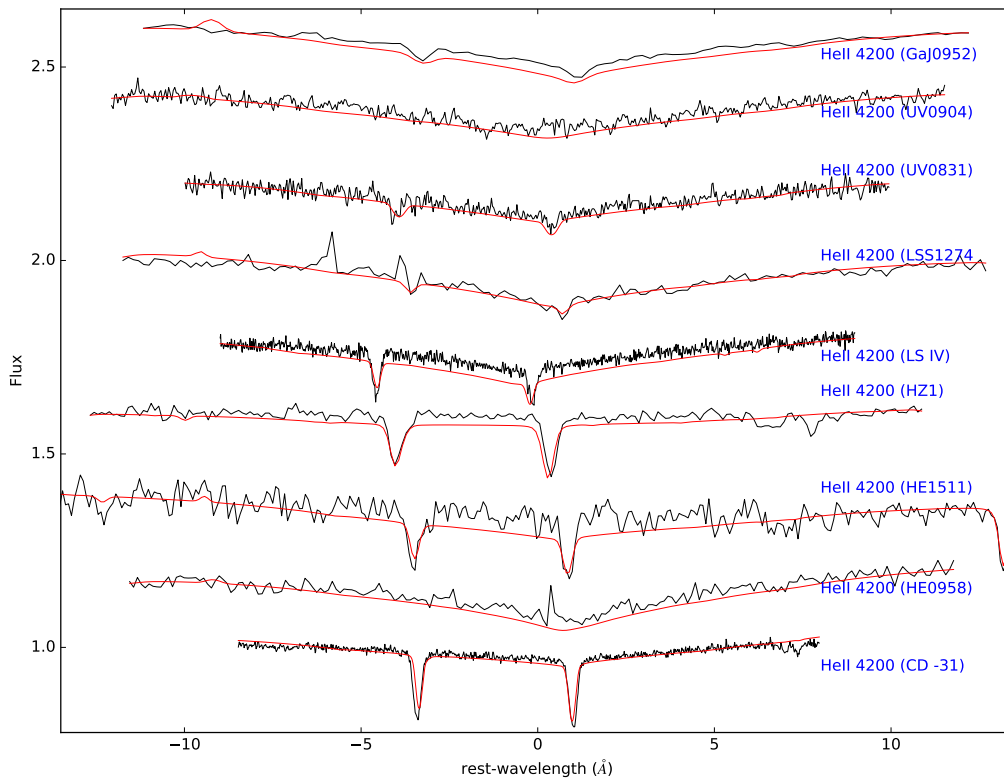


Figure 6.91: The He II 4200 Å line with the final model solution overplotted for different stars. The data have not been RV corrected.

taken by different echelle spectrographs, a common mistake in the data reduction, i.e. a wrong correction of the blaze function, is highly unlikely. The FORS (=longslit spectrograph) spectrum of CD-31° 4800 shows no signs of the Pickering problem, however the very low resolution can easily hide the deviations.

- **Stellar rotation**

Among the affected stars, some are rotating and some are not. In addition rotation would affect all lines, not only the Pickering ones and can therefore be excluded as a possible cause.

- **Helium abundance**

At a sufficient low helium abundance, the hydrogen components in the some of Pickering lines start to become visible and affect the line cores. But this cannot explain deviations in the 4200 Å and the 4542 Å lines as only at 4340 Å is a hydrogen line from the Balmer series contributes. Additionally, at such high helium abundances as observed in the He-sdO stars (especially in CD-31° 4800), hydrogen contribution is not visible in those lines.

- **Level dissolution**

For objects with a high surface gravity, pressure effects might lead to a dissolution of certain atomic states with high quantum numbers. According to Bauer and Husfeld [1995] this effect can be neglected for the Pickering Problem as the affected lines do not have appropriate quantum numbers.

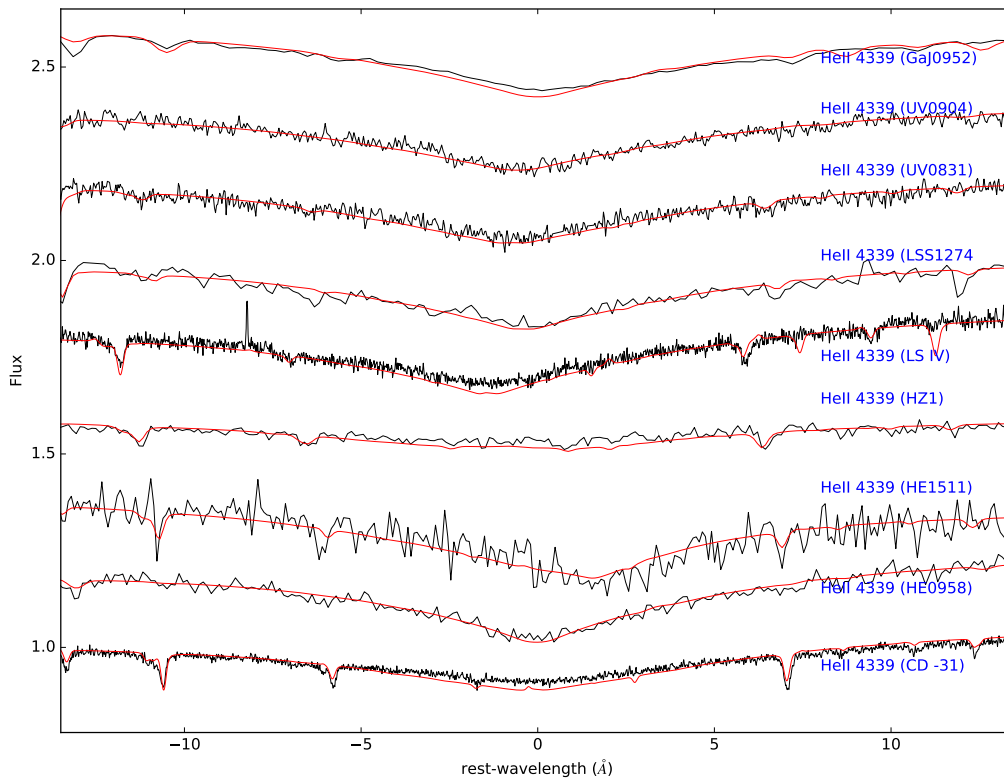


Figure 6.92: The He II 4339 Å line with the final model solution overplotted for different stars. The data have not been RV corrected.

- **Model atoms**

Bauer and Husfeld [1995] wondered if iron group elements in NLTE atmosphere might play an important role in explaining the Pickering problem. As all the model atmospheres representing the final parameters contained iron and nickel and still suffered from distorted lines, it is safe to claim that the additional opacity coming from iron and nickel (or the intermediate elements) can not compensate for the inadequate results concerning the Pickering lines.

- **Mass loss**

For CD-31° 4800 and LSIV +10 9 no signs of mass loss could be found. In the UV spectra, the lines have a symmetric shape and the C IV duplet consists of two lines with identical depths. For GALEX J095256.6-371940 no UV spectra are available and therefore potential mass loss is hard to detect.

- **Binarity**

None of the listed stars is known as binary system and none of the analyzed spectra seem to show a contribution from a possible companion. It is therefore difficult to imagine an undetected companion with a spectrum just appropriate to distort the Pickering lines and nothing but the Pickering lines..

Up to now, no knew theory on the cause of the Pickering problem is known. As stars from the N-rich subclass are as well affected as those from the CN-rich subclass, it is unlikely that the chemical composition of the atmosphere plays an important role. It may be that the used helium model atoms are still not sufficient enough to

describe all features of all lines or that the used broadening tables fail to account for pressure broadening by He^+ and He^{++} ions as they occur in large numbers in helium rich stellar atmospheres. As some of the He-sdO stars show no sign of the pickering lines, inadequate broadening parameters also become unlikely. The affected stars do not group in a certain area in a $T_{\text{eff}}/\log(g)$ plane. There are hotter and cooler stars in the sample, as well as ones with higher and lower surface gravity and helium abundance.

Up to now, no mechanism that could explain the observed behavior is known to the author.

7 Evolutionary scenarios

The following chapter discusses several formation scenarios for He-sdO stars. Matching the previous chapter, they are divided in scenarios for N-rich, C-rich and CN-rich stars. At the end, a short remark on the most likely formation scenario for BD+39° 3226 is presented.

7.1 Formation history of N-enriched He-sdOs

Fig. 7.1 shows the distribution of the nitrogen rich He-sdO stars from this work in comparison with other He-sdOs from the GALEX sample [Németh et al., 2012] and He-sdOs analyzed by Hirsch [2009]. For more information on the sample, see chapter 9. It can be seen that the stars seem to group in a small range for the

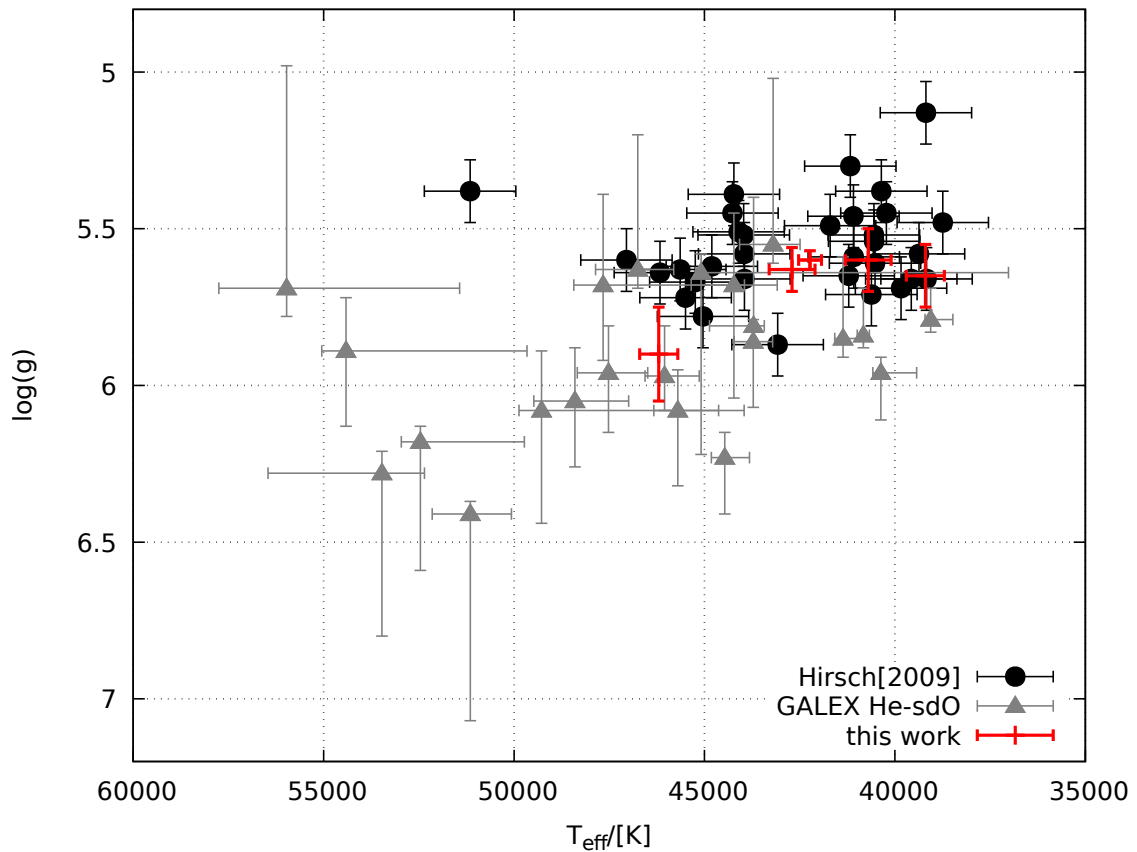


Figure 7.1: Comparison of the N-rich He-sdO subsample with the GALEX sample and the He-sdOs from Hirsch [2009].

surface gravity, clustering around 5.6, while the temperature spreads from 39200 K

to around 43000 K.

Fig. 7.2 shows the stars in a Kiel diagram with three tracks for the deep mixing hot flasher scenario and one track for the shallow mixing case [T.Battich, priv. comm.]. The later one can be excluded for all stars as it is clearly outside any errorrange. All stars from the compatible with the tracks for the deep mixing scenario, at least in theory.

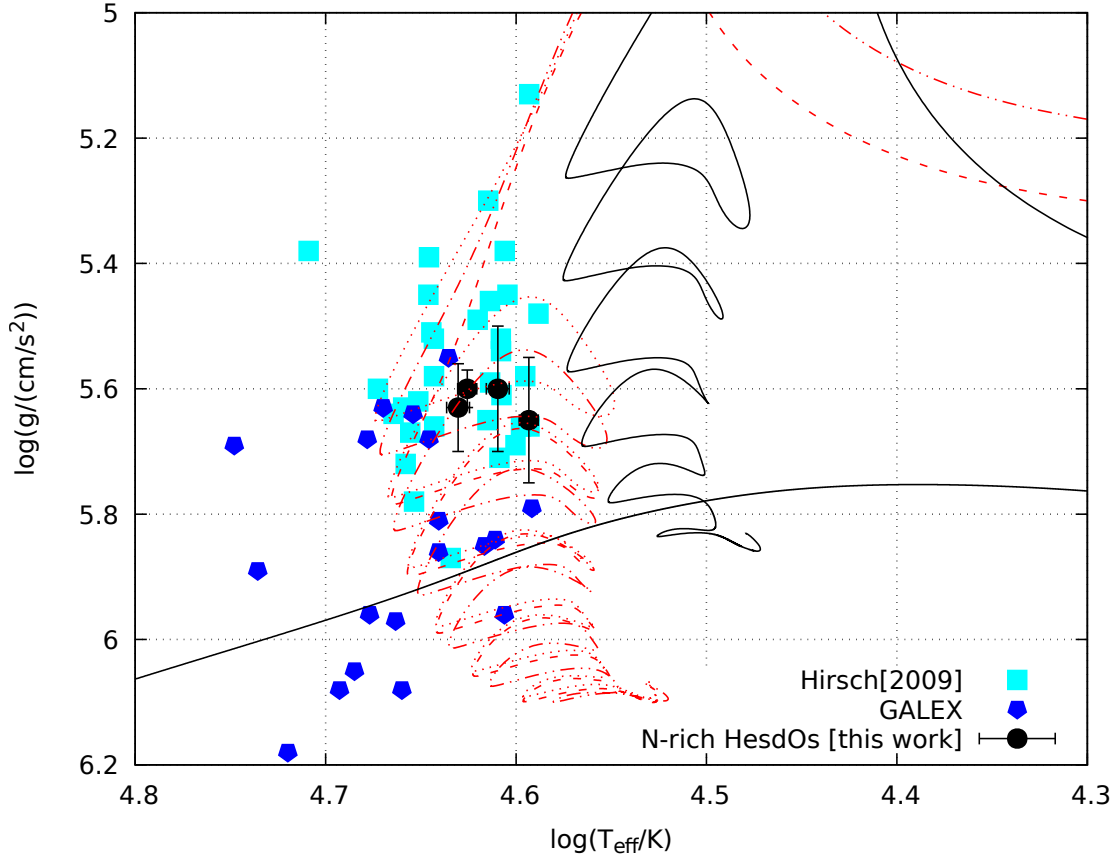


Figure 7.2: Kiel diagram for the N-rich sample of He-sdO stars. Included are the evolutionary tracks for shallow mixing(0.468 M_{\odot} /black) and different deep mixing scenarios (0.455 M_{\odot} /dashed, 0.460 M_{\odot} /dotted, 0.468 M_{\odot} /dashed-dotted) at an initial metallicity of $z=0.02$.

Table 7.1 shows the mass abundances for all elements in the four nitrogen rich sample stars. Their abundance pattern with the eye-catching CNO by-cycle abundance pattern is not compatible with the deep mixing late hot flasher scenario. Although the helium abundance would match, all other elements are more depleted in the stars than expected for a hot flasher. In addition the shallow mixing case can be ruled out as it would require higher oxygen abundances compared to the observed one (Miller-Bertolami, priv. comm.).

Hence the N-rich sample stars are in good agreement with a slow merger scenario in which two He core WDs in a binary system start to lose orbital energy by emitting gravitational waves. As the orbit shrinks, the less massive star sooner or later gets disrupted by the tidal forces of its companion and begins to form an accretion disk. From this disk, matter is transferred on the remaining star. In the cold merger

Element	CD -31° 4800	HE 1511-1103	HZ1	HZ44
H	-3.21	-1.60	-3.50	-1.17
He	$-4.36 \cdot 10^{-3} \pm 0.2$	-0.13 ± 0.19	$4.36 \cdot 10^{-3} \pm 0.28$	-0.47 ± 0.17
C	-4.46 ± 0.19	-4.03 ± 0.16	-4.54 ± 0.10	-4.62 ± 0.09
N	-2.34 ± 0.09	-2.39 ± 0.05	-2.50 ± 0.06	-3.25 ± 0.10
O	-4.21 ± 0.19	-3.65 ± 0.24	-4.60 ± 0.28	-4.32 ± 0.12
Ne	-2.91 ± 0.26	-2.55 ± 0.11	-2.99 ± 0.09	-3.77 ± 0.10
Mg	-3.42 ± 0.30	-3.15 ± 0.15	-3.39 ± 0.32	-4.30 ± 0.19
Al	-4.58 ± 0.18	-4.27 ± 0.16	-4.52 ± 0.14	-4.74 ± 0.12
Si	-3.19 ± 0.14	-3.09 ± 0.09	-3.34 ± 0.08	-4.03 ± 0.12
P	-	-5.31 ± 0.29	-5.41 ± 0.44	-6.58 ± 0.19
S	-4.51 ± 0.44	-3.99 ± 0.34	-4.40 ± 0.30	-3.97 ± 0.30
Fe	-3.32 ± 0.09	-	-	-4.09 ± 0.25
Ni	-4.46 ± 0.16	-	-	-3.30 ± 0.21

Table 7.1: Logarithmic mass abundances for the N-rich sample of He-sdO stars. For HZ1, the mass abundances were calculated from the averaged abundances resulting from XSHOOTER and UVES.

scenario, the accretion happens slowly and the temperatures remain low, resulting in a lack of occurring nuclear reactions. This means that the chemical composition of the matter in the accretion disk is not changed. The expected abundances would be dominated by composition of the (former) secondary star, hence the observed abundance pattern should match the one of a He core of a RGB star. Fig. 7.3 compares the observed mass abundances to those from a model of RGB He cores (Miller-Bertolami, priv. comm). As RGB cores naturally contain no hydrogen, no expected range is shown here. To get an idea about how much hydrogen is involved, it is necessary to know that He-WDs have comparatively massive hydrogen envelopes [Althaus et al., 2013a]. Their mass can vary roughly between $4 \cdot 10^{-4}$ and $4 \cdot 10^{-3}$ solar masses. As we are dealing with the slow merger scenario in which temperatures remain low, the present hydrogen is not burnt up. This leads to a mass abundance for hydrogen of something between 0.001 and 0.03 or the double values if the hydrogen envelope of the primary is taken into account (Miller-Bertolami, priv. comm.). As the gravitational settling of the elements takes place the hydrogen abundance might even be increased. This results in a large span for the possible hydrogen content which easily covers all of the analyzed N-rich stars in the sample. The abundances of helium, carbon and nitrogen are matching for all stars, except HZ44. For oxygen and neon, HZ1 and HE 1511-1103 respectively are slightly off. HZ44 is below the predictions for all elements. This is not surprising as all model calculations were carried out for a metallicity of $z=0.02$. HZ44 is thought to be a member of Population II, early formed stars with an overall lower content of metals compared with younger stars. But as all elements are below the predictions and the general distribution of the elements in Fig. 7.3 is also reproduced for HZ44, it is likely that it shares the

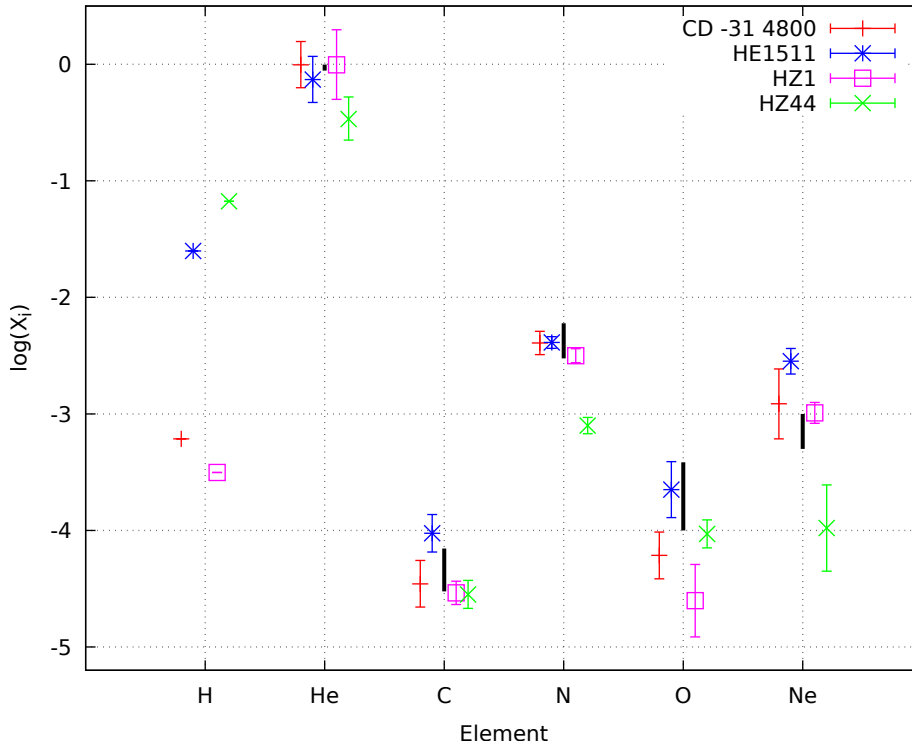


Figure 7.3: Comparison of mass abundances from the N-rich sample to those derived from model calculations of the RGB star He core. The black bars indicate the expected ranges for the mass abundances from nucleosynthesis theory.

same evolutionary history as the rest of the N-rich sample.

Although these considerations supports the theory of the He-WD slow merger, none of the stars shows significant rotation which would be expected after a merger of two stars [Németh et al., 2012]. None of the observed N-rich He-sdOs is known to host a strong magnetic field which might help in explaining the loss of rotation. Therefore, a profound statement on the evolutionary history and development of the N-rich He-sdO stars from this sample cannot be made.

7.2 Formation history of C-enriched He-sdOs

Fig. 7.4 shows the distribution of the carbon rich He-sdO stars from this work in comparison with other He-sdOs from the GALEX sample [Németh et al., 2012] and the He-sdOs analyzed by Hirsch [2009]. For more information on the sample, see chapter 9. With only two stars it is difficult to draw any conclusion from the diagram. The only apparent property is that both stars have quite different surface gravities while being closer together concerning their effective temperature.

Fig. 7.5 shows the position of [CW83] 0904-02 and HE 0958-1151 in a Kiel diagram together with tracks for deep mixing late hot flasher scenarios and a potential shallow mixing case (Tiara Battich, priv. comm.)

For both stars the shallow mixing case can be ruled out, based on the Kiel diagram. The position of [CW83] 0904-02, makes the low mass deep-mixing track

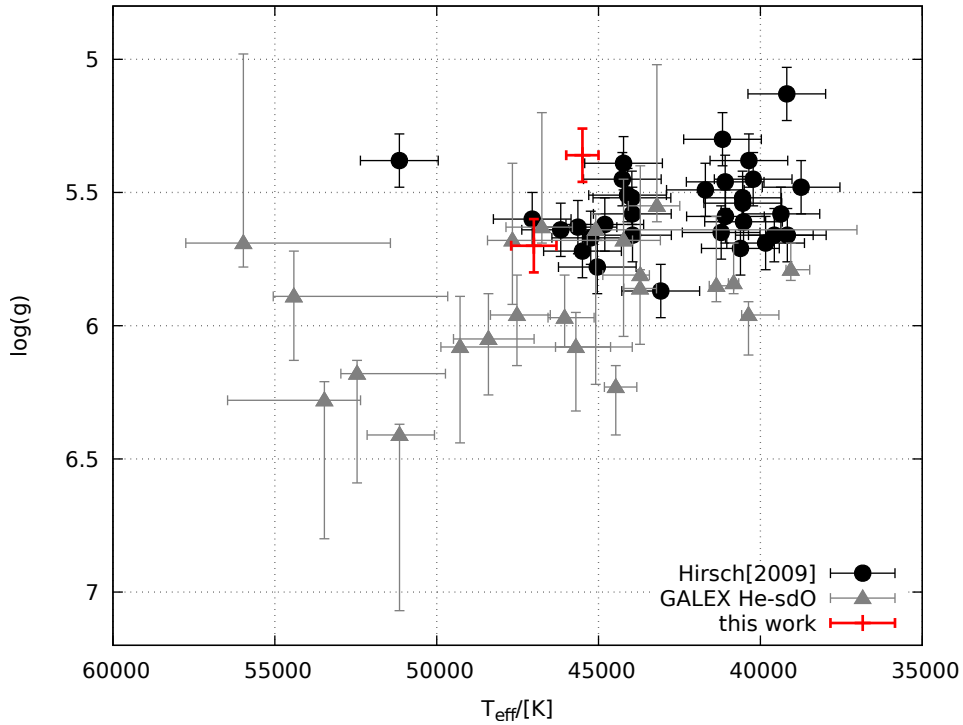


Figure 7.4: Comparison of the C-rich He-sdO subsample with the GALEX sample and the He-sdOs from Hirsch [2009].

unlikely and favors the solutions with heavier stars. HE 0958-1151 is not covered by any tracks and is closest to the intermediate mass deep mixing track. As it cannot be excluded that the errors on the atmospheric parameters have been underestimated, the deep mixing late hot flasher scenario is still the most likely one.

To better compare the element abundances to the predictions of theoretical evolutionary models, table 7.2 shows the mass abundances and errors for the two stars.

In Fig. 7.6 the abundances from table 7.2 are compared to the predictions of theoretical nucleosynthesis models. The overall agreement is quite good, only nitrogen shows clear deviations. As the formation history of the C-rich sample seems to be the same one as for the CN-rich sample, please see Sect. 7.3 for a detailed description on the evolutionary status and sequence.

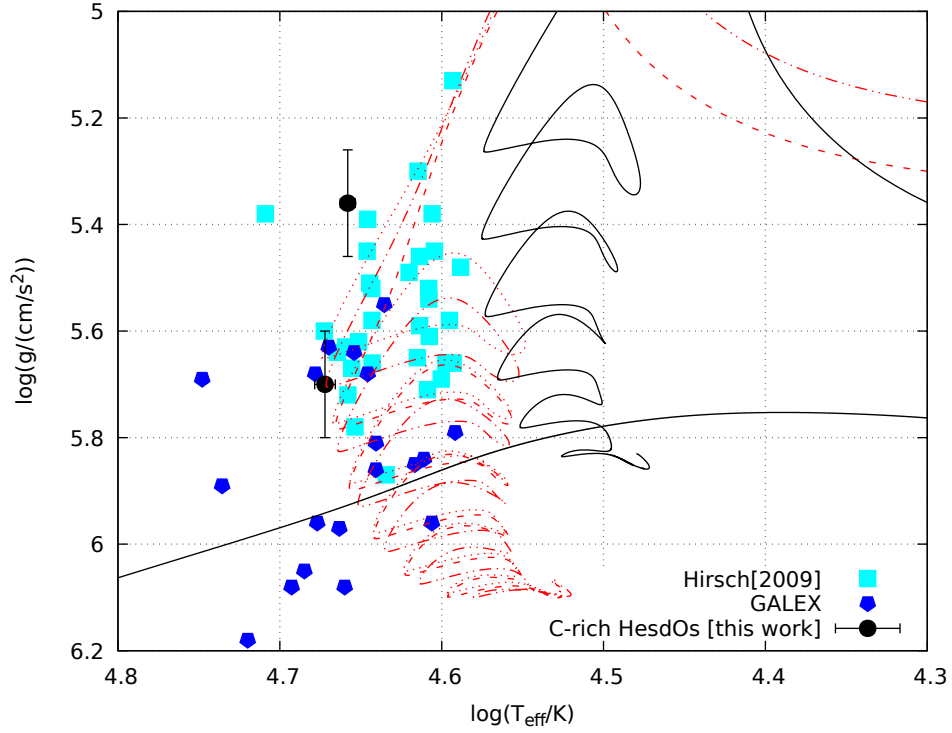


Figure 7.5: Kiel diagram for the C-rich sample of He-sdO stars. Included are the evolutionary tracks for shallow mixing($0.468 M_{\odot}$ /black) and different deep mixing scenarios ($0.455 M_{\odot}$ /dashed, $0.460 M_{\odot}$ /dotted, $0.468 M_{\odot}$ /dashed-dotted) at an initial metallicity of $z=0.02$.

Element	[CW83] 0904-02	HE 0958-1151
H	-2.62	-2.61
He	$1.78 \cdot 10^{-2} \pm 0.29$	$8.77 \cdot 10^{-3} \pm 0.20$
C	-1.65 ± 0.09	-1.87 ± 0.07
N	-3.07 ± 0.10	-3.07 ± 0.15
O	-3.13 ± 0.29	-3.23 ± 0.19
Ne	-2.23 ± 0.26	-2.60 ± 0.11
Mg	-3.43 ± 0.14	-3.60 ± 0.18
Al	-4.07 ± 0.18	-4.58 ± 0.25
Si	-3.67 ± 0.18	-3.64 ± 0.16
P	-4.98 ± 0.13	-5.08 ± 0.21
S	-3.68 ± 0.25	-4.24 ± 0.41
Fe	-3.68 ± 0.17	–
Ni	-4.41 ± 0.18	–

Table 7.2: Logarithmic mass abundances for the C-rich sample of He-sdO stars.

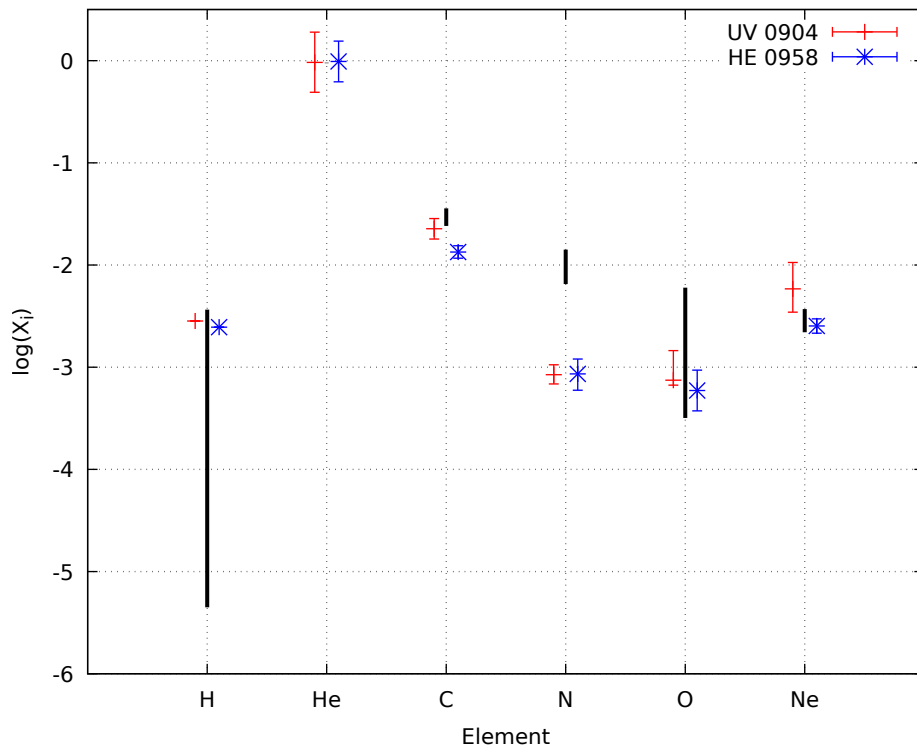


Figure 7.6: Comparison of mass abundances from the C-rich sample to those derived from model calculations. The black bars indicate the expected ranges for the mass abundances from nucleosynthesis theory.

7.3 Formation history of CN-enriched He-sdOs

Fig. 7.7 shows the distribution of the carbon/nitrogen rich He-sdO stars from this work in comparison with other He-sdOs from the GALEX sample [Németh et al., 2012] and He-sdOs analyzed by Hirsch [2009]. For more information on the sample, see chapter 9. In contrast to the nitrogen rich He-sdO stars, those enriched in car-

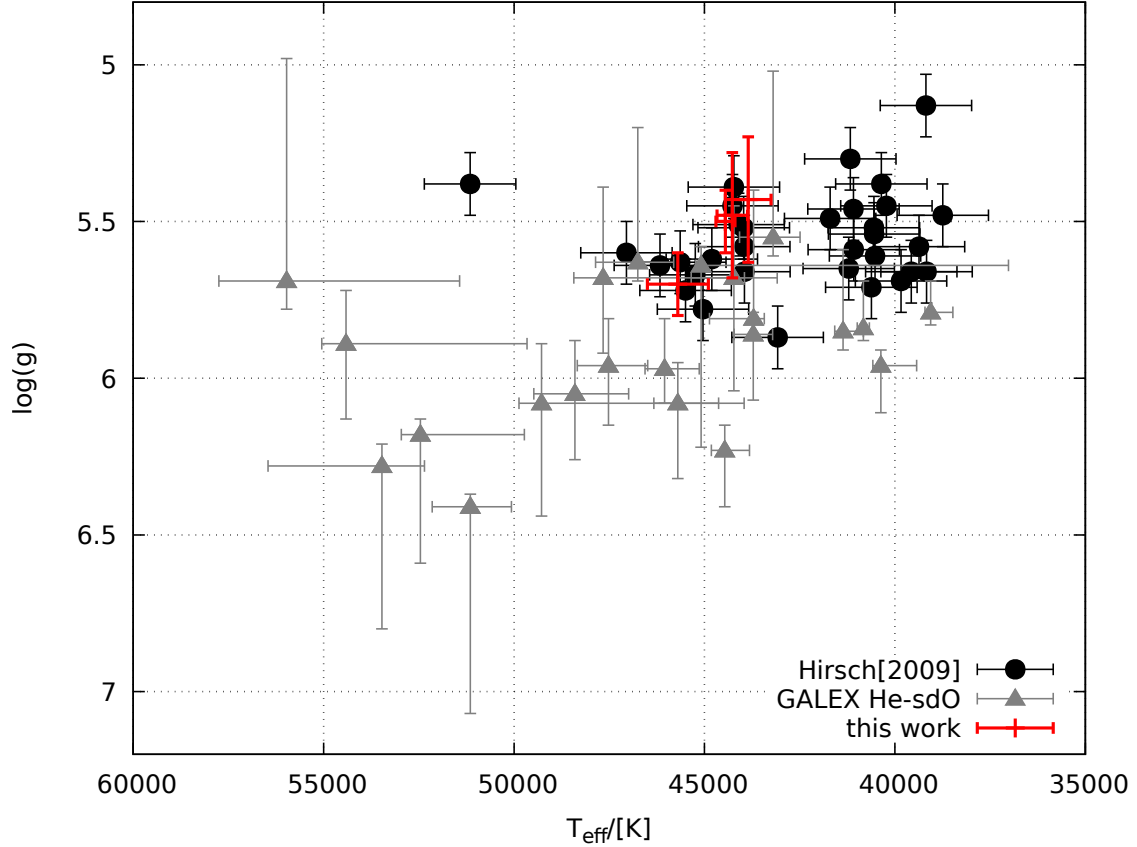


Figure 7.7: Comparison of the CN-rich subsample of He-sdOs with the GALEX sample and the He-sdOs from Hirsch [2009].

bon and nitrogen show a large spread when it comes to their surface gravity and a comparatively narrow temperature window. The later vary in between roughly 2000 K while the $\log(g)$ spans 0.3 dex.

Fig. 7.8 shows the location of the CN-rich sample stars in a Kiel diagram with evolutionary tracks for the deep mixing hot flasher scenario and a shallow mixing case (Tiara Battich, priv. comm.). The deep mixing tracks are plotted for different stellar masses. For all four stars, a shallow mixing scenario can be ruled out. Due to the comparatively large atmospheric parameters, it is not possible to make any estimates about the mass from the tracks. For GALEX J095256.6-371940, the low mass model of the deep mixing late hot flasher can be excluded. For the remaining ones, all deep mixing tracks are covered by the errorbars.

A potential He-WD merger scenario seems unlikely as it would require an extreme fine tuning of the merger properties and the final mass of the stars to get an enrichment of carbon and nitrogen at the same time [Zhang and Jeffery, 2012]. As

explained below, the deep-mixing late hot flasher scenario allows to explain the observed properties far more easily without fine tuning.

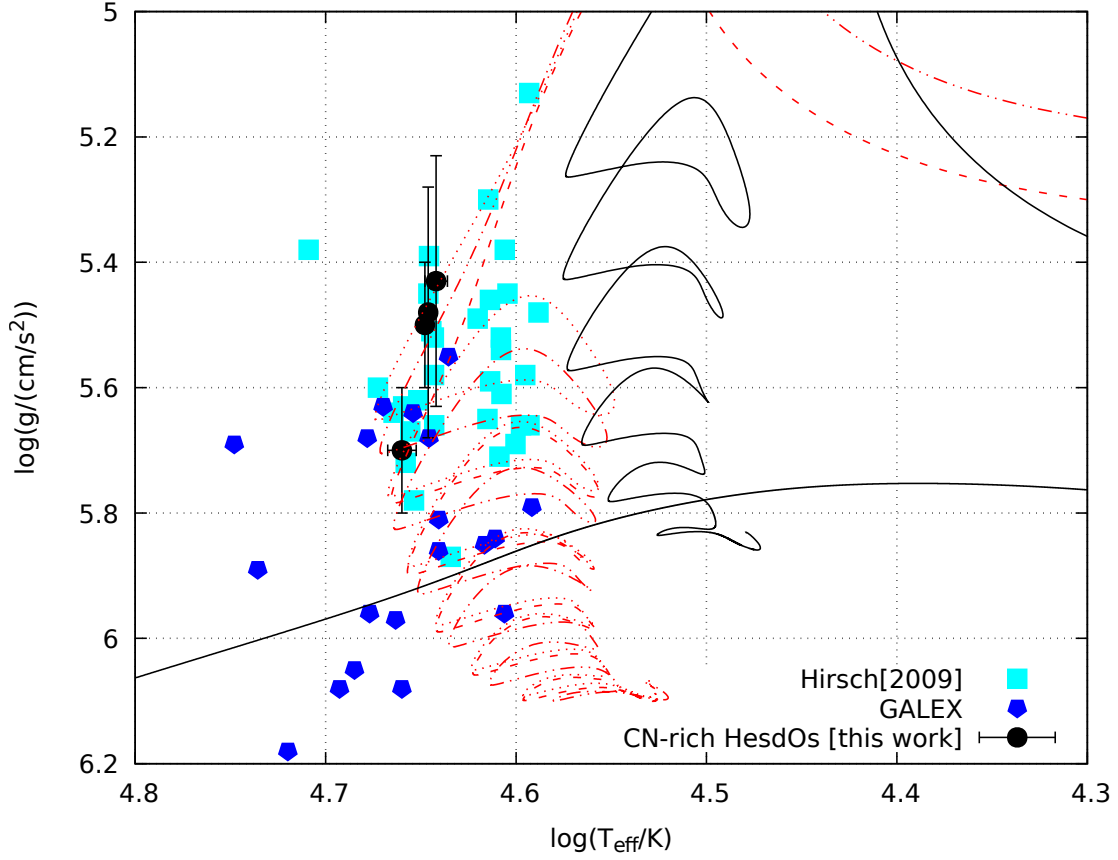


Figure 7.8: Kiel diagram for the CN-rich sample of He-sdO stars. Included are the evolutionary tracks for shallow mixing ($0.468 M_{\odot}$ /black) and different deep mixing scenarios ($0.455 M_{\odot}$ /dashed, $0.460 M_{\odot}$ /dotted, $0.468 M_{\odot}$ /dashed-dotted) at an initial metallicity of $z=0.02$.

To simplify the comparison with calculated evolutionary models, table 7.3 shows the mass abundances and the corresponding errors for all stars of the CN rich sub-sample.

In Fig. 7.9 the mass abundances of table 7.3 are compared to the predictions of nucleosynthesis theory in the case of a deep mixing event. The overall accordance is well visible. The hydrogen, helium and oxygen abundances are matching perfectly. While carbon and nitrogen are less abundant than predicted by the models, neon is enriched compared to the theoretical values. The deviations concerning nitrogen and neon might be linked to each other and caused by the shortcomings of a 1D modeling of the flashing event (M.M. Miller-Bertolami, priv. comm). If the modeling would be carried out in three dimensions, the convective regions of the He- and the H-flash would not be disconnected, which they are in the one dimensional case. Nitrogen being generated in the H-flash region could come in contact with the He-flash region where it can be burnt up to ^{22}Ne . The neon could leak back to the H-flash part of the star. This would enhance the neon abundance on the cost of nitrogen and bring observations and models closer together.

Element	LSS 1274	LS IV +109	[CW83] 0832-01	GaJ095256.6-371940
H	-2.79	-2.79	-3.61	-3.61
He	$-2.22 \cdot 10^{-2} \pm 0.20$	$-1.32 \cdot 10^{-2} \pm 0.24$	$-1.32 \cdot 10^{-2} \pm 0.20$	$-1.32 \cdot 10^{-2} \pm 0.19$
C	-1.69 ± 0.05	-2.11 ± 0.13	-1.74 ± 0.05	-2.03 ± 0.09
N	-2.75 ± 0.05	-2.39 ± 0.04	-2.71 ± 0.06	-2.44 ± 0.08
O	-3.39 ± 0.10	-2.85 ± 0.09	-3.05 ± 0.18	-2.64 ± 0.15
Ne	-2.23 ± 0.09	-1.94 ± 0.05	-2.01 ± 0.09	-2.10 ± 0.09
Mg	-3.37 ± 0.23	-3.16 ± 0.11	-3.22 ± 0.09	-3.20 ± 0.15
Al	-4.01 ± 0.12	-4.04 ± 0.07	-4.09 ± 0.09	-4.18 ± 0.14
Si	-3.44 ± 0.08	-2.96 ± 0.07	-3.35 ± 0.13	-2.88 ± 0.11
P	-5.21 ± 0.13	-4.98 ± 0.10	-4.73 ± 0.11	-4.89 ± 0.21
S	-4.04 ± 0.09	–	-3.68 ± 0.18	-3.64 ± 0.16
Fe	-3.47 ± 0.08	-3.38 ± 0.09	–	–
Ni	-3.64 ± 0.10	-4.07 ± 0.13	–	–

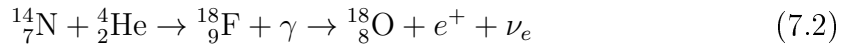
Table 7.3: Logarithmic mass abundances for the CN-rich sample of He-sdO stars.

To understand the development of the individual elements over time, Fig. 7.10 shows the evolution of carbon, nitrogen, oxygen and neon between the He-flash (at $t=0$) and the H-flash shortly after $t=1$.

During the He-flash the amount of ^{12}C is increased at the expense of helium by the triple α process.



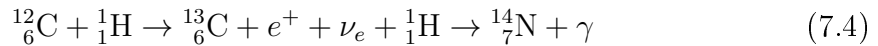
At the same time ^{18}O and ^{22}Ne are enriched while ^{14}N is depleted by the following reactions.



and



After the H-flash set in ^{12}C is enriched for a short time before being transformed to ^{14}N (and partly ^{13}C) by



Neon remains untouched at this stage as the temperatures are not high enough. Fig. 7.10 shows the development of the important element abundances in the convection zone between the He- and the H-flash in the simulation of a deep mixing event with an initial metallicity of $z=0.02$ (Tiara Battich, priv. comm.). It is based on the equations stated above. The intermediate mass elements like magnesium, aluminum, silicon, phosphorus and sulfur are expected to remain unaltered by the deep mixing hot flasher scenario as the temperatures are still too low to start nuclear

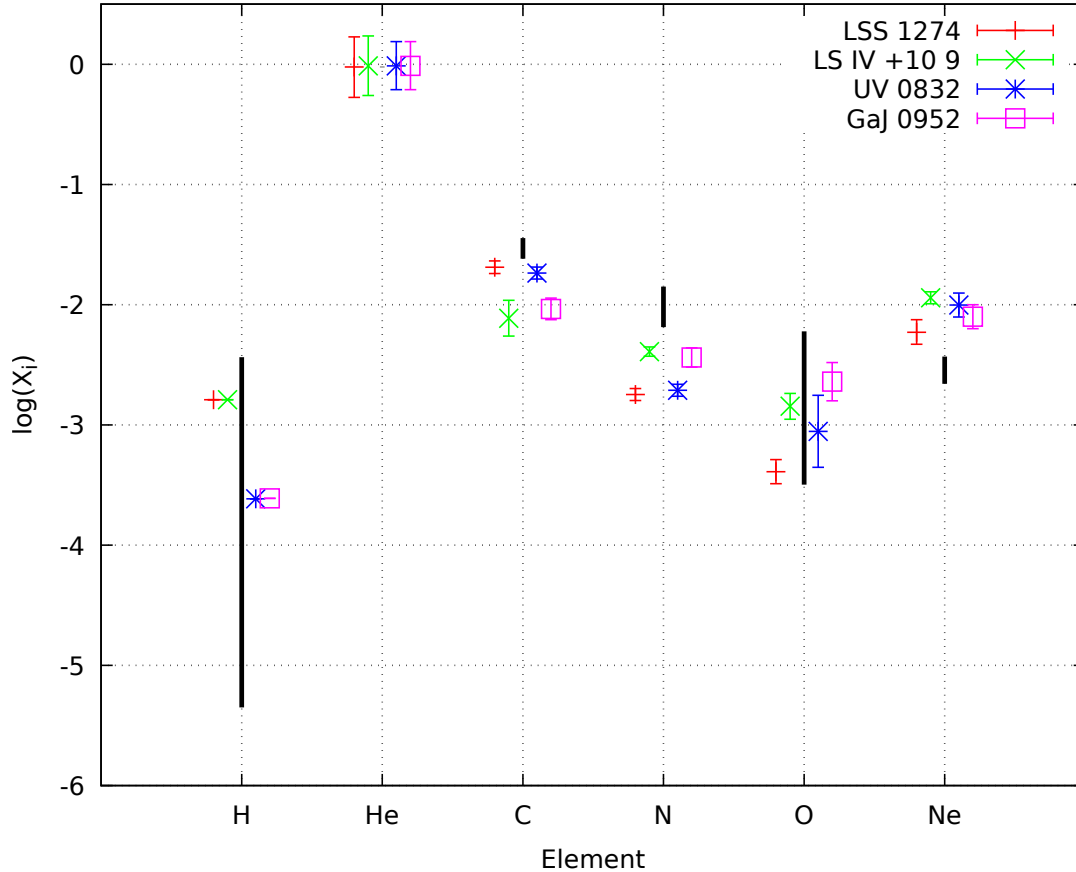


Figure 7.9: Comparison of mass abundances from the CN-rich sample to those derived from model calculations. The black bars indicate the expected ranges for the mass abundances from nucleosynthesis theory.

reactions with these elements.

As some of the C-rich and CN-rich stars show significant rotation the question if these stars can as well be explained by the deep mixing hot flasher scenario has to be asked. For the four questionable stars, [CW83] 0832-01, GALEX J095256.6-371940, [CW83] 0904-02 and HE 0958-1151 the alternative scenario of a composite merger seems considerable.

As already explained in Sect. 2.1.3.2, the composite merger scenario is a mixture of the slow/cool merger and the fast/hot merger of two He-core WDs. After the disruption of the less massive star, parts of the stellar matter form a disc around the remaining star from which matter is slowly accreted. This does not alter the chemical composition of the material. The other material forms a hot, spherical corona around the more massive star which could easily reach temperatures of about 10^8 K [Zhang and Jeffery, 2012]. Fig. 7.11 till Fig. 7.18 illustrate the expected mass abundances for carbon, nitrogen, oxygen and neon from the composite merger scenario. For carbon and nitrogen, tracks for a metallicity of $z=0.001$ and $z=0.02$ are shown while for oxygen and neon, only the higher metallicity is pictured. The displayed track for oxygen results from the combination of O16 and O18, while neon shows the combination of the two isotopes Ne20 and Ne22 (see Zhang and Jeffery [2012] Fig. 22 for details on the O16/O18 ratio for the different masses. For Ne20 a mass

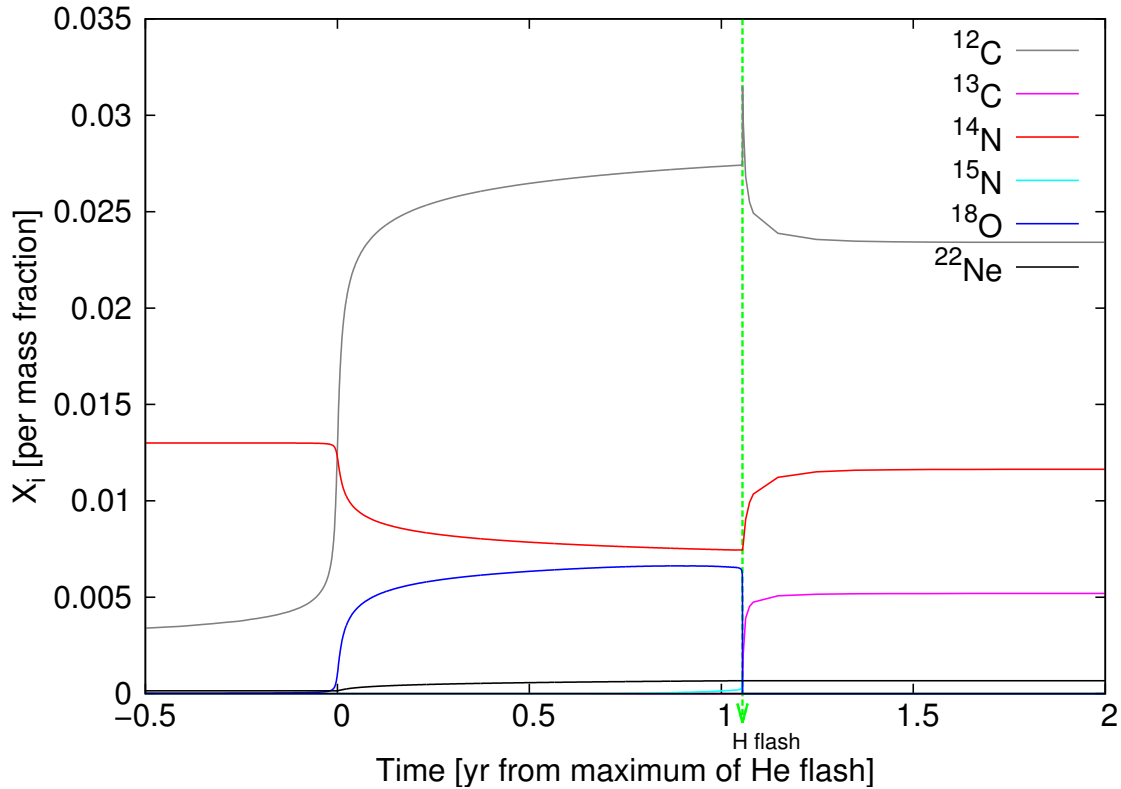


Figure 7.10: Development of chemical abundances after the He- and the H-flash.

abundance of $1.88 \cdot 10^{-3}$ was adopted (Miller-Bertolami, priv. comm.)

For [CW83] 0832-01 the expected abundances for carbon and nitrogen are matching with the observations and a mass around 0.8 solar masses can be concluded. The observed neon content is in accordance with this assumption while the predicted oxygen abundance is too high at this mass. To match oxygen, a composite mass of 0.6 solar masses or below would be required which is not compatible with the other elements.

When assuming the high metallicity of $z=0.02$ for GALEX J095256.6-371940, both carbon and nitrogen match the expectations from the merger model around 0.77 solar masses. In addition the neon abundance matches the predictions from around 0.72 to 0.78 solar masses. However the values for oxygen deviate and are only matching between 0.62 and 0.68 solar masses. This is not in good agreement with the other elements. As for around $0.78 M_{\odot}$ only the oxygen abundance is slightly off the composite merger cannot be ruled out completely for GALEX J095256.6-371940.

Concerning [CW83] 0904-02, carbon and nitrogen match the predictions. If a metallicity of $z=0.02$ is assumed, the mass has to be larger than 0.8 solar masses. While the measured neon abundances agrees well with the predictions, oxygen is too low. For HE 0958-1151, carbon and nitrogen are matching again, but neither oxygen nor neon match the predictions from the composite merger model.

To sum it up, GALEX J095256.6-371940 shows an acceptable agreement with the expectations from a composite merger, substantiated by its rotations.

For the other stars the composite merger scenario can be ruled out as the deviations between the measured abundances and model predictions are too large.

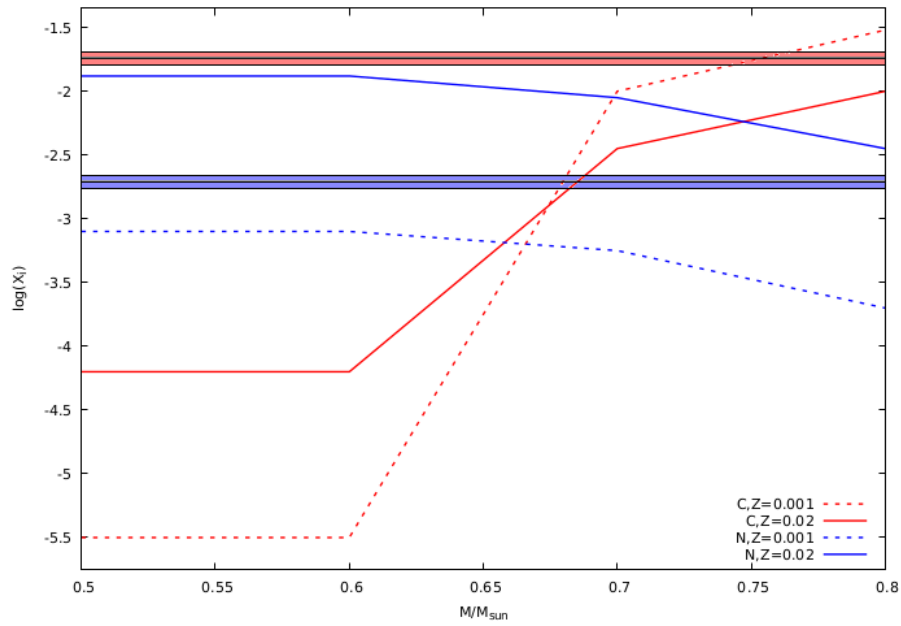


Figure 7.11: Mass abundances for C and N expected from the composite mixing scenario compared to those measured in [CW83] 0832-01. Adopted from Zhang and Jeffery [2012].

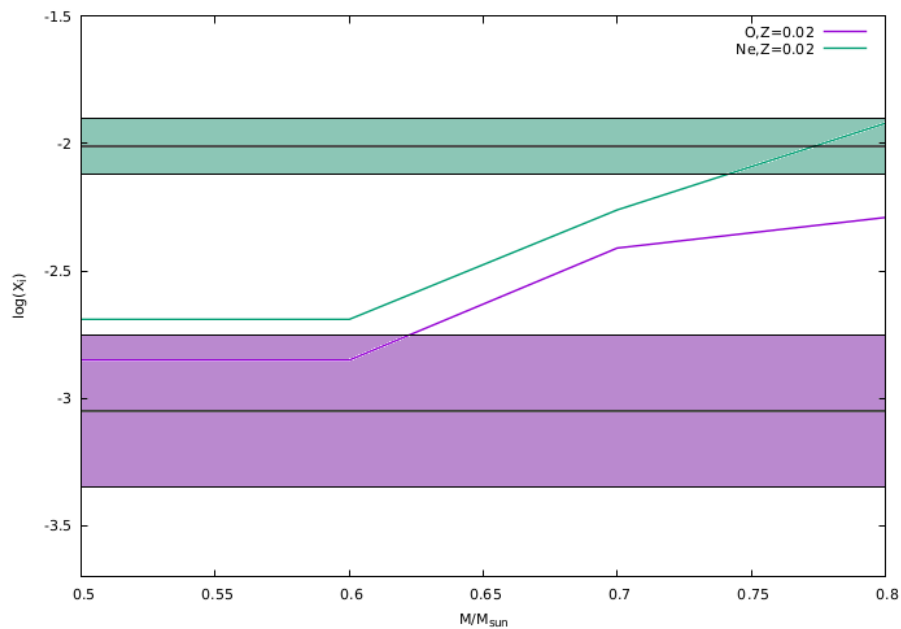


Figure 7.12: Mass abundances for O and Ne expected from the composite mixing scenario compared to those measured in [CW83] 0832-01. Adopted from Zhang and Jeffery [2012].

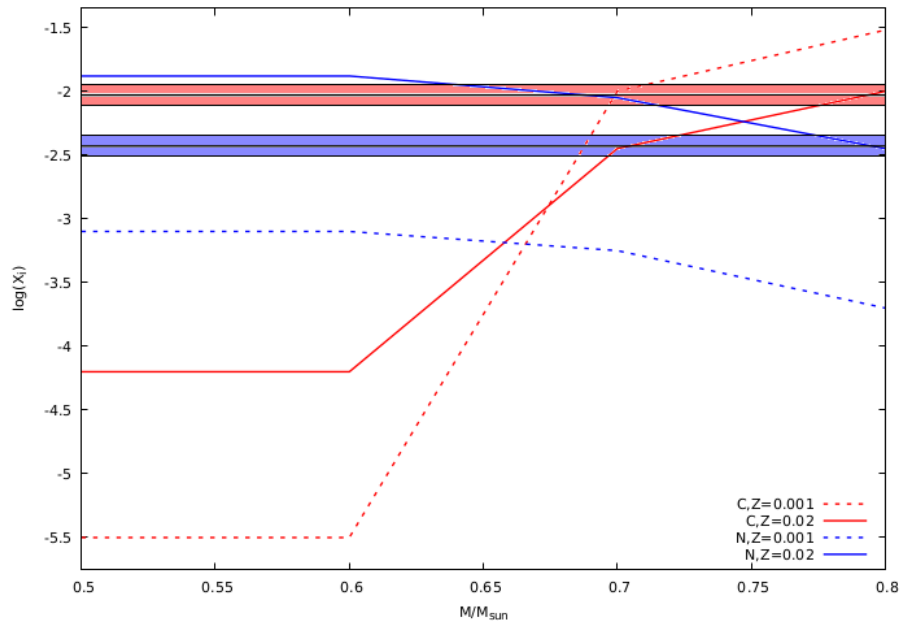


Figure 7.13: Mass abundances for C and N expected from the composite mixing scenario compared to those measured in GALEX J095256.6-371940. Adopted from Zhang and Jeffery [2012].

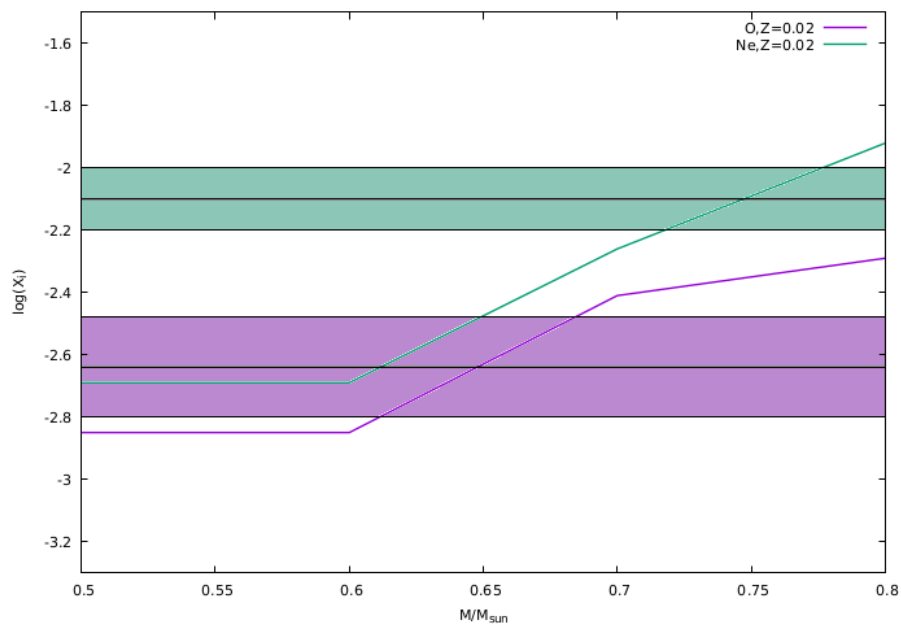


Figure 7.14: Mass abundances for O and Ne expected from the composite mixing scenario compared to those measured in GALEX J095256.6-371940. Adopted from Zhang and Jeffery [2012].

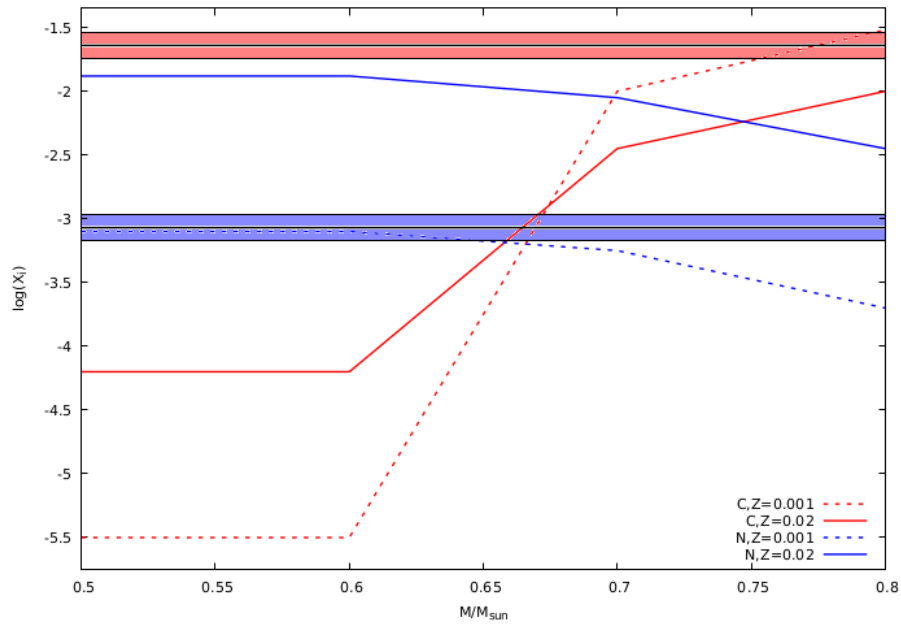


Figure 7.15: Mass abundances for C and N expected from the composite mixing scenario compared to those measured in [CW83] 0904-02. Adopted from Zhang and Jeffery [2012].

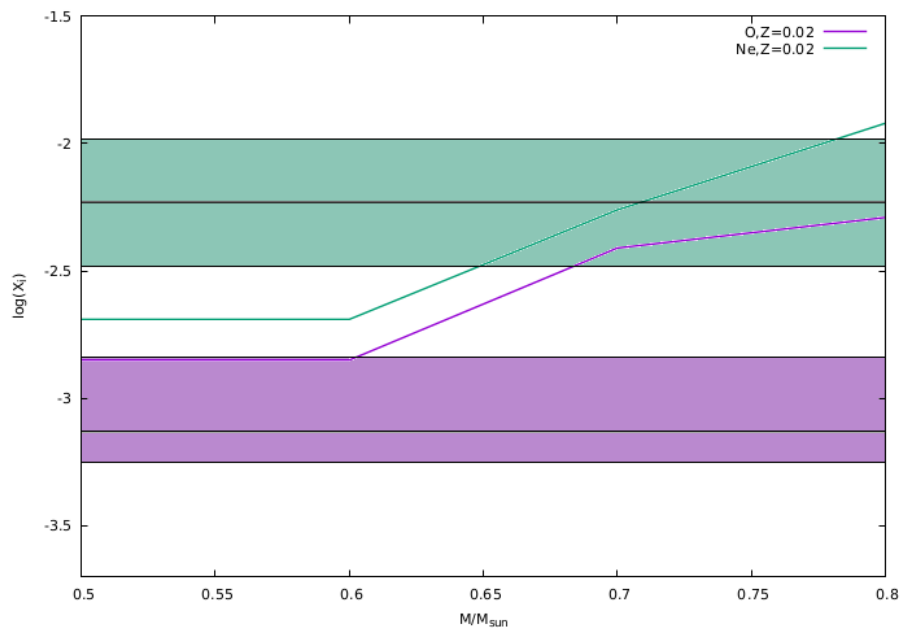


Figure 7.16: Mass abundances for O and Ne expected from the composite mixing scenario compared to those measured in [CW83] 0904-02. Adopted from Zhang and Jeffery [2012].

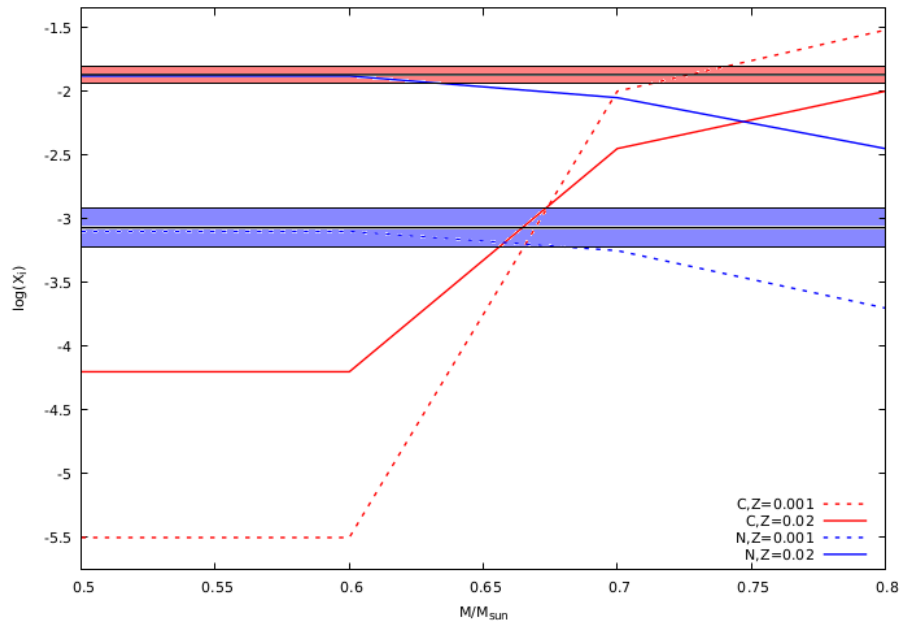


Figure 7.17: Mass abundances for C and N expected from the composite mixing scenario compared to those measured in HE 0958-1151. Adopted from Zhang and Jeffery [2012].

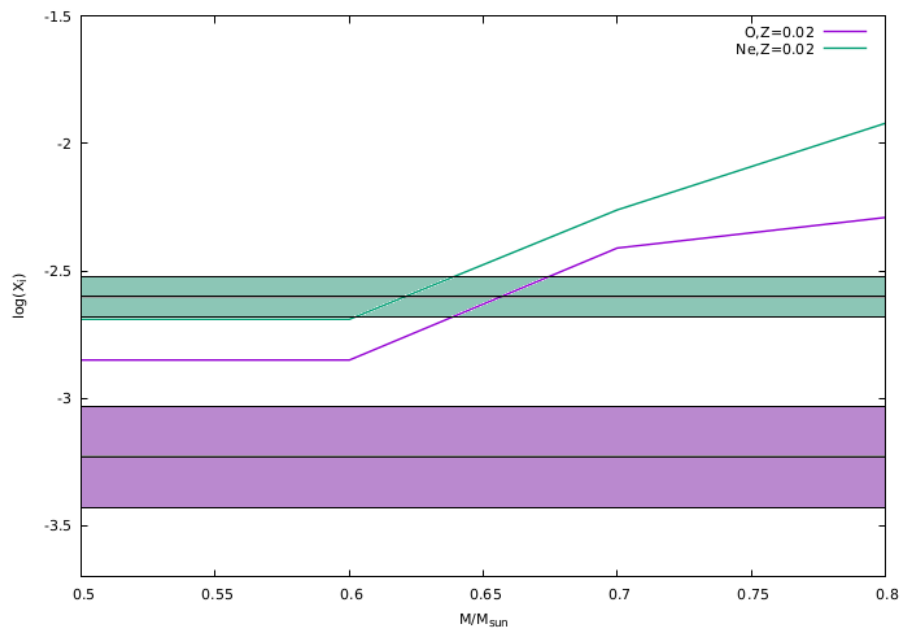


Figure 7.18: Mass abundances for O and Ne expected from the composite mixing scenario compared to those measured in HE 0958-1151. Adopted from Zhang and Jeffery [2012].

7.4 Remarks on the formation history of BD+39° 3226

BD+39° 3226 most likely belongs to the halo population, however a kinematic analysis would also allow for a thick disk origin [Heber 2018, priv. com.]. As expected for a halo star, the overall metallicity of BD+39° 3226 is low. BD+39° 3226 most likely belongs to Population II. These stars are very old and have an overall lower metallicity than those from later populations. The expected enrichment of the α -elements was not observed. Only magnesium is significantly enriched, while silicon is depleted compared to the rest of the intermediate mass elements. It is difficult to draw conclusion on the evolutionary history of this particular star, as the models available to the author do not cover such low metallicities. Regarding the clearly visible CNO bi-cycle abundance pattern, BD+39° 3226 looks like one the of the N-rich He-sdO stars that originated from the slow merger scenario. Having in mind that the intermediate mass elements are about solar in the sample stars analyzed so far, shifting all metal abundances up by a factor of ~ 50 would result in the well known distribution of elements.

It is therefore likely that BD+39° 3226 is indeed the result of a slow merger and proofs that this scenario already occurred in earlier days of our galaxy.

8 Analysis of US708

The He-sdO US708 was first discovered by Usher and Mitchell [1982] as a faint blue object at high galactic latitude during a survey conducted with the Palomar Schmidt camera. It was the second discovered Hypervelocity star [Hirsch et al., 2005] and got its name from the measured radial velocity of 708 km/s.

It is found at $\alpha = 09^{\text{h}}33^{\text{m}}20.87^{\text{s}}$ and $\delta = +44^{\circ}17'05.52''$ with a visible magnitude of 18.8.

A more recent examination by Geier et al. [2015a] concluded a higher radial velocity of 917 ± 7 km/s, resulting in a Galactic restframe velocity of 1157 ± 53 km/s. It is moving away from us and has a current distance of about 8.5 kpc. By computing orbit trajectories, Geier et al. [2015a] showed that US708 crossed the Galactic disk 14 ± 3.1 Myr ago and excluded the center of our Galaxy as a possible origin with very high confidence (and therefore also the acceleration by the supermassive black hole found there). US 708 is found in an evolutionary stage where it has already evolved away from the Extreme Horizontal branch.

Up to now, the most likely scenario for US708 having such a high velocity, is the supernova Ia ejection scenario, more precisely, the ejection as a result of the double detonation of a white dwarf. In this scenario, a low-mass helium star and a massive white dwarf are in a close orbit around each other. Usually the two stars approach each other and the orbit shrinks because of the emission of gravitational waves. Once a certain limit is reached, mass will be transferred from the helium star to the white dwarf via Roche lobe overflow. As a certain amount of helium had been accreted on the surface of the white dwarf, the criterion for helium burning is fulfilled, the helium is ignited and a shockwave travels through the white dwarf. This shockwave can be powerful enough to trigger the explosion of the CO material and therefore the dwarf itself, resulting in a supernova Ia.

A possible progenitor system for such an event, fulfilling all criteria has already been found, CD-30°11223.

But even for the supernova ejection scenario, the velocity of US708 is still very high. This would conclude that the progenitor system had been very close, with an orbital period of only about 10 min. Also the white dwarf companion would have to be comparatively massive. According to Geier et al. [2015a], the most likely configuration is a massive CO-WD with $1.1 \pm 0.1 M_{\odot}$ and a compact helium star with $0.3 M_{\odot}$. The resulting accretion rate for helium is 10^{-9} to $10^{-8} M_{\odot} \text{ yrs}^{-1}$. As one would expect for a supernova ejection, US708 shows a high rotational velocity v_{rot} (about 115 km/s), as the subdwarf experiences tidal influences that lead to a spin up.

$$v_{\text{rot}} = \frac{2\pi R_L}{P} \quad (8.1)$$

By demanding conservation of angular momentum, the fast rotation should remain even after the disruption of the system and the ejection of the companion.

But if an ultracompact binary progenitor is assumed, the measured rotation should

be about four times higher than it is [Geier et al., 2015a]. To solve this problem, it has to be taken into account that the supernova impact can trigger a loss of mass and angular momentum [Liu et al., 2013a]. This phenomenon is predicted for MS companions, however the effect should be smaller for more compact objects like US708.

Certainty on the acceleration mechanism (and the origin of the rotation) could only be achieved by finding direct evidence for a nearby supernova explosion in the atmosphere of US708. As outlined in Sect.2.4.1 this scenario is likely to change the surface abundances of the star and lead to an enrichment in iron and nickel [Pan et al., 2012, Liu et al., 2013b]. By determining their abundance and comparing it to other He-sdOs with a similar chemical composition, it is possible to detect over- (or under-) abundances that could be the key to a profound understanding of US708's past.

8.1 General procedure

The first approach to model the low-resolution UV data with the standard method of fitting certain lines/regions for one specific element and iterating this over all elements with atomic data available soon turned out to be not practical. The bad resolution (and fast rotation in the case of US708) led to a wide spread concerning the abundances which usually covered several magnitudes! Therefore it was decided to utilize XTGRID (see sect. 4.11) to model the spectra. Although XTGRID is capable of fitting atmospheric parameters and abundances in parallel, it was decided to determine the abundances from the available optical spectra using the HHeCNO grid and fixing these values. The fitting procedure for US708 and the comparison star (both optical and UV) was carried out by ASTROSERVER.ORG [Németh, 2017]. The analysis included the first 30 element from the periodic table (some under LTE conditions), although not all elements show visible lines in the optical and/or UV. Especially in the later one, the lines are heavily blended due to line crowding and the low resolution of the available UV spectra. This blending leads to the formation of a strong pseudocontinuum. By including more elements than directly visible, it became easier to place the pseudocontinuum and the quality of the fit improved. If strong interstellar lines were detected in the data, they were cut out to reduce systematic effects. As described in the following sections, The UV data were fitted alone and together with their optical counterpart. The two different wavelength ranges were fitted together, they were divided in smaller subranges and a weight was assigned to each of the subranges based on the S/N ratio of that particular region.

8.2 Revisiting CD -31° 4800

Before switching to the analysis of US 708, and old friend, CD-31° 4800, had to be revisited. As especially the abundances of iron and nickel are of interest, some reference level had to be set. Four of the stars in this thesis had usable UV spectra to determine the enrichment or iron and nickel¹, among which only CD-31° 4800 shows a similar chemical composition with the typical CNO pattern emerging from

¹At the time the analysis of US708 was finished.

the CNO burning bi-cycle. For this reason, it was chosen as a comparison star for US 708, meaning it had to be analyzed in the same way and with the same methods as its speeding counterpart.

or the analysis, two datasets were used: the HST-COS spectrum and the UVES spectrum, already used in Sect. 6.1.1 (see Sect. .1 for details on the spectra). The COS and KECK spectra were fitted together, in addition the COS spectrum was fitted alone. As the atmospheric parameters have already been well determined, it was decided to fix them to the values determined in Sect. 6.1.1. These are

- $T_{\text{eff}} = 42230 \pm 300 \text{ K}$
- $\log(g) = 5.60 \pm 0.03$
- $\log(n(\text{He})/n(\text{H})) = 2.61 \pm 0.06$
- $v_{\text{rot}} < 5 \text{ km/s}$

Model 2 with the higher surface gravity was not considered as most of the test made during this work pointed towards the lower $\log(g)$. Despite being fixed, errors were calculated for the atmospheric parameters.

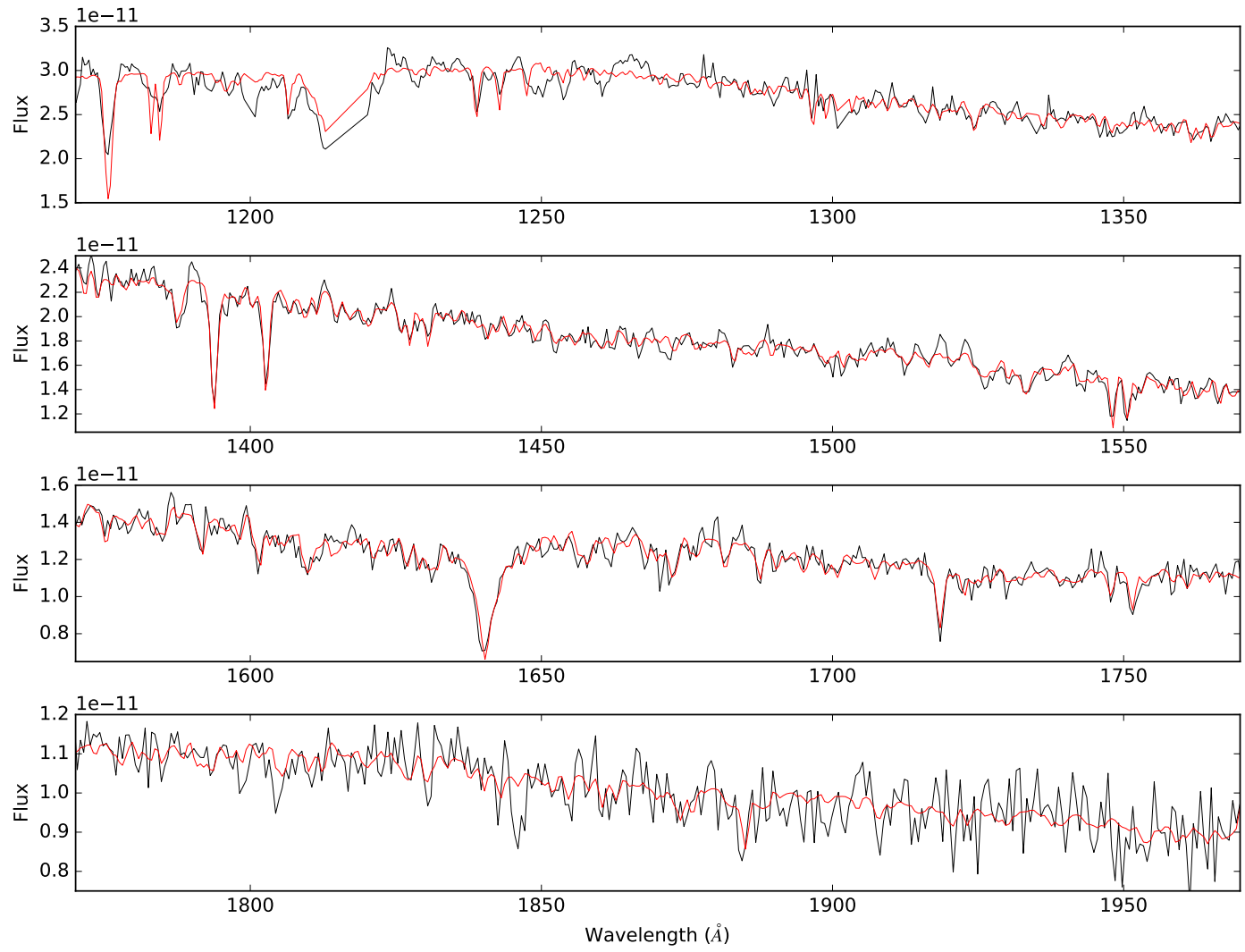


Figure 8.1: Fit to the COS spectrum of CD-31° 4800 with XTGRID.

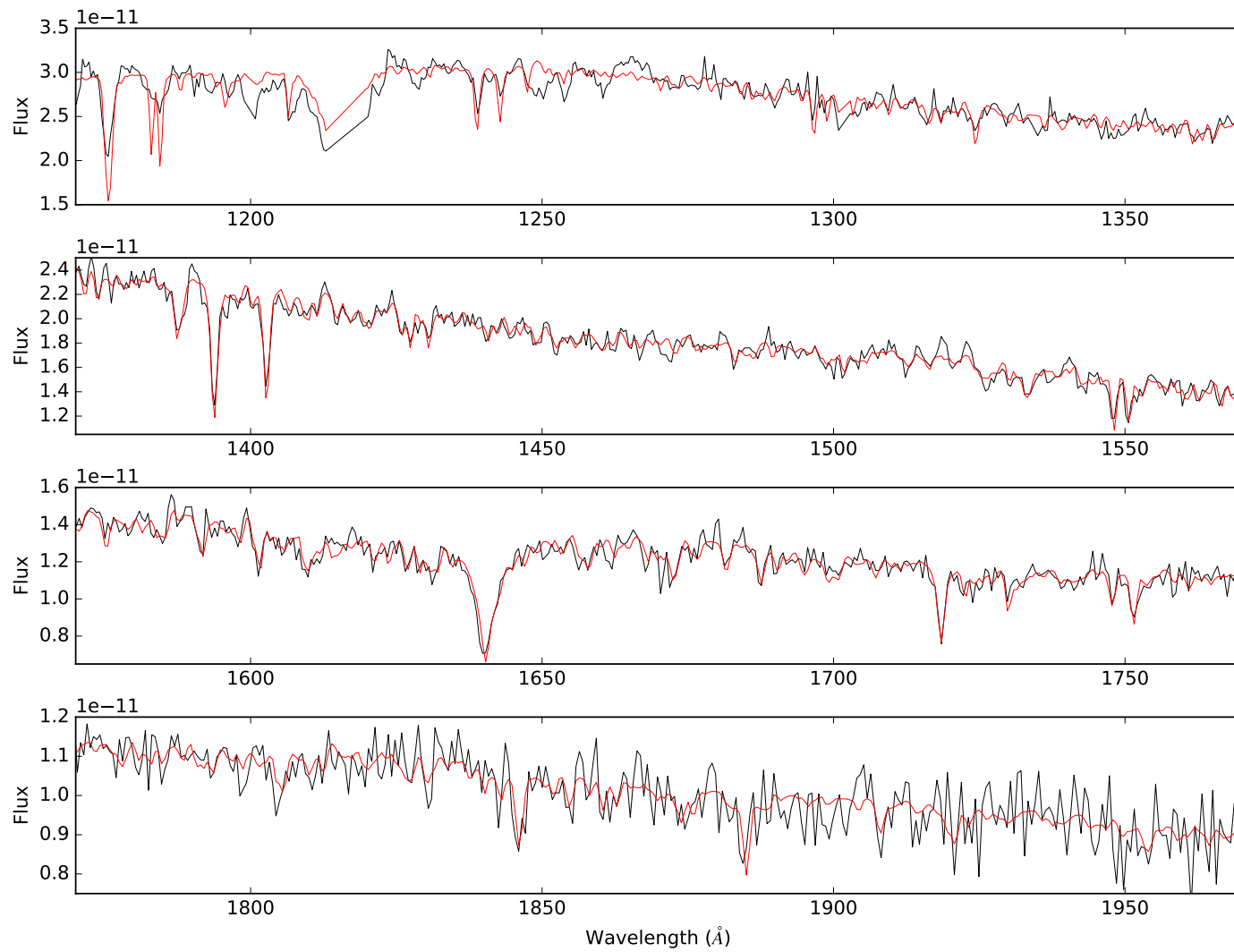


Figure 8.2: Fit to the COS part of the combined COS+UVES spectrum of CD-31° 4800 with XTGRID.

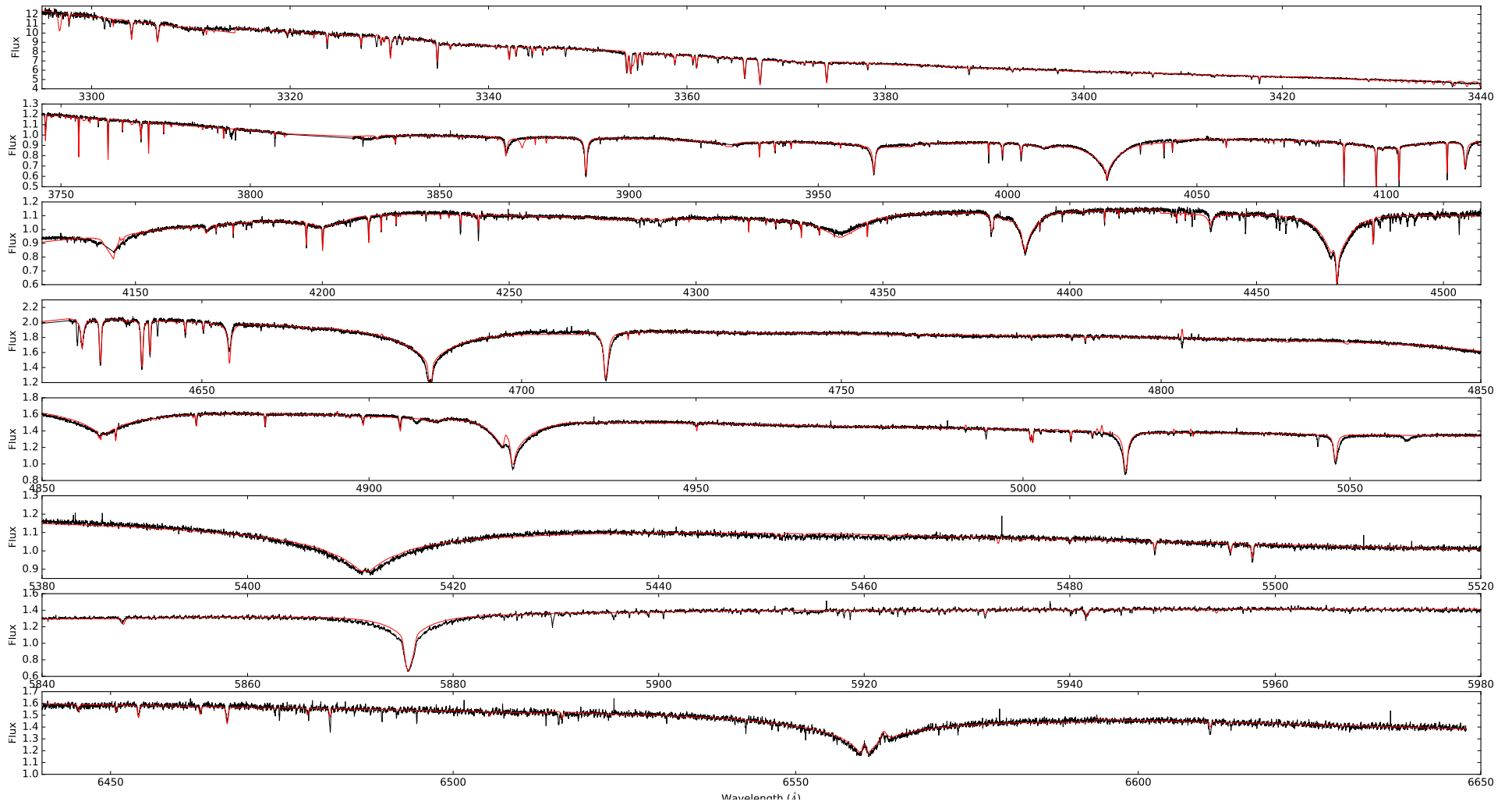


Figure 8.3: Fit to selected parts of the UVES spectrum of CD-31° 4800 with XTGRID.

In the fit of the UVES spectrum, the Pickering Problem is visible again, especially around 4340 Å. This proves that the way the models were calculated and fitted cannot be the cause of the non-matching lines. After all, the overall shape of the spectrum is well reproduced. Beyond 5050 Å, several regions were cut out, mostly because of the contamination of the spectrum by telluric lines. The important helium lines in this part of the spectrum were kept.

Regarding the COS spectrum of CD-31° 4800, the spectral part around the Lyman α line as well as several interstellar lines towards the blue end were cut out and omitted.

Especially in the wavelength range between 1350 Å and 1450 Å, the fit almost resembles the data, indicating a very low noise level. Towards the bluer or redder end, the deviations increase. Beyond 1700 Å the S/N ratio of the data decays rapidly. This behavior can be explained by looking at the COS throughput in the following image. While peaking around 1250 Å and still being very high in the wavelength

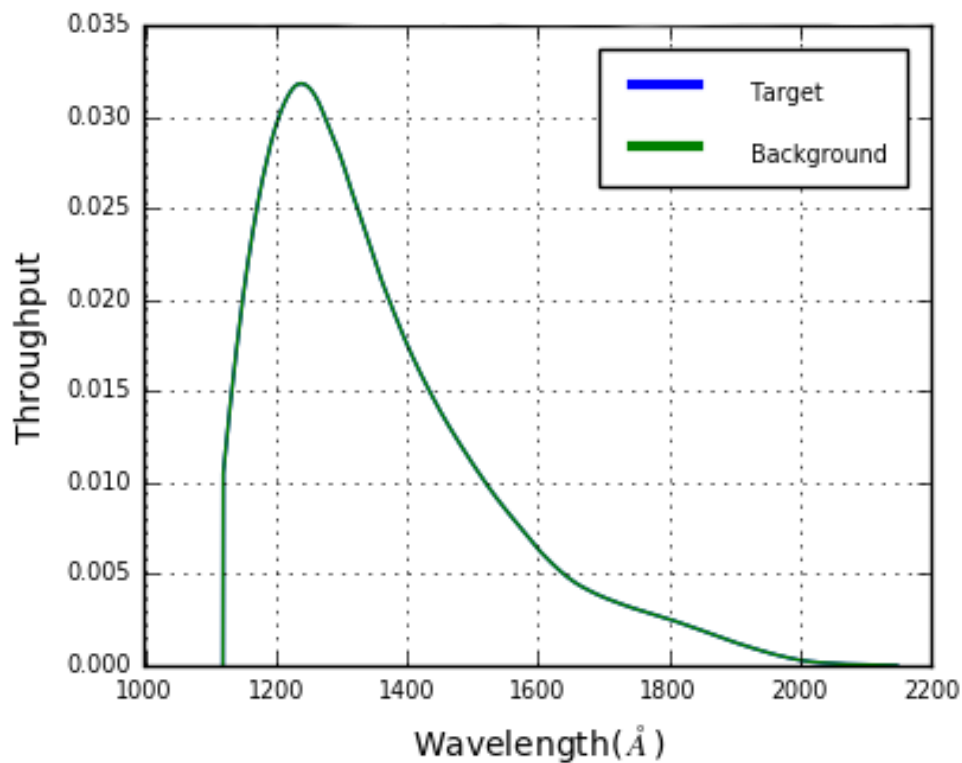


Figure 8.4: Throughput of the COS spectrograph using the G140 grating.(P.Németh, private communication)

window mentioned above, the general shape matches the S/N ratio of the data very well.

The following tables shows the relative mass abundances (with respect to the solar value) for the COS fit as well as the UVES+COS fit as determined by the XTGRID fitting procedure.

Element	β/β_{\odot} COS	β/β_{\odot} COS+UVES
H	$8 \cdot 10^{-4}$	$8 \cdot 10^{-4}$
He	$3.535^{+0.285}_{-0.598}$	$3.974^{+0.129}_{-2.023}$
C	$0.013^{+0.002}_{-0.002}$	$0.013^{+0.013}_{-0.005}$
N	$2.086^{+1.347}_{-0.559}$	$7.290^{+0.963}_{-0.737}$
O	$(0.002^{+0.003}_{-x})$	$(0.005^{+0.024}_{-x})$
F	(57.610^{+x}_{-x})	(45.320^{+x}_{-x})
Ne	$7.018^{+240.1}_{-5.832}$	$0.683^{+0.709}_{-0.083}$
Na	$(2.440^{+50.80}_{-x})$	(4.830^{+102}_{-x})
Mg	$(0.125^{+0.710}_{-x})$	$0.721^{+0.626}_{-0.373}$
Al	$(0.086^{+0.369}_{-x})$	$(0.290^{+2.312}_{-x})$
Si	$0.645^{+0.198}_{-0.159}$	$1.030^{+0.089}_{-0.329}$
P	$(0.004^{+0.403}_{-x})$	$(0.028^{+3.360}_{-x})$
S	$0.155^{+0.185}_{-0.107}$	$0.400^{+0.560}_{-0.127}$
Cl	$(0.203^{+3.152}_{-x})$	$(0.313^{+24.71}_{-x})$
Ar	$(5.017^{+32.630}_{-x})$	$(1.196^{+2.550}_{-x})$
K	(367^{+x}_{-x})	$(19.570^{+41.47}_{-x})$
Ca	$(0.875^{+3.32}_{-x})$	$(0.255^{+1.12}_{-x})$
Sc	(0^{+x}_{-x})	(100.5^{+x}_{-x})
Ti	$(0.662^{+8.00}_{-x})$	$0.375^{+1.0}_{-0.357}$
V	$(6.040^{+23.90}_{-x})$	(6.080^{+120}_{-x})
Cr	$4.140^{+3.770}_{-2.580}$	$(3.930^{+57.40}_{-x})$
Mn	$(1.301^{+1.25}_{-x})$	$(4.810^{+0.876}_{-x})$
Fe	$0.544^{+0.071}_{-0.121}$	$0.571^{+0.419}_{-0.205}$
Co	$(0.450^{+0.375}_{-x})$	$(0.397^{+0.717}_{-x})$
Ni	$0.512^{+0.21}_{-0.11}$	$0.510^{+2.766}_{-0.321}$
Cu	(569^{+x}_{-x})	(547^{+x}_{-x})
Zn	$16.29^{+41.20}_{-11.58}$	(20.10^{+111}_{-x})

Table 8.1: Relative mass abundances of CD-31° 4800 compared to the solar value for each element. Shown are the results from the COS and the COS+KECK fit. Given are the 1σ errors. An x indicated that no error could be calculated or the error was unrealistically large. Abundances in brackets are those with either no errors or only upper-/lower limits and have to be dealt with carefully.

The results are visualized in the following plots. Fig. 8.5 shows a direct comparison of the results from the COS and the COS+UVES fit, while Fig. 8.6 and Fig. 8.7 compare both fits to the results derived from the UVES and IUE spectra with the standard approach used in this thesis so far. In Fig. 8.5 only elements with proper errors are shown. For a graphical representation of all elements, see Fig. .8 in the appendix.

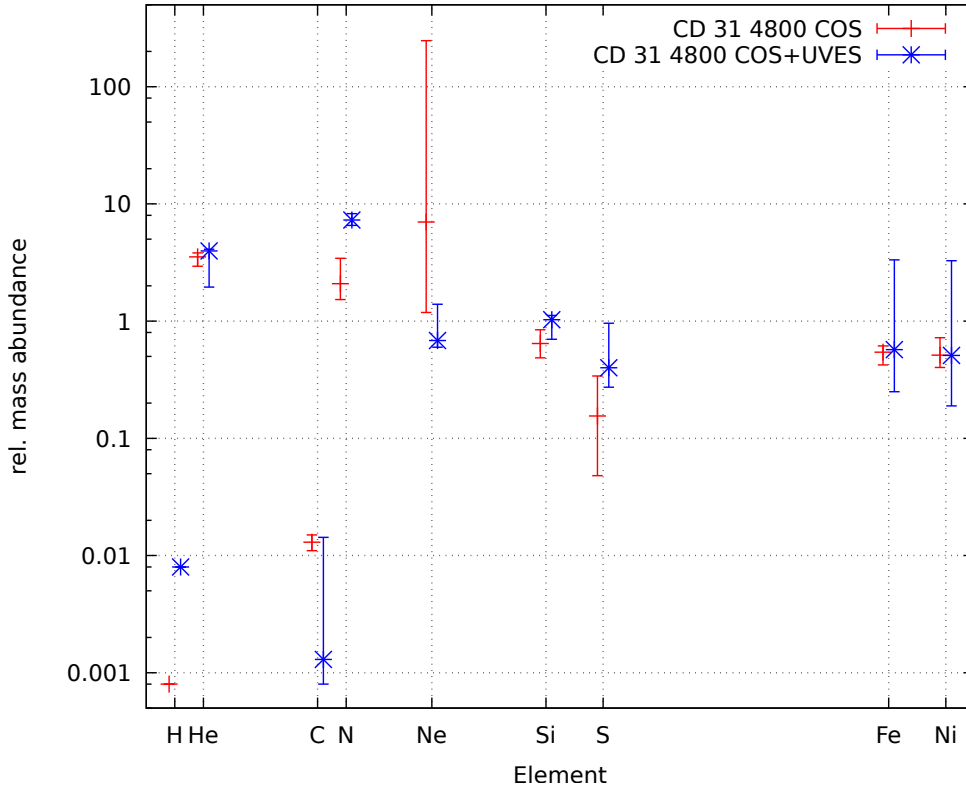


Figure 8.5: Relative mass abundances for CD-31° 4800 derived with XTGRID from a COS (red) and COS+UVES (blue) fit.

The abundances for lithium, beryllium and boron are undetermined and have no proper error calculation. They were therefore set to solar abundances and fixed at that value. The CNO bicycle pattern is clearly visible in both fits. While the carbon abundance is the same in both fits, nitrogen and oxygen are more abundant in the COS+UVES fit, with the oxygen values being an upper limit. Fluorine has no errors and is therefore undetermined. However, the most likely abundances from both fits are close together. Neon is well constraint in COS+UVES, while the error from the UV data only is very large and only overlapping very little with the optical+UV fit. For sodium, only upper limits can be given. Magnesium is in good agreement with the solar content from UVES but no error calculation was possible from COS only data. For aluminum the fit only gives back upper limits. Silicon is again well constraint in both fits, with abundances around the solar value. Phosphorus shows large deviations in the calculated abundances and gives only upper limits in addition. Sulfur shows proper errors, while chlorine and argon are only upper limits. Potassium has an upper limit from COS+UVES but is unconstrained from COS only. Calcium only has upper limits. Scandium is not constrained from both fits,

however the resulting scandium abundance from the COS fit was way above 10000 time the solar value. It is therefore not shown in the plot. Titanium is in agreement with the solar value from both fits, but being an upper limit from the UV. For the iron group elements, the constraint from the COS data is usually better than from COS+UVES. Both give only upper limits for vanadium. Chromium is above solar in the UV fit, the optical+UV fit results in the same abundance but fails to give a negative error. Manganese is an upper limit from both datasets. Iron (and Nickel) are both constraint from both fits, but the errors are significantly smaller in the COS only data while the abundances match very well. Copper is not constraint and zinc has an upper limit from the optical+UV while having proper errors in the COS fit.

As it has been shown, the XTGRID fits of both the UV as well as the UV+optical data manage to deliver comparable results, at least for most elements. The next step is comparing them to the abundances derived from UVES and IUE spectra with the standard method presented in this thesis. As the atmospheric parameters in XTGRID were set to match those of model one, only the comparison of both fits with the model one results is shown.

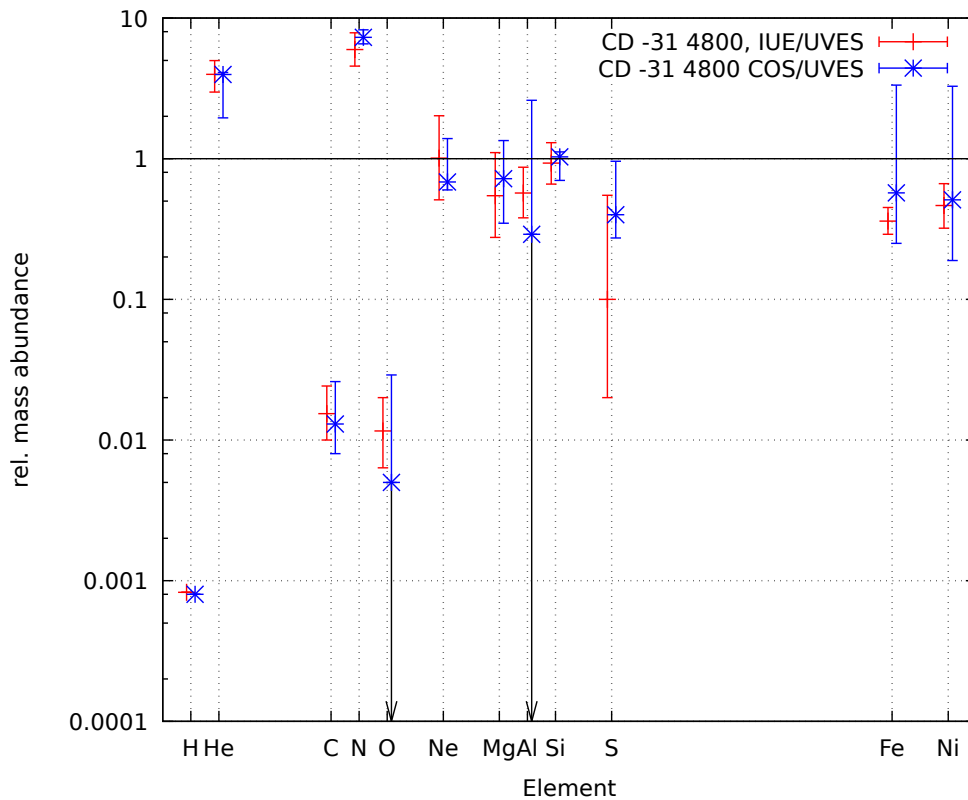


Figure 8.6: Comparison of derived abundances from the XTGRID COS+UVES fit (blue) and the UVES+IUE fit (red). All elements from the standard analysis are shown despite their errors. Upper and/or lower limits are indicated by black errors.

By comparing the COS+UVES fit, it is apparent that the abundances for all elements, are matching quite well to those derived with SPAS. For aluminum, no

negative error could be calculated with XTGRID, but the element is constraint from the previous SPAS analysis. The sulfur abundances are off by about 0.5 dex. Having the large error and the problems with fitting sulfur lines in mind, this doesn't come surprising. At least the errors are overlapping, meaning the results can be considered as consistent. As there are no iron or nickel lines in the optical, the errors and the respective elements are very large and not trustworthy.

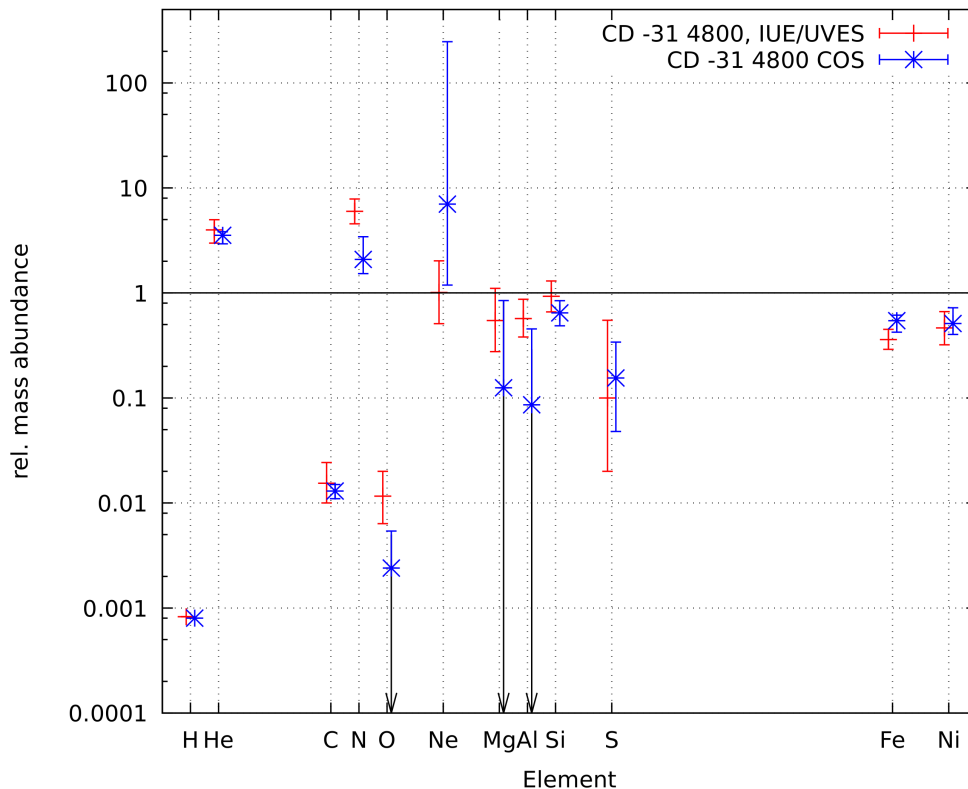


Figure 8.7: Comparison of derived abundances from the XTGRID COS fit (blue) and the UVES+IUE fit red. Upper and/or lower limits are indicated by black errors.

Regarding the abundances from the COS only fit, it is remarkable that for all elements, except neon, the XTGRID abundances are smaller than the ones from SPAS. This effect is negligible concerning iron and nickel. Neon sticks out as it shows a much higher XTGRID abundance. But in addition, the error is very large and it is overlapping with the possible neon range from SPAS. While magnesium has no errors and aluminum is an upper limit only, both elements are well constrained within the SPAS fit.

It is also remarkable how well the iron and nickel abundances are matching. Even the errors have about the same size.

It can be said that the COS+UVES fit seems to be closer to the SPAS results concerning the intermediate mass elements, while the COS only fit shows a higher level of agreement concerning iron and nickel. This is not surprising as the missing of both elements in the optical UVES spectrum significantly worsens the capability with which XTGRID can calculate the errors. Or in other words: To account for the absence of iron and nickel lines, a larger error is needed compared to a pure UV

fit, where there are plenty of iron-group lines and their effects (blending etc.) are far stronger.

Keeping these in mind, the XTGRID method proved to be reliable when it comes to fitting low resolution, low S/N UV data. Therefore it can be applied to the COS spectra of US708

8.3 Spectral analysis of US708

The spectral analysis of US 708 consisted of two main parts, the determination of the atmospheric parameters using the standard method and the analysis of the metal lines with XTGRID.

8.3.1 Atmospheric parameters

To get a first idea of the atmospheric parameters of US708, an optical spectrum¹, taken with the KECK ESI spectrograph, was analyzed. The spectrum consisted of eight single spectra which were coadded. Unfortunately it was very noisy and featured undesired emission spikes towards the red end. A cut off at 6700 Å had to be applied. Especially the H α line was influenced, worsening the fit there. The standard HHeCNO grid was utilized and the rotational velocity was set as a free parameter at first. As basically all fits crowded around a velocity of 115 km/s, the fit was fixed to that value. The results of the fit are as following.

- $T_{\text{eff}} = 47500 \pm 900 \text{ K}$
- $\log(g) = 5.50 \pm 0.20$
- $\log(n(\text{He})/n(\text{H})) = 1.50 \pm 0.15$
- $v_{\text{rot}} = 115 \pm 7 \text{ km/s}$

The combination of the poor S/N ratio and the high rotational velocity made it extremely difficult to get trustworthy results. As it can be seen in Fig. 8.8 the fit of the H α line seems far too shallow, as well as the He II lines at 4859 Å, and 5412 Å. The rest of the fitted lines matched very well. The Pickering lines at 4340 Å and 4200 Å are reproduced very well. If one assumes that the Pickering Problem is also present in this star, the line cores would usually be too deep. Together with the too shallow lines of the other He II lines, this might point to an imbalance in the ionization equilibrium, requiring a higher temperature. However, efforts to manually push the fit towards higher temperatures by using selected lines or adjusting the fit windows were not successful. This means that the atmospheric parameters listed above have to be regarded as legit at the moment. They will be revisited in Sect. 8.3.3.

Of course it was tried to determine metal abundances from the optical spectrum as well. This proved to be not practical as the rotational velocity and the S/N ratio smeared most of the lines and made them indistinguishable from noise. Only some nitrogen lines were significant enough to fit them, resulting in a large spread of abundances. The same holds for the UV COS spectrum with its even worse

¹Provided by Dr. Stephan Geier, priv. communication.

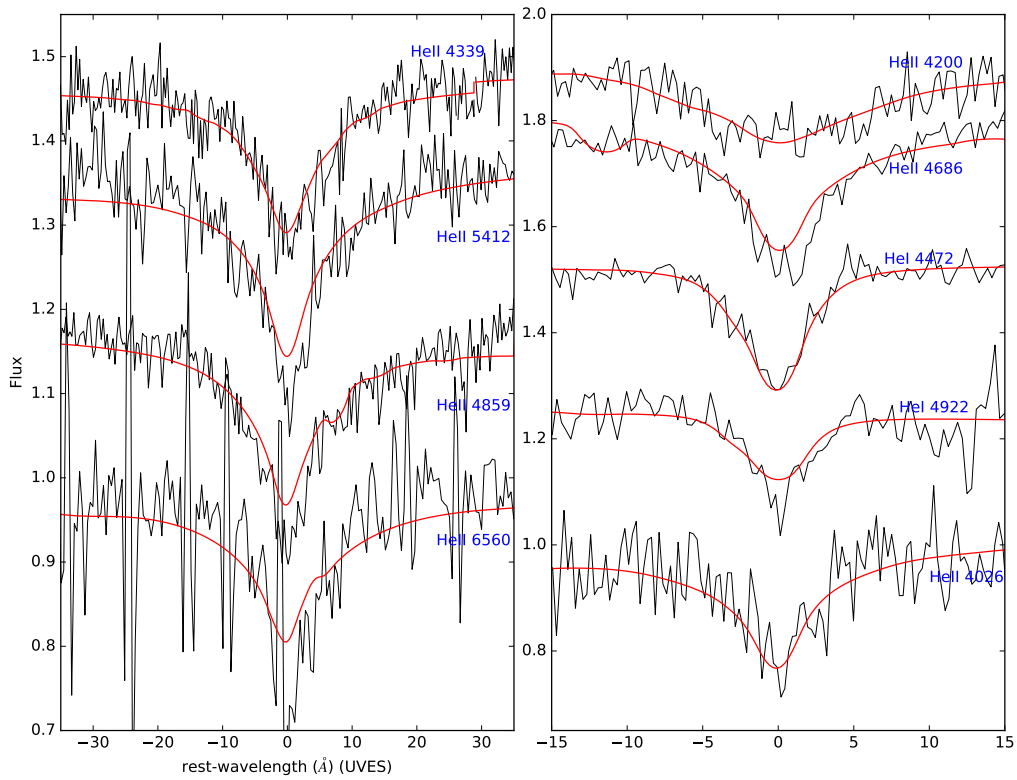


Figure 8.8: Visualization of several normalized Helium I and II lines of US 708. The black lines show parts of the ESI spectrum, the best-fitting model is represented by the red lines. The flux levels had been adjusted for better representation.

resolution. Therefore a new method had to be applied. The program XTGRID (see Sect. 4.11) looked promising and it was decided to give it a try.

8.3.2 Abundances of US708

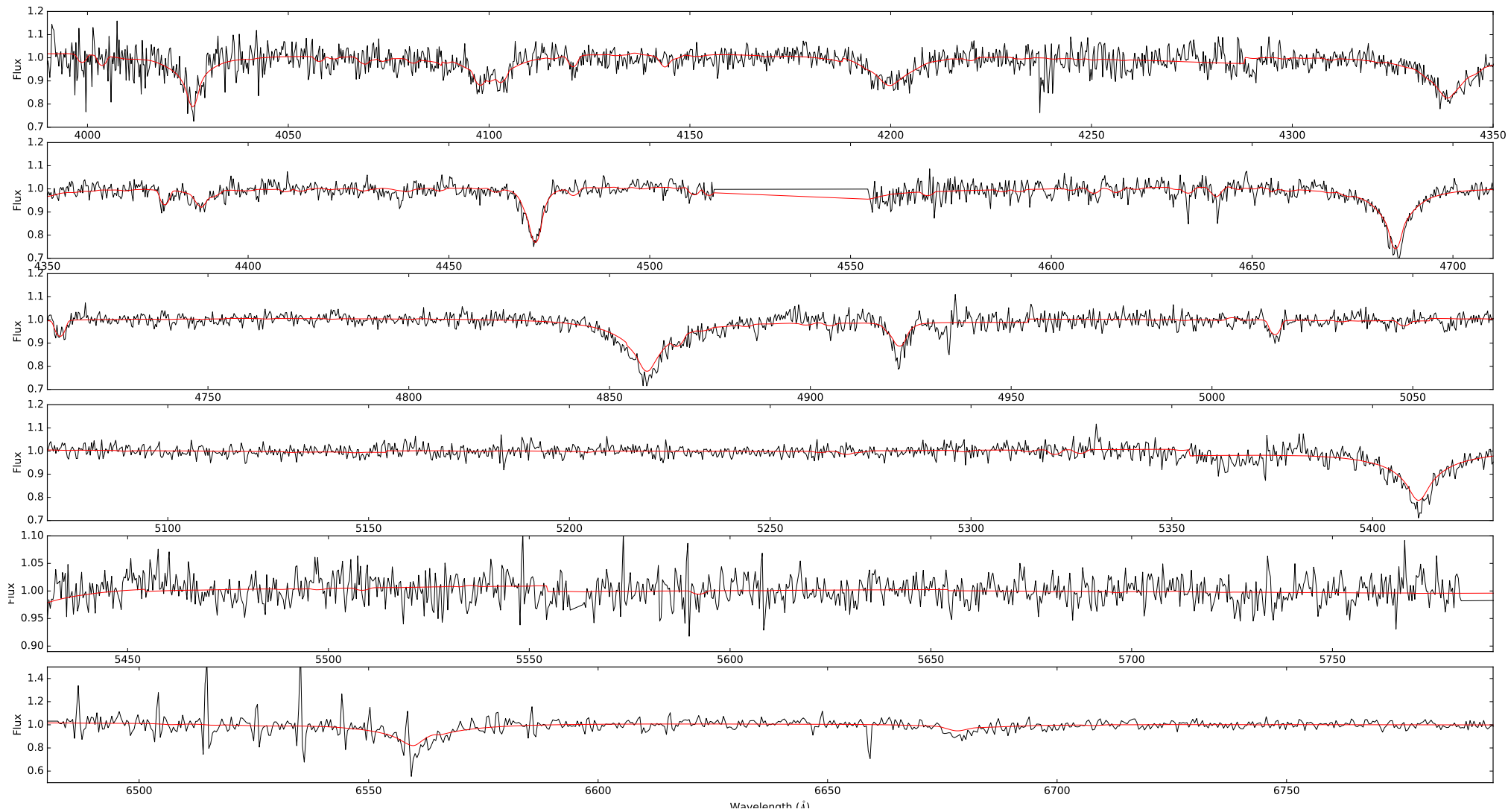


Figure 8.9: Fit to the KECK spectrum of US708 with XTGRID. The data in the lowest panel was not fitted, only overplotted.

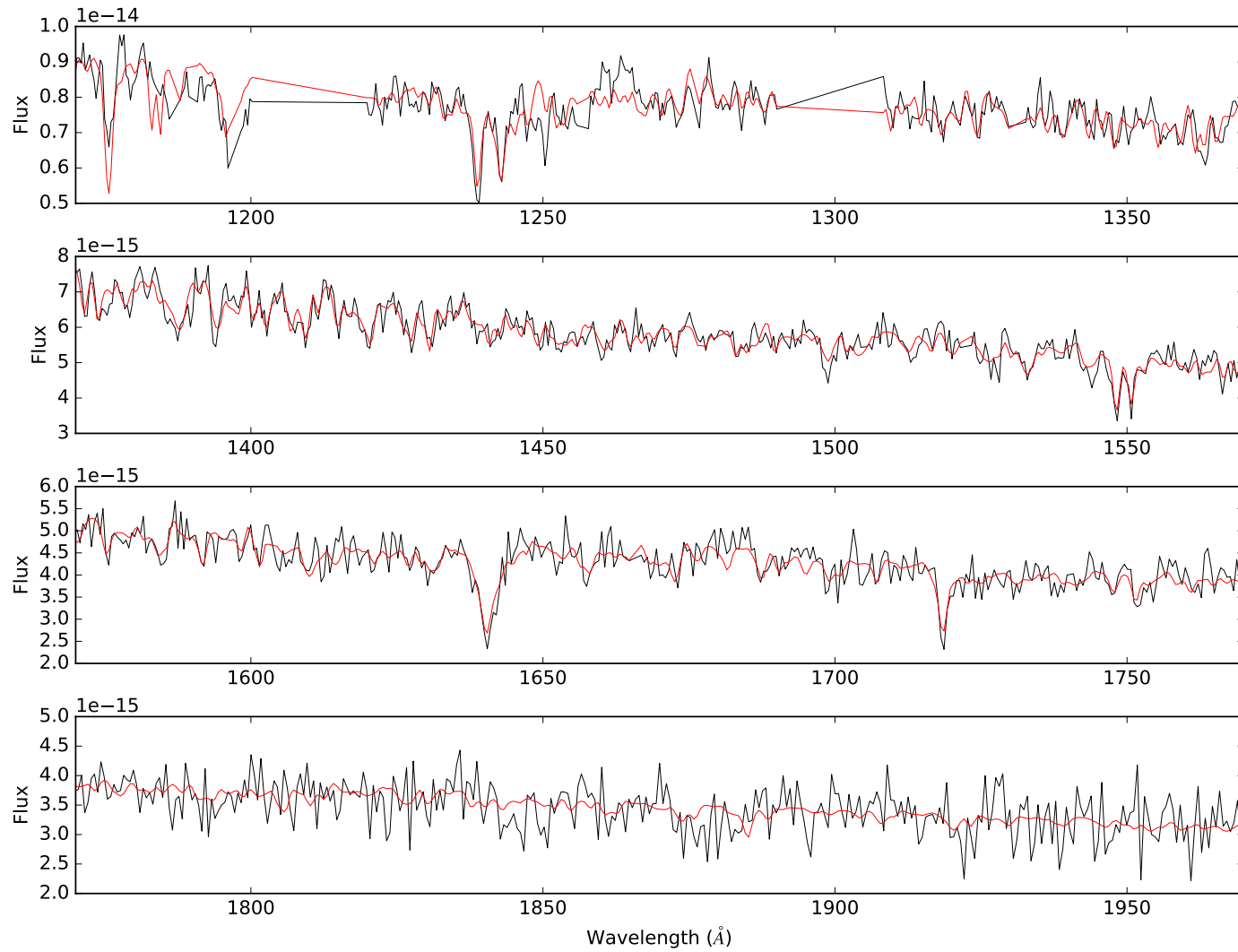


Figure 8.10: Fit to the COS part of the combined COS+KECK spectrum of US708 with XTGRID.

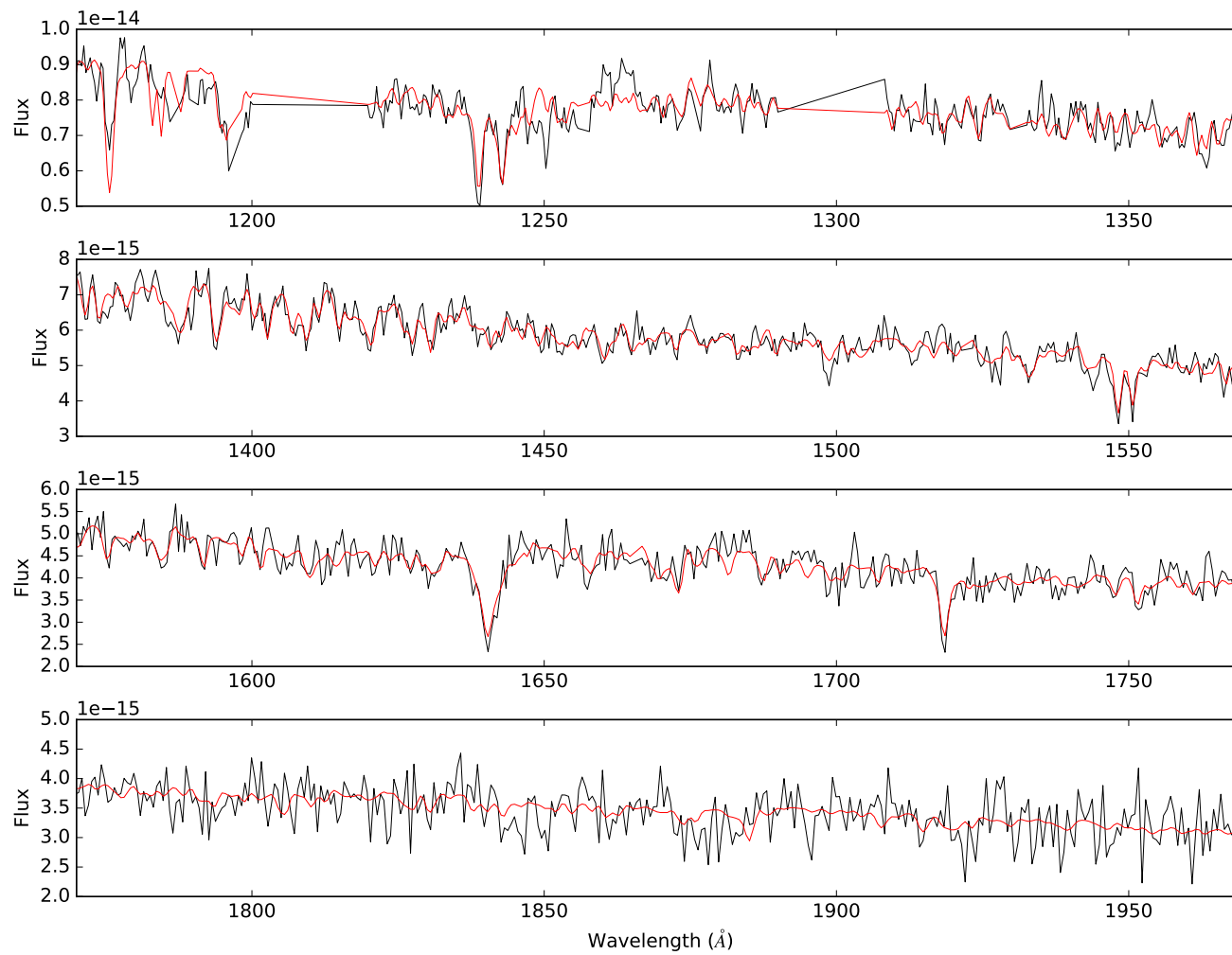


Figure 8.11: Fit to the COS spectrum of US708 with XTGRID.

Element	β/β_{\odot} COS	β/β_{\odot} COS+KECK
H	$7.3 \cdot 10^{-3}$	$9.5 \cdot 10^{-4}$
He	$2.996^{+0.396}_{-0.821}$	$3.854^{+0.626}_{-2.337}$
C	$0.006^{+0.056}_{-0.035}$	$(0.084^{+0.227}_{-x})$
N	$7.904^{+3.11}_{-3.247}$	$11.17^{+12.36}_{-9.30}$
O	$(0.014^{+0.347}_{-x})$	$(0.047^{+0.222}_{-x})$
F	(102.4^{+x}_{-x})	(942^{+x}_{-x})
Ne	$(6.662^{+16.24}_{-x})$	(6.361^{+x}_{-x})
Na	(57.60^{+x}_{-x})	(176^{+x}_{-x})
Mg	$(1.051^{+14.60}_{-x})$	(2.18^{+86}_{-x})
Al	$(0.682^{+12.95}_{-x})$	(1.022^{+101}_{-x})
Si	$(0.312^{+0.656}_{-x})$	$(0.142^{+1.765}_{-x})$
P	$(0.507^{+28.10}_{-x})$	(6.238^{+x}_{-x})
S	$(0.181^{+0.262}_{-x})$	(0.207^{+x}_{-x})
Cl	$(0.887^{+37.92}_{-x})$	(7.498^{+x}_{-x})
Ar	(3806^{+x}_{-x})	(0^{+x}_{-x})
K	(102.4^{+x}_{-x})	(284.0^{+x}_{-x})
Ca	$(0.441^{+11.73}_{-x})$	(2.683^{+x}_{-x})
Sc	(7423^{+x}_{-x})	(0^{+x}_{-x})
Ti	(3.457^{+174}_{-x})	(24.75^{+x}_{-x})
V	(170^{+x}_{-x})	(0^{+x}_{-x})
Cr	$(17.57^{+16.61}_{-x})$	(39.91^{+x}_{-x})
Mn	$(2.407^{+4.41}_{-x})$	(12.56^{+x}_{-x})
Fe	$2.064^{+1.194}_{-0.748}$	$3.044^{+5.759}_{-2.168}$
Co	$(1.516^{+8.19}_{-x})$	(3.98^{+100}_{-x})
Ni	$4.129^{+5.416}_{-1.934}$	$8.31^{+24.171}_{-7.248}$
Cu	(726^{+x}_{-x})	(0^{+x}_{-x})
Zn	(27.23^{+x}_{-x})	(281^{+x}_{-x})

Table 8.2: Relative mass abundances of US708 compared to the solar value for each element. Shown are the results from the COS and the COS+KECK fit. Given are the 1σ errors. An x indicated that no error could be calculated or the error was unrealistically large. Abundances in brackets are those with either no errors or only upper-/lower limits and have to be dealt with carefully.

Due to the poorer resolution and worse S/N ratio, the accuracy of the abundance determination is not on the same level as for CD-31° 4800, the amount of elements without any error determination is much larger. In general, the COS-only fit seemed to provide better results; More elements are constraint, at least with an upper limit. For fluorine, sodium, argon, potassium, scandium, vanadium, copper and tin no errors could be computed. The abundances resulting from the COS + KECK fit are in general higher than from the standalone UV fit.

As for CD-31° 4800 lithium, beryllium and boron were set to solar abundance and fixed. The CNO bi-cycle pattern is clearly visible in both fits. The two datasets deliver the same neon abundance, however, only the COS fit manages to give an upper limit. Magnesium, aluminum and silicon are represented as upper limits only from both fits, the abundances do not differ significantly. For phosphorus, argon and chlorine no errors are available from the optical + UV data, COS-only gives upper limits. While the abundances are matching very well for sulfur, phosphorus and chlorine are way off, but considering the poor errors, this is not surprising. The amount of argon determined from the COS + KECK was above 10000 and is therefore not shown in the plot, the same applies for scandium. While the iron group elements mostly have no proper errors, only iron and nickel are clearly constraint and both show an above solar enrichment. Fig. 8.16 shows a visualization of the abundance pattern, but uses only the few elements with proper errors. For a figure with all the elements in it, please see Fig. .10 in the appendix.

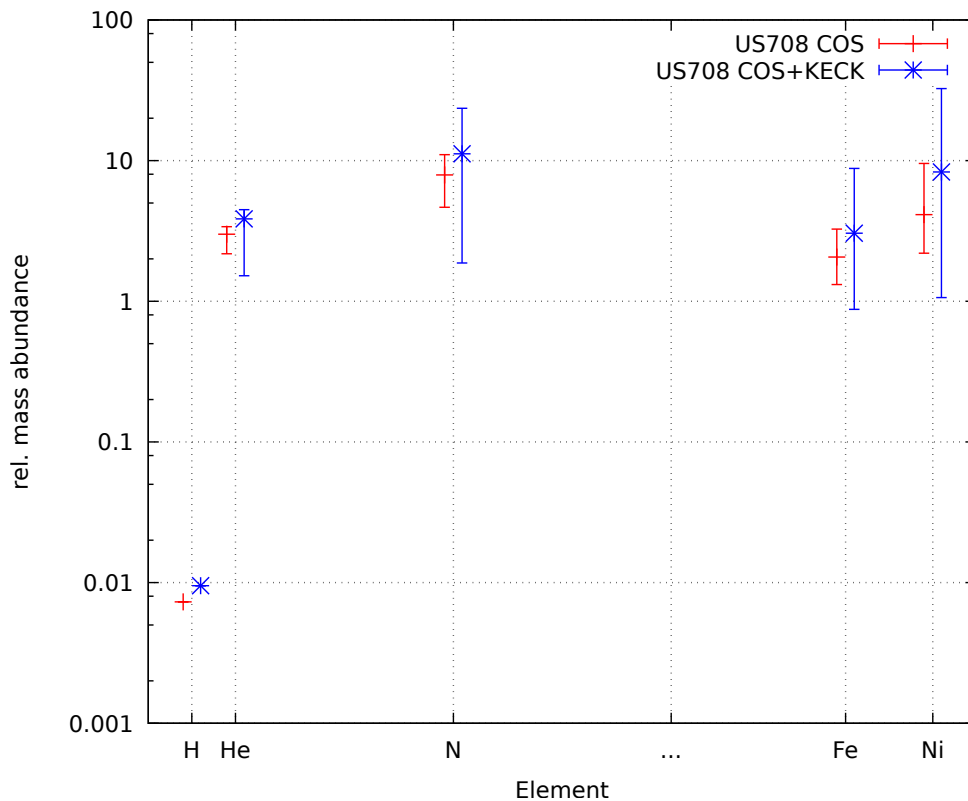


Figure 8.12: Relative mass abundances for US708 derived with XTGRID from a COS (red) and COS+KECK (blue) fit. For a plot with all elements, see Fig. .10 in the appendix.

8.3.3 Atmospheric parameters - revisited

As described in Sect. 8.3.1 there was an insecurity concerning the atmospheric parameters from the fit of the KECK spectrum with the HHeCNO model grid. For the fit with XTGRID, the atmospheric parameters were fixed, but taken into account concerning the error calculation. For each of the three parameters the 1D χ^2 distribution was calculated from the fit of the COS spectrum. A graphical illustration is shown in the following figures.

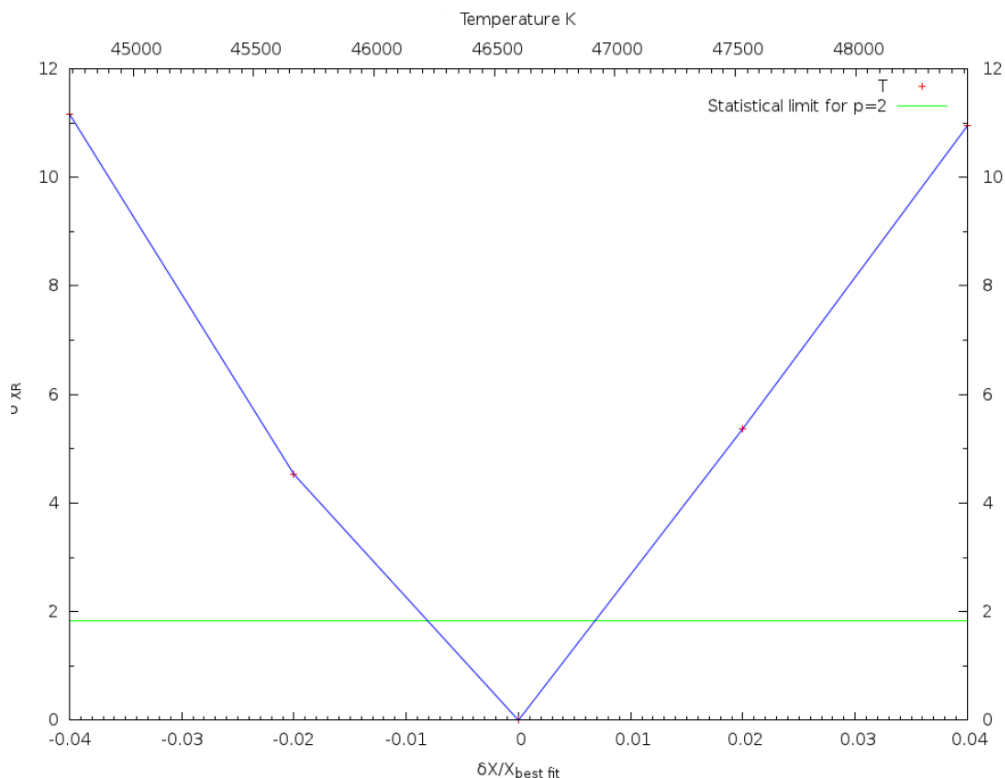


Figure 8.13: χ^2 distribution for the temperature of US708

A symmetric parabola centered around zero indicates that the found value lies in the deepest point of the χ^2 landscape. Asymmetric parabolas show that the found value for a parameters is not the best fit. In these cases, the deepest point of the parabola indicates the offset between the most likely - and the fitted value.

The shape of the parabola for the effective temperature is centered around zero and symmetric. Therefore the used temperature seems to be correct. The picture is different for the surface gravity and the helium abundance. For the gravity, an offset of about 0.15 dex is found. The true surface gravity of US708 is therefore around 5.65, not 5.50. However, the shift is still covered within the given error range of 0.2 dex, resulting from the SPAS fit of the KECK spectrum.

For helium, the parabola is asymmetric, but the the deepest point is at the used value. This points to asymmetric errors, but a reasonable abundance. In general the determined values seemed to match the observations very well. The slight shift in surface gravity is within the possible error and therefore not significant. This can serve as an other proof that the applied method of fitting single helium lines with a HHeCNO grid is able to deliver correct and trustworthy results.

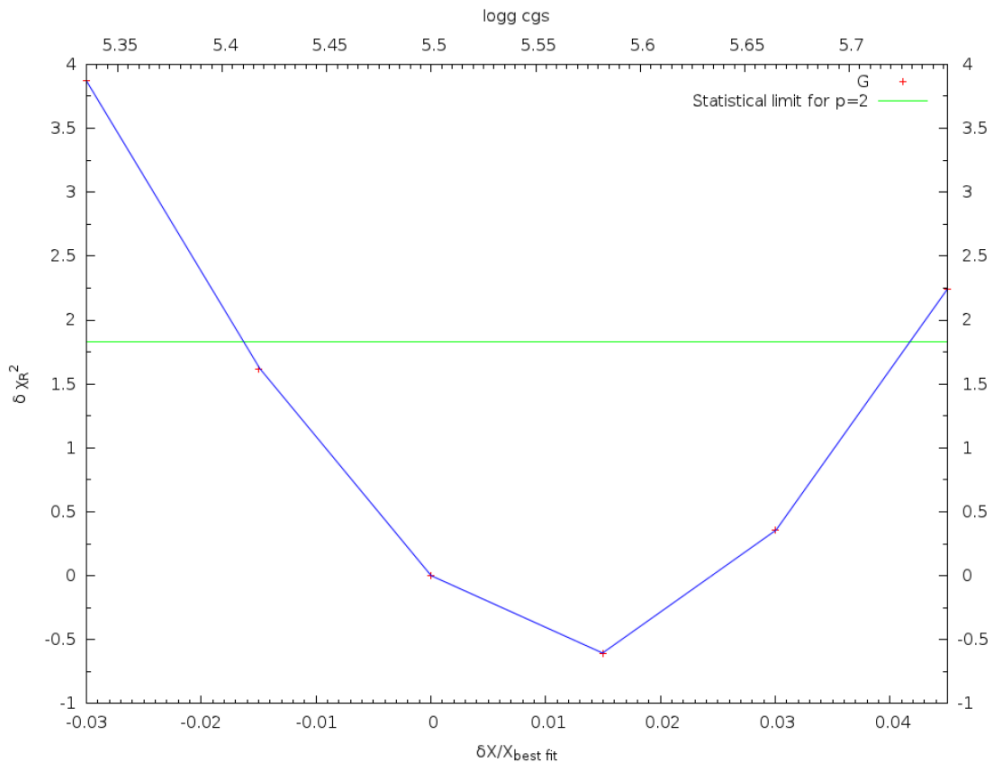


Figure 8.14: χ^2 distribution for the surface gravity of US708

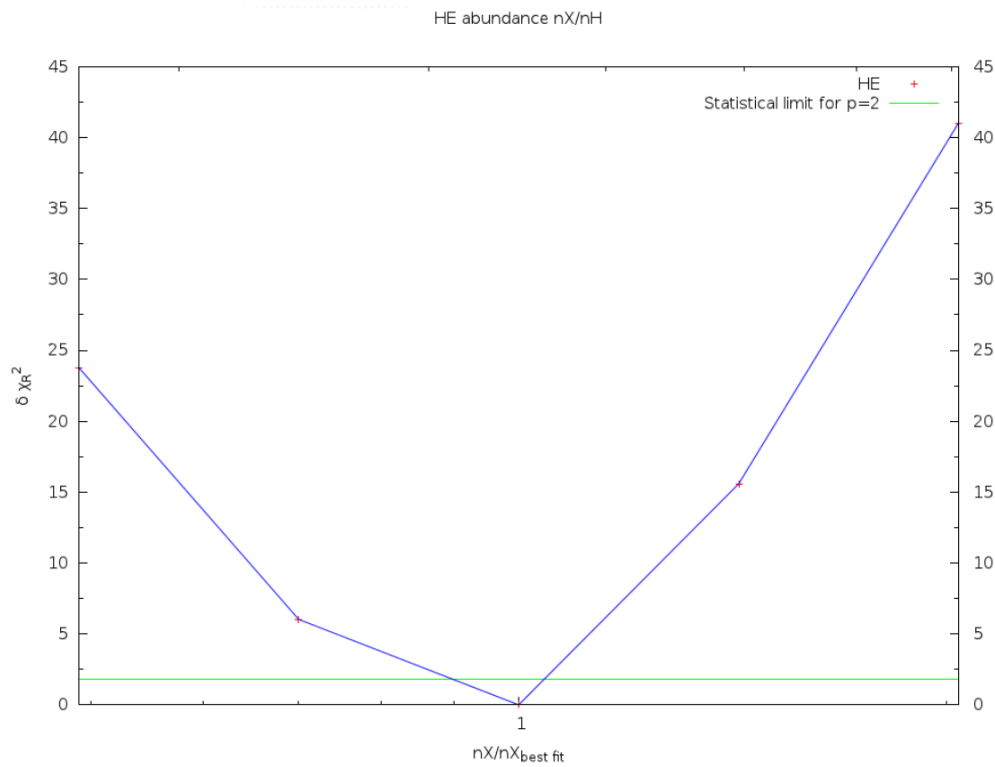


Figure 8.15: χ^2 distribution for the helium abundance of US708

8.4 Acceleration mechanism

If we want to know more about the acceleration mechanism which pushed US708 to its high speed, the first step is to look at metal abundances and compare the to those of CD -31° 4800.

8.4.1 Abundances of iron & nickel

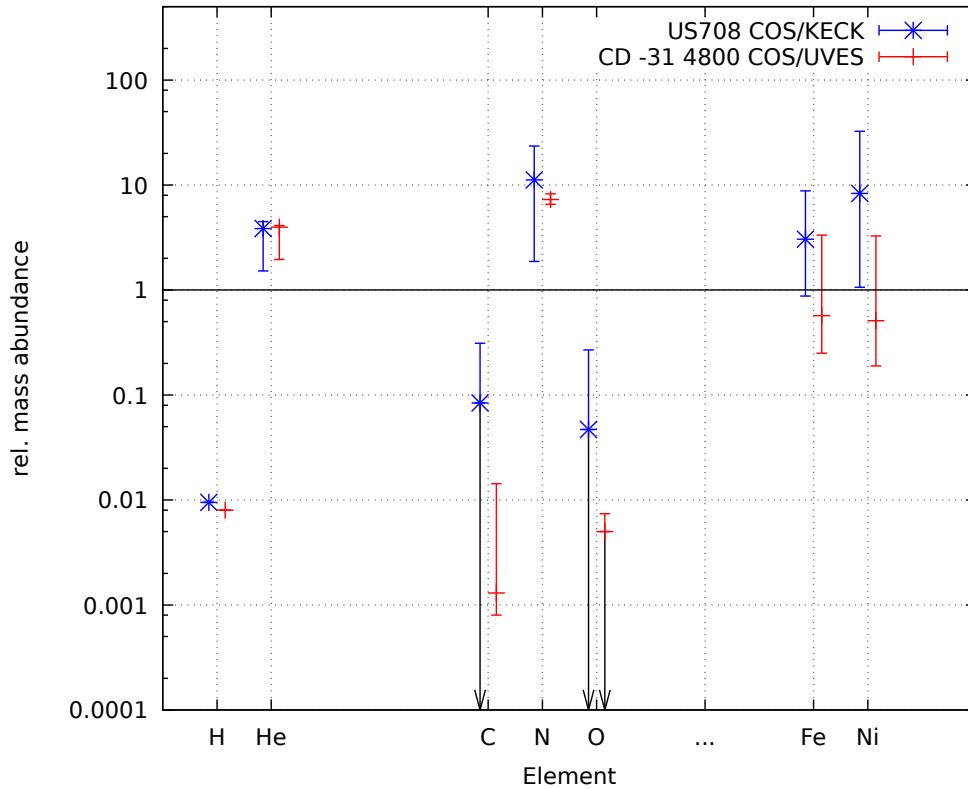


Figure 8.16: Comparison of relative mass abundances for CD-31° 4800 (red) and US708 (blue) derived from Optical + UV fits with XTGRID. For an overview with all elements, see Fig. 8.16 in the appendix.

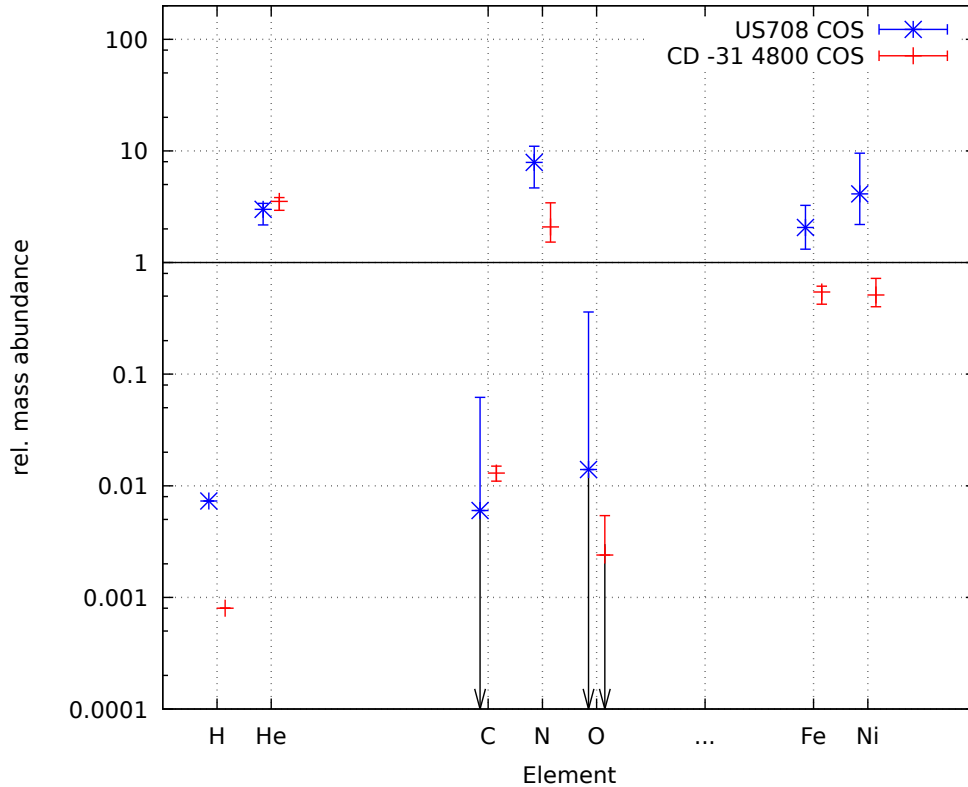


Figure 8.17: Comparison of relative mass abundances for CD-31° 4800 (red) and US708 (blue) derived from UV COS fits with XTGRID. For an overview with all elements, see Fig. .11 in the appendix.

From Fig. .11 it is clearly visible that US708 shows a significant enrichment concerning iron and nickel when compared to CD-31° 4800. However, the errors given in these plots are the 1σ errors. In addition, the 3σ errors were computed for iron and nickel in both stars (see table 8.3 and Fig. 8.18).

	CD-31° 4800	US708
Fe	$0.544^{+0.166}_{-0.176}$	$2.064^{+1.989}_{-1.074}$
Ni	$0.518^{+0.437}_{-0.240}$	$4.129^{+10.40}_{-3.056}$

Table 8.3: 3σ errors for iron and nickel in CD-31° 4800 and US708. Given are the relative mass abundances compared to the solar value of the corresponding element.

Even with the 3σ errors, the errorbars are still not overlapping. To give visual support on the enhancement of iron and nickel, the spectra and the best fit of US708 were overplotted with the best-fit model of CD-31° 4800 in Fig. 8.19. In addition the location of the strongest iron lines are marked in the second panel, where the S/N ratio of the data is best. Fig. 8.20 shows a magnification of the spectral part with the highest COS throughput and therefore the best S/N ratio.

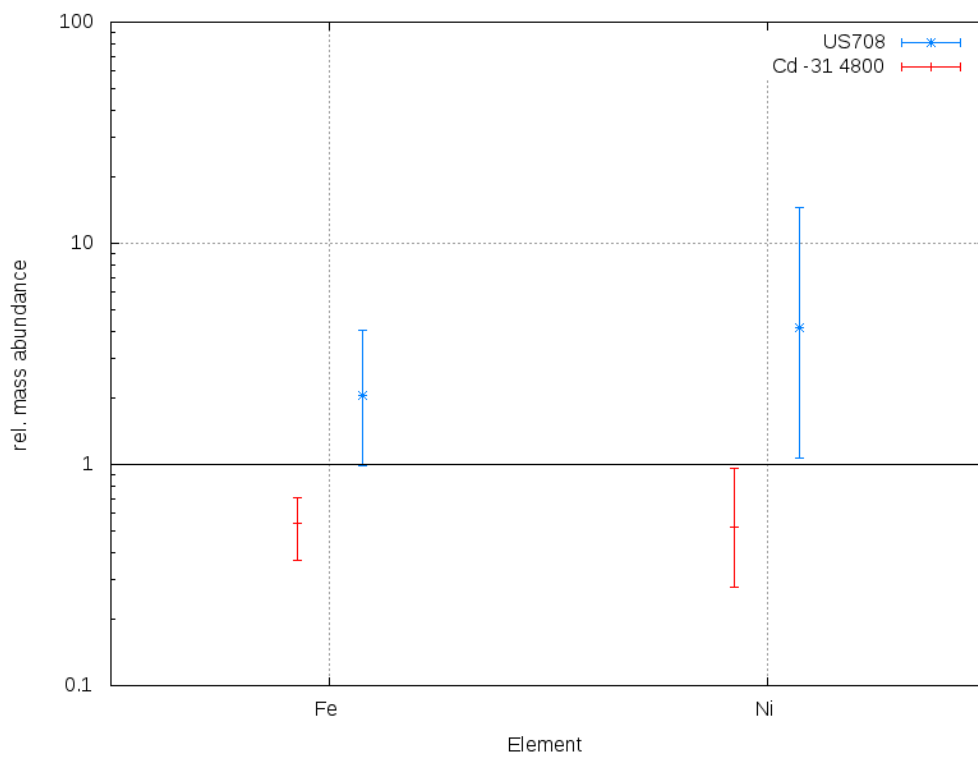


Figure 8.18: Abundances of iron and nickel in US708 and CD-31° 4800 with the corresponding 3σ errors.

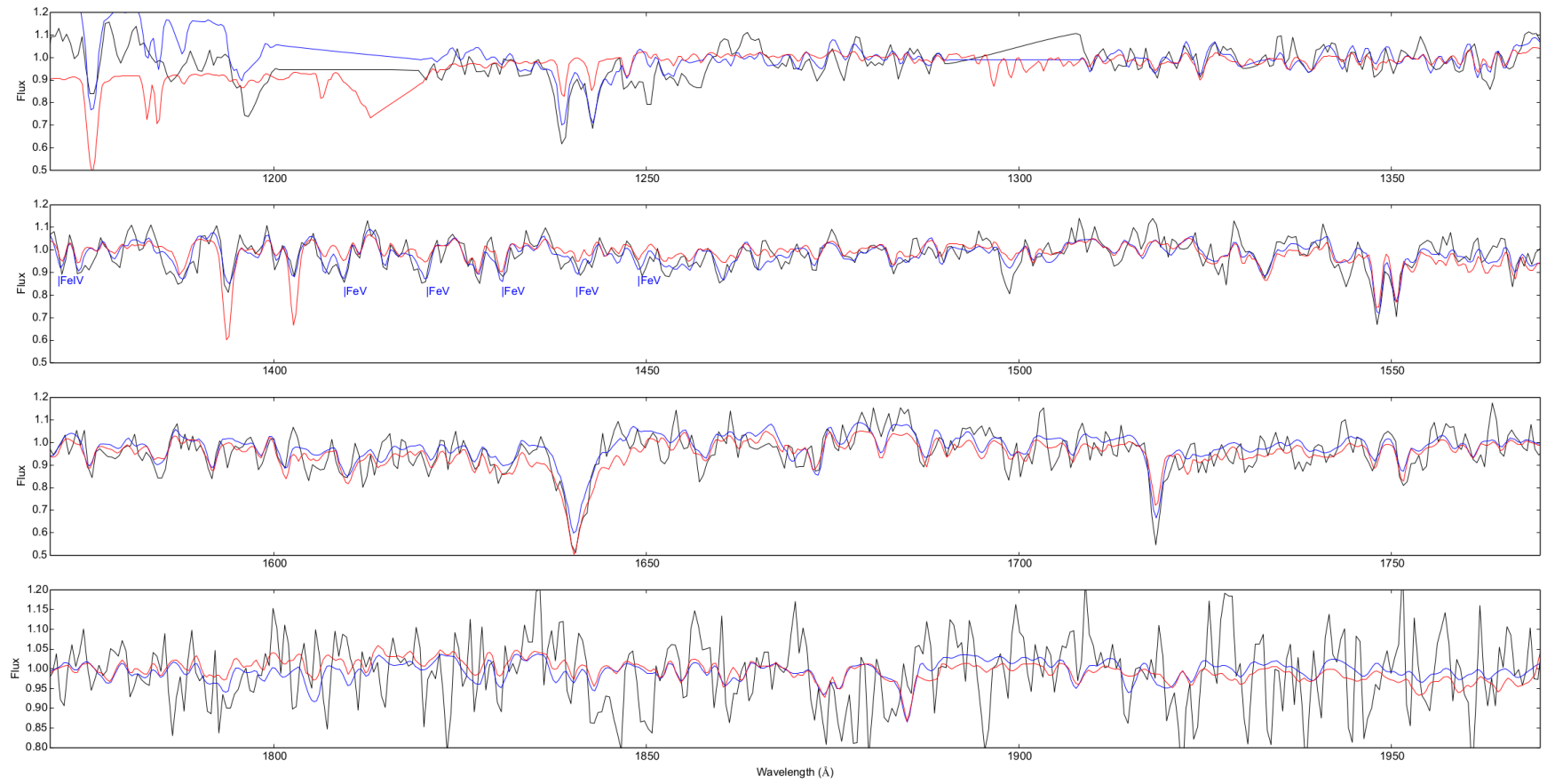


Figure 8.19: Overplot of US708 spectrum (black) and fit (blue) with best-fit model of the CD-31° 4800 (red) analysis.

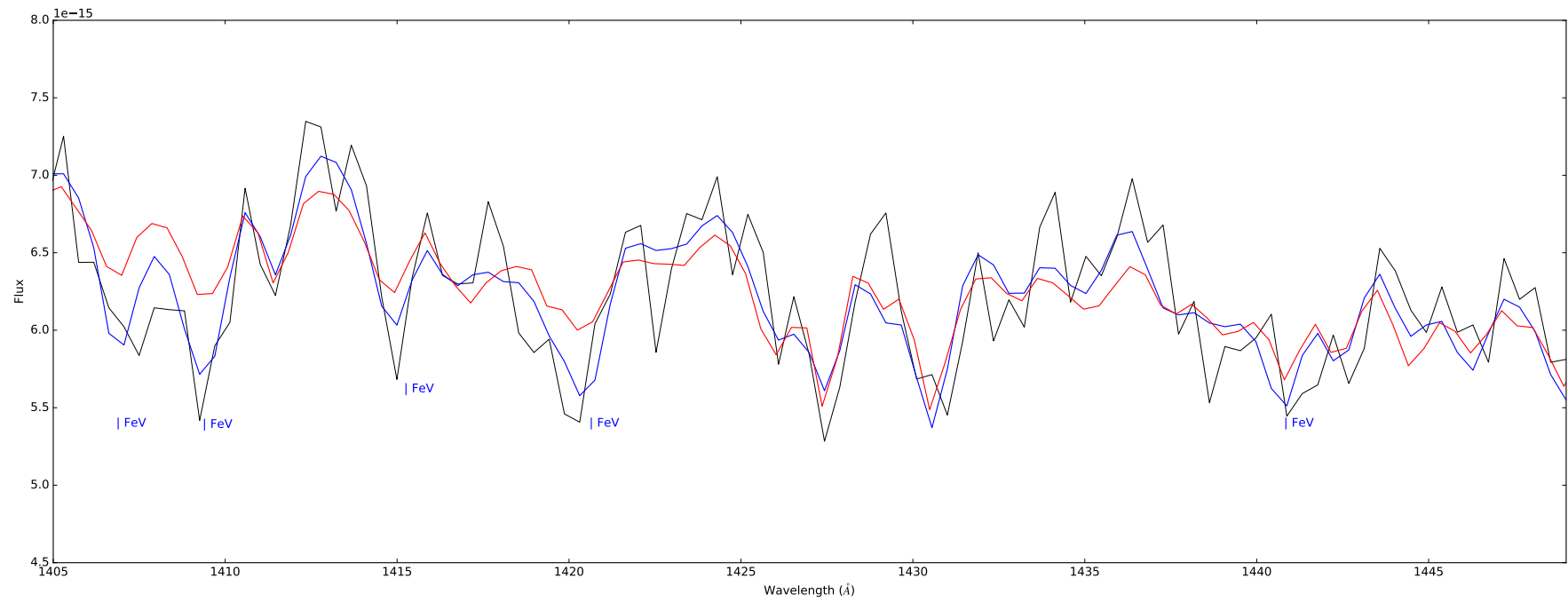


Figure 8.20: Magnification of Fig. 8.19, showing the spectral range with the highest COS throughput and therefore best S/N ratio.

It is striking that at the mentioned positions, a clear offset between both data and model of US708 and the CD-31°4800 fit is visible. Especially the iron lines around 1409.4 Å and 1420.5 Å show clear deviations. Of course no single lines are visible here as the rotation and poor resolution smears and blends all the lines. But an offset at different positions limits the chances that these are just coincident or caused by other elements.

This is consistent with the results of Liu et al. [2013b], who predict an enrichment of iron and nickel by using hydrodynamical simulations of the supernova ejecta and an He-rich companion. Their simulations of the SN explosion are based on the W7 model of Nomoto et al. [1984] and Maeda et al. [2010]. It has been adopted with a helium-rich companion (W7-He) with different orbital separation (W7-He01, W7-He02) Fig. 8.21, adopted from Liu et al. [2013b], shows the estimated enrichment of certain elements for the different supernova explosion models (black and gray symbols) as well as the corresponding composition after the decay of unstable isotopes (red, open circles). It is clearly visible that only the iron group elements, and here

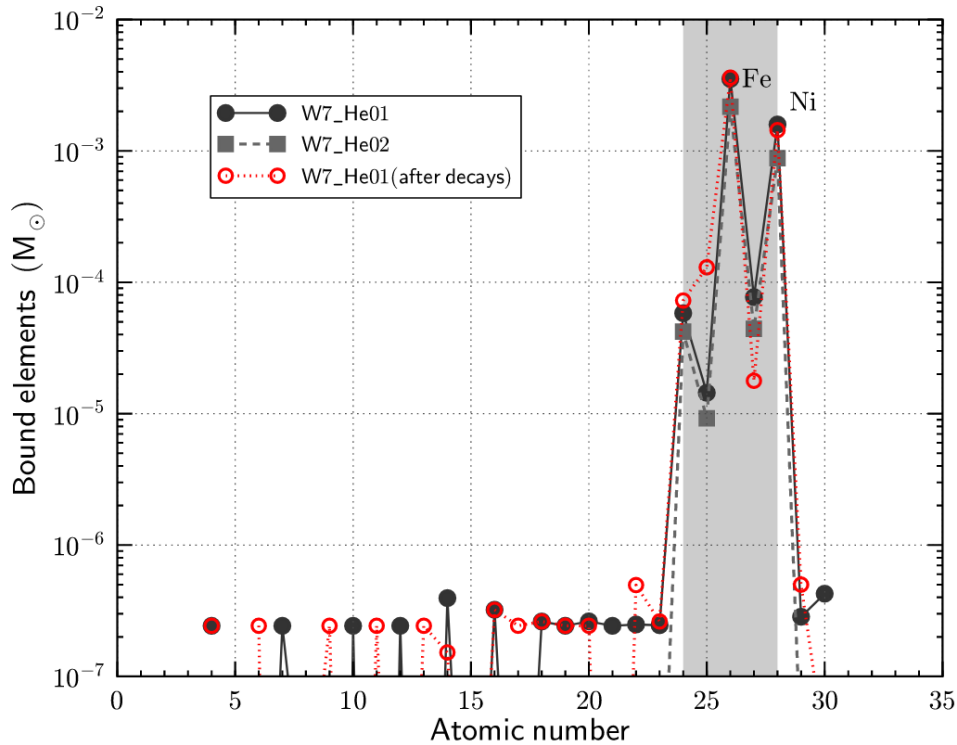


Figure 8.21: Predicted enrichment of certain elements for different supernova Ia explosion models 2000s after the explosion. The model with red, open circles described the element composition after the decay of unstable elements. Adopted from Liu et al. [2013b].

especially iron and nickel, are enriched up to 3 dex compared to the intermediate mass elements. This outcome shows only slight dependences of the actual model describing the supernova explosion. More than 10^{-3} solar masses of iron and nickel can be accreted on the helium-rich companion. But to get a valid and concrete idea of what caused US708's high speed it is not enough to just look at abundances of the iron group elements. It is also important to understand how US708 is moving through space and what we can learn from its trajectory.

$\mu_\alpha \cos \delta$	μ_δ	Reference
-8.0 ± 1.8	9.1 ± 1.6	Geier et al. [2015a]
-7.33 ± 0.58	2.28 ± 0.55	Brown et al. [2015]
-5.6 ± 1.8	1.3 ± 1.6	Tian et al. [2017]

Table 8.4: Proper motions of US708. Values are given in [mas/yr]

8.4.2 Kinematic properties

(This section is based on the paper “On the origin of US708“ by Németh&Schindewolf et al. (in prep.))

Geier et al. [2015a] already presented a kinematic analysis for US708. In the meantime, new proper motions have been measured, see table 8.4. The proper motions provided by Brown et al. [2015] are based on HST images, while data given by Tian et al. [2017] is from the GPS1 catalog, consisting of CCD-derived position measurements from 2MASS, SDSS and PS1. Data from GAIA DR1 is also part of this catalog, but US708 was not part of the first data release. The proper motions of Brown et al. [2015] and Tian et al. [2017] are consistent within their individual error ranges, but both show deviations concerning the declination component when compared to Geier et al. [2015a].

Concerning the atmospheric parameters of US708, this work presents more conservative uncertainties for the single parameters as well as slightly different values. Because of the different datasets and different approaches concerning the method of analysis, the two sets of results can be considered independent. As a concrete surface gravity is needed to continue with the kinematic interpretation, it was decided to adopt the average values from this work and Geier et al. [2015a] in combination with the larger errors presented in this thesis. This results in the following atmospheric parameters for US708, which were used hereafter.

- $T_{\text{eff}} = 47350 \pm 900 \text{ K}$
- $\log(g) = 5.60 \pm 0.20$

To derive the spectroscopic distance of a star, some assumption has to be put on the stellar mass. Because of the proposed evolutionary scenario for US708 (disk ejection from a very compact binary system), Geier et al. [2015a] adopted a stellar mass of $0.30M_\odot$ and received a distance of $8.0 \pm 1.0 \text{ kpc}$. As other scenarios might still be possible we present spectroscopic distances for three more different masses here, $0.40M_\odot$, $0.47M_\odot$, the canonical mass, and $0.80M_\odot$. This leads to the following spectroscopic distances.

- $0.30M_\odot \rightarrow 9.2^{+2.5}_{-2.0} \text{ kpc}$
- $0.40M_\odot \rightarrow 10.6^{+2.9}_{-2.3} \text{ kpc}$
- $0.47M_\odot \rightarrow 11.5^{+3.1}_{-2.5} \text{ kpc}$
- $0.80M_\odot \rightarrow 15.1^{+4.1}_{-3.2} \text{ kpc}$

To test these distances for consistency, the SED can be used to derive the photometric distance independently. Fig. 8.22 displays the SED of US708 with the available

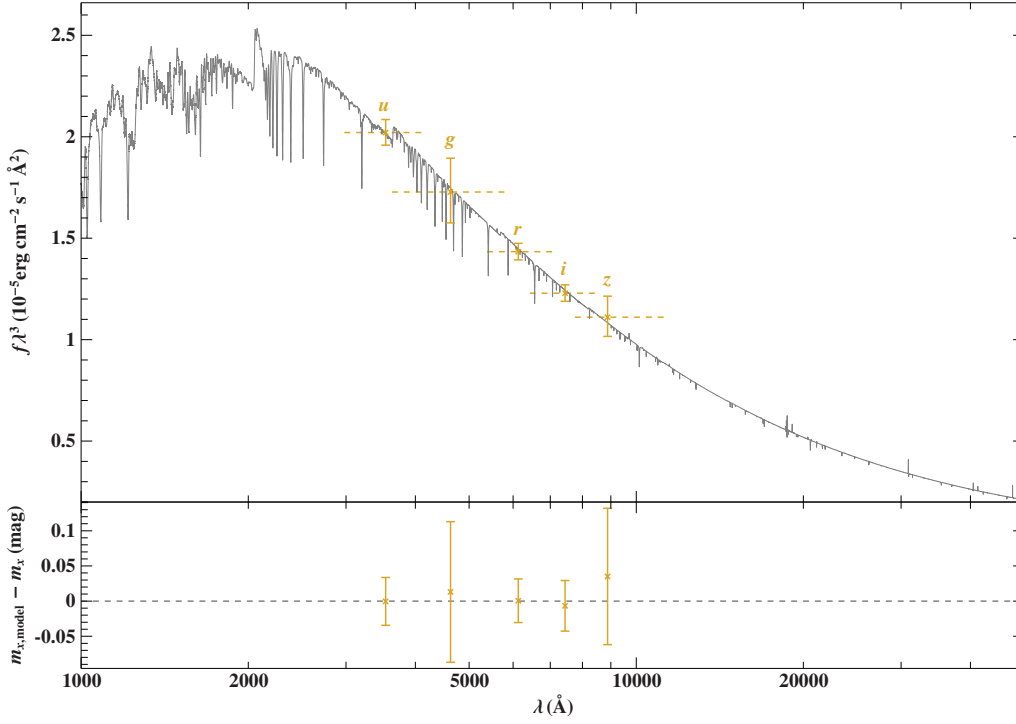


Figure 8.22: SED of US708 with selected photometric measurements used for fitting. The bottom panel shows the residuals for the magnitude measurements.

Filter	value	error	type	reference
u	18.232	0.014	magnitude	Alam et al. [2015]
g	18.645	0.08	magnitude	Alam et al. [2015]
r	19.155	0.011	magnitude	Alam et al. [2015]
i	19.524	0.018	magnitude	Alam et al. [2015]
z	19.821	0.077	magnitude	Alam et al. [2015]

Table 8.5: Photometric measurements for US708.

photometric measurements. Despite the SDSS u, g, r, i and z magnitudes, several Johnson magnitudes were available. The later one however did not match the SED at all and showed a large scatter. They were therefore not used for fitting. Despite having the possibility of computing a box magnitude from the COS spectrum, it was not used because the sensitivity is known to change over time which makes fluxing rather complex and less trustworthy. Two corrected FUV and NUV magnitudes from GALEX were thrown away as well as they scattered too much and may harbor unknown systematic shifts. The SDSS magnitudes however were in very good agreement during several data releases and seem trustworthy. The following table (8.5) lists the few available magnitudes that were used. To compute the photometric distance, a $\log(g)$ of 5.5 ± 0.2 was used as this was the surface gravity for which the SED was calculated. By adopting masses of $0.30M_{\odot}$, $0.40M_{\odot}$, $0.47M_{\odot}$ and $0.80M_{\odot}$, the following distances arise.

- $0.30M_{\odot} \rightarrow 10.58_{-2.17}^{+2.74}$ kpc

- $0.40M_{\odot} \rightarrow 12.22^{+3.16}_{-2.51}$ kpc
- $0.47M_{\odot} \rightarrow 13.25^{+3.43}_{-2.77}$ kpc
- $0.80M_{\odot} \rightarrow 17.28^{+4.48}_{-3.56}$ kpc

They are in good agreement with the spectroscopic distances, also being slightly higher in general. The errors are about 200 pc higher from the photometric fit. For the proceeding analysis, the spectroscopic distances will be used.

To reconstruct the Galactic velocity components and past trajectories, the approach described in Tillich et al. [2011] was applied. The three spectroscopic distances and proper motions were examined independently in all possible combinations. For the Galactic gravitational potential, model 1 from Irrgang et al. [2013] was used. Monte Carlo simulations with a depth of 100000 iterations were computed to trace back the trajectories until they crossed with the Galactic disc (see i.e. Ziegerer et al. [2017]). Table 8.6 shows the most important parameters from these calculations. As the parameters only changed insignificantly when switching between the different model potentials, only the results of potential I from Irrgang et al. [2013] are shown.

M_{sdO} [M_{\odot}]	v_X [km s^{-1}]	v_Y [km s^{-1}]	v_Z [km s^{-1}]	v_{grf} [km s^{-1}]	t_{flight} [Myr]	v_{ej} [km s^{-1}]
Geier et al. [2015a]						
0.30	-878 ± 88	679 ± 117	406 ± 86	1191 ± 93	17.3 ± 6.8	1053 ± 122
0.40	-922 ± 102	740 ± 138	362 ± 100	1247 ± 118	23.4 ± 10.4	1126 ± 150
0.47	-947 ± 110	776 ± 146	337 ± 108	1280 ± 129	28.0 ± 13.5	1170 ± 159
0.80	-1051 ± 144	926 ± 191	230 ± 141	1434 ± 186	52.1 ± 43.8	1327 ± 179
Brown et al. [2015]						
0.30	-854 ± 62	379 ± 32	449 ± 58	1040 ± 35	15.0 ± 5.4	922 ± 49
0.40	-890 ± 70	391 ± 37	414 ± 67	1061 ± 44	18.6 ± 7.3	952 ± 71
0.47	-912 ± 76	399 ± 40	393 ± 72	1075 ± 50	21.2 ± 8.9	976 ± 81
0.80	-1008 ± 99	431 ± 52	302 ± 94	1144 ± 76	37.7 ± 25.4	1079 ± 102
Tian et al. [2017]						
0.30	-796 ± 75	340 ± 73	505 ± 70	1009 ± 38	13.4 ± 4.7	911 ± 39
0.40	-824 ± 87	346 ± 86	479 ± 81	1023 ± 47	16.4 ± 6.6	924 ± 59
0.47	-840 ± 93	352 ± 92	463 ± 87	1033 ± 53	18.3 ± 7.6	935 ± 70
0.80	-914 ± 122	368 ± 122	394 ± 114	1078 ± 83	29.5 ± 19.6	1003 ± 105

Table 8.6: Kinematical parameters of US 708 as derived from Monte Carlo simulations.

The proper motions of Brown et al. [2015] and Tian et al. [2017] result in a significantly lower y component of the velocity compared to the results from the Geier proper motions. The flight time, galactic rest frame velocity and ejection velocity are less affected and more or less consistent among each other.

Fig. 8.23 shows the possible origin region for US708 resulting from different spectroscopic distances and proper motions. From almost all scenarios, the Galactic centre (black dot) can still be excluded as an origin of US708. Only from the GPS1 proper motions, a very slight chance remains. All the results are in agreement with those of Geier et al. [2015a].

8.4.3 Evolutionary and ejective scenarios

From all we know now about US708, it is possible to draw conclusion linked to the evolutionary and ejective scenario for this special star. On the following pages, the remaining, possible scenarios will be discussed and graded according to their likeliness.

8.4.3.1 Ejection by triple disruption in the Galactic centre

The disruption of a hierarchical triplet system by the SMBH in the Galactic centre was the first ejection mechanism proposed for US708 [Perets, 2009]. In this scenario, a triplet system consisting of a normal star and a close He-WD binary gets disrupted by the supermassive black hole and the binary part of the triplet system is accelerated and merges later on to form a single He-sdO star. Both, the high velocity of US708 and the evolutionary status as a single He-sdO can be explained. However, this scenario was rejected by Geier et al. [2015a] as the trajectory was not in agreement with an origin in the Galactic centre. But as Geier et al. [2015a] only assumed a low mass subdwarf, the centre origin might still be possible as the merger channel predicts masses up to $0.8 M_{\odot}$. In Fig. 8.23 we show possible origins for US708 for different masses and proper motions. Even for a mass of $0.8 M_{\odot}$, the Galactic centre can be ruled out as an origin of US708 almost certainly, making the ejection by triple disruption in the Galactic centre a highly unlikely scenario.

8.4.3.2 Ejection by an asymmetric core-collapse supernova

Tauris [2015b] proposed a mechanism that would also be capable to accelerate stars to such high velocities as seen in US708, the ejection by an asymmetric core collapse supernova. In this special case, the shockwave of a highly asymmetric supernova needs to hit the companion in the proper orbital phase. Depending on the size and mass of the companion, velocities up to 1200 km/s are proposed.

However, two properties of US708 make this scenario rather unlikely, the chemical composition and the rotational velocity.

Tauris [2015a] predict that the yield of a core collapse supernova leads to an enrichment of, among others, silicon on the surface of the companion. In the COS spectrum of US708, no strong silicon lines are detectable, in contrast to CD -31° 4800, which shows strong silicon lines around 1400 Å, see Fig. 8.19. In US708, only an upper limit for the silicon abundance could be determined. To assure for the unlikely case that the lines were not only smeared out by rotation, Fig. 8.24 shows a comparison between the synthetic spectra of CD -31° 4800 and US708 without rotation and

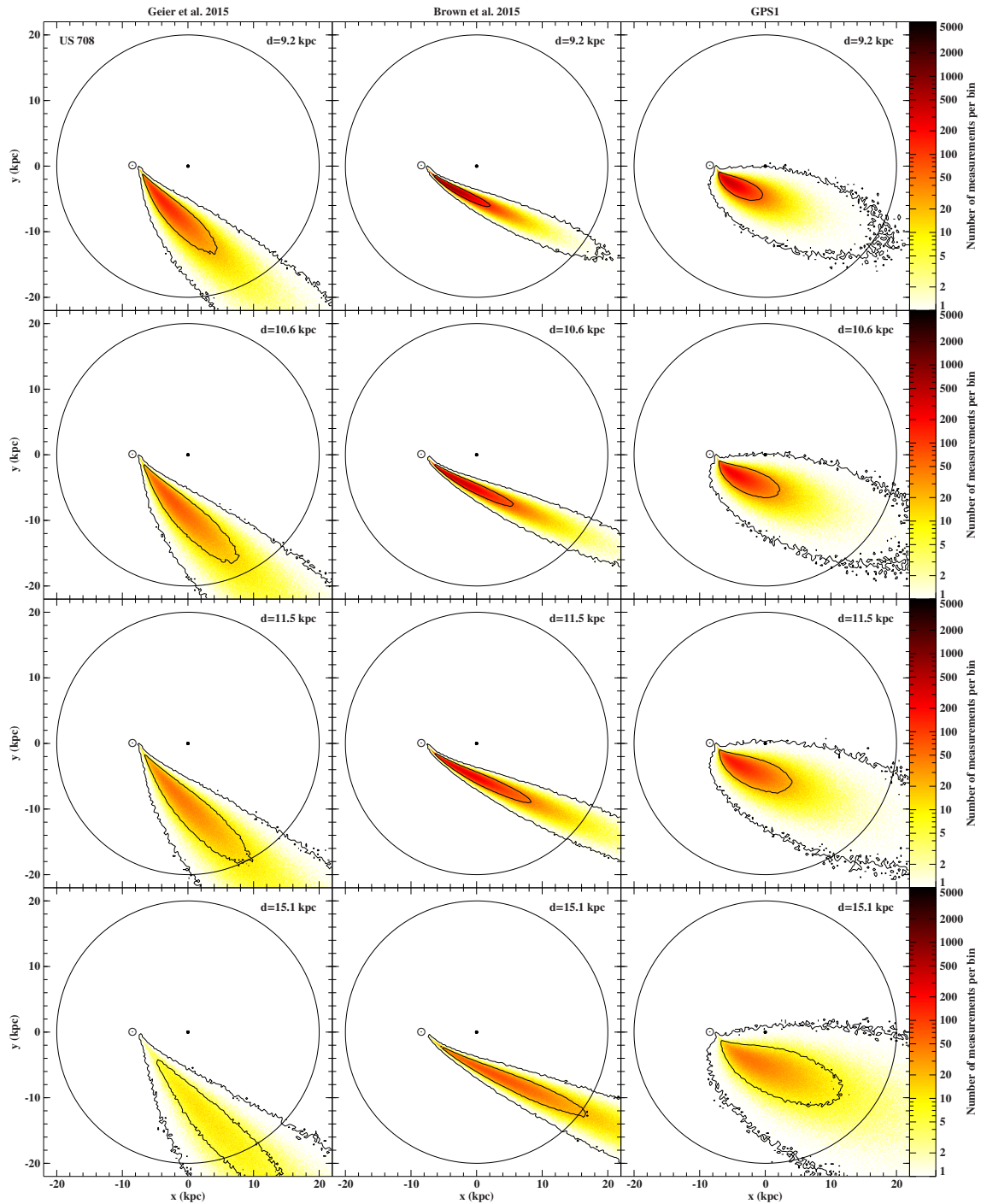


Figure 8.23: Origin plots for US708. Given are the x and y position in kpc for different spectroscopic distances and proper motions. The Galactic potential model I from Irrgang et al. [2013] was used for the simulations visualized here. The position where the star crossed the Galactic disk (which is shown pole-on) is marked with the color-coded bins. The contours correspond to the 1σ and 3σ confidence limits. The black dot marks the position of the Galactic centre, the star symbol the position of the Sun. US708's current position is indicated by a triangle.

proves that the silicon lines are indeed far less pronounced in US708 and not only

smearred out by rotation. The other smoking gun against an acceleration by an

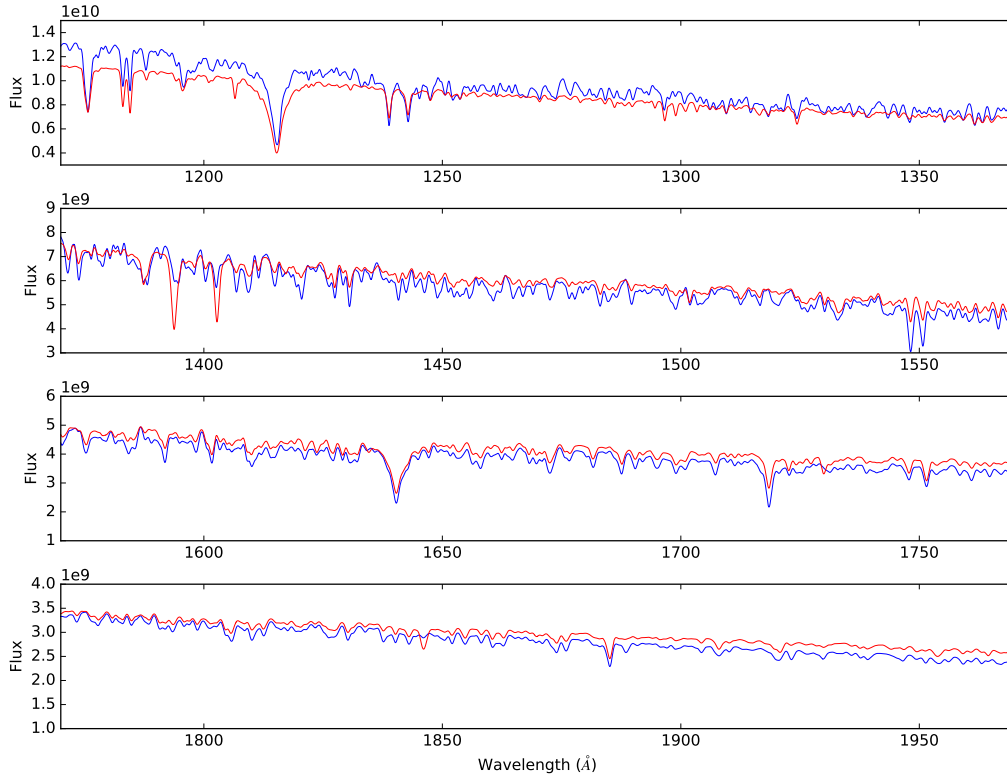


Figure 8.24: Comparison of the synthetic spectra without rotation for CD-31° 4800 (red) and US708 (blue).

asymmetric core collapse SN is the rotational velocity of US708. The pre-SN binary is expected to have an orbital period of several hours. The rotational velocity that can be conducted from tidal synchronization is far below the one of US708. The acceleration by an asymmetric core collapse supernova can therefore be ruled out with high certainty.

8.4.3.3 Ejection from the disk by a thermonuclear supernova

This scenario was already proposed by Geier et al. [2015a] as a double-detonation of a massive CO white dwarf. This star is part of a close binary together with a hot subdwarf star. Once the orbit has shrunk enough by emitting gravitational waves, the subdwarf can fill its Roche lobe and start to transfer matter, helium in this case, onto the surface of the White Dwarf. At some point, enough helium was accreted to start He-burning in an explosive way. This triggers the burning of carbon and oxygen in the WD and finally leads to its disruption via a thermonuclear supernova. The debris of the former WD are partly shot onto the surviving companion and should be detectable in its atmosphere as an enrichment in iron and nickel. This is what we observe in the case of US708.

To constrain the parameters of the progenitor system, the ejection velocity comes to help. The value of the ejection velocity can be directly linked to the orbital separation of the two binary stars. The tighter the orbit, the higher the resulting ejection velocity. But a tighter orbit requires a more massive WD as a consequence. Geier

et al. [2015a] already described how to compute the parameters of the progenitor system. They found consistent solutions for subdwarf masses between $0.30 M_{\odot}$ and $0.35 M_{\odot}$ in combination with a WD having more than one solar mass and an orbital period between 10 and 15 minutes.

Adopting their approach to the new measurements presented beforehand and using the average ejection velocity from all combinations, the following mass combinations can be obtained. Using the proper motions of Tian et al. [2017] results in a subdwarf mass of $0.40 M_{\odot}$, a WD with $1.50 M_{\odot}$ and a binary period of around 20 minutes. If the highest proper motions is used, the binary period drops to around 14 minutes and the subdwarf becomes more lightweight ($\sim 0.33 M_{\odot}$).

Such a low mass is rather unusual for a hot subdwarf stars with He-core burning but not impossible if the progenitor stars are more massive than $2.0 M_{\odot}$ and helium burning started under non-degenerate conditions. However, the same problem with the low mass as already mentioned by Geier et al. [2015a] is encountered. Fig. 8.25 shows the position of US708 in a $T_{\text{eff}}\text{-log}(g)$ diagram together with several evolutionary tracks. Only tracks for masses of $0.45 M_{\odot}$ are in accordance with the measured atmospheric parameters. This is a clear discrepancy with the low mass required from the ejection velocity. Geier et al. [2015a] argued that the further evolution of the subdwarf might not depend on the current mass as it was much more massive before the mass transfer started. If the helium in the core was already exhausted towards the end of the phase of mass-transfer, the further evolution would be influenced by the core mass rather than the total mass [Geier et al., 2015a]. However, even with the new proper motions and the resulting reduced ejection velocity, the discrepancy still concerning the stellar mass still remains significant and makes the ejection by a thermonuclear supernova from the disk at least more unlikely.

8.4.3.4 Ejection from the halo by a thermonuclear supernova

A possibility to resolve this unpleasant issue would be to re-think about the disk as the origin of US708 and the stellar type of our speeding friend.

Althaus et al. [2013b] recently found the closest sdB+WD binary known so far. With an orbital period of 44.7 minutes and a mass for the WD of $0.90 M_{\odot}$, OW J074106.0-294811.0 features a He-sdO primary of only $0.35 M_{\odot}$. It can therefore be described best as a pre-He-WD, a type of star which is not burning helium in its core. The evolutionary tracks for a star with almost the same mass of $0.34 M_{\odot}$ are matching the position of US708 in the $T_{\text{eff}}\text{-log}(g)$ diagram. Up to now, the possibility of US708 being a pre-He-WD was rejected as the evolutionary timescales of such an object are only around 1 Myr. This is a strong contradiction to the time of flight from the galactic disk to the current position of US708, which is about 1 magnitude larger. In addition, it was questioned if mass transfer from such an object was able to ignite a double-detonation supernova. Shen and Moore [2014] recently showed that even small amounts of helium on the surface of a CO white dwarf can be enough to trigger the detonation of the core. This implies that only a short period of mass transfer is necessary and different types of helium donors can be taken into account.

A very elegant solution to the problem would be to assume that US708 was ejected somewhere in the halo of our Galaxy. Some halo stars were shown to have rather extreme trajectories with Galactic restframe velocities of around 600 km/s. Corresponding hot subdwarfs and wide binaries have already been found ([Ziegerer et al.,

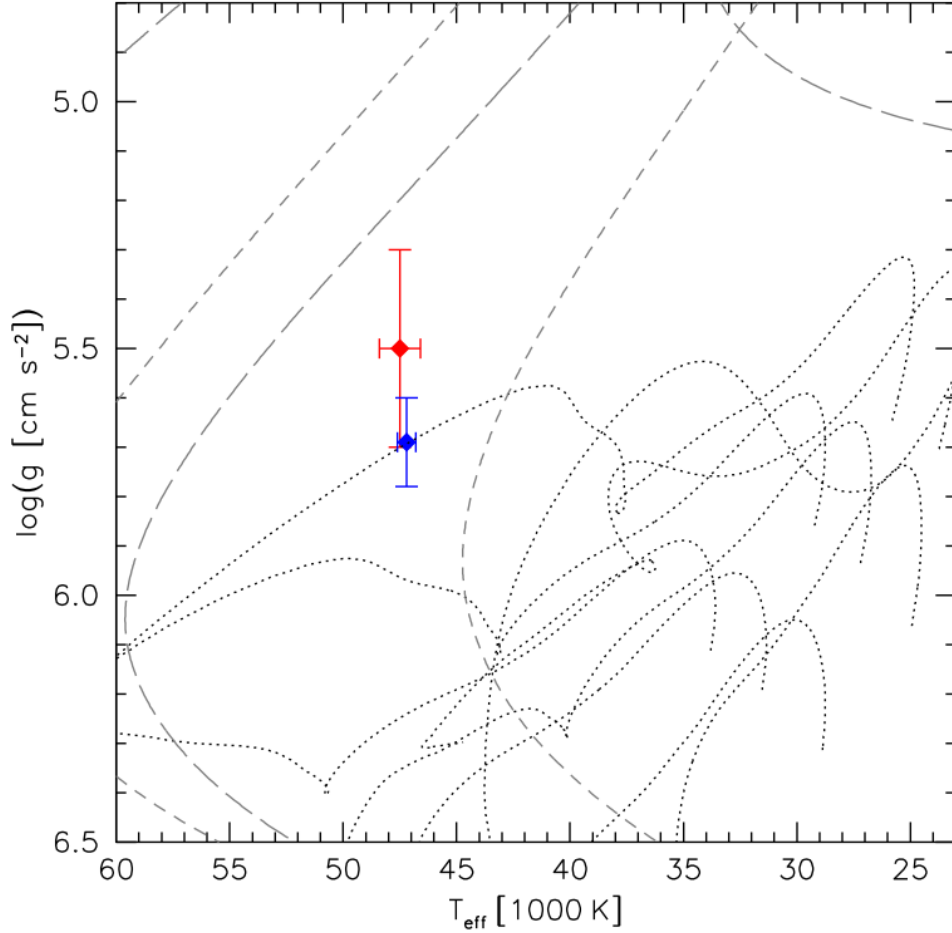


Figure 8.25: $T_{\text{eff}}\text{-log}(g)$ diagram showing the parameters of US708 derived in this work (red) and those derived by Geier et al. [2015a] (blue). The dotted lines show evolutionary tracks of core helium burning stars with solar metallicity ([Han et al., 2002]), with masses of $0.35 M_{\odot}$, $0.40 M_{\odot}$ and $0.45 M_{\odot}$ from lower right to upper left and different hydrogen envelope masses between zero and $0.005 M_{\odot}$ (from bottom to top). The dashed lines indicated evolutionary tracks for pre-He-Wds ([Althaus et al., 2013a]) with masses of $0.3207 M_{\odot}$ (short-dashed) and $0.3603 M_{\odot}$ (long-dashed).

2017], [Németi et al., 2016]). Such high velocities are already close to the escape velocity and only a comparatively small amount of extra energy would be required to set them unbound. Compared to ejection from the disk, the required RV semi-amplitude would need to be between 500 km/s to 600 km/s, not around 1000 km/s. This holds true for the most extreme halo star trajectories. For more moderate ones, the required orbital velocity goes up. This scenario would match the observed rotational velocity and the mass of US708 is likely to be consistent with the evolutionary tracks in the $T_{\text{eff}}\text{-log}(g)$ diagram.

To constrain the properties of the progenitor binary, the initial-to-final mass solution for white dwarfs can be applied with respect to the double-detonation supernova scenario. From this, the main sequence progenitor of the WD must have had a mass between $3.5 M_{\odot}$ and $8.0 M_{\odot}$. Using the current turnoff-mass of the Galactic halo,

an upper limit for the hot subdwarf mass is given by around $0.8 M_{\odot}$. As the initially more massive star has to evolve to the AGB-phase before forming a MS+WD binary after the common envelope phase, the orbital separation was expected to be around 100 AU, which then decrease to only 1 AU. Another common envelope phase after a long break of about 10 Gyrs then turned the main sequence star in a hot subdwarf, causing it to lose almost all of its envelope.

After having all these different options in mind, it seems most likely that US708 is indeed a pre-He-WD, being ejected from a close binary system somewhere in the halo by a double detonation SN Ia. Not only do we observe the predicted enrichment in iron and nickel, but also the required rotation. The possible halo tracks reduce the required orbital velocity and make the progenitor system appear less extreme.

9 Summary & Conclusion

Helium sdO stars represent a poorly understood phase of stellar evolution. Therefore, a detailed spectroscopic analysis of selected he-sdOs was carried out, supplemented by photometric and kinematic investigations. The spectroscopic analysis covered the atmospheric parameters and abundances of certain elements and was followed by an eye on photometric properties and evolutionary aspects.

A detailed study on spectroscopic grids, used to determine atmospheric parameters, with different metal contents was conducted. Starting with grid containing no metals, ones with additional nitrogen or carbon and ones with additional carbon, nitrogen and oxygen were used. If a “final“ model atmosphere (H, He, C, N, O, Ne, Mg, Al, Si, P, S, Fe, Ni) is considered as a reference it turned out that the different models show significant differences concerning the temperature stratification of the stellar atmospheres. The offset of the pure HHe model was largest. In the important line-forming region, the temperature differences went up to ~ 3000 K, while the HHeC/N or HHeCNO models showed much smaller deviations around several hundred Kelvin. The size of the deviations is of course dependent on the effective temperature and, to some extent, on the chemical composition of the atmosphere, so to speak which element with which opacity was included. A more realistic approach than comparing temperature stratification is a direct fit of helium lines, in which the differences between the grids start to diminish. Especially the resulting effective temperature was very similar. Differences in the surface gravity were much larger and caused by the effect of backwarming induced by the additional opacity. For future analysis, the pure HHe grids cannot be recommended. Grids with at least the most abundant metal affect the temperature stratification of the atmosphere in a positive way and allow for more precise determinations of the surface gravity.

From the sample of 12 stars, three subgroups were formed: The nitrogen rich He-sdO stars, showing the CNO by-cycle abundance patterns, the carbon and nitrogen rich He-sdO stars in which carbon and nitrogen are enriched above the solar level and the carbon rich He-sdO stars in which the carbon level is above the solar one and nitrogen is below or around solar (within the errorrange).

The nitrogen rich subsample is best explained with the merger of two He-core White Dwarfs. In contrast to the shallow - or deep mixing hot flasher scenario, almost all abundances can be explained. What is difficult to explain is the missing rotation. None of the analyzed N-rich stars shows any rotation above the significance level. This offers two plausible solutions. Either there is an effect or scenario that produces non-rotating stars from mergers or leads to a decline of rotation over time. The other possibility would be that the predictions on element abundances from the shallow mixing hot flasher scenario are not entirely correct, especially concerning hydrogen and oxygen.

After the abundance analyses it turned out that the distinction between C- and CN-rich He-sdOs was rather arbitrary. Both subsamples can be best explained by the deep-mixing hot flasher scenario, predicting all abundances correctly. Problems

with the nitrogen and neon abundances are most likely caused by the limitations of the evolutionary model. For the rotating stars from the C/CN-rich subgroup, the He-WD composite merger scenario was tested. For all stars the predictions of the composite merger model concerning the chemical abundances could not be completely reproduced. Especially the predicted level of oxygen and neon suffered from partially strong deviations compared to the measured abundances. Only for GALEX J095256.6-371940 the observed differences between observations and model are small enough to make a composite merger scenario appear possible although the deep-mixing hot flasher scenario offers a better agreement between measurements and predictions.

The possible halo star BD+39° 3226 shows an abundance pattern very similar to the N-rich subgroup and is most likely to share the same evolutionary history. It's general metal-poorness is not thought to have any direct influence on the formation mechanism.

The evolutionary scenario does usually not affect the intermediate mass elements (except neon) as the temperatures are not high enough to let any nuclear reactions at such high atomic numbers occur. This is plausible when considering the determined abundances. The intermediate mass elements all scatter around the solar value.

In all stars the iron abundance is below the nickel one. It can be argued that nickel is more sensitive to gravitational levitation as it features more possible, excitable states in the electron shells. But as iron also features a vast number of possible excited states, it remains questionable if the observed overabundance of nickel compared to iron is solely due to levitation or if, i.e., unstable iron isotopes are transformed to nickel by β -decay, resulting in a depletion of iron.

In theory heavier elements than iron should be observable in He-sdO stars. They could be created by the s-process, leading to an enrichment of heavy atoms. The seeds are i.e. iron or nickel atoms that capture free neutrons. Those particles are produced e.g. by the reaction



After being captured by a nucleus, a β -decay can occur and the neutron transforms into a proton, creating a new, heavier element.

Iron and nickel also play a keyrole for the understanding of one of the most spectacular He-sdO stars, US708, the fastest known hypervelocity star. In this thesis a detailed analysis of HST COS UV spectra of US708 and the comparison star CD-31° 4800 was performed. It was shown that US708 shows a significant enrichment in iron and nickel compared to CD -31° 4800. This supports the supernova ejection theory as an origin for its high velocity. This speed is the radial velocity semiamplitude of the companion of a progenitor binary and the additional kick by the explosion of the primary white dwarf itself. US708 was not only accelerated but also formed in a binary system. It is believed to have originated from a sdB+WD binary system in which the sdB had transferred most of its envelope onto a C/O white dwarf.

Geier et al. [2015a] assumed that the star was ejected from the Galactic disk. In this work a new theory, presenting US708 as the result of a double-detonation SN Ia in the Galactic halo was proposed. The possibility of inherently large Galactic restframe velocities and extreme trajectories allow to reduce the required orbital

velocity of US708 in the former binary system. The resulting mass range would be in good agreement with evolutionary tracks for a pre-He-WD . Together with the enrichment of iron and nickel and the fast rotation, the origin in a supernova explosion is highly likely. So far, no sdB+WD binaries close enough for a similar orbital velocity as suspected for the progenitor system of US708 have been found in the halo. Up to now, candidate progenitors were found in the disk population e.g. CD-30°11223. But there is no need for discouragement. The much higher density of stars towards the disk just makes a discovery there much more likely, putting a large selective bias on all numbers of sdB+WD binaries found there. As the ejection can happen at any point of the stellar trajectory, HVS moving towards the Galactic disc are also possible. The discovery of such a star would provide very strong evidence for the halo ejection scenario.

Unfortunately we were only able to compare the abundance pattern of US708 to one other star, CD-31° 4800, observed with the same instrument. This host potential for a large selection bias. It would have been better to compare it with a rather large sample of He-sdOs also showing the CNO bi-cycle abundance pattern. Various of these stars have been found by i.e. Hirsch [2009]. However, as none of the available sample used the combination of *tlusty*/*synspec* and did an abundance determination for iron and nickel, the number of possible comparison stars was limited. To avoid instrumental bias we wanted to use UV spectra from the same source for both US708 and the comparison star. Caused by the dimness of US708, the HST COS spectrograph was the only reasonable choice to obtain spectra. As for no star, all criteria for a comparison star were fulfilled at the same time, choosing CD-31° 4800 as a reference and obtaining the COS spectra directly after US708 seemed the best choice. However, keeping the difficulties encountered during the spectral analysis of CD-31° 4800 in mind, it might not have been the optimum choice as comparison star.

For most elements in CD-31° 4800 and US708, the abundances from the COS spectra are only upper limits or show no limits at all. This was either caused by the poor S/N ratio of the COS data, especially towards the red end and the poor resolution, smearing, in combination with the rotation of US708, all lines to a hardly distinguishable line porridge. Further COS observations would be helpful in enhancing the S/N ratio and therefore maybe allow to determine limits for more elements in US708. This would allow for further comparison with Supernova Ia models.

In a more general picture, it is important to understand not only the single evolution of certain stars, but also if and how atmospheric parameters might be grouping and emerging from different datasets. This can help to achieve a deeper understanding of the fitting process on the one hand and help to identify possible selection effects on the other hand.

To compare the properties of certain types of stars, it can be useful to put them in a $T_{\text{eff}}/\log(g)$ diagram (or a Hertzsprung-Russel diagram) and compare them to larger samples to investigate distributions and possible selection effects. A good base for comparison is the GALEX (GALaxy Evolution eXplorer) sample, more precisely the GALEX sample of hot subdwarfs as presented by Németh et al. [2012]. The selection of the hot subdwarf stars was based on color indices and the data consists of low resolution spectra. To determine the atmospheric parameters, XTGRID was used for the fitting process, based on *Tlusty* models. The parameters should be somewhat comparable as the same model atmosphere code was used as in this work. The fitting

procedure however was different (fitting single HeI and HeII lines vs fitting the complete spectrum) and the spectra only feature a comparatively low resolution. From this sample, the He-sdOs were selected by their identification label and a crosscheck of temperature, surface gravity and helium abundance to pick possible mismatches. Fig. 9.1 shows the GALEX sample of He-sdOs taken from Németh et al. [2012] in gray, the He-sdOs analyzed by Hirsch [2009] in black and the stars analyzed in this work in blue. It can be seen that the analyzed He-sdO stars lie in a regime typical for

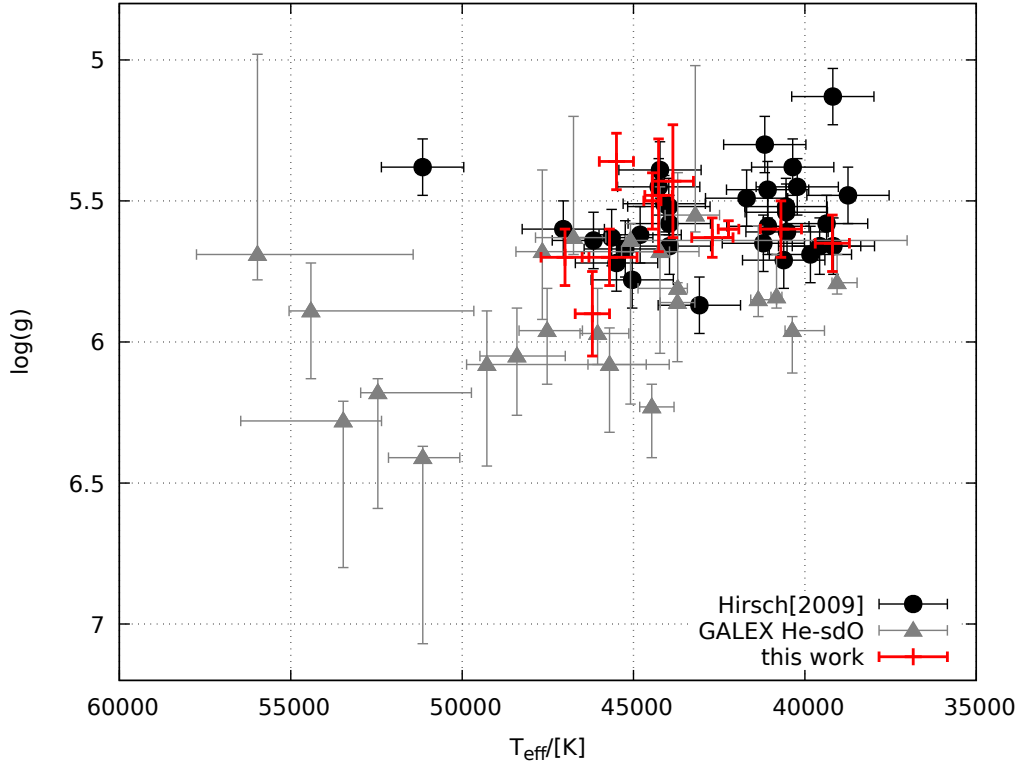


Figure 9.1: Comparison of the He-sdO stars analyzed in this thesis with He-sdO stars from the GALEX sample (taken from Németh et al. [2012]) and He-sdOs analyzed by Hirsch [2009].

these types of stars, the temperature is usually between 40000 K and 50000 K while the surface gravity varies around $\log(g)=5.5$. Compared to the sample of He-sdOs from Németh et al. [2012] it seems that the surface gravity is systematically lower, the sample tends to group slightly below the the GALEX sample. This reminds us of the problems concerning the lower surface gravity of CD-31° 4800 when compared to the results of Hirsch [2009] and the too low surface gravity of US708 as indicated by the χ^2 distribution of this parameter. For CD-31° 4800 the difference might be explained by the different atmosphere model codes that were used, but as XTGRID is also based on Tlusty models, the suspicion arises that the lower surface gravity must emerge either from the observed spectra (low vs high resolution) or from the fitting process itself. The parameter range for the surface gravity varied from 5.0 to 6.2 in our HHeCNO grid. The expected surface gravities were well covered by this grid and the starting values for the fit were usually set to 5.6, respectively the middle of the possible range. An effect might be induced by the resolution of the available

data. As already mentioned, the GALEX sample is based on low-resolution data, for CD-31° 4800 the analyzed UVES spectrum had a much higher resolution than the FEROS spectrum analyzed by Hirsch [2009]. Something similar can be applied for US708 for which the atmospheric parameters were obtained from the optical KECK ESI spectrum while the χ^2 distribution of the surface gravity resulted from a combined fit of the ESI spectrum with the low resolution COS spectrum or the COS spectrum itself. When compared to the sample provided by Hirsch [2009] no trend for too low or too high gravities or temperatures is visible.

An elegant solution to the $\log(g)$ problem would be to know the parallaxes of the corresponding stars as accurately as possible. However, measuring parallaxes is not easy. Up to now (February 2018), the best measurements for most He-sdOs are still the Hipparcos parallaxes which often are not as accurately as desired and gave uncertainties up to four mas. A milestone in Astronomy is ESA's GAIA satellite which is capable of measuring positions up to 200 times more accurately compared to Hipparcos. Unfortunately, none of the sample stars was contained within data release (DR) 1. They will be most likely included in DR2 which is planned to be made public in April 2018. Having the GAIA parallaxes, we will be able to determine the distance to the stars with unimagined precision which will automatically result in very precise estimates for the surface gravity and hopefully solve the inconsistencies encountered for some of the stars presented in this work.

Bibliography

- Lab course manual, Remeis Observatory. 2015.
- M. G. Abadi, J. F. Navarro, and M. Steinmetz. An Alternative Origin for Hyper-velocity Stars. *Astrophys. J.*, 691:L63–L66, Feb. 2009. doi: 10.1088/0004-637X/691/2/L63.
- C. Aerts, J. Puls, M. Godart, and M.-A. Dupret. On the origin of macroturbulence in hot stars. *Communications in Asteroseismology*, 158:66, July 2009.
- S. Alam, F. D. Albareti, C. Allende Prieto, F. Anders, S. F. Anderson, T. Anderton, B. H. Andrews, E. Armengaud, É. Aubourg, S. Bailey, and et al. The Eleventh and Twelfth Data Releases of the Sloan Digital Sky Survey: Final Data from SDSS-III. *Astrophys. J. Supp. Series*, 219:12, July 2015. doi: 10.1088/0067-0049/219/1/12.
- L. G. Althaus, M. M. Miller Bertolami, and A. H. Córscico. New evolutionary sequences for extremely low-mass white dwarfs. Homogeneous mass and age determinations and asteroseismic prospects. *Astronomy and Astrophysics*, 557:A19, Sept. 2013a. doi: 10.1051/0004-6361/201321868.
- L. G. Althaus, M. M. Miller Bertolami, and A. H. Córscico. New evolutionary sequences for extremely low-mass white dwarfs. Homogeneous mass and age determinations and asteroseismic prospects. *Astronomy and Astrophysics*, 557:A19, Sept. 2013b. doi: 10.1051/0004-6361/201321868.
- M. Asplund, N. Grevesse, A. J. Sauval, and P. Scott. The Chemical Composition of the Sun. *Annual Review of Astron. and Astrophys.*, 47:481–522, Sept. 2009. doi: 10.1146/annurev.astro.46.060407.145222.
- L. H. Auer. *Acceleration of Convergence*, page 101. 1987.
- L. H. Auer and D. Mihalas. Non-Lte Model Atmospheres. III. a Complete-Linearization Method. *Astrophys. J.*, 158:641, Nov. 1969. doi: 10.1086/150226.
- R. Barbier, F. Dossin, C. Jaschek, M. Jaschek, M. Klutz, J. P. Swings, and J. M. Vreux. Spectral classification of ultraviolet objects. *Astronomy and Astrophysics*, 66:L9–L10, June 1978.
- F. Bauer and D. Husfeld. Metal abundances in subdwarf O stars. *Astronomy and Astrophysics*, 300:481, Aug. 1995.
- J. Berger and A.-M. Fringant. Three new hot subdwarfs: AGK2 +81 266, BD +39 3226, BD +34 1543. *Astronomy and Astrophysics*, 64:L9–L11, Mar. 1978.
- J. Berger and A.-M. Fringant. A sample of new hot subluminoous stars taken from the list of ultraviolet objects detected by the S2/68 Sky Survey Experiment. *Astronomy and Astrophysics*, 85:367–369, May 1980.

- J. Biretta. STIS Instrument Handbook. 15, 2016.
- H. Bluhm, O. Marggraf, K. S. de Boer, P. Richter, and U. Heber. ORFEUS II echelle spectra: deuterium and molecular hydrogen in the ISM towards BD +39 3226. *Astronomy and Astrophysics*, 352:287–296, Dec. 1999.
- W. R. Brown. Hypervelocity Stars. *Annual Review of Astron. and Astrophys.*, 53: 15–49, Aug. 2015. doi: 10.1146/annurev-astro-082214-122230.
- W. R. Brown, J. Anderson, O. Y. Gnedin, H. E. Bond, M. J. Geller, and S. J. Kenyon. Proper Motions and Trajectories for 16 Extreme Runaway and Hypervelocity Stars. *Astrophys. J.*, 804:49, May 2015. doi: 10.1088/0004-637X/804/1/49.
- C. J. Cannon. Frequency-Quadrature Perturbations in Radiative-Transfer Theory. *Astrophys. J.*, 185:621–630, Oct. 1973. doi: 10.1086/152442.
- D. F. Carbon. *Line blanketing*, pages 395–426. 1984.
- P. Chayer, F. LeBlanc, G. Fontaine, F. Wesemael, G. Michaud, and S. Vennes. On the predicted abundances of iron and nickel supported by radiative levitation in the atmospheres of hot DA white dwarfs. *Astrophys. J.*, 436:L161–L164, Dec. 1994. doi: 10.1086/187657.
- R. M. Cutri, M. F. Skrutskie, S. van Dyk, C. A. Beichman, J. M. Carpenter, T. Chester, L. Cambresy, T. Evans, J. Fowler, J. Gizis, E. Howard, J. Huchra, T. Jarrett, E. L. Kopan, J. D. Kirkpatrick, R. M. Light, K. A. Marsh, H. McCallon, S. Schneider, R. Stiening, M. Sykes, M. Weinberg, W. A. Wheaton, S. Wheelock, and N. Zacarias. VizieR Online Data Catalog: 2MASS All-Sky Catalog of Point Sources (Cutri+ 2003). *VizieR Online Data Catalog*, 2246, June 2003.
- R. M. e. Cutri. VizieR Online Data Catalog: WISE All-Sky Data Release (Cutri+ 2012). *VizieR Online Data Catalog*, 2311, 2012.
- J. Debes. Cosmic Origins Spectrograph Instrument Handbook. 2016.
- W. Demtröder. *Experimentalphysik - Atmoe, Moleküle und Festkörper*. 2010.
- W. V. Dixon, D. J. Sahnou, P. E. Barrett, T. Civeit, J. Dupuis, A. W. Fullerton, B. Godard, J.-C. Hsu, M. E. Kaiser, J. W. Kruk, S. Lacour, D. J. Lindler, D. Massa, R. D. Robinson, M. L. Romelfanger, and P. Sonnentrucker. CalFUSE Version 3: A Data Reduction Pipeline for the Far Ultraviolet Spectroscopic Explorer. *Publications of the ASP*, 119:527–555, May 2007. doi: 10.1086/518617.
- D. Dravins, H. Jensen, S. LeBohec, and P. D. Nuñez. Stellar intensity interferometry: astrophysical targets for sub-milliarcsecond imaging. In *Optical and Infrared Interferometry II*, volume 7734, page 77340A, July 2010. doi: 10.1117/12.856394.
- S. Dreizler. Spectral Analysis of Extremely Helium Rich Subdwarf O-Stars. *Astronomy and Astrophysics*, 273:212, June 1993.
- J. S. Drilling and U. Heber. Radial velocities of hot SDO stars. In A. G. D. Philip, D. S. Hayes, and J. W. Liebert, editors, *IAU Colloq. 95: Second Conference on Faint Blue Stars*, pages 603–606, 1987.

- M. M. Dworetzky, P. A. Whitelock, and D. J. Carnochan. Optical observations of ultraviolet objects. II - Classification and photometry / $l = 0$ to 145 deg/. *Monthly Notices of the RAS*, 201:901–922, Dec. 1982. doi: 10.1093/mnras/201.4.901.
- H. Edelmann, R. Napiwotzki, U. Heber, N. Christlieb, and D. Reimers. HE 0437-5439: An Unbound Hypervelocity Main-Sequence B-Type Star. *Astrophys. J.*, 634:L181–L184, Dec. 2005. doi: 10.1086/498940.
- D. Egret, P. Didelon, B. J. McLean, J. L. Russell, and C. Turon. The TYCHO Input Catalogue - Cross-matching the Guide Star Catalog with the HIPPARCOS INCA Data Base. *Astronomy and Astrophysics*, 258:217–222, May 1992.
- ESA, editor. *The HIPPARCOS and TYCHO catalogues. Astrometric and photometric star catalogues derived from the ESA HIPPARCOS Space Astrometry Mission*, volume 1200 of *ESA Special Publication*, 1997.
- P. N. Fedorov, V. S. Akhmetov, and V. V. Bobylev. Residual rotation of the Hipparcos/Tycho-2 system as determined from the data of the XPM catalogue. *Monthly Notices of the RAS*, 416:403–408, Sept. 2011. doi: 10.1111/j.1365-2966.2011.19045.x.
- D. H. Ferguson, R. F. Green, and J. Liebert. Hot subdwarfs in detached binary systems and thick-disk cataclysmic variables from the Palomar-Green survey. *Astrophys. J.*, 287:320–333, Dec. 1984. doi: 10.1086/162691.
- F. R. Ferraro, B. Paltrinieri, F. Fusi Pecci, C. Cacciari, B. Dorman, and R. T. Rood. Hubble Space Telescope Ultraviolet Observations of the Cores of M3 and M13. *Astrophys. J.*, 484:L145–L148, Aug. 1997. doi: 10.1086/310780.
- E. L. Fitzpatrick. Correcting for the Effects of Interstellar Extinction. *Publications of the ASP*, 111:63–75, Jan. 1999. doi: 10.1086/316293.
- R. F. Garrison and W. A. Hiltner. CPD -31 1701, an extremely helium-rich subluminescent, O-type star. *Astrophys. J.*, 179:L117, Feb. 1973. doi: 10.1086/181129.
- S. Geier, F. Fürst, E. Ziegerer, T. Kupfer, U. Heber, A. Irrgang, B. Wang, Z. Liu, Z. Han, B. Sesar, D. Levitan, R. Kotak, E. Magnier, K. Smith, W. S. Burgett, K. Chambers, H. Flewelling, N. Kaiser, R. Wainscoat, and C. Waters. The fastest unbound star in our Galaxy ejected by a thermonuclear supernova. *Science*, 347:1126–1128, Mar. 2015a. doi: 10.1126/science.1259063.
- S. Geier, T. Kupfer, U. Heber, V. Schaffenroth, B. N. Barlow, R. H. Østensen, S. J. O’Toole, E. Ziegerer, C. Heuser, P. F. L. Maxted, B. T. Gänsicke, T. R. Marsh, R. Napiwotzki, P. Brünner, M. Schindewolf, and F. Niederhofer. The catalogue of radial velocity variable hot subluminescent stars from the MUCHFUSS project. *Astronomy and Astrophysics*, 577:A26, May 2015b. doi: 10.1051/0004-6361/201525666.
- R. Genzel, F. Eisenhauer, and S. Gillessen. The Galactic Center massive black hole and nuclear star cluster. *Reviews of Modern Physics*, 82:3121–3195, Oct. 2010. doi: 10.1103/RevModPhys.82.3121.

- J. R. Giddings. PhD thesis, , University of London, (1981), June 1981.
- K. N. Gourgouliatos and C. S. Jeffery. On the angular momentum evolution of merged white dwarfs. *Monthly Notices of the RAS*, 371:1381–1389, Sept. 2006. doi: 10.1111/j.1365-2966.2006.10780.x.
- R. F. Green, M. Schmidt, and J. Liebert. The Palomar-Green catalog of ultraviolet-excess stellar objects. *Astrophys. J. Supp. Series*, 61:305–352, June 1986. doi: 10.1086/191115.
- J. L. Greenstein. The Nature of the Faint Blue Stars. *Astrophys. J.*, 144:496, May 1966. doi: 10.1086/148633.
- A. Gualandris and S. Portegies Zwart. A hypervelocity star from the Large Magellanic Cloud. *Monthly Notices of the RAS*, 376:L29–L33, Mar. 2007. doi: 10.1111/j.1745-3933.2007.00280.x.
- S. Haas. PhD thesis, PhD thesis, University of Erlangen-Nürnberg, Germany, (1997), 1997.
- Z. Han, P. Podsiadlowski, P. F. L. Maxted, T. R. Marsh, and N. Ivanova. The origin of subdwarf B stars - I. The formation channels. *Monthly Notices of the RAS*, 336:449–466, Oct. 2002. doi: 10.1046/j.1365-8711.2002.05752.x.
- B. Hauck and M. Mermilliod. VizieR Online Data Catalog: uvby-beta Catalogue (Hauck+ 1997). *VizieR Online Data Catalog*, 2215, Oct. 1997.
- U. Heber. Subluminous O Stars – Origin and Evolutionary Links. In A. Werner and T. Rauch, editors, *Hydrogen-Deficient Stars*, volume 391 of *Astronomical Society of the Pacific Conference Series*, page 245, July 2008.
- U. Heber. Hot Subdwarf Stars. *Annual Review of Astron. and Astrophys.*, 47: 211–251, Sept. 2009. doi: 10.1146/annurev-astro-082708-101836.
- U. Heber. Hot Subluminous Stars. *PASP*, 128(8):082001, Aug. 2016. doi: 10.1088/1538-3873/128/966/082001.
- U. Heber, A. Irrgang, and J. Schaffenroth. Spectral energy distributions and colours of hot subluminous stars. *ArXiv e-prints*, Dec. 2017.
- A. A. Henden, M. Templeton, D. Terrell, T. C. Smith, S. Levine, and D. Welch. VizieR Online Data Catalog: AAVSO Photometric All Sky Survey (APASS) DR9 (Henden+, 2016). *VizieR Online Data Catalog*, 2336, Jan. 2016.
- J. G. Hills. Hyper-velocity and tidal stars from binaries disrupted by a massive Galactic black hole. *Nature*, 331:687–689, Feb. 1988. doi: 10.1038/331687a0.
- H. A. Hirsch. *Hot subluminous stars: On the Search for Chemical Signatures of their Genesis*. PhD thesis, Friedrich-Alexander University Erlangen-Nürnberg, Oct. 2009.
- H. A. Hirsch, U. Heber, S. J. O’Toole, and F. Bresolin. <ASTROBJ>US 708</ASTROBJ> - an unbound hyper-velocity subluminous O star. *Astronomy and Astrophysics*, 444:L61–L64, Dec. 2005. doi: 10.1051/0004-6361:200500212.

- E. Høg, C. Fabricius, V. V. Makarov, S. Urban, T. Corbin, G. Wycoff, U. Bastian, P. Schwekendiek, and A. Wicenec. The Tycho-2 catalogue of the 2.5 million brightest stars. *Astronomy and Astrophysics*, 355:L27–L30, Mar. 2000.
- I. Hubeny and T. Lanz. Accelerated complete-linearization method for calculating NLTE model stellar atmospheres. *Astronomy and Astrophysics*, 262:501–514, Sept. 1992.
- I. Hubeny and T. Lanz. Non-LTE line-blanketed model atmospheres of hot stars. 1: Hybrid complete linearization/accelerated lambda iteration method. *Astrophys. J.*, 439:875–904, Feb. 1995. doi: 10.1086/175226.
- I. Hubeny and T. Lanz. Model Photospheres with Accelerated Lambda Iteration. In I. Hubeny, D. Mihalas, and K. Werner, editors, *Stellar Atmosphere Modeling*, volume 288 of *Astronomical Society of the Pacific Conference Series*, page 51, Jan. 2003.
- I. Hubeny, S. Stefl, and P. Harmanec. How strong is the evidence of superionization and large mass outflows in B/Be stars? *Bulletin of the Astronomical Institutes of Czechoslovakia*, 36:214–230, July 1985.
- P. Hudelot, J.-C. Cuillandre, K. Withington, Y. Goranova, H. McCracken, F. Magnard, Y. Mellier, N. Regnault, M. Betoule, H. Aussel, J. J. Kavelaars, P. Fernique, F. Bonnarel, F. Ochsenein, and O. Ilbert. VizieR Online Data Catalog: The CFHTLS Survey (T0007 release) (Hudelot+ 2012). *VizieR Online Data Catalog*, 2317, Sept. 2012.
- M. L. Humason and F. Zwicky. A Search for Faint Blue Stars. *Astrophys. J.*, 105:85, Jan. 1947. doi: 10.1086/144884.
- A. Irrgang. Origin of runaway ob stars, 2014.
- A. Irrgang, N. Przybilla, U. Heber, M. F. Nieva, and S. Schuh. The Nature of the Hyper-Runaway Candidate Hip 60350. *Astrophys. J.*, 711:138–143, Mar. 2010. doi: 10.1088/0004-637X/711/1/138.
- A. Irrgang, B. Wilcox, E. Tucker, and L. Schiefelbein. Milky Way mass models for orbit calculations. *Astronomy and Astrophysics*, 549:A137, Jan. 2013. doi: 10.1051/0004-6361/201220540.
- N. V. Kharchenko. All-sky compiled catalogue of 2.5 million stars. *Kinematika i Fizika Nebesnykh Tel*, 17:409–423, Oct. 2001.
- D. Kilkenny and S. Muller. Radial velocities and spectral types for a sample of faint blue stars. *South African Astronomical Observatory Circular*, 13:69–82, 1989.
- D. Kilkenny, U. Heber, and J. S. Drilling. A catalogue of spectroscopically identified hot subdwarf stars. *South African Astronomical Observatory Circular*, 12, 1988.
- D. Kilkenny, D. O’Donoghue, C. Koen, R. S. Stobie, and A. Chen. The Edinburgh-Cape Blue Object Survey - II. Zone 1 - the North Galactic CAP. *Monthly Notices of the RAS*, 287:867–893, June 1997. doi: 10.1093/mnras/287.4.867.

- R. P. Kudritzki. The formation of weak metal lines in the atmosphere of O-stars - The role of microturbulence and transonic matter outflow. *Astronomy and Astrophysics*, 266:395–401, Dec. 1992.
- A. U. Landolt and A. K. Uomoto. Optical Multicolor Photometry of Spectrophotometric Standard Stars. *Astronomical J.*, 133:768–790, Mar. 2007. doi: 10.1086/510485.
- T. Lanz, T. M. Brown, A. V. Sweigart, I. Hubeny, and W. B. Landsman. Flash Mixing on the White Dwarf Cooling Curve: Far Ultraviolet Spectroscopic Explorer Observations of Three He-rich sdB Stars. *Astrophys. J.*, 602:342–355, Feb. 2004. doi: 10.1086/380904.
- Y.-W. Lee, S.-J. Joo, S.-I. Han, C. Chung, C. H. Ree, Y.-J. Sohn, Y.-C. Kim, S.-J. Yoon, S. K. Yi, and P. Demarque. Super-Helium-rich Populations and the Origin of Extreme Horizontal-Branch Stars in Globular Clusters. *Astrophys. J.*, 621:L57–L60, Mar. 2005. doi: 10.1086/428944.
- P. J. T. Leonard. The maximum possible velocity of dynamically ejected runaway stars. *Astronomical J.*, 101:562–571, Feb. 1991. doi: 10.1086/115704.
- Z.-W. Liu, R. Pakmor, F. K. Röpkke, P. Edelmann, W. Hillebrandt, W. E. Kerzendorf, B. Wang, and Z. W. Han. Rotation of surviving companion stars after type Ia supernova explosions in the WD+MS scenario. *Astronomy and Astrophysics*, 554:A109, June 2013a. doi: 10.1051/0004-6361/201220903.
- Z.-W. Liu, R. Pakmor, I. R. Seitenzahl, W. Hillebrandt, M. Kromer, F. K. Röpkke, P. Edelmann, S. Taubenberger, K. Maeda, B. Wang, and Z. W. Han. The Impact of Type Ia Supernova Explosions on Helium Companions in the Chandrasekhar-mass Explosion Scenario. *Astrophys. J.*, 774:37, Sept. 2013b. doi: 10.1088/0004-637X/774/1/37.
- K. Maeda, S. Benetti, M. Stritzinger, F. K. Röpkke, G. Folatelli, J. Sollerman, S. Taubenberger, K. Nomoto, G. Leloudas, M. Hamuy, M. Tanaka, P. A. Mazzali, and N. Elias-Rosa. An asymmetric explosion as the origin of spectral evolution diversity in type Ia supernovae. *Nature*, 466:82–85, July 2010. doi: 10.1038/nature09122.
- J. C. Mermilliod. VizieR Online Data Catalog: Homogeneous Means in the UBV System (Mermilliod 1991). *VizieR Online Data Catalog*, 2168, Sept. 1997.
- D. Mihalas. *Stellar atmospheres /2nd edition/*. 1978.
- D. G. Monet, S. E. Levine, B. Canzian, H. D. Ables, A. R. Bird, C. C. Dahn, H. H. Guetter, H. C. Harris, A. A. Henden, S. K. Leggett, H. F. Levison, C. B. Luginbuhl, J. Martini, A. K. B. Monet, J. A. Munn, J. R. Pier, A. R. Rhodes, B. Riepe, S. Sell, R. C. Stone, F. J. Vrba, R. L. Walker, G. Westerhout, R. J. Brucato, I. N. Reid, W. Schoening, M. Hartley, M. A. Read, and S. B. Tritton. The USNO-B Catalog. *Astronomical J.*, 125:984–993, Feb. 2003. doi: 10.1086/345888.

- R. Napiwotzki, L. Yungelson, G. Nelemans, T. R. Marsh, B. Leibundgut, R. Renzini, D. Homeier, D. Koester, S. Moehler, N. Christlieb, D. Reimers, H. Drechsel, U. Heber, C. Karl, and E.-M. Pauli. Double degenerates and progenitors of supernovae type Ia. In R. W. Hilditch, H. Hensberge, and K. Pavlovski, editors, *Spectroscopically and Spatially Resolving the Components of the Close Binary Stars*, volume 318 of *Astronomical Society of the Pacific Conference Series*, pages 402–410, Dec. 2004.
- J. J. Nassau and C. B. Stephenson. Luminous Stars in the Northern Milky Way. *Hamburger Sternw. Warner & Swasey Obs.*, 1963.
- P. Nemeth. *Non-LTE luminosity and abundance diagnostics of classical novae in x-rays*. PhD thesis, Florida Institute of Technology, June 2010.
- P. N emeth. Astroserver - Research Services in the Stellar Webshop. *Open Astronomy*, 26:179–186, Dec. 2017. doi: 10.1515/astro-2017-0434.
- P. N emeth, A. Kawka, and S. Vennes. A selection of hot subluminous stars in the GALEX survey - II. Subdwarf atmospheric parameters. *Monthly Notices of the RAS*, 427:2180–2211, Dec. 2012. doi: 10.1111/j.1365-2966.2012.22009.x.
- P. N emeth, E. Ziegerer, A. Irrgang, S. Geier, F. F urst, T. Kupfer, and U. Heber. An Extremely Fast Halo Hot Subdwarf Star in a Wide Binary System. *Astrophys. J.*, 821:L13, Apr. 2016. doi: 10.3847/2041-8205/821/1/L13.
- K. Nomoto, F.-K. Thielemann, and K. Yokoi. Accreting white dwarf models of Type I supernovae. III - Carbon deflagration supernovae. *Astrophys. J.*, 286:644–658, Nov. 1984. doi: 10.1086/162639.
- G. L. Olson and P. B. Kunasz. Short characteristic solution of the non-LTE transfer problem by operator perturbation. I. The one-dimensional planar slab. *Journal of Quantitative Spectroscopy and Radiative Transfer*, 38:325–336, 1987. doi: 10.1016/0022-4073(87)90027-6.
- S. J. O’Toole. Beyond the iron group: Heavy metals in hot subdwarfs. *Astronomy and Astrophysics*, 423:L25–L28, Aug. 2004. doi: 10.1051/0004-6361:200400027.
- K.-C. Pan, P. M. Ricker, and R. E. Taam. Impact of Type Ia Supernova Ejecta on Binary Companions in the Single-degenerate Scenario. *Astrophys. J.*, 750:151, May 2012. doi: 10.1088/0004-637X/750/2/151.
- E. Paunzen. A new catalogue of Str omgren-Crawford $uvby\beta$ photometry. *Astronomy and Astrophysics*, 580:A23, Aug. 2015. doi: 10.1051/0004-6361/201526413.
- M. J. Penston. Photoelectric UVB observations made on the Palomar 20-inch telescope. *Monthly Notices of the RAS*, 164:133, 1973. doi: 10.1093/mnras/164.2.133.
- H. B. Perets. Runaway and Hypervelocity Stars in the Galactic Halo: Binary Rejuvenation and Triple Disruption. *Astrophys. J.*, 698:1330–1340, June 2009. doi: 10.1088/0004-637X/698/2/1330.

- A. Poveda, J. Ruiz, and C. Allen. Run-away Stars as the Result of the Gravitational Collapse of Proto-stellar Clusters. *Boletín de los Observatorios Tonantzintla y Tacubaya*, 4:86–90, Apr. 1967.
- P. Renson and J. Manfroid. VizieR Online Data Catalog: General Catalogue of Ap and Am stars (Renson+ 2009). *VizieR Online Data Catalog*, 3260, Apr. 2009.
- C. Rodríguez-López, A. Ulla, and R. Garrido. The first extensive search for sdO pulsators. *Monthly Notices of the RAS*, 379:1123–1132, Aug. 2007. doi: 10.1111/j.1365-2966.2007.11989.x.
- S. Roeser, M. Demleitner, and E. Schilbach. The PPMXL Catalog of Positions and Proper Motions on the ICRS. Combining USNO-B1.0 and the Two Micron All Sky Survey (2MASS). *Astronomical J.*, 139:2440–2447, June 2010. doi: 10.1088/0004-6256/139/6/2440.
- F. Rufener. *Catalogue of stars measured in the Geneva Observatory photometric system : 4 : 1988*. 1988.
- G. B. Rybicki and D. G. Hummer. An accelerated lambda iteration method for multilevel radiative transfer. I - Non-overlapping lines with background continuum. *Astronomy and Astrophysics*, 245:171–181, May 1991.
- V. Schaffenroth, N. Przybilla, K. Butler, A. Irrgang, and U. Heber. Observations of the extreme runaway HD271791: nucleosynthesis in a core-collapse supernova. *ArXiv e-prints*, Jan. 2015.
- D. Schonberner and J. S. Drilling. Effective temperatures and luminosities of very hot O type subdwarfs. *Astrophys. J.*, 278:702–710, Mar. 1984. doi: 10.1086/161839.
- M. Schork. Die unterleuchtkräftigen O-Sterne HZ44 und BD +75 325, Mar. 2017.
- A. I. Sheinis, M. Bolte, H. W. Epps, R. I. Kibrick, J. S. Miller, M. V. Radovan, B. C. Bigelow, and B. M. Sutin. ESI, a New Keck Observatory Echellette Spectrograph and Imager. *Publications of the ASP*, 114:851–865, Aug. 2002. doi: 10.1086/341706.
- K. J. Shen and K. Moore. The Initiation and Propagation of Helium Detonations in White Dwarf Envelopes. *Astrophys. J.*, 797:46, Dec. 2014. doi: 10.1088/0004-637X/797/1/46.
- M. A. Stark and R. A. Wade. Single and Composite Hot Subdwarf Stars in the Light of 2MASS Photometry. *Astronomical J.*, 126:1455–1471, Sept. 2003. doi: 10.1086/377017.
- A. Stroeer, U. Heber, T. Lisker, R. Napiwotzki, S. Dreizler, N. Christlieb, and D. Reimers. Hot subdwarfs from the ESO supernova Ia progenitor survey. II. Atmospheric parameters of subdwarf O stars. *Astronomy and Astrophysics*, 462:269–280, Jan. 2007. doi: 10.1051/0004-6361:20065564.

- B. Strömberg. Two-dimensional spectral classification of F stars through photoelectric photometry with interference filters. *Vistas in Astronomy*, 2:1336–1346, 1956. doi: 10.1016/0083-6656(56)90060-5.
- T. M. Tauris. Maximum speed of hypervelocity stars ejected from binaries. *Monthly Notices of the RAS*, 448:L6–L10, Mar. 2015a. doi: 10.1093/mnrasl/slu189.
- T. M. Tauris. Maximum speed of hypervelocity stars ejected from binaries. *Monthly Notices of the RAS*, 448:L6–L10, Mar. 2015b. doi: 10.1093/mnrasl/slu189.
- H.-J. Tian, P. Gupta, B. Sesar, H.-W. Rix, N. F. Martin, C. Liu, B. Goldman, I. Platais, R.-P. Kudritzki, and C. Z. Waters. A Gaia-PS1-SDSS (GPS1) Proper Motion Catalog Covering 3/4 of the Sky. *ArXiv e-prints*, Mar. 2017.
- A. Tillich, U. Heber, S. Geier, H. Hirsch, P. F. L. Maxted, B. T. Gänsicke, T. R. Marsh, R. Napiwotzki, R. H. Østensen, and R.-D. Scholz. The Hyper-MUCHFUSS project: probing the Galactic halo with sdB stars. *Astronomy and Astrophysics*, 527:A137, Mar. 2011. doi: 10.1051/0004-6361/201015539.
- A. Ulla and P. Thejll. Infrared flux excesses from hot subdwarfs. II. 72 more objects. *Astronomy and Astrophysics Supplement*, 132:1–12, Oct. 1998. doi: 10.1051/aas:1998439.
- P. D. Usher and K. J. Mitchell. Faint blue objects at high galactic latitude. III - Palomar Schmidt field centered on selected area 28. *APJS*, 49:27–52, May 1982. doi: 10.1086/190789.
- G. Valyavin, S. Bagnulo, S. Fabrika, A. Reisenegger, G. A. Wade, I. Han, and D. Monin. A Search for Kilogauss Magnetic Fields in White Dwarfs and Hot Subdwarf Stars. *Astrophys. J.*, 648:559–564, Sept. 2006. doi: 10.1086/505781.
- F. van Leeuwen. Validation of the new Hipparcos reduction. *Astronomy and Astrophysics*, 474:653–664, Nov. 2007. doi: 10.1051/0004-6361:20078357.
- S. Vennes, A. Kawka, and P. Németh. A selection of hot subluminescent stars in the GALEX survey - I. Correlation with the Guide Star Catalog. *Monthly Notices of the RAS*, 410:2095–2112, Jan. 2011. doi: 10.1111/j.1365-2966.2010.17584.x.
- J. Vernet, H. Dekker, S. D’Odorico, L. Kaper, P. Kjaergaard, F. Hammer, S. Randich, F. Zerbi, P. J. Groot, J. Hjorth, I. Guinouard, R. Navarro, T. Adolfsen, P. W. Albers, J.-P. Amans, J. J. Andersen, M. I. Andersen, P. Binetruy, P. Bristow, R. Castillo, F. Chemla, L. Christensen, P. Conconi, R. Conzelmann, J. Dam, V. de Caprio, A. de Ugarte Postigo, B. Delabre, P. di Marcantonio, M. Downing, E. Elswijk, G. Finger, G. Fischer, H. Flores, P. François, P. Goldoni, L. Guglielmi, R. Haigron, H. Hanenburg, I. Hendriks, M. Horrobin, D. Horville, N. C. Jessen, F. Kerber, L. Kern, M. Kiekebusch, P. Kleszcz, J. Klougart, J. Kragt, H. H. Larsen, J.-L. Lizon, C. Lucuix, V. Mainieri, R. Manuputy, C. Martayan, E. Mason, R. Mazzoleni, N. Michaelsen, A. Modigliani, S. Moehler, P. Møller, A. Norup Sørensen, P. Nørregaard, C. Péroux, F. Patat, E. Pena, J. Pragt, C. Reinero, F. Rigal, M. Riva, R. Roelfsema, F. Royer, G. Sacco, P. Santin, T. Schoenmaker, P. Spano, E. Sweers, R. Ter Horst, M. Tintori, N. Tromp, P. van Dael, H. van der

- Vliet, L. Venema, M. Vidali, J. Vinther, P. Vola, R. Winters, D. Wistisen, G. Wulterkens, and A. Zacchei. X-shooter, the new wide band intermediate resolution spectrograph at the ESO Very Large Telescope. *Astronomy and Astrophysics*, 536:A105, Dec. 2011. doi: 10.1051/0004-6361/201117752.
- S. S. Vogt, S. L. Allen, B. C. Bigelow, L. Bresee, B. Brown, T. Cantrall, A. Conrad, M. Couture, C. Delaney, H. W. Epps, D. Hilyard, D. F. Hilyard, E. Horn, N. Jern, D. Kanto, M. J. Keane, R. I. Kibrick, J. W. Lewis, J. Osborne, G. H. Pardeilhan, T. Pfister, T. Ricketts, L. B. Robinson, R. J. Stover, D. Tucker, J. Ward, and M. Z. Wei. HIRES: the high-resolution echelle spectrometer on the Keck 10-m Telescope. In D. L. Crawford and E. R. Craine, editors, *Instrumentation in Astronomy VIII*, volume 2198 of *Proc. SPIE Instrumentation in Astronomy VIII*, page 362, June 1994. doi: 10.1117/12.176725.
- A. R. Walker. Spectroscopy of four subdwarf O stars. *Monthly Notices of the RAS*, 197:241–246, Oct. 1981. doi: 10.1093/mnras/197.2.241.
- R. F. Webbink. Double white dwarfs as progenitors of R Coronae Borealis stars and Type I supernovae. *Astrophys. J.*, 277:355–360, Feb. 1984. doi: 10.1086/161701.
- K. Werner and S. Dreizler. The classical stellar atmosphere problem. *Journal of Computational and Applied Mathematics*, 109:65–93, Sept. 1999.
- N. Zacharias, D. G. Monet, S. E. Levine, S. E. Urban, R. Gaume, and G. L. Wycoff. The Naval Observatory Merged Astrometric Dataset (NOMAD). In *American Astronomical Society Meeting Abstracts*, volume 36 of *Bulletin of the American Astronomical Society*, page 1418, Dec. 2004.
- N. Zacharias, C. T. Finch, T. M. Girard, A. Henden, J. L. Bartlett, D. G. Monet, and M. I. Zacharias. VizieR Online Data Catalog: UCAC4 Catalogue (Zacharias+, 2012). *VizieR Online Data Catalog*, 1322, July 2012.
- X. Zhang and C. S. Jeffery. Evolutionary models for double helium white dwarf mergers and the formation of helium-rich hot subdwarfs. *Monthly Notices of the RAS*, 419:452–464, Jan. 2012. doi: 10.1111/j.1365-2966.2011.19711.x.
- E. Ziegerer, U. Heber, S. Geier, A. Irrgang, T. Kupfer, F. Fürst, and J. Schaffenroth. Spectroscopic twin to the hypervelocity sdO star US 708 and three fast sdB stars from the Hyper-MUCHFUSS project. *Astronomy and Astrophysics*, 601:A58, May 2017. doi: 10.1051/0004-6361/201730437.

List of Figures

2.1	The equivalent width of several elements and ionization stages plotted versus temperature and spectral class. Taken from: ¹	5
2.2	A Hertzsprung-Russell diagram. The luminosity is plotted versus the effective temperature.	6
2.3	Typical spectra of sdB and sdO stars with indication of important hydrogen and helium lines. Taken from Heber [2009].	8
2.4	Kippenhahn diagram for the deep mixing scenario, Adopted from: Hirsch [2009].	10
2.5	Kippenhahn diagram for the shallow mixing scenario. Adopted from Hirsch [2009].	11
2.6	Kippenhahn diagram for the composite mixing scenario. Adopted from Hirsch [2009].	11
2.7	Schematic overview on the three different merging models for helium white dwarfs. Taken from Zhang and Jeffery [2012].	12
2.8	Binding energy per nucleon plotted versus number of nucleons. Taken from: ¹	15
2.9	Schematic overview on the pp-chain mechanism. The resulting helium is colored blue, while the burnt hydrogen is red. Taken from Irrgang [2014].	16
2.10	Schematic overview on the CNO bi-cycle. The resulting helium is colored blue, while the burnt hydrogen is red. Taken from Irrgang [2014].	18
2.11	Onion-like structure of an evolved, massive star, not to scale. Taken from Irrgang [2014].	20
2.12	Distribution of late-type stars (red) and early-type stars (blue) within one parsec around the central galactic region.	25
2.13	Orbits of several S-stars. Taken from ²	25
2.14	Aitoff projection showing stars from a disrupted satellite galaxy (red) and HV stars with velocities $> 400\text{km/s}$ in the tidal stream (blue)	26
2.15	Visualization of dynamical interaction between binary systems.	27
3.1	Measuring of angle Θ . Adopted from Irrgang et al. [2013].	31
3.2	Overview on the different stellar coordinate systems and their starting & end values.	32
3.3	Influence of the rotational velocity on a line profile at different velocities.	39
4.1	Comparison between actual cross sections (upper panel) and the ODF constructed from it (lower panel)	46
4.2	Superlevels and -lines for FeII and FeIII in a Grotrian diagram.	49
4.3	ODFs computed for three different depth points.	50
4.4	Comparison of selected helium lines of a TLUSTYmodel spectrum (red) and a TMAP model spectrum (black).	52

4.5	Screenshot of SPAS output, showing fits to several Balmer lines of a faint sdB star.	54
4.6	Relative temperature stratification of the atmosphere of CD-31° 4800	57
4.7	Relative temperature stratification of the atmosphere of [CW83] 0904-02	58
4.8	Fits to several He I and HeII lines derived from a synthetic spectrum of CD-31° 4800 using the HHeCNO grid.	59
4.9	The different stroemgren filter passbands. Adopted from: ¹	66
5.1	Schematic overview on the UVES optical layout.	70
5.2	Schematic overview on the XSHOOTER optical layout. Taken from: Vernet et al. [2011]	71
5.3	Schematic overview on the FEROS optical layout.	72
5.4	Schematic path of light in the HIRES spectrograph.	73
5.5	Schematic path of light in the ESI spectrograph operating in echellette mode.	74
5.6	Layout of the STIS spectrograph with its most important components; Adopted from Biretta [2016].	76
5.7	Schematic layout of the COS optical layout, including FUV and NUV chanel. Taken from Debes [2016].	77
5.8	Schematic layout of the COS FUV chanel. Taken from ?	77
5.9	Layout of the IUE satellite with its most important components.	79
5.10	Optical layout of the FUSE spacecraft.	80
6.1	Visualization of several HeI and HeII lines of CD-31° 4800	85
6.2	Fits to several HeI and HeII lines of CD-31° 4800 (FEROS data)	86
6.3	Fits to several HeI and HeII lines of CD-31° 4800 (FORS data)	87
6.4	Fouler lines of CD-31° 4800	88
6.5	Fits to several nitrogen lines of CD-31° 4800(optical)	91
6.6	Fits to several oxygen lines of CD-31° 4800(optical)	92
6.7	Fits to several neon lines of CD-31° 4800(optical)	92
6.8	Fits to several nitrogen lines of CD-31° 4800(UV)	93
6.9	Fits to several carbon lines of CD-31° 4800(UV)	94
6.10	Comparison of UV- and optical abundances for CD-31° 4800	94
6.11	Mass abundances of CD-31° 4800	95
6.12	SED for model 1 of CD-31° 4800	96
6.13	SED for model 2 of CD-31° 4800	97
6.14	Visualization of several HeI and HeII lines of HE 1511-1103	99
6.15	Fits to several nitrogen lines of HE 1511-1103(optical)	101
6.16	Fits to several neon lines of HE 1511-1103(optical)	102
6.17	Fit to one magnesium lines of HE 1511-1103(optical)	102
6.18	Mass abundances of HE 1511-1103	103
6.19	SED of HE 1511-1103	105
6.20	Visualization of several HeI and HeII lines of HZ1	108
6.21	Fits to several nitrogen lines of HZ1 (XSHOOTER UVES/SPY)	111
6.22	Fits to several neon lines of HZ1 (XSHOOTER UVES/SPY)	112
6.23	Mass abundances of HZ1	114
6.24	SED of HZ1(XSHOOTER)	116
6.25	Visualization of several Hydrogen, HeI and HeII lines of HZ44	118
6.26	Fits to several carbon lines of HZ44 (UV)	121

6.27	Fits to several nitrogen lines of HZ44 (optical)	122
6.28	Fits to several oxygen lines of HZ44 (UV)	122
6.29	Fits to several neon lines of HZ44 (optical)	123
6.30	Fits to several silicon lines of HZ44 (optical)	123
6.31	Mass abundances of HZ44	124
6.32	SED of HZ44	125
6.33	Visualization of several HeI and HeII lines of [CW83]0904-02	127
6.34	Visualization of several optical carbon lines of [CW83]0904-02	129
6.35	Visualization of several carbon lines from the UV spectrum of [CW83]0904-02	130
6.36	Visualization of several nitrogen lines from the UV spectrum of [CW83]0904-02	131
6.37	Visualization of several oxygen lines from the UV spectrum of [CW83]0904-02	131
6.38	Visualization of of the mass abundance ratio of [CW83]0904-02	132
6.39	SED of [CW83]0904-02	134
6.40	Visualization of several HeI and HeII lines of HE 0958-1151	135
6.41	Visualization of several optical nitrogen lines of HE 0958-1151	137
6.42	Visualization of several optical oxygen lines of HE 0958-1151	137
6.43	Visualization of several optical neon lines of HE 0958-1151	138
6.44	Mass abundances of HE 0958-1151	139
6.45	SED of HE 0958-1151	140
6.46	Visualization of several HeI and HeII lines of LSS 1274	142
6.47	Fits to several carbon lines of LSS 1274(optical)	144
6.48	Fits to several carbon lines of LSS 1274(UV)	144
6.49	Fits to several nitrogen lines of LSS 1274(optical)	145
6.50	Fits to several nitrogen lines of LSS 1274(UV)	145
6.51	Fits to several oxygen lines of LSS 1274(optical)	146
6.52	Fits to several neon lines of LSS 1274(optical)	146
6.53	Fits to several phosphorus lines of LSS 1274(UV)	147
6.54	abundance pattern of LSS 1274	148
6.55	SED of LSS 1274	150
6.56	Visualization of several HeI and HeII lines of LSIV +109	152
6.57	Visualization of several carbon lines of LSIV +109 (UV)	154
6.58	Visualization of several nitrogen lines of LSIV +109 (UV)	155
6.59	Visualization of several oxygen lines of LSIV +109	155
6.60	Visualization of several neon lines of LSIV +109	156
6.61	Visualization of several silicon lines of LSIV +109	156
6.62	Visualization of several phosphorus lines of LSIV +109 (UV)	157
6.63	abundance pattern of LSIV +109	158
6.64	SED of LSIV +109	160
6.65	Visualization of several HeI and HeII lines of [CW83]0832-01	161
6.66	Visualization of several carbon lines of [CW83]0832-01	163
6.67	Visualization of several nitrogen lines of [CW83]0832-01	164
6.68	Visualization of several oxygen lines of [CW83]0832-01	164
6.69	Visualization of one MgII line of [CW83]0832-01 (UVES spectrum) in comparison with the final synthetic spectrum.	165
6.70	Mass abundances of [CW83]0832-01	166

6.71	SED of [CW83]0832-01	167
6.72	Visualization of several HeI and HeII lines of GALEX J095256.6-371940.	169
6.73	Visualization of several carbon lines of GALEX J095256.6-371940 . .	170
6.74	Visualization of several nitrogen lines of GALEX J095256.6-371940 .	171
6.75	Visualization of several oxygen lines of GALEX J095256.6-371940 . .	172
6.76	Visualization of several neon lines of GALEX J095256.6-371940 . . .	172
6.77	Mass abundances of GALEX J095256.6-371940	173
6.78	SED of GALEX J095256.6-371940	174
6.79	Visualization of several HeI and HeII lines of BD+39° 3226	176
6.80	Fits to the CIII septuplet of BD+39° 3226(UV)	178
6.81	Fits to several nitrogen lines of BD+39° 3226(UV)	179
6.82	Fits to several nitrogen lines of BD+39° 3226(UV)	180
6.83	Fits to several oxygen lines of BD+39° 3226(UV)	180
6.84	Fits to several magnesium lines of BD+39° 3226(optical)	181
6.85	Fits to one silicon line of BD+39° 3226(UV)	181
6.86	Visualization of of the mass abundance ratio of BD+39° 3226.	182
6.87	SED of BD+39° 3226	184
6.88	Comparison of carbon lines UV fit for [CW83]0904-02	186
6.89	CIII triplet around 1165.65 Å in [CW83]0904-02 with adopted con- tinuum level.	187
6.90	Comparison of models with different iron contents for NIII lines in HE 1511-1103. The (almost invisible) red line represents the model with a solar iron abundance.	188
6.91	The He II 4200 Å line with the final model solution overplotted for different stars. The data have not been RV corrected.	194
6.92	The He II 4339 Å line with the final model solution overplotted for different stars. The data have not been RV corrected.	195
7.1	Comparison of the N-rich He-sdO subsample with the GALEX sample and the He-sdOs from Hirsch [2009].	197
7.2	Kiel diagram for the N-rich subsample	198
7.3	Comparison of mass abundances from the N-rich sample to those derived from model calculations	200
7.4	Comparison of the C-rich He-sdO subsample with the GALEX sample and the He-sdOs from Hirsch [2009].	201
7.5	Kiel diagram for the C-rich subsample	202
7.6	Comparison of mass abundances from the C-rich sample to those derived from model calculations	203
7.7	Comparison of the CN-rich subsample of He-sdOs with the GALEX sample and the He-sdOs from Hirsch [2009].	204
7.8	Kiel diagram for the CN-rich subsample	205
7.9	Comparison of mass abundances from the CN-rich sample to those derived from model calculations	207
7.10	Development of chemical abundances after the He- and the H-flash. .	208
7.11	Mass abundances for C and N expected from the composite mixing scenario compared to those measured in [CW83]0832-01	209
7.12	Mass abundances for O and Ne expected from the composite mixing scenario compared to those measured in [CW83]0832-01	209

7.13	Mass abundances for C and N expected from the composite mixing scenario compared to those measured in GALEX J095256.6-371940	210
7.14	Mass abundances for O and Ne expected from the composite mixing scenario compared to those measured in GALEX J095256.6-371940	210
7.15	Mass abundances for C and N expected from the composite mixing scenario compared to those measured in [CW83]0904-02	211
7.16	Mass abundances for O and Ne expected from the composite mixing scenario compared to those measured in [CW83]0904-02	211
7.17	Mass abundances for C and N expected from the composite mixing scenario compared to those measured in HE 0958-1151	212
7.18	Mass abundances for O and Ne expected from the composite mixing scenario compared to those measured in HE 0958-1151	212
8.1	Fit to the COS spectrum of CD -31° 4800 with XTGRID.	217
8.2	Fit to the COS part of the combined COS+UVES spectrum of CD-31° 4800 with XTGRID.	218
8.3	Fit to selected parts of the UVES spectrum of CD-31° 4800 with XTGRID.	219
8.4	Throughput of the COS spectrograph using the G140 grating.(P.Németh, private communication)	220
8.5	Relative mass abundances for CD -31° 4800 derived with XTGRID	222
8.6	Comparison of derived abundances from the XTGRID COS+UVES fit (blue) and the UVES+IUE fit (red)	223
8.7	Comparison of derived abundances from the XTGRID COS fit (blue) and the UVES+IUE fit red.	224
8.8	Visualization of several normalized Helium I and II lines of US 708	226
8.9	Fit to the KECK spectrum of US708 with XTGRID.	227
8.10	Fit to the COS part of the combined COS+KECK spectrum of US708 with XTGRID.	228
8.11	Fit to the COS spectrum of US708 with XTGRID.	229
8.12	Relative mass abundances for US708 derived with XTGRID	231
8.13	χ^2 distribution for the temperature of US708	232
8.14	χ^2 distribution for the surface gravity of US708	233
8.15	χ^2 distribution for the helium abundance of US708	233
8.16	Comparison of relative mass abundances for CD -31° 4800 (red) and US708 (blue) derived from Optical + UV fits with XTGRID. For an overview with all elements, see Fig. 8.16 in the appendix.	234
8.17	Comparison of relative mass abundances for CD -31° 4800 (red) and US708 (blue) derived from UV COS fits with XTGRID. For an overview with all elements, see Fig. .11 in the appendix.	235
8.18	Abundances of iron and nickel in US708 and CD -31° 4800 with the corresponding 3σ errors.	236
8.19	Overplot of US708 spectrum (black) and fit (blue) with best-fit model of the CD -31° 4800 (red) analysis.	237
8.20	Magnification of Fig. 8.19, showing the spectral range with the highest COS throughput and therefore best S/N ratio.	238
8.21	Predicted enrichment of certain elements for different supernova Ia explosion models 2000s after the explosion.	239

8.22	SED of US708 with selected photometric measurements used for fitting. The bottom panel shows the residuals for the magnitude measurements.	241
8.23	Origin plots for US708	245
8.24	Comparison of the synthetic spectra without rotation for CD -31° 4800 (red) and US708 (blue).	246
8.25	$T_{\text{eff}}\text{-log}(g)$ diagram showing the parameters of US708 derived in this work (red) and those derived by Geier et al. [2015a] (blue).	248
9.1	Comparison of the He-sdO stars analyzed in this thesis with He-sdO stars from the GALEX sample (taken from Németh et al. [2012]) and He-sdOs analyzed by Hirsch [2009].	253
.1	Fits to several carbon lines of HZ1 (optical-XSHOOTER)	287
.2	Fits to several oxygen lines of HZ1 (optical-XSHOOTER)	288
.3	Fits to several aluminium lines of HZ1 (optical-XSHOOTER)	288
.4	Fits to several silicon lines of HZ1 (optical-XSHOOTER)	289
.5	Fits to several carbon lines of HZ1 (optical-SPY/UVES)	290
.6	Fits to several oxygen lines of HZ1 (optical-SPY/UVES)	290
.7	Fits to several silicon lines of HZ1 (optical-SPY/UVES)	291
.8	Relative mass abundances for CD -31° 4800 derived with XTGRID	292
.9	Relative mass abundances for US708 derived with XTGRID	293
.10	Comparison of relative mass abundances for CD -31° 4800 (red) and US708 (blue) derived from Optical + UV fits with XTGRID.	294
.11	Comparison of relative mass abundances for CD -31° 4800 (red) and US708 (blue) derived from UV COS fits with XTGRID.	294

List of Tables

2.1	Luminosity classes of different types of stars	5
4.1	Summary of the different number abundances of helium, carbon, nitrogen and oxygen in the calculated HECNO grid	56
4.2	The different ionization stages and number of levels (L)+superlevels (SL) used in the standard model atmosphere. For *, see the following text	61
4.3	Comparison of the results of fitting atmospheric parameters with grids containing different amounts of metals.	63
4.4	Overview on the different Stroemgren filters with their center wavelength and FWHM	65
6.1	Comparison of ionization equilibriums for CD-31° 4800	86
6.2	Metal abundances derived from the optical UVES spectra of CD-31° 4800	89
6.3	Metal abundances derived from the optical UVES and ultraviolet IUE spectra of CD-31° 4800.	89
6.4	Metal abundances derived from a Far-UV FUSE spectrum of CD-31° 4800. Given in brackets is the number of lines used for each element and model.	90
6.5	Mass abundances for the different elements in CD-31° 4800 compared to the solar mass abundance.	95
6.6	Photometric measurements for CD-31° 4800.	98
6.7	Metal abundances derived from the optical SPY/UVES spectra of HE 1511-1103(without Fe/Ni)	100
6.8	Metal abundances derived from the optical SPY/UVES spectra of HE 1511-1103	101
6.9	Abundances by mass for the different elements in HE 1511-1103 compared to the solar mass abundances.	103
6.10	Photometric measurements for HE 1511-1103.	104
6.11	Metal abundances derived from the optical XSHOOTER and SPY/UVES spectra of HZ1	109
6.12	Metal abundances derived from the optical XSHOOTER and SPY/UVES spectra of HZ1 (with Fe/Ni)	110
6.13	Mass abundances for the different elements in HZ1 compared to the solar mass abundance.	113
6.14	Photometric measurements for HZ1.	115
6.15	Metal abundances derived from the optical HIRES spectra of HZ44	119
6.16	Metal abundances derived from optical and UV spectra of HZ44 (with Fe/Ni)	120
6.17	Mass abundances for the different elements in HZ44 compared to the solar mass abundance.	120

6.18	Photometric measurements for HZ44.	125
6.19	Overview on the number abundances for [CW83] 0904-02 determined from the optical FEROS spectrum. Given is the $\log(n(X)/n(H))$ in number abundances. (Models without Fe/Ni). The second column gives the number of lines used for the fit of a specific element. Values in brackets show very large errors and have to be dealt with care.	128
6.20	Overview on the number abundances (log) for [CW83] 0904-02 determined from different spectra.	128
6.21	Mass abundance ratio for [CW83] 0904-02.	130
6.22	Photometric measurements for [CW83] 0904-02.	133
6.23	Metal abundances derived from the optical SPY spectra of HE 0958-1151 (without Fe/Ni)	136
6.24	Metal abundances derived from the optical SPY spectra of HE 0958-1151	136
6.25	Mass abundances for the different elements in HE 0958-1151 compared to the solar mass abundance.	138
6.26	Photometric measurements for HE 0958-1151.	140
6.27	Overview on the number abundances (log) for LSS 1274 determined from UVES+CASPEC spectra.	142
6.28	Overview on the number abundances (log) for LSS 1274 determined from different spectra.	143
6.29	Mass abundance ratio for LSS 1274.	149
6.30	Photometric measurements for LSS 1274.	150
6.31	Overview on the number abundances (log) for LSIV +10 9 determined from UVES spectra.	153
6.32	Overview on the number abundances (log) for LSIV +10 9 determined from different spectra.	154
6.33	Mass abundance ratios for LSIV +10 9.	159
6.34	Photometric measurements for LSIV +10 9.	159
6.35	Metal abundances derived from the optical FEROS spectra of [CW83] 0832-01(without Fe/Ni)	162
6.36	Metal abundances derived from the optical FEROS spectra of [CW83] 0832-01	162
6.37	Mass abundances for the different elements in [CW83] 0832-01 compared to the solar mass abundance.	163
6.38	Photometric measurements for [CW83] 0832-01.	167
6.39	Metal abundances derived from the optical XSHOOTER spectra of GALEX J095256.6-371940(without Fe/Ni)	169
6.40	Metal abundances derived from the optical XSHOOTER spectra of GALEX J095256.6-371940(with Fe/Ni)	170
6.41	Mass abundances for the different elements in GALEX J095256.6-371940 compared to the solar mass abundance.	171
6.42	Photometric measurements for GALEX J095256.6-371940.	174
6.43	Overview on the number abundances (log) for BD+39° 3226 determined from the optical HIRES spectrum	176
6.44	Overview on the number abundances (log) for BD+39° 3226 determined from different spectra.	178
6.45	Mass abundance ratio for BD+39° 3226.	179

6.46	Photometric measurements for BD+39° 3226.	183
6.47	Solar photospheric abundances taken from Asplund et al. [2009]. NLTE elements are marked with an N, a * indicates that an indirect method was used to determine the abundance.	190
6.48	Comparison of photometric magnitudes J, H and K from Ulla and Thejll [1998] and Cutri et al. [2003].	192
7.1	Logarithmic mass abundances for the N-rich sample of He-sdO stars .	199
7.2	Logarithmic mass abundances for the C-rich sample of He-sdO stars.	202
7.3	Logarithmic mass abundances for the CN-rich sample of He-sdO stars.	206
8.1	Relative mass abundances of CD-31° 4800	221
8.2	Relative mass abundances of US708	230
8.3	3 σ errors for iron and nickel in CD-31° 4800 and US708.	235
8.4	Proper motions of US708. Values are given in [mas/yr]	240
8.5	Photometric measurements for US708.	241
8.6	Kinematical parameters of US 708 as derived from Monte Carlo simulations.	243
.1	Table with details on the properties of spectra of CD-31° 4800 analyzed during this work. The FORS spectrum was provided by Prof. U.Heber [priv. comm.]	277
.2	Table with details on the properties of spectra of [CW83]0904-02 analyzed during this work.	278
.3	Table with details on the properties of spectra of LSS 1274 analyzed during this work.	279
.4	Table with details on the properties of spectra of LS IV +10 9 analyzed during this work.	280
.5	Table with details on the properties of spectra of [CW83]0832-01 analyzed during this work.	280
.6	Table with details on the properties of spectra of HE 1511-1103 analyzed during this work.	281
.7	Table with details on the properties of spectra of HE 0958-1151 analyzed during this work.	281
.8	Table with details on the properties of spectra of HZ1 analyzed during this work.	282
.9	Table with details on the properties of spectra of HZ44 analyzed during this work. The error for the HIRES spectra was selected higher than suggested by the fit to account for the poor wavelength calibration.	283
.10	Table with details on the properties of spectra of GALEX J095256.6-371940 analyzed during this work.	284
.11	Table with details on the properties of spectra of BD+39° 3226 analyzed during this work. The available IUE spectra were likely shifted to a radial velocity of zero. The error for the HIRES spectra was selected higher than suggested by the fit to account for the poor wavelength calibration.	285
.12	Table with details on the properties of spectra of US 708 analyzed during this work.	286

Acknowledgements

MS acknowledges funding by the Deutsche Zentrum für Luft und Raumfahrt (grant No. 50 OR 1406). This research has made use of ISIS functions provided by ECAP/Remeis observatory.

Some of the data presented in this paper were obtained from the Mikulski Archive for Space Telescopes (MAST). STScI is operated by the Association of Universities for Research in Astronomy, Inc., under NASA contract NAS5-26555. Support for MAST for non-HST data is provided by the NASA Office of Space Science via grant NNX09AF08G and by other grants and contracts.

Based on observations at the Paranal Observatory of the European Southern Observatory.

Based on observations at the La Silla Observatory of the European Southern Observatory.

Some of the data presented herein were obtained at the W.M. Keck Observatory, which is operated as a scientific partnership among the California Institute of Technology, the University of California and the National Aeronautics and Space Administration. The Observatory was made possible by the generous financial support of the W.M. Keck Foundation. The author wish to recognize and acknowledge the very significant cultural role and reverence that the summit of Mauna Kea has always had within the indigenous Hawaiian community. We are most fortunate to have the opportunity to conduct observations from this mountain.

This research has used the services of ASTROSERVER.ORG.

So many people contributed to this thesis in a direct or an indirect way.

First of all I want to thank Dr. Peter Németh not only for being my officemate for about two years, but also for his continuous support, his help with python, gnuplot and above all Tlusty and Synspec. Not to forget the ASTROSERVER.ORG services which really helped a lot. Without you, the work on this thesis would have been much harder and much more frustrating. Thank you!

I express my gratitude towards Prof. Ulrich Heber and Prof. Stephan Geier who gave me the opportunity to work on this topic and always had an open ear for questions and discussions.

I thank Tiara Battich and Marcelo M. Miller-Bertolami for providing me with simulation results for the different evolutionary scenarios and for answering my questions on this topic.

Lot's of people contributed to the unique working atmosphere at the Remeis Observatory and I cannot address all of you personally.

But I want to mention my office mates in the Drechsel room, Jonathan Knies, David Schneider and Max Woltz who sometimes had a hard time with my jokes. A special

thank goes to Dr. Andreas Irrgang for his help with all the ISIS functions and his little scripts that turned out to save me a lot of time and nerves.

An institute like the Remeis Observatory would not be imaginable without the gang of admins, keeping all the computers and servers running. You guys rock! Special greetings to my favorite (Ex-) admin Dr. Fritz Walther Schwarm!

Working on a project like this for several years is not possible without support from friends and family who never fail to encourage you or cheer you up. I thank my parents for supporting me throughout the years, for believing in me and helping me in fulfilling my dreams. Ein besonderer Dank gilt auch meiner Großmutter, nicht nur für ihre Unterstützung in den letzten Jahren. I am very thankful that I have found so many new friends in Bamberg and my heartfelt thank goes to my “Neu in Bamberg“ and “GBSSG“ gang: Alina, Fred, Marina, Michael, Sebastian, Sonja, Stefan and many more.

However, there is always need for friends who understand and share even the weirdest thoughts in one’s head. With this in mind, Steffi, Björn, you know what I mean.

Thank you!

Appendix

.1 Data of analyzed spectra

In this section, the most important data on the spectra used in this work are listed. In some cases, more spectra are available but were neglected due to poor S/N ratio, reduction artefacts or wrong classification of the observed object. Those spectra are therefore not shown in this list. If not indicated otherwise in the corresponding section, the individual spectra were coadded before analyzation to improve the quality of the data.

Low resolution IUE data that were only used to get the photometric value from the box-filters in the SED analysis are not listed here. If not indicated otherwise, all IUE, FUSE and HST spectra were obtained from the Mikulski Archive for Space Telescopes: archive.stsci.edu

If not indicated otherwise, all optical spectra were obtained from the ESO Phase3 Science archive: http://archive.eso.org/wdb/wdb/adp/phase3_main/form. The S/N ratio was not calculated for the spectra but taken from the archival information, if available.

.1.1 CD -31° 4800

Instrument	Obs. date	Program ID	wavelength range [Å]	exposure time [s]	R	SNR	RV[km/s]
UVES	2002-06-03;23:31:23	69.C-0171(A)	3281...4562	2700	68642	205	30 ± 2
UVES	2002-06-03;23:31:23	69.C-0171(A)	4583...6686	2700	107200	163	30 ± 2
FEROS	2005-02-25;02:29:200	074.B-0455(A)	3527...9216	600	48000	85.5	37 ± 2
FORS*			3480...5890				28 ± 4
HST-COS	2014-03-31;13:57	LCA802010	1230...2050	1732	1800	x	29 ± 6
IUE	1978-07-21;22:32	swp02074	1150...1980	10800	10000	x	25 ± 3
IUE	1982-07-02;22:55	lwr13594	1850...3350	4800	10000	x	24 ± 5
FUSE	2004-04-12;14:22	p2050603000	900...1190	11747	22000	x	27 ± 4

Table .1: Table with details on the properties of spectra of CD -31° 4800 analyzed during this work. The FORS spectrum was provided by Prof. U.Heber [priv. comm.]

.1.2 [CW83] 0904-02

Instrument	Obs. date	Program ID	wavelength range [Å]	exposure time [s]	R	SNR	RV[km/s]
FEROS	2005-02-24;04:24:19.126	074.B-0455	3527...9216	1000	48000	45.2	22 ± 4
FEROS	2005-02-24;06:20:23.803	074.B-0455	3527...9216	1000	48000	34.4	22 ± 4
CASPEC	1984-04-04;00:46	x	3900...4900	2400	18000	x	25 ± 5
HST-STIS	2011-05-06 14:35	OBIE13010	1140...1740	1732	14000	x	24 ± 2
FUSE	2004-05-04;05:19	p2051302000	900...1190	3157	22000	x	30 ± 5
FUSE	2004-05-05;04:34	p2051303000	900...1190	2385	22000	x	30 ± 5
IUE	1993-12-23;09:48	swp49676	1150...1970	12000	10000	x	25 ± 4
IUE	1993-12-23;13:45	swp49677	1150...1970	9300	10000	x	25 ± 4
IUE	1994-03-16;04:22	swp50226	1150...1970	9560	10000	x	24 ± 4

Table .2: Table with details on the properties of spectra of [CW83] 0904-02 analyzed during this work.

.1.3 LSS 1274

Instrument	Obs. date	Program ID	wavelength range [\AA]	exposure time [s]	R	SNR	RV[km/s]
UVES	2006-04-10;01:29:49	077.C-0547(A)	4726...6835	2100	66320	106	13 ± 1
UVES	2006-04-10;00:53:37	077.C-0547(A)	4726...6835	2100	66320	94	13 ± 1
UVES	2006-04-10;01:29:32	077.C-0547(A)	3024...3884	2100	49620	94	13 ± 1
UVES	2006-04-10;00:53:45	077.C-0547(A)	3024...3884	2100	49620	85	13 ± 1
CASPEC	1985-04-05;00:58	x	3900...4900	x	18000	x	40 ± 7
FUSE	2002-03-11;12:13	p2051701000	900...1190	13927	22000	x	17 ± 4
FUSE	2002-03-08;06:00	p2051702000	900...1190	7935	22000	x	16 ± 4

Table .3: Table with details on the properties of spectra of LSS 1274 analyzed during this work.

.1.4 LSIV +109

Instrument	Obs. date	Program ID	wavelength range [\AA]	exposure time [s]	R	SNR	RV[km/s]
UVES	2001-07-01;09:42:48	67.D-0047(A)	3281...4562	1500	53750	106.8	-32 ± 3
CASPEC	1988-05-25;06:54	x	3900...4900	3600	18000	x	-28 ± 5
IUE	1983-04-29;10:36	swp19852	1150...1980	14400	10000	x	-3 ± 3
FUSE	2002-07-03;17:49	p2050901000	900...1190	6639	22000	x	-35 ± 4
FUSE	2002-07-04;18:46	p2050902000	900...1190	5585	22000	x	-30 ± 3
FUSE	2004-05-10;18:11	p2050903000	900...1190	45577	22000	x	-6 ± 4

Table .4: Table with details on the properties of spectra of LSIV +109 analyzed during this work.

.1.5 [CW83] 0832-01

Instrument	Obs. date	Program ID	wavelength range [\AA]	exposure time [s]	R	SNR	RV [km/s]
FEROS	2016-09-21;07:07:18	074.B-0455(A)	3527.8...9216.5	900	48000	61.5	12 ± 4
CASPEC	1984-04-04;23:57	x	3900...4900	3000	18000	x	15 ± 3

Table .5: Table with details on the properties of spectra of [CW83] 0832-01 analyzed during this work.

.1.6 HE 1511-1103

Instrument	Obs. date	Program ID	wavelength range [Å]	exposure time [s]	R	SNR	RV [km/s]
UVES	2013-09-24;16:50:10.6	165.H-0588(A)	3258...4563	300	19540	17.6	64 ± 3
UVES	2013-09-24;17:31:35.6	165.H-0588(A)	3258...4563	300	19540	22.4	64 ± 4
UVES	2013-09-24;16:50:10.6	165.H-0588(A)	4584...6686	300	18770	3.9	64 ± 3
UVES	2013-09-24;17:31:35.6	165.H-0588(A)	4584...6686	300	18770	6.1	64 ± 4

Table .6: Table with details on the properties of spectra of HE 1511-1103 analyzed during this work.

.1.7 HE 0958-1151

Instrument	Obs. date	Program ID	wavelength range [Å]	exposure time [s]	R	SNR	RV [km/s]
UVES	2013-09-24;17:35:44	165.H-0588(A)	3258...4563	300	119540	36.2	59 ± 5
UVES	2013-09-24;17:41:51	165.H-0588(A)	3258...4563	300	119540	37.6	58 ± 4
UVES	2013-09-24;17:35:44	165.H-0588(A)	4584...6686	300	18770	13.3	59 ± 5
UVES	2013-09-24;17:41:51	165.H-0588(A)	4584...6686	300	18770	15.1	58 ± 5

Table .7: Table with details on the properties of spectra of HE 0958-1151 analyzed during this work.

.1.8 HZ1

Instrument	Obs. date	Program ID	wavelength range [Å]	exposure time [s]	R	SNR	RV [km/s]
XSHOOTER	2015-12-26;06:35:23.753	096.D-0055(A)	5336..10200	300	18000	69.5	-1 ± 4
XSHOOTER	2015-12-26;06:27:40.913	096.D-0055(A)	5336..10200	300	18000	68.4	0 ± 4
XSHOOTER	2015-12-26;06:14:51.880	096.D-0055(A)	9940..24789	300	11000	42.4	3 ± 3
XSHOOTER	2015-12-26;06:04:24.383	096.D-0055(A)	2989..5559	300	9800	108.6	5 ± 2
XSHOOTER	2015-12-26;06:20:01.150	096.D-0055(A)	9940..24789	300	11000	41.6	3 ± 3
XSHOOTER	2015-12-26;06:04:30.546	096.D-0055(A)	5336..10200	300	18000	74.1	-1 ± 4
XSHOOTER	2015-12-26;06:12:07.276	096.D-0055(A)	2989..5559	300	9800	103.9	5 ± 2
XSHOOTER	2015-12-26;06:19:56.710	096.D-0055(A)	5336..10200	300	18000	71.0	-1 ± 4
XSHOOTER	2015-12-26;06:19:50.496	096.D-0055(A)	2989..5559	300	9800	99.0	4 ± 2
XSHOOTER	2015-12-26;06:35:17.523	096.D-0055(A)	2989..5559	300	9800	91.9	5 ± 2
XSHOOTER	2015-12-26;05:49:03.540	096.D-0055(A)	5336..10200	300	18000	71.8	-1 ± 4
XSHOOTER	2015-12-26;05:49:06.903	096.D-0055(A)	9940..24789	300	11000	44.0	3 ± 3
XSHOOTER	2015-12-26;06:09:42.183	096.D-0055(A)	9940..24789	300	11000	43.2	4 ± 3
XSHOOTER	2015-12-26;06:12:13.436	096.D-0055(A)	5336..10200	300	18000	72.6	-2 ± 4
XSHOOTER	2015-12-26;05:48:58.360	096.D-0055(A)	2989..5559	300	9800	108.2	5 ± 2
XSHOOTER	2015-12-26;06:04:34.696	096.D-0055(A)	9940..24789	300	11000	44.2	3 ± 3
XSHOOTER	2015-12-26;05:54:15.583	096.D-0055(A)	9940..24789	300	11000	41.0	3 ± 3
XSHOOTER	2015-12-26;05:56:47.543	096.D-0055(A)	5336..10200	300	18000	71.1	-1 ± 4
XSHOOTER	2015-12-26;05:59:23.213	096.D-0055(A)	9940..24789	300	11000	43.9	3 ± 3
XSHOOTER	2015-12-26;05:56:41.353	096.D-0055(A)	2989..5559	300	9800	105.0	3 ± 2
XSHOOTER	2015-12-26;06:27:33.870	096.D-0055(A)	2989..5559	300	9800	92.9	5 ± 2
UVES	2002-02-27;01:50:46.730	167.D-0407(A)	4583..6686	300	18770	38.7	1 ± 3
UVES	2002-02-27;01:50:47.556	167.D-0407(A)	3281..4562	300	19540	58.4	1 ± 3
UVES	2003-01-11;04:38:15.753	167.D-0407(A)	4583..6686	300	18770	65.5	5 ± 4
UVES	2003-01-11;04:38:15.956	167.D-0407(A)	3281..4565	300	19540	52.2	5 ± 4

Table .8: Table with details on the properties of spectra of HZ1 analyzed during this work.

.1.9 HZ44

Instrument	Obs. date	Program ID	wavelength range [Å]	exposure time [s]	R	SNR	RV [km/s]
HIRES	2005-12-08;05:59:25.44	G10H	3180...6050	500	40000	39	-14 ± 10
HIRES	2005-12-08;08:09:58.15	G10H	3180...6050	500	40000	25	-15 ± 10
FUSE	2004-03-23;03:31	P302	900...1190	5919	22000	x	-17 ± 2

Table .9: Table with details on the properties of spectra of HZ44 analyzed during this work. The error for the HIRES spectra was selected higher than suggested by the fit to account for the poor wavelength calibration.

.1.10 GALEX J095256.6-371940

Instrument	Obs. date	Program ID	wavelength range [Å]	exposure time [s]	R	SNR	RV [km/s]
XSHOOTER	2016-01-26;03:52:28.970	096.D-0055(A)	9940..24789	300	11000	21.5	60 ± 7
XSHOOTER	2016-01-26;04:33:38.876	096.D-0055(A)	5336..10200	300	18000	39.9	59 ± 6
XSHOOTER	2016-01-26;04:33:32.666	096.D-0055(A)	2989..5559	300	9800	83.	62 ± 2
XSHOOTER	2016-01-26;04:10:23.766	096.D-0055(A)	2989..5559	300	9800	100.6.	62 ± 2
XSHOOTER	2016-01-26;04:18:17.600	096.D-0055(A)	9940..24789	300	11000	16.7	60 ± 7
XSHOOTER	2016-01-26;03:55:03.523	096.D-0055(A)	5336..10200	300	18000	49.5	58 ± 6
XSHOOTER	2016-01-26;04:18:06.696	096.D-0055(A)	2989..5559	300	9800	92.3.	62 ± 2
XSHOOTER	2016-01-26;03:47:18.943	096.D-0055(A)	5336..10200	300	18000	53.3	58 ± 6
XSHOOTER	2016-01-26;04:18:12.866	096.D-0055(A)	5336..10200	300	18000	44.4	59 ± 6
XSHOOTER	2016-01-26;04:02:48.853	096.D-0055(A)	5336..10200	300	18000	47.5	58 ± 6
XSHOOTER	2016-01-26;04:07:59.420	096.D-0055(A)	9940..24789	300	11000	18.3	60 ± 7
XSHOOTER	2016-01-26;04:25:49.526	096.D-0055(A)	2989..5559	300	9800	87.8.	62 ± 2
XSHOOTER	2016-01-26;04:02:51.266	096.D-0055(A)	9940..24789	300	11000	18.3	60 ± 7
XSHOOTER	2016-01-26;03:57:37.126	096.D-0055(A)	9940..24789	300	11000	19.0	61 ± 7
XSHOOTER	2016-01-26;04:13:08.240	096.D-0055(A)	9940..24789	300	11000	17.9	60 ± 7
XSHOOTER	2016-01-26;04:10:29.926	096.D-0055(A)	5336..10200	300	18000	48.7	58 ± 6
XSHOOTER	2016-01-26;03:47:13.813	096.D-0055(A)	2989..5559	300	9800	108.8.	62 ± 2
XSHOOTER	2016-01-26;03:47:22.146	096.D-0055(A)	9940..24789	300	11000	21.8	60 ± 7
XSHOOTER	2016-01-26;04:02:40.543	096.D-0055(A)	2989..5559	300	9800	98.3.	62 ± 2
XSHOOTER	2016-01-26;03:54:57.353	096.D-0055(A)	2989..5559	300	9800	101.5.	62 ± 2
XSHOOTER	2016-01-26;04:25:55.676	096.D-0055(A)	5336..10200	300	18000	42.1	58 ± 6

Table .10: Table with details on the properties of spectra of GALEX J095256.6-371940 analyzed during this work.

.1.11 BD+39° 3226

Instrument	Obs. date	Program ID	wavelength range [Å]	exposure time [s]	R	SNR	RV [km/s]
HIRES	2006-06-04;15:10:04.34	U157Hb	2970...5950	300	85000	52	-285 ± 10
HIRES	2006-06-04;15:14:44.24	U157Hb	2970...5950	300	85000	52	-285 ± 10
HIRES	2006-06-04;15:21:19.954	U157Hb	2970...5950	300	85000	52	-285 ± 10
FUSE	2004-05-21;19:06	P302	900...1190	5183	22000	x	-283 ± 5
IUE	1981-10-16;14:30	lwr11789	1850...3350	5040	10000	x	0 ± 2
IUE	1981-10-16;15:58	swp15275	1150...1970	3600	10000	x	0 ± 2
HST-STIS	2011-07-24;02:14	OBIE09010	1140...1700	1757	11000	x	-277 ± 5

Table .11: Table with details on the properties of spectra of BD+39° 3226 analyzed during this work. The available IUE spectra were likely shifted to a radial velocity of zero. The error for the HIRES spectra was selected higher than suggested by the fit to account for the poor wavelength calibration.

.1.12 US 708

Instrument	Obs. date	Program ID	wavelength range [Å]	exposure time [s]	R	SNR	RV [km/s]
KECK-ESI	2013-03-03;06:05:56	C253E	4000...10100	1800	6000	x	911 ± 9
KECK-ESI	2013-03-03;06:40:16	C253E	4000...10100	1800	6000	x	913 ± 9
KECK-ESI	2013-03-03;07:12:59	C253E	4000...10100	1800	6000	x	914 ± 9
KECK-ESI	2013-03-03;07:45:38	C253E	4000...10100	1800	6000	x	912 ± 8
KECK-ESI	2013-03-03;08:17:23	C253E	4000...10100	1800	6000	x	913 ± 9
KECK-ESI	2013-03-03;08:49:39	C253E	4000...10100	1800	6000	x	913 ± 9
KECK-ESI	2013-03-03;09:23:49	C253E	4000...10100	1800	6000	x	917 ± 9
KECK-ESI	2013-03-03;09:54:06	C253E	4000...10100	1800	6000	x	913 ± 7
HST-COS	2014-01-31;16:55	13290	1230...2050	4800	1800	11	825

Table .12: Table with details on the properties of spectra of US 708 analyzed during this work.

.2 Additional spectral fits for HZ1

.2.1 XSHOOTER

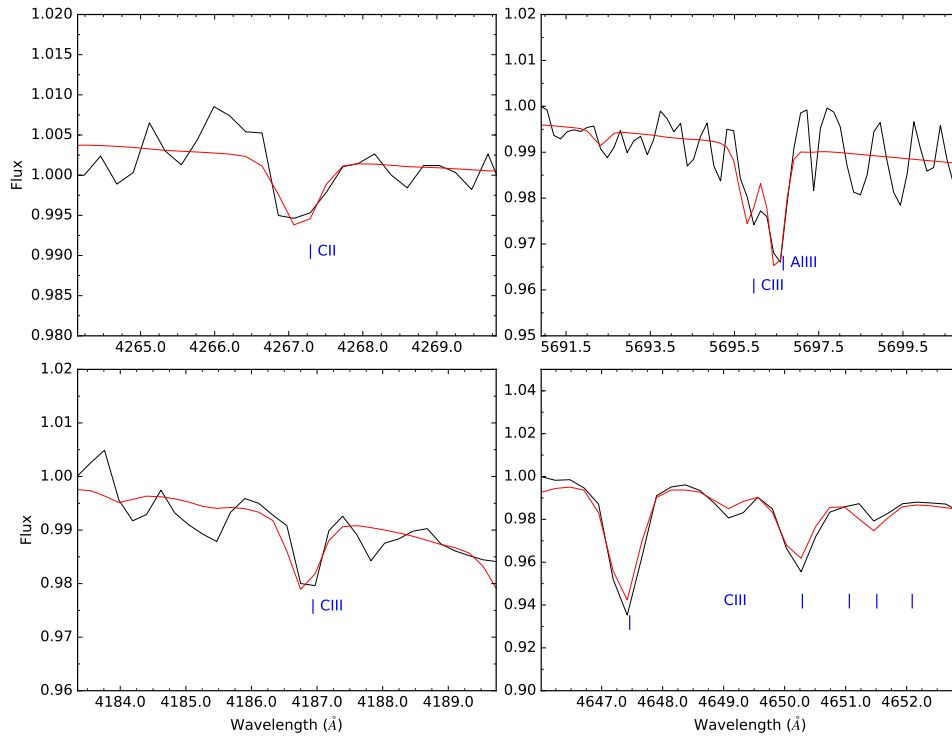


Figure .1: Visualization of several carbon lines with different ionization stages of HZ1 (XShooter spectrum) in comparison with the final synthetic spectrum.

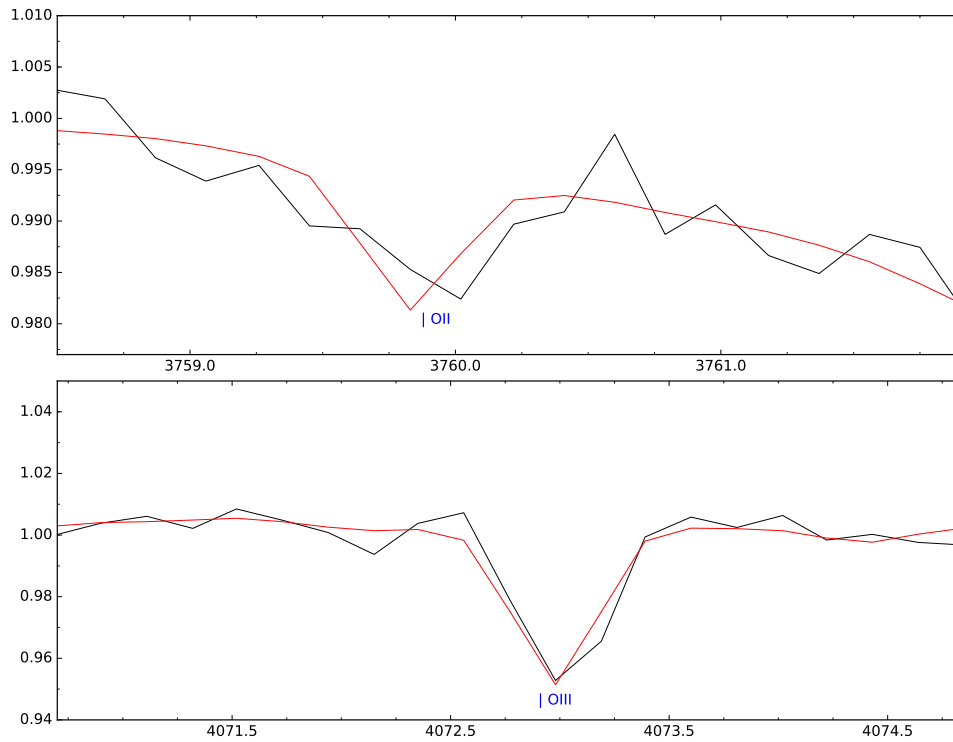


Figure .2: Visualization of several OII lines of HZ1 (XShooter spectrum) in comparison with the final synthetic spectrum.

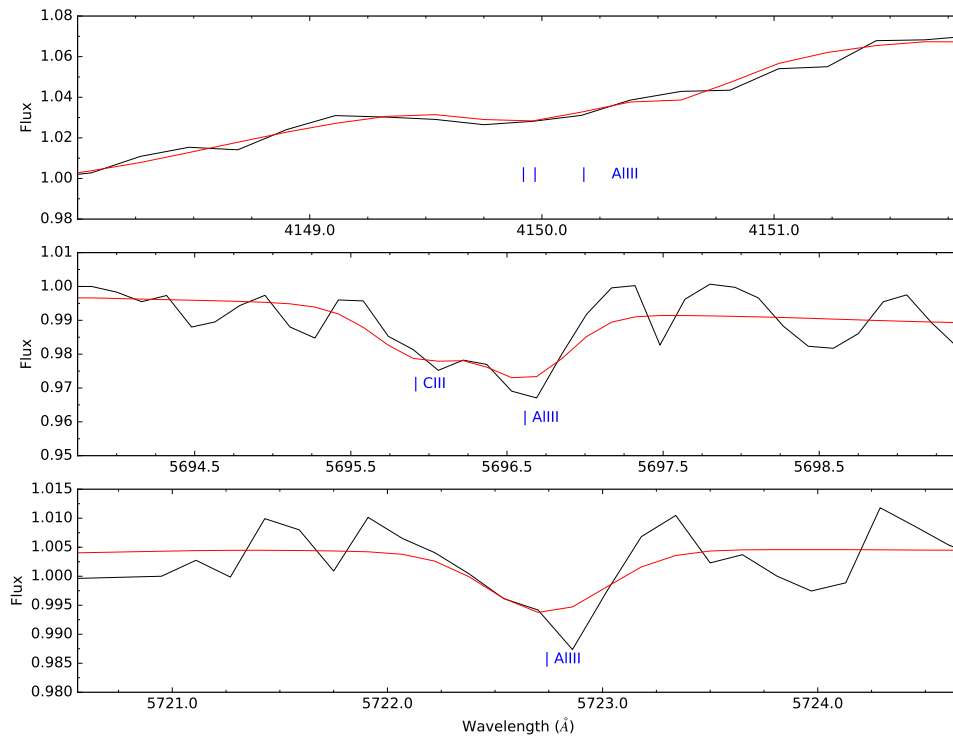


Figure .3: Visualization of several AlIII lines of HZ1 (XShooter spectrum) in comparison with the final synthetic spectrum.

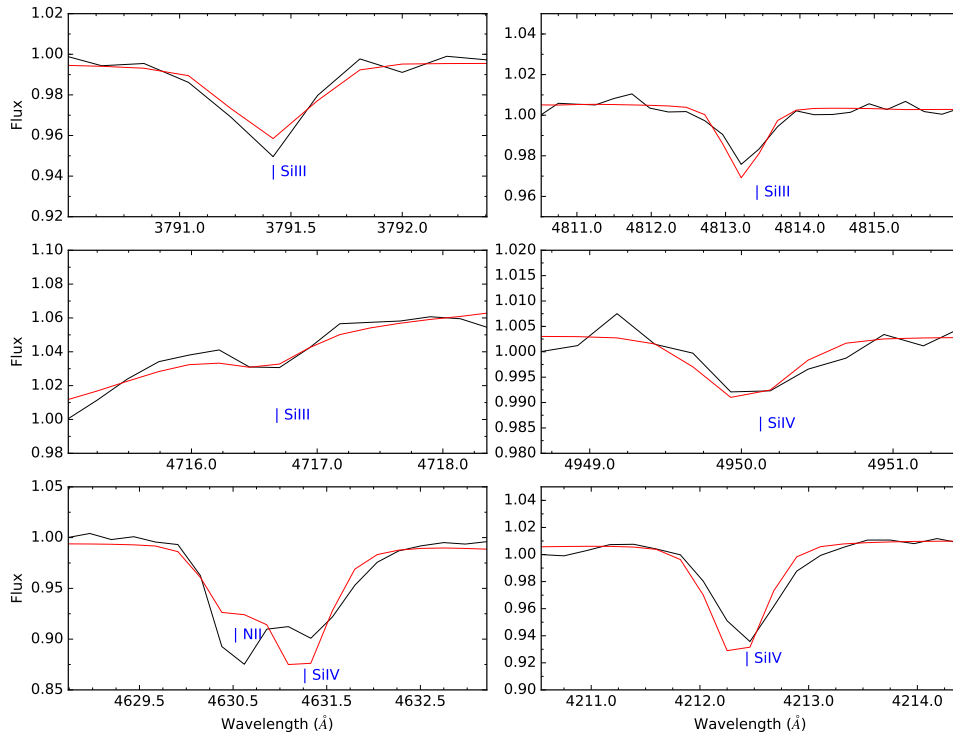


Figure .4: Visualization of several silicon lines with different ionization stages of HZ1 (XShooter spectrum) in comparison with the final synthetic spectrum.

.2.2 SPY/UVES

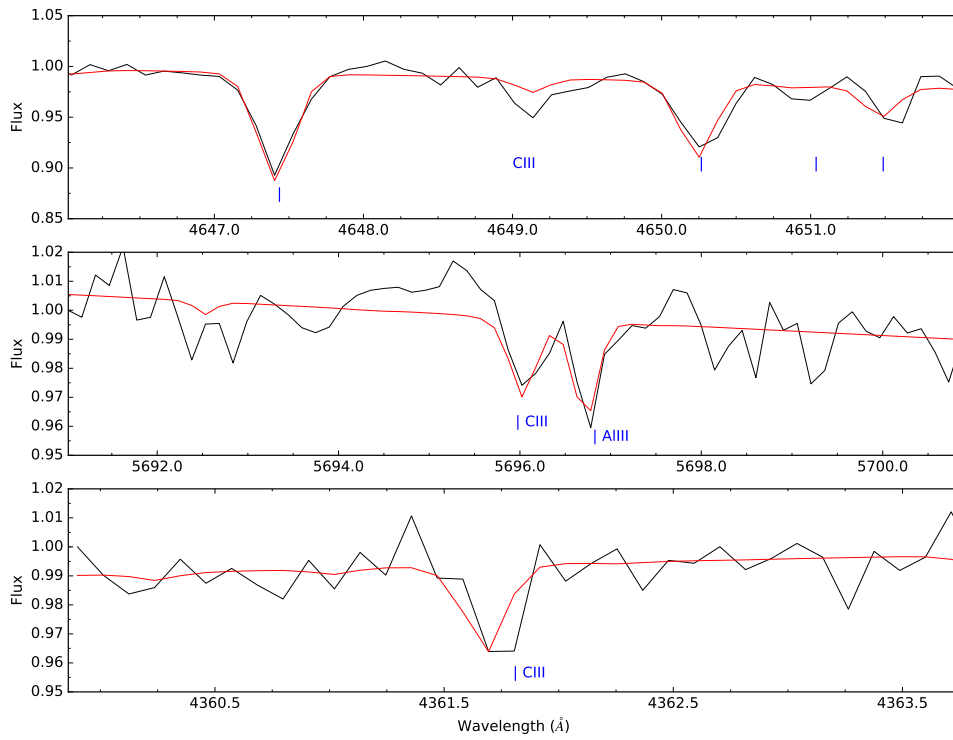


Figure .5: Visualization of several CIII lines of HZ1 (SPY/UVES spectrum) in comparison with the final synthetic spectrum.

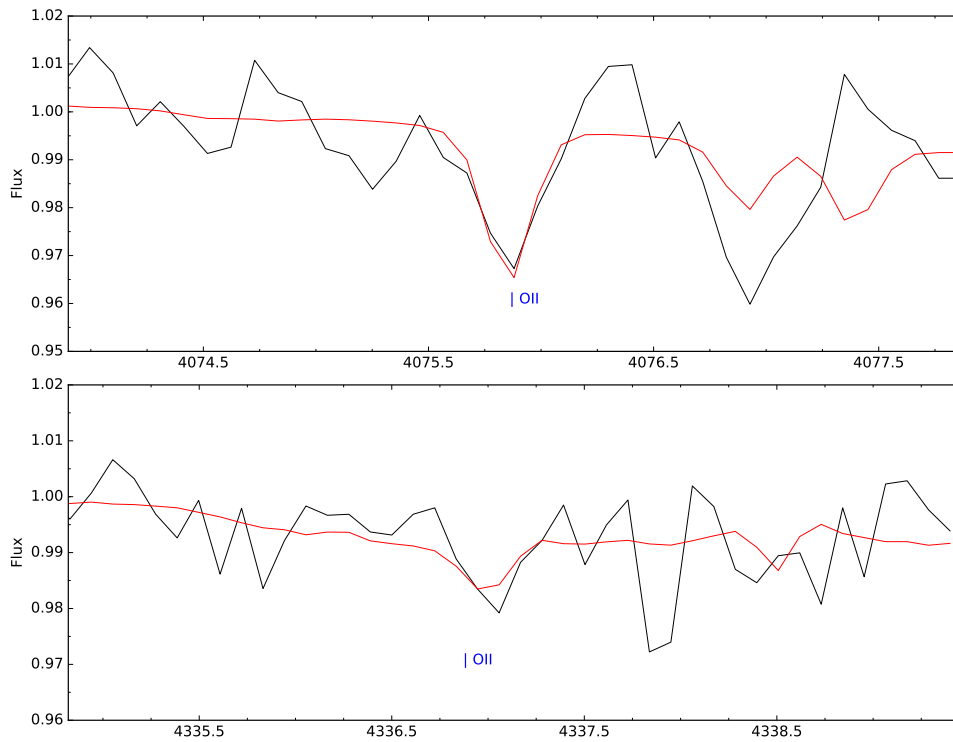


Figure .6: Visualization of several OII lines of HZ1 (SPY/UVES spectrum) in comparison with the final synthetic spectrum.

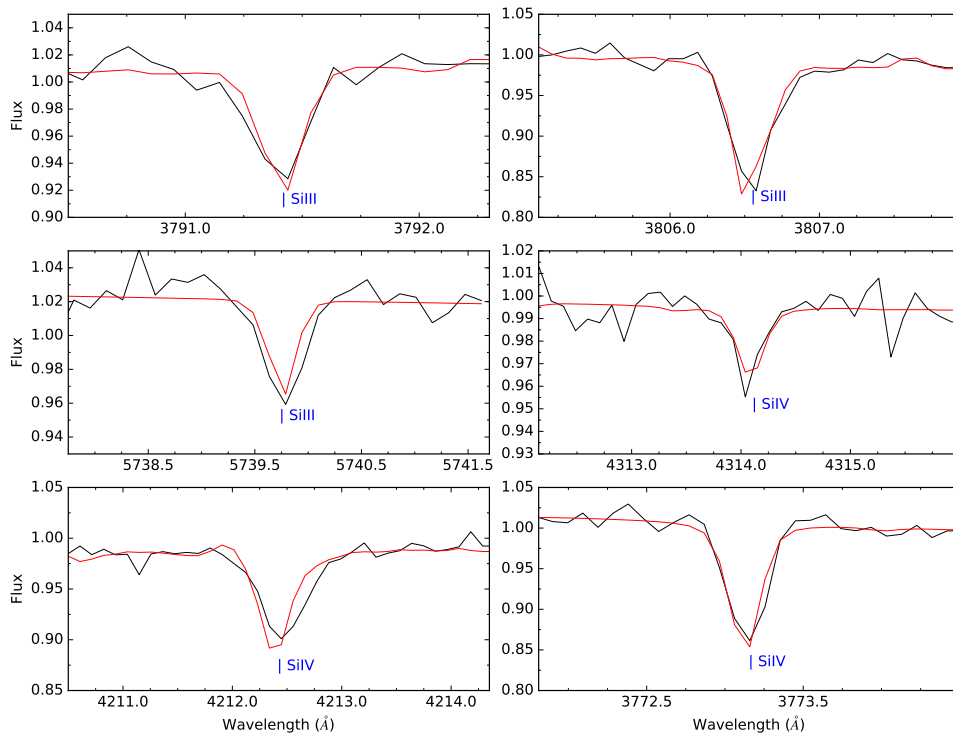


Figure .7: Visualization of several silicon lines with different ionization stages of HZ1 (SPY/UVES spectrum) in comparison with the final synthetic spectrum.

.3 Abundance plots for CD-31° 4800 and US708

The following section hosts the abundance plots for CD-31° 4800 and US708 with all elements, independent from their errors.

.3.1 CD-31° 4800

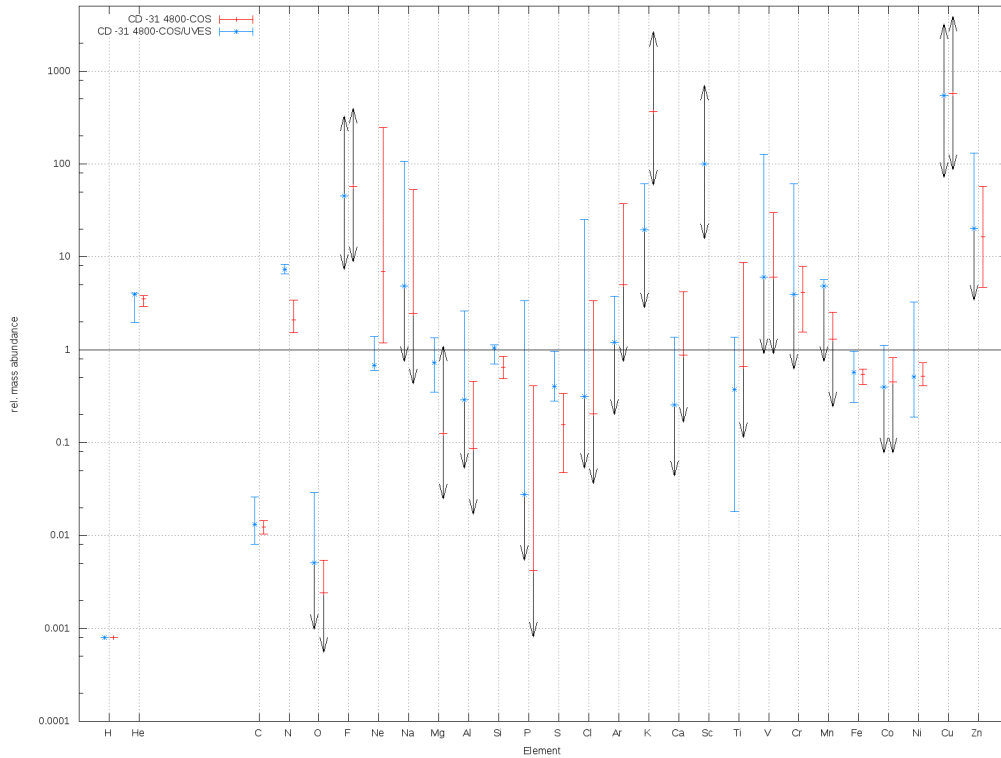


Figure .8: Relative mass abundances for CD-31° 4800 derived with XTGRID from a COS (red) and COS+UVES (blue) fit. Missing limits are indicated by black arrows.

.3.2 US708

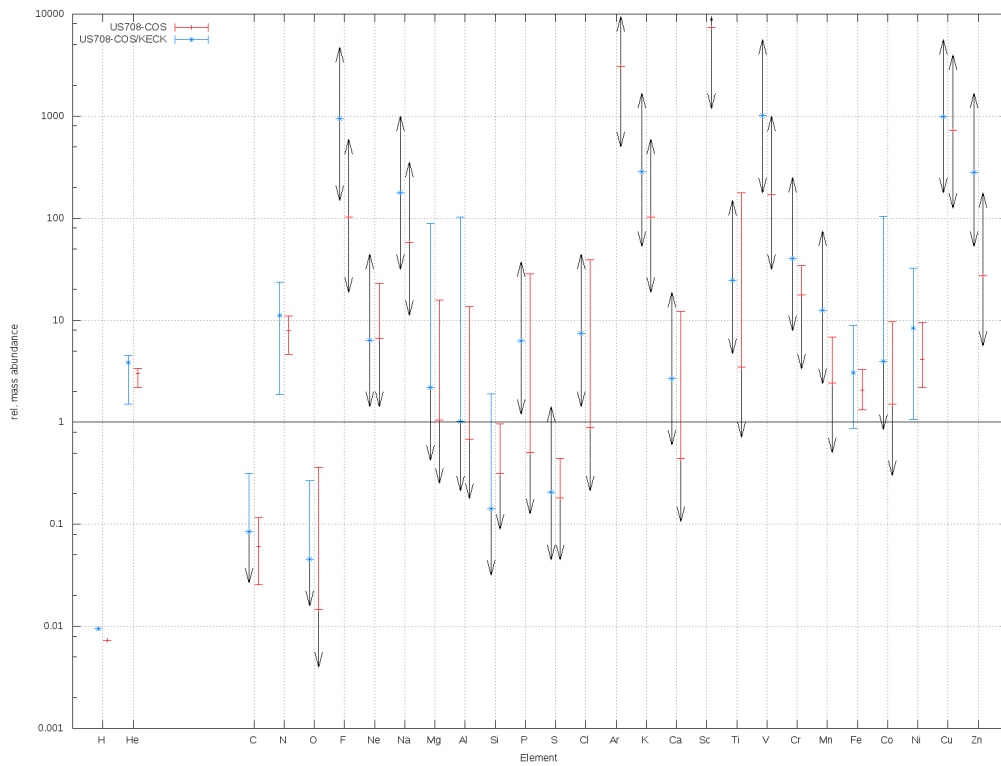


Figure .9: Relative mass abundances for US708 derived with XTGRID from a COS (red) and COS+KECK (blue) fit.

.3.3 Comparison of CD -31° 4800 and US708

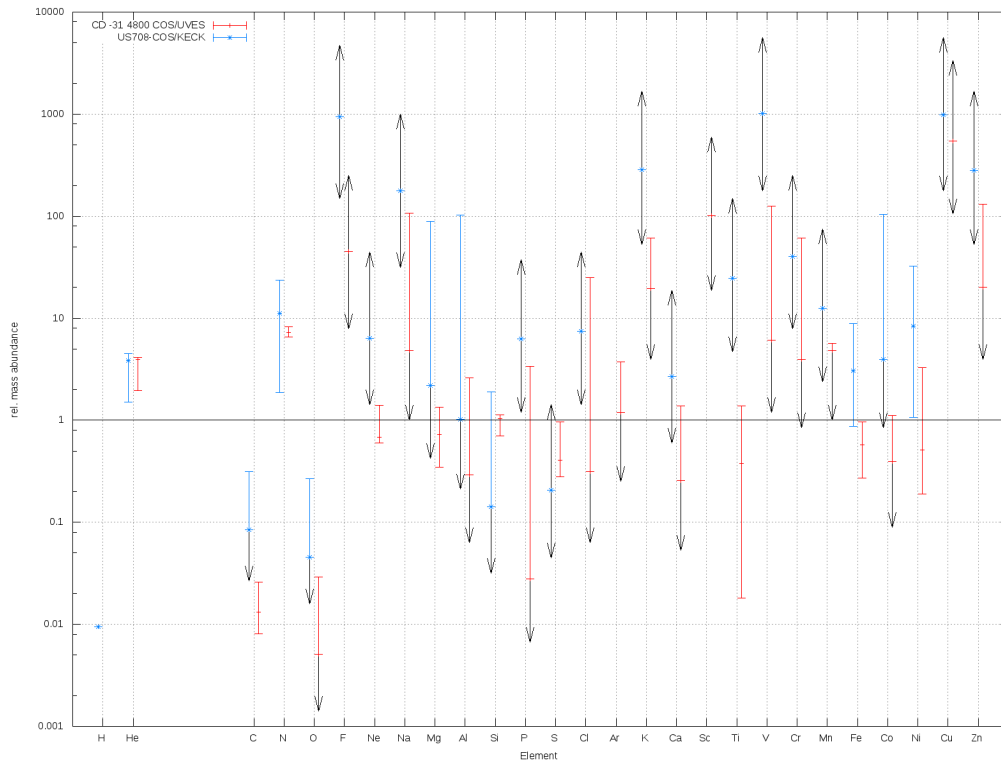


Figure .10: Comparison of relative mass abundances for CD-31^o 4800 (red) and US708 (blue) derived from Optical + UV fits with XTGRID.

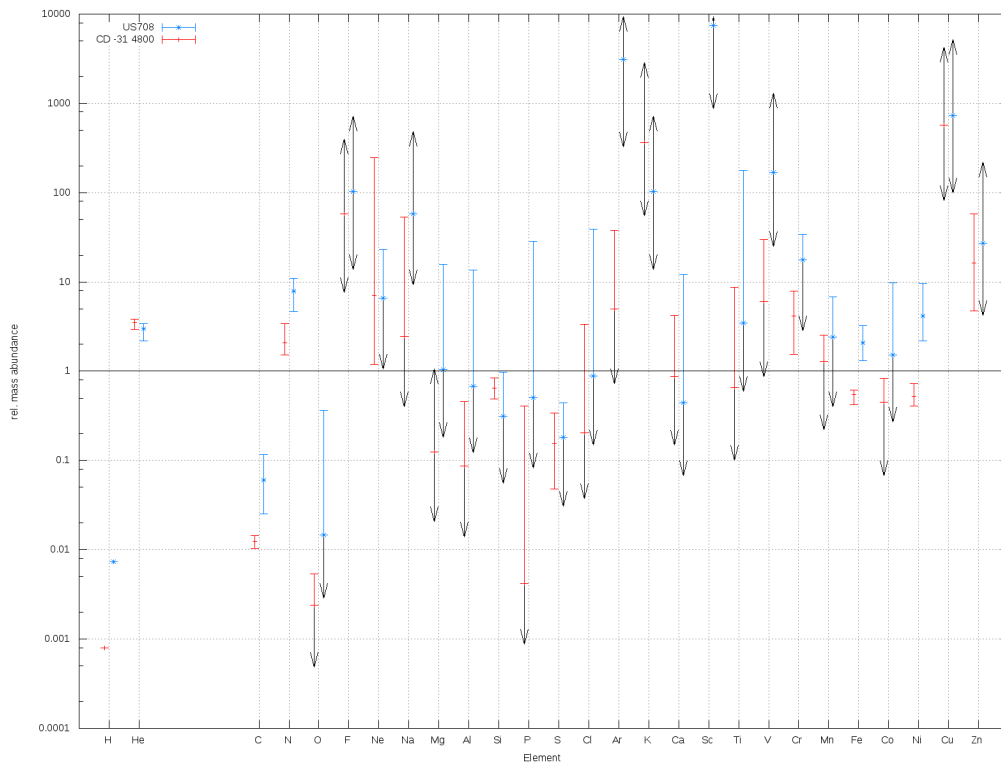


Figure .11: Comparison of relative mass abundances for CD-31^o 4800 (red) and US708 (blue) derived from UV COS fits with XTGRID.

.4 Linelist

Following are several linelist, containing all the possible lines used during the analysis of the He-sdO stars shown in this work. They are separated between optical and UV lines. In some cases one line is listed more than one time. Once as a single line and once as a part of multiple lines, depending on the conducted task/measurement one or the other type was used. Wavelengths marked with a * are part of the multiplet listed directly above. In the UV, the lines from a multiplet could usually not be resolved and were taken from the synspec linelist. This list does not claim to be complete in terms of containing all relevant lines that could be used for a specific element.

.4.1 Optical Helium lines

Ion. stage	wavelength [\AA]
He I	3888.65
He II / H I	3968.44 / 3970.08
He II / He I	4025.61 / 4026.19
He II / H I	4100.05 / 4101.71
He II	4199.84
He II / H I	4338.68 / 4340.47
He I	4387.93
He I	4437.55
He I	4471.48
He II	4541.59
He II	4685.70
He I	4713.15
He II / H I	4859.32 / 4861.35
He I	4921.93
He I	5015.68
He I	5047.74
He II	5411.51
He I	5875.75
He II / H I	6560.09 / 6562.79
He I	6678.15

.4.2 Optical metal lines

Element+Ion. stage	Wavelength [Å]	Element+Ion. stage	Wavelength [Å]
C III	3883.81	N II	4788.13
C III	*	N II	4803.29
*	3608.78	N II	4987.38
*	3609.05	N II	5002.80
*	3609.07	N II	5007.32
*	3609.62	N II	5010.62
*	3609.68	N II	5025.66
C III	4056.06	N II	5045.10
C III	*	N II	5495.67
*	4067.94	N II	5666.63
*	4068.91	N II	5676.02
*	4070.26	N II	5679.56
C III	4121.85	N II	5686.21
C III	4186.90	N II	5710.77
C III	4247.31	N II	5931.78
C III	4325.56	N III	3004.03
C III	4361.85	N III	3330.11
C III	4382.90	N III	3342.09
C III	4516.79	N III	*
C III	*	*	3353.98
*	4647.42	*	3354.32
*	4650.25	N III	*
*	4651.02	*	3360.98
*	4651.47	*	3365.80
*	4652.05	N III	*
C III	5695.92	*	3365.80
C III	*	*	3367.30
*	6149.28	*	3374.07
*	6154.16	N III	*
*	6155.12	*	3754.62
*	6156.69	*	3757.65
*	6160.01	*	3762.60
C IV	4658.30	N III	*
C IV	*	*	3771.05
*	5016.62	*	3771.36
*	5018.40	N III	3792.97
C IV	*	N III	3938.52
*	5801.33	N III	3942.88
*	5811.97	N III	*
N II	3838.37	*	3998.63
N II	3842.19	*	4003.58
N II	3995.00	N III	4097.33
N II	4176.16	N III	4103.39
N II	4227.74	N III	4195.70
N II	4447.03	N III	4200.02
N II	4694.27	N III	4215.77
N II	4779.72	N III	4318.78

Element+Ion. stage	wavelength [\AA]	Element+Ion. stage	wavelength [\AA]
N III	*	N IV	*
*	4318.78	*	3478.71
*	4321.22	*	3482.99
*	4325.43	*	3484.96
*	4327.88	N IV	4057.76
N III	*	N IV	6380.77
*	4332.91	O II	3759.87
*	4337.01	O II	3857.16
N III	*	O II	4069.89
*	4345.68	O II	4072.15
*	4345.81	O II	4075.86
*	4351.11	O II	*
N III	*	*	4307.23
*	4514.86	*	4312.10
*	4518.91	*	4313.44
N III	4523.56	*	4317.14
N III	4530.86	*	4317.70
N III	4534.58	*	4319.63
N III	4547.30	*	4325.75
N III	*	O II	4349.42
*	4589.18	O II	4336.87
*	4591.98	O II	6152.56
N III	4634.14	O III	3340.74
N III+ He II&H β	*	O III	3459.48
*	4858.82	O III	3715.08
*	4861.22	O III	3757.21
*	4867.15	O III	3759.87
N III	4873.10	O III	5592.37
N III	4884.14	O III	6507.55
N III	*	Ne II	3323.73
*	5260.86	Ne II	3327.15
*	5270.57	Ne II	3388.41
*	5272.68	Ne II	3406.94
*	5282.43	Ne II	*
N III	*	*	3416.91
*	5297.75	*	3417.69
*	5298.95	Ne II	3542.84
N III	*	Ne II	*
*	5314.35	*	3565.82
*	5320.32	*	3568.50
*	5327.18	*	3571.23
N III	*	*	3574.61
*	5817.79	Ne II	*
*	5820.57	*	3643.93
N III	5847.94	*	3644.86
N III	5954.70	Ne II	3664.07
		Ne II	3694.21

Element+Ion. stage	wavelength [Å]
Ne II	3709.62
Ne II	3713.08
Ne II	3727.11
Ne II	3766.26
Ne II	3777.13
Ne II	4150.69
Ne II	*
*	4217.17
*	4219.37
*	4219.74
Ne II	4250.64
Ne II	*
*	4290.37
*	4290.60
Ne II	4379.55
Ne II	4397.99
Ne II	*
*	4409.30
*	4412.59
Ne II	*
*	4428.52
*	4428.63
*	4430.90
*	4431.81
Mg II	4242.45
Mg II	*
*	4481.13
*	4481.33
Mg II	*
*	5916.43
*	5918.16
Mg II	5928.23
Mg II	*
*	6346.74
*	6346.96
Al III	3601.63
Al III	4149.96
*	4159.91
*	4149.96
*	4150.17
Al III	*
*	4479.83
*	4479.97

Element+Ion. stage	Wavelength [Å]
Al III	4512.57
Al III	5722.73
Al III	5696.60
Si III	3486.91
Si III	3791.41
Si III	3806.54
Si III	3924.47
Si III	4552.65
Si III	4567.87
Si III	4574.78
Si III	4716.66
Si III	4813.39
Si III	4819.72
Si III	5739.73
Si IV	3773.15
Si IV	4088.86
Si IV	4116.10
Si IV	4212.41
Si IV	4314.10
Si IV	4631.24
Si IV	4654.32
Si IV	4950.11
P IV	3347.74
P IV	3364.47
P IV	4249.66
P IV	4728.37
P V	5122.19
S III	3632.02
S III	3662.01
S III	3717.77
S III	3747.85
S III	3794.68
S III	3837.79
S III	3928.61
S III	3961.51
S III	4099.15
S III	4253.59
S III	4284.99
S III	4361.47
S IV	5488.25
S IV	5497.75

.4.3 UV lines

Element+Ion. stage	wavelength [Å]	Element+Ion. stage	wavelength [Å]
HeI	2829.08	NII	2709.84
HeI	2945.11	NII	2879.75
HeII	1215.15	NII	*
HeII	1640.46	*	2537.48
HeII	2306.19	*	2537.74
HeII	2385.40	N III	*
HeII	2511.20	*	1005.99
HeII	2733.33	*	1006.04
CIII	1240.28	N III	*
CIII	1247.03	*	1038.61
CIII	1785.02	*	1038.98
CIII	1880.6	*	1039.00
CIII	1991.80	N III	*
CIII	2162.94	*	1055.95
CIII	2289.98	*	1055.97
CIII	2296.87	N III	1103.05
CIII	*	N III+N IV	*
*	2671.32	*	1104.07
*	2671.34	*	1104.12
CIII	*	*	1104.54
*	2683.92	N III	1106.34
*	2683.94	N III	*
CIII	*	*	1120.60
*	2697.25	*	1120.81
*	2697.42	N III	*
*	2697.71	*	1140.05
*	2698.13	*	1140.12
CIII	2727.55	N III	
CIII	*	*	1182.97
*	2796.46	*	1183.03
*	2796.48	N III	*
CIII	*	*	1184.51
*	2806.16	*	1184.55
*	2806.23	NIII	*
CIV	*	*	1288.74
*	1027.28	*	1289.65
*	1031.27	*	1290.54
C IV	1107.98	NIII	*
CIV	*	*	1324.16
*	1230.04	*	1324.31
*	1230.52	*	1324.36
CIV	1550.77	*	1324.40
NII	*	*	1324.40
*	2309.06	NIII	1387.37
*	2309.53		

Element+Ion. stage	wavelength [\AA]	Element+Ion. stage	wavelength [\AA]
NIII	*	NII+NIII	*
*	1449.31	*	2486.24
*	1449.53	*	2486.43
NIII	1574.31	NIII	2862.32
NIII	1729.95	NIII	*
NIII	1732.08	*	2713.98
NIII	1747.85	*	2714.07
NIII	1763.16	N IV	955.34
NIII	*	N IV	*
*	1804.44	*	1036.12
*	1804.49	*	1036.15
*	1805.67	*	1036.20
NIII	1835.51	*	1036.23
NIII	1885.10	*	1036.24
NIII	*	*	1036.33
*	1919.30	N IV	1117.93
*	1919.56	N IV	*
*	1919.78	*	1132.02
NIII	1947.04	*	1132.23
NIII	*	N IV	*
*	2083.35	*	1132.68
*	2084.59	*	1132.94
NIII	2107.56	*	1133.12
NIII	2121.52	N IV	1135.25
NIII	*	N IV	1188.01
*	2146.56	NIV	1486.50
*	2156.92	NIV+NIII	*
*	2147.31	*	1195.51
*	2147.85	*	1195.57
*	2147.99	*	1195.59
*	2148.09	*	1195.68
*	2148.51	*	1195.73
*	2148.99	NIV	2080.33
*	2149.02	NIV	2219.61
*	2149.45	NIV	2278.78
*	2150.06	NV	1238.82
NIII	2185.15	NIII+NV	*
NIII	2242.81	*	1242.80
NIII	2244.42	*	1242.85
NIII	2267.32	NV	1616.31
NIII	2269.32	NV	1619.70
NIII	*	OII	2020.33
*	2274.14	OII	*
*	2274.82	*	2027.10
NII+NIII	*	*	2027.60
*	2486.24	OII	*
*	2486.43	*	2411.60
		*	2411.65

Element+Ion. stage	wavelength [Å]	Element+Ion. stage	wavelength [Å]
OII+OIII	*	OIII	3059.28
*	2425.57	OIII	3121.64
*	2425.63	OIV	1106.93
*	2425.90	OIV	1164.55
*	2426.31	OIV	1338.61
*	2426.57	OIV	1343.5
OII+OIII	*	OIII+OIV	*
*	3024.36	*	3004.34
*	3024.54	*	3004.59
*	3024.81	OIV	3063.42
OII	3025.78	OIV	*
OII+OIII	*	*	3039.80
*	3035.20	*	3040.73
*	3035.41	OV	1371.29
OII	3113.62	Ne II	1133.92
OII	3139.68	Ne II	*
O III	*	*	1139.11
*	1007.88	*	1139.36
*	1008.10	Ne II	1143.89
*	1008.40	NeII	1854.04
O III	1033.15	NeII	1907.5
O III	1040.32	NeII	1930.04
O III	1138.54	NeII	1938.83
O III	*	NeII	1945.45
*	1150.88	NeII	3037.72
*	1150.99	NeII	3039.59
O III	*	NeII	1688.36
*	1153.02	NeII	1916.08
*	1153.21	NeII	*
O III	1153.77	*	2876.33
O III	1157.64	*	2876.47
OIII	1193.03	NeII	2955.73
OIII	1476.9	NeII	*
OIII	1590.05	*	3034.34
OIII	1767.78	*	3034.44
OIII	1771.67	*	3034.46
OIII	2496.55	NeII	*
OIII	2959.69	*	3062.48
OIII	*	*	3062.49
*	2983.68	NeII	3094.01
*	2983.78	Ne III	*
OIII	*	*	1044.94
*	3023.43	*	1044.96
*	3024.36	Ne III	*
OIII	3035.41	*	1076.71
OIII	3042.07	*	1076.79
OIII	3047.12	*	1077.02

Element+Ion. stage	wavelength [Å]	Element+Ion. stage	wavelength [Å]
NeIII	1810.13	AlIII	*
NeIII	1842.09	*	1935.84
NeIII	1849.72	*	1935.86
NeIII	*	*	1935.95
*	2159.44	ALiii	*
*	2159.60	*	2154.61
NeIII	*	*	2154.64
*	2163.52	Si III	997.39
*	2163.70	Si III	*
*	2163.77	*	1113.17
NeIII	*	*	1113.20
*	2412.73	*	1113.23
*	2412.94	Si III	1140.50
*	2413.18	Si III	1144.31
*	2413.54	Si III	1161.58
*	2413.78	SiIII	*
NeIII	2803.67	*	1192.23
NeIII	*	*	1193.26
*	2822.94	SiIII	1301.15
*	2823.14	SiIII	1361.59
NeIII	2825.28	SiIII	1506.07
NeIII	3077.34	SiIII	1160.25
NeIII	2161.04	SiIII	*
NeIII	2678.64	*	2075.03
MgII	1734.85	*	2075.04
MgII	*	*	2075.05
*	2790.54	*	2075.08
*	2790.78	*	2075.09
MgII	2795.33	SiIII	2559.22
MgII	2802.71	SiIII	*
MgII	2936.51	*	3040.93
MgIII	1748.92	*	3040.94
MgIII	1879.49	*	3041.02
MgIII	2039.55	SiIII	3093.42
MgIII	2064.90	Si IV	996.87
AlIII	1071.74	Si IV	*
AlIII	*	*	1154.62
*	1162.59	*	1154.62
*	1162.62	SiIV	1727.38
AlIII	1384.13	SiIV	1797.5
AlIII	*	SiIV	2120.17
*	1611.81	SiIV	*
*	1611.87	*	2287.05
AlIII	1854.72	*	2287.06

Element+Ion. stage	wavelength [Å]	Element+Ion. stage	wavelength [Å]
SiIV	*	SiV	*
*	2675.11	*	1227.35
*	2675.12	*	1227.53
*	2675.25	SiV	1624.01
SiIV	*	SiV	1944.18
*	2723.80	SiV	1964.54
*	2723.81	SiV	3096.48
SiIV	2895.13	S V	1122.04
SiIV	2904.5	S VI	933.38
P IV	*	S VI	944.53
*	1030.51	FeIII	1141.27
*	1030.52	FeIII	1142.96
P IV	1033.10	FeIV	1156.53
P IV	1064.61	FeIV+FeIII	*
P IV	1118.55	*	1270.69
P IV	1187.57	*	1270.76
PV	997.60	FeIV	1281.56
PV	1117.98	FeIV	1299.32
PV	1128.01	FeIII+FeIV	*
SIII	911.77	*	1300.02
SIII	1194.04	*	1300.34
SiV	1062.70	FeIV	1320.81
SiV	1072.97	FeIV+2FeV	1351.6
SiV	1073.52	*	1351.52
SiV	1098.36	*	1351.55
SiV	1098.92	*	1351.76
SiV	1111.04	FeIV	1357.24
SiV	1117.16	FeIV+FeV	*
SiV	*	*	1361.42
*	1138.07	*	1361.45
*	1138.21		

Element+Ion. stage	wavelength [Å]	Element+Ion. stage	wavelength [Å]
FeIII+FeV	*	FeV	*
*	1408.90	*	1116.05
*	1409.02	*	1116.16
*	1409.03	FeIV+FeV	*
*	1409.06	*	1124.83
*	1409.23	*	1124.89
*	1409.28	FeV	1118.38
*	1409.46	FeV	1133.57
*	1409.55	FeV	1149.12
FeIV	1425.48	FeV	1153.80
FeIV	1458.76	FeV	1161.92
FeIV	1483.58	FeV	1165.71
FeIV	1499.79	FeV	*
FeIV	1503.25	*	1227.63
FeIV	1503.25	*	1227.66
FeIV	*	*	1227.79
*	1508.85	FeIV+FeV	*
*	1508.86	*	1281.36
FeIII+FeIV	*	*	1281.37
*	1676.75	FeV	*
*	1676.79	*	1287.05
FeIV+FeIII	*	*	1287.10
*	1681.36	*	1287.17
*	1681.49	FeV	*
*	1681.50	*	1293.30
*	1681.58	*	1293.35
*	1681.72	*	1293.38
*	1681.88	FeV	1311.82
*	1681.90	FeV	*
*	1681.95	*	1321.49
*	1682.08	*	1321.85
*	1682.44	FeV	*
*	1682.49	*	1370.30
*	1682.65	*	1370.94
FeIV	1685.82	FeV	1385.69
FeV	*	*	1385.68
*	1101.07	*	1385.69
*	1101.21	FeV	1416.22
FeIV+FeV	*	FeV	1422.5
*	1111.89	FeV	*
*	1112.17	*	1456.16
*	1112.21	*	1456.29

Element+Ion. stage	wavelength [Å]
FeV	*
*	1479.39
*	1479.48
Niiv+NiV	*
*	1152.67
*	1152.68
Niiv+NiV	*
*	1158.86
*	1158.98
*	1158.02
*	1159.04
*	1159.09
Niiv+NiV	*
*	1187.84
*	1187.67
*	1187.79
Niiv	1191.66
Niiv+NiV	*
*	1195.85
*	1196.02
Niiv+NiV	*
*	1201.30
*	1201.21
*	1201.56
*	1201.58
*	1201.64
*	1201.76
Niiv+NiV	*
*	1251.90
*	1252.08
*	1252.13
*	1252.18
*	1252.25
Niiv+NiV	*
*	1253.19
*	1253.19
*	1253.20
*	1253.22
*	1253.29
Niiv+NiV	*
*	1254.00
*	1254.03
*	1254.04
*	1254.14
*	1254.42

Element+Ion. stage	wavelength [Å]
Niiv+NiV	*
*	1342.14
*	1342.15
*	1342.17
*	1342.20
Niiv	1408.71
Niiv	1411.45
Niiv	1414.60
Niiv	*
*	1418.69
*	1418.73
Niiv	*
*	1419.45
*	1419.57
*	1419.58
*	1419.73
Niiv	*
*	1430.19
*	1430.38
Niiv	1435.24
Niiv	*
*	1437.94
*	1437.98
*	1287.17
Niiv+NiV	*
*	1342.14
*	1342.15
*	1342.17
*	1342.20
Niiv	1408.71
Niiv	1411.45
Niiv	1414.6
Niiv	*
*	1418.69
*	1418.73
Niiv	*
*	1419.45
*	1419.57
*	1419.58
*	1419.73
Niiv	*
*	1430.19
*	1430.38
Niiv	1435.24

Element+Ion. stage	wavelength [Å]	Element+Ion. stage	wavelength [Å]
NiIV	*	NiV	1195.19
*	1174.19	NiV	1227.49
*	1174.20	NiV	*
NiV	*	*	1229.39
*	1178.80	*	1229.57
*	1178.81	NiV	*
*	1178.82	*	1232.52
*	1178.92	*	1232.54
*	1178.94	NiV	*
*	1179.16	*	1237.12
NiV	*	*	1237.20
*	1182.54	*	1237.25
*	1182.62	*	1237.29
*	1182.71	*	1237.34
NiV	*	*	1237.63
*	1190.28	NiV	*
*	1190.32	*	1244.03
NiV	*	*	1244.05
*	1193.88	*	1244.15
*	1193.99	*	1244.17
*	1194.10	*	1244.24
*	1194.22	NiV	1252.76
*	1194.25	NiV	1279.72
*	1194.28	NiV	1300.98
*	1194.49	NiV	1317.45

Erklärung

Hiermit bestätige ich, dass ich diese Arbeit selbstständig und nur unter Verwendung der angegebenen Hilfsmittel angefertigt habe.

Bamberg, den 23.02.2018

Markus Schindewolf